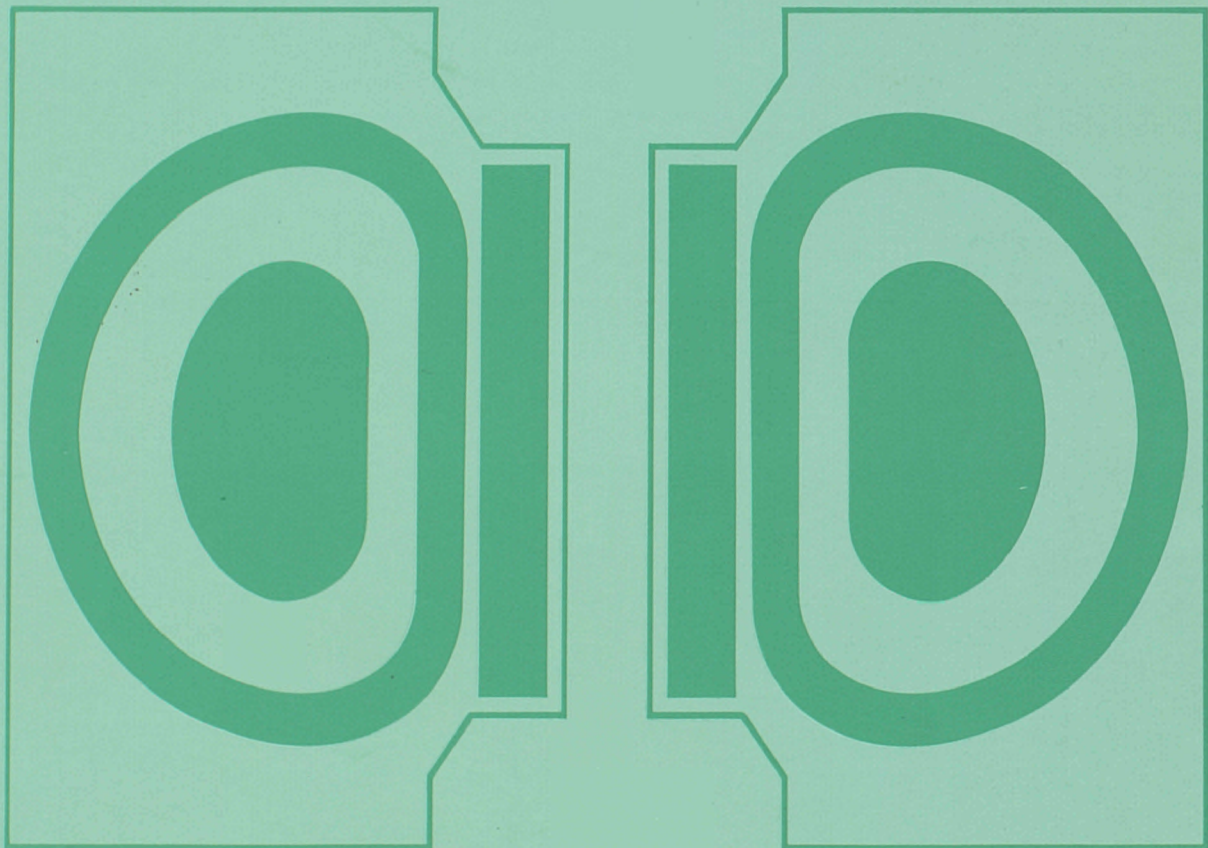


11/7/95

**JET  
JOINT  
UNDERTAKING**

**PROGRESS  
REPORT  
1994**





**EUR 16474-EN-C**

**EUR-JET-PR12**

**JET  
JOINT  
UNDERTAKING**

**PROGRESS  
REPORT  
1994**

**APRIL 1995**

*This document is intended for information only  
and should not be used as a technical reference.*

EUR16474 EN (EUR-JET-PR12) April 1995.  
Editorial work on this report was carried out by B.E.Keen.  
The preparation for publication was undertaken by  
JET Publications Group, JET Joint Undertaking, Abingdon, UK.

**© Copyright ECSC/EEC/EURATOM, Luxembourg 1995**

Enquiries about copyright and reproduction should be addressed to:

The Publications Officer, JET Joint Undertaking, Abingdon, Oxon. OX14 3EA, UK.

**Legal Notice**

Neither the commission of the European Communities nor any person acting on behalf of the Commission is responsible for the the use which might be made of the following information.  
Catalogue number : CD-NB-16474-EN-C for the Report EUR 16474-EN-C

*Printed in England*

# Contents

<b>Introduction, Background and Summary</b>	<b>1</b>
<b>Technical Achievements during 1994</b>	<b>11</b>
- Torus Systems	11
- Power Supplies and Magnet Systems	15
- Neutral Beam Heating Systems	31
- RF Heating Systems	42
- Operations Systems	57
- Remote Handling Systems	61
- Waste and Beryllium Handling	65
- Vacuum Systems	67
- Control and Data Acquisition System (CODAS)	69
- Data Management	74
- Diagnostic Systems	76
- Summary of Machine Operations	100
- Summary of Technical Achievements	103
<b>Scientific Achievements during 1994</b>	<b>107</b>
- High Performance	108
- Divertor Assessment and Divertor Physics	115
- Tokamak Concept Improvements	141
- Transport and Fluctuations	154
- MHD and Beta Limits	164
- Physics Issues relating to Next Step Devices	166
- Data Analysis and Modelling	168
- Summary of Scientific Progress and Perspective	183
<b>Developments and Future Plans</b>	<b>187</b>
- Pellet Injection	189
- Advanced Divertor Development	192
- Tritium Handling	193
- Technical Preparation for D-T Experiments	197
- Future Plans	202
<b>Appendices</b>	<b>205</b>
I JET Task Agreements 1994	205
II List of Articles, Reports and Conference Papers published in 1994	208



# Foreword

This is the twelfth JET Progress Report, which provides an overview summary and puts into context scientific and technical advances made on JET during 1994. This Report presents a more detailed account of JET's progress than that contained in the JET Annual Report. It is aimed not only at specialists and experts engaged in nuclear fusion and plasma physics, but also at a more general scientific community. To meet these aims, the Report contains a brief summary of the background of the Project, and describes the basic objectives of JET and the principal design aspects of the machine. In addition, the Project Team structure is included, as it is within this structure that activities and responsibilities for machine operation are carried out and the scientific programme is executed.

JET entered 1994 nearing the end of the longest and most extensive modification since the initial assembly of the device. Two faulty toroidal magnetic field coils had been replaced and the new pumped divertor configuration (Mark I) had been installed. The interior of the torus had been completely rebuilt to include four new divertor coils, an inertially-cooled divertor target structure and a cryogenic vacuum pump. The heating and current drive systems had been modified and included an upgraded neutral beam system to inject 7.8MW of power at 140keV and 13.6MW at 80keV, new Ion Cyclotron Resonance Frequency heating antennae (designed to couple 20MW) and

a new Lower Hybrid launcher (designed to couple 10MW). Other new installations included a system for plasma current and shape control, a Fast Radial Field Amplifier for vertical position control, eight Saddle Coils inside the vacuum vessel for disruption control and the study of Toroidal Alfvén Eigenmodes and an extensive array of new diagnostics, especially for divertor measurements.

The shutdown was successfully completed with pumpdown of the torus in January 1994. The first plasma in the new pumped divertor configuration was produced in February and by mid-March successful 2MA diverted plasmas had been established.

The general objectives of the experimental programme with the Mark I divertor were to assess the performance of the pumped divertor configuration, using the horizontal target tiles and, within their limitations, the vertical side tiles. The relatively open geometry of the Mark I divertor accepts a wide range of plasma equilibria, and divertor physics studies, high performance operation and advanced tokamak concept studies are possible for this configuration within the designed maximum plasma current capability of 6MA.

1994 has seen significant progress in optimising peak fusion performance and extending operation to the reactor relevant steady-state ELMy H-mode, which has now been obtained under a variety of conditions: plasma currents up

to 4MA, power levels up to 26MW, in the high  $\beta_p$  regime, in discharges with negative central magnetic shear, and at high  $\beta_N$ . The high  $\beta_p$  regime has also been extended to steady-state and to the reactor relevant domain.

The high power handling capability of the Mark I divertor target has been demonstrated and the severe impurity influxes (carbon “blooms”), which previously terminated high performance plasmas, have been eliminated. The cryopump reduces recycling, eliminates the effects of wall saturation (observed in previous long pulse operation), allows effective particle control, and generally allows higher plasma performance.

The best steady-state results (achieved in ELMy H-modes at 4MA/3.4T with more than 18MW of additional heating) show a stored energy of  $\approx 8$  MJ and a fusion triple product ( $n_D T_i \tau_E$ ) of  $2.6 \times 10^{20} \text{m}^{-3} \text{keVs}$  being maintained for more than four energy confinement times. The best transient results (achieved at the end of the ELM-free phase of hot-ion H-modes) were comparable to the best of past campaigns even though plasmas are now  $\approx 15\%$  smaller in volume. The highest stored energy was 11.3MJ and the fusion triple product ( $n_D T_i \tau_E$  greater than  $8 \times 10^{20} \text{m}^{-3} \text{keVs}$ ) and neutron rate ( $4 \times 10^{16} \text{s}^{-1}$ ) were within 10% of the best obtained with deuterium in 1991/92.

The two neutral beam injectors have routinely injected up to 19MW and 140MJ has been injected during a 20s ELMy H-mode. 13MW of ICRF power has also been coupled, but this is limited by a combination of unsatisfactory control electronics, unequal coupling of the straps of the antennae array and low power transfer to the plasma under some phase conditions. New control electronics systems are currently being installed and will be tested with plasmas in February 1995. Further antenna modifications are scheduled for the beryllium tile exchange shutdown and the Mark II divertor shutdown planned to start in March and June 1995, respectively. Combined NB and ICRF powers of 26MW have been injected and 3MA has been driven non-inductively with 6MW of LH power.

The saddle coils have been used for initial experiments on TAEs and the disruption feedback stabilisation system is in the final stages of commissioning. Only the lower saddle coils are now available, since the upper saddle coils were disabled in September 1994 after being damaged.

The 1994/95 campaign (scheduled to end in June 1995) has still to address: high power combined heating; further exploration of the detached divertor regime and its compatibility with ELMy H-mode operation; helium pumping and transport using argon frost on the cryopump; work on current profile control; toroidal magnetic field ripple studies; use of the saddle coils for disruption feedback control; and extension of X-point operation towards 6MA. In March 1995, the CFC divertor target tiles will be exchanged for beryllium target tiles and a comparison will then be made between CFC and beryllium tiles for a few specific plasma configurations. One RF antenna, modified to incorporate a bumper limiter, will also be tested.

The next major milestone will be to demonstrate compatibility between the high confinement reactor-relevant ELMy H-mode regime and detached divertor operation. However, this may require the more closed Mark II divertor structure. This will be installed in 1995 and tested in 1996 with particular emphasis on the effect of geometry on gas target/radiative divertor plasmas, which form the physics basis for the divertor concept favoured by the ITER Joint Central Team.

During the second half of 1996, a limited period of D-T operation (DTE-1, producing up to  $2 \times 10^{20}$  neutrons) will demonstrate long pulse fusion power production (fusion amplification factor,  $Q > 1$  with more than 10 MW of fusion power for a few energy replacement times) and will make important contributions to D-T physics (including H-mode threshold, ELM and confinement behaviour, and some D-T specific radio frequency heating studies) which JET alone can provide in an ITER-relevant divertor configuration. DTE-1 would allow the original

four areas of JET work to be completed and would provide timely input to the ITER EDA. It would also address the important technology issues of reactor relevant tritium processing and remote handling. In particular, it would demonstrate the ability of the Active Gas Handling System to process tritium while supporting a reacting tokamak plasma.

A proposal for the extension of the JET Programme to the end of 1999, which is supported by the JET Council, is currently being sent to the Council of Ministers for approval. It would include divertor studies aimed at providing data in support of the ITER divertor, while satisfying the requirements of high performance D-T operations. The remote handling exchange of the Mark II divertor target structure after DTE-1 would demonstrate, for the first time, one of the central technologies required for ITER and for a fusion reactor. The 1997/98 operations

period would validate high power, high performance physics in a divertor configuration specifically for ITER. The subsequent programme would then progress to divertor/plasma optimisation studies before a more extensive period of D-T operation (DTE-2) in 1999. In DTE-2, D-T plasmas would be studied with substantial alpha-particle heating, capitalising on the performance improvements achieved in the preceding experimental campaigns. DTE-2 experiments could produce up to  $5 \times 10^{21}$  neutrons, but every effort would be made to reduce the activation produced while still satisfying JET's role in supporting ITER and the World Fusion Programme.

JET has made impressive advances in recent years, and I am confident that, with the continued dedication of its staff, the Project will meet the challenges ahead and will continue to provide crucial information for a Next Step tokamak and a reactor.

Dr M Keilhacker  
Director  
April 1995



# Introduction, Background and Summary

## Introduction

JET Progress Reports are aimed both at specialists in plasma physics and nuclear fusion research and at the more general scientific community. This contrasts with the JET Annual Reports, which provide overview descriptions of the scientific, technical and administrative status of the JET programme, and is directed at the average member of the public.

To meet these general aims, the Progress Report contains a brief summary of the background to the Project, describes the basic objectives of JET and sets out the principal design aspects of the machine. In addition, the Project Team structure is detailed, since it is within this framework that machine activities and responsibilities are organized and the scientific programme is executed.

The main part of the 1994 Report provides overview summaries of scientific and technical advances made during the year, supplemented by detailed cross-references to the more important JET scientific and technical articles produced during the year. The final part of the Report briefly sets out developments underway to further improve JET's performance and plans for future experiments through to its foreseen completion.

## Background

### Objectives of JET

The Joint European Torus (JET) is the largest single project of the nuclear fusion research programme of the European Atomic Energy Community (EURATOM). The project was designed with the essential objectives of obtaining and studying plasma in conditions and with dimensions approaching those needed in a fusion reactor. These studies are aimed at defining the parameters, the size and working conditions of a tokamak reactor. The

realisation of this objective involves four main areas of work:

- (i) the scaling of plasma behaviour as parameters approach the reactor range;
- (ii) the plasma-wall interaction in these conditions;
- (iii) the study of plasma heating; and
- (iv) the study of alpha-particle production, confinement and consequent plasma heating.

Two of the key technological issues in the subsequent development of a fusion reactor are faced for the first time in JET. These are the use of tritium and the application of remote maintenance and repair techniques. The physics basis of the post-JET programme will be greatly strengthened if other fusion experiments currently in progress are successful. The way should then be clear to concentrate on the engineering and technical problems involved in progressing from an advanced experimental device like JET to a prototype power reactor.

### Basic JET Design

To meet these overall aims, the basic JET apparatus was designed as a large tokamak device with overall dimensions of about 15m in diameter and 12m in height. A diagram of the apparatus is shown in Fig.1 and its principal parameters are given in Table I. At the heart of the machine, there is a toroidal vacuum vessel of major radius 2.96m having a D-shaped cross-section 2.5m wide by 4.2m high. During operation of the machine, a small quantity of gas (hydrogen, deuterium or tritium) is introduced into the vacuum chamber and is heated by passing a large current through the gas. Originally, the machine was designed to carry 4.8MA, but has already been modified to achieve 7MA. This current is produced by transformer action using the massive eight-limbed

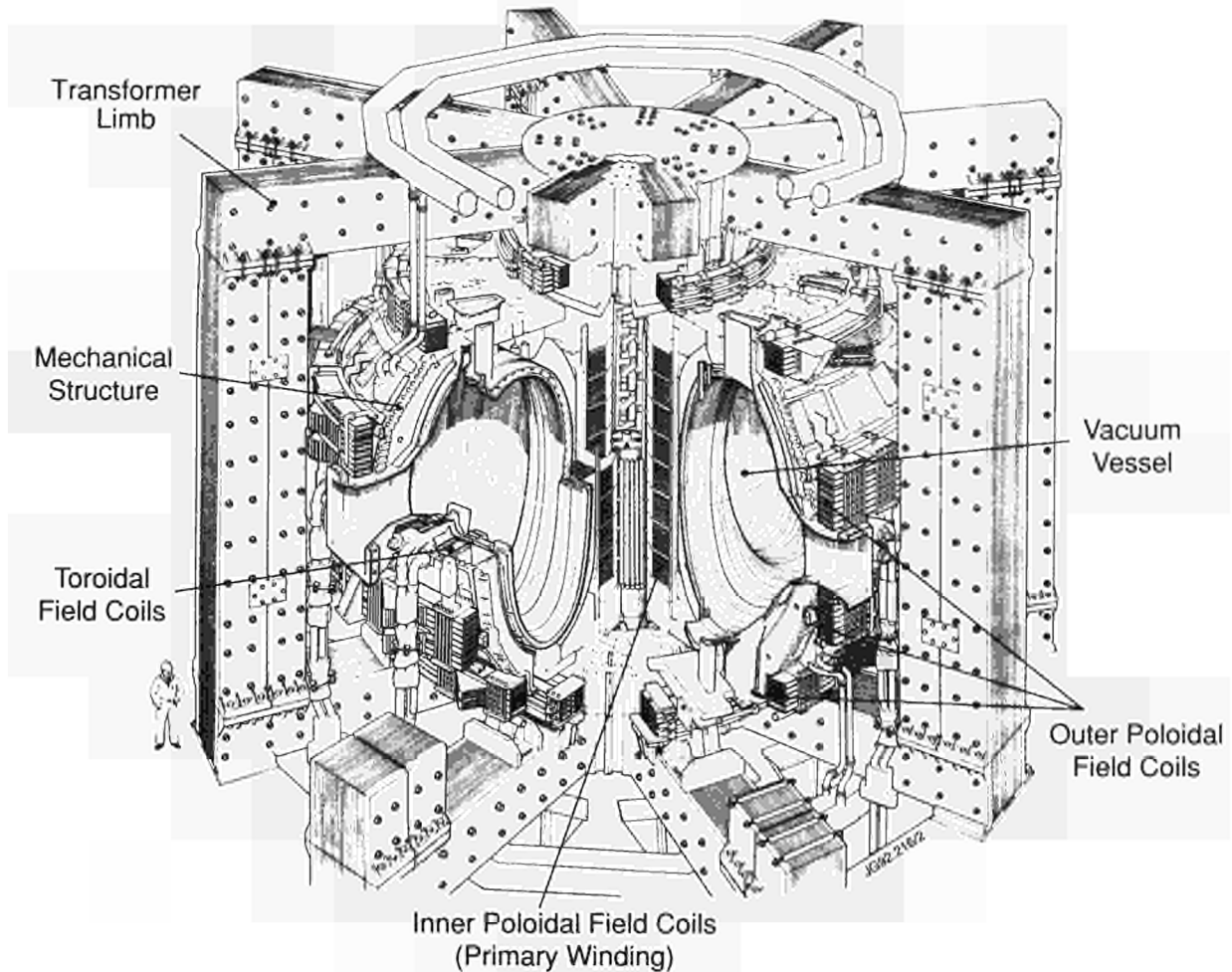


Fig.1: Diagram of the JET Tokamak.

Table I  
Principal Parameters

Parameter	Value
Plasma minor radius (horizontal), a	1.25m
Plasma minor radius (vertical), b	2.10m
Plasma major radius, $R_0$	2.96m
Plasma aspect ratio, $R_0/a$	2.37
Plasma elongation ratio, $\epsilon=b/a$	1.68
Flat top pulse length	60s
Toroidal magnetic field (plasma centre)	3.45T
Plasma current, D-shaped plasma	7.0MA
Volts-seconds available	54Vs
Toroidal field peak power	380MW
Poloidal field peak power	300MW
Additional heating power (into torus)	~50MW
Weight of vacuum vessel	108t
Weight of toroidal field coils	364t
Weight of iron core	2800t

magnetic circuit, which dominates the apparatus (see Fig.1). A set of coils around the centre limb of the magnetic circuit forms the primary winding of the transformer with the plasma acting as the single turn secondary. Additional heating of the plasma is provided by the propagation and absorption of high power radio frequency waves in the plasma and by the injection of beams of energetic neutral atoms into the torus.

The plasma is confined away from the walls of the vacuum vessel by a complex system of magnetic fields, in which the main component, the toroidal field, is provided by 32 D-shaped coils surrounding the vacuum vessel. This field, coupled with that produced by the current flowing through the plasma, forms the basic magnetic field for the tokamak confinement system, which provides a full design field at the plasma centre of 3.45T. The poloidal coils, positioned around the outside of the vacuum vessel, shape and position the plasma in operation.

Experiments have been carried out mainly using hydrogen or deuterium plasmas, although during 1991, experiments were performed in helium-3 and helium-4 and a preliminary experiment was performed using 10% tritium in deuterium. In the final stage of the programme, it is planned to operate with deuterium-tritium plasmas so that abundant fusion reactions occur. The alpha-particles liberated from the reactions should produce significant heating of the plasma. During this phase, the machine structure will become radioactive to the extent that any repairs and maintenance would have to be carried out using remote handling systems.

To reach conditions close to those relevant to a fusion reactor, plasma densities of  $\sim 10^{20} \text{m}^{-3}$  at temperatures of 10-20keV would be needed. Even with plasma currents up to 7MA in JET, this would be inadequate to provide the temperature required using ohmic heating alone. Consequently, additional heating is required and two main systems are being used at JET, as follows:

- Injection into the plasma of highly energetic neutral atoms (Neutral Injection Heating);

- Coupling of high power electromagnetic radiation to the plasma (Radio Frequency (RF) Heating).

In 1991, the lifetime of the Project was extended to the end of 1996 to allow JET to implement a new Pumped Divertor phase of operation. This would assist the aim of establishing in deuterium plasmas "reliable methods of plasma purity control under conditions relevant for the Next Step Tokamak". During 1992/93, an axisymmetric pumped divertor was installed inside the vacuum vessel, together with all necessary auxiliary equipment.

The new plasma shapes of the divertor configuration required a complete redesign of the vacuum vessel first wall to accommodate the relevant plasmas. Upon completion, the inside of the vessel had been almost completely rebuilt and JET was effectively a new machine.

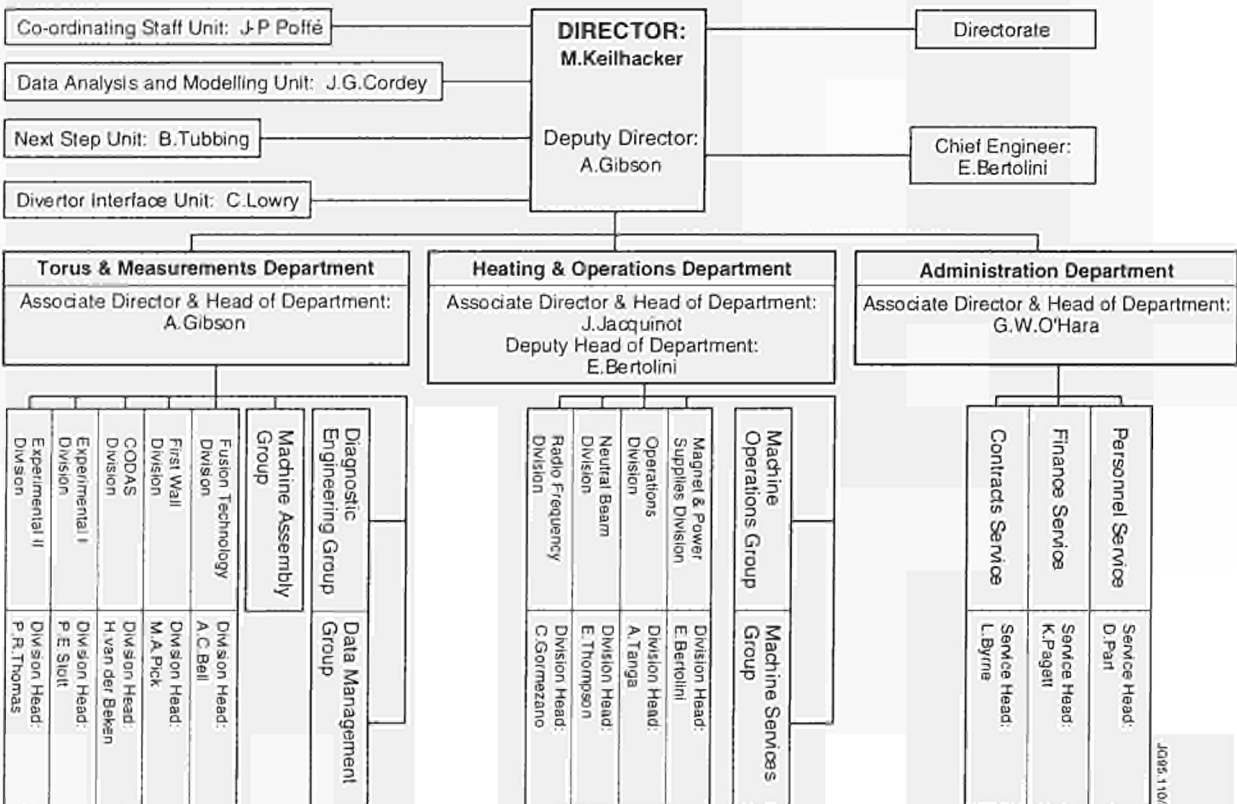
### Project Team Structure

The Project structure adopted, for management purposes, is divided into three Departments (see Table II):

- Torus and Measurements Department;
- Heating and Operations Department;
- Administration Department.

Table II

## JET Departmental and Divisional Structure



J095 1108

In addition, some scientific and technical duties are carried out within the Directorate and in Supporting Units.

The main duties of the Administration Department have been described in previous JET Annual Reports. This Report concentrates on progress made in the scientific and technical areas during 1994. To aid this description, the functions of these Departments are described below.

### **Torus and Measurements Department**

The Torus and Measurements Department has overall responsibility for the performance capacity of the machine: this includes enhancements directly related to this (excluding heating) and the long term planning associated with integration of these elements to achieve ultimate performance. The Department is also responsible for: fusion technology requirements for the active phase including tritium handling and processing; for construction and operation of necessary measurement diagnostic systems and the interpretation of experiment data; and for data systems comprising data control, acquisition and management. The main functions of the Department are:

- to design, procure and implement enhancements to the JET device;
- to provide and maintain clean conditions inside the vessel which lead to high quality plasma discharges;
- to conceive and define a set of coherent measurements;
- to be responsible for construction of necessary diagnostics;
- to be responsible for diagnostics operation, quality of measurements and definition of plasma parameters;
- to organise and implement data acquisition and computing;
- to design and develop remote handling methods and tools to cope with JET requirements;
- to design and construct facilities for handling tritium and for waste management.

The Department consists of five Divisions and three Groups (Machine Assembly, Diagnostic Engineering and Data Management):

(a) *First Wall Division*, which is responsible for the vital area of plasma wall interactions. Its main tasks include the provision and maintenance inside the vacuum vessel of conditions leading to high quality plasma discharges. The Division develops, designs, procures and installs the first wall systems and its components

such as limiters, wall protections and internal pumping devices. The area of responsibility encompasses the mechanical integrity of the vacuum vessel as a whole and the development and implementation of mechanical and Remote Handling techniques;

- (b) *Fusion Technology Division*, is responsible for all nuclear engineering aspects of this Project including tritium and gas handling, vacuum systems, waste management and regulatory approvals;
- (c) *Control and Data Acquisition System Division (CODAS)*, which is responsible for the implementation, upgrading and operation of computer-based control and data acquisition systems for JET;
- (d) *Experimental Division 1 (ED1)*, which is responsible for specification, procurement and operation of about half the JET diagnostic systems. ED1 undertakes electrical measurements, electron temperature measurements, surface and limiter physics and neutron diagnostics;
- (e) *Experimental Division 2 (ED2)*, which is responsible for specification, procurement and operation of the other half of the JET diagnostic systems. ED2 undertakes all spectroscopic diagnostics, bolometry, interferometry, the soft X-ray and neutral particle analysis.

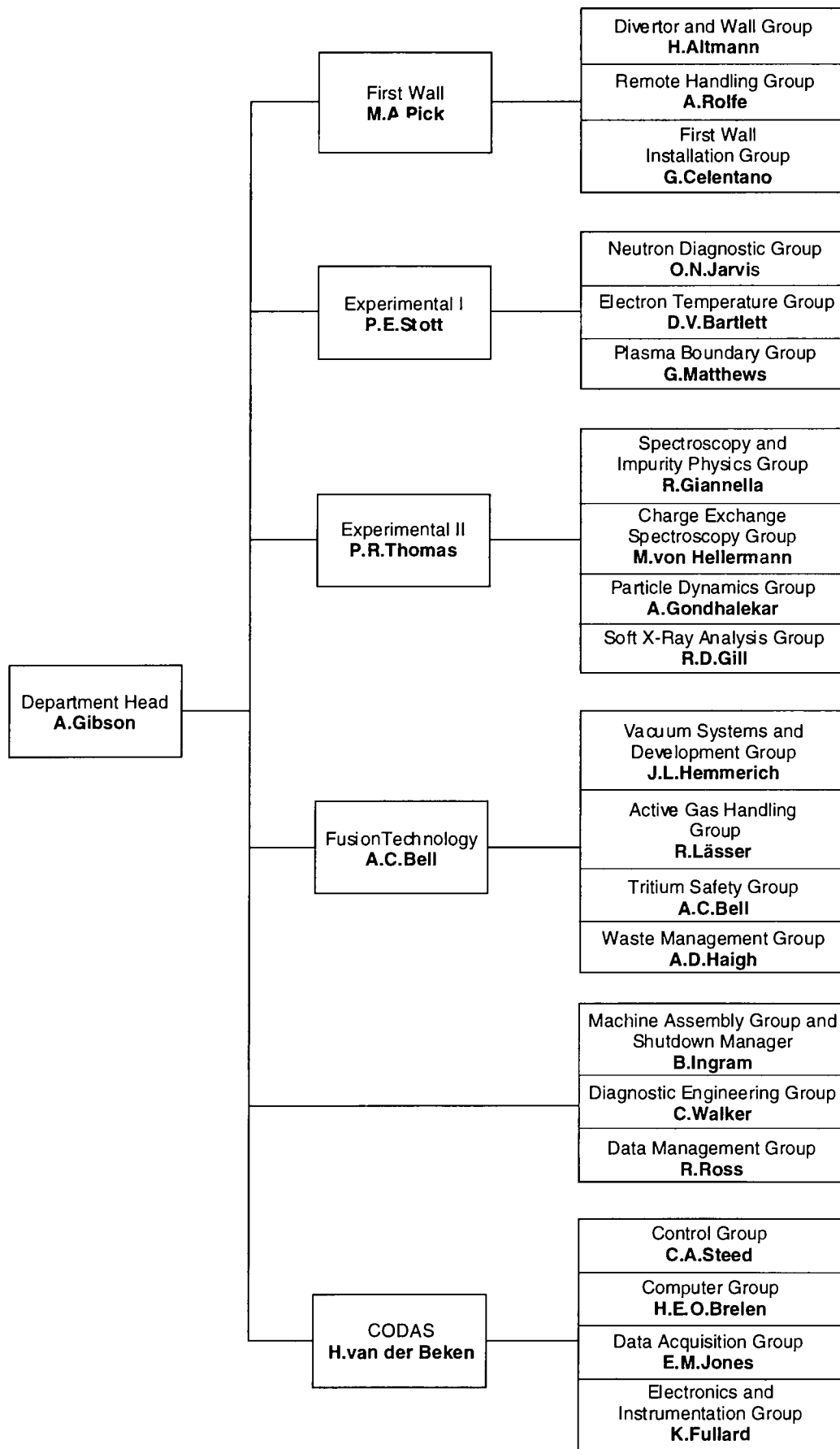
The structure of the Torus and Measurements Department to Group Leader level is shown in Fig. 2 and the list of staff within the Department is shown in Fig. 3.

### **Heating and Operations Department**

The overall responsibility of the Heating and Operations Department is for the efficient and effective day-to-day operation of the machine. In addition, the Department has responsibility for plasma heating and auxiliary equipment and related physics; the design and operation of power supplies as well as contributing to the execution and evaluation of JET's experimental programme. The main functions of the Department are:

- preparing and co-ordinating operation of the machine across Departments and Divisions;
- heating and current drive and analysis of its effects in the plasma;
- plasma fuelling, including pellet injection;
- designing and employing power supplies for ensuring efficient operation and control of the machine.

The Department consist of two Groups (Machine Operations and Machine Services) and four Divisions:



JG95.1102

Fig.2: Torus and Measurements Department, Group Structure (December 1994)

**TORUS AND MEASUREMENTS DEPARTMENT**

*Head of Department: A. Gibson*

C. Earl	Mrs. P. Longworth	R. T. Ross	R. Smith
C. Hancock	J. Lundquist	P. Sagar	A. Tiscornia
J. Hocking	J. Reid	Miss. D. Samuel	C. Walker
B. Ingram	Mrs. J. Roberts	P. Smeulders	C. Wilson

**FUSION TECHNOLOGY DIVISION**

*Head: A.C. Bell*

S. Bryan	J. L. Hemmerich	M. Laveyry	J. Orchard
H. Buttergeit	D. Holland	J. Lupo	R. Pearce
C. J. Caldwell-Nichols	H. Jensen	J. Mart	Mrs J. Pointer
C. Callaghan	Mrs. M. E. Jones	A. Miller	K. D. Walker
Mrs. J. Campbell	J. F. Jaeger	P. Milverton	R. Warren
N. Green	R. Lässer	G. Newbert	T. Winkel
A. Haigh			

**FIRST WALL DIVISION**

*Head: M.A. Pick*

H. Altmann	E. Deksnis	M.A.Irving	J. Palmer
G. Benali	C. Froger	L.P.D.F. Jones	A. Peacock
G. Brown	L. Galbiati	J.F. Junger	T. Raimondi
T.V. Businaro	F. Hurd	A.B. Loving	S. Scott
R.A. Cusack	Mrs. I. Hyde	B. Macklin	R.L. Shaw
G. Celentano	G. Israel	A. Nowak	T. Szabo
Mrs. D. Cranmer			

**CONTROL AND DATA ACQUISITION SYSTEMS DIVISION**

*Head: H. van der Beken*

M. B. Baronian	P. J. Card	E. M. Jones	C. A. Steed
Mrs. A. M. Bellido	J. J. Davis	F. J. Junique	C. Terella
H. E. O. Brelen	S. Dmitrenko	N. G. Kidd	G. Wolfers
W. J. Brewerton	S. E. Dorling	J. G. Krom	I. D. Young
T. Budd	K. Fullard	C. Perry	

**EXPERIMENTAL DIVISION I**

*Head: P. E. Stott*

S. Ali-Arshad	J. Fessey	M. Loughlin	P. Roberts
Miss. N. Avery	C. Gowers	F. B. Marcus	G. Sadler
D. Bartlett	Mrs. M. Harper	G. Matthews	B. Schunke
H. Bindslev	P. J. Harbour	G. Neill	A. Stevens
B. W. Brown	M. Hone	P. Nielsen	D. Summers
S. Clement	J. Hoekzema	H. Oosterbeek	P. van Belle
J. P. Coad	I. Hurdle	R. Prentice	J. Vince
J. Ehrenberg	O. N. Jarvis		

**EXPERIMENTAL DIVISION II**

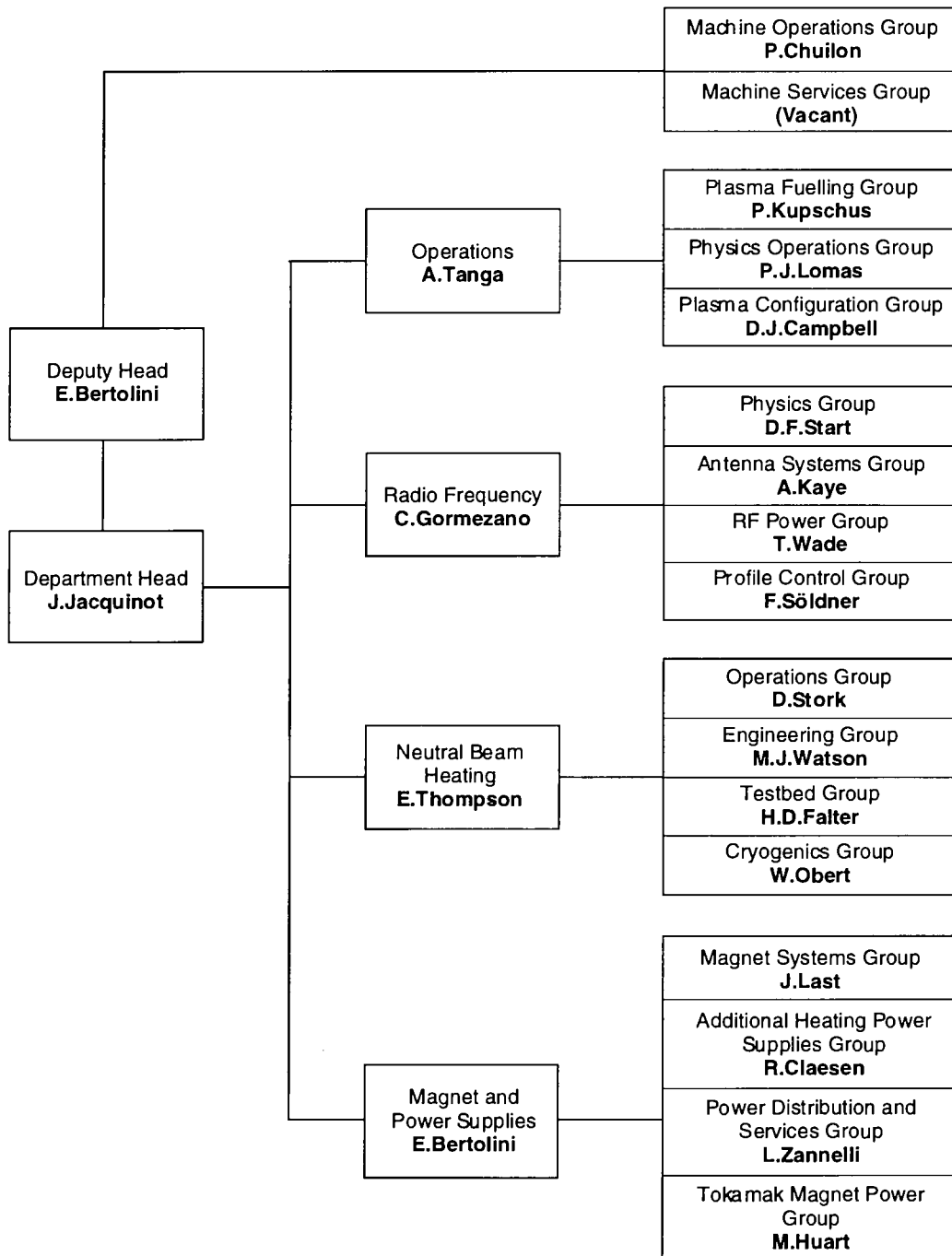
*Head: P. R. Thomas*

B. Alper	R. Giannella	R. König	M. Stamp
Mrs. K. Bell	R. Gill	P. Morgan	S. A. Staunton-Lambert
G. Braithwaite	A. Gondhalekar	C. Nicholson	W. Studholme
J. L. Bonnerue	L. D. Horton	R. Reichle	M. von Hellermann
P. Breger	A. Howman	J. Ryan	B. Viaccoz
A. Edwards	H. Jäckel		

*Fig.3: Project Team Staff in the Torus and Measurements Department  
(December 1994)*

(a) *Operations Division* plays a major role in the efficient planning and execution of JET's experimental programme and in the integration of existing or imminent systems into an effective experimental programme. In addition, it is responsible for effective methods of fuelling the plasma including the development of methods based on solid high speed hydrogen pellets; development of new plasma wall conditioning techniques; plasma control systems; development

of disruption control methods; training of operations staff; and monitoring of machine operations;  
 (b) *Neutral Beam Heating Division*, which is responsible for construction, installation, commissioning and operation of the neutral injection system, including development towards full power operation. The Division is also responsible for all cryo-systems and also participates in studies of physics of neutral beam heating;



JG95.110/4

Fig.4: Heating and Operations Department, Group Structure  
 (December 1994)

**HEATING AND OPERATIONS DEPARTMENT**

*Head of Department: J. Jacquinot*

*Deputy Head of Department: E. Bertolini*

K. Adams	T. Dale	R. Meadows	W. Smith
V. Bhatnagar	R. Greenfield	C. Rayner	K. Taylor
C. Birks	M. Hughes	B. Regan	J. Watt
M. Bolton	M. Macrae	Miss. V. Shaw	B Workman
P. Chuilon			

**MAGNET AND POWER SUPPLIES DIVISION**

*Head: E. Bertolini*

T. Bonicelli	C. Folco	V. Marchese	G. Sannazzaro
D. Chiron	J. Goff	G. Marcon	S. Shaw
R. Claesen	M. Huart	Mrs. H. Marriott	A. Tesini
E. Daly	F. Jensen	G. Murphy	S. Turley
N. Dolgetta	J. R. Last	P. Noll	J. van Veen
P. Doyle	H. McBryan	R. Ostrom	C. R. Wilson
H. T. Fielding	J. McKivett	P. Presle	L. Zannelli

**OPERATIONS DIVISION**

*Head: A. Tanga*

D. J. Campbell	J. How	T. Martin	A. Santagiustina
S. Cooper	M. Johnson	S. Puppin	Ms. R. Sartori
M. Gadeberg	P. Kupschus	L. Rossi	A. C. C. Sips
M. Garribba	P. J. Lomas	Miss. G. Saibene	M. Tabellini

**NEUTRAL BEAM HEATING DIVISION**

*Head: E. Thompson*

A. Bickley	D. Ewers	C. Mayaux	D. Raisbeck
A. Browne	H. Falter	Mrs. D. Noyes	D. Stork
C. D. Challis	Mrs. S. Humphreys	W. Obert	L. Svensson
J. F. Davies	T. T. C. Jones	S. Papastergiou	J. Waterhouse
A. Dines	F. Long	A. J. Parfitt	M. J. Watson
H. P. L. de Esch	D. Martin		

**RADIO FREQUENCY HEATING DIVISION**

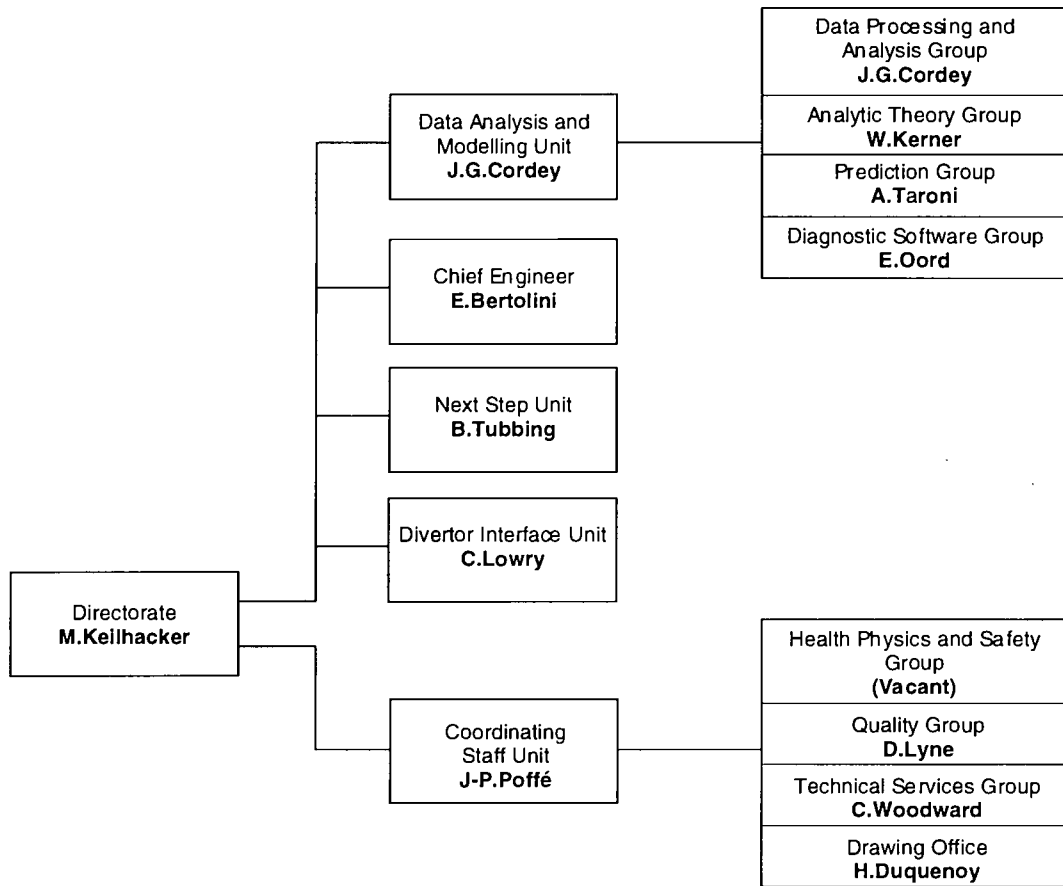
*Head: C. Gormezano*

S. C. Booth	T. Dobbing	G. Jessop	M. Schmid
M. Brandon	D. T. Edwards	A. Kaye	A. Sibley
M. Bures	A. Franklin	M. Lennholm	F. Söldner
Miss. M. Casson	P. Finberg	J. Plancoulaine	D. F. Start
G. Cottrell	M. Gammelin	F. Rimini	C. Steele
P. Crawley	R. Horn	P. Schild	T. Wade
Mrs. R. Deitrich			

*Fig.5: Project Team Staff in the Heating and Operations Department  
(December 1994)*

JG95.110/5

- (c) *Radio Frequency Heating Division*, which is responsible for the design, construction, commissioning and operating RF heating and current drive systems during the different stages of its development to full power. The Division is also responsible for the TAE excitation system and also participates in studies of the physics of RF heating;
- (d) *Magnet and Power Supplies Division* is responsible for the design, construction, installation, operation and maintenance of the electromagnetic system and plasma control. The area of responsibility encompasses the toroidal, poloidal and divertor magnets, mechanical structure; and all power supply equipment needed for magnets, plasma control, additional heating and auxiliaries.



JG95.110/6

Fig.6: Directorate and Support Units, Group Structure (December 1994)

The structure of the Heating and Operations Department to Group Leader level is shown in Fig. 4 and the list of staff in the Department is shown in Fig. 5.

In addition, both Departments are involved in:

- execution of the experimental programme;
- interpretation of results;
- making proposals for future experiments.

**Directorate**

Within the Directorate, are four technical units and a Chief Engineer, reporting directly to the Director. The main responsibilities are as follows:

(a) *The Co-ordinating Staff Unit* is responsible for the availability of a comprehensive health physics and safety project organisation; and for the provision of centralised engineering support services. It comprises four Groups:

- Health Physics and Safety Group;
- Quality Group;
- Technical Services Group;
- Drawing Office.

(b) *The Data Analysis and Modelling Unit* is responsible for the provision of software for the acquisition and processing of the data from JET diagnostics; for confirming the internal consistency of the processed data and assembling it into public databases; and the development and testing of theoretical models against JET data. In addition, the Unit is responsible for prediction by computer simulation of JET performance, interpretation of JET data and the application of analytic plasma theory to gain an understanding of JET physics.

It comprises three groups;

- Analytic Theory Group
- Simulation Group
- Data Processing and Analysis Group

(c) *The Next Step Unit* is responsible for co-ordinating contributions from JET to the European effort in support of the ITER-EDA. This responsibility includes drawing up proposals, initiating relevant work programmes on JET and taking part in their execution and evaluation.

**DIRECTORATE AND SUPPORT UNITS***Director: Dr M. Keilhacker*Mrs. C. Johnson  
C. Lowry  
J. McMahonT. O'Hanlon  
Ms. R. ThormahlenB. Tubbing  
G. VlasesD. Ward  
M. L. Watkins**COORDINATING STAFF UNIT***Head: J-P. Poffé*Ms. L. Ashby  
M. Axton  
P. Barker  
D. Campling  
N. DaviesH. Duquenoy  
A. Gibson  
J. A. Green  
H. D. Jones  
R. LitchfieldMiss. K. Luker  
M. Page  
H. Panissie  
B. Patel  
Mrs. J. ReidK. Sandland  
P. Schofield  
M. Scotcher  
C. Woodward**DATA ANALYSIS AND MODELLING UNIT***Head: J. G. Cordey*B. Balet  
K. Blackler  
J. Christiansen  
L. G. Eriksson  
J. JeralW. Kerner  
D. O'Brien  
E. Oord  
M. Ottaviani  
F. PorcelliR. Simonini  
K. Slavin  
E. Springmann  
Mrs. P. Stubberfield  
A. TaroniK. Thomsen  
J. Wesson  
D. Wilson  
W. Zwingmann**NEXT STEP UNIT***Head: B. Tubbing***DIVERTOR INTERFACE UNIT***Head: C. Lowry**Fig.7: Project Team Staff in Directorate and Support Units  
(December 1994)*

JG95.1107

(d) *The Divertor Interface Unit* is responsible for assessing the impact of developments in the experimental programme and operation on the design requirements for JET divertors. This includes a high level of participation in the JET experimental programme on divertor physics, the mechanical analysis of plasma induced loads on the divertor, and the definition of advanced divertor concepts.

In addition, there is a *Chief Engineer*, who reports to the Director, and is responsible for ensuring the overall coherence of technical aspects of JET operations.

The structure of the Directorate to Group Leader level is shown in Fig. 6 and the list of staff in these areas is shown in Fig. 7.

## Report Summary

The first section of this Report provides a brief introduction and background information relevant to the Report. The

second and third sections set out an overview of progress on JET during 1994 and with a survey of scientific and technical achievements during 1994 sets these advances in their general context. This summary is specifically cross-referenced to reports and articles prepared and presented by JET staff during 1994. The full list of articles is given in Appendix II, and copies can be obtained by application to JET Publications Office.

The fourth section is devoted to future plans and certain developments which might enable enhancements of the machine to further improve its overall performance. Some attention has been devoted to methods of surmounting certain limitations and these are detailed in this section.

The Appendices contain a list of work topics which have been carried out under Task Agreements with various Association Laboratories. In addition, a full list is included of all Articles, Reports and Conference papers published by JET authors in 1994.

# Technical Achievements during 1994

## Introduction

In late-January 1994, JET completed its planned major shutdown, that had lasted for almost two years. The main objective had been to install the components of the pumped divertor and undertake its associated system modifications. These included:

- lower divertor structure with Mark I CFC target plates (inertially cooled);
- four internal divertor coils and power supplies;
- pumping chamber and cryopump;
- poloidal limiters;
- new ICRF antennae (A2) and modified protections;
- full lower hybrid current drive (LHCD) system with modified launcher (L1), grill and protections;
- divertor diagnostics;
- disruption control system using internal saddle coils.

The first plasma was produced in mid-February and the experimental campaign started.

During 1994, three manned in-vessel interventions were carried out in full air-suits (since beryllium evaporation had been used). In late-March, following first experiences with the restart of operations, an inspection showed that no significant in-vessel damage had occurred. In September/October, damage to the upper saddle coils was stabilised and a further diagnostic system was installed. In early November, the beryllium evaporator heads were removed, strengthened and reinstalled.

Intensive design and procurement activities for the Mark II pumped divertor components to be installed in the 1995 shutdown have continued. The complexity of the new configuration has required close attention to the sequence in which components are installed and means that it is important for all components to be ready for installation in accordance with the shutdown schedule.

Significant effort continues to be devoted to preparation of a comprehensive suite of remote handling equipment, which will be used when activation of the vessel prevents man-access, especially during the final phase of full D-T operations. In addition, the active gas handling system, which will handle tritium during the active phase, has been essentially completed and is now being operated in an integrated way under conditions relevant to the actual tritium processing cycle.

The following sections detail the main technical achievements made during 1994.

## Torus Systems

The main activities throughout 1994 were:

- design and procurement of components for the Mark II divertor support structure;
- the Mark IIA divertor tile carriers;
- the preparation and planning for the major Mark II installation shutdown in 1995;
- the initial conceptual design studies for the Mark II Gas-Box divertor tile carriers;
- the design and testing of Remote Handling equipment for the time when manned access to the vessel will not be possible;
- maintenance work inside the vessel during a year of plasma operations on the Mark I divertor.

The Mark I shutdown, the longest and most difficult since the initial assembly of the JET machine, began at the end of February 1992 and ended in January 1994. All the critical stages of the starting up operation (i.e. the pumping down of the vessel, the baking of the vessel, the locking of the vessel with the refurbished MVP vertical

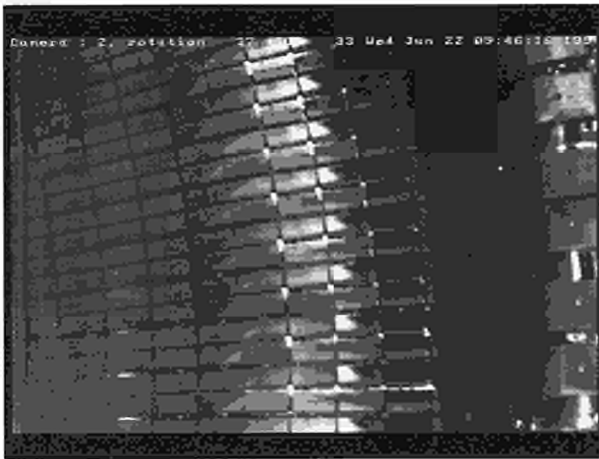


Fig.8: Divertor CFC tiles seen by In-Vessel Inspection System

restraints, the first introduction of water into the cooling system of the divertor modules, the first introduction of liquid nitrogen and liquid helium into the divertor pumps, etc.) were successfully completed in a short time.

Plasma operation on the Mark I divertor during 1994 showed an absence of the so-called "carbon blooms". This indicated that the divertor target plates performed as expected and that the carbon fibre reinforced graphite tiles, attached to the water cooled stainless steel beams of the divertor structure, had been installed and aligned within the very precise limits set.

### Vessel Maintenance during Operations Interventions

Two short in-vessel interventions were carried out in 1994 as well as a further intervention planned for the routine maintenance of the beryllium evaporators; as follows:

- The first in-vessel intervention was in March 1994. Showers of sparks had been observed in the vacuum vessel by a CCD camera. A thorough examination of the in-vessel components did not reveal the cause of the sparks. This was later found to be associated with the conditioning of the vessel and the behaviour of the Fast Radial Field Amplifiers. All the in-vessel components were in good condition except for some earth straps which were deformed due to unexpected changes in the direction of the halo currents.
- The second intervention, initially scheduled to carry out maintenance of beryllium evaporators, took place in September 1994. An in-vessel inspection (IVIS) carried out just before starting the shutdown, showed damage to the upper inner saddle coil conductors caused by large unexpected currents flowing in the

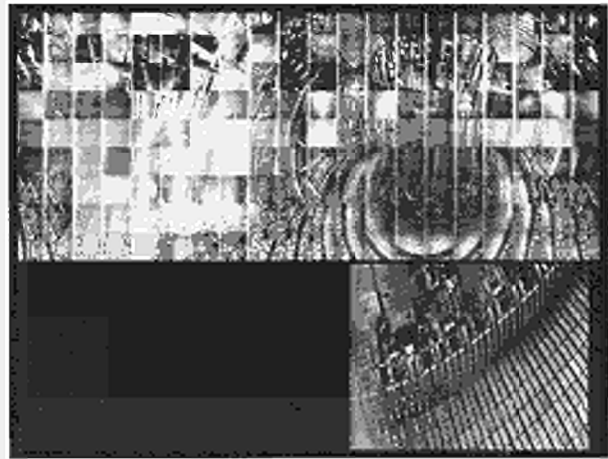


Fig.9: Picture mosaic of inside of JET vessel

coils. A more careful inspection carried out later inside the vessel, gave a clear picture of the damage. This required that some refurbishment work to the damaged upper saddle coils had to be added to that planned on the evaporators.

This work involved the renewal of all inner and outer flexible laminated saddle coil power links. Electrical isolation tests were carried out in-vessel to determine the degradation of the coil insulation due to metalisation of the alumina balls. Most elements were found to be adequately isolated but with wide variations in resistance at breakdown. One short section of outer coil element at Octant No.3 was found to have relatively low resistance and was removed with the adjacent elements and clamps refitted to carry protection tiles. The upper crossover bars were grounded to the vessel by welding an earthing plate at the inner ends. The inner elements of each coil were linked and grounded at the mid point using a special earth strap. The outer coil element assemblies were broken down into shorter lengths by unbolting links and then grounding at the mid-point. The measures taken left the lower saddle coils operational.

A third in-vessel intervention took place at the beginning of November 1994. This was due to a sheared CFC support tube of a beryllium evaporator head which had subsequently fallen into the divertor. Two heads with a similar potential problems were replaced.

### New In-Vessel Inspection System (IVIS)

The new In-Vessel Inspection System (IVIS), installed during the 1992/93 shutdown, has been in operation since January 1994. It consists of four newly designed viewing probes and additional lighting units and its upgraded enhancement. As a result, clearer pictures and a wider

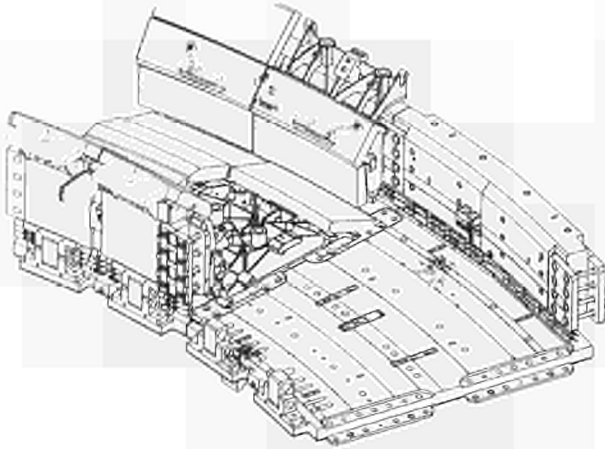


Fig.10: Mark II divertor support structure

range of view, including the direct view of the divertor (Fig.8) have been obtained. Consequently, the system has become an increasingly important instrument in machine operation, allowing early detection of any damage occurring during plasma operations and for calibrating several in-vessel diagnostics. IVIS campaigns, during which the entire vessel is scanned, are presently carried out on a weekly basis. Results are available in the form of picture mosaics (Fig.9), from which individual pictures can be easily chosen and enlarged for display on the monitor of any workstation connected to the internal network.

### The Mark II Divertor Design and Procurement

The new Mark II Divertor for JET has been designed to investigate the effects of divertor geometry on plasma performance. Actively cooled divertor target systems are difficult to exchange easily, quickly and, in particular, using remote handling tools. The Mark II design relies on the thermal inertia of the target tiles to maintain acceptable target surface temperatures. The Mark II divertor, shown in Fig.10, consists of a toroidally continuous U-shaped structure which is internally stable and a set of three rings of tile carriers bolted onto the bottom and sides of the structure. The structure itself consists of 24 individual water-cooled modules bolted together into a continuous ring in the vessel and attached to the vessel via the 36 main clamps of the two central divertor coils. It provides a flat and rigid base and cylindrical inner and outer sides for the attachment of the tile carriers. The rigid U-shaped structure is the basis for the precise alignment of the tiles. The tile carriers can vary depending upon the chosen divertor shape. The divertor thus exhibits the

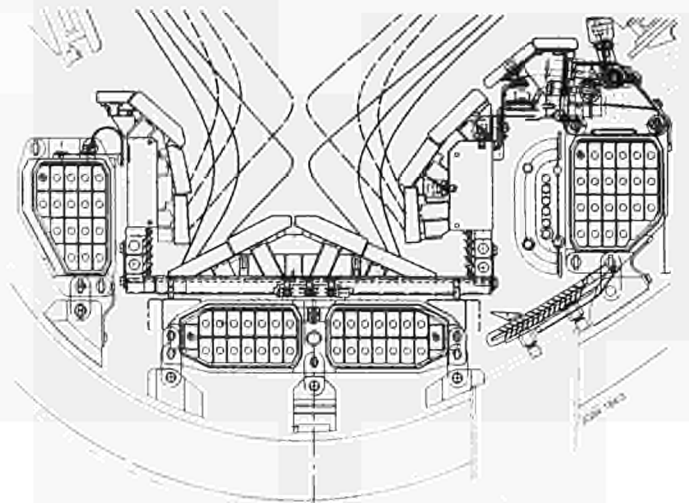


Fig.11: Mark IIA tile carriers showing two examples of plasma configurations expected to be run

required flexibility by permitting an easy and rapid change of the divertor geometry by the exchange of the tile carriers. The tile carriers are fully equipped with tiles and any associated diagnostic systems prior to being installed in the vessel. Access to the fixing bolts of the carrier to the support structure is through gaps between the tiles. The exchange of tile carriers can be performed by the remote handling tools presently being developed.

The Mark IIA tile carriers to be initially installed (Fig.11) allow the investigation of a large variety of plasma configurations, including high power discharges and discharges with the separatrix impinging on either the side or the lower target tiles. To allow for the highest power handling capability, the total area wetted by the plasma has been increased as far as practicably possible, in both toroidal and poloidal direction. This has been achieved by a number of design features.

The toroidal wetted length is optimised by using target tiles which are long in the toroidal direction, Fig.12, mounted in a way which guarantees a minimum tile-to-tile misalignment. The diagram shows how each tile is attached to the tile carrier by a single spring loaded central bolt attached to a dumb-bell shaped rod inserted in a hole drilled into the tile, and supported on four corner pads. Each tile carrier is fitted with its own tiles but adjacent tiles always share the corner support pads so that the tile-to-tile step accuracy is not dependent on the exact alignment of adjacent tile supports, but only upon the tolerance of the tile thicknesses. Large tiles produce fewer toroidal gaps between tiles. A definite tile-to-tile step must be incorporated into the design at each gap, so as to shield the edge of the adjacent tile from direct power loading. The size of this step is determined by the largest perpendicular

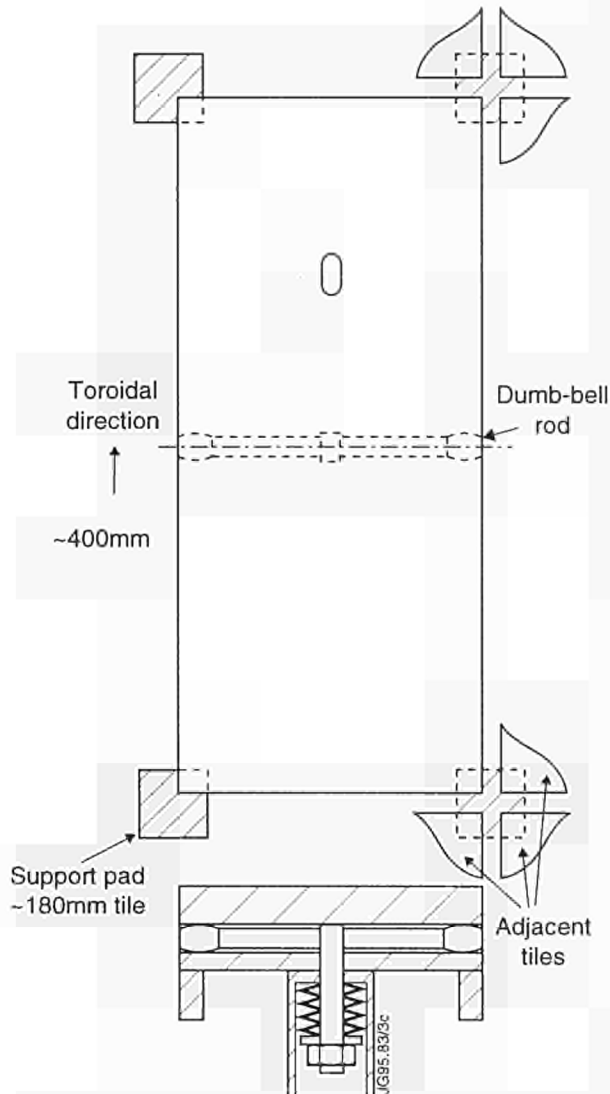


Fig.12: Tile and tile mounting for the Mark IIA tile carriers showing how each tile shares its four support pads with the adjacent tiles

angle between the field lines and the tile surfaces (as determined for all envisaged plasma configurations), the largest width of the gap between the tiles (as given by the required width plus the tolerances of the tile carriers and the tile lengths) and the tolerance in the tile thicknesses. Tiles long in the toroidal direction need only be inclined a small angle compared to short tiles in order to achieve the same protection of the adjacent tile, thereby increasing the wetted area of tiles.

The poloidal inclination of the target tiles was chosen so that the poloidal area wetted by the plasma scrape-off is increased as far as possible for the plasma configurations envisaged. Steps designed to protect tile edges are also included in the poloidal direction and these are shown in Fig.12.

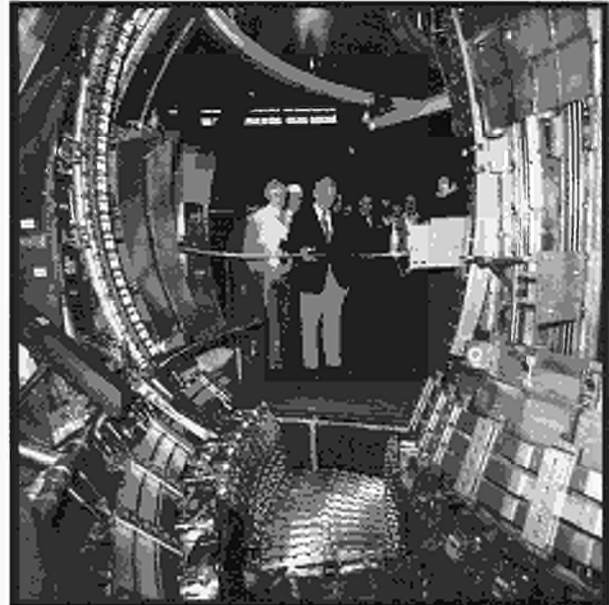


Fig.13: The official opening of the In-Vessel Training Facility, a full-scale replica of four Octants of the inside of the vessel.

Keeping the front surface of the tiles, without exception, free of holes or cut-outs either for attachment or for diagnostic purposes, ensures that hole edges are not exposed to direct power influx and that there is no loss of wetted surface area due to the requirement that a complex shape be machined into the tile surface to shield the edges of the hole.

One of the main activities related to the tendering, placing and supervising of the manufacturing contracts for the Mark II Divertor support structure, tile carriers, and instrumentation for diagnostic cabling including remote handling plugs and sockets. The detailed analysis of the final designs were undertaken with regard to thermal and mechanical stresses on the structure, covering a wide range of load cases on the plates, rings, joints, hinges, and supports, expected during operations.

### The Mark IIA Tile Material

The Mark II divertor is designed around carbon fibre reinforced carbon (CFC) tiles, which are typically 400 x 180 x 40 mm in size. CFC was chosen as the tile material for the first installation, as it provides a robust and forgiving solution. It can be followed up by a beryllium tile design once the optimum divertor geometry has been identified.

The design was based on material properties such as thermal conductivity, thermal expansion coefficient and flexural strength, which were known to be readily achievable from a number of CFC manufacturers. The final

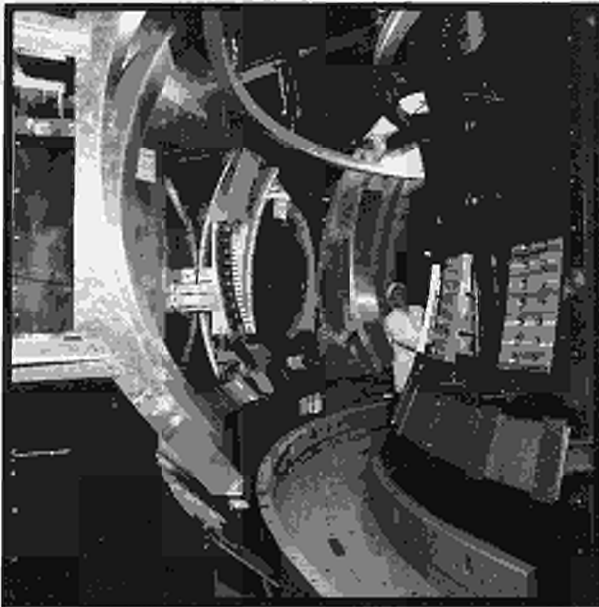


*Fig.14: A section of the In-Vessel Training Facility designed to study the remote handling aspects of in-vessel work.*

decision for a particular material was based on mechanical and high heat flux tests performed in the Neutral Beam Test Facility.

### The In-Vessel Training Facility

In 1994, an In-Vessel Training Facility has been built, which is a realistic full-scale replica of Four Octants of the inside of the JET vessel and all of the important aspects of the in-vessel components (Fig.13). This facility has three main uses:

- A major concern for future shutdowns has been the provision of adequate training for in-vessel workers. Due to the beryllium contamination of the vessel, all the work in the vessel is performed by workers wearing pressurised suits and three pairs of gloves and having a limited visibility. In addition, as the number of high performance plasmas increases, the background radiation levels in the vessel increases. To remain within JET's self imposed radiation exposure limit of 10% of the legal limit, a large number of trained fitters, engineers, welders and inspectors are required. The facility is used to train in-vessel personnel in the conditions that await them in the vessel and prior to their actually going into the vessel so that all in-vessel work can be done correctly, safely, efficiently and with the absolute minimum of radiation exposure;
- The facility is used to check the details of new components, develop and test all new installation proce-

dures, handling and installation tools, new in vessel flooring, and interface problems in order to ensure that the Mark II divertor can be installed to the desired accuracy and within the boundary conditions prevailing;

- The facility will be used for remote handling operations trials. The preparation of equipment and operators for the fully remote exchange of the tile carriers will include the full-scale testing and proving of each individual task both under normal operating conditions and under failure case conditions. All of these trials will be performed within the facility. The facility has incorporated into it a full-scale space frame representation of all in-vessel components considered to potentially offer a manoeuvring, viewing or access constraint under fully remote conditions, (e.g. Poloidal Limiters, Lower Saddle Coils and Inner Wall Guard Limiters (see Fig.14)). The facility will be closed with curtains to prevent extraneous light entering the working environment and will be operated fully remotely from the Remote Handling Control Room with viewing from the IVIS system and remote handling cameras. The forthcoming mock-up task trials will include extensive testing and proving of the capability to recover from worst case Remote Handling equipment failures and also the capability to recover from worst case failure of in-vessel components such as seizure of bolts or fractured tiles.

## Power Supplies and Magnet Systems

The purpose of the JET electromagnetic system is to establish, maintain and control the tokamak magnetic configuration (Fig.15). It includes: the toroidal coils, which establish the toroidal magnetic field; the poloidal coils P1, acting as primary windings of the tokamak transformer, and coils P2, P3 and P4 to control plasma radial position, vertical position and shape; and the divertor coils D1, D2, D3, D4, to establish and control the new divertor magnetic configuration. To perform these functions, these coils are energised by suitable power supplies. Voltages and currents of the poloidal coils are controlled in real-time by the plasma position and current control (PPCC) system. Other DC power supplies energise the neutral beam injectors (NB) and ion cyclotron

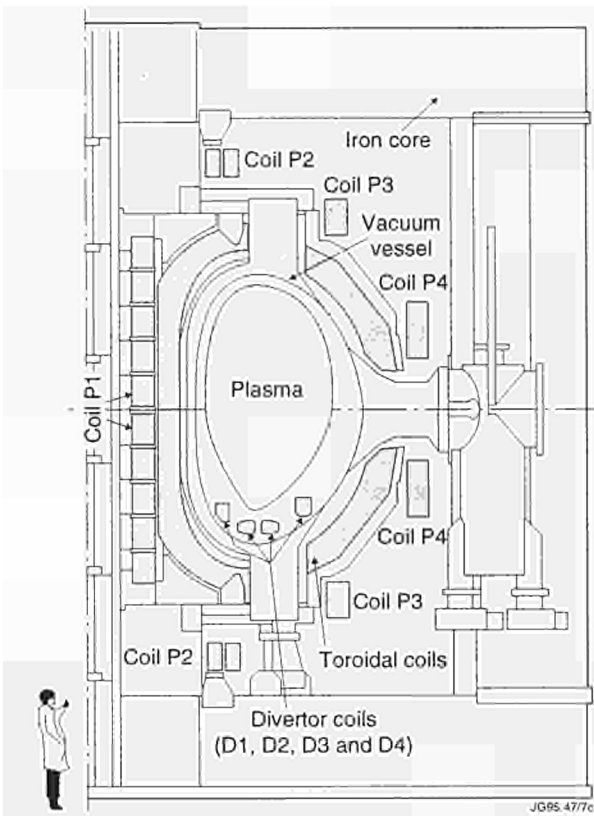


Fig15: Cross-section of JET showing toroidal, poloidal and divertor coils

radio frequency (ICRF) system for plasma heating, and the lower hybrid current drive (LHCD) system for plasma current profile control.

The total installed DC power exceeds 1500 MVA, capable of delivering a peak power above 1000MW and an energy per pulse above 10,000MJ. More than half of the power and of the energy is taken directly from the UK National Grid at 400kV and the rest is provided by two vertical shaft flywheel generators. Consequently, a major feature of JET is the 400kV-36kV distribution system. Auxiliary power is supplied by the 20MVA, 11kV/3.6kV/415V distribution system.

JET development, an essential part of the Project's programme towards enhanced plasma performance, calls for continuous modification and upgrading of the electromagnetic system, of the plasma control and of the additional heating power supplies. The overall objective of 1994 activities has been the commissioning of all new systems, installed during the 1992-93 shutdown, including the four new divertor coils, four DC power supplies to energise the coils, the fast radial field amplifiers (FRFA) for the vertical stabilisation of divertor plasmas, a completely new PPCC system and a new Coil Protection

Table III. Divertor Coil Cooling System Capability for  $\Delta T_{\text{Freon}} = 15^{\circ}\text{C}$

Coil	D1	D2	D3	D4
Main pump cooling capability (kW)	22	24	28	43
Emergency pump cooling capability (kW)	8	8	7.5	10.5
Heat input with vessel at 250°C with uncooled target assembly (kW)	4	4.5	5	7

System (CPS). To cope with the new demands and to maintain the voltage drop and the reactive power swing at the 400kV interconnecting points a new Reactive Power Compensation Unit of 50MVAR has been installed, commissioned and integrated with the already existing 3 x 50 MVAR units.

### Magnet System

Major tasks have been the commissioning of the four new divertor coils and of the CPS (Coil Protection System) and the installation of the air cooled busbars for the toroidal magnetic field ripple experiment in the Basement and in the Torus Hall.

### Divertor Coils

The divertor coils were progressively commissioned in line with experimental requirements, and this was most activity centred around the thermal performance of the coils and cooling system. The coils are heated from two sources; ohmically generated heat due to coil current and heat transfer from the surrounding vacuum vessel and in-vessel components. The coils are cooled by freon which is pumped through the conductor cooling channels.

### The Coil Cooling System

The divertor coils use the same heat exchanger and coolant as the toroidal field (TF) coils but have their own independent pumps to give high flow rate and control of differential temperature. The cooling system is designed to maintain the measured temperature difference across the coils to 15°C (Table III). This limits the thermally developed shear stress in the inter-turn insulation to 10MPa.

Each divertor coil has its own cooling pump and control valves but is fed with cold freon from the TF coil

system. During a power pulse, the divertor cooling system is put into closed-loop mode: as the coil and coolant heat up, hot coolant is re-circulated through the coil thus limiting the differential temperature across the coil. After the pulse, a control valve is progressively opened under the control of a feedback system which controls the temperature difference across the coil, during cooling. An "emergency cooling system" is also installed, in parallel with the four coils with a common pump, connected to an un-interruptable power supply. This operates only in open-loop mode and is capable of extracting the thermal power input to the coil.

### Heating by Surrounding Components

Since the restart of operation, the thermal performance of the coils has been monitored in order to interpret the measured heat power load to the coils, and the temperatures measured on the Inconel casing. The aim is to estimate whether any part of the epoxy-glass insulation might be subjected to temperatures which could degrade its properties as an insulating or structural material. Direct measurements of the epoxy temperature are not possible. The present Mk.1 divertor target plate assembly is supported on the divertor coils, and its alignment ultimately relies on the mechanical stability of the epoxy. Calculations were also made to evaluate faults such as loss of vacuum or failure of the coil cooling system.

The divertor coils, are enclosed in thin Inconel casings (thickness 1.2mm), which were also their impregnation-curing mould. These are anchored to the vessel by 32 clamps, which allow for radial expansion due to forces and to temperature variations. Pads welded on the casing top surface of coils D2 and D3 support the target plate structure. The target plate is generally water-cooled, but operation with uncooled target plate proceeded for several months, and this may still be required for conditioning baking of the vessel. The coils are provided with radiation heat shields over about 75% of their surface and the remaining 25% (in particular, the sections at the clamps, pads and coil termination) are unshielded.

The shields considerably reduce the heat power load, which would otherwise require 50% of the available cooling power. However, at the clamps and target support pads, combined heat radiation and conduction may produce a concentration of heat flux. For this reason, the coil assembly includes copper plates, at the top and bottom of the coil, spreading the heat and protecting the

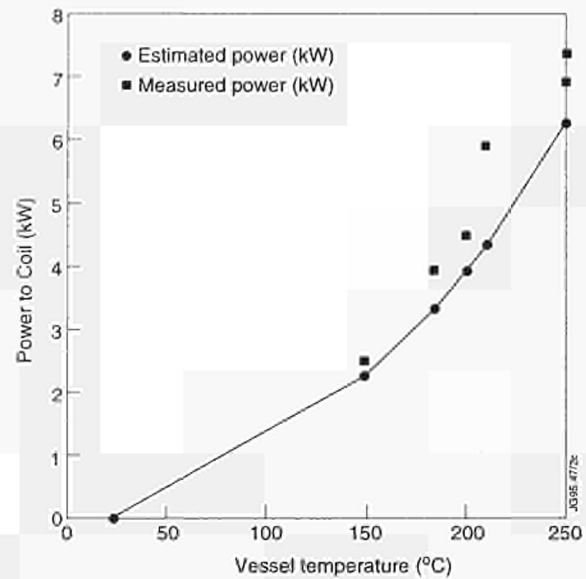


Fig16: Heating power to Coil D4 with target plates uncooled;

ground insulation. From the thermal point of view, the epoxy is a matter of concern, since it is not protected by this feature. For structural purposes, this fills the gap between casing and electrical insulation of copper plates. The temperature of the casings is monitored, at four points per coil, by thermocouples welded to the casing 20mm from the clamps.

The cooling system is used for the thermal power load measurements, since, in steady state conditions, the power is related to the coolant mass flow, the specific heat and the difference  $\Delta T$  between outlet and inlet temperatures.

To assess the power scaling and the main heat transfer mechanism to the coils, measurements were performed with the vacuum vessel at several temperatures in steady state conditions, between 150°C and 250°C, with and without target plate cooling and at 320°C with target plate cooling. Tests were performed, to assess the effect of a vacuum loss in the vessel.  $H_2$  and  $N_2$  gases were injected up to 10mbar pressure, with the vessel at 150°C and 250°C, respectively, and the increased heat power measured (see Fig.16 and Table III). A model representing the coil in its thermal environment has been developed. The measured thermal power load dependence with the vessel temperature scales as the radiation law. Casing surfaces screened by the heat shields contribute about 10% of the heat power load to the coil and the underlying epoxy insulation is less than 5°C higher than the coil copper. The radiated power is essentially transmitted through the unshielded casing parts, where the underlying epoxy insulation is about 30°C higher than the coil copper.

Molecular conduction is the main means of heat transfer across the inter-space between casing and epoxy insulation. This inter-space, which is pumped down to about 1 millibar was formed during resin polymerisation.

The power transmitted by conduction through the clamps appears to be small compared to the radiated power, possibly due to low contact pressure at the hinge pins linking the clamp to the vessel. The contact pressure depends on coil and target plate weight and also on the deflection profile of vessel and could not be estimated beforehand.

The epoxy layer under coils D2 and D3 pads is the most critically affected by the vessel temperature, because of the larger than expected, heat conduction from the target plate graphite tiles to the support structure. Baking and operation with the target plate uncooled is now restricted to a maximum vessel temperature of 200°C per hour, and with target plates cooled to 320°C.

### **Pulse Operation**

Divertor coils D2 and D3 were commissioned for operation at 40kA and coils D1 and D4 for operation at 20kA. The current in D4 is limited by the power supply configuration, and for D1, higher currents have not been required for operation. The coil ( $I^2t$ ) is presently limited to  $13 \times 10^9 \text{A}^2\text{s}$  and can only be increased if the freon inlet temperature is reduced.

### **Coil Protection System (CPS)**

#### **General**

The new Coil Protection System (CPS) detects electrical faults and protects the coils against mechanical and thermal over-stressing due to operation outside safe limits. Protective actions include immediate removal of the voltage from the coils. CPS detailed design started in March 1993, and the system became operational in May 1994. The system required new voltage and current transducers, pick up coils, flux loops, Rogowski coils and temperature sensors for most of the circuits. Measurements or computed quantities are compared with suitable thresholds. If a threshold is exceeded an alarm is generated and protective actions are taken.

#### **Fault Detection Algorithms and Protective Actions**

The protection algorithms can be classified into five categories, as follows:

#### **(a) Conventional over-current and over-voltage protection for all the circuits**

Over-voltage and over-current protection has been implemented for both poloidal and toroidal systems, and the protection is active at all times. A simple deglitching technique makes this protection more "robust", against unwanted intervention especially in case of plasma disruption. Three levels of protection are defined for currents and voltages; two during a pulse, 5% and 10% above nominal maximum, and one, 10% of nominal maximum, outside pulses. A special protection for the P1 coils reduces the current in the end coils to an acceptable level in case of full inversion of amplifier PFX when the coil currents are close to the limits.

#### **(b) Thermal stresses (eg. $I^2t$ ) in all coils**

Limits on  $I^2t$  are a function of the initial temperature of the coolant and, for a given cooling rate of the coils, affect the pulse repetition rate.

#### **(c) Mechanical stresses on the coils and vacuum vessel**

The protection system makes real-time computations of the forces using flux loops and ampere-turn measurements or analytic coefficients. The tensile and shear stress in each coil is computed as a linear combination of vertical and radial forces and temperature (computed from the energy dissipated).

#### **(d) Circuit equation integration and comparison with the measured currents**

This protection based on circuit equation integration in real-time, has been implemented for the toroidal field circuit and will be implemented for the poloidal circuit. The inputs to the circuit models are the coil terminal voltages. In either case, the computed currents are compared with the measured currents. A large difference would indicate a possible fault and would terminate the pulse.

#### **(e) Thermal model for the divertor coils**

A simple model will be used to estimate the temperature of the epoxy insulation and copper windings of the divertor coil. The inputs to the model are the vessel temperature, coil case temperature, coil currents, coolant flow and coolant inlet and outlet temperatures. The protective actions taken are that two fail-safe commands are sent individually to the PF and TF power supplies, a Voltage Off and a Circuit Breaker Open command. These direct interlocks are backed-up by actions performed via the Pulse Termination Network (PTN) and the Central Interlock and Safety System (CISS).



### Implementation

CPS is a multiprocessor and multi-tasking system based on VME. Data is continually collected from the Analogue and Digital I/O boards by the DSP Master Board, via the VME Bus. These values are used to provide continual protection of the coils.

While JET is not pulsing, it is possible to suspend the protection for a short period of time and to load from the Level 1 software on the host computer a new set of operating parameters. As a pulse is started messages are received from the host computer via the Crate Controller, preparing the CPS software for the next pulse. The information in these messages instructs CPS what data channels to collect during the next pulse and also indicates the state of other parts of the plant. From this point, CPS monitors the progress of the pulse using the status information from the Service module together with values from some of the digital inputs.

While JET is pulsing, further data is collected from the Pre-processor card, by the DSP Slave board. This board provides drift and offset compensation of the integrated signals received from the Pre-processor. This data is then combined with the data already being collected by the SDP Master board, to provide the large number of inputs upon which the full range of protective algorithms are run. If a fault is detected, appropriate actions are taken directly using the digital outputs to issue commands to the remainder of the plant, while at the same time messages are sent to the host indicating the source of fault and the actions taken.

During the pulse, samples of the collected and calculated signals are simultaneously stored in a Shared Memory block on the DSP Master board. After each pulse these stored values are collected by the GAP program on the host, via the Crate Controller, and archived.

### Operating Experience

CPS became operational in May 1994 and was progressively commissioned, debugged and upgraded to include new requirements. CPS statistics for the four months July to October 1994 are given in Table IV. The protective actions were mainly caused by parameters being outside limits due to induced currents and voltages during disruptions. Early experience indicates that CPS will be useful and reliable. Due to its flexibility, protection functions not included in the original design have already been implemented and others are planned.

Table IV. CPS Statistics, July to October 1994, Pulse Nos: 30443 to 32600

No. of pulses	% of total	CPS action
1898	88	no fault detected
219	10	protective action successfully generated
35	1.6	pulse incorrectly stopped
5	0.2	system off-line

### TF Ripple Busbar

A busbar running from the Torus Hall to Building J1H via the Basement, connecting the centre point of the TF coils to the power supply busbar has been designed and the parts manufactured. The busbar is designed to carry a pulse current of 40kA (or 50kA) and a fault current of 300kA. Installation began in December 1994.

### Error Field Coils

Coils for compensating error fields due to imperfect axisymmetry of the poloidal coils have been designed, to give an  $m=2$ ,  $n=1$  component of field with a maximum amplitude of 5G in the plasma volume. The coil system consists of four coils mounted on the mechanical structure upper ring and four on the lower ring, each coil carries a maximum 60kA-turns. When operation with the new divertor coils restarted, the error fields were less than in previous configurations and error field compensation was not required so this project was curtailed.

### Irradiation Tests on Divertor Coil Insulation

In the D-T phase, the divertor coils will operate under neutron and gamma fluxes which may affect the characteristics of the electrical insulation. To assess the effect of radiation damage, test samples were irradiated in conditions close to those during the active phase. The test samples consisted of two aluminium bars electrically insulated with glass/kapton and impregnated with epoxy resin contained in an aluminium box. Aluminium was used instead of copper to avoid activation problems. Irradiation conditions achieved were:  $2.7 \times 10^{15} \text{nm}^{-2} \text{s}^{-1}$  fast neutron fluence rate ( $E > 0.1 \text{MeV}$ ) corresponding to a dose rate of  $6 \text{Gys}^{-1}$  and a gamma rate of  $5 \text{Gys}^{-1}$ . The

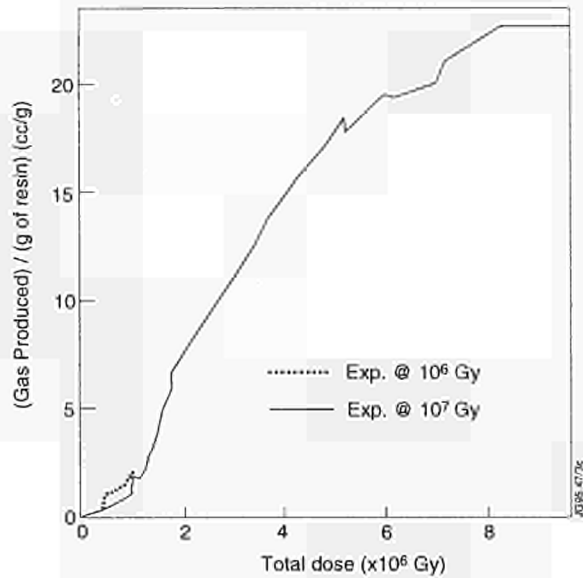


Fig.17: Gas released under irradiation

samples temperature was kept below 80°C. Three irradiations were performed at total doses of 10<sup>5</sup>, 10<sup>6</sup> and 10<sup>7</sup>Gy, respectively.

Under irradiation, covalent bonds of the epoxy resin atoms were broken forming free radicals, which recombined in new compounds with alteration of physical, mechanical and chemical properties. The material lost tensile, shear and impact strength and became brittle. Moreover, freed protons and methylic groups recombined producing hydrogen (mostly) methane and ethane. Up to 4x10<sup>5</sup>Gy gas was released during the three exposures, with a production rate in the range 0 - 2 cc/g/10<sup>6</sup>Gy with a slight regular increase with increasing doses. At higher doses, the production rate strongly increased with increasing doses, sometimes with abrupt changes, as shown in Fig.17 (~2x10<sup>6</sup>Gy). During the experiment at high dose (10<sup>7</sup>Gy), gas release rate up to 7cc/g/10<sup>6</sup>Gy was observed (Fig.18). This behaviour can be explained by the presence of cavities in the resin, either formed during impregnation and/or formed due to material degradation under irradiation. The gas produced filled the cavities, then it was slowly released.

It was concluded that:

- Loss of the insulation mechanical properties preceded loss of electrical properties. The resin started to become brittle at doses higher than 10<sup>6</sup>Gy, but at a dose of 10<sup>7</sup>Gy, the electrical resistivity value was still acceptable for insulation purposes;
- Radiolysis was the actual insulation life limiting phenomenon;

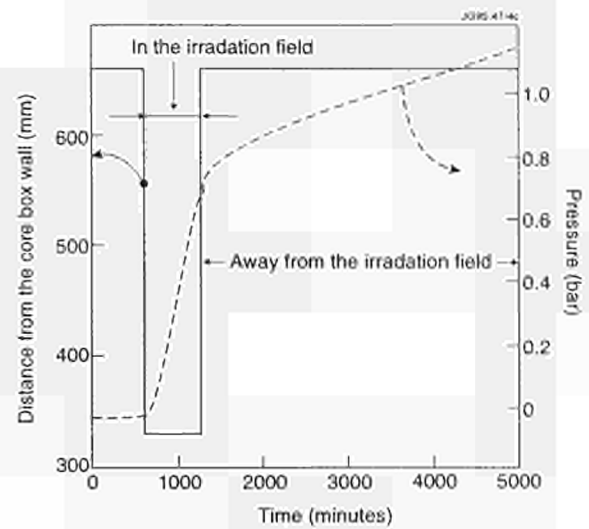


Fig.18: Gas release after the end of irradiation, as a function of time

- Gas release was not significant up to 10<sup>3</sup>Gy, but at higher doses, it caused swelling and a pumping system would be required to evacuate the gas from the divertor coils cases.

### Magnet Power Supplies

The toroidal field power supplies consist of a flywheel generator diode rectifier, (rated 67kA DC, 9kV no-load voltage, 2600MJ delivered energy) and of two transformer-thyristor rectifiers, supplied directly from the 36kV distribution, (each rated 67kA, 2kV DC open circuit). These three power supplies are connected in series (67kA DC, 13kV open circuit)

The poloidal field power supplies consist of a flywheel generator diode rectifier (identical to the toroidal field supplies), a DC switching network and a transformer-thyristor PVFA 5-6, rated 2.8kV DC no-load voltage, 40kA DC. This establishes and sustains the plasma current, up to 6MA, in the new divertor configuration.

In addition, the poloidal field power supplies include: the amplifiers PVFA3-4 and PVFB, rated 12kV at 1kA, 4.7kV at 6kA and 2kV at 40kA DC, for the control of the radial position; PVFA1, rated 1.4kV (no load), 40kA DC for the control of the plasma shape; the PDFA Amplifier system, PDFA1,4 rated 500V, 40kA, DC; PDFA2,3 rated 650V, 40kA DC to supply the four divertor coils; and the FRFA 1,2,3,4 system (based on switched mode full four quadrant GTO inverters) each one rated 2.5kV, 2.5kA DC with a switching frequency of 1250Hz, for a fast control of the plasma vertical position.

Finally, the DFAS, based on IGBT's and made up of four units each are rated 1.5kV, DC with an output frequency of 0-10kHz and a current of 3kA (0-1kHz) and 3kA/f(Hz) (1-10kHz), to supply the four saddle coils in pairs, installed inside the vacuum vessel fan at the top and fan at the bottom.

### **Poloidal Vertical Field Amplifiers (PVFA)**

The Poloidal Vertical Field Power Supply consists of a 12 pulse thyristor rectifier PVFA3-4, (rated 2.8kV DC no-load voltage, 40kA DC load current) and a boost amplifier PVFB, (rated 9.2kV DC no load voltage, 6kA DC load current (short time rated)). The Boost Amplifier is electrically connected in parallel to a freewheeling diode stack capable of carrying the rated current of PVFA3-4. The combination PVFA3-4 and PVFB provides the required DC voltage/current for the control of the plasma radial position. The boost amplifier only operates during the plasma initiation when a high voltage is required on the coil P4.

In addition, the vertical field circuit is configured with a mid-point link between the power supply and the P4 coil to provide a radial field by an imbalance current between the upper and lower P4 coil. The imbalance voltage is provided by the amplifier PVFA3-4 (the circuit is rated  $\pm 500\text{V}$ ,  $\pm 10\text{kA DC}$ ).

To provide better control of the divertor configuration at high plasma current, both the voltage and current capability of the imbalance circuit were upgraded. To this effect, the spare PVFA2 thyristor rectifier was converted to four quadrant operation and the output busbars were connected, to the output busbars of PVFA3-4.

The conversion of PVFA2 to four quadrants involved computer simulation to check that both the 300Hz ripple and the transient excursion of the circulating current were satisfactory with the DC chokes already fitted within the thyristor rectifier. In addition, it involved modification of the DC busbars, of the control and protection system of PVFA1,2 and PVFA3-4 as well as the interface with CODAS. After commissioning on dummy load during the September shutdown, the upgraded Poloidal Vertical Field Power Supply was commissioned on the coils in October 1994. The converted PVFA2 behaved well with a circulating current of typically 500A under steady conditions and peak of no more than 1300A during transition conditions. The imbalance voltage is controlled by means of a sequential controller with a cross-over voltage set at  $\pm 500\text{V}$ . For

demand lower than  $\pm 500\text{V}$ , PVFA3-4 provides the imbalance voltage while PVFA2 is operating at zero voltage. For higher demand, PVFA3-4 imbalance voltage is limited to  $\pm 500\text{V}$  and PVFA2 provides the additional imbalance voltage. The new rating of the imbalance circuit is  $\pm 2500\text{V}$ ,  $\pm 16\text{kA}$ . Further commissioning work is required to increase the current to the design value of 18kA.

### **Poloidal Divertor Field Amplifiers (PDFA)**

The Poloidal Divertor Field Amplifiers (PDFAs) were connected for the first time to the divertor coils in early 1994. During integrated commissioning from the Control Room, the current was progressively increased in the divertor coils and the current control loops and current limit loops were optimised for each PDFA to avoid oscillations due to strong magnetic coupling between coils. Unlike the dummy load used for the acceptance tests of the PDFAs, the divertor coils are active loads where voltages and currents can be induced either from the other coils of the Tokamak or from plasma disruptions. This has led to two slight modifications of the electronics. The first one consisted in the improvement in the transition between two different operation modes of the PDFAs, namely from bridge mode to block mode, to avoid induced current at the start up of the plasma current. The second was to install an intertrip connection between the PDFAs to avoid an increase of induced current over the limits in some specific fault cases. These two modifications were carried out during integrated commissioning and, since then, the PDFA amplifiers have operated satisfactorily.

### **Fast Radial Field Amplifiers (FRFA)**

The Fast Radial Field Amplifier, installed on-site and commissioned on a Dummy Load in 1993, was operated on the Radial Field Coils during the re-commissioning after the 1992-93 shutdown. After re-tuning the current control loop to take care of the long cable connections to the coils, which modified the apparent impedance of the load at high frequencies, the amplifier was successfully tested up to its full performance in February. This was followed by the integration of the amplifier in the new Vertical Stabilisation Control system and, finally plasma operation started. During the whole experimental campaign in 1994, the FRFA was operated in open-loop and in Configuration B, providing an output voltage of up to  $\pm 10\text{kV}$  and an output current of up to  $\pm 2.5\text{kA}$ .

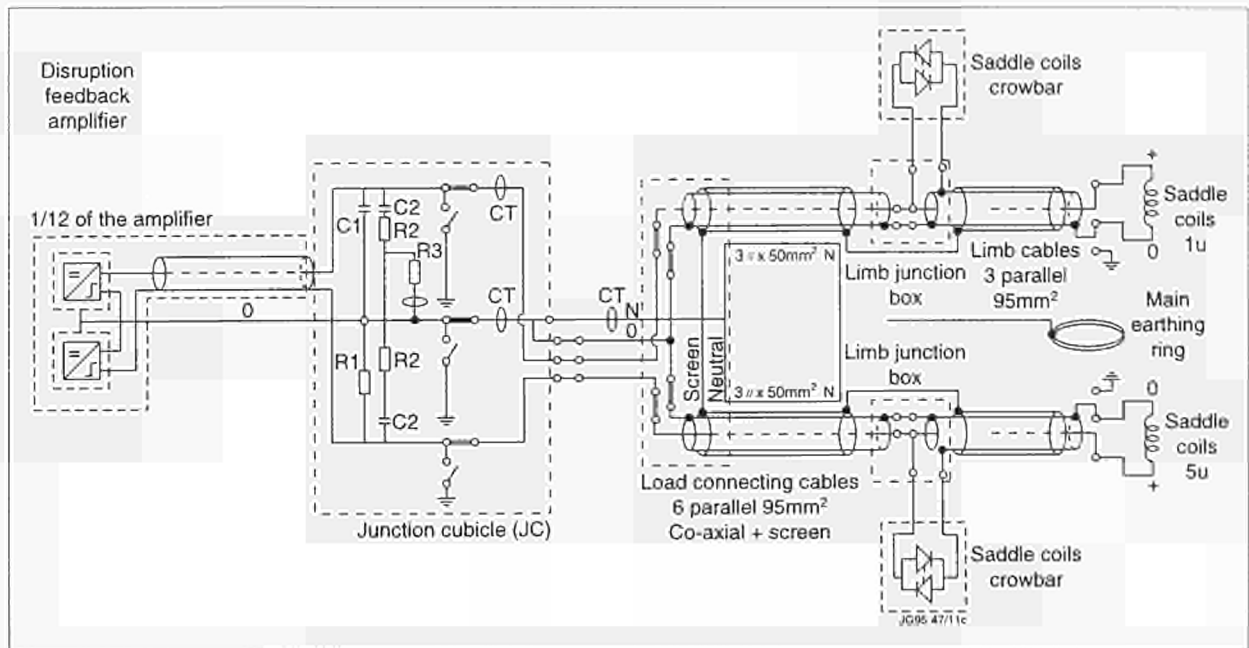


Fig19: Layout of the saddle coils showing crowbar connections

The reference signal produced by the plasma vertical position controller and driving the FRFA was heavily affected by parasitic magnetic pick-up and noise mainly produced by the current ripple in the divertor coils. As a consequence, unnecessarily large amplitude oscillations of the amplifier output voltage were produced, which were responsible for “sparkling” inside the vessel. The input/output characteristic of the amplifier was therefore modified to make it less sensitive to this parasitic signal and, at the same time, it was made more “linear”. This modification, together with other changes in the magnetic measurements and control systems allowed the sparking phenomena to be eliminated and, since then, satisfactory control of the plasma vertical position has been achieved.

### Disruption Feedback Amplifier System

Several modifications have been undertaken to the Disruption Feedback Amplifier due to changes in the internal earthing. The mid-point of two series connected coils is now solidly earthed to limit the induced voltage in case of disruptions and faults. To limit the voltage on the saddle coils when faults occur the protection logic has been changed so that zero voltage is applied, similar to a crowbar action, instead of inverting the voltage. The current will now take longer to go to zero but the coils will be less stressed in voltage.

Operation with two of the four Disruption Feedback Amplifier Systems (DFAS) on the lower saddle coils has

started. The current is limited to 500A and the voltage to <500V. So far, these have operated without problems.

### Saddle Coil Crowbar System (SCCS)

In case of the occurrence of disruptions or internal faults in the saddle coils, the voltage from the power supplies must be removed as quickly as possible to limit the energy in the fault. For this reason crowbars were installed close to the saddle coils. These were operational at the end of June 1994 according to the original planning.

The SCCS is composed of eight crowbar units (one per coil), each composed of two thyristors in anti-parallel connection with related control and protection equipment, and one Local Control Unit (LCU), for system supervision and interaction with other JET units. The layout of the saddle coils power supplies with the crowbars and a pair of coils is shown in Fig.19. Three different power supplies can be connected to the saddle coils: the Disruption Feedback Amplifier System (DFAS); the Error Field Compensation Amplifier (EFCA); and the Toroidal Alfvén Eigenmodes (TAE) system. These three power supplies have different requirements. In addition, the crowbar must be installed as close as possible to the coils. The optimum position found was in the Basement, but even there the components would be subject to radiation during the D-T phase of operation. The saddle coil crowbar must cope with all of these requirements. Table V gives an overview of the main technical specification for the crowbar.

Table V: Technical Specification for the Saddle Coil Crowbar

dV/dt	4kVs <sup>-1</sup> , between ±2kV
dl/dt	250 As <sup>-1</sup> , up to 10kA
I <sub>max</sub>	15kA
I <sup>2</sup> t	3.6 × 10 <sup>2</sup> A <sup>2</sup> s
Fluence (n)	3 × 2 × 10 <sup>11</sup> n/cm <sup>2</sup> (1MeV)
Dose (n)	40Rad (Si)
Dose (γ)	3.0 × 10 <sup>2</sup> Rem

As can be seen from the Table V, the main constraints on the crowbars due to the power supplies are the high fault energy of the Error Field Compensation Amplifier, the operation at RF frequencies with TAE (sinusoidal output 50 to 500kHz, V<sub>peak</sub> = 1000V, P = 3kW), and DFA switching (f<sub>max</sub> = 70kHz with dV/dt<sub>max</sub> = 4kV/s between ±2kV including over-voltages). Resonances of the transmission lines should also be considered.

To prevent a flash-over on the coils or reduce the energy dissipated in the fault and possibly extinguish the arc, the SCCS was designed to produce a fast short at the coil terminals keeping very low voltages across the coils (±30V) with fault current up to 15kA. Hence, it has been necessary to minimise the distance between the crowbars and the coils, and locate the crowbars where the neutron fluence and gamma dose are close to the limits for silicon device damage.

The SCCS was tested successfully first with the DFA on dummy load and then on the real coils without problems. These are now permanently connected to the coils and used during operation even if no power supply is connected to the saddle coils. In this case, they are permanently triggered to keep the saddle coils short circuited.

**Maintenance and Operation**

Both Flywheel-Generator-Convertor sets continued to run satisfactorily throughout the year with regular access for preventative maintenance and fault correction. The generator excitation systems DC circuit breakers became a source of operational concern and a call-for-tender has been issued for the supply of replacement breakers.

In the ohmic heating area, the commissioning of a new measurement and protection cubicle was completed. Initial problems experienced with the replacement fibre

optic measurement links were overcome with a revision of the shielding arrangements of the field transmitters. Some further problems continued with operational failures of the main reversal switches but these have been identified and the sources of faults have been reduced and controlled by increased and improved maintenance routines. The PF crowbar switch was re-installed and commissioned to operate under the command of the main Coil Protection System.

**Plasma Control And Magnetic Forces**

Loss of control of the plasma vertical position is one of the main causes of major plasma disruptions leading to high induced forces on the vacuum vessel and on in-vessel components.

**Vertical Stabilisation**

Stabilisation of the plasma vertical position plasma is achieved by feedback control of the new fast radial field amplifier (FRFA). The FRFA is a DC/DC converter with up to nine switched output voltage levels (0, ± 2.5, ± 5, ± 7.5, ± 10kV), power rating 25 MVA, and maximum response delay time 0.2ms. The FRFA includes a hysteric controller. The stabilisation is based on proportional feedback to the vertical speed of the current centroid, weighed with the plasma current. The average FRFA current is kept near zero on average by a slower proportional-integral current feedback. The system is designed to stabilise plasmas with instability growth rates up to 1000s<sup>-1</sup>.

After first operation with plasma, a number of modifications had to be made. The switching frequency was unexpectedly high and the highest switching level ±10kV was often invoked at a high rate, causing “sparkling” at in-vessel components and poor plasma behaviour. This problem was due to a large interference at 600Hz caused by the divertor coil power supplies (12 pulse 50Hz ac/dc converters) on the plasma feedback signal, and by the high noise sensitivity of the original FRFA hysteric controller.

The interference was suppressed by abandoning compensation of the feedback signal for the unwanted contribution from the divertor currents and also by omission of the signal contributions from the lower set of poloidal field pick up coils. The presently used signal no longer represents the vertical speed of the plasma current centroid. Therefore, it is sensitive to external field and plasma current changes.

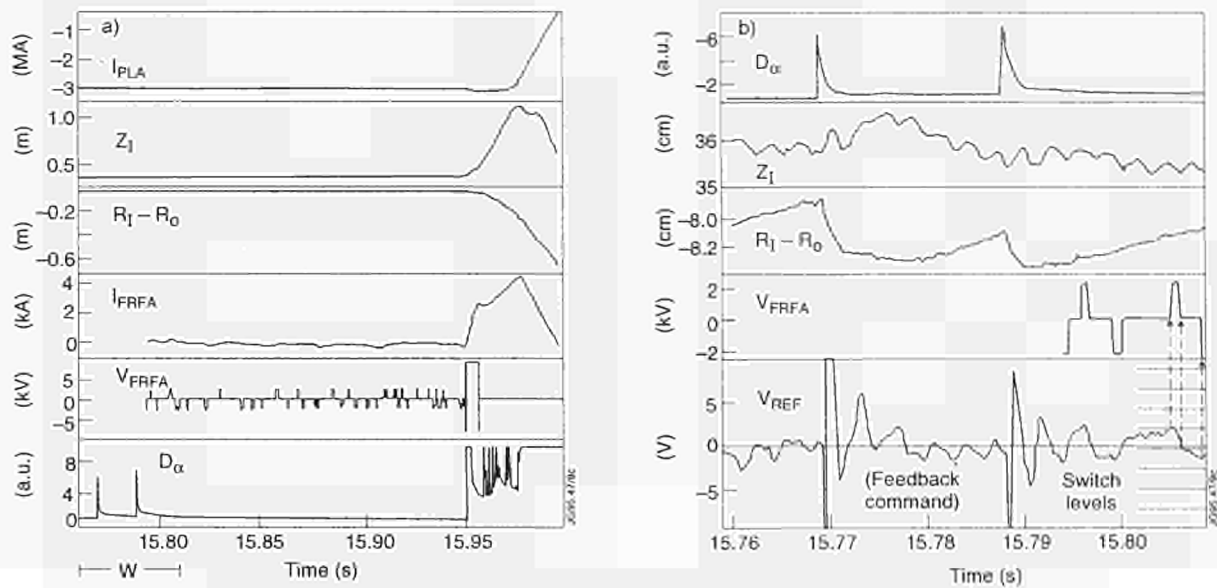


Fig20: (a) Plasma and FRFA signals of Pulse No:32732 before and during disruption;  
 (b)  $D_\alpha$ , plasma position and FRFA signals during ELMs

The FRFA hysteretic controller algorithm was altered to avoid multiple switching by noise and to achieve a closer similarity with a linear voltage control. Hysteresis is now set to one switch level (2.5kV), independent of the instantaneous output level. In the previous algorithm, a positive output voltage was only reduced if the demand decreased below -2.5kV or more. Typical behaviour of the FRFA output voltage is shown in Fig.20(a) (labelled  $V_{FRFA}$ ). During the ELM free interval 15.79-15.95s only short low level pulses ( $\sim 1\text{ms}$ ,  $\pm 2.5\text{kV}$ ) are required for stabilisation, producing FRFA current steps of  $\sim 0.1\text{kA}$  (the full range is 2.5kA). The switching frequency of  $\sim 200$  pulses/s is moderate.

Another modification is the introduction of a time dependent proportional gain for the plasma feedback signal. At the plasma start up a high gain is required within a narrow window. When the plasma current and hence the plasma signal increases the gain can be reduced. Typically, the gain is reduced by 60% after the first second of the plasma pulse. This measure allowed a substantial reduction of the limit cycle frequency. The present vertical stabilisation has been examined and it was concluded that there was still room for optimisation of the efficiency using other control algorithms and improving the plasma displacement measurement.

Practically all disruptions and also giant ELMs caused a voltage saturation and a current limit trip of the FRFA, leading subsequently to a vertical instability and large

vertical forces on the vessel, Figure 20(a) illustrates a typical case of sudden saturation, probably caused by a giant ELM at  $t = 15.95\text{s}$ . The stabilisation is not re-gained and the plasma becomes unstable and disrupts. Figure 20(b) indicates the response on smaller ELMs. The feedback signal  $V_{REF}$  shows synchronous perturbations even though the vertical current centroid location  $z_1$  remains almost constant as opposed to the radial position  $R_1$ . This behaviour suggests that the resaturation of the originally intended plasma current derivative method could be advantageous. As an alternative, the implementation of soft X-ray cameras is proposed for feedback stabilisation. This measurement will be free from magnetic noise and insensitive to ELMs.

The system analysis of the vertical stabilisation is still unsatisfactory because measured instability growth rates are in general substantially smaller than growth rates derived from simulations with the MAXFEA and PROTEUS equilibrium evolution codes. During divertor experiments, five instability tests were performed, where the feedback signal was set zero at a fixed time. Table VI shows the growth rates derived experimentally and obtained from simulations, assuming flux conservation at PF circuits except P4 coil imbalance and plasma ( $I_p$  is constant).

The discrepancy between experiment and simulation is large for the cases with higher growth rate (ie. when the theoretical growth rate approaches the MHD limit). The

Table VI: Growth rates from Experiments and Simulations

Pulse No:	30123	30211	30522	31420	31610
$I_{po}$ (MA)	-1.06	-.97	-2.95	+2.0	-2.1
b/a	1.66	1.61	1.62	1.65	1.51
$f_i$	1.37	1.36	.98	.97	1.08
Exp. Growth rate ( $s^{-1}$ )	140	280	120	160	115
MAXFEA ( $s^{-1}$ )	320	1200	110	220	90
PROTEUS ( $s^{-1}$ )	-	-	210	-	-

disagreement between MAXFEA and PROTEUS simulations for Pulse No:30522 may be due to different assumed current density/poloidal flux relationships. A test case using the same relation gave good agreement. Further studies are intended to improve the understanding of the vertical instability. The effect of eddy currents in the mechanical shell and of varying currents in the scrape off layer (halo currents) will be considered.

### Electromagnetic Forces

A continuous assessment of forces on machine components is required to clear new operating scenarios, and to assess the effect of the plasma disruptions on such components.

### Toroidal Field Coils

Sideways forces at the TF coils must be limited, in particular, in the vicinity of the upper and lower collars and rings of the mechanical structure. These forces are monitored using ten flux loops mounted along the TF coil perimeter. Computations with the MAXFEA equilibrium code permit a cross check and a verification of intended

Table VII: Measured and Calculated Vertical Forces for Pulse No:32737\*

	D2(MN)	D3(MN)	Total(MN)
Computed (MAXFEA)	1.11	1.62	2.7
Measured (from flux)	1.25	1.79	3.0
Vessel support force	-	-	2.3
F-number (static)	-	-	1.9

\*(5MA FAT plasma, no currents in coils D1 and D4)

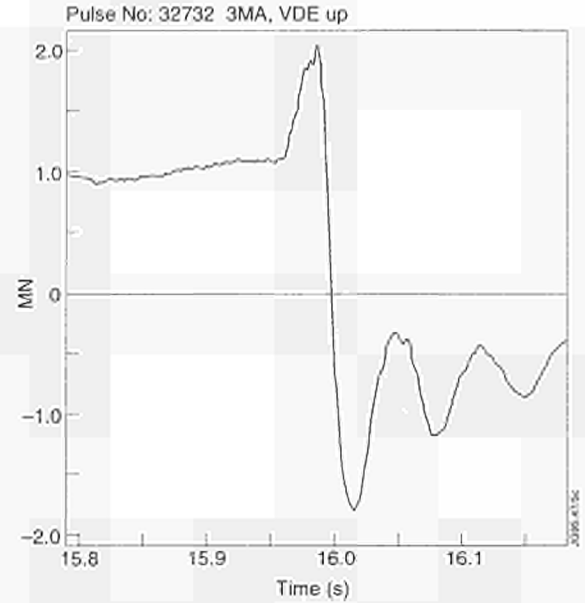


Fig21: Total vertical force on vessel at vessel supports

plasma configurations. Measurements and computations are in reasonable agreement. In a recent 5MA current pulse (Pulse No:32838), the traverse flux-current product at loop No:7 reached 13Wb.kA, which is close to the limit 15Wb.kA set out in an Operation Instruction. This implies that pulses with 5MA plasma current or higher must be carefully planned.

### Static Forces at Divertor Coils

Extensive computations have been performed with various plasma configurations to assess the forces and stresses at the D-coils. The computed forces can be compared with forces measured with flux loops mounted on the coils, and with the vertical forces measured with strain gauges at the vessel supports.

The vertical forces are of particular interest. For example, Table VII presents the peak vertical forces obtained for the 5MA Pulse No:32838. The "static F-number" is a simplified second order polynomial of PF currents with force coefficients obtained with the MAXFEA code. It is used, in combination with a "dynamic F-number", for validation of pulse schedules and for "Soft-stop" when reaching 5MN. The relatively small value of the vessel support force may be partially attributed to the fact that only the forces at the main vertical supports are accounted for the static F-number is significantly smaller than the measured D-coil forces. Investigations are on-going to improve the precision of predictions and measurements.

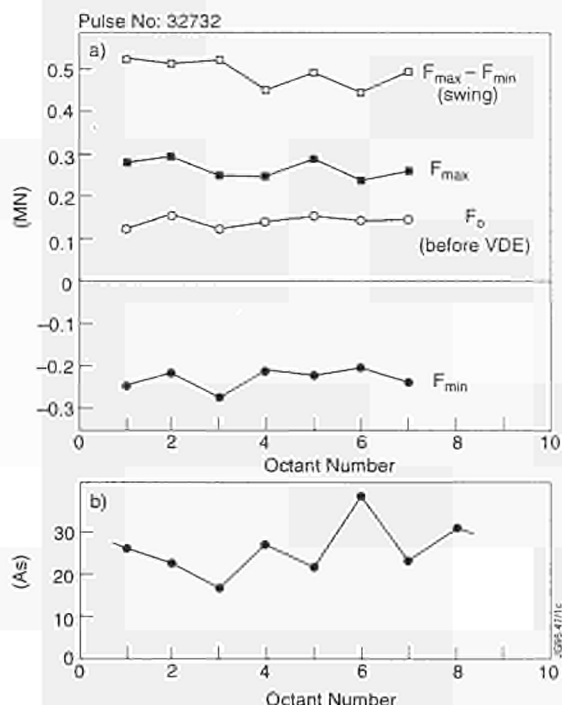


Fig.22: (a) Vertical forces at vessel supports at different Octants, for Pulse No:32732 (3MA upward VDE); (b) Charge collected during VDE at mushroom tiles, at eight toroidal positions and the same poloidal position

### Global Vertical Disruption Forces - Toroidal Asymmetry

During disruptions, the global forces can increase, in particular, during upward vertical displacement events (VDEs). The typical evolution of vessel support forces is shown in Fig.21, for an upward VDE of a 3MA plasma with elongation 1.8, similar to that of a SLIM plasma. The force rises from 1 to 2MN and swings then to -1MN with substantial overshoot due to inertial effects. The static F-number is 1.5MN before the VDE, indicating an over-estimate of the static force. The total F-number (static and dynamic) is 1.8MN before the VDE, anticipating fairly well the peak force arising from the VDE. Scaling up to 5MA the peak vertical vessel support force would be 5.6MN which is somewhat smaller than the value of 8MN estimated previously for a VDE in a 5MA SLIM plasma.

Of particular concern are toroidal asymmetries of the force distribution. The main contribution to asymmetries is believed to be due to a non-uniform distribution of halo currents, while forces due to toroidal eddy currents in the vessel and D-coil forces are expected to be toroidally symmetric. The toroidal distribution of vessel support forces has been examined in a series of disruptions. Figure 22(a) shows, the forces at seven octants before the VDE of Pulse No:32732, together with positive and

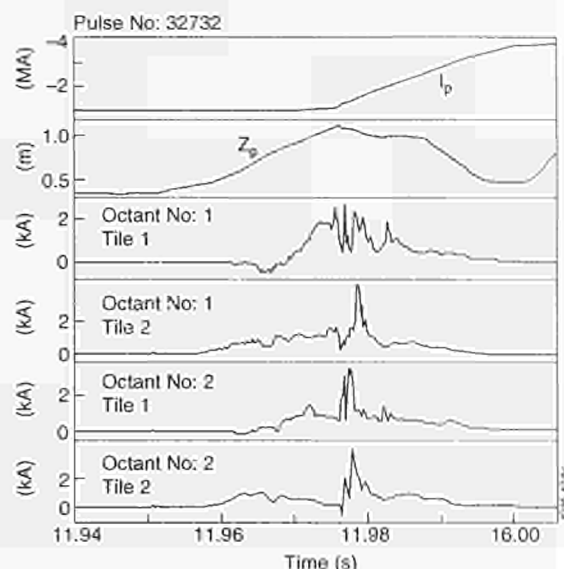


Fig.23: Currents intercepted by four mushroom tiles at locations  $R=3.15$  and  $3.30m$  in the upper part of the vessel, for Pulse No:32732. The plasma current and displacement signals are included to indicate the correlation with the VDE

negative peak forces arising from the VDE. The departures from toroidal symmetry are within about 10%. In some other disruptions significantly larger deviations were observed and the asymmetries of peak forces were found to vary in different disruptions.

Measurements of the total halo current are presently not available. However, it is possible to obtain an estimate of the toroidal distribution of halo currents by inspection of halo currents intercepted by mushroom shaped tiles at eight toroidal positions. Figure 22(b) shows, for example, the charges collected by the mushroom tiles during the VDE of Pulse No:32732. The departures from toroidal uniformity are larger than those of the vessel support forces shown in Fig.22(a) and there is no apparent correlation. Figure 23 shows the currents in two pairs of mushroom tiles at two neighbored Octants, together with the plasma current and vertical displacement. The poloidal separation of the tiles of each pair is only 0.2m. The signals indicate that the halo current density distribution has large fluctuations on a small scale length. The variations of the total halo current per octant is expected to be smaller than small scale variations.

### Forces at In-Vessel Components

During 1994, various in-vessel components have been re-examined as part of a reliability assessment. The forces on components due to circulation of eddy and halo currents have been considered. The basic assumption for the

design had been that the total poloidal halo current could be 20% of the plasma current before disruption (1.2MA for  $I_p = 6\text{MA}$ ), and that the plasma current could decrease to zero in a time  $>15\text{ms}$ . Due to the uncertain toroidal asymmetry of the halo current, a guideline figure of 1.5MA had been assumed for the maximum total halo current. The re-circulation of the halo current in the in-vessel elements and the vessel itself depends on the resistances of the network of interconnections (earthing straps etc). In some cases, such as the target plates the sharing of current with other elements was ignored giving, in general, an overestimate of currents and forces.

With the above assumptions, the "safety factors" (yield stress/max calculated stress) were found to be close to unity:

- poloidal limiter upper support;
- weld of inner wall guard limiter at upper restraining ring;
- localised bending stress at central target support beams;
- inner target plate support, weld pad to D1 coil casing;
- upper support of a vertical water pipe.

Experiments have not caused undue stresses in these components, as implied by current shunt measurements at earthing straps and the moderate level of global forces at vessel supports experienced.

Problems were however found with the following components:

- bending and buckling of the upper earthing straps at the outer poloidal limiter;
- unexpected large current in "French horn" type water connections for target cooling, but no damage;
- bending and severe damage of disruption feedback saddle coils;
- break-off of one Beryllium evaporator;
- bending of glow discharge electrode;
- break-off of one reciprocating probe.

These problems were analysed, and, in most cases, satisfactory explanations were found. The cause of saddle coil damage is still not fully understood. Currents induced in short-circuited coils were originally estimated to be  $<6\text{kA}$  for 5MA current quench in 15ms, but induced voltages derived from magnetic measurements were not excessive except for occasional short peaks during the energy quench phase of disruptions.

Remedial actions have been taken or planned. In the case of the saddle coils, it has been decided to remove the damaged upper coils and to observe closely the behaviour of the lower ones.

### **Additional Heating Power Supplies**

The key objectives of these activities have been re-commissioning and reliable operation, and the design of modification/improvements to meet the requirements the experimental programme.

### **Ion Cyclotron Resonance Frequency (ICRF) Heating**

At the beginning of the year, routine maintenance was carried out to these power supplies before operation started. Since then, they have been regularly used with the RF generators as load. No major problems have been encountered and no changes were made to the control or other components.

### **Lower Hybrid Current Drive (LHCD)**

The power supplies were initially operated with all the klystrons on load at the same time for commissioning purposes. Since then, they have been used on a routine basis with the klystrons either for testing of the klystrons on dummy load or for operation on the machine.

### **Neutral Beam Injection (NBI)**

Since the start of the campaign, the Neutral Beam power supplies have been used routinely for injection of the beams on the machine. Although reliability has been good, due to the complexity of the system, faults must be expected on the power supplies. In fact, one fault which gave great concern was that, although the measured voltage waveforms did not show any deviation with the set value, the actual voltage was much lower. This resulted in beams which were not at optimum perveance and hence much wider than they should have been. As a result, the deflected ion beam travelled outside the ion dump and caused damage to other components inside the NB box. Many investigations were carried out and the cause of the problem was located.

During the year, additional refrigerators/coolers were introduced to reduce the temperature inside the protection systems. This measure was most effective in improving the reliability of the system. The air temperature blown into the protection system was at  $8^\circ\text{C}$ . When the

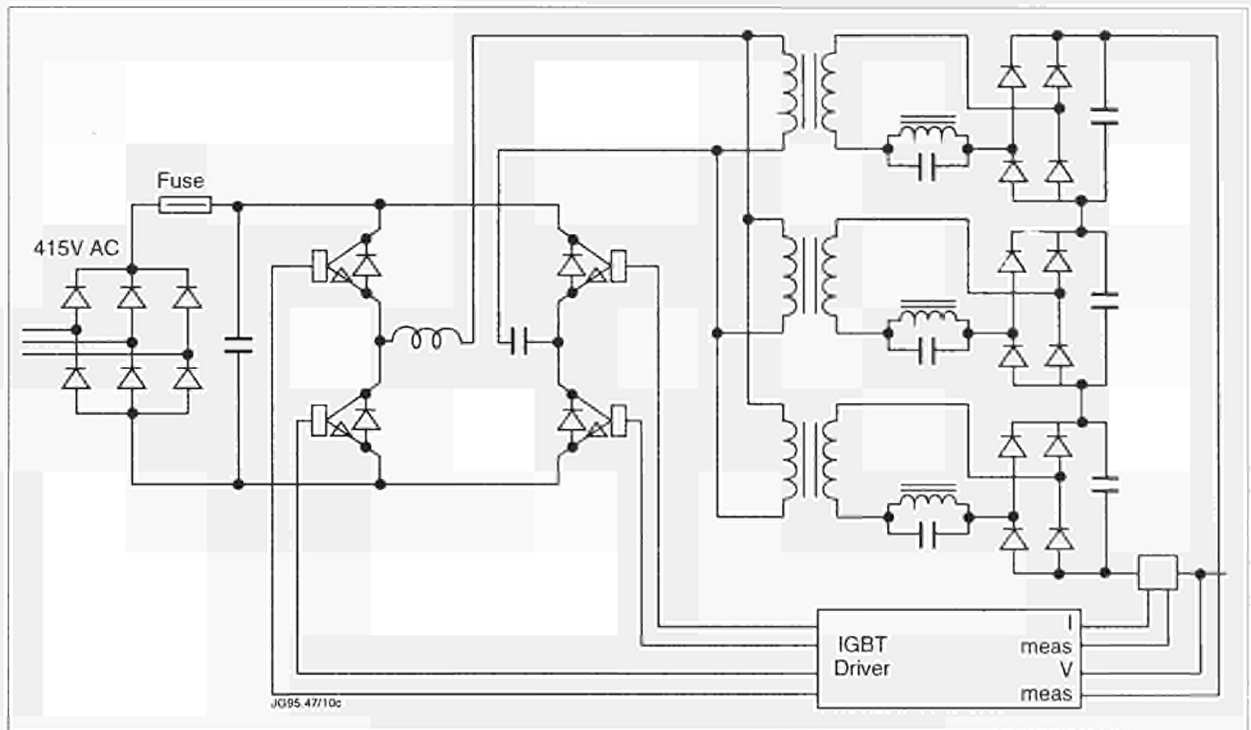


Fig24: Schematic of the GDC power supply system

temperature inside the protection system fell below a set level, the cooler was stopped, and as a result the dew point of the air inside the system rose, and condensation formed on the coolest surface. One of these surfaces was the voltage measuring divider. An additional protection circuit is now being studied which compares the reading of the voltage divider with another divider; if they differ by a set amount the pulse is terminated. In the meantime, the problem has been corrected by operating the protection system without refrigeration/cooler, and should not adversely effect the system reliability (at least in the winter period) while the additional protection circuit is procured.

Another problem with operating the beams in synchronous operation, is that the drop on the 36kV network prevents the power supply from being used at its maximum design value. The reason is that the voltage across the tetrode in the protection system drops too low causing the pulse to be terminated by an increase in screen grid current. A redesign is now in progress to keep the voltage across the tetrode constant when a certain value of screen grid current is obtained. This results in a lower voltage to the injector during that time. This is a relaxation of the original design values, but recent developments have shown that a voltage drop of 10 to 15% can be tolerated for 50ms. In addition, modifications to the beam modulation are in progress. This will suppress the spikes on the output during the off-period of the beams.

### Discharge Cleaning

The Glow Discharge Cleaning (GDC) power supplies consist of four independent supplies. Each one is connected to one electrode inside the vessel. The overall schematic of the power supply is shown in Fig.24. Each cubicle houses one power supply and the RF generator to facilitate the start of the glow. The power supply is a current source based on a full bridge series and parallel resonant power converter working in discontinuous current operation, its output is fully floating. Table VIII gives the main parameters of the power supply.

The series resonant circuit is composed of an inductor,  $L_s$ , and the parallel connection of three capacitors  $C_p$ . The capacitor,  $C_d$ , is used only as a decoupling capacitor. The parallel resonant circuit is formed by the three  $L_p$  and  $C_p$  circuits in parallel. Table VIII gives the values of the main

Table VIII: Main Parameters of GDC Power Supplies

Max. output (V)	1500 V
Max. output (I)	20 A
Max. energy in arc before trip	10 J
Output	Floating
Output isolation level	10 kV
Duty cycle	Continuous
Series Resonant Frequency	$\pm 100$ kHz
Parallel Resonant Frequency	$\pm 20$ kHz

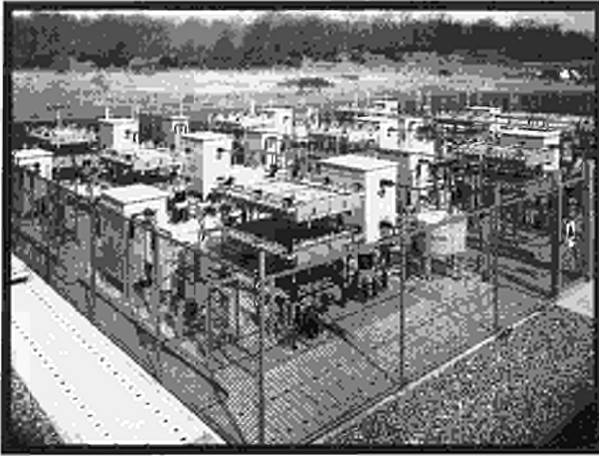


Fig25: 200 MVAR Reactive Power Compensation System

parameters of the circuit. The load is protected by two voltage protections (eg. minimum and maximum voltage level). The minimum voltage level is used to protect against arcing and is set just below the actual voltage level during operation. If during operation, the voltage drops below this set value the power supply trips, only the energy in the bridge  $C_1$  and output  $L_0$  is transferred to the load. No significant energy is added from the inverter because the under voltage detection circuit reacts within 10ms. The maximum voltage level prevents the voltage rising too high in case the glow extinguishes. The system is now used routinely for cleaning the vessel.

### Power Distribution

Activities during 1994 have been directed towards completion of shutdown work, routine maintenance, and repairs/modifications to the major distribution systems.

### 36kV Electrical Distribution

Half of the 200MVAR system (Fig.25) was unavailable for several months due to widespread failures of the 36kV insulators fitted on the capacitor banks. More than half of the installed insulators were affected. It appears that these insulators may not have been appropriate for outdoor applications in spite of the manufacturer's assurance that they were suitable. One Reactive Power Compensation (RPC) Unit was returned to service after "cannibalising" two other faulty units. The most recently installed unit was not affected as a different type of insulator was involved. Replacement insulators are now available and will be installed at the next available opportunity.

Unavailability of part of the RPC unit, did not affect operations, since full performance with all subsystems operating at full capacity was not required at that time.

Table IX: Expenditure on Electricity in 1994

	Units (kWh)	p/kWh	ECU
National Grid	-	-	125,103
National Power	18,999,980	4.46	1,074,989
Southern Electric	50,038,605	4.18	2,694,350
AEA Culham	2,107,263	5.70	153,996

### 415V Distribution

During the year, continuous upgrading of the low voltage distribution for building services and ancillary supplies for experimental machine sub-systems required the fabrication and installation of 12 new distribution boards and associated cabling in the following areas: J1S Cryoplatfrom, J25 E.D. System, J1A Clean Room, J1H S.C. Crowbar System and external welding bay. The total installed power for these upgrades has resulted in an increase in excess of 800kVA.

### Service, Design and Installation Work

The Electrical Drawing Office has undertaken several major power distribution studies such as AGHS chiller work buffer system, pellet injector compressors and gas collection system, saddle coil crowbar, TAE system, and Health Physics laboratory. Installation activities included completion of CPS and PPCC cabling and components, FRFA, DFAS and PVFA power supply, surge arrestors in the 400kV/36kV substation sealing of cable penetrations all around the machine.

### Supply of Electricity

There are four contracts for the supply of electrical energy to JET: with National Power for the supply of 400kV and National Grid for the supply of 400kV for the pulse systems. Southern Electric and AEA Culham for the supply of 11kV power for the outlay system (the latter is used as a back-up during maintenance periods and/or failure of the Southern Electricity supply). The make-up of the bill for supply of electricity for 1994 is shown in Table IX.

### Machine Services

The operation of the divertor coils inside the vacuum vessel, which are cooled with the fluid trichlorotrifluoroethane (CFC 113), required full commissioning tests of the fluid cooling control system to be carried out at the commencement of operations in 1994.

In addition, full commissioning tests were also carried out on the new water cooled target plates, cryogenic baffles and other in-vessel water cooled components.

To ensure secure operation of the NB cooling system and to avoid the possibility of freezing the water within the components located close to the cryogenically cooled panels within the Neutral Injector Box (NIB), an additional NIB cooling pump circuit, control cubicle and instrumentation were installed and fully commissioned for both Neutral Beam Systems at Octant No.4 and Octant No.8. For early detection of leakage of freon (CFC 113) from the toroidal and divertor coils cooling circuits, a new Infra-Red Freon Detection Analyser with automatic multi-point sampling was also designed, installed and commissioned for operation during the 1994/95 programme.

### **Divertor Coils Cooling System**

Commissioning of the divertor coils cooling system started in January 1994, and progressed until the closed loop control system was made operational. Initial difficulties were encountered and overcome, the measured coolant flows reaching their nominal values and the cooling rate matched the estimated one.

The divertor cooling system is connected in parallel to the TF cooling system providing a large reservoir of cold fluid at 5 bars. During operation, the system is set in full re-circulation at the start of a new pulse, following which the cooling is controlled, via a pneumatically operated mixing valve, limiting the differential temperature to a set value.

Commissioning of the cooling system in closed loop was performed independently of operation, heating the coolant and, therefore, the coils up to 50°C, with the system of full re-circulation, by means of the main pumps friction losses. Adjustments to the control parameters were made to obtain a fast response with no overshoot. The maximum differential temperature of the coolant is now limited to 15°C, limiting the shear stress in the interturn insulation. Operation of the controller and mixing valve proved consistently satisfactory.

As a precautionary measure, operational pulses are at present only allowed with the coil initial temperature below 30°C, but this limitation will be removed as soon as the necessary pre-pulse checks are implemented in the Level 1 software of the overall machine control. To upgrade the operational limits on the allowed divertor pulse  $I^2t$ , a new chiller is under consideration.

### **In-Vessel Component Cooling**

In-vessel water-cooled components were fully commissioned and made operational, as follows:

- Divertor target plates - Octants No:1 to No:8
- Divertor Cryogenic baffles - Octants No:1 to No:8
- Soft X-ray diodes diagnostic - Octant No:1
- Rotary high vacuum valves - Octants No:4 and No:8
- Neutral beam duct scrapers - Octants No:4 and No:8
- Lower hybrid window - Octant No:3
- Lower hybrid cryostat flap - Octant No:3
- Lower hybrid cryostat shield - Octant No:3

Tests were carried out with the new control system, to nitrogen cool each component, with the main vessel at high temperature (>250°C), down to a lower temperature (<80°C) to avoid excessive heat stress occurring during refilling with cold water.

Each cryogenic baffle was cooled using this method, so that with a nitrogen inlet pressure of 4 bar and the outlet to atmosphere, it took about 1 hour to cool the component down to 80°C. The components cooling circuit was then evacuated down to 100mbar pressure, with a water ring pump, ready for filling with demineralised water.

To avoid the cryogenically cooled target plates and the lower hybrid flaps and shields from freezing the water, due to loss of flow, an automatic sequence is initiated from a flow sensor located within each cooling loop. The sequence automatically closes the inlet and outlet valves to the component from the low flow signal and then proceeds to drain down the component by opening the drain valves and purging out the water with nitrogen into the drain ring.

In the event of pressure rise in the main vacuum vessel of >15mbar, which could be caused by a water leak into the vessel, an automatic draining sequence is initiated. This sequence immediately closes all in-vessel components, inlet and outlet valves from receipt of this high pressure signal from the vacuum local unit control system. The system then checks at 1 minute intervals up to a maximum of 3 minutes, to ensure that the signal is not spurious in any way, then after the final 1 minute check, opens all in-vessel components drain valves and allows the water to be drained out of each in-vessel component.

The target plates and the lower hybrid flaps and shields are also purged continuously with nitrogen to avoid the possibility of the water freezing-up during and after the drain-down period.

### **Infra-Red Freon Analyser**

This system automatically scans the remote points located around the torus and in the Basement area and receives back a sample of air from each point which is automatically analysed for freon in air content in ppm. The level of freon detected is transmitted back to the main Control Room. When the level exceeds 500ppm an alarm is raised. Should the level exceed 2000ppm, then in addition to an alarm, an automatic drain sequence is initiated. This drains the toroidal coils of all freon down to below the lower manifold of the toroidal coils cooling circuit. The freon cooling to the divertor coils is maintained at all times, during and after this drain down period.

The infra-red analyser is a single beam multi-wavelength infra-red to soft UV process analyser. This unit was incorporated into the design of the multi-point sampling system which is controlled by a PLC directly interfaced to the CODAS subsystem. The detailed design and construction of the system including the PLC software was carried out in-house and the system is now fully commissioned and operational.

### **TF/PF Cooling Control System**

A new enhanced design is being carried out for the remote control and monitoring of the following cooling systems associated with the toroidal and poloidal coils.

- TF Coils fluid (CFC 113) cooling system;
- PF Coil 2 and miscellaneous demineralised water cooling systems;
- PF 3/4 coils demineralised water cooling system;
- PF demineralised water leak detection system.
- Turbomolecular Pumps demineralised water cooling system

The design will incorporate a new PLC for automatic control of the 10 existing cooling pumps, three new cooling control cubicles, mimic diagram and new control instrumentation. This new system will be designed and constructed in-house commissioned and ready for operation at the end of the 1995 shutdown period.

## **Neutral Beam Heating Systems**

1994 has been particularly successful in terms of the contributions from the Neutral Beam Heating Systems.

- All engineering work undertaken during the major shutdown was completed within the planned

timescales. This included essentially a complete disassembly and reassembly of both injectors, installation of the pumped divertor cryopump inside the torus in addition to new duct liners and the LHCD cryopump. No engineering problems or failures have been encountered to date with these systems. Studies of the fatigue life of some injector components, operating beyond their original design parameters, show the need for replacement by upgraded components;

- The neutral beam injectors have been available and used throughout 1994 and have operated with impressive reliability at power levels in excess of the original design values;
- The in-vessel pumped divertor cryopump has been commissioned in conjunction with the new helium liquefier/refrigerator. Operation of the cryopump has proved to be a major feature in obtaining high fusion performance plasmas and also in being able to demonstrate long-pulse (20s) plasma operation. These latter discharges, which were heated throughout by NBI, achieved steady-state equilibrium values of all significant parameters (density, temperature, impurity content, and current profile);
- The NBI Testbed has continued to play an essential supporting role in NBI operations via the pre-testing of PINIs. New methods of diagnosing the optical properties of the beams has resulted in a reassessment of the operation of the injectors, which may open up the possibility of further enhancing their performance. Tests of beryllium-clad high heat flux components have established that the limiting value of heat flux of up to  $18\text{MWm}^{-2}$  appears to be governed by the strength of the beryllium metal itself and not the brazed joint between the beryllium and the water-cooled CuCrZr high heat flux element;
- Work relating to the provision of up to 12MW of tritium neutral beams for the next D-T experiment is presently being planned.

Details are given in the following sections.

### **Neutral Beam Operations**

The major work has related to the recommissioning of the two injection systems and their subsequent operation to meet the heating power requirements for the experimental programme. Both tasks were accomplished successfully and the neutral beam system operated on nearly every day of the 1994 campaign.

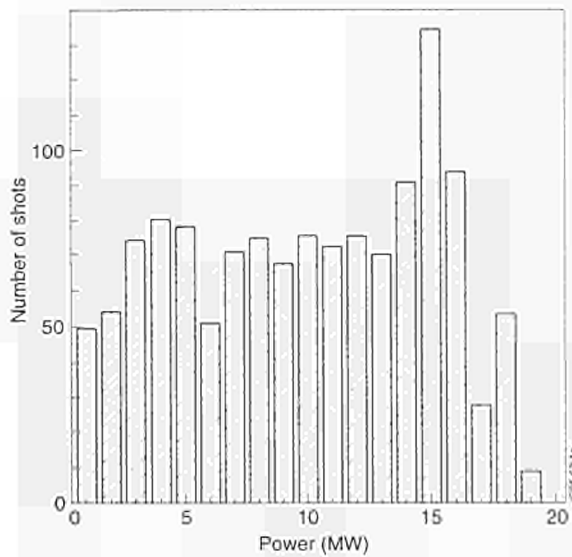


Fig.26: Histogram of injected power during 1994.

Recommissioning of the system involved bringing the injectors up to routine operation at high power, as well as commissioning the new remotely operated vertical and horizontal steering systems for each of the positive ion neutral injectors (PINIs), which provide the eight beams integrated within each injector. The new vertical steering facility allowed the NB power deposition profiles to be optimised for the upwardly shifted plasma equilibria, characteristic of the pumped divertor phase of operation.

In addition, the new extended protection assemblies for both the neutral beam drift injection ducts were commissioned together with their extensive thermocouple instrumentation. This extended protection allowed safe injection of neutral beams down to plasma currents ~1MA, compared to previous campaigns, where injection had been limited to  $\geq 1.5$ MA. This proved invaluable in the programme of high  $\beta_p$  experiments.

The configuration of the NB system installed for the 1994 campaign consisted of one 'high voltage' injector with eight beam sources (PINIs) in the 140/160kV triode configuration and one 'high current' injector with eight 80/85kV PINIs in the tetrode configuration. The high voltage injector routinely delivered up to 7.8MW to the plasma (~5% above the original design value) whereas the injected power level of the high current injector was progressively increased up to 11.5-12MW (50% above the original design value).

Although at the start of the campaign, this beamline was equipped with eight modified high current PINIs, which deliver ~55A of ion beam, two were replaced with

Table X: Statistics on NB Power to JET 1988-94

Year	No NB Pulses	No pulses $P \geq 15$ MW	% $P \geq 15$ MW	Max. <sup>†</sup> Power (MW)
1988	993	100	10.1	21.0
1989	621	99	15.9	18.5
1990	813	72	8.9	18.5
1991	1265	78	6.2	17.5
1992	339*	12	3.5	17.5
1988				
-1992	4031	361	9.0	-
1994	1313	325	24.8	21.0

\*Dominated by low-neutron yield experiments

<sup>†</sup> Maximum installed power has varied from year-to-year due to the varying mix of 80kV and 140kV PINIs

80kV PINIs in the original 'standard' 43A configuration due to relatively minor faults, which appeared during the early phases of the experimental campaign. High current PINIs will be re-installed during the planned shutdown in 1995. Safe operation of the injector at power levels in excess of 50% of the design value has only been achieved by paying great care to beam alignment and optics and by a continuing assessment of the safe levels of power and

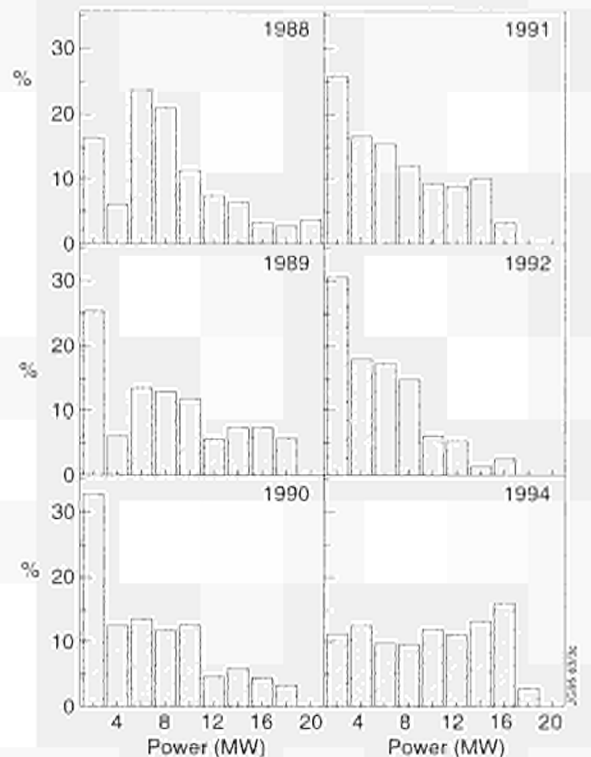


Fig.27: Comparison of 1994 power with previous campaigns

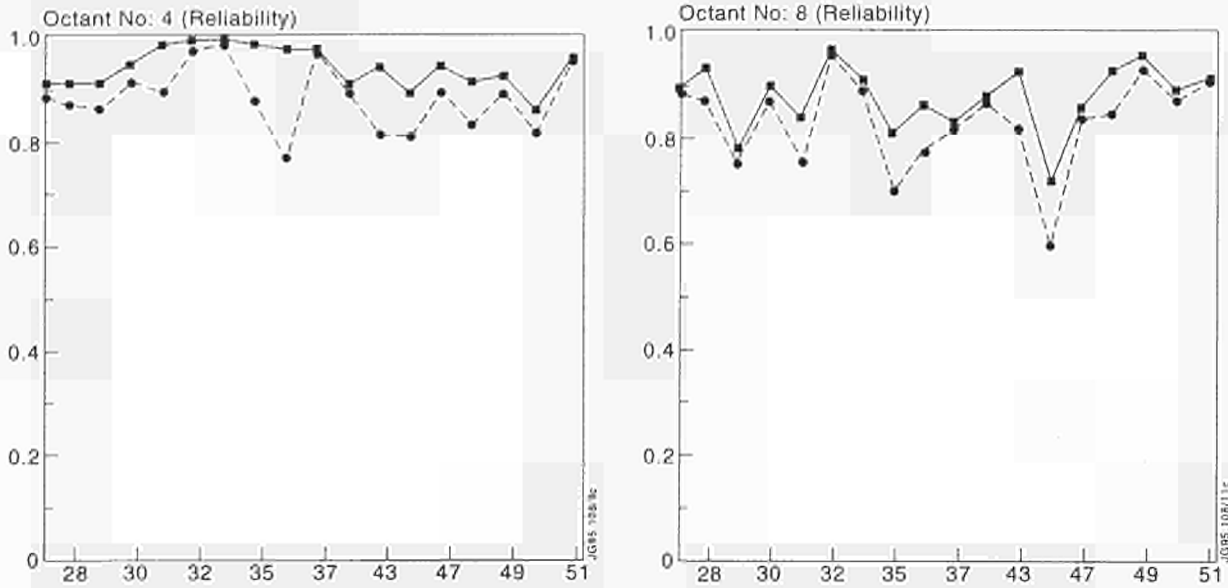


Fig.28: Measured reliability of (a) Octant No. 4 and (b) Octant No. 8 injection systems

power density intercepted by various beam defining scrapers and other components.

This work, combined with recent results from the Testbed, has led to a new insight of the beam optics, which could lead to enhanced efficiency of the injectors and even higher power levels delivered to the torus (>13MW from the high current injector).

### Operational Statistics, Power Delivered, Reliability and Availability

The overall statistics for power injected into JET with the NBI system are shown in Fig.26 and also Table X, compared with previous campaigns (1988-1992). The NBI system was more heavily used in 1994 than any previous year and the proportion of pulses at high power (one quarter of all pulses) exceeded previous campaigns. Figure 26 shows that the spectrum of injected power was nearly uniform up to 16MW, reflecting the wide variety of experiments, in which the NB system was used, and not a shortfall in performance. Above 16MW, the number of pulses is reduced as the system only attained these power levels reliably from October onwards.

Comparative performance of the NBI system in the campaigns of 1988-1994 is shown in Fig.27, where it is evident that the system now performs much more routinely at high power levels. As in previous campaigns, the system reliability and availability have been closely monitored, where reliability is defined as:

$$R = [\text{Energy injected during pulse (MJ)} / \text{Energy requested before the pulse (MJ)}] \times 100\%$$

Levels of  $R > 85\%$  were obtained throughout the campaign on both injectors. A high value of  $R$  is a clear prerequisite for the efficient execution of the experimental programme. The system reliability in 1994 is shown in Fig.28. The reliability of the system was uniform as a function of the requested power (ie, number of PINIs). There was no significant difference between the high voltage and the high current injectors.

The availability of the system (SA) is defined as

$$SA = [(TS - \sum(FD_i \times FS_i)) / TS] \times 100\%$$

where  $TS$  = total duration of operational shifts and  $FS$  is the fraction of the injector not available for a time  $FD$ . The availability exceeded 90% throughout the campaign and equals the levels achieved in previous years.

### Long Pulse Injector Operation

The neutral injectors are designed for a nominal 10s pulse length. Although this facility has been available for many years, pulse lengths of >3s have been used rarely due to the problems of handling the injected power, when it exits from the plasma. This limitation to long pulse, high power, additionally heated plasmas is exemplified by the phenomena of the so-called carbon bloom due to limitations in the previous divertor targets (prior to 1992). This problem has now been eliminated by the improved Mark I divertor target tiles combined with sweeping of the strike points. Consequently, the use of high power NBI for long pulse lengths has become a much more common feature of the programme. NB pulse lengths up to 20s were obtained using combinations of 10s pulse lengths on

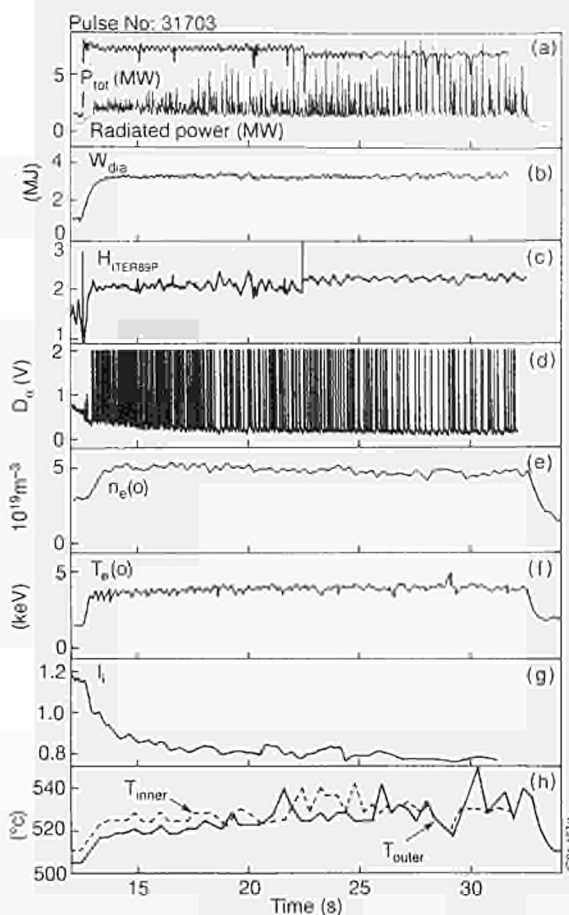


Fig.29: Overview of long pulse NBI to produce steady-state ELMy H-mode plasma

different groups of PINIs. The record NBI pulse duration of 20s at ~6.5 MW, injected into an X-point plasma, is shown in Fig.29.

### Neutral Beam Engineering

Following successful completion of the major shutdown activities, completed on schedule, a wide range of engineering development has been carried out to meet the future needs of NBI for the programme. Experimental and theoretical studies of the brazing of beryllium cladding to CuCrZr high heat flux elements have brought this important technological study to a successful conclusion.

### Support Activities

The major aspects are summarised, as follows:

- Definition of operational limits of beamline components in view of enhanced injector performance, reconfiguration and exchange of PINIs;
- Manufacture of components for cryogenic forevacuum system for the torus; and installation and modification

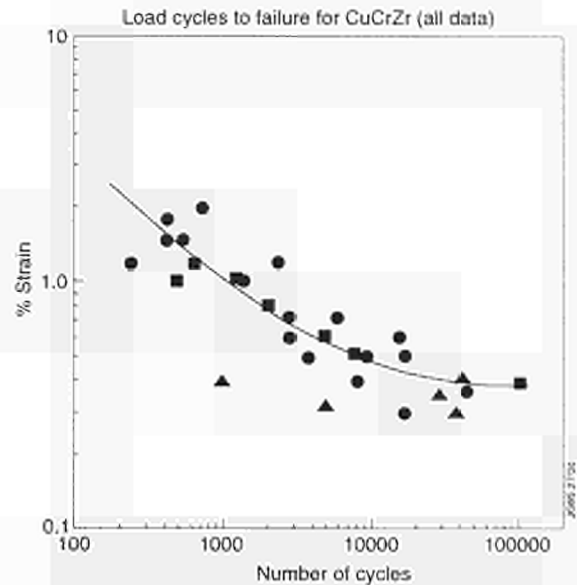


Fig.30: Measured fatigue failure of CuCrZr alloy used for beamline components

of cryo-transfer lines for the divertor and injector cryopumps;

- Design, manufacture, assembly and instrumentation of test assemblies for high heat flux tests in the Testbed and the installation of a new beryllium-compatible test facility;
- Extensive detailed computations to predict the operational safety limits of the in-vessel pumped divertor cryopump and surrounding in-vessel components under normal and abnormal operation scenarios. Good agreement has been obtained between the model predictions and experimental measurements obtained under defined conditions.

### Engineering Development

The intensive use of the injection systems at power levels 50% above their original design values has led to a reappraisal of the fatigue life of injector components. In particular, the beamline calorimeter and the water-cooled accelerator grids have been identified as the components most at risk from fatigue.

### Beamline Calorimeter

Figure 30 shows the experimentally determined cycles to failure as a function of percentage strain for the CuCrZr alloy which is used for the manufacture of all high heat flux hypervapotron elements in the beamlines. The data were obtained as part of the manufacturing contracts for the existing components by two differing manufacturers.

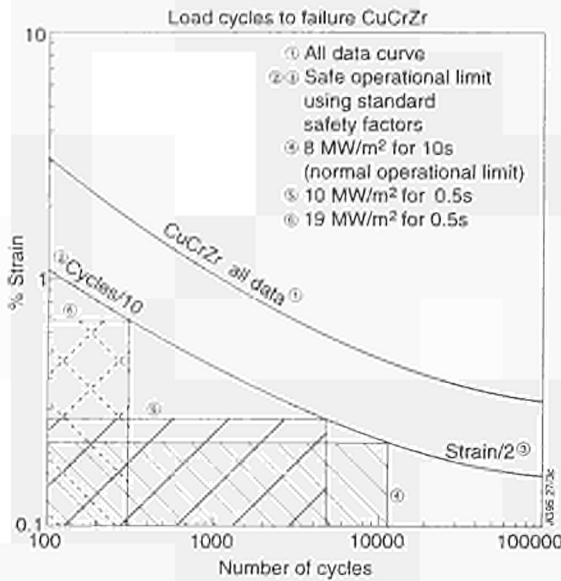


Fig.31: Derived safe operating region against fatigue failure, showing strain values derived from measured operating conditions of the present injectors

The majority of data was obtained using test samples with dimensions well in excess of the grain size of the material but the lower values (D) refer to tests on samples having a large grain structure (comparable to the sample size).

The fit to the data is replotted in Fig.31 together with the derived curve corresponding to normally accepted engineering limits placed upon fatigue data: (ie, cycles x 0.1 and strain x 0.5). The various shaded areas on Fig.31 correspond to strain data computed from injector operation at differing measured values of power which have been intercepted by the calorimeter during the 1994 campaign. Clearly, the values of strain imposed by the enhanced beamline performance, which is comparable to that which is to be expected for tritium operation at 160 kV, leads to an unacceptably low safety margin against fatigue failure. Even the values of strain resulting from the lower power high-voltage operation give rise to concern in the context of the accumulated cycles to date and continued operation at the present intensive level irrespective of future scenarios using tritium.

Consequently, a new design of calorimeter has been undertaken as a matter of urgency for installations during the shutdown planned for mid-1995. Although the hypervapotron cooling technique developed to accept power densities near  $20\text{MWm}^{-2}$  in continuous operation, chosen a system has been based upon thermal inertia with interpulse cooling in the interests of time and cost.

The existing beamline calorimeter support structure and actuating mechanism will be retained and the existing

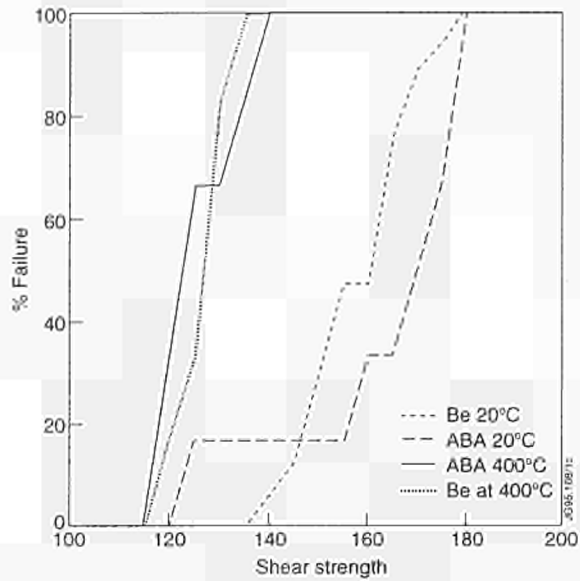


Fig.32: Measured shear strength of test samples of pure Be compared to that of identical samples of Be brazed to CuCrZr. Shear test data obtained at 20°C and at 400°C

hypervapotrons (limited to  $10\text{MWm}^{-2}$  for continuous operation) will be replaced by inertial elements capable of accepting  $20\text{MWm}^{-2}$  for a 1s pulse length. An innovative feature is the use of copper, which is explosively bonded on to stainless steel. This results in a much enhanced stiffness and hence reduced bending of the elements during operation. In addition, the requirement for brazed joints is completely eliminated since the interpulse cooling water, which will be carried in the stainless steel, will be of an all-welded construction.

**Brazing of Be to CuCrZr**

The limiting values of heat flux of up to  $18\text{MWm}^{-2}$  have been obtained for castellated beryllium tiles brazed on to CuCrZr hypervapotrons. In the course of demonstrating the transfer of this technology successfully to another industrial firm and hence demonstrating its potential as a viable manufacturing technology, considerable insight and understanding of the limiting performance has been gained. The findings are supported by extensive computational and theoretical analyses.

Further tests of uncastellated 2mm tiles again resulted in failure of the brazed joint at a power density of  $\sim 18\text{MWm}^{-2}$ . However, it was observed that the failure of the brazed joint occurred during the cooldown of the element 350ms after the high power density beam had been switched off. This is the result of plastic deformation on the surface of the tile during the high power beam pulse, which after a small number of cycles increases the

stress in the Be at the interface, subsequently resulting in fracture of the joint. The results of mechanical shear tests of braze samples for two test temperatures are shown in Fig.32 where the percentage failure refers to the percentage of the number of samples tested (typically ~6), which failed at a given value of applied stress. Also shown are data obtained using identical samples composed of solid beryllium which exhibits behaviour remarkably similar to that of the brazed joint. Visual examination of the surfaces of sheared joints revealed in some cases flakes of Be metal still attached to the braze. Surface analysis of the surfaces confirmed the presence of beryllium on the sheared joint.

Taking together the striking similarity of the behaviour of the brazed tiles and the shear results shown in Fig.32, it could be concluded that the brazed joint strength is limited to the yield strength of the beryllium itself. Therefore, this would highlight the importance of the choice of beryllium grade as a critical factor for brazed components.

Finite element computations have been carried out to examine the role of the unavoidable pre-stressing of the system by the brazing process itself. In addition, the dependence of the stress at the joint as a function of the thickness of the beryllium has also been studied. It is concluded that the design of beryllium-clad structures is a compromise between the beneficial effect of castellating the front surface of the Be, to reduce the stresses due to plastic deformation, and the deleterious effect of the notch at the base of the castellation leading to enhanced local stresses.

### *Duct Protection*

Extra duct protection has been designed to enable safe operation of the injectors at low values of plasma current (~1MA) used for high- $\beta$  experiments, over a much wider range of plasma configurations than is available at present and also for 160kV tritium reionisation products, due to their greater stiffness. Since this protection is in a region beyond that which can be introduced from the exterior of the torus (due to the shape of the JET large port), an additional assembly which must be installed from inside the vacuum vessel is required. A compact system of copper tiles mounted on an inconel sub-frame will be installed during the 1995 shutdown. The extended protection relies upon the thermal capacity of the tiles to absorb the energy during an injection pulse and this is subse-

quently emitted by radiative cooling during the interpulse period. Thermocouple instrumentation will be routed via feedthroughs in the middle port adapters, one of which is being replaced to provide access for a new plasma diagnostic.

### *NBI Work in Support of ITER*

A limited effort has been devoted in support of neutral beam activities for ITER. Conceptual designs for the following components have been supplied under contract for ITER.

- Alignment of the NBI vacuum vessel-duct-torus interface to handle the large dimensional changes when the cryostat is cooled;
- Fast shutter, including a proposal for a magnetic actuator;
- Outline of a calorimeter drive mechanism;
- Electrostatic beam dump;
- Suggested overall concepts for the injector layout/assembly.

Some work related to the brazing of Be to CuCrZr has been carried out to fulfil ITER requirements for thick ~10mm Be cladding.

### **Neutral Beam Testbed**

The NB Testbed has executed a full and varied programme in support of the injectors installed on the tokamak and in preparation for operation with tritium planned for 1996. Tests and developments related to high heat flux components for divertor and first wall applications have continued to produce interesting and relevant results. In addition, the development of new beam diagnostic systems has led to a deeper insight into the beam optics of the PINIs and this may lead to increased injected power combined with reduced power loading on the beamline components of the injectors.

### **Infra-red Calorimetry**

The footprint of the beam sources can be visualised by infra-red thermography on a high conductivity unidirectional carbon fibre composite (CFC) target. This novel technique has a resolution of approximately  $2 \times 2\text{mm}^2$  on a  $200 \times 400\text{mm}^2$  target and allows the diagnosis of structure in the beam alignment and steering, not visible with the previously available conventional calorimetric technique. Figure 33 shows the power density contours of a helium beam, which is measured 8m from the beam

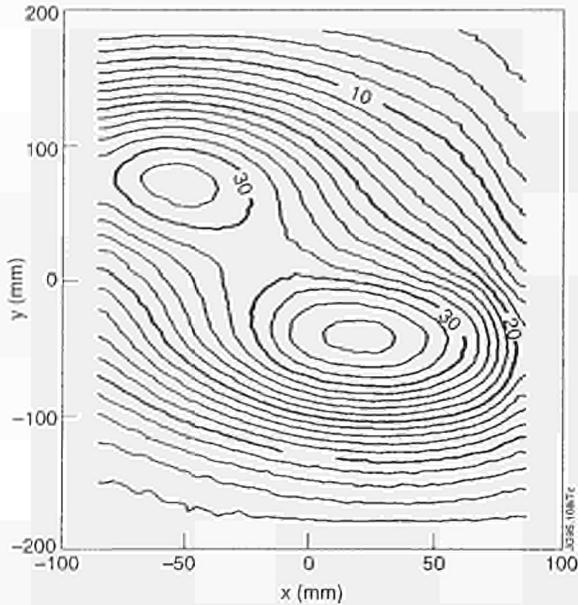


Fig.33: Contours of constant beam power density. The two areas of peak power density correspond to beams from each half grid. The horizontal displacement reveals previously unobserved differences in the axes of the two beams

extraction plane. Particles from the two separate grid halves of the beam source are clearly separated and of particular importance is the difference in the alignment of the beams from the two grid halves which results in the considerable shift of the beam centres, seen in Fig.33. This misalignment can lead to unacceptable power loadings on beam scrapers and also higher power density on the full energy beam dumps. A new support structure for this diagnostic is being manufactured to allow this measurement to be made at varying distances from the beam extraction plane, in order to measure any serious misalignment at the locations corresponding to the beam scrapers in the injectors.

### Doppler-shifted Balmer- $\alpha$ Spectroscopy

Doppler-shifted Balmer- $\alpha$  spectroscopy has been used in the past to measure the species composition of the extracted beam. By adding a two-dimensional CCD detector array and optimising the optical train, the resolution and the sensitivity of the system have been greatly improved. Spectra can now be obtained under all operating conditions with excellent signal-to-noise ratio and with full separation of the individual beam components, as shown in Fig.34. The improved sensitivity is such that this can now be used to quantify the isotopic exchange in the ion source when the operating gas is exchanged and can even measure the release of one implanted isotope by

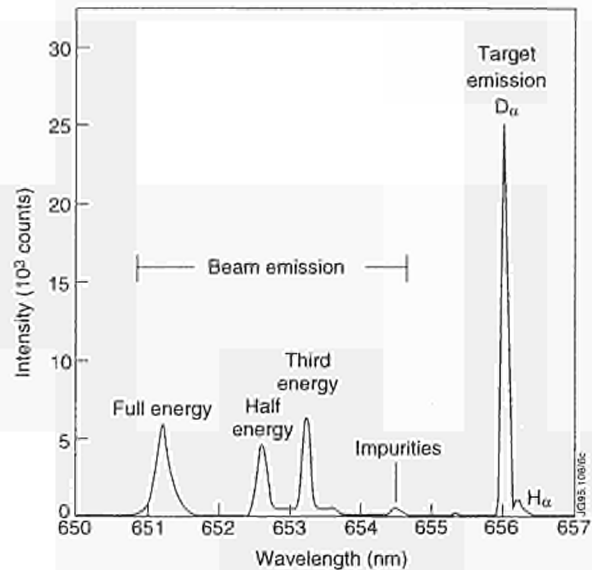


Fig.34: Typical output for the improved beam emission spectrometer

another from the beam dump. Both of these applications are highly relevant for the preparation for tritium neutral beam injection.

The improved resolution allows the local divergence of the differing beam species to be obtained using the measured line width. This suggests an extremely powerful application, since it can be used to measure instantaneous values of divergence and perveance-match independently of beam transmission. The spatial resolution of these measurements is such that a multi-channel version will be used to measure the spatial variation in the beam divergence due to possible plasma non-uniformities in the ion source.

The use of these two new high resolution beam diagnostic systems will provide much more detailed information on the optical properties of the beams than available previously. This offers the possibility of enhancing the power delivered due to improved injector efficiency.

### Component Tests

Operating parameters of the Neutral Beam Testbed (heat flux  $3\text{--}100\text{MWm}^{-2}$ , pulse duration 20ms - 20s, exposed area  $400 \times 300 \text{mm}^2$ ) make this the most powerful facility available in Europe for testing high heat flux components. The facility has been used to test large area CFC components such as the NET divertor prototype module or the full-sized Mark II divertor module ( $400 \times 160 \times 40 \text{mm}^3$ ) using two beams.

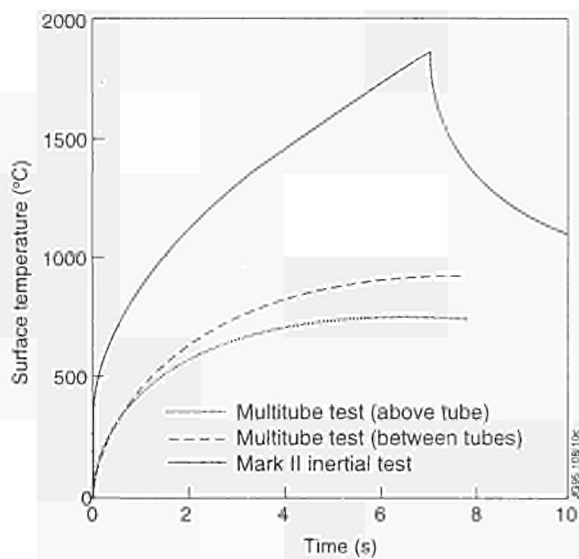


Fig.35: Measured surface temperature of cooled and uncooled CFC tiles

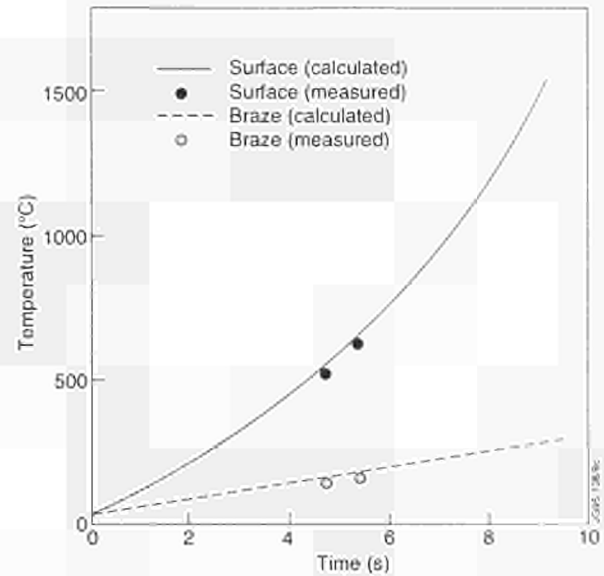


Fig.36: Surface temperature of 10mm thick Be brazed onto CuCrZr hypervapotron versus incident power density

### CFC Components

Very promising results have been obtained on CFC blocks which are actively cooled by six parallel OFHC tubes (three with swirl type inserts). Tests were performed on three  $155 \times 200 \text{ mm}^2 \times 36 \text{ mm}$  thick two-dimensional CFC blocks (Dunlop DMS 704 and SEPCARB N11) with peak beam power densities in the range  $5\text{--}20 \text{ MWm}^{-2}$  and with water flow velocities ranging between  $3\text{--}6 \text{ ms}^{-1}$ . The results of these tests can be summarised as follows:

- CFC material could be successfully bonded to an OFHC tube in the large area multitube configuration. Surface temperature distribution was uniform although some hot spots originating from poor contact between the tubes and CFC material were visible. No evolution of these hot spots was observed after long beam exposure;
- Thermal equilibrium was reached after  $\sim 6 \text{ s}$  and the cooling effect of the tubes could be observed after  $\sim 1 \text{ s}$  (Fig.35). Since the measured surface temperatures were much lower than those measured for an inertially cooled tile, this would result in much lower mechanical deformation of the structure;
- The swirl tube inserts and the water flow velocity did not appear to have a major effect on the cooling.

### Beryllium Components

It has been established that the limiting critical heat flux for 2mm thick brazed beryllium tiles is  $\sim 20 \text{ MWm}^{-2}$ . An endurance test of 1000 cycles (temperature ramped be-

tween room temperature and  $600^\circ\text{C}$ ) has been performed successfully and the tiles show no signs of fatigue cracks due to the ductile-brittle transition of beryllium which occurs at  $\sim 100^\circ\text{C}$ . Tiles of 10mm thickness have been tested at power densities of up to  $6 \text{ MWm}^{-2}$ . From these measurements, it can be derived that surface melting will occur at power densities above  $8 \text{ MWm}^{-2}$  (Fig.36). Figure 37 shows the measured surface temperature of a 10mm thick beryllium tile versus time for an incident flux density of  $5.9 \text{ MWm}^{-2}$ . From this, it is estimated the time to melt the surface for differing assumed values of the incident power density (eg for  $20 \text{ MWm}^{-2}$ , which is an ITER design value) surface melting would occur in less than 2s for a 10mm tile bonded to a vapotron cooled with room temperature water.

### Use of a Defrosting Technique to observe Braze Integrity

A method to test the braze integrity is of paramount importance for the application of armour tiles attached to actively cooled heat sinks, if they are to be applied for divertor or first wall components. A simple test has been developed, which can be carried out without the use of sophisticated equipment. The component is cooled to a temperature of  $-15^\circ\text{C}$ . When subsequently exposed to humid air, the test section covers with a white frost and when room temperature water is subsequently made to flow through the cooling channels, the test section heats up and the frost disappears when the surface passes

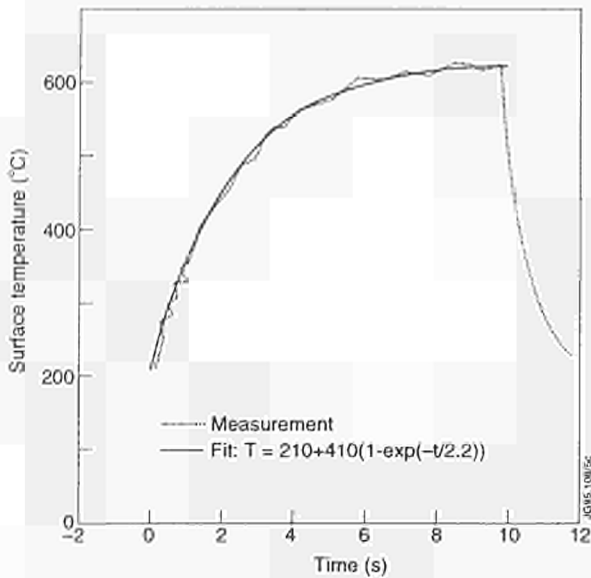


Fig.37: Surface temperature of 10mm thick cooled beryllium as a function of time. Incident power flux is  $5.9\text{MWm}^{-2}$

through  $0^{\circ}\text{C}$ . This defrosting process is easily recorded using a video camera. A reduced thermal contact of the surface with the heat sink is immediately obvious due to a delay in the defrosting. This test in practice has shown agreement with the results from tests using high power exposure on various components.

## Cryogenics

1994 has been a particularly intensive period for the cryogenics work in view of the much increased demands within the Project. The new helium refrigerator/liquefier was commissioned and became fully operational by mid-1994. The two new cryopumps installed during the major shutdown have also been brought into full operation and have made a significant contribution to the experimental programme.

The LHCD cryopump has proved to be essential for conditioning the launcher and subsequent successful operation of the LHCD system at high power, but the in-vessel pumped divertor cryopump has had an even greater positive impact on operations and is now routinely required for essentially all aspects of the programme. In particular, this pump has been essential in obtaining plasmas with the highest fusion performance, in addition to its originally foreseen role of allowing quasi-steady-state (20s) duration pulses. The on-going commissioning of the active gas handling system (AGHS) now requires regular supplies of liquid helium in addition to those required for the long-standing users (eg. pellet and neutral

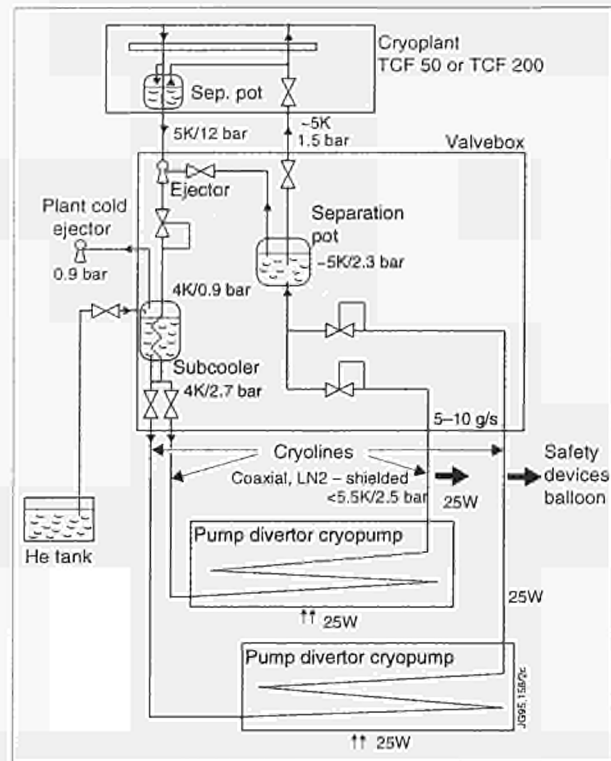


Fig.38: Schematic of supercritical helium loop for pumped divertor cryopump

beam testbeds and the pellet and neutral beam injectors in the Torus Hall).

## Torus Cryopump and Supercritical Loop

The supercritical helium loop used to supply the pumped divertor cryopump is shown schematically in Fig.38. The basic flow from the refrigerator of  $\sim 6\text{g/s}$  is enhanced by the use of the cold ejector to give a total available flow of supercritical helium  $\sim 16\text{g/s}$ . Prior to connection to the in-vessel pump, the loop and the new refrigerator were commissioned "off-line" using a spare quadrant of the cryopump installed adjacent to the cryoplant. This "cryo-testbed" incorporated an electrical heater to allow absolute calibration of the heat input into the cryo-loop and also the performance of the supercritical loop. Figure 39 shows data obtained from this test loop: the slope of the curve yields a mass flow rate of supercritical helium of  $\sim 17\text{g/s}$  and the intercept for zero enthalpy difference between the input and output to the pump gives the thermal heat load to the helium structure of  $\sim 18\text{W}$ . This value is somewhat higher than results from the measured temperature increase of cold gas flowing in the cooling tubes, which have been obtained during acceptance tests. The in-vessel pump was connected to the cryoloop in July and, following a relatively short period of commission-

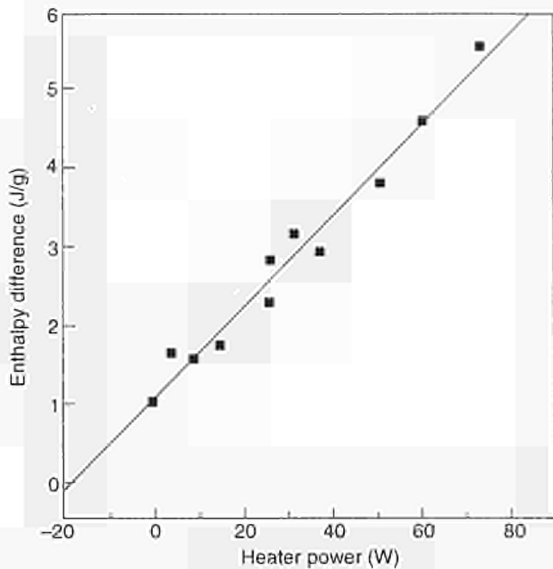


Fig.39: Measured performance of supercritical loop using cryo-test loop. Enthalpy difference is that calculated from measured temperature difference between input and output at measured value of pressure of supercritical flow

ing, entered routine operation. Figure 40 shows the decay of the torus vacuum pressure following the introduction of gas pulses of deuterium which is cryocondensed, followed immediately by a similar pulse of helium gas which is not pumped by cryocondensation. The decay of the torus pressure yields an effective pumping speed of  $\sim 200,000 \text{ l/s}$  for the divertor structure plus the cryopump. This should be compared to the calculated speed of the naked cryopump itself of  $\sim 500,000 \text{ l/s}$ . In operation, the pump has proved to be resilient to all plasma operation scenarios and is unaffected by plasma disruptions.

Although helium gas is not pumped by cryocondensation, it can be pumped using cryosorption onto a pre-deposited layer of argon frost. This technique has previously been used successfully in the neutral beam injectors and will be applied to the torus cryopump using an argon spray system integrated into the liquid nitrogen cooled chevron structure of the pump. Commissioning of the dedicated argon gas introduction system is well advanced.

### LHCD Cryopump

Following preliminary operation to confirm satisfactory performance, this pump was installed onto the torus at the beginning of the year and brought into routine operation by mid-1994. The pump has proved to be a necessary prerequisite to obtaining high power operation of the LHCD system. The performance of the pump, measured

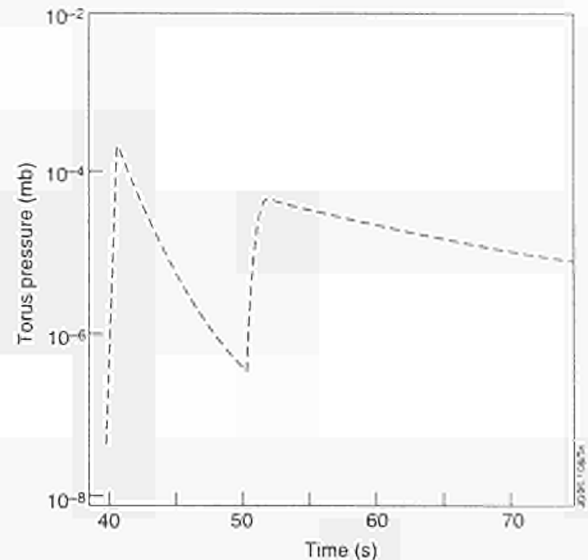


Fig.40: Measured decay of torus pressure as function of time for gas puff of  $D_2$  followed by identical puff of He. The two traces correspond to gauges in differing locations in the torus. Only one half of the cryopump was in operation

during the limited time available for acceptance tests, conforms to the design values. Figure 41 shows data obtained prior to installation on to the torus which demonstrates that the pumping speed is  $\sim 90,000 \text{ l/s}$  compared to the design value of  $\sim 100,000 \text{ l/s}$ . The pump has demonstrated continuous and stable operation for periods of several weeks, including periods of overnight helium glow discharge cleaning. Regeneration of the pump during glow cleaning is prevented by isolating the cryopump from the torus using the 1m diameter regeneration flap which effectively seals the input of the pump from the torus. Any minor leakage of helium gas from the torus into the pump is cryosorbed by the charcoal at 4.2°K which was incorporated as a design feature of the pump.

### Preparations for DTE I

Following the successful introduction of tritium using NBI for the replacing deuterium-tritium experiment (PTE), preparations are underway for a more extensive use of tritium NBI in the next deuterium-tritium experiment (DTE I). This experiment is scheduled for the end of 1996 and the various aspects of the NBI-related work are again being carried out. Provisions are being made to convert all 16 PINIs to full tritium operation. The existing 140kV configuration which will be operated at 160kV in tritium should deliver  $\sim 12.5 \text{ MW}$  of  $T^0$  beams into the plasma (compared to the 1.5MW used in PTE). The high current 80kV injector is viewed principally as a deuterium injec-

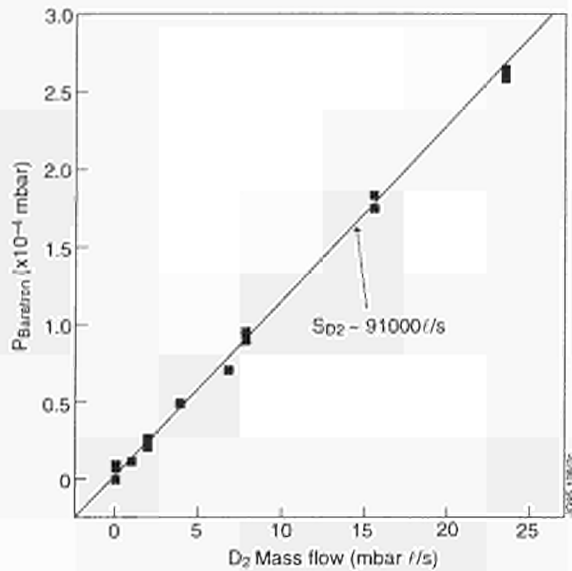


Fig.41: Determination of pumping speed of LHCD cryopump for deuterium

tor for these experiments, but nevertheless it will also be made fully compatible for 80kV operation in tritium as a fall-back option should the need arise. Progress is summarised as follows:

### PINI Conversion for full D-T operation

This entails modifications to the gas introduction feed developed previously for PTE and enables the source plus the neutraliser gas to be introduced by a common single feed at earth potential. In addition, water drainage points have to be provided to handle tritiated water in the event of a water leak developing during tritium operation. Each PINI requires a total of 90 QA Class 1 welds to be carried out during their conversion in addition to replacement of elastomer by metallic seals and the over-wrapping of the large PINI main insulator by glass fibre reinforced epoxy.

Each refurbished PINI is operationally tested and fully characterised in the NBI Testbed prior to being installed on the tokamak injectors. Present planning calls for all 16 PINIs in the Torus Hall to be fully converted before the end of 1995. Four fully tritium-compatible sources have already been installed to gain operation experience during the 1995 on-going experimental campaign.

### Tritium Gas Introduction

The tritium gas for the injectors will be provided by and returned to the AGHS system. To meet the requirement for mixed D and T operation within one injector, the gas

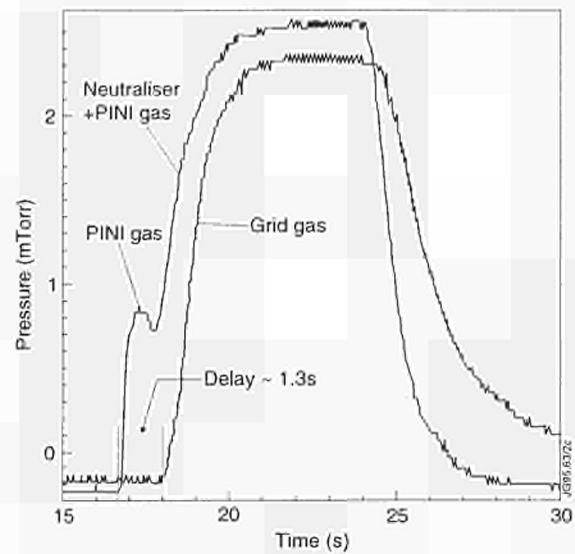


Fig.42: Measured operational response of simulated  $T_2$  gas introduction system compared to that of "standard" system using separate feed for plasma source and neutraliser

introduction system is now in the final stages of detailed design. It will allow any pair of PINIs (coupled via the common beam deflection magnet for each quadrant) to be operated with either  $D_2$  or  $T_2$  as the working gas. This will enable injection at full power with varying fuelling ratios of deuterium to tritium in the JET plasma.

An identical system will be provided for the 80kV injector as a fall-back option. The mechanical design for these systems and the associated double containment vessels are already well advanced in preparation for installation during the 1995 shutdown. The outline of the control and interlock system is essentially defined with an emphasis on fail-safe operation. The long pipe runs supplying the gas from the AGHS Building to the control valves, pressure regulators etc and the large distance from this system to the PINIs, leads to an unavoidably distributed system whose performance in terms of time constants is difficult to predict accurately. Hence, a complete simulation of the pipe runs has been carried out in the NB Testbed, in conjunction with an operating PINI in order to measure the overall system response. This is illustrated in Fig.42, where the pressure response is shown for the normal combination of source plus neutraliser gas and the "grid gas" configuration which corresponds to that for  $T_2$  operation.

The measured time delay of  $\sim 1.3s$  and time to equilibrate of  $\sim 1s$  are both acceptable and can be accommodated in the overall timing/control system.

## Cryosystem

The impact of DTE 1 on the cryosystem is relatively minor and is limited to minor changes to the system handling the boil-off from the LN systems. The boil-off gas will be routed via the Torus Hall to allow the short-lived activity produced during a D-T pulse to decay and also to act as a fire suppression system for the Torus Hall.

The torus and injector cryopumps will utilise a forced regeneration scenario in order to minimise the overall time for returning tritium to the AGHS and to eliminate cold spots which could retain condensed tritium. This forced regeneration has already been adopted as the routine mode of regeneration of the cryopumps to gain operational experience.

## RF Heating Systems

JET is equipped with two different high power radio frequency systems: the Ion Cyclotron Resonance Frequency heating (ICRF) and the Lower Hybrid Current Drive (LHCD) systems. In addition, a new low power system exciting Toroidal Alfvén Eigen-modes (TAEs) is being built. Each system has very distinctive roles.

The ICRF heating system is used for high power centralised heating of the JET plasma, with the capability of producing Fast Wave Current Drive (FWCD) with the new A2 antennae. The localisation depends mainly on the magnetic field and is insensitive to parameters such as density and temperature. Wide band operation between 23-57 MHz allows variation in both the choice of minority ion species heated and the localised position of the heating. So far with the previous A1 antennae, up to 3.5MW on one antenna and 22.7MW total coupled power for 2s have been achieved. Preliminary experiments on Fast Wave Ion Current Drive have been successful showing that the plasma current gradients near the  $q=1$  surface were modified by changing the phase between straps of the antennae. New ICRF antennae have been installed and optimised to the geometry of the divertor plasmas. Their location in the torus has been revised to give four arrays of two adjacent antenna. Each array has four RF radiating conductors, or straps, which provide an enhanced radiated spectrum. Variation in the relative phase of the RF currents in the straps allows this spectrum to be varied for both heating and current drive experiments. In addition, the control electronics has been completely rebuilt to allow operation with four straps closely coupled and to improve the reliability of the ICRF plant by

reducing the cross-talk between modules. The start of operations has been made difficult by the fact that both the control electronics and the antennae are new systems and have required large commissioning time. Several problems have been identified and remedial action has been taken. In spite of these early difficulties, a record power of 13.5MW has been launched in a divertor plasma, compared to 12MW in X-point plasmas in the preceding campaign.

The LHCD system operates at 3.7GHz and is capable of driving a significant fraction of the plasma current. This is achieved by launching an RF wave predominantly in one toroidal direction. This wave accelerates the high energy electrons in the plasma and so drives a current. It may be used to stabilise sawtooth oscillations, thereby increasing central electron temperatures. It is the system on JET for controlling the plasma current profile which is considered to be the main tool to stabilise high beta poloidal plasmas with a large proportion of bootstrap current, the so called advanced tokamak scenarios but it can also be used to optimise JET performances. With a prototype launcher, LO, up to 2.3MW of LHCD was coupled to the plasma. Full current drive was demonstrated in 2MA low density plasma. This prototype has provided engineering, operational and physical experience of LHCD on JET on a variety of plasma configurations. An upgraded launcher, L1, was installed in 1993. Launched power in excess of 5MW have been produced and full current drive of plasmas up to 2.5MA have been achieved. Performance can still be increased up to, the maximum design launched power of 10MW.

The TAE will excite Alfvén Eigen-modes (AE) which are discrete global modes of Alfvén waves in confined toroidal plasmas. In particular, AE appear in the frequency gaps for shear Alfvén waves corresponding to toroidicity, ellipticity or triangularity induced harmonic coupling (whence, the denominations TAE, EAE, ...). Modes based on finite  $\beta$  coupling between Alfvén and sound waves also exist in the Alfvén frequency range ( $2\pi f \sim v_A/2qR$ ) with  $f$  ranging for the different TAE and EAE from 20kHz to 500kHz. AE have been predicted to be of fundamental importance in tokamak reactor relevant conditions, since these can be destabilised by fast particles (such as fusion produced alpha-particles) and, in turn, may expel fast particles from the plasma core via resonance wave-particle interaction. The saddle coil antennae in JET, in conjunction with the ICRF and NBI

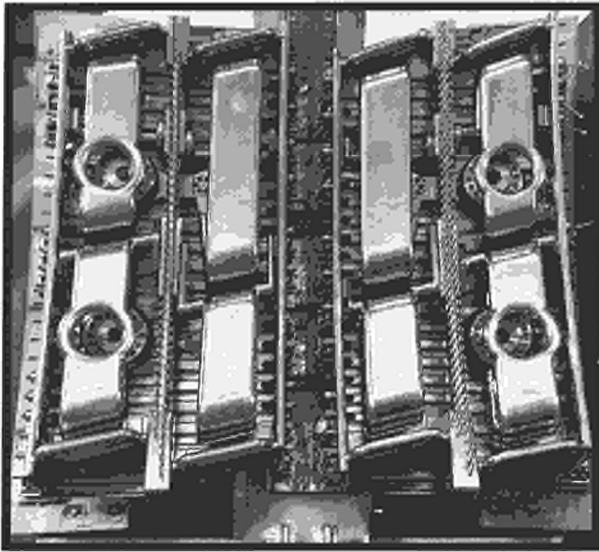


Fig. 43: The new A2 antenna

heating methods, offers the unique possibility of exploring in a systematic way the importance of these modes, which can be excited in a controlled way by a devoted RF system, the TAEE system. This system has been brought successfully into operation within the framework of a Task Agreement with CRPP-Lausanne, Switzerland. The excitation of TAE modes has been assessed and a large data base of AE activity and damping rates has been collected and are being analysed.

## ICRF Technical Achievements

### *Ion Cyclotron Heating*

JET has a powerful and highly versatile ion cyclotron resonant heating system with the potential for delivering up to 24MW of power to the plasma. The operating frequency range is 23MHz to 57MHz which allows fundamental heating with hydrogen, deuterium, He<sup>3</sup> and He<sup>4</sup> minority ions, and second harmonic heating with hydrogen, deuterium, tritium and He<sup>4</sup> ions. The power deposition can be made on-axis or off-axis depending only on the ion species and the ratio of the frequency to the magnetic field. The fast magnetosonic wave excited by the antennae can access dense plasmas and so there is no difficulty in providing central heating at high densities relevant to reactor operation. The antennae are multi-strap units in which the currents can be phased to launch waves either with no net toroidal directivity for heating purposes, or with up to 75% toroidal directivity for both ion and electron current drive applications.

During the shutdown, the ICRF system was equipped with a new set of four antennae specifically designed to

match the geometry of the divertor plasmas. As shown in Fig.43, these A2 antennae have four phase-coherent current straps which produce better defined  $k_{\parallel}$  spectra and are three times narrower than those excited by the old A1 antennae. There is also a wider choice of spectra available for heating since  $0\pi/0\pi$ ,  $0\pi\pi/0$ ,  $00\pi\pi$  and  $0000$  phasings are all possible compared with only dipole and monopole phasings with the A1 antennae which had only two straps. The four current straps of the A2 module are electrically coupled both inductively and capacitively. This complicates the matching procedure since the impedance that each strap presents to the feed lines depends on the voltage and phasings applied to the other straps. Thus all four straps must be tuned simultaneously. This requirement has necessitated a new set of electronics to control the power, frequency, phase, conjugate box, trombones (line stretchers) and stub lengths. The new control system also has narrow band filters on the reflected power signals to remove "cross-talk" from antennae operating at different frequencies. Such cross-talk is observed in low single pass absorption scenarios and leads to spurious tripping of system protecting against arcs.

Two major improvements have been made to the power transmission. Longer trombones have been added to many of the lines to cope with the requirements of tuning four antenna straps, and conjugate box decouplers are installed on three modules to compensate for power coupled across straps of an antenna when phased for current drive operation. So far the system has coupled up to 13.5MW to JET divertor plasmas. In addition 11MW of hydrogen minority ICRF has been combined with 15MW of neutral beam injection to give a total additional heating of 26MW into 2MA with a toroidal field of 2.8T.

## Commissioning and Initial Operation

Most of the plant commissioning was completed in the first three months of 1994 and comprised the following:

- Installation and testing of the various electronic control modules, which included the frequency reference units, the phase and frequency control modules, the amplitude and phase detection modules, the matching control modules, trip and limit modules and frequency conversion modules;
- Multipactor conditioning of the antennae and transmission lines, obtaining trombone and stub settings for matching the antennae to vacuum, and performing short pulse, high voltage conditioning of the antennas

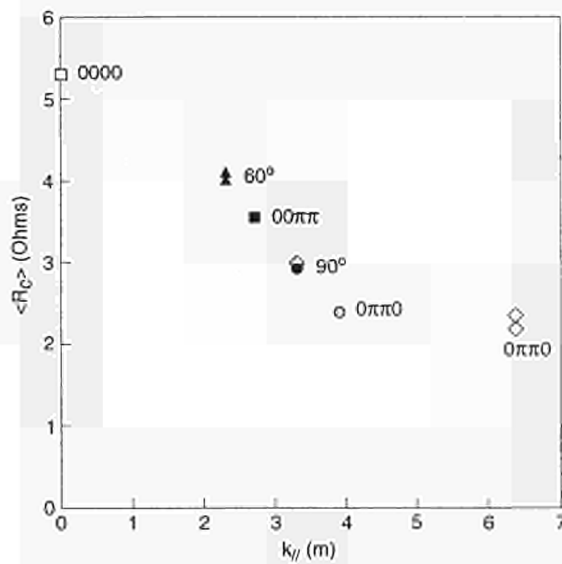


Fig. 44: Coupling resistance ( $R_c$ ) as a function of wavenumber,  $k_{||}$

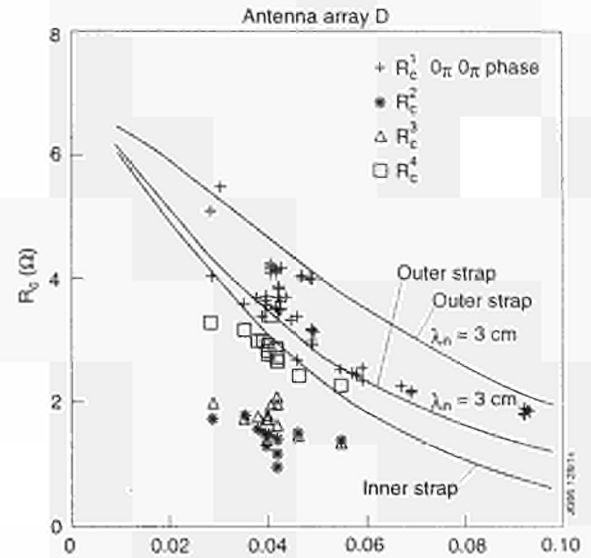


Fig.45: Coupling resistance ( $R_c$ ) as a function of seperatrix-antenna distance

and vacuum transmission lines. These procedures were carried out at frequencies of 32MHz, 43MHz, 48MHz and 52MHz. In addition, vacuum matches were obtained at 43MHz and 52MHz for phasings of 0000, 60°, 90°, 00ππ and 0π0π. The high voltage conditioning reached main transmission line voltages ~30kV quite rapidly, suggesting that the removal of the ceramic supports had made the new antennas and vacuum transmission lines rather robust towards breakdown. This has been confirmed subsequently during plasma heating experiments when operation at over 30kV has been achieved;

- Modifications and commissioning of the operation of the plant and data acquisition through CODAS;
- Long pulse high voltage conditioning in asynchronous timing with tokamak operation. This was performed particularly cautiously with stringent limits set on the allowable pressure rise to avoid damage due to arcing;
- Calibration of almost one hundred directional coupler signals, testing the automatic matching system with feedback on frequency trombones and stubs, and verification of the matching algorithms. The automatic matching facility made a major improvement in performance, since it allowed almost perfect matches to be achieved speedily and to be maintained during coupling variations due to edge density changes. Good matches are also maintained as the phase is varied say from 0π0π to 90° in a few seconds and this feature is particularly useful for finding good operat-

ing parameters for new phasings. However, the system had difficulty with rapid and large variations caused by giant ELMs, which changed the coupling resistance from typically 3Ω to 9Ω on a timescale of a few tens of microseconds. More frequently, smaller amplitude (“grassy”) ELMs, which occur during high power combined heating with neutral beam injection, can often be accommodated by the system;

- Commissioning and interfacing the plasma position feedback control, which keeps the average coupling resistance of the antennas constant, with the new tokamak gap control plasma shaping system.

This period of setting up and proving the ICRF system revealed a substantial problem in the feedback loop which controls both the phase and the frequency. The correct operation of this loop was being jeopardised by RF interference, which resulted in the production of sidebands to the main RF frequency. The problem became more serious as the power level is increased and effectively limited the system to about 1MW per antenna strap. The presence of sidebands also meant that the narrow band filters on the arc protection system could not be used. As a result, the system was particularly sensitive to cross-talk between antennae that were operating at similar frequencies. Thus, spurious tripping of the plant became especially severe in scenarios where the single pass absorption was low.

The problem is being solved by several changes to the design of the electronic modules. In particular, the phase

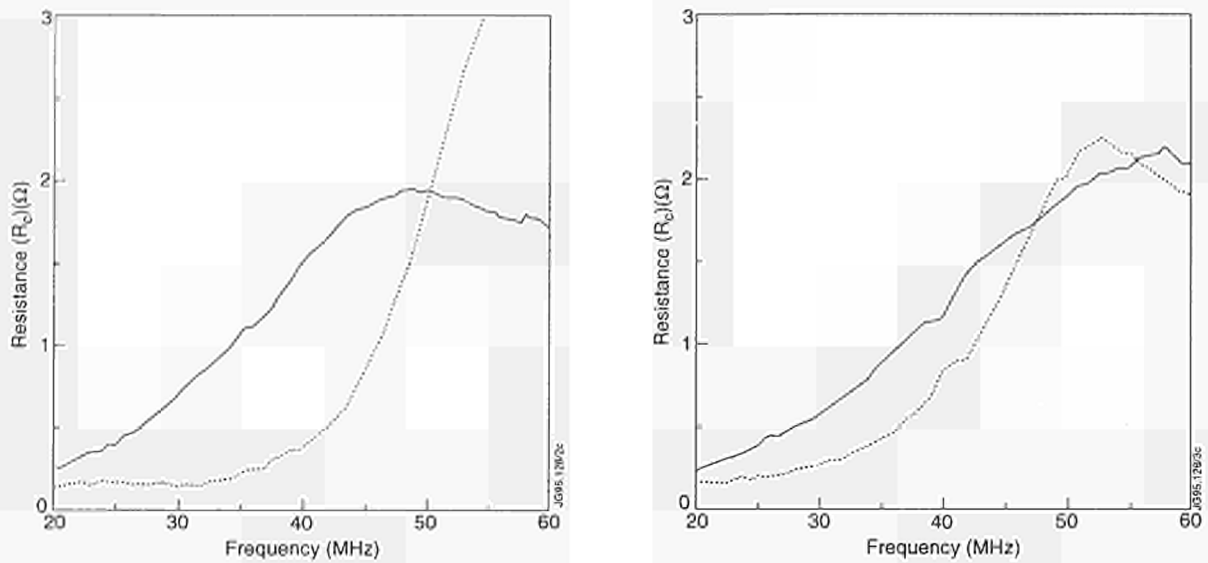


Fig.46: Coupling resistance ( $R_c$ ) as a function of frequency

and frequency control loops have been made independent of one another. Initial operation with the prototypes have allowed the main transmission lines to reach 30kV.

### Coupling to Plasma

The coupling of the A2 antennae to plasma has been assessed over a frequency range of 32MHz to 52MHz with phasings of  $0000$ ,  $00\pi\pi$ ,  $0\pi\pi0$ ,  $60^\circ$  and  $90^\circ$  and as a function of the distance of the plasma separatrix from the antenna. The coupling resistance  $R_c$  is defined as the characteristic impedance of the transmission line ( $30\Omega$ ) divided by the voltage standing wave ratio on the main transmission line. The value of  $R_c$  averaged over current straps varies with frequency from  $1.5\Omega$  at 32MHz to  $2.5\Omega$  at 52MHz. The variation of  $R_c$  with phasing is shown in Fig.44 where the average value is plotted against  $k_{||}$ . The coupling is maximum for monopole phasing and decreases as  $k_{||}$  increases to its highest value for dipole ( $0\pi0\pi$ ) phasing. This scaling is similar to that of the A1 antennas. The reduction in  $R_c$  with increasing distance between the antenna and the separatrix is shown in Fig.45 for dipole phasing and a frequency of 43MHz. Also shown are model calculations for density decay lengths of 1cm and 3cm; probe measurements give values within this range for most cases. The model represents the values of  $R_c$  reasonably well for the outer straps. However, the values for the inner straps of the antenna array are less than those of the outer straps by a factor of two and are considerably below the model predictions. This large and

unexpected imbalance in  $R_c$  between the inner and outer straps is a feature of dipole phasing for all frequencies up to 43MHz. At 48MHz, there is some reduction in the imbalance and at 52MHz the inner straps have the same values of  $R_c$  as the outer straps. For monopole phasing the imbalance is less than a factor of two for frequencies up to 43MHz but, in this case, the inner straps are predicted to have a larger value of  $R_c$  than the inner straps.

The origin of this reduction in coupling resistance of the inner straps has been identified as due to an impedance transformation by the crossover link which connects the inner straps to the main transmission line; there is no such link for the outer straps. The cause of the problem was found from scattering matrix measurements both for the antennae in the torus and for the prototype two strap "half" antenna. A new way of determining the matrix elements with the antenna coupled to plasma has been developed and uses the forward and reflected voltage measurements on the main transmission line. The method involves making measurements for several different phasings of the antenna whilst operating with identical plasma conditions. In fact it can be performed most readily in one pulse by making a phase ramp which is sufficiently slow to allow the automatic matching to keep the system in tune. A least squares fit to the amplitudes and phases of the transmission line signals then allows the scattering matrix elements to be evaluated.

The key feature in connection with the coupling imbalance is the difference between the diagonal elements for

the inner and outer straps, the latter being smaller than the former. Thus the coupling imbalance is not due to an effect of mutual coupling between straps but is due to a difference between the individual straps. The obvious candidate was the crossover link and this was verified as the main source of the problem by measurements on the two-strap prototype antenna. Fig.46(a) shows the values of  $R_c$  versus frequency measured using a network analyser with absorbent foam loading the prototype. The coupling resistance of the inner strap is more than a factor of two less than that of the outer strap for frequencies up to 43MHz but at 52MHz the values are almost equal as seen on plasma with the full four strap system. Calculations indicated that the characteristic impedance of the crossover strap was closer to  $70\Omega$  rather than the ideal  $30\Omega$  (the impedance of the feed-lines). The impedance of the crossover link has been reduced by increasing its capacitance and reducing its inductance and this has brought the coupling resistance closer to that of the outer strap as shown in Fig.46(b). However, the two straps have not yet been made identical and further optimisation is required. Modifications to the antennae in the vessel are planned for the 1996 shutdown. Meanwhile, the low coupling of the inner straps is a substantial impediment to high power operations at frequencies below 43MHz.

### Ion Cyclotron Heating Results

The ICRF system has coupled up to 13.5MW of power to divertor plasmas and has combined 11MW with NBI to generate 26MW total power. Such heating power levels have led to the following achievements:

- generation of H-modes with RF alone;
- increased the D-D reactivity during the ELM-free phase of H-modes in high flux expansion discharges;
- combined heating powers up to 26MW in advanced tokamak discharges to produce plasmas with poloidal beta values up to 2.5, normalised beta values up to 2.7 and H-factors greater than 2;
- improved confinement of 2.5MA, high density radiative divertor discharges by central power deposition.

The following sections give some details of these results and show how the heating efficiency depends on the antenna phasing.

### RF-only H-modes

RF H-modes have been produced both by hydrogen minority heating at the fundamental ion cyclotron fre-

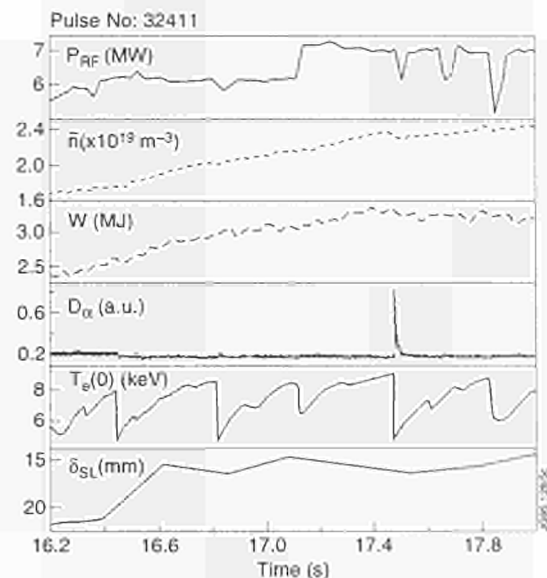


Fig.47: Example of variations in RF-only H-mode

quency and by second harmonic hydrogen heating. An example of the former in a 3MA discharge is shown in Fig.47. The toroidal field was 2.8T and the RF frequency was 42.7MHz which places the hydrogen minority ion resonance close to the magnetic axis. The H-mode was formed at 16.46s as indicated by the reduction in  $D_\alpha$  signal and the increase in the time derivative of the density. The H-mode was ELM-free for about 1s. The RF power level was switched on at 6MW of which half was with  $90^\circ$  phasing and half with dipole phasing. The antennae phased at  $90^\circ$  have somewhat better coupling but are only 65% as efficient as those phased in dipole in terms of power deposited in the plasma centre. Nevertheless, the energy content reached 4MJ after the power is stepped up to 7MW. The central electron temperature was 9keV and the fast ion energy content was 0.9MJ.

The coupling resistances were typically  $3.5\Omega$  for the outer straps and  $2\Omega$  for the inner straps and were kept constant by the plasma position feedback system. The distance between the separatrix and the limiter is shown in Fig.47. The feedback control moves the plasma outwards to reduce the gap from 2.1cm to 1.5cm as the H-mode is formed. There is no more than a 10% change in coupling during this transition and no generator trips. For each antenna, the forward voltages on the main transmission lines were equalised to optimise the power and, during the programme leading up to Pulse No:32411, the maximum voltage could be steadily raised. This conditioning eventually allowed one module to reach

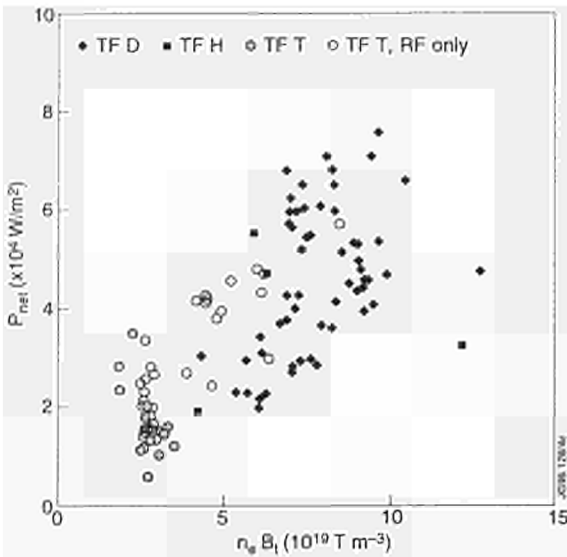


Fig.48: Power threshold level ( $P_{net}$ ) as a function of product of line average density and toroidal field ( $n_e B_t$ )

30kV on the main transmission lines. Subsequent operation with the new control electronics has allowed voltages above 30kV to be attained almost routinely with a need for only minor conditioning.

In Fig.47, the H-mode is triggered with the plasma only 2.1cm from the limiter and the ELM-free phase persists for over 1s with the distance reduced to 1.5cm. A study has been made of the quality of H-modes with both RF and NBI as a function of the plasma distance from the limiter with the following conclusions:

- H-modes can be triggered and maintained for distances down to  $\approx 1$ cm from the limiter in both standard and triangular plasmas.
- The power thresholds are comparable in the small and large distance shots.
- The duration of the ELM-free phase and the behaviour of the ELMs do not appear to be affected by distance.

The power threshold levels for RF-only H-modes are shown in Fig.48 as a function of the product of line average density and toroidal field. The quantity  $P_{net}$  is the total input power minus the radiated power inside the separatrix and the time derivative of the stored energy. The lowest power levels correspond to second harmonic hydrogen ICRF at 43MHz in 1MA/1.4T discharges. H-modes have also been produced with  $90^\circ$  phasing but so far attempts to produce H-modes with  $00\pi\pi$  phasing have been unsuccessful, probably due to the reduced heating efficiency with this phasing. The solid line in

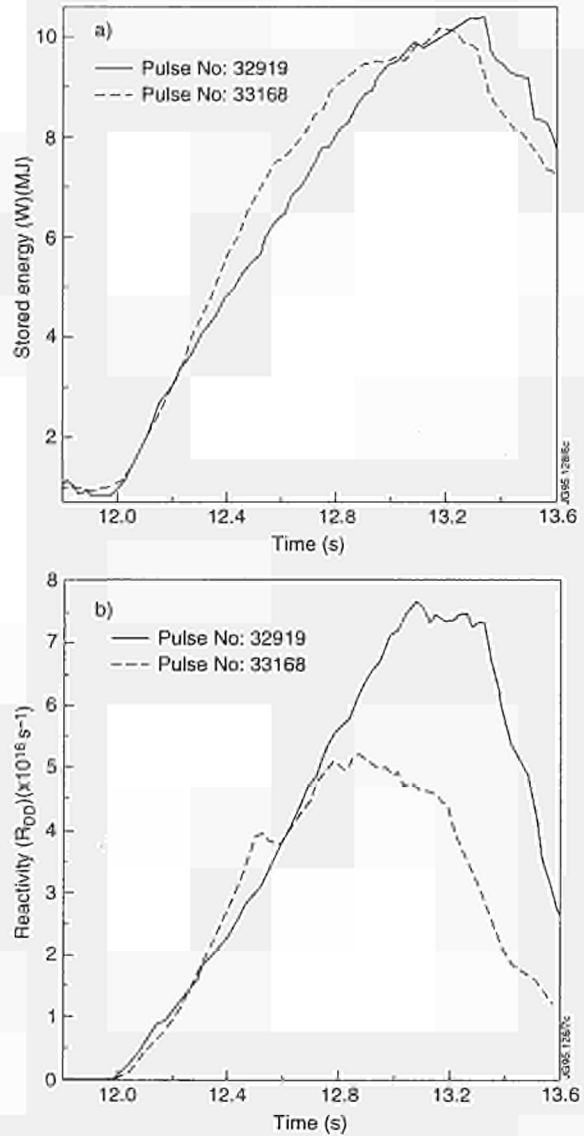


Fig.49: (a) Stored energy (W); (b) Reactivity as a function of time; for Pulse Nos: 32919 and 33168

Fig.48 is the best fit to H-mode threshold measurements using NBI in discharges with  $q_{95} = 3.0$ . The RF threshold is also close to this line indicating no significant difference between heating schemes in this area.

### ICRF Heating in High Flux Expansion Discharges

Hydrogen minority heating at a frequency of 51.7MHz has been applied to 3.5MA X-point plasmas with high flux expansion in the divertor region. This magnetic configuration was similar to that in which the longest ELM-free period and the highest D-D fusion reactivity have been achieved during the present campaign. With combined heating, the addition of even a modest amount of RF power has an impact on the rate of rise of both stored energy and reactivity. Fig.49 shows the effect of adding

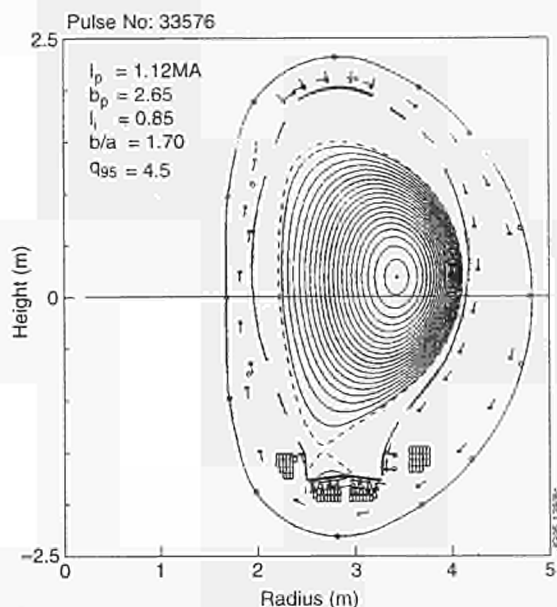


Fig.50: Poloidal flux contours for Pulse No: 33576

4MW of H-minority heating to 18MW of NBI during a 3.5MW ELM-free H-mode (Pulse No: 32919). For comparison, an NBI-only pulse is also shown for 19MW of power (Pulse No: 33168). The rate of rise of the stored energy and the neutron production is enhanced in the combined heating case. The rapid rise of the reactivity is prematurely curtailed by a sawtooth at 12.5s. During the ELM-free phase, the RF power diminishes as the coupling resistance decreases to  $1.8\Omega$ . Actions to improve and prolong these high performance periods, including profile control, are being studied.

### Combined Heating in High Beta Plasmas

Plasmas with a high value of poloidal beta are particularly good for RF coupling which is, at first sight, is surprising in view of their large triangularity and consequent mismatch to the shape of the antenna (Fig.50). The radius of curvature of the last closed flux surface in front of the antenna is less than the radius of curvature of the antenna itself. In such a case, those field lines which just miss the limiter will cross the midplane at a major radius larger than that at which the limiter intersects midplane. Thus plasma is able to penetrate behind the limiter with a corresponding improvement in antenna coupling.

The configuration shown in Fig.50 corresponds to a discharge with a plasma current of 1MA and a toroidal field of 2.8T into which was injected 16MW of NBI and 8MW of ICRH in  $0\pi\pi 0$  phasing. The evolution of the plasma parameters are shown in Fig.51. During the ELMy H-mode phase the poloidal beta reaches 2.5. Between

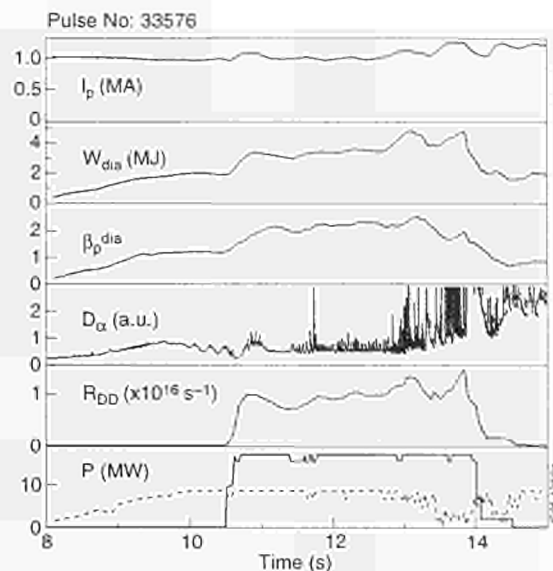


Fig.51: Overview for a high  $\beta_p$  plasma (Pulse No: 33576)

12.5s and 13.5s, the current is increased from 1MA to 1.2MA. During this current ramp the plasma transiently forms a VH-mode with an H-factor of 3 and the poloidal beta increases slightly to 2.7. This plasma qualifies as an "advanced tokamak scenario", which requires simultaneously  $\beta_p > 2$ ,  $H > 2$  and  $4 < q_{95} < 6$ .

### Heating of Radiative Divertor Plasmas

In a reactor operating with a divertor a large fraction of power crossing the separatrix must be radiated to prevent excessive heat loading of the divertor tiles. This type of high density plasma ( $n_e = 7 \times 10^{19} \text{m}^{-3}$ ) with up to 70% of the power radiated has been produced in JET using nitrogen as the radiative element. The heating was a combination of RF and NBI power. An example is shown in Fig.52 for 7MW of hydrogen minority ICRF and 17MW of  $D^0$  NBI power. The discharge has a plasma current of 2.5MA and a toroidal field of 2.6T. The RF has good coupling in such discharges which produce grassy ELMs. In this case, the value of  $R_c$  was about  $3.5\Omega$ . The fast waves have no problem penetrating such high density plasmas and are able to deposit power in the plasma centre, where the energy is best confined, in order to optimise performance. This produces central electron temperature of  $\sim 5.5\text{keV}$  for a plasma density of  $7 \times 10^{19} \text{m}^{-3}$ . During the beam only phase the H-factor is 1.45 and rises to 1.6 during the RF phase. Such an increase is expected since the RF power deposition is in the plasma centre even at these high densities.

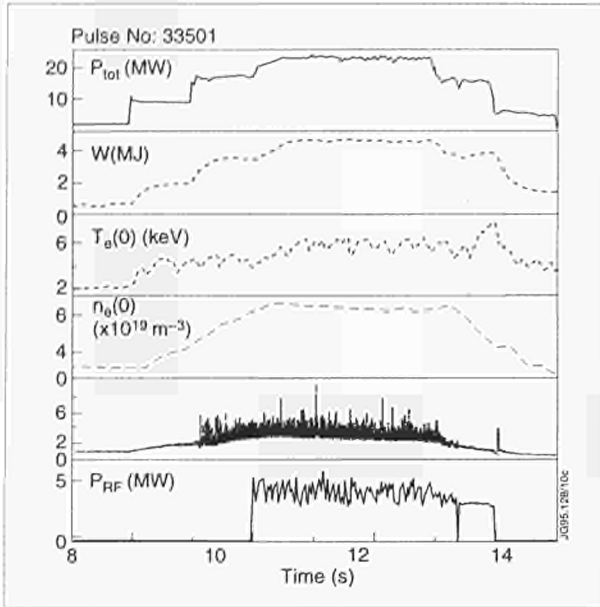


Fig.52: Combined plasma heating in Pulse No: 33501

### Heating Efficiency

The heating efficiency of the A2 antennae has been measured for a variety of different phasings. Dipole phasing ( $0\pi0\pi$ ) produces the largest stored energy per unit input power. With this phasing, the heating efficiency is similar to that obtained with NBI. Moreover, the efficiency, the fast ion energy content and central electron temperature are similar to those achieved in the previous campaign for the same input power and discharge conditions. However, it was noted early in the present campaign that for phasing with low values of  $k_{\parallel}$  the heating efficiency was significantly reduced. To quantify this effect a series of modulation experiments were carried out using three antennae in dipole phasing to ensure a substantial fast ion population and the fourth antenna in the phasing being studied. A detailed analysis showed that  $00\pi\pi$  phasing was only half as efficient as dipole phasing. On the other hand,  $0\pi\pi0$  is as efficient as dipole and had better coupling. For this reason, many of the high power pulses used  $0\pi\pi0$  phasing. Current drive phasing of  $90^{\circ}$  was 65% as efficient as dipole.

The phasings which produce poor heating also generate hot spots on the limiter at a power level of 1-2MW per antenna. An example is shown in Fig.53. Estimates of the power producing these hot spots was much less than the power deficit required to explain the reduced plasma heating. However, there was enhanced impurity influx which could lead to disruptions. The reduced efficiency and the limiter heating is thought to be connected with RF sheath rectification effects which was substantially greater

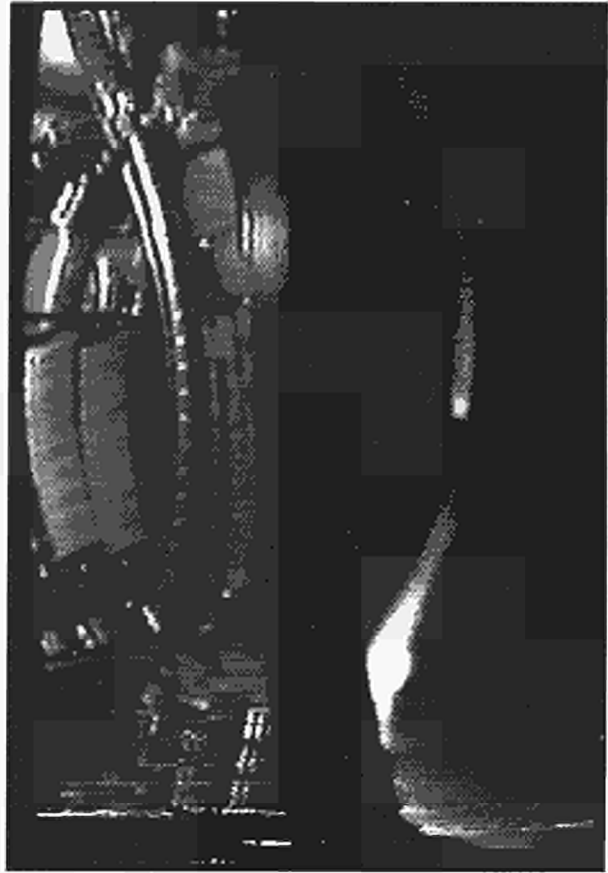


Fig.53: Hot-spots on the limiter (Pulse No: 30553)

in the A2 antennae since these with three times wider than the A1 antennae. Supporting evidence for this interpretation is the lack of observation hot spots when the field lines are aligned with the antenna screen bars. During the shutdown for the beryllium tile installation, a limiter will be inserted at the centre of one antenna to reduce sheath rectification. If this is successful all antennae will be fitted with these limiters during the 1995 shutdown for the MarkII divertor. In this case, good heating efficiency should be restored for the phasings which produce good coupling and ensure a substantial improvement in the power delivered by the ICRF system.

### LHCD Technical Achievements

The full Lower Hybrid (LH) system started operation in spring 1994 at the start of the experimental campaign in the new divertor configuration. LH power was injected into the plasma during with the first discharges. Full current drive conditions at 2MA plasma current were achieved in the first dedicated LH experiments in mid-year, and at 3MA with about 6 MW LH power coupled towards the end of the year. The variation of LH power deposition profiles was studied with extensive code

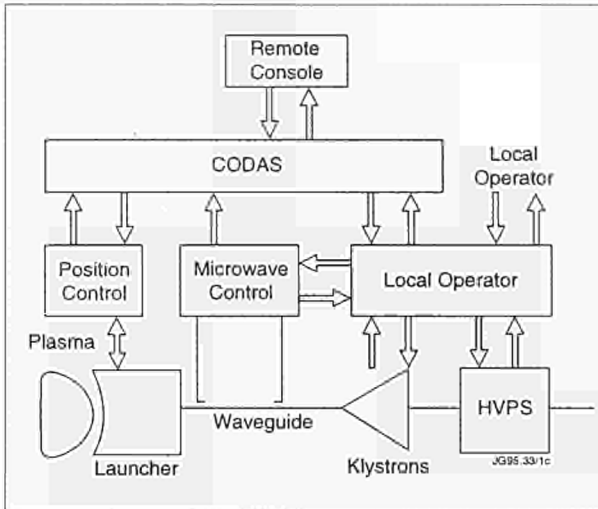


Fig.54: Block diagram of the power transmission from the LHCD plant to the plasma.

modelling of the experimental data in preparation for profile control experiments. Strong broadening of the current profile was obtained with off-axis LH current drive (LHCD). Sawteeth were stabilised with near-axis LHCD. Deep shear reversal configurations, as required in advanced tokamak scenarios, were established with the application of LHCD and ICRF heating power during fast plasma current ramps. Profile control scenarios and the outline of a LHCD system on ITER were also studied.

### LHCD System

The Lower Hybrid generator consists of 24 klystron amplifiers operating at 3.7GHz. Each klystron is rated at a maximum power output of 650kW. The total generator power is 15MW in pulses up to 10s and 12MW up to 20s. The main parameters of the LHCD system are given in Table XI. A block diagram of the power transmission is shown in Fig.54. The power is transmitted from the generator on waveguides to the LHCD launcher, which is installed on the main horizontal port of Octant No:3. In the launcher, the power is progressively split to feed a phased array of 384 waveguides at the grill mouth facing the plasma. The front end of the launcher as seen from inside the vessel is shown in Fig.55. Three vertically superposed areas of the waveguide array can be phased independently. This allows for high flexibility in the wave spectrum composition.

The control system for the generator includes a number of automatic software routines to simplify operation of the plant. One of these is used to condition the launcher vacuum waveguides, without a plasma load. This routine pulses the generator modules at the maximum rate



Fig.55: View of the front-end of the LHCD launcher inside the vessel

Table XI: Main Parameters of LHCD System

Plant	
Frequency	3.7GHz
Number of klystrons	24
Power (generator)	12MW, (15MW)
Pulse duration	20s, (20s)
Duty cycle	1/30
Efficiency	42%
Phase control	10kHz
Phase accuracy	10°
Maximum VSWR	1.8
Transmission line	
Length	40 m
Insertion loss	1 dB
Launcher	grill type, 48 multijunctions (copper coated stainless steel)
Number of waveguides	384 (12 rows x 32 columns)
Dimensions (waveguides)	height = 72 mm, width = 9mm, wall: 2mm
Position control	hydraulic actuators
Radial movement	5ms <sup>-2</sup> , 33mms <sup>-1</sup>
Radial stroke	210mm
Baking temperature	450°C
Pumping	cryopump, 85 000ℓ/s <sup>-1</sup>
Total weight	15tonnes
Coupling control	launcher position control, plasma position control, local gas puff
Wave spectrum	
Maximum	N <sub>  </sub> = 1.4 - 2.3, adjustable
Full width	ΔN <sub>  </sub> = 0.46

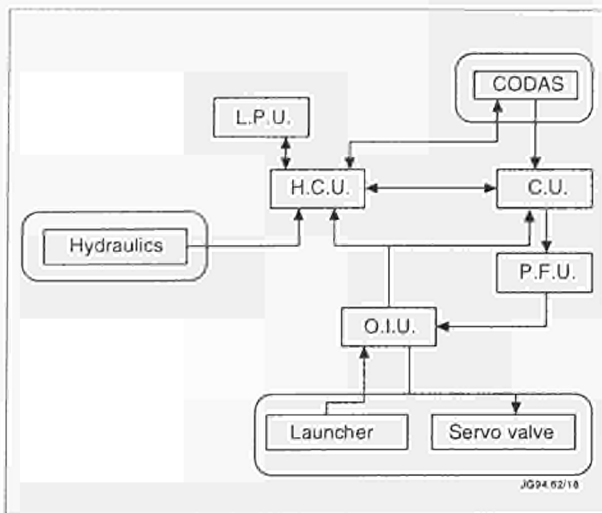


Fig.56: Block diagram of the hydraulics position control system of the LHCD launcher

allowed and automatically adjusts the power to the maximum that the launcher can handle. This software was later modified to trigger the generator modules in sequence to produce ECRH plasmas in quasi-continuous burst mode. A second software routine optimises the power within an LH pulse into plasma to the maximum possible by ramping up the power until there is an arc in the launcher. The power is then removed for a pre-set time and reapplied at a level 20kW below that which caused the arc.

Before the start of plasma operation, the generator was operated routinely on test load to condition the klystrons and commission the various parts of the system. The first LH pulse on the L1 launcher with the torus under vacuum was in February. Within five days, 21 of the 24 klystrons had been pulsed with the launcher up to a power level of 50/100kW each for 1s and 1MW launched into vacuum. The first LH pulse with plasma was in mid-March. The power level achieved both in vacuum and with plasma steadily improved as the Launcher vacuum waveguides were conditioned. At the start of the campaign in the new divertor phase, the first LH current drive experiments were performed with 4MW coupled to the plasma.

### Position Control

The radial position of the launcher is controlled with a hydraulic position control system, consisting of three subsystems. The first, the Offset Circuit, is composed of four hydraulic actuators, which compensate the vacuum load. The second, the Servo Circuit, has two cylinders, which move and control the launcher position. The third, the Legs Circuit, has three cylinders, which determine the maximum in-vessel position of the launcher. These three

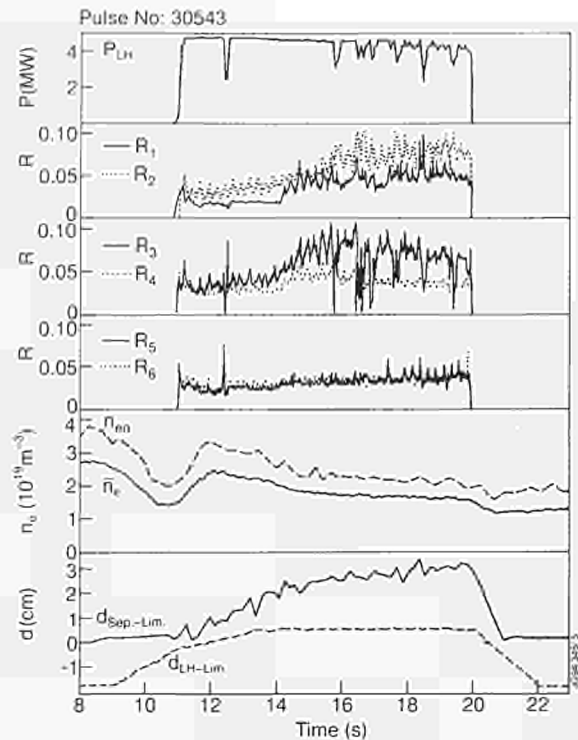


Fig.57: Waveforms of total coupled LH power, reflection coefficients on the six vertically staggered rows of multijunctions, plasma density and separatrix and launcher positions

cylinders, also called legs, are adjustable to fit the requirement of the LH operation. All the cylinders of the Servo and Legs Circuits are fitted with position transducers. The hydraulic system is controlled either locally or from the Control Room, as shown in Fig.56. Here LPU is the Local Panel Unit situated in the local control area and CODAS stands for any authorised X-terminal; the opto-isolation unit (IOU) isolates the signal from/to the torus from the cubicle; the Hydraulic Control Unit (HCU) controls all operations involving the hydraulic system itself (open/close valves, start/stop pump, etc...) and defines the status of the system; the Control Unit (CU) transmits the requested position to the Position Feedback Unit (PFU) and defines the position corresponding to the actual requirement (in/out of JET pulses, position waveform, position feedback). The Position Feedback Unit acts on the servo valve to move the launcher to the required position.

The present system allows positioning the launcher front end in the range of -100mm to +27mm, relative to the poloidal limiter position. The legs can be set anywhere within that range. The maximum speed available for real time position movements is  $0.04\text{ms}^{-1}$ .

The position of the launcher has been varied during pulses in order to improve coupling, while still ensuring

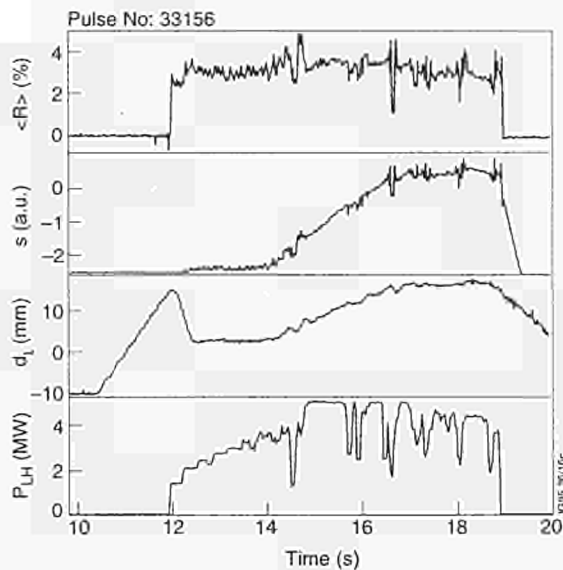


Fig.58: Waveforms of average reflection coefficient ( $R_f$ ), feedback loop error signal ( $s$ ), feedback controlled launcher position and total coupled LH power

that the last closed flux surface was at an adequate distance from the front of the launcher. Initially the launcher was moved using a pre-programmed position waveform. In this case, the coupling may degrade due to uncontrolled variations of the plasma boundary. Figure 57 shows such a case, where during pre-programmed launcher positioning the plasma shape changed and the clearance between plasma and launcher increased. In consequence, the reflection coefficient on four of the six vertically staggered rows of multijunctions increased.

Feedback control of the launcher position was therefore developed, using a feedback loop which adjusts the launcher position upon a requested reflection coefficient. The feedback was allowed to move the launcher in a band of 20mm around the position given by a pre-programmed waveform. In this way, even if the feedback loop did not respond correctly, the launcher would not stray too far into the plasma. The feedback works reliably, and has kept the reflection coefficient constant at the requested value in the range between 2-10%. An example for high power LHCD operation with feedback controlled launcher position is shown in Fig.58. The upper part shows the actual measured reflection coefficient, averaged over all waveguides. The requested value of 3% is well met during the whole pulse. The second curve gives the error signal produced in the feedback loop. The third box shows resulting launcher position controlled by the feedback system within the allowed excursion band. The total LH power coupled is shown in the lower box.

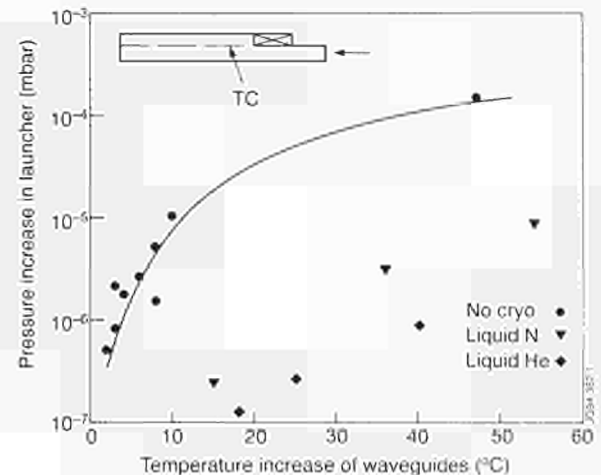


Fig.59: Pressure increase in LHCD launcher during conditioning

The bandwidth of the feedback loop is 1-5Hz. As the reflection coefficient is an exponential function of the distance between the launcher and the last closed flux surface, the actual bandwidth depends on the reflection coefficient which is requested. The performance of the LH system has been seen to be critically dependent on the coupling. The maximum power can only be launched if the reflection coefficient is in the range 2-5%. Using the feedback control to sustain a reflection coefficient of 3% during pulses has significantly improved on the power that could be coupled into divertor plasmas.

### Launcher Conditioning

To increase the conditioning speed of the LHCD launcher an automatic conditioning system has been developed. When RF power is transmitted through the multijunctions into vacuum, total reflection of the wave occurs and the resulting RF power losses lead to an increase in the temperature of the waveguides. By pulsing the klystrons into vacuum at high repetition rate, efficient baking and conditioning of the launcher is obtained. If the klystron protection system detects any increase or decrease in reflected power in a waveguide during the pulse, indicating an arc or plasma formation, the corresponding klystron is switched off for 100ms. Depending on the number of trips, the klystron power is increased, decreased or kept constant for the next pulse.

A temperature interlock on the graphite loads in the multijunctions has also been implemented, which stops a klystron when the load reaches the temperature limit, thereby avoiding excessive outgassing from the graphite

loads. After one day of vacuum conditioning the temperature of the launcher increases by  $100^{\circ}\text{C}$  in average. At the start of operation of the LHCD system and before the LHCD cryopump was available, vacuum conditioning would increase the pressure in the launcher from  $10^{-6}$  mbar up to  $10^{-4}$  mbar. High outgassing of  $\text{H}_2\text{O}$ ,  $\text{CO}$  and  $\text{CO}_2$  was then observed. With the cryopump fully operational, the launcher pressure is normally kept at  $10^{-8}$  -  $10^{-7}$  mbar and can increase to  $10^{-6}$  mbar after heavy conditioning. The pressure increase with the waveguide temperature during RF conditioning of the launcher is shown in Fig.59 for various pumping conditions [2].

After about six months of operation and conditioning, the outgassing became negligible and, after venting the torus, the previous conditioning status of the launcher can be recovered after a few days of vacuum conditioning.

### ECRF Heated Plasmas

The Lower Hybrid system has been used as an ECRF heating system to produce low density plasmas in a low toroidal magnetic field for vessel conditioning. LH has been operated in quasi-continuous pulsed mode with pulse lengths of 0.5, 1, 2 and 3s and a duty cycle between 1/20 and 1/5. The total power was varied between 100 and 400kW, with only one module pulsing at a time. A low steady-state toroidal magnetic field alone has been applied, with no poloidal field. A low filling pressure of  $1.6 \times 10^{-6}$  mbar was used with continuous gas flow, aiming at plasma densities  $n_e < 10^{17} \text{m}^{-3}$ . Plasmas in this range have been studied in start-up experiments on RTP [3]. The non-confined plasma provided homogeneous wetting of all interior vessel walls. With values of 0.1, 0.13 and 0.16T, the location of the electron cyclotron frequency for the frequency of 3.7GHz has been varied between positions near the inner wall and near the LH launcher. The discharges were run in helium, and plasmas were reliably produced in all conditions. The dominant feature in the RGA spectrum was an increase of the water pressure. Initially, part originated from the LH launcher, as seen from LH vacuum pulses. After the LH experiments, no increase across the whole RGA spectrum was no longer seen with LH pulses into vacuum. The LH launcher therefore was conditioned during this operation.

### Coupling

The LHCD system has coupled power into plasmas in a wide range of different configurations. The coupling has

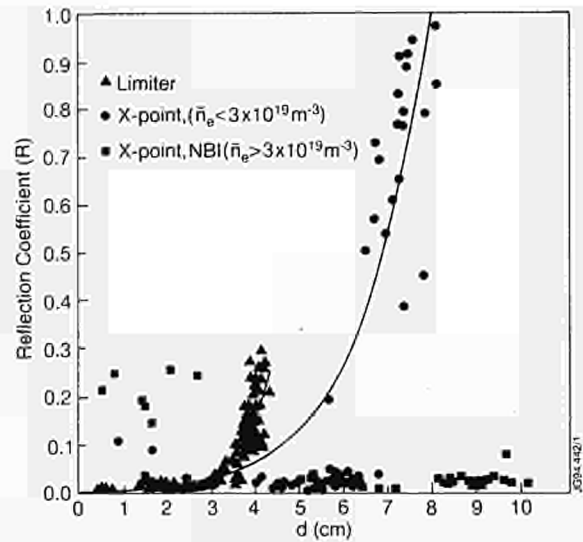


Fig.60: Reflection coefficient versus distance between the LHCD launcher and separatrix for various operational conditions ( $I_p = 2\text{MA}$ ,  $B_t = 2.8\text{T}$ )

depended critically, as expected - on the distance between the last closed flux surface and the front of the launcher. The coupling was basically determined by the plasma density in the scrape off layer (SOL) immediately in front of the launcher. This in turn depended on the plasma density at the last closed flux surface (LCFS), the connection length in the SOL, and local perturbations in front of the launcher.

The reflection coefficient seen from the LH plant is the parameter that indicates the coupling and its value depended exponentially on the distance from the launcher to the LCFS. The exponential decay length was determined by the connection length in the SOL. This led to a long decay length in divertor plasmas, and a short decay length in limiter plasmas.

Although the distance from the launcher to the LCFS was the most important parameter determining the coupling, other factors played an important role. The coupling degraded severely when the ICRF antenna next to the launcher was used. This degradation depended on the RF power, and resulted in a much steeper dependence of the coupling on the distance from the plasma. On the contrary, very good coupling was observed in certain cases when LH was used in conjunction with neutral beam injection. The dependence of the coupling coefficient on distance between launcher and the LCFS is shown in Fig.60 for ohmic limiter, divertor plasmas and NBI-heated divertor plasmas. With divertor plasmas, the reflection stayed low for larger distance.

The power handling capability of the LH system depends critically on the achieved reflection coefficient. High power could only be coupled when the reflection was in the range 2-5% of the incident power. If the reflection became too low, indicating a high plasma density in front of the launcher, breakdown could occur in the launcher, probably caused by plasma, or gas entering the waveguides. If, on the other hand, the reflection was too high, the electric field inside the waveguides became excessive, again leading to a breakdown.

Due to the critical dependence of the power handling on the distance between the launcher and the LCFS, it was important to assure a plasma shape which followed closely the shape of the limiters (and thereby the launcher).

## Code Development

### Ray Tracing

Development work on the LHCD ray tracing code aimed at three different directions: proper calculation of single-null X-point equilibria for LHCD modelling in the JET divertor configuration, considerable reduction of CPU time consumption to allow a link of the LHCD code to a transport code and revision of 2D Fokker Planck codes.

The ray tracing and Fokker Planck packages have been modified to enable modelling in single null X-point divertor configurations. The numerical solution of the equilibrium problem by the EFIT code is used for the magnetic field instead of the three moments approximation employed in a previous version of the LHCD code [6]. All major parameters are taken from the experiment. A bicubic spline approximation is used for description of the plasma density and temperature profiles. The scrape-off layer is taken into account. The calculations of the ray trajectories are carried out in Cartesian coordinates.

Considerable acceleration of ray tracing calculations was achieved by using several new numerical methods. The mapping technique was employed for solving the ray equations. In this method a ray trajectory in the phase space is presented as a discrete set of points generated by an area-preserving transformation. The application of this approach to the current drive simulation requires a significant modification of the procedure. Other important features of the fast ray tracing code (FRTC) are: calculation of the power deposition separately from ray tracing; effective ray trajectory memorising; special treatment of over long trajectories; use of a conservative scheme for the diffusion coefficient calculation.

The 2D Fokker Planck (FP) code [7] implemented on JET was supplemented by a diagnostic code which allows to transform the calculated distribution function from spherical (momentum, pitch angle) into cylindrical (parallel and perpendicular momentum) coordinates and to perform integration over the perpendicular momentum to obtain parallel and perpendicular tail temperatures. The parameters can be used in a different 2-D (parallel momentum, radius) Fokker-Planck code which takes into account spatial diffusion. Hard X-ray emission produced by fast electrons during LHCD can be simulated for distribution functions from both FP codes.

### Beam Tracing Code

A new Lower Hybrid (LH) current drive and power deposition code has been developed. The code makes use of a new beam tracing technique for the description of LH wave propagation and absorption in a plasma [8]. The 1D Fokker-Planck equation is solved in the code for the treatment of fast electron kinetics. The beam tracing (BT) approach contains the conventional ray tracing (RT) as a particular case. In addition, it includes also the wave phenomena such as diffraction and interference which are not described by the commonly used RT techniques. The BT based code is about a factor of ten faster than the RT code. This allows efficient usage of the BT codes as a built-in subroutine for advanced transport codes. The BT LH programme package has been included into the transport codes ASTRA, JETTO and TRANSP. First results obtained from modelling calculations with the code TRANSP are presented below.

New physics features of the LH wave propagation in a tokamak plasma were obtained with the BT code already in its stand-alone version. The effect of diffraction results in a strong LH wave envelope broadening, both in configurational and spectral spaces. In particular, the spectral gap filling occurs much earlier on the wave path than it is predicted by the ray tracing modelling. As a result, substantial absorption is already seen during the first wave passage over the minor plasma radius, for the conditions where the conventional ray tracing codes show no absorption at all. Simultaneously, LH power deposition profiles as obtained from the BT approach are broader and smoother than those determined by ray tracing calculations. For plasma parameters with dominating first pass absorption, the BT code gives good agreement with measurements of the fast electron

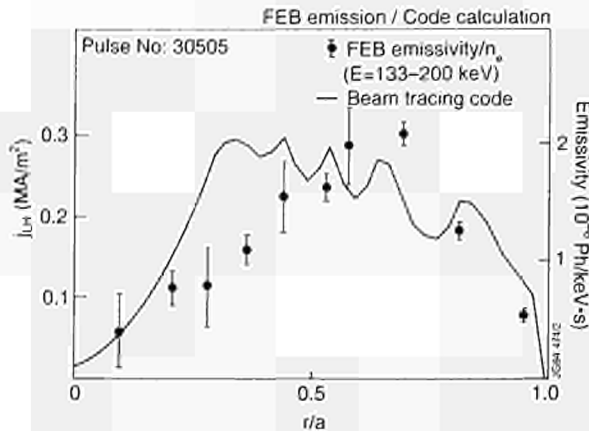


Fig.61: Comparison of the LH current profile from beam tracing with the FEB profile

bremsstrahlung (FEB). Figure 61 shows a comparison of the calculated LH driven current profile and the Abel inverted profile of the FEB emission for Pulse No. 30505.

An example of transport modelling with the code TRANSP is shown in Fig.62 for the Pulse No. 29711. For the injected LH power of 4 MW and the plasma current of 2MA, an LH-driven current of  $I_{LH} = 1.5-1.8\text{MA}$  is calculated. The temporal evolution of the loop voltage in the experiment is well reproduced by the code. The same transport modelling without account of the LH current drive gives results qualitatively very different from the experiment.

## ITER Studies

### Profile Control Scenarios on ITER

The models developed and validated on the basis of the experimental results on JET have been used to study the application of LHCD to ITER and reactor grade plasmas [9]. LH power and current deposition profiles are determined in these studies with ray tracing and beam tracing codes. The temporal evolution of the plasma profiles is calculated with the 1.5-D transport code JETTO. Full current drive and real time profile control on ITER can be achieved by a combination of LHCD and Fast Wave current drive (FWCD) with a high fraction of bootstrap current in the H-mode at high  $\beta_p$ . The off-axis current drive capability of LHCD is essential to establish and maintain stable shear reversal configurations. A scenario with 74% bootstrap current, 20% LH-driven current and a small fraction of FWCD-driven current for central q control has been developed. Steady-state operation at a plasma current of 13.5MA is then provided by a combination of FW and LH systems, with 50MW each. The

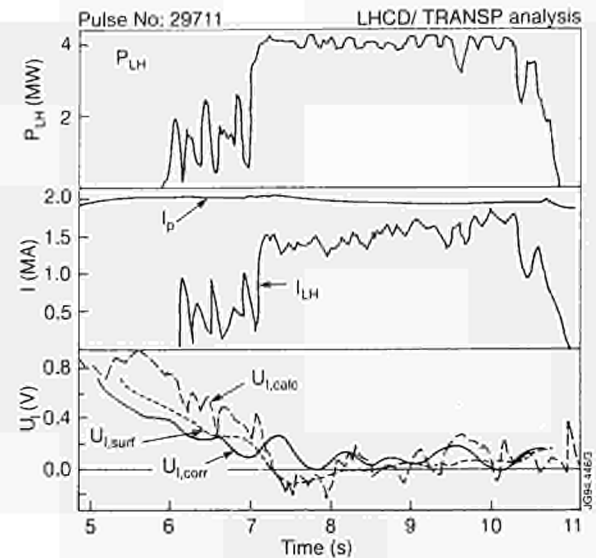


Fig.62: LH power, plasma current and LH-driven current, and loop voltage from experiment and beam tracing calculation

start-up of the currents is shown in Fig.63. A non-monotonic q-profile with negative shear over the inner half radius and a minimum q-value of about 3 is established already in the current ramp-up phase

### LHCD Launcher Design for ITER

The outline design is based on TAC-4 Report parameters. The physics of LH current drive defines the frequency (5GHz) and optimum spectrum ( $N_{ll,peak} = 2$ ). This defines the wavelength across the grill as about 30mm. The total width of the port thus represents about 40 wavelengths, resulting in a very narrow spectrum with high directivity.

Cooling of the waveguides at the grill mouth, which are subject to the intense neutron flux and plasma radiation at the first wall, requires the provision of active cooling channels close to the mouth. A convenient means of providing space for such channels is the use of passive waveguides for every second guide at the grill [10]. The

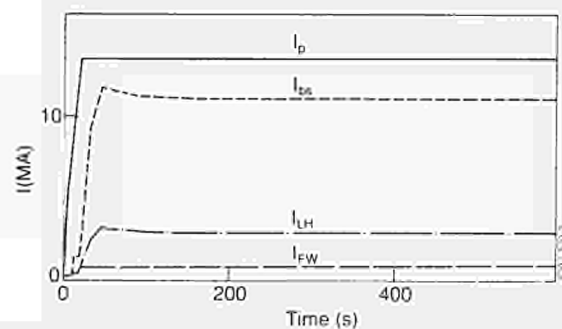


Fig.63: Full noninductive current drive with LHCD, FWCD and bootstrap currents in ITER

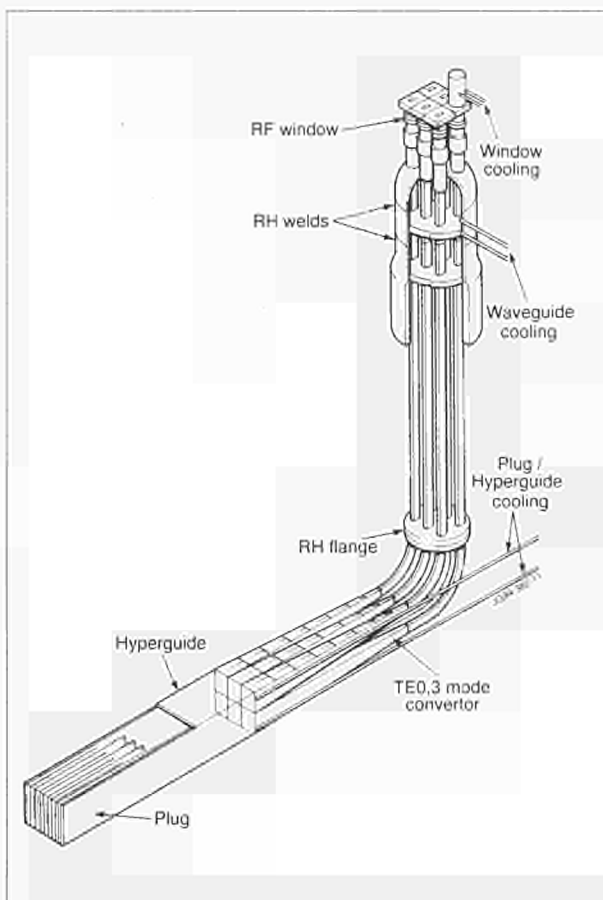


Fig.64: Schematic view of a module of a LHCD launcher design for ITER

depth of the passive waveguides is chosen to optimise the spectrum. This enables cooling of the grill mouth by conduction to cooling channels behind the passive waveguides, provided high conductivity materials are used, for example, copper alloys or possibly beryllium.

A consequence of this active/passive waveguide structure is that the overall coupled power for a given area of grill is reduced by a factor of two for a given power density in the active waveguides. The acceptable power density is a function of frequency and reflection coefficient. For the conditions anticipated, a power density of  $3.8\text{ kW/cm}^2$  is safe [11], given low reflection at the grill and good conditioning, a peak value of  $6\text{ kW/cm}^2$  may be achieved. For the available port area, the coupled power is therefore in the range 15 - 24MW per port for the passive waveguide launcher.

A benefit of the passive waveguide structure is that the grill is typically 60% dense in this region, and can therefore provide substantial neutron shielding. The length of this 'plug' may be increased to improve the shielding, each metre giving typically two orders of magnitude reduction. The grill may then be viewed as an integral part

of the shield. This in particular enables the full area of the port to be used for waveguides without exposing the TF coils to excessive radiation.

This length of the plug now conveniently accommodates phase shifters and multijunction splitting networks to give the required phase distribution at the grill mouth combined with low reflection from the plug. The plug in turn is excited by 'hyperguides' - large highly overmoded waveguides which offer simple construction, low losses, and excellent vacuum pumping. A total of eight such modules conveniently fills the available area.

Each module corresponds to up to 3MW of coupled power, reasonably provided by six klystrons each of 0.5 MW, with one vacuum window per klystron, all based on present technology. Mode converters are used to couple the six incoming waveguides to the hyperguide. A schematic view of one module is given in Fig.64.

The launcher is enclosed within a vacuum vessel rated at 20bar internal pressure as for the torus vessel. The launcher vessel extends through the cryostat inside a double bellows to maintain the cryostat internal 6 bar pressure. The RF windows are outside the cryostat where the neutron flux can be comfortably below the allowable flux for degradation of the ceramic.

Remote maintenance of the grill is limited to exchange of the hyperguide/plug modules, or their support structure, from outside of the cryostat. These may be refurbished off-line if required.

### Toroidal Alfvén Eigenmode Exciter

The 1994 experimental campaign has seen the start of operation of the active diagnostic for the excitation and detection of Alfvén Eigenmodes (AE). This allows a systematic study of AE physics in terms of frequency spectrum, mode structure and damping. It uses 3kW RF amplifier to excite up to four of the eight saddle coils inside the JET vacuum vessel. The other saddle coils, toroidally and poloidally distributed magnetic pick up coils, ECE and reflectometry signals are used as detectors. Signals from these are fed to specially designed electronics, which extract from the background noise the real and imaginary components of the signals driven by the saddle coil currents (synchronous detection). The pick up coils allow spacial resolution of the TAE mode. The detection system is sufficiently sensitive to detect magnetic field oscillations of  $10^{-7}\text{ T}$  for driver currents of about 5A in the saddle coils. The operating frequency is

repetitively swept across the range of interest in the region of the Alfvén continuum gap frequency. Several global eigenmode resonances have been clearly observed in different plasma conditions. Their damping rates have been directly measured.

The coils are protected by earth leakage detection and shortened turn detection both of which trip the RF drive to the amplifier.

The main system parameters are:

• Amplifier output power	3kW
• Maximum frequency range	30-500 kHz
• Maximum voltage across the coils	500V
• Maximum saddle coil current	10A
• Number of detector channels	42

**References**

- [1]. Söldner, F.X., et al, IAEA Meeting on Radio-Frequency Launchers for Plasma Heating and Current Drive, Naka, Japan 1993.
- [2]. Froissard, Ph., et al., 18th Symposium on Fusion Technology, Karlsruhe, Germany 1994.
- [3]. Polman, R.W., et al., 18th Europ. Conf. on Contr. Fusion and Plasma Physics, Berlin 1991, Vol. III, 317.
- [4]. Söldner, F.X, et al., 21st Europ. Conf. on Contr. Fusion and Plasma Physics, Montpellier 1994, Vol. III, 1126.
- [5.] Holties, H.A., et al., 21st Europ. Conf. on Contr. Fusion and Plasma Physics, Montpellier 1994, Vol. I, 234.
- [6]. Baranov, Y.F., et al., 20th Europ. Conf. on Contr. Fusion and Plasma Physics, Lisbon 1993, Vol. III, 881.
- [7]. M.Shoucri, I.Shkarofsky. Computer Physics Communications, Vol. **82**, 287,1994.
- [8]. G.V. Pereverzev, Nuclear Fusion **32**, 1091 (1992).
- [9]. ITER Task Report IVA-LH (1994), to be published.
- [10]. Bibet, Ph, et al., IAEA Meeting on Radio-Frequency Launchers for Plasma Heating and Current Drive, Naka, Japan 1993.
- [11]. Kaye, A., Plasma Phys. and Controlled Fusion **35A** 71-90 (1992).

**Operations Systems**

**Disruption Feedback Stabilization System**

The aim of the disruption stabilization system, which is shown schematically in Fig.65, is the detection and suppression of the  $m=2, n=1$  MHD modes, which are commonly observed to precede, and ultimately cause, major disruptions in tokamaks. While extension of the tokamak

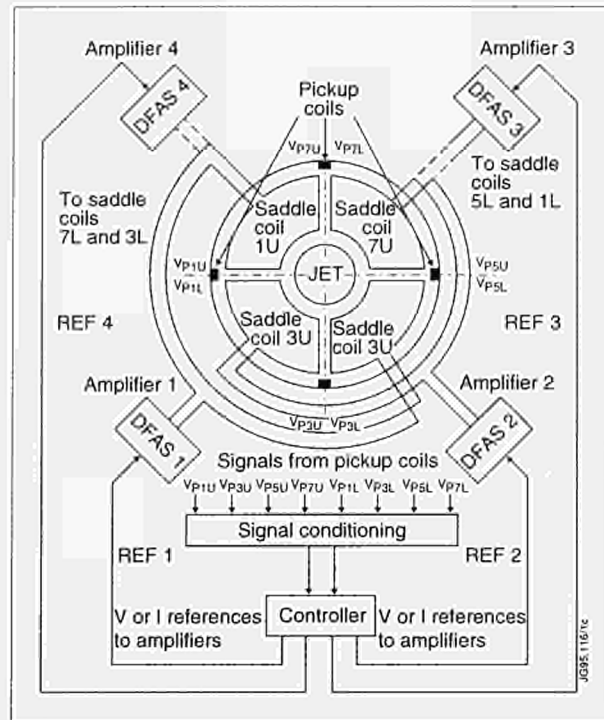


Fig.65: Schematic of disruption feedback stabilization system

operating regime by suppression of disruptions would be a major achievement, the capability of working more closely to the existing operational limits with a greater margin of safety would, in itself, represent a significant advance. Thus, the system is potentially of great value to tokamak operations, in particular, in the context of steady-state operation of a reactor, where a major disruption may have both technical and economic consequences.

The disruption feedback stabilization system consists of:

- four disruption feedback amplifiers (DFAS) operating in the range 0-10kHz;
- eight saddle coils in the vacuum vessel;
- the saddle coil protection system, which includes the saddle coil crowbars (SCC);
- the disruption feedback controller (DFC) with associated magnetic detection system.

Installation of the eight saddle coils was completed during the major shutdown. Each saddle coil covers one quadrant of the vacuum vessel in the toroidal direction and approximately 60° in the poloidal direction, as illustrated in Fig.66, which shows a schematic overview of part of the system. As a result of analysis of induced voltages during disruptions and vertical displacement events, it was decided that it would be necessary to short-circuit the coils during such events to prevent arcing, and a crowbar system was designed to perform this task. Before installation of the crowbar system, the saddle coils

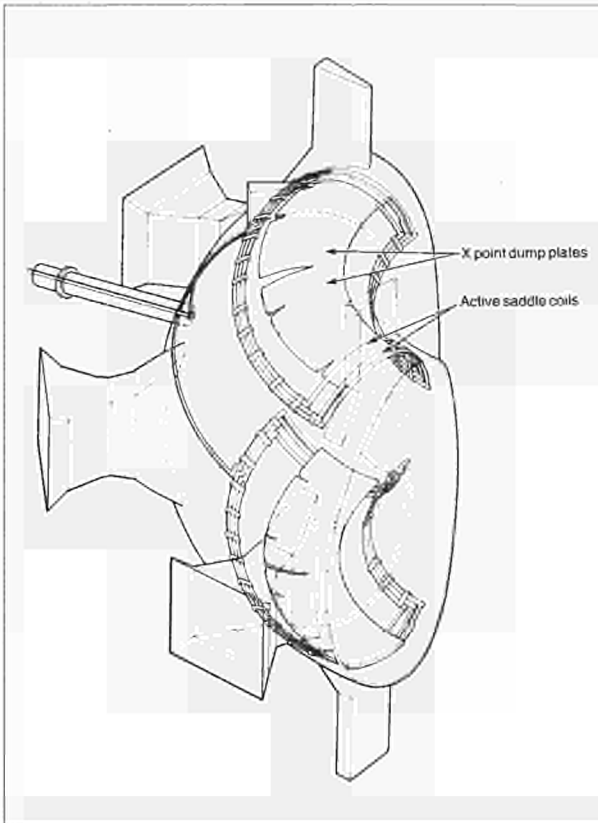


Fig.66: Overview of saddle coils in one Octant of the vessel

were protected by a fixed short-circuit, though an inductive coupling allowed the TAE system to be used at low power.

Following installation of the saddle coil crowbar system in July 1994, power commissioning of the DFAS with the saddle coils was undertaken. Each of the four DFSS circuits (Fig.67) consists of a single disruption feedback

amplifier, with a power of 4.5MVA driving two saddle coils in antiphase. This provides an  $n=1$  magnetic structure in the plasma, with each saddle coil protected by a crowbar. Each of the circuits has been tested to full current, that is up to 3kA over the range 0-1kHz, thereafter falling to 300A at 10kHz. In September 1994, damage was discovered to the upper saddle coils resulting from plasma interactions and it was decided to remove sections of the coils to prevent further damage. Experimental work has, therefore, been restricted to the lower saddle coils.

The saddle coil protection system is designed to protect the coils from arcs generated either by the amplifiers, in the course of normal operation, or by disruption induced voltages. The system consists of earth fault protection, short-circuit protection and disruption detection. Following detection of a short-circuit, which is determined by a voltage imbalance of the two saddle coils in each circuit, the amplifier is switched off in 20ms, reducing the energy delivered to the fault to ~10-20J. To prevent disruptions causing arcs which might be associated with substantial energies, a disruption detection system has been implemented which detects both locked  $n=1$  modes and vertical displacements of the plasma, as well as responding to large induced voltages on the saddle coils. If any of these three protection circuits is triggered, the saddle coils are short-circuited in less than 100ms by the saddle coil crowbar, thereby reducing the possible induced voltages and arc current, which could result. These protections have performed well and the crowbars have fired with 100% reliability during disruptions.

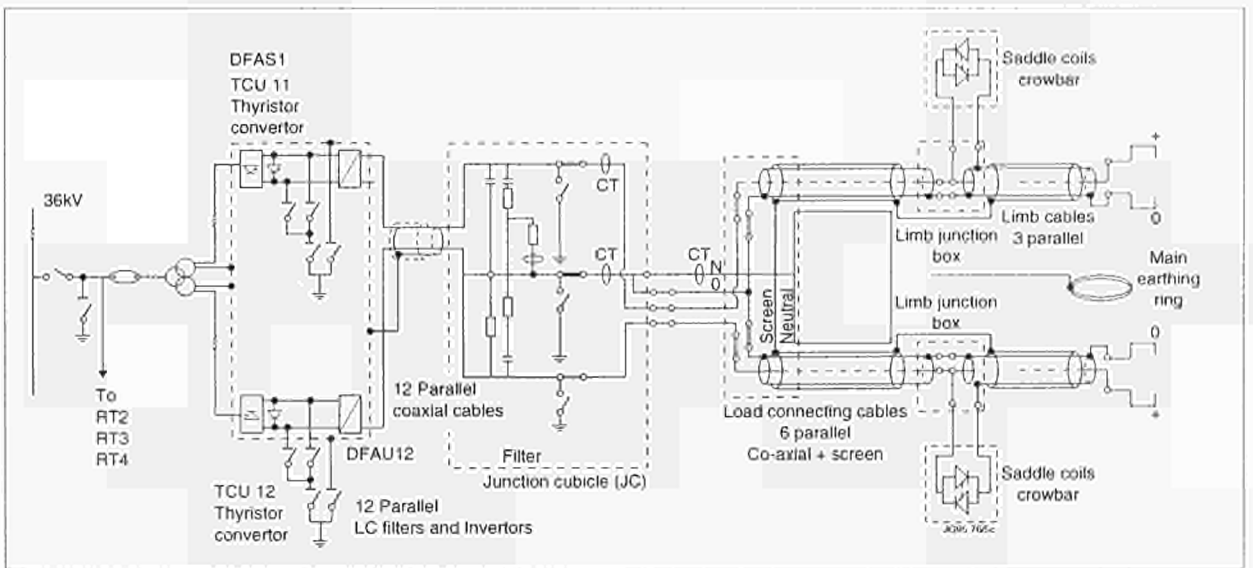


Fig.67: Schematic of one DFSS circuit, showing the arrangement of one disruption feedback amplifier, transmission lines, two saddle coils and crowbar protection.

The disruption feedback controller, which is the key component in the DFSS, receives input from four magnetic pick-up coils inside the torus, from which the amplitude, phase and frequency of the precursor are determined. The necessary magnetic correction signals are then calculated and control signals sent to the DFAS, which operates in current control. This produces an appropriate magnetic correction field, via the saddle coils, to stabilize the mode growth.

The detection system for the feedback control circuit is based on identification of the mode by analysis of magnetic ( $B_\theta$ ) pickup coils. New coils were installed as part of the upgrade to the magnetic diagnostic for the Pumped Divertor Phase. The detection system encompasses eight coils, located on the vessel midplane. Only four coils are used for detection, the remaining four being held in reserve in case of faults developing in the primary set. Each set of four coils is divided into two pairs, the members of each pair being separated by  $180^\circ$  toroidally and the pairs being rotated by  $45^\circ$  toroidally relative to each other. This permits amplitude and phase of the  $n=1$  component of the MHD activity to be measured. The coils have a surface area of  $\sim 0.07\text{m}^2$  and a flat amplitude and phase response up to 250kHz, so that appropriate filtering can be applied within the detection and control circuit.

Since the feedback control system is designed to deal with precursor activity at frequencies of up to 10kHz, the feedback loop must respond on a very fast timescale, in order to minimize phase delays. The target for the system is to achieve loop delays of  $<20\text{ms}$ . Therefore, to optimize the speed of the system and to provide flexibility in operation, a digital approach has been implemented. The DFC is a VME-based system, consisting of a cluster of 6 TMS320C40 digital signal processors (DSP) which process the input signals, apply necessary calibration, compensation and phase correction, and generate required control signals for the DFAS. Input from the magnetic detection system and four Rogowski coils monitoring the saddle coil currents is via eight 16 bit/500kHz ADC's which have only 2ms delay, and the output to the DFAS is via four 12 bit DAC's with only 2ms delay. In addition, a fast TAXI link to the magnetics diagnostic provides additional information, required to compensate the magnetic signals.

To optimize the signal processing delays, a judicious distribution of activities between the DSP's has been implemented. Two DSP's are dedicated to the fast processing loop and the input/output tasks, while two others

perform the JET Pulse File data collection. A further DSP performs calculations required for the adaptation of the control signals to the plasma conditions and the final processor is responsible for the TAXI interface to the magnetics diagnostic, as well as providing overall supervision of the system. The processors exchange data and are synchronized through C40 communication links and the system is interfaced to CODAS via Ethernet. A program cycle time of 5ms and a total controller delay of 8ms have been achieved. To date a relatively simple control algorithm has been developed, but future improvements include the adaptation of control parameters as a function of mode frequency and plasma conditions, using data transmitted over the TAXI link from the magnetic diagnostic, KC1D.

Commissioning of the system is underway and initial open loop power experiments have been performed in the presence of plasma. Although the principal aim of the system is stabilization of disruption precursors, a wide range of further experiments is possible. Non-rotating modes due to error fields are of major concern in the design of ITER and did limit the operation regime of JET in the past. The DFSS system will allow the physics of such modes to be investigated in detail. Several aspects of the physics of the  $m=2, n=1$  mode can also be addressed. In addition, the influence of error fields and MHD activity on the core and edge plasmas can be investigated.

### **Plasma Fuelling**

The Plasma Fuelling Group is responsible for pellet injection systems, the control of plasma density, co-ordination of vessel conditioning and analysis of the torus exhaust gas. There are two main pellet injection systems.

#### ***The Pellet Centrifuge***

The pellet centrifuge for the shallow deposition of pellet fuelling mass beyond the recycling layer at high equivalent flow rates is intended as an intermediate radius particle source tool in connection with divertor pumping. The centrifuge is in an advanced construction and commissioning phase and its implementation on the machine is now planned for early 1995. Figure 68 shows the centrifuge on its stand in the Assembly Hall.

#### ***The High-Speed Pellet Launcher***

The high-speed pellet launcher is based upon two-stage gun technology and has been for some years under

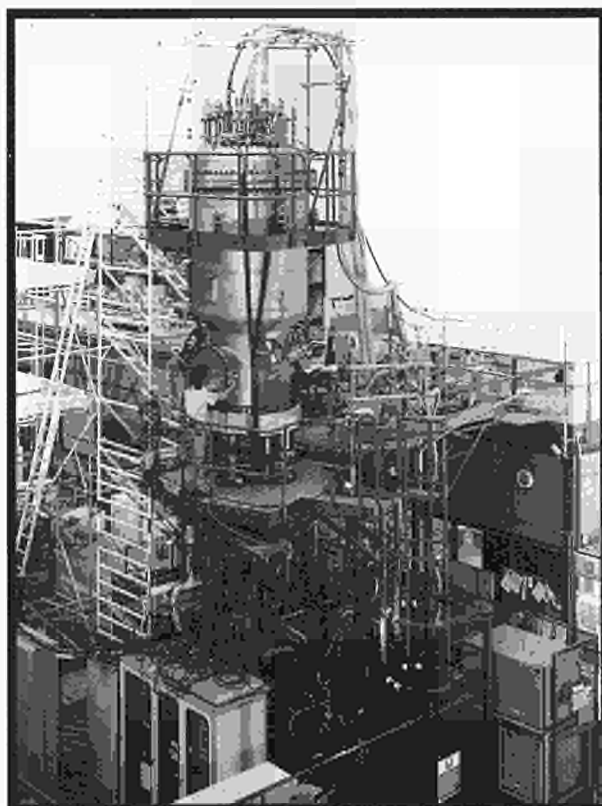


Fig68: The Pellet Centrifuge

development. This system has now been installed on the machine and is being commissioned with plasma.

First pellet launches into the plasma have been performed. During a sequence of successful pellet shots into the plasma, it unfortunately turned out that the bursting discs loaded in the respective bushing batch were wrongly etched and this resulted in too low a break-away pressure. Bushings are the mobile sections of the gun barrel in which the bursting discs, the sabot and the condensed deuterium pellets are wheeled into the breech. This led to pellet speeds in the range of only 1.6 to 2 km/s. Figure 69 shows the pressure pulse of the two stage gun, the microwave signal traces of an interferometer whose two cavities are successively traversed by the pellet and the  $D_{\alpha}$  signal. Magnified in the cut-out, is the time-of-flight delay giving the speed and the magnitude of the signal indicating pellet size. The plasma commissioning of deuterium pellets with speeds in excess of 3 km/s is being continued.

A sabot is a plastic (polyethylene or propylene) carriage to protect the deuterium pellet from the driver gas of the two-stage gun. To benchmark the effect on the plasma of an accidentally delivered sabot which might fail to properly be eliminated by the shear cone, a hollowed out plastic cylinder of 6 mm diameter and 4 mm

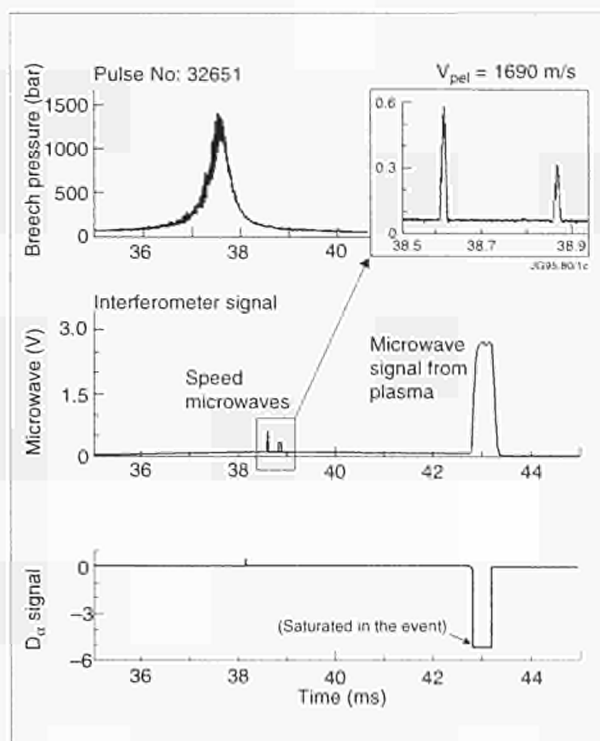


Fig69: Pellet flight summary

length ( $7 \times 10^{-2}$  mg) at  $\sim 1200$  ms<sup>-1</sup> was deliberately shot into a 2MA X-point plasma. The second purpose of this experiment was to investigate whether a plasma could be intentionally terminated by this technique. This would avoid unduly high disruption forces. It was hoped that both the thermal and the magnetic energy would be dissipated into radiation by the cold-shocked plasma with its now high carbon contents. The preliminary result was positive in that the position of this plasma decaying in about 20 ms could be maintained and the energies went mainly into radiation. The resulting disruption created only moderate forces on the vessel and the immediate recovery in the next pulse indicated low de-conditioning of the first wall and auxiliary limiters. Cultivating this kind of termination may well turn out to be of essential benefit to the next generation of fusion experiments but needs further experimental evaluation.

### Plasma Density Control

Based upon micro processor controlled CAMAC units, a new control for the gas introduction system to the machine (the plasma density feed-back system (PDF)) and an update of the plasma density validation (PDV) have been brought successfully into operation. PDF contains two hierarchical loops. The first one commands any combination of the ten gas inlet valves at various loca-

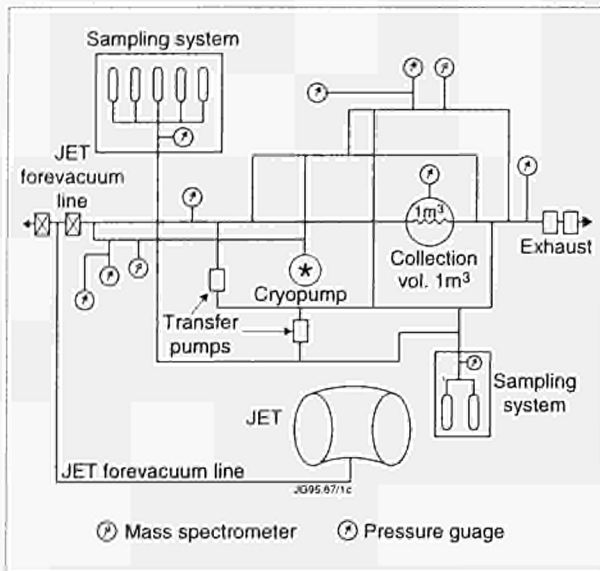


Fig70: Schematic of the gas collection system (GCS)

tions on the torus with reference to the validated density, a safe combination of the (FIR) laser interferometer signals and the Bremsstrahlung signal, in case of interferometer fringe jumps. The second one can be linked to any other monotonic signal and has been successfully referenced to the boundary probe signal (KY4D) and the Bolometer (KB1). A more flexible and sophisticated version of PDF and PDV, VME units, is under preparation and ready for commissioning.

### Gas Collection System

A new gas collection system (GCS) for the analysis of the torus exhaust gas has been completed with respect to its procurement and installation and is being in part commissioned and in part operated. It is connected to the torus forevacuum crown pumping line, in such a way that it can take over the pumping of the torus exhaust for certain times up to a total capacity of 1000 bar<sup>l</sup> of gas. The GCS (Fig.70) features two sections; one on the low pressure side (torus forevacuum line); and one equipped with a 1m<sup>3</sup> vessel at higher pressure, into which the gas can be compressed by a transfer pump. Both sections are equipped with various pressure gauges, sampling stations and mass spectrometers for the analysis. The first section also features a cryopump which can either accumulate the exhaust of many pulses up to the GCS capacity or take the gas from the torus cryopump after its regeneration in one batch. The GCS cryopump, which can be operated with and without the use of carbon fibre cloth for the cryogenic pumping of helium, will then re-generate into the 1m<sup>3</sup> volume of the second section for further analysis.

## Remote Handling Systems

A comprehensive suite of Remote Handling equipment is being prepared to support operations during periods when man-access to the machine is not possible. During and immediately after periods of D-T operation, parts of the machine will become activated to an extent, where man-access is severely limited and under these conditions all maintenance and remedial work in the restricted areas will be performed by trained operators utilising remote handling equipment.

The remote maintenance philosophy is based on the principle that maintenance tasks must be undertaken by trained operators using remote handling machines. The operators position and deploy the equipment so that remote maintenance becomes a direct extension of the 'hands-on' maintenance operations. The inbuilt intelligence and adaptability of the human operator is retained and is aided and enhanced by the robotic devices, which provide force reflection from the work face and include functions, which enable the equipment to learn and repeat particular motions/procedures, etc. The resultant Remote Handling System is essentially general purpose and has only a limited amount of task specific equipment.

This approach has enabled the overall remote handling equipment development to be minimally affected by the continual modification and development of JET since 1983. As an example, the 1992/3 shutdown of resulted in a complete reconfiguration and replacement of hardware within the torus. The only significant effect on the remote handling system equipment was in the area of specialised tooling where development of new cutting, welding and handling tools was required. All other major elements of the remote handling system remained unaffected.

The design, development and proving of remote handling equipment has taken place in line with the need to apply much of the equipment to maintenance tasks during hands-on shutdowns. The Articulated Boom and special tooling have been used extensively since 1985 as well as, to a lesser extent, the TARM, ROLLT and various end-effectors.

During 1994, the Remote Handling Articulated Boom and special tooling were used to facilitate the final phase of Mark I Divertor installation, including installation of the Mark I divertor modules and the welding of the divertor module cooling pipework in-vessel.

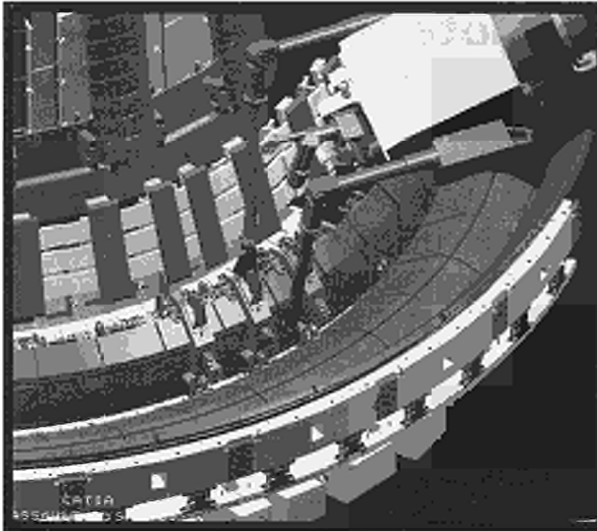


*Fig.71: Computer generated image of Mascot servo-manipulator attached to the end of the Articulated Boom performing in-vessel tasks*

In the remainder of 1994, all effort within the Remote Handling Group was focused on preparing for the installation of the Mark IIA divertor system due to take place during 1995 and the fully remote exchange of Mark IIA tile carriers by the Mark IIB tile carriers planned immediately after DTE1. This remote tile exchange will be the first fully remote task undertaken on the machine and will also be the most significant fully remote handling task undertaken on any fusion device in the world. Accordingly, extensive preparations are being made for the proving of the equipment function, performance and reliability together with the derivation and development of task techniques and operator training using full scale mock-ups. The operations will be performed in-vessel by use of the Mascot servo-manipulator mounted on the end of the Articulated Boom entering from Octant No:5 (see Fig.71). Special tools will be used to handle the tile carriers and all components will be transferred into and out of the torus through Octant No:1 main horizontal port.

During and after DTE1, the activation of the torus will also restrict personnel access in a limited way ex-vessel. Direct access to systems at the main horizontal and vertical ports will not be possible for extended periods. Accordingly, the possibility of it being necessary to undertake some limited ex-vessel remote handling tasks is being investigated.

### **Remote Handling Equipment Reliability Test**

The reliability of remote handling equipment will be critical to the success of any remote handling mainte-

nance operation. Reliability of the Articulated Boom and special tools have been proven by extensive use during hands-on shutdowns since 1985. In addition, a Mascot servo-manipulator system of the same mechanical design as the one used at JET has been proven in use at CERN since 1971. The remainder of the remote handling system and the integration of the various elements into a fully operational system needed to be proven reliable. This will be done implicitly by the application of Remote Handling equipment to tile carrier task trials in extensive full scale mock-ups during the next two years. However, to demonstrate the reliability of remote handling equipment explicitly as early as possible it was decided to undertake a controlled set of operational experiments using as much of the relevant remote handling equipment as possible.

This "so-called" 1000 hour test was undertaken over a six-week period operating the remote handling equipment for 24 hours per day, six days per week. The equipment in use comprised the Articulated Boom, Mascot servo-manipulator, various handling tools, Man-Machine Interface system, gas supply service system for gaiters and cooling, camera packages, video/audio multiplexing system, Control Room infrastructure and the overall Control Communications Network. The system was operated under fully remote control with a duty cycle typical of that expected during the remote tile exchange. Over the entire six week period, there was only one occasion when the equipment was unavailable for operations due to a small problem with one drive of the Articulated Boom which was diagnosed and repaired within one eight hour shift.

The tests were highly successful and extensive information and confidence in the performance and reliability of the equipment was obtained.

### **Articulated Boom**

The Articulated Boom was used during the final phase of the Mk I Divertor installation shutdown to transfer into the torus and position all 48 divertor modules. The Articulated Boom was subsequently stripped down for routine maintenance, rebuilt and characterised before being used during the 1000 hour test programme. The Boom performance and condition was closely monitored and re-characterised during and after the 1000 hour test programme, in order to detect any changes within the Boom actuators during operation. No significant changes to function or performance were detected.

In a separate development programme, and making use of the newly commissioned Boom Development Test Rig, a study was undertaken into the feasibility of implementing torque loop control on the Articulated Boom servo-actuators. Computer analysis was used to show that considerable improvements to Articulated Boom performance could be obtained using this technique and experimental work confirmed this.

## Manipulators

The Mascot servo-manipulator was used extensively during the 1000 hour trials and also throughout the year for various small-scale bench tests associated with remote handling tool development. Significant progress was made in the use of air-cooling for Mascot slave actuators by directing cooled air from a vortex tube mounted within the slave actuator housing. From a single air supply, vortex tubes passively generate two streams of air, one 20°C cooler and the other hotter than the incoming air temperature. The effectiveness of this type of cooling was confirmed during the 1000 hour trials, when just one of the two Mascot arms was cooled in this way. Modification of the airflow distribution within the slave arm housing have been shown to offer potential for yet further improvements.

The Mark IIA divertor tile carriers are expected to be of a weight significantly greater than the capability of the Mascot slave arms. Whilst it will be possible to upgrade Mascot in the long term, it is not possible to achieve this and prove it within the timeframe for DTE1. Accordingly, the operational scenario for the remote tile exchange has been derived making use of a new 40kg winch attached to the Mascot slave between the pair of arms. This winch has been designed, built and tested this year.

A long term programme of work to upgrade Mascot to 35kg capacity per arm has been initiated. This involves changes to the mechanical structure, the actuators and the control system. In 1994, the feasibility of making the changes to the control system have been proven and prototypes of the new actuators have been designed.

## Special Tools

In the early part of 1994, there was extensive use of the 50mm diameter alignment and welding tools in-vessel for final installation of the divertor water cooling system. Ex-vessel, considerable use was made of the lip-welding and cutting trolleys and circular port tools as various systems

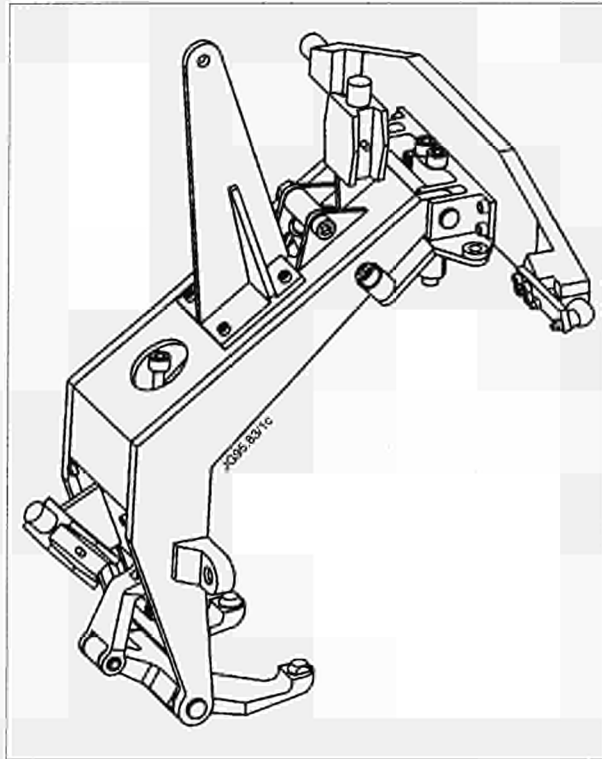


*Fig.72: Special Remote Handling Tool to install and remove a tile carrier whilst protecting the edges of protruding tiles*

were re-installed on the machine. Also in this period the 4000 Mark I Divertor tile packs were installed in-vessel using the remote handling tile tools and the poloidal limiter and Lower Hybrid Current Drive protection tiles were also installed using remote handling tile tools.

In the remainder of 1994, there was considerable design effort and prototype testing of tools for the handling of Mark IIA divertor tile carriers. It is required to pick up each of the six types of tile carrier using the Mascot servo-manipulator assisted by the 40kg winch. It is critical that during the handling process no damage is done to any part of the tile faces or sharp corners and each tile carrier must be aligned and fitted adjacent to other tile carriers with a gap between them of a few mm. A special handling tool was designed both to handle the weight of the tile carriers and to ensure that removal or installation of a tile carrier from between two adjacent tile carriers was achieved with no risk of clashing or rubbing the close fitting tiles (see Fig.72). The concept derived was proven in a simple bench test rig and fully detailed prototypes of the tools have been designed and are being built.

The installation of divertor coils within the torus has resulted in extremely limited access to the lower 91mm diameter circular ports. In many cases, these are not possible to reach without displacing the coils and so these ports are blanked off with a welded plug. The remaining

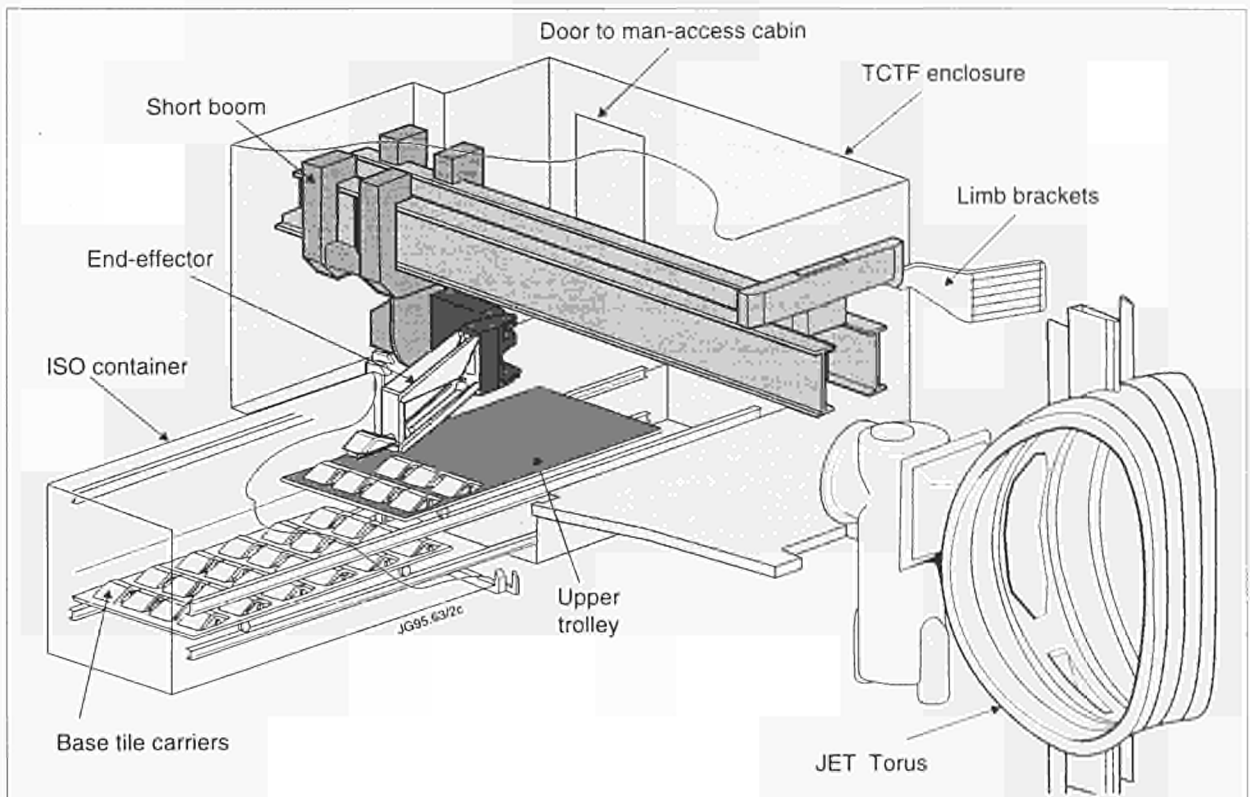


Fig.73: The new Octant No.1 Facility designed to transport tile carriers and tools fully remotely into and from the torus

lower circular ports, which have equipment installed, cannot be reached using the original cutting and welding tools and so new tools have been designed and the cutting tool has been manufactured.

During the removal of the Mark I Divertor in 1995, it will be necessary to cut all 96 of the 48mm diameter water feed pipes in-vessel, in order to remove the divertor modules. This will be done using a new cutting tool. During DTE1, it is required that the Remote Handling Group be prepared and able to change any of the in-vessel first wall tiles. Accordingly a concept design for a generic tool for bolted tile handling has been derived and the first version is being built.

### Remote Handling Control Room and Man-Machine Interface

The Remote Handling Control Room was used in 1994 for command and control during the 1000 hour trials and also for all Mascot based bench tests. The Control Room is being refurbished and rewired to control the new equipment required for the remote tile exchange.

All remote handling equipment can be controlled by means of a customised control panel delivered with the specific equipment. This control panel or Man-Machine Interface (MMI) facilitates stand-alone control of the

equipment during acceptance testing, development and for hands-on use. The Man-Machine Interface for remote handling equipment under fully remote control will be installed on PC machines running under Windows NT and communicating to the individual equipment controllers through Ethernet and dedicated serial links. A software utility is being designed and generated which will facilitate the creation of an MMI for any piece of remote handling equipment by an operations JRO with minimal programming experience. This MMI framework programme is now being applied to the command and control of the hydraulic and pneumatic power supply System and the Boom Interface Cubicle for use in 1995.

### Remote Handling Viewing System

A new camera package for deployment at the end of the Articulated Boom, TARM and Mascot has been designed and built. The package weighs less than 2 kg and comprises a Pulnix CCD camera with integrated zoom lens, microphone, roll axis and lights housed within a sealed case. To position and orientate the new camera package, the original two camera arms envisaged for use at the end of the Articulated Boom and TARM have been reduced to a single, shorter camera arm. This camera arm and the

associated cable reeling system were designed and developed during 1994.

To accommodate the full suite of cameras and monitors required during the remote tile exchange, the video/audio crossbar has been expanded to its full size of 70 video inputs switchable to 40 video outputs.

### **Remote Handling Tile Carrier Transfer Facility**

The remote tile exchange concept requires the transfer of tile carriers and tools into and from the torus through the Octant No:1 main horizontal port. This transfer task and the placing of tile carriers in a transport container will be carried out fully remotely by means of a new Tile Carrier Transfer Facility which will be installed and operated at Octant No:1 (see Fig.73). The facility comprises a so-called Short Boom with an end-effector suitable for carrying the various tile carriers and tools housed within a sealed enclosure for contamination control but with interface doors for a man-access module and tile carrier transfer containers. The removed tile carriers are placed on the end-effector in-vessel and then removed from the torus by operation of the Short Boom which then places the tile carrier at a pre-determined location on one of two trolleys positioned within the main enclosure. Transfer into the torus of new tile carriers will be achieved by substituting the tile carrier storage cabin containing removed tile carriers with a cabin containing new tile carriers and reversing the process. Concept design for the whole facility has been completed and a contract for detail design and manufacture of the Short Boom has been placed. The new end-effector design is complete, the enclosure interface to transfer containers is complete and prototype double doors are being manufactured. The control system for the entire facility has been designed and prototype testing of critical functions have been completed.

## **Waste and Beryllium Handling**

The Waste Management Group is responsible for provision of facilities in support of interventions and shutdowns, respiratory protection equipment and disposal of radioactive and beryllium wastes. This involves the operation of five controlled areas, including the Torus Access Cabin (TAC), Building K7 complex, the two Beryllium Handling Facilities and the Waste Handling

Facility (WHF) in Building J30, together with operation of the liquid waste drainage system.

At the beginning of 1994, all staff were involved in the final stages of the divertor shutdown. During the remainder of the year, the emphasis has been on the sorting, volume reduction and despatch of wastes from the site, support for ad-hoc machine interventions and preparations for the facilities which will be required for the remote exchange of divertor components planned to take place after DTE1. The main features of the work are described in the following sections.

### **Torus Access Cabin**

The Torus Access Cabin (TAC) enables personnel to access the JET vessel in a manner which prevents the spread of radioactive or beryllium contamination beyond controlled areas and includes decontamination, workshop and waste transfer facilities. The latter includes the ability to transfer both drummed waste and waste in ISO containers. These can be docked onto the TAC by means of a special double PVC membrane which avoids the need for Health Physics clearance. It is designed in such a way as to present a clean, closed face on both controlled area openings to the torus hall environment. The containers, presenting a clean outside surface, can then be transferred through uncontrolled areas and docked onto the J30 Waste Handling Facility. The arrangements which are shown in Fig.74 have reduced the transfer time from one shift to 45 minutes.

Although the TAC attached to the JET vacuum vessel was a semi-permanent arrangement operating continuously for 22 months of the divertor shutdown, it has been designed and improvements made to permit rapid docking to the machine to permit access for emergency interventions. The TAC is normally parked in the Assembly Hall and is craned into the Torus Hall when required. Three interventions were made during 1994 and the in-line time involved in connection of the TAC (including opening of the pumping chamber door, establishment of services and preparation for entry in pressurised suits has been reduced to less than one shift).

### **PVC Handling Facility (Building K7)**

The Building K7 facility includes a pressurised suit cleaning and inspection area, a PVC workshop, and a suit training area. The facility was more heavily used in 1994, since all three ad-hoc vessel interventions required pres-

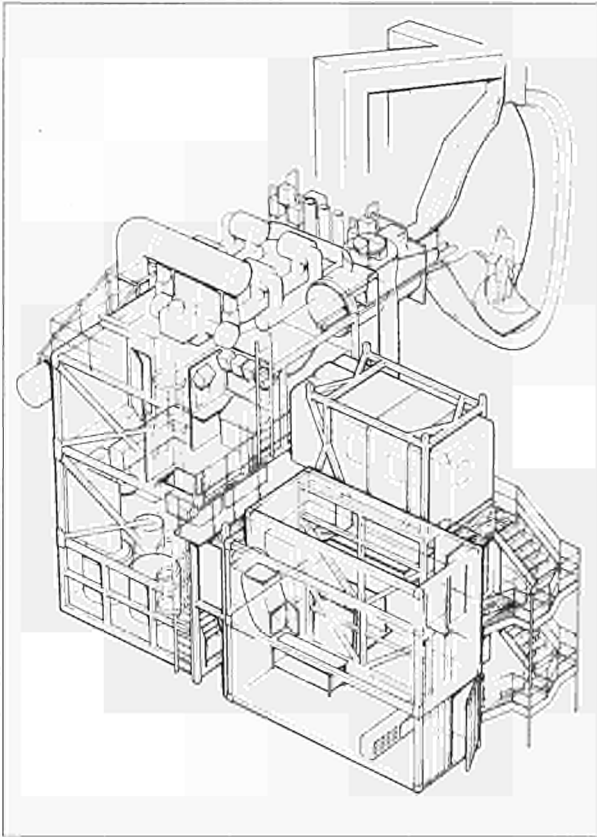


Fig.74: Torus Access Cabin

surised suit working. JET has a stock of about 350 suits plus half-suits and other respiratory protection equipment, which is required to be maintained in readiness for any intervention. The daily throughput of cleaning, inspection and repair is about 20 suits.

The PVC workshop continues to provide PVC isolators and tents, including a tented facility for decommissioning of the prototype LHCD launcher. In preparation for future shutdowns, a suit training area has been established in Building K7.

### **Beryllium Handling Facilities**

The Beryllium Handling Facilities have been operated continuously during 1994. These provide containment and contamination facilities to enable Waste Management Group and other Divisions to carry out cleaning and maintenance on beryllium-contaminated components.

### **Waste Management Facility**

This facility is used to sort and segregate waste from re-usable components, carry out volume reduction and package waste for consignment off-site. It has been enhanced by additional glove box facilities to improve the ability to sort bags and separate different classes of waste.

During 1994, over 700 packages containing potentially radioactive waste were produced at JET. Approximately 80% was classed as "housekeeping" or compressible, with the remainder classed as irregular waste which is likely to require detailed sorting and subsequent streaming of material types. The facility has prepared 177 drums of waste and 114 of these have been despatched to the Harwell Laboratory (for subsequent disposal mainly at the BNFL site at Drigg). The mixture of materials processed during the year includes a variety of plastics, sealed sources, aqueous acidic waste, carbon tiles, metal components and organic liquids. Rigorous 'Quality Assurance' procedures are required to demonstrate that the waste is properly categorised. Improvements to the waste management database have been made and sets of analysis results have been made for the above consignments.

### **Waste Drainage System**

A number of improvements have been made, including more robust arrangements for the interlocking of transfer between tanks in the system. A total of 1140m<sup>3</sup> in 19 batches was discharged from the JET holding/assay tanks at the Culham Laboratory tank farm.

### **Waste Characterisation**

The lower threshold for radioactive waste is 0.4Bq/g. As it is not possible to detect tritium at such a low level using conventional techniques without resorting to costly destructive analysis, a technique of tritium extraction from certain materials using humidified nitrogen and air has been developed in conjunction with Politecnico di Milano, Italy. The results of tests on samples in the extractor rig were compared with destructive analysis. The technique has the capability of detection below 0.4Bq/g and will assist in segregating material which may be disposed of via a non-radioactive route.

### **Preparations for Remote Tile Exchange**

The remote tile exchange, planned to take place after DTE1, will involve suited personnel access to enclosures situated at Octant No 1 and Octant No.5, and facilities for transfer of a large number of activated and Be-contaminated tile modules from the Torus Hall. Transportable controller/dresser units to provide support and services for four men and an improved double door system to ease docking of ISO containers onto a controlled area have been designed and are being procured.

# Vacuum Systems

## Gas Introduction

In preparation for the next tritium plasma operation, design of gas supply lines connecting the Active Gas Handling System (AGHS) with the torus and both Neutral Injection Boxes (NIBs) has started. The AGHS will supply  $D_2$  and  $T_2$  to the NIBs and  $T_2$  to a single piezo-valve on the torus.

For glow discharge cleaning, a new supply system has been designed and is being procured. The new system is based on permanently installed individual supply lines for  $D_2$ ,  $H_2$ ,  $^4He$  and one other (exchangeable) gas. Each supply line has a mass flow controller, which can be remotely set for optimum operating pressure. The new system will permit fast and easy start-up (always with a  $D_2$  gas puff). Changeover from one gas supply to another can be performed instantly without even switching off the glow discharge.

## Leak Detection

The detection of leaks using a standard  $^4He$  mass spectrometer leak detector with  $^4He$  as a tracer gas is severely restricted on equipment releasing substantial amounts of  $H_2$  and, in particular,  $D_2$ . Previous attempts using a standard regenerable getter pump for  $H_2$  and  $D_2$  at the leak detector-inlet improved this background signal by about 2 orders of magnitude. A new, improved getter pump ( $1/2$  Ø tube, 500mm long, filled with getter pellets) improves this suppression to >5 orders of magnitude: a  $D_2$  leak connected to the  $^4He$  mass spectrometer and adjusted to  $1 \times 10^{-4} mb \ell^{-1}$  indication was suppressed to  $\sim 5 \times 10^{-10} mb \ell^{-1}$  when the gas flow was passed through the getter system. As a result, it would now be able to perform and scrutinise leak detection on the torus at operating temperature of 250-300°C, if the use of  $^4He$  for glow discharge cleaning could be abandoned.

## Insulating Breaks in Forevacuum Lines

Forevacuum lines were at torus potential, and could rise to 2000V in an accident scenario. As the amount of new equipment in the area where the vacuum lines exited from the Basement steadily increased, it became more difficult to prevent access to these lines. Therefore, insulating breaks were required for reasons of personnel safety. Breaks were developed to sustain 2000V even at pressures in the Paschen breakdown minimum. The breaks

consist of ten equipotential planes connected to a linear voltage divider. Since distance and hole size in the equipotential grid could not be made sufficiently small to avoid breakdown (for vacuum conductance reasons), an auxiliary homogeneous magnetic field parallel to the equipotential planes of  $\sim 200$  Gauss (0.02T) was necessary to achieve the required hold-off voltage.

## Baking Plant Gas Purifier Loop

The Baking Plant will have  $^4He$  as operating medium during D-T operation. To remove permeated tritium and inleaking air from the circulating gas, a purifying system was designed and manufactured. A bypass "polishing" flow of  $\sim 30 m^3 s^{-1}$  passes through two molecular sieve beds which adsorb HTO and then through a cryogenic (77K) activated charcoal adsorber to remove air. The purified gas is returned to the Baking Plant, the absorbed air is periodically regenerated through the AGHS Exhaust Detritiation system. Tritium monitors at several points in the loop serve to assess loop efficiency and permit decisions on regeneration of the molecular sieve beds.

## New Torus Vacuum Vessel Supports

The vacuum vessel supports of previous design often caused problems by not moving freely during vessel temperature changes. Furthermore, due to their inherent backlash, they needed preloading which could only be achieved by a vessel temperature increase. This made any operating temperature change of the torus a rather time-consuming procedure. The new design, successfully tested in a prototype employs large needle bearings which guarantee smooth and free rotation of the eccentrically pivoted lever arm drum. A disc brake incorporated on one side of the drum permits fixation at any time or vessel temperature. Preload is no longer required, since the redesigned mechanism is free of backlash. However, an arrangement of lever arms and springs (or counter-weights) will be incorporated to permit partial compensation of the increased weight of the vacuum vessel (divertor and other in-vessel equipment).

## Coil Case Pumping

The epoxy impregnated divertor coils, situated inside the vacuum vessel, are encompassed by a 1.2mm thick metal casing which at the electrical connector end protrudes through the vacuum vessel wall. A vacuum tight flexible pumping connection between coil casing and epoxy was

required to facilitate pumping of the degassing products of the epoxy, in particular, during neutron bombardment in the active phase. Pumping is also required to avoid rupture of coil casings due to ambient pressure entering the space between the protruding epoxy and the metal coil tail. Four pumping boxes are foreseen with expansion bellows and are seal welded onto the metal coil case tail end.

Using an automated syringe, the sealing to the epoxy was effected by the in situ casting of a poly-urethane rubber seal. After setting of the compound, the rubber seal was mechanically compressed to form a lasting vacuum seal. In conjunction with the coil case pumping system, the expected pressure range 0.1-1.0mb has been obtained without problems. The vacuum connections from the pumping boxes to the metal pumping lines had to be flexible and in addition, to avoid equipment damage due to spurious machine voltages, had to provide for a 2kV isolation. Paschen breakthrough tests were carried out over the pressure range from 1bar -  $10^{-4}$ mb using various lengths of 12mm ID Hyperlon hose as an electrical break. By using 80cm length of this hose, no Paschen breakthrough was observed and this type of break was consequently installed.

### Vacuum Interfaces

With respect to leak testing during the DTE1 and DTE2 phase considerable progress has been made, in particular, by specifying the interspace policy governing the ~450 interspaces on the machine. The principles presently being put in to practice rely on the manifolding of interspaces into ~35-40 groups. Each manifold will carry several 1/4 inch metal toggle valves, one for each connecting interspace line. In addition, the manifold will have a Bourdon pressure gauge, a pressure release valve, an isolation toggle valve and a suitable automatic vacuum coupling for attachment to the portable service set. Each system will be pumped down individually and back filled to 500mb with a suitable tracer gas and sealed off using the manifold isolation valve to provide secondary containment. The individual toggle valves to the interspaces will be left open at this stage.

On a leak indication, increase of the tracer gas partial pressure in the torus, suspected manifolds will be re-pumped, where a reduction in the tracer gas partial pressure is used as a leak indicator. Once the offending manifold has been located the toggle valves of the individual interspace lines will be used in a similar fashion to

find the leaking interspace. The choice has then to be made for repair or to pump down and valving off the interspace creating a guard vacuum which will significantly reduce the effects of the leak. In a later stage all the connections will be extended, possibly along side the vertical limbs, to a position in the Torus Hall or Basement accessible from floor level.

To aid helium leak testing a pressure release valve is planned near the manifold isolation valve which can be used to distribute helium, for "fire hosing", in the area near the manifold by pressurising the line from the Torus Hall ground floor or Basement.

### Control and Instrumentation

The commissioning of the many vacuum and conditioning systems spearheaded the transition from shutdown to operations. The reconnection subsequent testing of more than 600 torus jumper cables associated with pumping, valves, baking, vessel conditioning, gas introduction, vacuum and in-vessel instrumentation initiated the restart activity. Substantial effort was made to quickly bring on-line and commission more than 40 electrical cubicles for new, old and upgraded vacuum systems. Equipment which had supposedly been left untouched during almost two years of shutdown, presented the most re-commissioning challenges.

In general, the vacuum systems performed reliably over the year. Old systems such as the turbomolecular pumps and rotary baking pumps have operated with significantly improved reliability following the preventive maintenance programme which was performed on their control cubicles during the shutdown. The divertor coil case pumping system which was designed for high reliability and integrity has operated continuously, without fault, preventing the out-gassing of about 100mbar/day of gas causing ballooning of the divertor coil case. The torus 15mbar interlock which is used for draining the water systems in case of a pressure rise, is another new high reliability system which has functioned well. The vacuum system in support of the Lower Hybrid cryopump and new divertor gas introduction system have been used extensively and performed well. The in-vessel current shunts and the divertor coil case thermocouples, respectively, have produced very valuable data for analyses of forces on internal components and thermal interactions.

The new glow discharge cleaning system has been used routinely and effectively for vessel conditioning. Various

problems have been experienced with both the hardware and control software but these have been solved and the equipment enhanced throughout the year. The standard cleaning scenario used Helium gas at the  $10^{-3}$  mbar pressure range and 3-4A DC current on each of the four electrode with RF assistance. A lower pressure higher voltage scheme was also developed which was found to be particularly effective at cracking heavier molecules but tended to impregnate carbon tiles with the cleaning gas.

The vacuum vessel was generally held at 250°C by the Gas and Electrical Baking System for vessel conditioning and plasma operations. The vessel has been cooled approximately 10 times for intervention, leak testing and filling of water circuits. The new circuitry to allow the upper and lower vessel brakes to be locked at different temperatures, giving better control over the support preload, has been used routinely with the lower and upper brakes being locked at 70°C and 40°C, respectively, below operating temperature. Baking at 320°C has been performed. This is the highest temperature at which there is confidence that in case of a fault the divertor coils would not be degraded. To perform this higher temperature baking, the gas baking plant needed to be upgraded to supply up to 900kW of power. The increase in power required to heat the vessel is mainly due to the heat transfer into cooled components such as the divertor coils, target plate and cryobaffles.

The control equipment for the argon gas introduction system (cryopump frosting), has been completed. Commissioning work has been carried on a test vessel and initial argon frosting trials on the torus are ready to commence.

## Control and Data Acquisition System

The JET Control and Data Acquisition System (CODAS) is based on a network of minicomputers. It is the only interface to operate JET and it provides centralised control, monitoring and data acquisition. The various components of JET are logically grouped into subsystems like Vacuum, Toroidal Field, Lower Hybrid additional heating, etc. Each subsystem is controlled and monitored by one dedicated computer interfaced to the machine and its diagnostics through distributed front-end instrumentation. Signal conditioning and some data conversions are made using EUROCARD modules. The rest of the instru-

mentation is based on CAMAC and VME standards. Embedded front-end intelligence is implemented through microprocessors that are also used for real-time applications. The actions of the various computers are coordinated by supervisory software running in the Machine Console computer. This supervisory function includes the countdown sequence for the control and data acquisition during each plasma discharge.

During 1994, the main efforts of the Division have been focused on completion of the move of CODAS to a UNIX environment, the support of the restart of JET operation in its new configuration and the implementation of a significant number of VME-based front-end applications. This required full integration of the new control systems into the operation and deployment of new front-end intelligence based on the VME standard and connected by a dedicated network. The following sections describe the main activities and report on the current status and plans for 1995.

### Control System Integration

JET had to be restarted with a completely new magnetic configuration and a new control system that had never been exposed to the full brunt of operation but only to tests attempting to emulate the operation. The Man Machine Interface, now based on X-terminals, was also completely new. In the first months of the year, the end-to-end commissioning of all subsystems was completed. This was followed by the restart of JET operation which was controlled from the new Control Room. No serious problems were experienced which showed the quality of the original CODAS design and the dedication of all the staff involved in the move of CODAS to the new UNIX environment.

### Computer Network Topology and Implementation

The network described in the 1993 Report has been slightly modified and is working well with no performance problems. This confirms that the concept of computer clusters with local servers and the network structure based on multiple segments connected by bridges is suitable for the needs of JET. In order to monitor the performance of the network, equipment has been installed on the ETHERNET systems and statistic gathering implemented. The information collected about the network status is shown in a series of MIMICs which

assist in tracking down possible ETHERNET problems. Some status information is collected by active processes "pinging" specific destinations to further check the integrity of the network.

Following the decision to connect JET users to Internet and to provide host facilities to selected external users, the technical and security arrangements to provide such a service have been designed and implemented. The connection should be made available to users in early-1995.

## Diagnostic Support

The first VME diagnostic applications have been implemented and are part of the daily operation. The magnetic measurement diagnostic (KC1D) is fully operational. It sends calibrated and corrected data to the Plasma Position and Current Control (PPCC), the Disruption Feedback Stabilisation System (DFSS), to the real time plasma boundary identification system, XLOC, and collects JPF data. The data transfer to PPCC and DFSS is via TAXI links while that to XLOC is via two transputer links. As this diagnostic provides the reference signals used by PPCC, the data are checked automatically after each pulse for consistency and warnings to the operation team are generated if any anomaly is observed. Other VME based diagnostics now in operation include the interferometer based density measurement (KG1), where the performances of Digital Signal Processors provide enhanced accuracy and the diagnostic (KL4) which monitors the tile temperatures and stores the resulting data in the JPF. The VME based systems for the XUV and VUV Spectroscopy (KT7D), and the Neutron Profile Camera (KN3) are under construction. There are now 66 diagnostics operating on the UNIX system with 12 in various stages of development. A further four new diagnostic interfaces to CODAS are being specified.

## New Developments

### *Real Time Fusion Control*

Due to lack of available effort the development of the Real Time Power Control (RTPC) has been much slower than expected. The design of the main components for the first application is now complete. The hardware is in place and the first feedback tests are expected to take place before March 1995. Each additional heating source, Neutral Beam (NB), Ion Cyclotron Resonance Heating (ICRH) and Lower Hybrid (LH), will be driven by a local controller which can take its reference signal either from

a pre-programmed waveform or from a central controller. The central controller performs the main function of controlling a selected plasma variable whilst the local controller helps to actuate the heating source so that the power requested by the central controller is provided. A signal server collects all diagnostic signals that are of interest for control purposes. It also provides the central controller with the signal corresponding to the variable that has been selected for control. The first experiments to be carried out with this system will be electron temperature control and D-D reaction rate control by means of the ICRF system.

### *VME Electronics*

The 1993 Progress Report mentioned the concept of using a 3U commercial VME board carrying a 68030 processor and combining it with a 3U VME board based on re-programmable gate arrays. This has now been deployed successfully and several 6U VME board designs have been built in this way. The main modules are:

**VPL1 Logic module:** A 10,000-gate-equivalent array (Xilinx 4010) is surrounded by a flexible set of digital input and output buffers. There are also positions for small mezzanine printed boards; these have been used for extra memory in the first applications. The module is intended to implement general purpose logical functions. Twelve modules have been in use throughout the year converting 800 new ADC channels into transient recorder channels, with flexible sampling times, data storage and data access. The ADCs are of the new UXT1 and UXD1 types. Arrays of these 8-channel, 10kHz, 16-bit, isolated Eurocard modules have been used most successfully, both as low-drift integrators for magnetic-coil signals and as amplifiers with Langmuir probes.

**VPLS Service module:** One of these modules is installed in each CODAS VME crate. It is related to the VPL1 but has some specialised I/O buffers, including a fibre optic receiver for the Composite Timing and Trigger signal. This signal is used to provide precise JET timing pulses and clocks to all local modules. A special port allows two subracks of the JET standard low-speed digital I/O cards to be used (LSD) in support of VME. Local power supplies and cooling air are monitored also.

**VPLC Latching scaler:** Two Xilinx 4010 arrays are used in this module to provide 32 20-bit, 70MHz counters. When a latch command is received, every counter is stopped, its count quickly stored, and the counting re-

Table XII  
Quantitative Information on CODAS Installation

ITEM	End 1993	End 1994
CODAS Interface Cubicle	161	167
CAMAC Crates	204	212
CAMAC Modules	2,624	2,739
Eurocard Modules (Signal Conditioning and Power Supplies)	6,302	6,835
VME modules	122	252
CAMAC Serial Loop (Fibre Optic)	24	24
On-line Computers	45	54
Off line and Commissioning Computers	8	19

starts. The stored counts are gathered by the 68030 processor and made available for data collection programs. In this module, fast I/O buffers are fitted to accept the 32 differential pulse trains to be counted. Again mezzanine sites add flexibility to the design.

The flexibility and re-usability of the Xilinx design led to consideration of developing a CAMAC module based on Xilinx that could be programmed to emulate a normal CAMAC module. This type of approach will be developed in 1995 to replace CAMAC modules that are no longer in production or which cannot be procured in an economical way.

### Control Rooms

A set of forty 15-inch colour monitors has been installed to show additional non-interactive displays at low cost. The displays can be pictures from TV cameras or computer-generated graphics as seen on the main interactive terminals. The displays are mounted at head-height, mainly against the walls of the control rooms. These use Super-VGA standard and are driven by five Personal Computers running commercial software to emulate X-terminals.

### Evolution of Existing Systems

Tables XII and XIII give some quantitative data on the CODAS installation. The present computer configuration is also summarised in Table XIV. The extensions to the systems from 1993 are detailed in the following sections.

- To support the increasing load on off-line UNIX systems, a new development cluster has been set up using one server and 6 computers;

Table XIII  
Review of CODAS Electronics Stock Holding (Installed, pre-procurement, loaned and spares).

ITEM	End 1993	End 1994
CAMAC system modules	911	911
CAMAC digital I/O modules	842	843
Timing system (CAMAC, VME & Eurocard)	1,589	1,681
CAMAC analogue I/O modules	1,460	1,435
CAMAC auxiliary controllers	151	151
CAMAC powered crates	280	280
U-port adapter	215	215
CISS modules	1,078	1,079
CCTV	684	684
Cubicle frames	354	396
Power supply modules	2,122	2,163
Intercom, Public Address, Computer terminal network	826	844
Pool instruments	1,009	1,021
Analogue I/O in Eurocard	3,045	3,206
Digital I/O in Eurocard	5,043	5,080
Eurocard sub-racks	995	1039
JETnet active devices	341	372
VME modules and sub racks	243	672
<b>Totals</b>	<b>21,440</b>	<b>22,072</b>
	<b>Increase</b>	<b>2.9%</b>

- The operation required a larger number of X-terminals than originally envisaged and users are making heavy use of multiple windows. This led to an overload of the Man Machine Interface (MMI) computers. This has been corrected by adding more MMI computers, increasing their power by installing Weitek CPUs and increasing the installed memory to 64 MByte. For very demanding users, Engineers-in-Charge and Session Leaders, three workstations have been installed;
- One more diagnostic computer has been required due to the increase in the number of diagnostic systems;
- With increasing numbers of computers, the load associated with executing the corresponding number of console processes overloaded the computer in which they used to run. A separate system was necessary to support these console processes. Also a separate computer for network monitoring was installed and this accounts for the increase in number of host systems;

Table XIV: CODAS Computer Configuration and Allocation.

Category	Quantity end 1993	Quantity end 1994	Machine type	Memory size MByte (1)	Disk size in GByte
Server	9	10	Sun SPARCserver2	64(32)	0.424 (swap) 5*1.6 RAID
MMI	10	13	Sun SPARCserver2	64(32)	0.424 (swap)
		3	Sun Workstation	32(N/A)	0.424 (swap)
Host systems (2)	2	4	Sun SPARCserver2	32(32)	0.424 (swap)
Control system	17	17	Sun SPARCserver2	32(32)	0.424 (swap)
Diagnostic system	9	10	Sun SPARCserver2	32(32)	0.424 (swap) 1 (Volatile data)
Communication (3)	2	2	Sun 4/670	128(128)	1.6 (JPF)
		5	Sun SPARCserver2	32(32)	0.424 (local swap)
Off line development	4	7	Sun SPARCserver2	64(64)	0.424 (swap)
		1	Sun SPARCstation I+	32(32)	
		1	Sun IPCWorkstation	32(32)	
X-terminals	85	87			

- Notes:
- 1 - Numbers between brackets indicate the memory size at the end of 1993.
  - 2 - Host systems include Yellow Page Master (YPmaster), Host of all users home directories (Home), Concentrators for all console devices (Consoles) and network monitoring (NM)
  - 3 - Includes the IBM gateway and Internet interface computers.

- The complex Saddle Coil system required a new subsystem computer of its own. It proved to be extremely convenient to have an independent system on which tests and commissioning procedures could be run and to be able to include the system in the operational countdown sequence when requested by the experimental programme without interfering with other work;
- The off-line computers were also upgraded with faster CPU's and the memory increased to 64Mb. More disk volume was also added to meet increasing program development activities;
- It was decided that connection to Internet should be extended to all systems at JET. To protect the systems but still allow external access, an Internet interface comprising fire-wall and mail-server systems has been configured. This accounts for the increase in number of communication system computers.

**Electronic Enhancement**

The overall amount of CODAS installed electronic hardware grew by 8% during 1994. This reflects a strong

growth in systems using the recently adopted VME standard. Eight new cubicles were designed, constructed and installed, 565 fully-documented hardware improvements were made and 286 maintenance interventions were recorded. The safety system, CISS, has been extended by the addition of a new processor and cubicle to service the Saddle Coil systems. Twelve new cubicles were fitted with UNIX equipment in the computer room.

**CAMAC Interface**

As previously reported, the interface to the serial CAMAC loops is via a VME module connected by a VME/Sbus adapter to the host computers. It has continued to work with extremely high reliability.

**Link to the IBM**

This link via two SUN670 computers fitted with SUNlink channel interface boards is now fully operational. The initial services for transferring QPF (Quick Pulse File used for immediate data analysis on the IBM), JPF (JET Pulse Files) and LPF (Late Pulse Files for data collected up to few minutes after the pulse) data have been expanded to

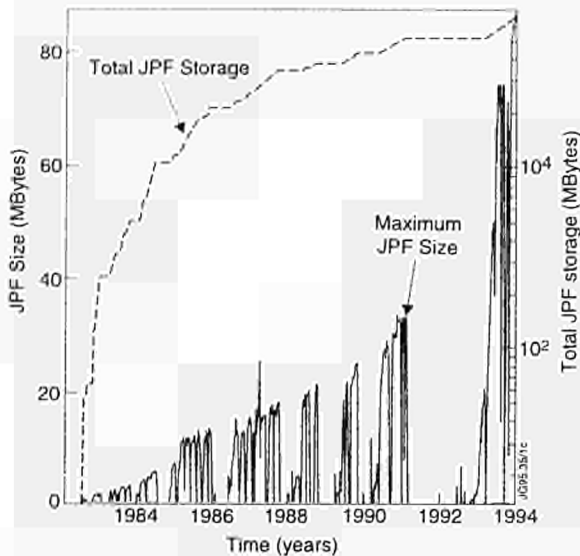


Fig.75: Evolution of CODAS data collection over the years

include automatic archiving of various CODAS log files and continuous recording data to the IBM.

### **New Data Collection Scheme**

The new data collection scheme implemented under UNIX which now includes facilities to collect data from VME and PC based diagnostics is running successfully. Transfer rates from individual subsystems to the IBM are in the range 200 to 550B/s depending on the size of the subsystem JPF. The overall transfer rate when several systems are transferring simultaneously is in excess of 1.5 MB/s. The QPF and JPF transfers and collection are in use and the first LPF data is expected early in 1995. The current JPF size is between 75 and 84 MBytes (see Figure 75) which agrees well with the forecast figure at this stage of 80 MB. The overall collection and transmission time to the IBM is around 280s increasing to 500s when disruption data is collected. Efforts to improve this performance are continuing.

### **Control of User Actions**

The protection scheme has been expanded to tailor the control of user actions to the operational state of JET. For example, this allows some actions to be restricted to a few authorised users during operational periods and the restrictions to be relaxed during maintenance periods. In addition the right to issue special types of communication messages or to send messages to specific communication ports can also be restricted to specified users.

### **Level 1**

During the restart period, a significant extension of the Level 1 software was made to cover all new front end application. Without the power of this tool, commissioning of systems like the new Plasma Control would have been extremely difficult. This tool is now used routinely by users to prepare pulse schedules in advance of the experimental sessions and to set all parameters for each pulse. This system is being expanded by the addition of more validation and calculation algorithms.

### **JETnet**

JETnet is the off-line network connecting all offices and user areas within JET. Its usage has grown by 20% about through the year. During the day, an average of 280 of the 610 users are logged-in. They are supported by six Vines servers and 14GB of disk storage.

### **System upgrade**

#### **Central Interlock and Safety System**

As in previous years, the Central Interlock and Safety System (CISS) has undergone a series of modifications and extensions to accommodate new JET equipment and to reflect new operating scenarios. An additional PLC has been added to the network to cover additional power amplifiers such as those used for the Saddle Coils. More importantly, in the framework of a possible extension of JET until 1999, a study has been made to review the maintainability and performance aspects of the existing PLCs which form the core of CISS. Based on the results of this study and on the outcome of a preliminary enquiry, it has been decided to proceed with a progressive replacement of the old units by more modern but fully compatible PLCs. The selected supplier will be identified in January 1995 and the first PLC will be installed in March 1995.

#### **Plasma Density Feedback**

The demand of operations created by the additional gas introduction modules has reached the maximum capability of the existing Plasma Density Feedback system (PDF) which was running in a CAMAC based TMS9900 front-end microprocessor. This system has been moved to VME and uses the more powerful 68040 based processor. The full commissioning and operational tests will be carried out in January 1995. The new platform for PDF will allow installation of an adaptive controller as a second stage improvement. One difficulty in controlling

the plasma density is that the dynamic properties of the plant keep changing which in turn affects the control performance. An adaptive controller capable of handling this complication is now under implementation. This controller is to identify the changing plant dynamics and re-tune itself accordingly in order to maintain required control performance. This system has been run on simulated data and, in this environment, showed a convergence time compatible with the operational demands.

## Data Management

The Data Management Group is responsible for the provision of the central computing services based on three separate networked computing environments - the IBM mainframe system, a cluster of networked high performance UNIX systems, and the site-wide network of PCs and Apple Macintosh machines. The Group is also responsible for the management of JET data and for organisation and control of routine data processing.

### The Mainframe Computing Service

The mainframe computing service is based on an IBM 3090/300J with 160 GigaBytes (GB) of disc storage and a further 2000 GB of automated cartridge tape storage. The service has been operating since June 1987 and the central computer was upgraded in February 1990 from an IBM 3090/200E to an IBM 3090/300J with three processors, two vector facilities and 384 Mega Bytes (MB) of memory (128 MB central and 256 MB expanded), almost doubling the processing capacity.

In February 1992, a Memorex-Telex automated cartridge tape library (ATL) with a capacity of about 1000 GB was installed. The ATL not only provides storage for all the raw JET data (JPFs) and archived processed JET data (PPFs), but also provides storage for backup and dump tapes, that were previously handled using manually operated cartridge tape drives. This together with the introduction of automated operations via the product AutoMate/MVS has completely eliminated the requirement for operator cover. In December 1993, the eight tape drives of the ATL were upgraded doubling the data recording density, and this doubled the capacity of the ATL. The disc system hardware was enhanced in two stages during 1994, with the addition of a further 53 GB of a more recent generation of IBM discs.

The JET IBM Computer Centre was originally established at the UKAEA Harwell Laboratory but was relo-

cated to Building J2 at JET in July 1992. The service has run successfully from the JET location, providing the expected improvement in communications, integration with the UNIX and PC systems, and a reduction in staff. The integration was further improved early in 1994 with the introduction of TCP/IP services on the mainframe using the Interlink SNS/TCP access software to provide more accessible means of data transfer between the mainframe and the UNIX and PC or Macintosh systems. It also improved the terminal emulation access from the PCs and UNIX systems.

The mainframe plays a major role as the data server and archiver, but also provides a powerful computer facility used by about 200 staff. The workload includes the main Drawing Office CAD system (CATIA) supporting 31 CAD stations, interactive data manipulation and extensive scientific data processing including the high priority Intershot data processing.

### The JET Analysis Cluster

The JET analysis cluster computing service was established during 1994. This was initially based on three IBM RS/6000 model 370 UNIX (AIX) systems. Due to the increasing demand for this type of computing power, the cluster was enhanced towards the end of the year with the installation of a further four systems, three model 380s and one model C10 file server. The cluster has a total of 30 GB of disc storage. These systems have now taken much of the computationally intensive computing away from the mainframe. This work includes transport analysis studies and plasma edge modelling (such as the EDGE2D program), and also some of the structural analysis work (mainly Abaqus and Patran). One workstation with a powerful graphics processor is used primarily to run the CATIA (CAD system) robotics design work for remote handling. This integrates well with the main CATIA work run on the mainframe. The UNIX systems act as a clustered computer server by running the Load Leveller work sharing (batch) system, distributing work to any of the work stations that has spare capacity. If interactive service is required on that system, the background work is temporarily suspended. Furthermore the different classes of work have priority on different systems, giving a guaranteed level of service to certain users, but also ensuring that the system can be fully utilised even when the priority work is absent. This mechanism means, for example, that outside Drawing

Office hours the UNIX Workstation dedicated for CATIA Robotics use can be incorporated in the cluster to process background batch overnight.

The total compute power of the Analysis Cluster in terms of the standard numerical benchmarks (Linpack Double Precision) corresponds to about 230 Mega flops (Mflops) (with a theoretical peak performance of 770 Mflops), compared to about 50 Mflops for the IBM mainframe in scalar mode or up to peak values of 140 Mflops on each of the two vector processors. For the right kind of work, the Analysis Cluster thus provides a very powerful compute environment and also provides high performance interactive graphics even when run to an X-terminal over the Network. However, the mainframe is much better suited for sharing facilities between large numbers of simultaneous tasks (150 users, and several batch streams), and for frequent access to multi-Gigabyte shared databases.

### **The Management of JET Data**

Since the restart of JET operations, there has been an explosion in the amount of JET data with JPF size up to 85MB per pulse (compared with 35MB during the operations period up to March 1992), yielding typically 2 GB of data each day of operation. The major development work in the areas of data transmission from the CODAS UNIX systems has lead to data transmission speeds of about 600 kBytes per second ensuring that JET data is available for analysis on the mainframe promptly after collection on the CODAS systems. The development of a very sophisticated data archiving and retrieval system based on a cache of 32 GB of on-line disc backed by tape storage on the ATL accommodates the storage of about 500 GB of original JET data (JPF) (before compression). The mechanism gives almost instant access to any JPF data that is available on disc (currently the preceding five weeks of data), and access typically within two minutes to restore the complete JPF for a given shot from the automated tape library, for any shots back to day one.

The Intershot Analysis is run automatically when the data are received on the IBM and the analysed results are fed to the Processed Pulse File (PPF) data base system. This corresponds typically to about 7 MB of analysed data per shot. The total data stored in the PPF system is about 90 GB. A major upgrade to the PPF system was made in 1994, converting the system to a client server architecture. This has lead to the full PPF system on the

mainframe being available on the UNIX and PC systems (running Windows NT). to provide an essential centralised data storage and retrieval system for use with a distributed analysis environment.

The Central Physics File (CPF), stored and used under the SAS environment, forms a complete higher level data selection and storage system. A subset of all data is extracted at time points of interest, determined by the Time-slice program and the interactive time slice editor (TED) and stored in the SAS databases. These data are the basis for extended statistical analysis, and the source for other extracts such as the TRANSPORT and EDGE data base. This system which has been extensively overhauled for the new operations, is fully automated, and used by many physicists in the Project. A new version of the JOTTER system which stores all the control room information for each session and pulse has also been developed in SAS and is available for all users as soon as it is entered. The JET data display facilities have also been extensively overhauled to provide efficient access to the JET data within the limitations of the mainframe terminal graphics.

### **Personal Computer Support**

There are about 600 Personal Computers (PCs), and 90 Apple Macintosh systems, the vast majority of which are connected to the site-wide ethernet (JETNet). The Macs are used mainly by the secretarial staff for word-processing. The PCs are used for a wide variety of tasks including word processing, data analysis, data acquisition, program development, terminal emulation, CAD, project planning and circuit design and analysis. The Networked services are provided from six servers running the Banyan VINES network operating system. This brings services such as electronic mail (integrated with other e-mail systems on site such as the UNIX and mainframe systems), shared file access with central backup service, centrally provided software, access to shared printers and to the UNIX and IBM computer systems. The number of users on the PC network continues to increase, with typically about 300 simultaneous users logged on. During 1994, there have been some enhancements to server disc systems and the associated software, together with the installation of a centralised CD-ROM server. The JETnet services have become essential tools for the work of many of the JET staff and the reliability of the network over the past year has been very high.

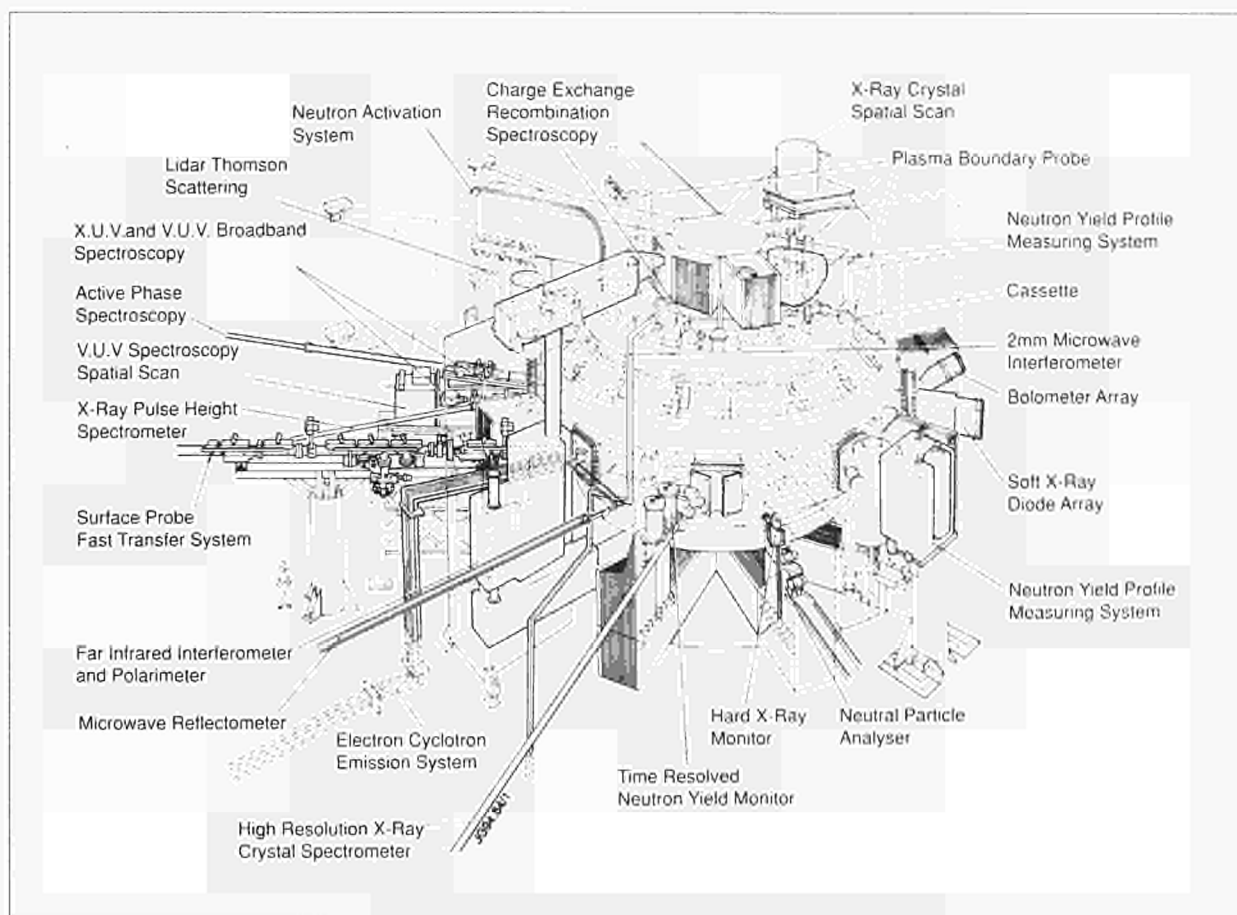


Fig.76: General layout of diagnostics on the machine

The Group has worked closely with CODAS in the provision of the JETnet services, co-ordinated by the regular NeST (Network Service Team) meetings. One major area of work has been the progress toward the secure connection of the site networks to the outside world via the Internet connection. This will go live early in 1995 and provide outgoing File Transfer (FTP) and remote computer access (Telnet) services from all systems on the JET site networks, and incoming access to the IBM mainframe for authorised users subject to various security restrictions.

## Diagnostics Systems

The status of JET's diagnostic systems at the end of 1994 is summarized in Tables XV and XVI and their general layout in the machine is shown in Fig76. The staged introduction of the diagnostic systems onto JET has proceeded from the start of operation in June 1983. The present status is that 48 systems are in existence. 35 of these systems were diagnostics which had existed from the 1992 campaign but had been modified or upgraded for operation in the new phase of JET or in the active D-T

phase. Table XVI sets out the list of 23 additional diagnostics, which were specifically prepared for divertor operation, and shows their present status. Operational experience on the existing diagnostics has been good and most of the systems have operated automatically with minimal manual supervision. The resulting measurements have been of high quality in terms of accuracy and reliability, and have provided essential information on plasma behaviour in JET. Further details on specific diagnostics systems are given below.

## Magnetics

Since the new JET plasma configurations are further away from the original set of magnetic sensors, a new set of magnetic probes, saddle loops and full flux loops were installed inside the vessel to maintain the boundary reconstruction accuracy. The new sensor configuration was designed using simulated JET plasmas to assess the reconstruction accuracy. Operation in 1994 has demonstrated boundary reconstruction in the new configuration accurate to within a few centimetres using the EFIT and XLOC codes. The main diagnostics

Table XV  
Status of JET Diagnostics Systems, December 1994  
Existing Diagnostics

System	Diagnostic	Purpose	Association
KB1	Bolometer array	Time and space resolved total radiated power	IPP Garching
KC1	Magnetic diagnostics	Plasma current, loop volts, plasma position, shape of flux surface, diamagnetic loop, fast MHD	JET
KE3	Lidar Thomson scattering	$T_e$ and $n_e$ profiles at 4Hz and 8Hz for short periods	JET and Stuttgart University
KF1	High energy neutral particle analyser	Ion energy distribution up to 3.5MeV	Purchased from Ioffe St Petersburg
KG1	Multichannel far infrared interferometer	$\int n_e ds$ on four vertical chords and four horizontal chords	CEA Fontenay-aux-Roses
KG3	O-mode microwave reflectometer	$n_e$ profiles and fluctuations	JET and FOM Rijnhuizen
KG4	Polarimeter	$\int n_e B_\theta ds$ on eight chords	JET and CEA Fontenay-aux-Roses
KH1	Hard X-ray monitors	Runaway electrons and disruptions	JET
KH2	X-ray pulse height spectrometer	Monitor of $T_e$ , impurities, LH fast electrons	JET
KK1	Electron cyclotron emission spatial scan	$T_e(r,t)$ with scan time of a few milliseconds	NPL, UKAEA Culham and JET
KK2	Electron cyclotron emission fast system	$T_e(r,t)$ on microsecond time scale	FOM Rijnhuizen
KK3	Electron cyclotron emission heterodyne	$T_e(r,t)$ with high spatial resolution	JET
KL1*	Plasma viewing	Monitor plasma in visible light	JET
KL3	Surface temperature	Surface temperature of target tiles	JET
KM1	2.4MeV neutron spectrometer	Neutron spectra in D-D discharges, ion temperatures and energy distributions	UKAEA Harwell
KM3	2.4MeV time-of-flight neutron spectrometer		NFR Studsvik
KM7	Time-resolved neutron yield monitor	Triton burnup studies	JET and UKAEA Harwell
KN1	Time-resolved neutron yield monitor	Time resolved neutron flux	UKAEA Harwell
KN2	Neutron activation	Absolute fluxes of neutrons	UKAEA Harwell
KN3	Neutron yield profile measuring system	Space and time resolved profile of neutron flux	UKAEA Harwell
KN4	Delayed neutron activation	Absolute fluxes of neutrons	Mol
KR2	Active phase neutral particle analyser	Ion distribution function, $T_i(r)$	ENEA Frascati
KS1	Active phase spectroscopy	Impurity behaviour in active conditions	IPP Garching
KS3	H-alpha and visible light monitors	Ionisation rate, $Z_{eff}$ , impurity fluxes from wall and limiter	JET
KS4	Charge exchange recombination spectroscopy (using heating beam)	Fully ionized light impurity concentration, $T_i(r)$ , rotation velocities	JET
KS5	Active Balmer $\alpha$ spectroscopy	$T_D$ , $N_D$ and $Z_{eff}(r)$	JET
KS6*	Bragg rotor X-ray spectrometer	Monitor of low and medium Z impurity radiation	UKAEA Culham
KS7*	Poloidal rotation	Multichannel spectroscopic measurement of poloidal rotation	UKAEA Culham
KT2*	VUV broadband spectroscopy	Impurity survey	UKAEA Culham
KT3	Active phase CX spectroscopy	Full ionized light impurity concentration, $T_i(r)$ , rotation velocities	JET
KT4*	Grazing incidence+visible spectroscopy	Impurity survey	UKAEA Culham
KX1	High resolution X-ray crystal spectroscopy	Central ion temperature, rotation and Ni concentration	ENEA Frascati
KY3*	Plasma boundary probes	Vertical probe drives for reciprocating Langmuir and surface collector probes	JET, UKAEA Culham
KZ3*	Laser injected trace elements	Particle transport, $T_i$ , impurity behaviour	JET
K $\gamma$ 1	Gamma rays	Fast ion distribution	JET

\* Not compatible with tritium

Table XVI  
Status of JET Diagnostics Systems, December 1994  
New Diagnostics

System	Diagnostic	Purpose	Association	Status
KB3D	Bolometry of divertor region	Power balance of divertor plasma	JET	Operational.
KB4	In-vessel bolometer array	Time and space resolved radiated power	JET	Partially operational.
KC1D	Magnetic pickup coils	Plasma geometry in divertor region	JET	Operational.
KD1D	Calorimetry of Mark I divertor targets	Power balance of divertor plasma	JET	Operational.
KE4	Fast ion and alpha-particle diagnostic	Space and time resolved velocity distribution	JET	In installation.
KE9D	Lidar Thomson scattering	$T_e$ and $n_e$ profiles in divertor plasma	JET	Commissioning.
KG6D	Microwave interferometer	$\int n_e dl$ along many chords in divertor plasma	JET	Installed.
KG7D	Microwave comb reflectometer	Peak $n_e$ along many chords in divertor plasma	JET	In installation.
KG8	E-mode reflectometer	Measurement of density fluctuations and profiles in edge and SOL	JET and CFN/IST Lisbon	In installation.
KJ3	Compact soft X-ray cameras	MHD instabilities, plasma shape	JET	Operational.
KJ4	Compact soft X-ray camera	Toroidal mode number determination	JET	Operational.
KK4D	Electron cyclotron absorption	$n_e T_e$ profile along many chords in divertor plasma	JET	Commissioning.
KM2	14MeV neutron spectrometer	Neutron spectra in D-T discharges, ion temperatures and energy distributions	UKAEA Harwell	In installation.
KM5	14MeV time-of-flight neutron spectrometer		NFR Gothenberg	In installation.
KT1D	VUV spatial scan of divertor	Time and space resolved impurity densities	JET	Not operational, vacuum system fault.
KT5D	Toroidal view visible spectroscopy of divertor plasma from Octant No: 7 mid-plane	$T_z$ and $V_z$ , ion temperature and toroidal velocity of impurities	JET	Waiting for installation.
KT6D	Polooidal view visible spectroscopy of divertor plasma using a periscope	Impurity influx, 2-D emissivity profile of lines	JET	Operational.
KT7D	VUV and XUV spectroscopy of divertor plasma	Impurity influx, ionization dynamics	JET	Operational.
KY4D	Langmuir probes in divertor target tiles and limiters	$n_e$ and $T_e$ in the divertor plasma and limiters	JET	Operational.
KY5D	Fast pressure gauges	Neutral flow in divertor region	JET	Operational.
KY6	50kV lithium atom beam	Parameters of the scrape-off-layer plasma	JET	Commissioning.
KY7D	Thermal helium beams	$n_e$ and $T_e$ in the divertor plasma	JET	Installed.
K $\alpha$ 1	Thin-foil charge collectors	Lost alpha-particle detection	JET	Waiting for installation.

JG95.110/1a

used in verifying the calculated boundary position are the divertor Langmuir probes, reciprocating probe and plasma viewing cameras.

The XLOC code is also used in the real-time plasma position and current control system (PPCC) to control the current in the coils which shape and position JET plasmas. Reliable magnetic data is essential for safe operation of JET. Therefore, data quality is monitored by post-pulse validation software which warns of potential errors in the magnetics data. A minimal set of analogue signals is also connected to the PPCC system for safe termination of the pulse in the event of a loss of the digital communication through which the majority of the magnetic data is received.

## Probe Measurements

Langmuir probes are one of the oldest plasma diagnostics and still play a crucial role in diagnosing the plasma boundary. In JET, there are 39 triple and 32 single Langmuir probes in the divertor and a further 22 single probes in the limiters. This system (KY4D) is fully operational and due to its self testing and configuring, it is highly autonomous. The triple probe system can measure electron density and temperature at up to 5kHz which is essential for the study of ELMs and discharges where the strike zones are swept across the divertor. Figure 77 shows an example of triple probe data taken during ELMs. There are large spikes on the ion-saturation current (ion flux) and to a lesser extent in the temperature.

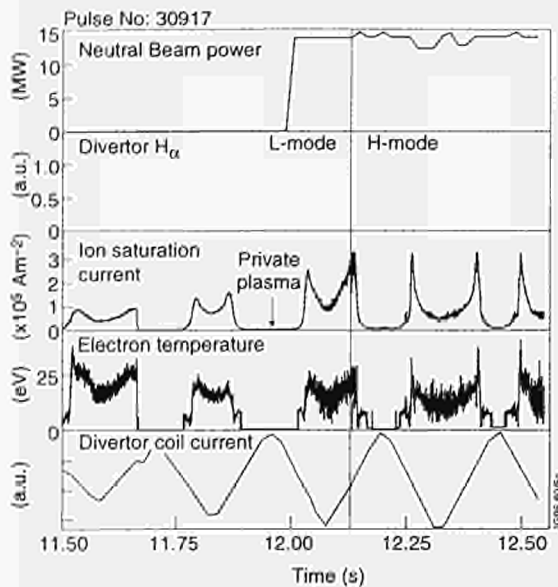


Fig.77: Divertor triple probe ion-saturation current and electron temperature in a discharge, in which the strike zone is swept repeatedly across the probe

Through a Task Agreement with CIEMAT, Spain, measurements at frequencies up to 250kHz are being made and this will be shortly be extended to 2MHz. This time resolution is essential for detailed ELM and turbulence studies. Figure 78 shows an example of the ion-flux and floating potential recorded on two toroidally adjacent probes during an ELM. These data were recorded at 250kHz and the floating potential shows a growing precursor oscillation.

In the scrape-off layer (SOL) at the top of the machine the two reciprocating Langmuir probe systems (KY3) provide measurements of the electron density, electron temperature, electron pressure, plasma flow velocity and floating potential. This data provides the best indication of separatrix parameters which are crucial boundary conditions for modelling the SOL plasma. Figure 79 is an example of the plasma pressure recorded with the reciprocating probe. Also shown is the electron pressure profile in the divertor from a triple Langmuir probe, which had the outer strike zone swept across it, this has been mapped around the magnetic surfaces to the same coordinate system as the reciprocating probe. One of the reciprocating probe systems has an exchange chamber, which allows collector probes to be mounted. These have been extensively used to monitor beryllium evaporations and metallisation during glow cleaning.

### Infra-red Measurements

The surface temperature of the divertor target is crucial for safe operation of JET and for addressing boundary

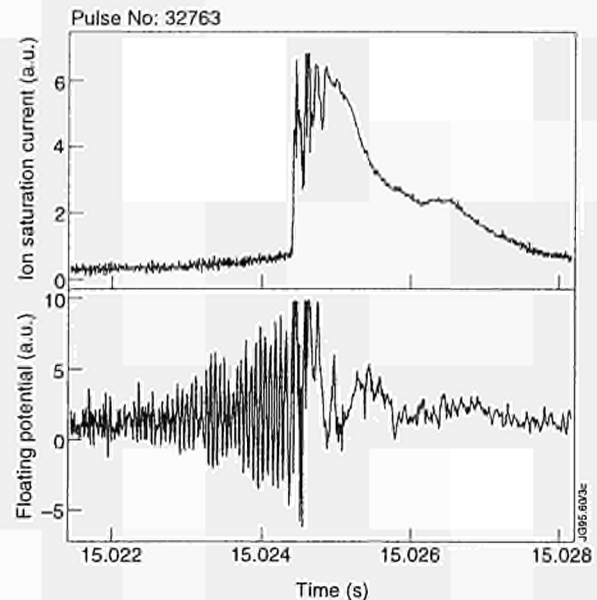


Fig.78: Data recorded at 250kHz during an ELM on two toroidally adjacent probes. One records ion-saturation current (which shows a burst in ion flux), and the other monitors floating potential (which shows a clear precursor to the ELM)

physics issues. This has been measured with a linear infra-red (IR) array (KL3.1) sensitive in the range 800-1650nm giving a 3mm spatial resolution across most of the target. Figure 80 is an example of target temperature contours plotted as a function of radius and time. It can be seen that neutral beam heating raises the surface temperature and then ELMs spread out the power. Development of a two dimensional IR camera (KL3.2) operating in the wavelength range 3000-5000nm is progressing and is now scheduled for installation during the Mark II divertor shutdown.

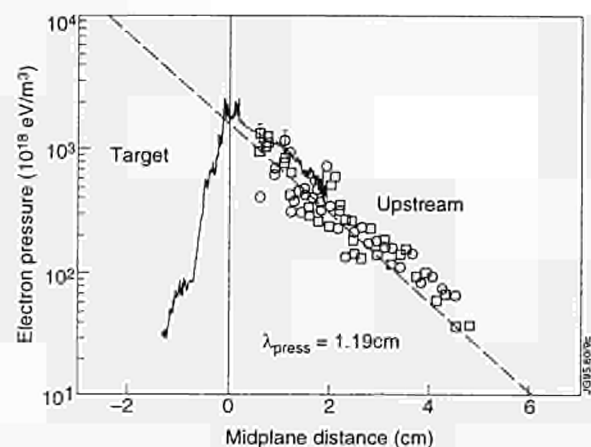


Fig.79: Comparison of electron pressure profile from the reciprocating probe at the top of the machine with the electron pressure profile in the divertor measured with a triple probe in the outer divertor leg, during a sweep of the strike point

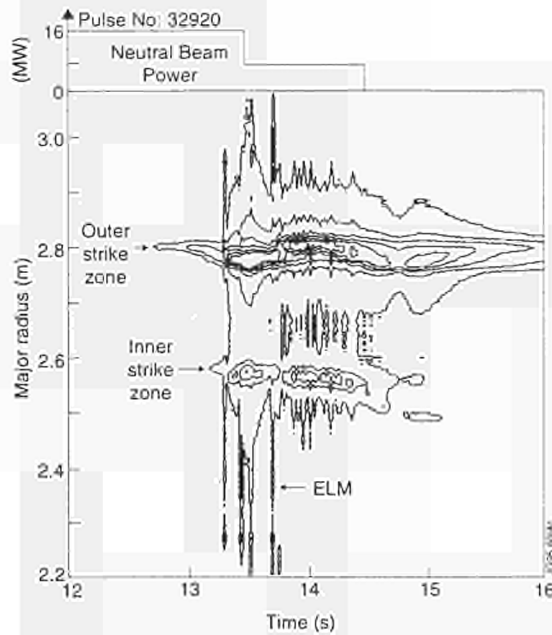


Fig.80: Target temperature during an unswept discharge with neutral beam heating. The inner and outer strike zones can clearly be seen, as can the broadening of the temperature profiles during ELMs

Extraction of the incident power from the IR camera data requires a three dimensional thermal model of the divertor tiles. This calculation can be performed by the TILE3D code developed at JET. Unfortunately, the CPU intensive nature of these calculations precludes routine evaluations on the JET mainframe computer. For this reason, TILE3D has been implemented on a 12 processor Parsytec parallel computer but the necessary systems integration is still underway. Until this work is completed power calculations will continue to be carried out using a much faster one-dimensional approximation.

A code TILO, has also been used to simulate the power deposited on the divertor target for real plasma conditions. This code imports the real tile geometry, the magnetic equilibrium and data from codes or databases available at JET, and allows thermal calculations with the finite element code ABAQUS. The preliminary results are in good agreement with measurements, and it is foreseen that this code will be used in conjunction with TILE3D.

### Plasma Viewing

Camera systems (KL1.1) operating in the visible also play a dual role. The wide angle camera which views a slice of the plasma extending from the upper wall down to the divertor target is one of the primary diagnostics during operations. Filtered views of the divertor target are

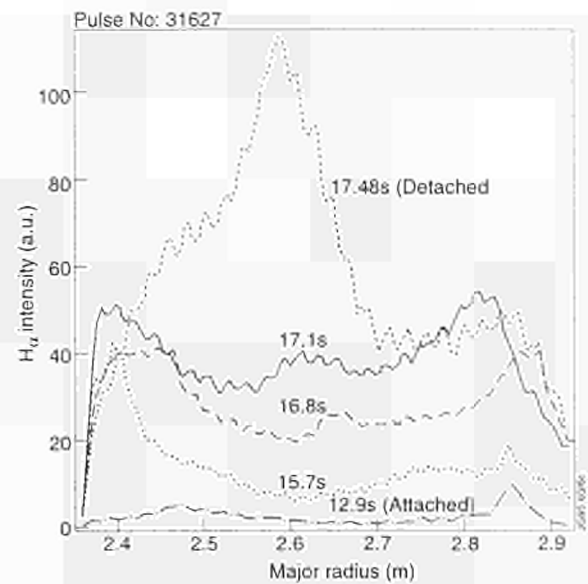


Fig.81: Evolution of the radial  $H_{\alpha}$  profiles recorded with one of the cameras viewing the target from the top of the machine. Data was recorded during a density ramp in which the plasma detaches. Initially the emission is mainly from the strikes points but in the detached state is predominantly from the X-point

available, from which radial profiles of  $H_{\alpha}$  and  $CH$  radiation can be extracted. Such data is important for the study of impurity production and recycling. Figure 81 shows the time evolution of the radial profile of  $H_{\alpha}$  in a plasma which detaches. The  $H_{\alpha}$  which initially peaks at the strikes zones develops a large peak near the X-point in the detached state. This behaviour can also be seen through the camera which views the X-point through a toroidally orientated divertor periscope. An electronic variable integration time system (developed at UKAEA Culham Laboratory, UK) has been used on all these cameras and greatly increases the useful dynamic range.

Commissioning has started on three spectroscopic filtered cameras (KL1.2), which view the divertor target from the top of the machine. These have a higher time resolution (5ms) and are directly digitised, thus making the data more readily available for quantitative analysis than the conventional camera systems, which use video tape. However, to keep the data storage requirements to a manageable size, the data is compressed to one-dimension by averaging the pixels toroidally.

Colour images of the divertor target are being recorded between pulses. Significant changes have been observed and the possibility of using colourimetry to quantify the erosion/deposition rate is being evaluated in collaboration with KFA Julich, Germany.

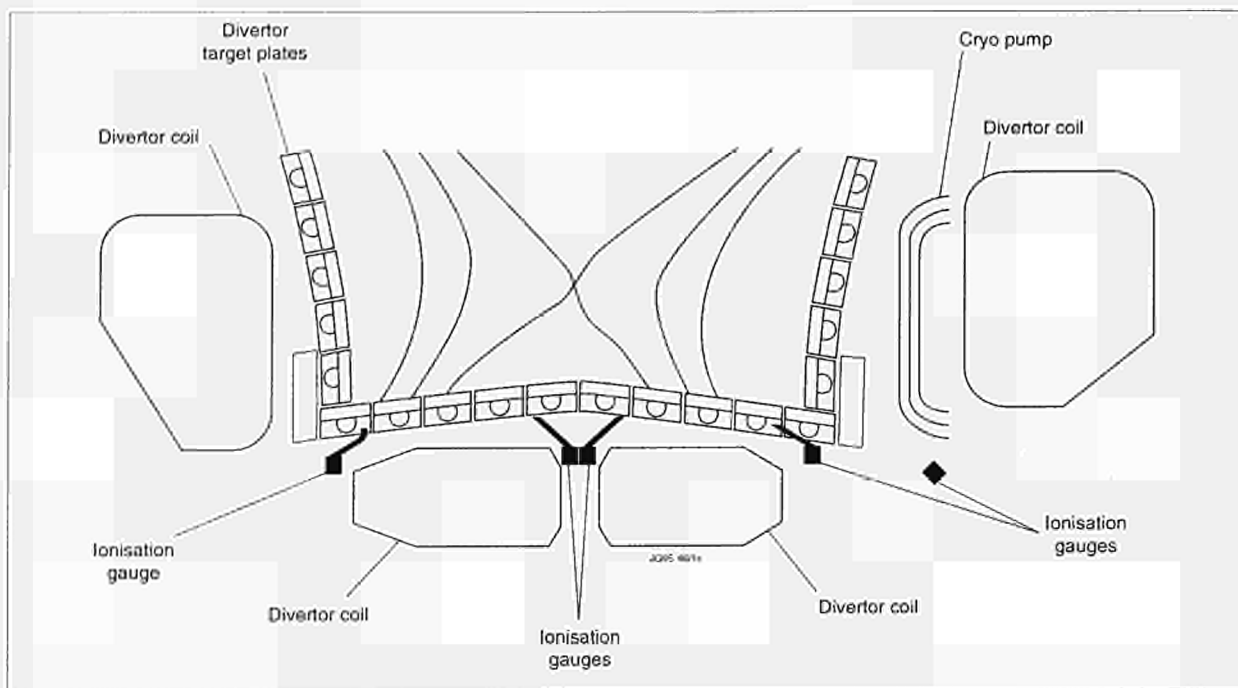


Fig.82: Poloidal distribution of the divertor pressure gauges

### Divertor Neutral Pressure

New ionisation gauges were developed and installed during the last shutdown. These are distributed along a major radius, although displaced by 7° toroidally. Figure 82 shows a projection of the gauges onto a major radius. There are a total of 15 gauges distributed in similar groups of five in three different Octants. Apart from the gauge which sits in front of the cryopump, the neutral particle flux, or equivalent pressure, is sampled through lengths of tube which limits the time response to about 5ms. The data acquisition and analysis system is fully operational and automatically processes the results intershot.

An example of the equivalent neutral pressure recorded by one of the gauges located near one of the strike zones in the private flux region is shown in Fig.83. This data was obtained in heated discharge which goes from L-mode to an ELMy H-mode and the neutral flux is clearly correlated to the ion flux recorded on the divertor triple probe. At each giant ELM, there is huge increase in divertor neutral pressure and a decrease in the line averaged density. Oscillations in pressure due to strike point sweeping can also be seen. The difference in response is due to the integrating effect of the gauge volume.

### Neutron Diagnostics

Progress in returning to full coverage of plasma discharges with the established Neutron Diagnostics has

been slower than that anticipated at the start of the 1992 shutdown. This has been due to a variety of factors, including the need to advance rapidly with the installation of the 14MeV diagnostics in preparation for the brief period of tritium operation that had been planned for Autumn 1994, manufacturers delays in delivering new

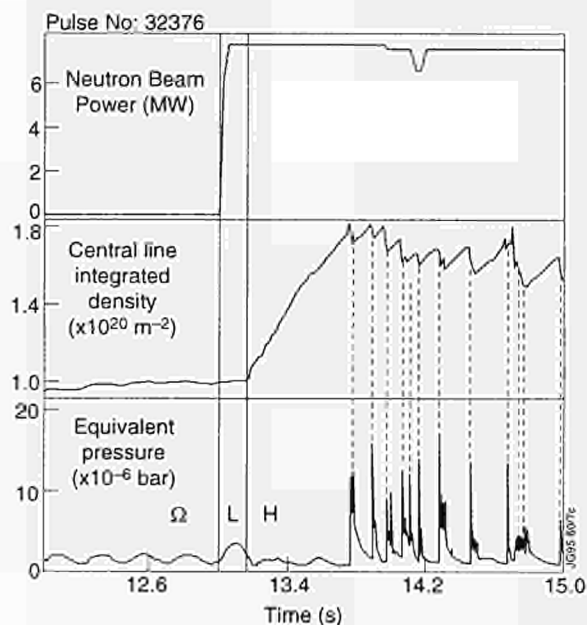


Fig.83: Equivalent neutral particle pressure (assuming particle flux isotropy) in the divertor volume under the inner strike zone in various plasma phases: ohmic, L-mode, ELM free H-mode, and ELMy H-mode. The underlying pressure oscillations are due to sweeping of the strike zone over the pressure gauge

hardware, commissioning problems associated with the change to a new CODAS computer system and access to experimental areas being restricted to non-operational periods. However, the only impact on the JET programme has been the lack of the 2.5MeV neutron spectrometer (KM3) and the continued use of the old neutron profile monitor (KN3), which has required repeated exchanges of detector boxes when changing between studies of LHCD bremsstrahlung emission and neutron emission.

Nevertheless, considerable progress has been made in the implementation of the new diagnostics. The upgrade neutron profile monitor (KN3-U) is nearly ready for installation on the machine, the two 14MeV neutron spectrometers (KM2 and KM5) will soon be ready for commissioning and a third 14 MeV spectrometer (KM9), (to be provided by the Swedish Association), is under construction. In addition, a lost alpha-particle detector has been designed and will be installed in the vacuum vessel during the 1995 shutdown.

### Neutron Yield Monitors (2.5 and 14MeV)

The most important diagnostic for the assessment of the fusion performance of the tokamak is the time-resolved neutron yield monitor (KN1), comprising three pairs of fission chambers arrayed around the tokamak. This is a highly reliable diagnostic for relative measurements but its absolute calibration has to be determined anew whenever significant changes are made to the hardware within and surrounding the machine. Sufficient experience of hardware changes has been acquired over the years that new calibrations can now be predicted with some confidence, in terms of the preceding calibrations. For the new divertor configuration, many changes have been made. The divertor itself was not expected to affect the fission chamber calibrations, unlike the changes in disposition of R.F. feeder lines. The predicted 2.5MeV neutron calibration for 1994 operations has been confirmed with measurements of neutron activation using the pneumatic transport system (KN2).

14MeV neutrons from triton burnup in deuterium plasmas are measured with a simple silicon diode (KM7) located close to one of the horizontal ports. Assuming that fast particles are fully confined in the plasma and slow down classically, then the burn-up ratio (the ratio of 14MeV to 2.5MeV neutron yields) is approximately proportional to  $(n_D/n_e)T_e$  and provides a useful measure of

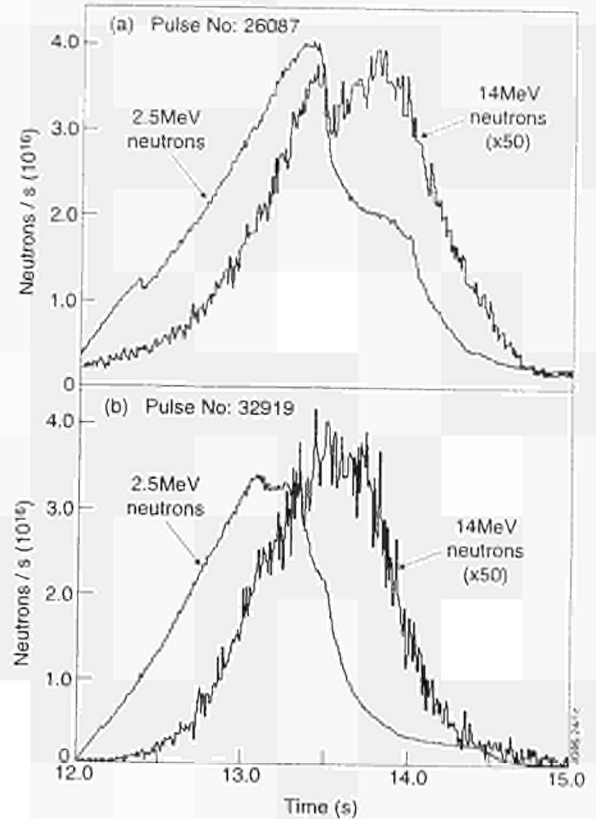


Fig.84: Comparison of 2.5MeV neutron emission with the resulting 14MeV emission from triton burn-up in D-D discharges (Pulse Nos:26087 and 32919). The 2.5MeV neutron time-traces are broadly similar during their ramp-up phases, although their terminations are accompanied by different phenomena, a carbon bloom for Pulse No:26087 and ELMs for Pulse No:32919. The effect of carbon influx is noticeable on the 14MeV neutron time-trace for Pulse No:26087. The 14MeV neutron signals have been multiplied by 50

the quality of a plasma discharge. For a NBI-heated ( $I_p > 3\text{MA}$ ) discharges, a burnup fraction of 2% is considered excellent. A comparison of the 2.5 and 14MeV neutron emission time-traces (Fig.84) between Pulse No: 26087 (which provided the previous record D-D neutron emission of  $4.3 \times 10^{16} \text{ns}^{-1}$ , with 15MW of beam heating) with those for Pulse No: 32919 (the best hot-ion mode discharge since the pumped divertor was installed, with  $3.9 \times 10^{16} \text{ns}^{-1}$  and 18MW of beam heating) illustrates the present behaviour of JET discharges. In Pulse No: 26087, the termination of the rise of the 2.5MeV neutron emission was accompanied by an influx of impurity ions (the carbon bloom) occurring well before the end of the beam heating period at 14s. Pulse No: 32919 behaved differently, with the rise of the 2.5MeV neutron emission apparently being halted by an internal event, followed by a large ELM just before the end of the heating period at 13.5s. Despite the shorter beam heating period of Pulse

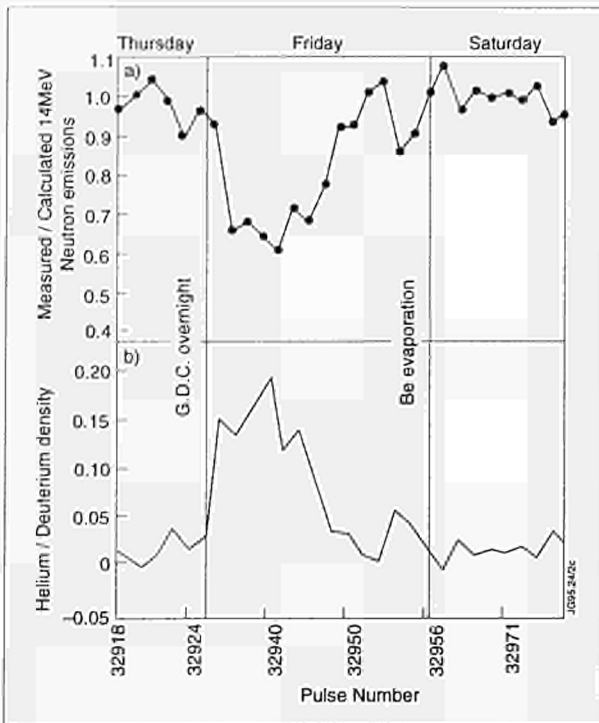


Fig.85: Illustrates the use of triton burn-up to determine the level of helium in the plasma following overnight helium glow discharge cleaning. (a) the ratio of measured to calculated 14MeV neutron emission levels due to triton burn-up; (b) the level of helium (helium to deuterium density ratio) required for consistency with the classical burn-up calculations

No: 32919, the burn-up fraction was as high (1.8%). The initial rate of rise of the 2.5MeV neutron emission is related to the step in beam heating injection rates, the D-D fusion reactivities for the injected beam ions and the  $(n_p/n_e)$  ratios; after applying the appropriate corrections and noting that the  $Z_{\text{eff}}$  values are similar ( $<2$ ), the rates of rise are similar. This indicates that the benefit obtained by pre-heating with beams for Pulse No: 26087 is forfeited by loss of power available for the step increase, as is expected when the energy confinement time is shorter than time taken to reach the peak neutron emission ( $\sim 1$ s).

The triton burnup studies also provide valuable information on the level of light impurity ions in the plasma. Figure 85(a) illustrates the fall in the ratio of measured to calculated burnup after helium glow discharge cleaning (GDC) had been used overnight. The calculations use the measured  $Z_{\text{eff}}$  data and assume carbon to be the main impurity, together with a small hydrogen content. The discrepancy between calculation and measurement following GDC is most readily explained by the persistent presence of residual helium in the plasma, causing the burnup to fall to about 60% of the predicted value. The helium content in the plasma (Fig.85(b)) can be deduced by using it as an adjustable parameter to ensure agreement

between measured and calculated burnup fractions. About 20 clean-up discharges were required to return the burn-up to its former level. A fall to 60% in the burn-up signal corresponds to falls to 60% in beam-plasma D-D neutron emission and a simultaneous fall to 36% in thermal fraction. The key feature of the burn-up measurement is that the burn-up prediction is based upon the measured D-D neutron emission and enables  $(n_p/n_e)$  to be determined, whereas direct interpretation of the D-D neutron emission is difficult since it depends sensitively on both ion density and temperature data.

### The Activation System

The activation system (comprising KN2 and KN4) has been seriously compromised by the installation of the divertor and saddle coils. Only a single irradiation end is now a suitable subject for the detailed neutron transport calculations that are necessary to obtain accurate estimates of the absolute levels of neutron emission. The automatic operation of the pneumatic transport system is no longer implemented on CODAS computers; instead, it will be controlled with a stand-alone computer. The new controller has not yet been commissioned. However, the transport system can be operated manually when required, which is acceptable for a diagnostic whose function is to provide absolute calibrations for KN1 and KM7 only after significant changes have been made to these two diagnostics or to the hardware arrayed around the machine. Full implementation of automatic operation will be carried out during the next shutdown.

### Neutron Spectrometers.

The 2.5MeV neutron diagnostic (KM1) comprises a massive shield positioned in the Torus Hall, close to Octant No:4. It contains a compact  $^3\text{He}$  ionization chamber spectrometer which offers the same overall efficiency as the time-of-flight spectrometer (KM3), better energy resolution, but considerably inferior count-rate capability and is overwhelmed with background gamma-radiation at high neutron emission levels. The shield has also been used for testing a variety of neutron detectors, including a small prototype for the 14MeV neutron spectrometer (KM2). Since this work is now complete, the KM1 shield will be removed as soon as KM3 is once again operational and its support tower and remotely adjustable collimator will be transferred for further service with the new 14MeV spectrometer (KM2).

Prior to the last operating campaign, the original time-of-flight spectrometer (KM3) was upgraded in efficiency and performance by utilizing (on a temporary basis) the detectors provided for the 14MeV neutron spectrometer (KM5) - which could not be installed at that time since there was no free line-of-sight available. During the last major shutdown, extensive changes were made in the Roof Laboratory, including realignment of the collimation lines-of-sight, and both KM3 and KM5 can now co-exist. Consequently, the KM5 detectors had to be returned and a new set assembled for KM3. This work is now essentially complete and commissioning will commence soon.

The tandem-radiator spectrometer (KM2) was originally planned for location inside the torus Hall, within a massive concrete shielding structure for D-T operation. With the withdrawal from the tokamak of the surface probe fast transfer system (KY2), a viewing location from the Diagnostic Hall became available. A new beam-line for KM2 was therefore designed and construction is now essentially complete. Its main feature is a large concrete blockhouse in the Diagnostic Hall which should prove ideal not only for the 14MeV neutron spectrometer but also as a test-bed for other detectors. A  $^3\text{He}$  spectrometer that is currently being tested with deuterium plasmas has shown that the beam-line meets expectations and that the background radiation levels within the blockhouse are very low.

The second 14MeV neutron spectrometer, KM5, is located in the Roof Laboratory, as mentioned. The beam-line and all the neutron detectors have been installed. Since this is a D-T phase diagnostic, completion of installation and its commissioning have now been postponed until the next major shut-down.

A third neutron spectrometer (KM9), based on magnetic analysis of knock-on protons from neutron interactions in a hydrogenous foil, has been proposed by the Swedish Association for use in ITER with ignited plasmas. To establish its suitability for ITER, it is desirable to test it at JET. Accordingly, it is planned to be installed at Octant No: 4, where space will become available following the removal of KM1. The advantage of such a location is that the overall spectrometer response will be at least an order of magnitude higher than is offered by the other two spectrometers, although this is gained at the cost of loss potential energy resolution and inconvenience of access once the D-T phase commences.

### **The Neutron Profile Monitor.**

The neutron profile monitor (KN3) provides detailed information on the fusion performance of JET plasmas that cannot easily be obtained by other means. The profile monitor is also furnished with alternate detector boxes, appropriate to the study of bremsstrahlung emission from fast electrons (FEB) accelerated by the lower hybrid current drive launcher. The FEB diagnostic is regarded as essential for LHCD studies. Due to this dual function for the profile monitor, the detector boxes have to be exchanged according to the needs of the programme. As a result, the neutron camera was not in place when many interesting discharges were run. The upgrade profile monitor is designed to provide simultaneous acquisition of FEB and neutron data.

While the FEB detector boxes were constructed specifically in support of the LHCD programme, they can also be applied to the study of runaway electrons. As the FEB detectors are sensitive to neutron emission, the bremsstrahlung emission (of between 0.1 and 1MeV) from runaway electrons is detectable only at low neutron emission strengths. Observations have been made on the generation of runaway electrons during the current ramp-up phase of low density discharges, which generate significant currents of electrons in the central region of the plasma in conditions such that the signal from electron ion collisions are detectable. Examination of the radial spreading of the X-ray emission indicates that the radial diffusion coefficient for the runaway electrons is very small,  $\sim 0.2 \text{ m}^2\text{s}^{-1}$ . At later phases of a plasma discharge, weak currents of low energy runaway electrons are detectable only through collisions of the energetic electrons with the plasma limiting surfaces; obviously, such observations are only possible when the outermost magnetic field flux surfaces are expanding or otherwise moving across a limiting surface. Such few observations that have been made leave the impression that runaway electrons are probably generated in the outer, low density, region of the plasma whenever the plasma current is ramped up. Finally, a strong production of runaway electrons is expected to accompany major plasma disruptions, as observed in the early years of operation, but no such events have yet been recorded while the FEB camera was installed.

During the present experimental campaign, the neutron profile monitor has been used to show that the shape of the neutron emission profiles is sensitive to the vertical

height of the plasma axis above the machine geometrical midplane. This is important because the neutral beam injection could not be adjusted fully to accommodate the new plasma position. The most sharply peaked neutron emission profiles are obtained with the plasma axis about 15cm above the machine midplane, whereas its natural position with the new divertor configuration is about 30cm above the midplane. More generally, a wide variety of plasma operating conditions has been explored, including studies of different gas puffing and gas recycling conditions, and it is found that very different neutron emissivity profiles and total rates are encountered due to effects of beam deposition and transport. Hot-ion H-mode plasmas are a continuing source of interest, since the termination of the high neutron emission phase is unpredictable. There appears to be an underlying MHD effect which has a noticeable influence on the development of the neutron emissivity profile.

Considerable effort has been devoted to the construction and fitting-out of the new profile monitor. It will be provided with separate detectors for bremsstrahlung radiation, 2.5MeV neutrons and 14MeV neutrons and will possess remotely changeable collimation to provide coarse optimization of the rate of detected events for differing plasma conditions. The existing profile monitor will be used until the new one is installed, but the new signal cables and the signal conditioning and associated CODAS cubicles are already in use. It is now expected that this upgraded diagnostic will be installed early in 1995.

### **Lost Alpha-Particle Detector**

A detailed design for the lost alpha-particle detector has now been elaborated. To obtain an early indication of the level of electromagnetic pickup inside the tokamak, a prototype detector (essentially, a charge collector) is to be installed during the beryllium tile-exchange shut-down in March 1995. The full diagnostic, comprising seven individual detectors mounted on a single support structure, will be installed during the main 1995 shutdown.

### **Fusion Gamma-Ray Emission**

A new gamma-ray detector has been acquired as part of a collaboration with the Colorado School of Mines, USA. It has been installed above the time-of-flight neutron spectrometer in the Roof Laboratory so that both diagnostics can share the same line-of-sight into the plasma. It consists of a central 10.16cm diameter by 12.70cm long

sodium-iodide scintillator, surrounded by an active anti-coincidence scintillator to discriminate against Compton scattered gamma-rays and also cosmic rays. The energy resolution and detection efficiency have both been determined in extensive accelerator studies; typically, the full energy peak energy resolution of this detector for 16MeV gamma-rays is about 1% and the absolute detection efficiency is approximately 2%. Perhaps as a result of the new mezzanine floor in the Roof Laboratory, it has been found that the magnetic field intensity during a discharge is appreciable, leading to large gain shifts. This has necessitated the provision of extra magnetic shielding. The detector has not been exploited for gamma-ray measurements during 1994 due to the poor coupling of the ICRF power to the plasma prevented the previous levels of gamma-radiation from being generated.

### **Electron Cyclotron Emission System**

Major modifications were completed to the Electron Cyclotron Emission (ECE) system during the 1992/93 shutdown. At the interface with the machine, new antennae to adapt to the new plasma configuration and a quasi-optical collection system for the heterodyne radiometer were installed. All systems now view the plasma through double vacuum windows. While the Michelson interferometer (KK1) and grating polychromator (KK2) hardware were largely unchanged, the heterodyne radiometer (KK3) was substantially upgraded to further enhance its measurement performance.

A new antenna array which provides three horizontal sightlines passing close to the new plasma centre (typically ~0.3 m above the vessel midplane) replaces the old fan-shaped array which had sightlines spread across the whole poloidal cross-section. There is also one obliquely viewing antenna directed towards the plasma centre. The original array of four horizontally viewing antennae has been retained. To realise the high resolution capability of the heterodyne radiometer, a Gaussian beam (or quasi-optical) collection system, employing two mirrors inside the vacuum vessel and scalar feed horns outside, was also installed. This gives a small antenna spot size in the plasma (~0.08 m diameter) which minimises the effect of flux surface averaging of temperature measurements. Figure 86 shows the locations of the most important sightlines now installed.

The Michelson interferometer was successfully calibrated after these changes, despite the potential loss of

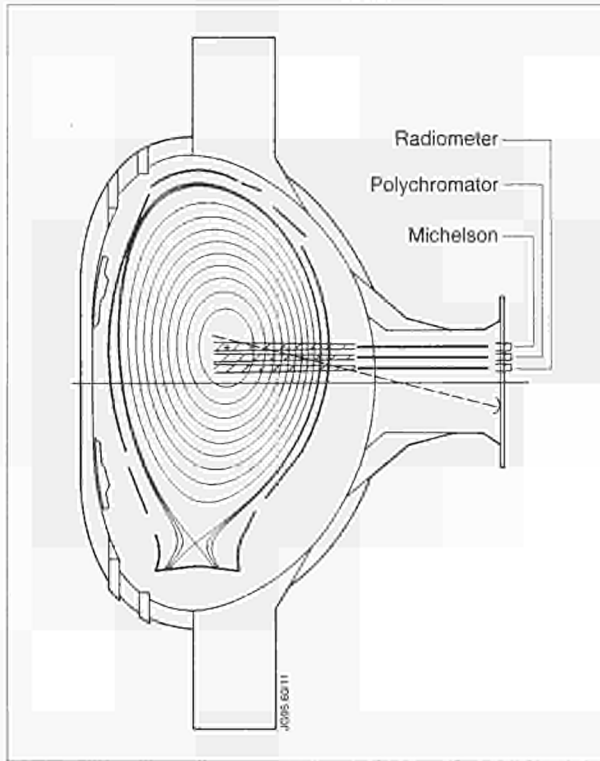


Fig.86: Poloidal cross-section of JET showing location of the horizontal ECE sightlines of the conventional antennae, and the near-horizontal sightline of the quasi-optical collection system. The sightlines employed by the different ECE measurement instruments are marked.

signal due to the double windows. It continues to provide routine electron temperature profile measurements with moderate spatial and temporal resolutions ( $\sim 0.15\text{m}$  and  $\sim 15\text{ms}$ , respectively) on all plasma pulses. It is also used as a reference for the cross-calibration of the grating polychromator and heterodyne radiometer which are difficult to calibrate using black-body sources.

The upgrade to the multi-channel heterodyne radiometer consisted principally of the addition of two further mixers (bringing the total to six) continuous spectral coverage from 73GHz to 139GHz. This enables it to measure electron temperature profiles, using both first and second harmonics of the ECE, across the whole minor radius of the plasma at all toroidal magnetic fields above about 1.7 Tesla. The radial coverage, and typical locations of the channels on an electron temperature profile of a 2.8T plasma, are shown in Fig.87. To share the radiation power from a single waveguide among the six mixers, beamsplitters are used in the oversized waveguide at the entrance to the radiometer. Wire grid beamsplitters have been employed to date. Although simple and inexpensive to manufacture, they have very little frequency selectivity, and therefore allow each mixer to receive only a small

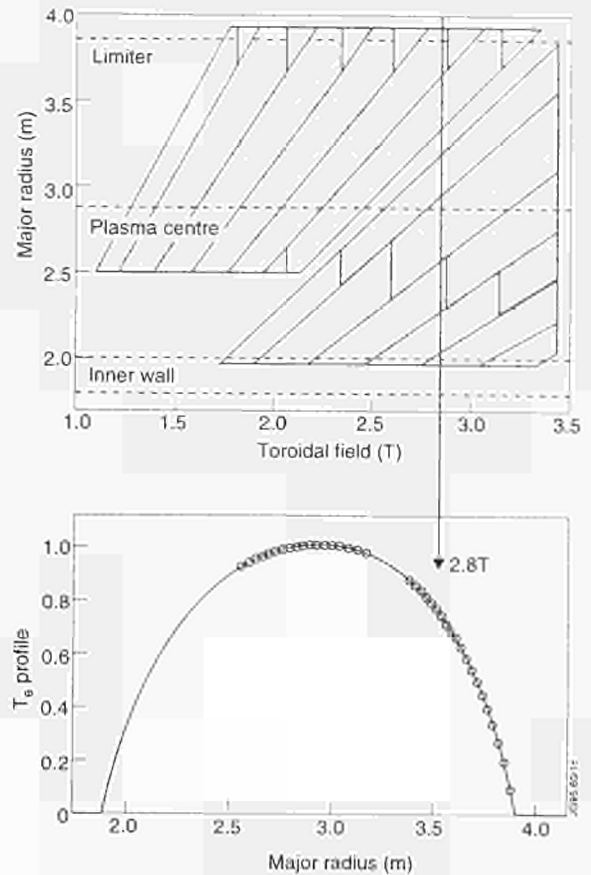


Fig.87: The upper part shows the radial coverage of the upgraded ECE heterodyne radiometer (KK3) as a function of the central toroidal magnetic field. Each band represents the frequency range of one mixer, the group on the left being for second harmonic E-mode measurements and the group on the right for the first harmonic O-mode. The lower part shows typical channel locations on an electron temperature profile for a field of 2.8T.

fraction of the incident power. A development contract with a UK manufacturer has shown that it is possible to make frequency selective splitters, which meet the requirements of the radiometer:  $45^\circ$  incidence in oversized waveguide, selectivity for both incident polarisations, and a narrow ( $\sim 12\text{GHz}$ ) transition from reflection to transmission. It is planned to replace all the beamsplitters in the instrument with these improved devices, giving an improvement in signal levels of about 3dB.

The other area of development for the heterodyne radiometer is the optimisation of its spatial resolution. This is achieved by the combination of the improved antenna pattern, and improved spectral resolution, by reducing the bandwidth of the intermediate frequency (IF) filters. The frequency selective beamsplitters offset the reduction in signal-to-noise ratio resulting from the use of narrower IF filters. The limiting spatial resolution, set by spectral broadening of the ECE, has been studied

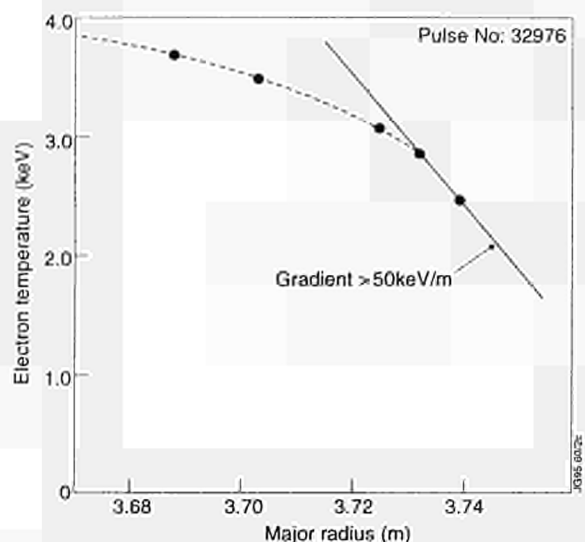


Fig.88: Edge electron temperature profile of an H-mode plasma, measured by the ECE heterodyne radiometer with optimised spatial resolution. At the maximum radius accessible to the measurement, the temperature gradient exceeds  $\sim 50 \text{ keV.m}^{-1}$

in detail to determine how narrow the IF filter widths should be in order to have optimum spatial resolution without undue loss of signal. By using filter widths in the range 100 to 250 MHz, spatial resolutions less than 10mm are achievable for many edge measurements in JET. Measurements of the edge plasma with a set of such IF filters, closely spaced, have been made. This allows the steep edge electron temperature profile to be studied in more detail than previously possible. Figure 88 shows the edge temperature profile of an H-mode plasma, where the gradient is in excess of  $\sim 50 \text{ keV.m}^{-1}$ .

### Microwave Reflectometry

The O-mode reflectometer (KG3) has been operating routinely throughout the experimental campaign, following major modifications to the antennae and waveguides during the shutdown, and continuing improvements to the data acquisition and data analysis. The antenna and waveguide modifications were required to make the instrument compatible with the new plasma configuration. This involved raising the antennae and waveguides by 0.3m, to be closer to the new plasma centre, and extending the antenna length to bring them closer to the plasma edge. Double vacuum windows were also installed.

New analogue fringe counters have been installed, to give improved phase resolution for profile measurements, while a fast data acquisition system for fluctuation measurements is also being installed. Further improvements have been made to the analysis software, which

calculates the group delay for each probing frequency from the measured phase difference resulting from the frequency sweep. The density profiles calculated from the frequency sweeps are refined by making use of the phase evolution during the fixed frequency period between sweeps. The inversion process automatically corrects for fringe jumps in the phase data, weights the data points according to their individual measurement uncertainties, assumes a continuous density gradient outside the measurement region, and corrects for the effect of the finite frequency sweep. It also employs the correct relativistic formulation of the refractive index, using electron temperature data from the ECE diagnostic. With the improved analysis software,  $\sim 75\%$  of the data gives reliable density profiles. The remaining data is too perturbed by density fluctuations to be reliably analysed.

During 1994, a new E-mode correlation reflectometer (KG8B) was constructed and commissioned. The design of this instrument is based on experience with previous experiments on correlation reflectometry, which have shown that it is necessary to measure both the phase and amplitude of the return signal to be able to deduce the density fluctuation level. In addition, resolving the propagation behaviour of the fluctuations unambiguously requires measurements in the toroidal, poloidal and radial direction in the same plasma.

The device uses an array of four antennae and combines three separate microwave sub-systems. One operates at 80GHz and provides measurements separated poloidally or toroidally, a similar system provides the same measurements at 105GHz, while a third system is a two channel correlation reflectometer, operating in the range 92 - 96GHz. In every case, the amplitude and phase of the reflected signal is recorded. Sample rates of up to 2MHz are available through a PC-based data acquisition system. Spectral analysis of preliminary measurements indicate that the region of significant fluctuation power can extend up to 250kHz. The first measurements of poloidal correlation in ohmic plasmas indicate that the fluctuations propagate in the electron diamagnetic direction at speeds of order three times the electron diamagnetic drift velocity, as illustrated in Fig.89.

Another E-mode reflectometer (KG8A) for measuring the density profile in the scrape-off layer (SOL) and edge plasma is presently under construction. This is a broad band swept system operating in two frequency ranges, 50 - 75GHz and 75 - 100GHz. Specially designed antennae

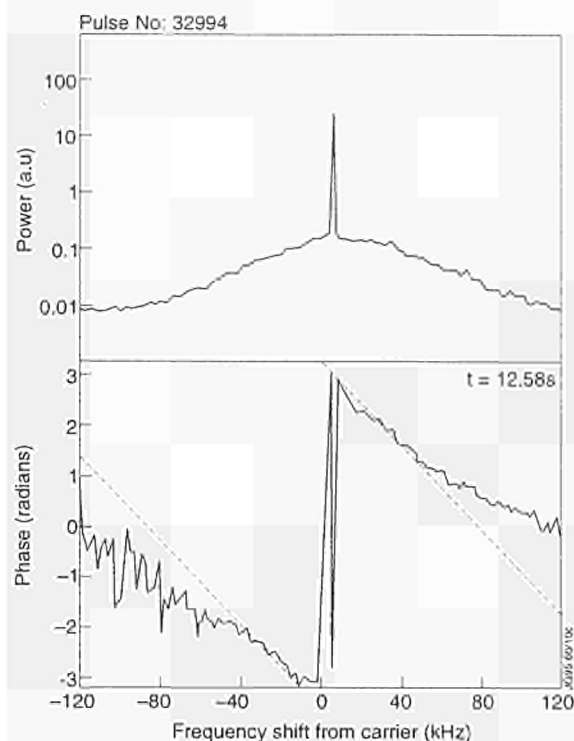


Fig.89: The upper part shows the spectrum of the returned power in a channel of the E-mode correlation reflectometer (KG8B) at 80GHz, as a function of the frequency shift from the microwave carrier frequency. The reflection is from a cutoff located at a radius of  $\sim 3.5m$ . The lower part shows the cross-phase between two reflectometer channels separated by 25 mm in the poloidal direction for the same pulse. The straight line corresponds to a propagation velocity  $\sim 4.7km/s$ . The diamagnetic drift velocity for this pulse is  $\sim 1.5km/s$ .

and waveguide couplers have been installed in the vacuum vessel for this system. The development of this instrument is being carried out in collaboration with Centro de Fusão Nuclear, Associação Euratom/IST, Lisbon and a contract has been placed with CFN/IST to supply the source and detection systems, which includes state-of-the-art fast sweep ( $\sim 10\mu s$ ) solid state sources and active multipliers.

### Microwave Divertor Diagnostics

Three microwave diagnostics share a single set of waveguides and antennae for divertor plasma measurements. These are a dual frequency interferometer for line-integrated electron density measurements (KG6D), a "comb" reflectometer for estimating the peak density along a sightline (KG7D), and an electron cyclotron absorption diagnostic (KK4D) for the determination of the local electron temperature-density product (the electron pressure).

The source, detection and data acquisition systems for the interferometer were supplied under contract by AEA

Fusion, Culham Laboratory, UK. The system has two probing frequencies, at 130GHz and 200GHz, so that phase shifts due to the effects of mechanical movements and vibrations in the plasma arm waveguides can be distinguished from those due to the divertor plasma. To minimise losses at the high frequencies employed, the microwave circuits are constructed from quasi-optical rather than waveguide components. The attenuation of the waveguide/antenna system in the measurement arm of the interferometer is estimated to be 65 dB, so the transmit and receive sections are mounted on opposite faces of a vertical support plate to minimise local cross-talk between these systems. The system has been delivered and installed, and is currently being commissioned. Some promising preliminary results have been obtained.

The comb reflectometer is being developed in collaboration with Centro de Fusão Nuclear, Associação Euratom/IST, Lisbon. Eight probing frequencies will be used; four in the waveguide band 50 - 75GHz and four in the 75 - 100GHz band. The frequencies have been chosen to give approximately equal intervals in cutoff density. The source and detection system has been delivered to JET and will be installed for initial tests once the interferometer is fully commissioned.

An Electron Cyclotron Absorption (ECA) diagnostic is being developed, as it is not possible to determine the electron temperature from electron cyclotron emission measurements in the optically thin divertor plasma. The plasma is not sufficiently opaque to re-absorb the intense ECE from the core plasma, which radiates at the same frequencies. By measuring the absorption of radiation from an external source, the optical depth will be determined directly. From this measurement the electron density-temperature product (the electron pressure) will be deduced. The diagnostic will measure the attenuation by the divertor plasma of radiation from swept frequency microwave sources. These will be located, together with the detection system and a  $\sim 100m$  long quasi-optical reference arm, outside the biological shield. Commissioning of the system has been delayed by problems with the supply of the Backward Wave Oscillator source, which is a key component of the system. In the meantime, development of the complex real-time signal processing algorithms which are required for frequency sweep linearisation and the first level data analysis has continued. It is expected that the diagnostic will be able to measure the spatial profile of the  $n_e T_e$  product in the

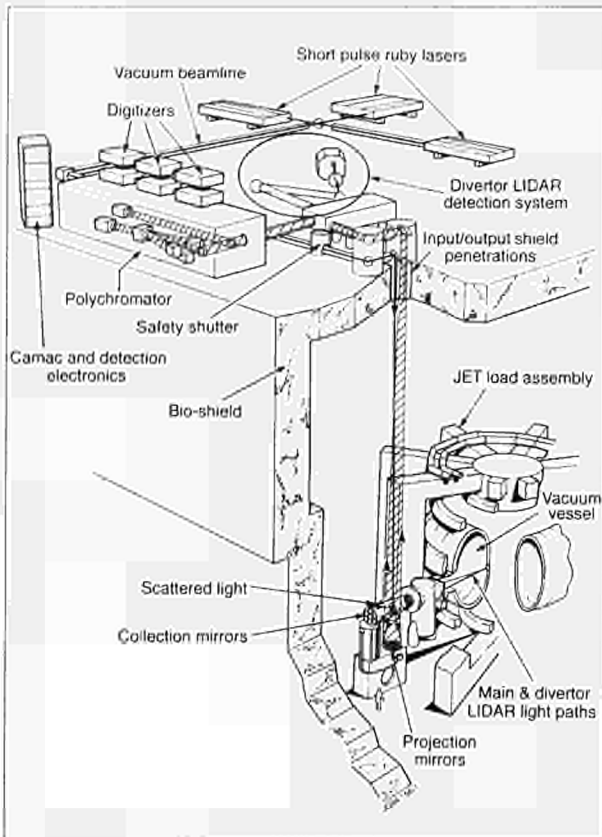


Fig.90: Cutaway section of the LIDAR Thomson Scattering System.

range  $2.5 \times 10^{20}$  to  $5 \times 10^{21} \text{ m}^{-3} \text{ eV}$  at most values of toroidal field, with an accuracy of  $\sim \pm 20\%$ , on a timescale of  $\sim 1 \text{ ms}$ .

### The Main LIDAR Thomson Scattering System

Installation and testing of all the new components for the main LIDAR system were completed on time ready for integrated commissioning (see Fig.90). The first successful LIDAR Thomson scattering profile measurements at the new standard rate of 4Hz throughout a pulse were obtained in March. Figure 91 shows an example of LIDAR  $T_e$  and  $n_e$  profiles during a recent JET pulse.

During the year, the diagnostic has also demonstrated an 8Hz repetition rate capability of the system for a 7s burst during a pulse. To do this, the layout of the laser beam paths were reorganized in the Roof Laboratory. By using a dielectric polarizer as a beam combiner and a pulsed magneto-optic polarization rotator to correct the polarization, the beams of both the available 4Hz lasers were combined along the main LIDAR path. The two lasers used were the new 4Hz main LIDAR ruby laser and the in-house upgraded, 4Hz, Stimulated Brillouin Scat-

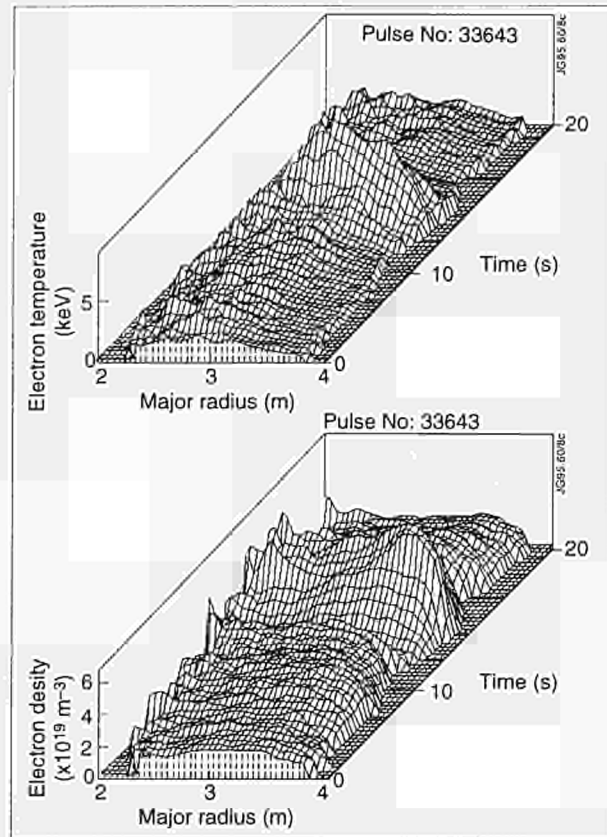


Fig.91: Temperature ( $T_e$ ) and density ( $n_e$ ) profiles obtained by the LIDAR System on Pulse No: 29177.

tering pulse compressed ruby laser. Better matching of the pulse energy between the two lasers is required to make this scheme a regular option. The old LIDAR 0.5Hz ruby laser has been switched to the Divertor LIDAR application where the higher pulse energy has significant advantages.

A better method of analysing the results from the old high resolution LIDAR detection system, has been developed in which the nature of fluctuations in signal strength is assessed in a global way to obtain a maximum likelihood profile rather than simply a series of unrelated fits at each spatial point. The profiles are generally in good agreement with those from the main LIDAR system at the same instant. In addition, a higher fraction of the results produce good quality data. Data is currently being prepared for storage in the JET Processed Pulse File (PPF) database. The maximum likelihood profile analysis is being evaluated for use on data from the main LIDAR system.

### The Divertor LIDAR Thomson Scattering System

A new LIDAR Thomson Scattering system was installed during the shutdown. The system employs in-vessel

mirrors to deflect the laser beam and the collected light from the divertor region out through the main horizontal port of Octant No:5. The mirrors are held in a drive assembly off the top of the pumping box. The mirrors are adjustable through double bellows drives mounted on the main port flange, coupling to long driveshafts on the mirror assembly. The silver coated mirrors failed during the final thermal cycling tests and new aluminium coatings had to be applied to the substrates. The reduced reflectivity of aluminium relative to silver combined with the fitting of double windows on the vacuum vessel unfortunately means a halving of the expected signal.

A separate laser was built for the diagnostic. The laser is based on the original laser from the single-point Thomson scattering system. Optical modifications to this laser have been made in collaboration with the Kurchatov Institute, Russia. The power supplies were also upgraded and the laser now operates at 4Hz with 300 ps pulses of ~1J energy. The short pulses are obtained by twice passing the laser beam through Stimulated Brillouin Scattering (SBS) pulse compression cells. These cells also work as conjugate phase mirrors. As a result of using this technique, the divergence of the laser beam is a few times the diffraction limit, a most valuable feature when passing the beam through the very restricted beam path of the system. In the end we decided to use the old more powerful 0.5Hz laser for the divertor region and the modified laser as an 8Hz option on the main LIDAR system.

The detection end consists of a grating polychromator and a streak camera fitted with a cooled CCD camera. A holographic notch filter at the entrance of the polychromator rejects the laser stray light by a factor  $\sim 10^3$ . The complete system was tested while the vacuum vessel was still at atmospheric pressure. Spurious stray laser light was at a sufficiently low level to allow Rayleigh scattering measurements confirming the expected transmission of the optical system. These measurements were made with the holographic notch filter removed from the spectrometer.

Alignment of the system has proved a problem. The in-vessel mirror system does not allow a direct view of the divertor structure outside the very narrow field of view of the actual collection area. When the laser strikes the divertor target, not only large stray light pulse is observed, but an intense white light signal corresponding to an incandescent object at ~35000C. The streak camera is

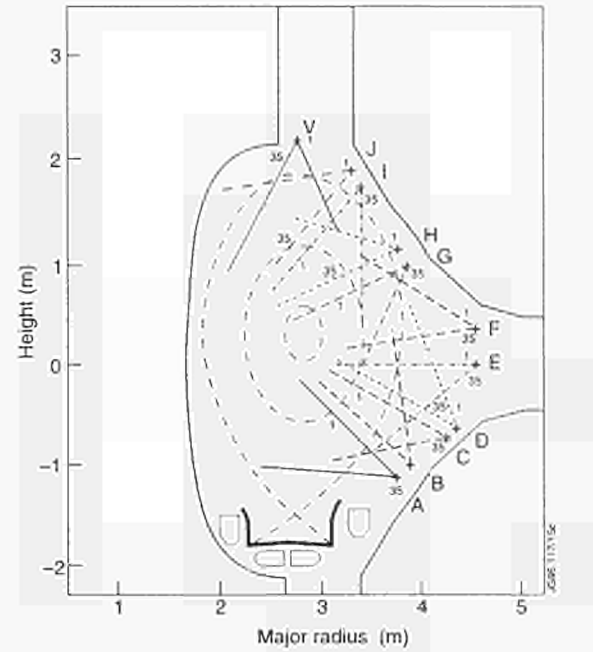


Fig92: Central lines of sight of soft X-ray cameras

presently unable to handle this signal even when it occurs outside the streak period. The gating of the streak camera will be improved so that this signal can be handled. The combination of poor transmission, alignment difficulties and "wall pulse" has prevented plasma measurements.

### Soft X-ray Measurement

The new compact soft X-ray cameras (KJ3,KJ4) were installed on the machine in early 1994. These assemblies provide viewing of the plasma from a large number of different directions with many lines-of-sight. This will provide much better data for tomographic reconstructions and will also allow good identification of MHD mode numbers. The development of the data acquisition system continued, resulting in the manufacture of large numbers of electronic modules and their installation and initial operation towards the end of the year. Parallel software developments have been made to allow for the collection and storage of the large data volumes which will be generated by this diagnostic.

The pulse height analysis system (KH2) was recommissioned early 1994 and has collected data on the impurities in the plasma. The thermal part of the spectrum was determined from three Si (Li) detectors and work has continued to reinstall the Ge detector system, which can be used to measure the non-thermal parts of the X-ray spectrum up to ~500 keV. A new collimation system was designed and built to control the intensity of the X-ray

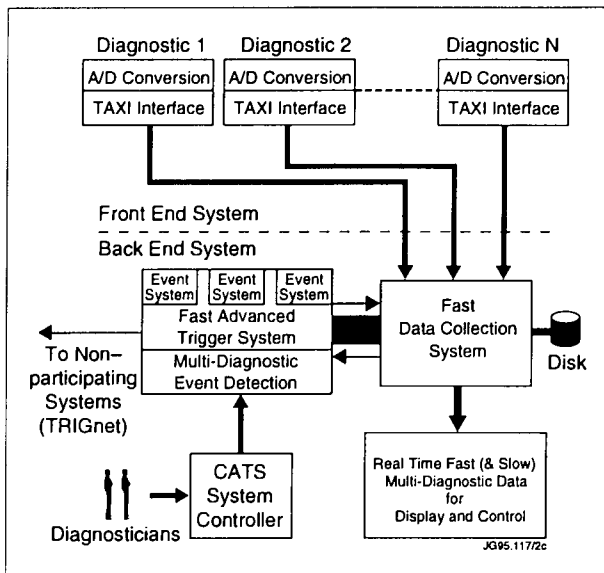


Fig.93: Outline design of Soft X-ray data acquisition system.

flux falling on the detector and the electronics and data acquisition system have been upgraded to allow simultaneous observation of the thermal and non thermal parts of the spectrum. These systems should be fully installed and working in early 1995.

**Compact Cameras (KJ3,KJ4)**

These are based on the use of single Si chips each of which has 35 elements sized 5 x 1 mm. Each detector is mounted to form a short focus (35-45 mm) pin-hole camera. In some of the cameras alternate elements only are used with the unused elements grounded. The cameras are mounted within pipes in a secondary vacuum, cooled by water at room temperature, and view the plasma through vacuum tight 250mm Be windows. The general arrangement of the cameras and their lines of sight in Octant No:2 are shown in Fig.92.

A further vertical camera is mounted in Octant No:7 to provide information on toroidal mode numbers. For tomographic reconstructions, a knowledge of the camera pin-hole positions and the lines-of-sight of the detector is important and these have been determined to an adequate accuracy by a combination of measurements on the assemblies before installation on the machine and from an in-vessel survey.

**Fast Central Data Acquisition System**

A new data acquisition system (FAST CATS) has been developed for the soft X-ray camera systems which will be able to handle the very high data rates that will be produced. A similar system will also be used to collect

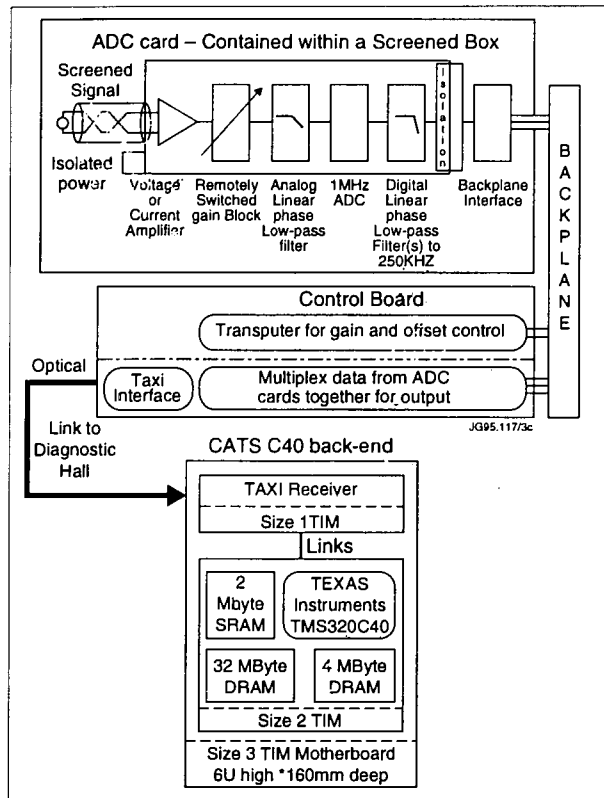


Fig.94: Torus Hall and back-end electronics

high volume fast data from other diagnostics. The soft X-ray system is based on the idea of placing the signal processing electronics and ADC as close as possible to the detectors and transmitting the digital data via optical fibres from the Torus Hall to the Diagnostic Hall, where further digital signal processing and storage take place. The outline system design is shown in (Fig.93).

The schematic, in Fig.94, shows the main components of the Torus Hall electronics. To reduce noise, each card is electrically isolated from its neighbours and is powered from a separate linear power supply. The ADC card can accommodate either a trans-impedance or a differential amplifier for current or voltage sources, respectively. To accommodate diverse plasma operating levels, the signals are then amplified with a gain that is fully adjustable. An eight-pole linear phase analogue filter is included to prevent aliasing of out of band signals or noise that could be present above the Nyquist sampling frequency. The ADC has twelve-bit sampling at 1MHz. The digitised signal can be optionally fed through a digital filter chain to lower the sampling rate and bandwidth as desired.

The ADC cards are mounted in racks of 19 and connected to a common back plane. A control card assembles the data from the cards and sends it via a TAXI transmitter down the optical fibre to the Diagnostic Hall, where a

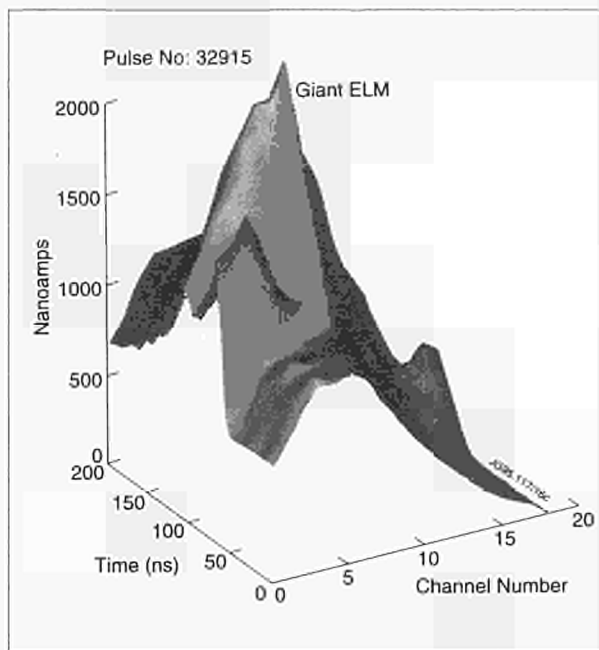


Fig.95: A giant ELM

TAXI receiver converts the data back to electrical signals. The clocking of the ADCs is arranged so that every signal is digitised at exactly the same time. The manufacture and installation of all these electronic components is now completed.

In addition to the front end electronics a back end system (Fig.94) has been developed to collect and process the data transmitted down the optical fibres. This is based on microprocessors which makes the system modular in design and easy to extend. A trigger system is included to allow the physicist to select events of interest. The overall system includes diagnostics other than soft X-rays and the number of channels for the other systems is shown in Table XVII. In addition to the fast data acquisition each channel can be digitally filtered to also give low frequency data which can be fed to the JPF.

The first results have already been obtained and have shown interesting structure of giant elms (Fig.95) and various complex MHD events have been observed in the central channels. The understanding and evaluation of these will be undertaken in 1995.

Table XVII: Diagnostic Channel Systems

Diagnostic	No. of Channels
Soft X-ray	264
Magnetics	70
ECE	48
Reflectometry	23
H-alpha	10

## Interferometry and Polarimetry (KG1,KG4)

The modifications and enhancements of the far-infrared interferometer/polarimeter system were successfully completed and the system brought into routine operation during the year. Several new features of note have arisen.

As expected in limiter plasmas the interferometer chords crossing the plasma centre in the vertical and lateral directions give equal line-averaged electron density,  $\int n_e d\ell$ . However, in X-point plasmas one vertical chord picks up an additional contribution while crossing the divertor plasma. Thus a determination of absolute  $\int n_e d\ell$  along one path in the divertor plasma is made, complementing several local measurements of  $n_e$  in the divertor plasma.

ELMS have become a regular feature of H-mode operation in diverted plasmas, severely disrupting  $\int n_e d\ell$  measurements along central vertical chords, plasma density validation and density feedback system (PDV). Since the  $\int n_e d\ell$  measurement on lateral chords is largely immune to ELMS, one of these has been incorporated into the density validation and feedback system, serving to enhance reliability of operation. In addition, the lateral measurement of  $\int n_e d\ell$  has been incorporated into the NBI-interlock system, as it corresponds to plasma density seen by NBI. The lateral  $\int n_e d\ell$  measurements are effected using a double-pass method employing mirrors mounted on the inner-wall of the vacuum vessel. A useful advantage of this arrangement is that a time-resolved precision measurement of inner-wall movement is routinely made, complementing other measurements of vessel movement.

The number and disposition of interferometer chords available is not adequate for determination of the electron density profile in the bulk plasma. Therefore, chord measurements of  $\int n_e d\ell$  from diagnostic KG1 are used in conjunction with flux-surface geometry determined from the FAST or EFIT equilibrium solvers to calibrate absolutely the electron density profile measured with the LIDAR Thomson scattering system.

The polarimeter KG4 is intended for measurement of  $\int n_e B_\theta d\ell$  along eight chords and, thereby, deducing  $\int B_\theta d\ell$ , which is then used to constrain the plasma equilibrium constructed from magnetic measurements. Two of the vertical chords have been deployed and the remaining will soon come into operation. With this constraint on magnetic field strength, instead of an assumed shape for the current density profile, a better correspondence can be made between measured and deduced pressure profile.

## Calorimetry of Pumped-Divertor Targets (KDID)

Two arrays of divertor target tile thermocouples have been installed in the Mark I divertor, one in Octant No:4 and the other in Octant No:8, with fourteen thermocouples each. Each array covers the entire poloidal extent of the divertor trough, monitoring heat loads on the horizontal and vertical divertor targets. The thermocouples measure the bulk temperature of individual tiles with only  $\sim 1$  s time and 8 cm poloidal resolution. Nevertheless, the thermocouples provide a useful cross check of target surface temperature measurements using infrared (IR) cameras. Confirmation of toroidal symmetry in divertor target loading is necessary to deduce total power load from IR measurements at one toroidal location, and for evaluating permissible tolerances in alignment of divertor structures.

## Neutral Particle Analysers (KR2, UFI)

The low energy Neutral Particle Analyser, KR2, was successfully reinstalled and operated during 1994. Many aspects of plasma operation have been hampered by high levels of hydrogen in the plasma, such as tail formation and efficient electron heating during D(H) ICRF heating, or shortfall in fusion reactivity in high performance regimes. KR2 measurements are in use to enlighten the hydrogen issue, and other recycling questions. The high energy neutral particle analyzer KF1, intended for measurement of MeV energy D-T and D-D fusion products and ICRF driven minority protons, was successfully deployed and operated during the year.

Analysis and interpretation of the MeV energy hydrogen flux measured by the NPA has been carried out using a model and code, which treats the electron donor impurities in the ground state with semi-classical rate coefficients. An improvement is under development in which the equilibrium of fully ionized and hydrogen-like impurities in an infinite homogeneous plasma is treated using a collisional-radiative model, which includes excited states. This is done to take into account that, although the population of impurity ions in excited states is usually small, the cross-section for proton neutralization from excited states of the donor impurity ions can be much larger than that from the ground state. A more accurate deduction of the energy distribution function of ICRF driven protons,  $f_p(E)$ , will be made.

Simulation of the measured  $f_p(E)$  is undertaken with the intent to verify adequacy of models used and validate

them for application in D-T experiments. In modelling ICRF driven  $f_p(E)$ , consideration must be given to:

- ion trajectories, characterized by guiding centre orbit widths comparable to their mean radial position, such that non-standard orbit effects may occur;
- spatial distribution of the heating wave fields, which depends on ion species mix and details of wave launching and propagation in the plasma, with effects due to modification of the fields by the evolving  $f_p(E)$ ;
- effects of radial fast ion transport due to neoclassical, ripple, RF- and MHD-driven mechanisms. Simulations of  $f_p(E)$  are made using Stix's approximate analytical model, which has proven successful in modelling average quantities such as stored energy;
- a bounce-averaged Fokker-Planck model, which treats trapping effects but is restricted to small banana width ion orbits on large aspect ratio circular flux surfaces; and a formulation without the above restrictions, in which the Fokker-Planck equation is solved by Monte Carlo methods.

## Investigation of Opacity in the Tokamak Divertor Region

Recently, JET experiments have concentrated on higher density and lower temperature divertor plasmas, in order to reduce sputtering of material from the divertor wall and to improve the containment of impurities in the divertor. In these conditions, the absorption of radiation can alter the power balance of the plasma. Consequently, knowledge of the plasma's opacity has become an issue.

To determine the opacity of the divertor plasma, a collisional radiative model of deuterium level populations is used. This assumes a first order escape probability method to determine the line escape probabilities and provides a self consistent model of population structure and the emergent line intensities from the plasma. The model consists of a finite number of uniform rectangular slabs and finds the optical thickness of each of these as a function of frequency and angle. It assumes emission and absorption profiles to be Doppler, but allows for variation of the profile width and the frequency from slab to slab.

Opacity increases linearly with density so that locations of maximum densities are expected to correspond to those where maximum radiation absorption is occurring. In a normal 'attached' divertor the density is greatest at the targets, where Langmuir probe measurements are available. However, investigations have shown that a

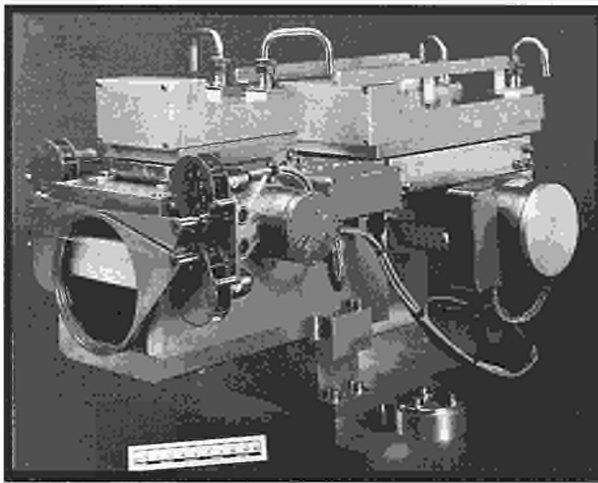


Fig.96: Assembled Bragg spectrometer

high densities, momentum loss due to recycling neutrals can result in the peak density occurring about the targets. Two types of divertor plasma models have been used to simulate these 'detached', plasmas:

- (i) A onion skin model of the SOL [1] has been modified to include momentum loss by ion-neutral collisions;
- (ii) The results of a full two dimensional fluid code [2].

The conditions from these simulations are averaged up to particular slab heights and used as input data for the population code.

Future improvements to the investigation are to consider charge exchange and impurity contamination effects. Also, the treatment of line transfer could be extended to a second order escape probability method or a full solution of the radiative transfer problem if the optical depths from the studies are considered large enough. Radiation absorption increases linearly with the size of the tokamak, so Next Step devices such as ITER will suffer from the effects of opacity even more greatly than present day fusion devices. Hence by incorporating different geometries, the population code could be extended to investigate these effects.

### VUV/XUV and Soft X-ray Spectroscopy of Bulk Plasmas

Three spectrometers were used to record the VUV, XUV and soft X-ray emission from the bulk plasma during the 1994 operations, a crystal spectrometer and two grating instruments. These spectral regions are of particular value since they permit characteristic spectral lines to be monitored of all the intrinsic impurities found in JET plasmas.

The Bragg crystal spectrometer consists of four scanning monochrometers. This has proved to be particularly

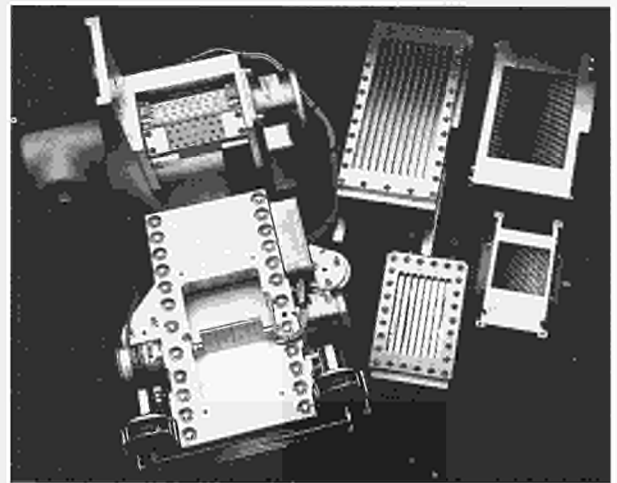


Fig.97: Main components of Bragg spectrometer

valuable during 1994, since the instrument was available from the beginning of the campaign. A balance has to be made between the temporal resolution and the number of lines accessed. Initially, a time resolution of  $\sim 400$ ms was used and seven lines were routinely monitored. With the increasing availability of spectroscopic data, a much improved temporal resolution, of  $\sim 80$ ms, was adopted with five lines being recorded. Figures 96 and 97 show the assembled spectrometer and the spectrometer's individual components, respectively. The four crystal holders can be seen in the foreground of Fig.96.

The SPRED spectrometer is a VUV, grating instrument providing coverage of the wavelength region from 100 to 1100Å with a spectral resolution of  $\sim 3$ Å. The XUV, SOXMOS instrument is a grazing incidence spectrometer with two detectors. Each views a wavelength range of  $\sim 40$ Å and can be moved to record the spectrum at positions between 15 and 340Å.

Both systems have been extensively upgraded for the present operations, the detectors being modified to extend their dynamic range. The number of channels has been doubled in the SPRED system. The existing data acquisition systems have been replaced with new PC-based systems. The new arrangement has resulted in an improved temporal resolution of 11ms for the full spectral coverage of both instruments. Installation of the SPRED and SOXMOS spectrometers began in January 1994 and commissioning took place during the start-up phase of plasma operations with the first spectrum being recorded in May. The SPRED has a fixed near-horizontal line-of-sight close to the vessel midplane, while the SOXMOS can be tilted to look at angles between the horizontal and a near-divertor view.

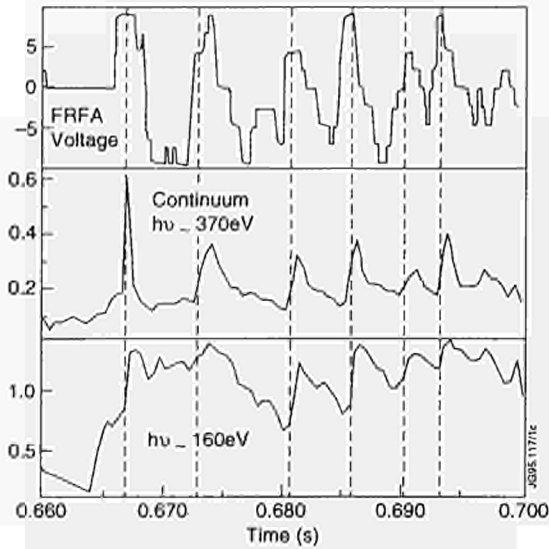


Fig.98: Correlation between KS6 features and FRFA voltage swings

During the restart phase of the plasma operations, the Bragg spectrometer revealed a connection between the Fast Radial Field Amplifier (FRFA), which controls the vertical plasma position, and a series of unstable discharges. Quasi-periodic features in the soft X-ray continuum, attributable to a type of minor disruption, were correlated with switching transients in the FRFA. Figure 98 illustrates that these features in two soft X-ray channels occur on positive swings of the FRFA voltage. The instabilities, which lead to large influxes of metal impurities, were most serious when the in-vessel lower pick-up coils were used to provide inputs to the FRFA feedback system. Modifications to the FRFA and use of different input signals have all but eliminated this effect.

The dominant low-Z element observed during 1994 was carbon (being the element from which the limiter and divertor tiles were constructed). Spectral features of Be, following a Be evaporation, and O were also observed, but were generally much weaker. The period was also characterised by significant levels of metals, such as Ni and Cr. These originate in the Inconel of the vessel walls. Figures 99 and 100 show, respectively, typical SPRED and SOXMOS spectra. In Fig.99, intense lines due to Ni and Cr are clearly seen and features due to Fe, which is a constituent of stainless steel are evident. The other intense lines are due to C and CV and CVI lines can be seen in the SOXMOS spectra in Fig 100. This figure compares the spectra recorded with two different lines-of-sight, one near-horizontal and the other towards the divertor. The latter passes through the edge of the plasma and not only

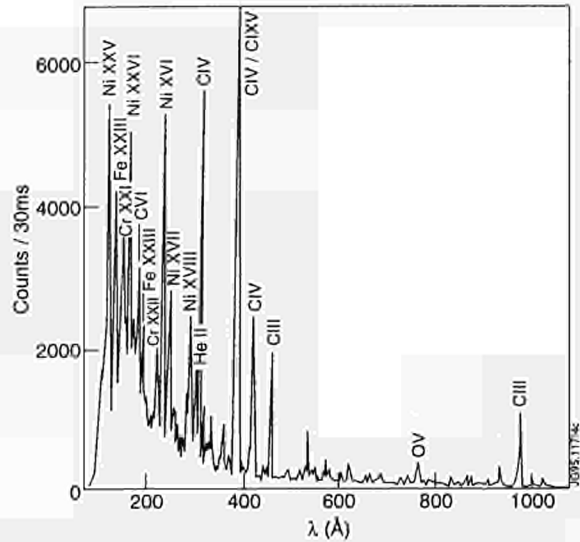


Fig.99: Typical VUV spectrum from the SPRED instrument

are the CV lines more intense relative to CVI, which is indicative of the cooler edge plasma regions, but features resulting from recombination and charge exchange are evident in the strength of the CV intercombination line at 40.73 Å and in the distortion of the CVI Lyman series.

Another impurity seen during 1994, as during previous campaigns, was Cl. During some periods, this element gave rise to significant radiation. Figure 101 shows the elemental radiated power components for Cl and O, together with the bolometric measurement of the total radiated power at 4s plotted against pulse number. A general increase in the level of Cl is evident, the Cl eventually accounting for about half of the radiated power at this time in the discharge. The components were

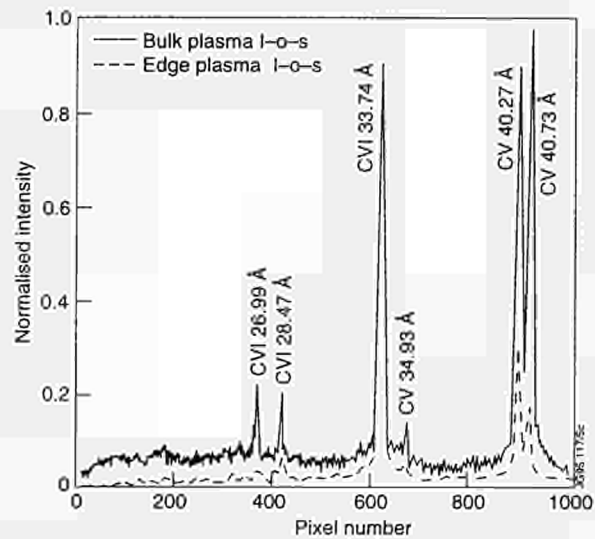


Fig.100: CV/VI XUV spectrum from the SOXMOS instrument

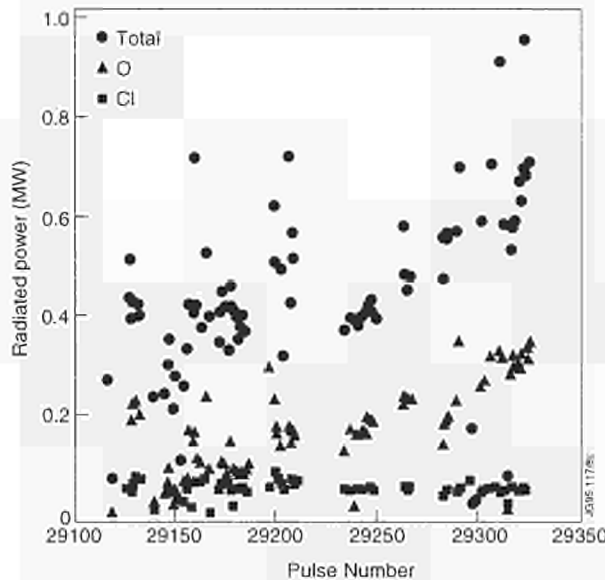


Fig.101: Total Oxygen and Chlorine radiated power at 4s versus pulse number.

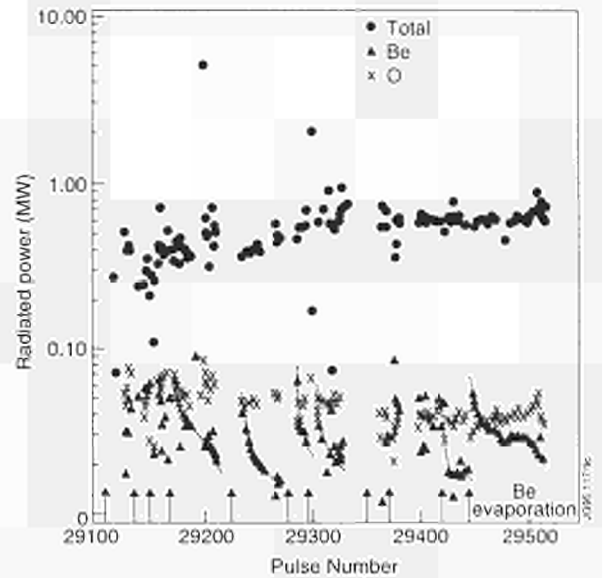


Fig.102: Total Beryllium and Oxygen radiated power at 4s versus pulse number.

derived by normalising the sum of particular line intensities to the total radiated power. The Cl is thought to arise from previous contamination, its levels decreasing after a few months of plasma operations.

Figure 102 shows a similar diagram for the Be and O elemental radiated power components. In this diagram, the timings of the Be evaporations are indicated and the decay in the Be levels following an evaporation are clearly seen. The condition of the machine was studied using dedicated reference discharges. Figure 103 shows a radiated power analysis for one such discharge, (Pulse

No:32114). The time history of the elemental radiated power components are shown together with their sum and the total radiated power. The plasma, after being formed on the outboard limiter, goes to an X-point magnetic configuration, followed by a phase on the outboard and then inboard limiters; this permits the condition of each surface to be assessed. In this pulse, Cl and C are the main contributors to the radiated power, there also being a significant contribution from Ni.

In Fig.103, the C signal can be seen to drop significantly when the plasma goes from a limiter to an X-point

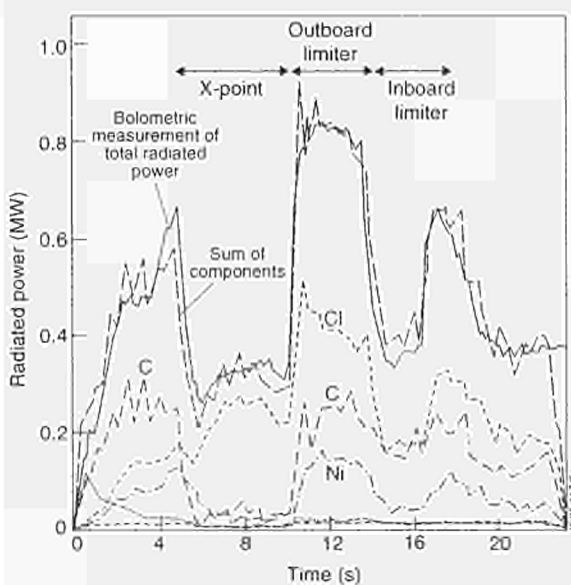


Fig.103: Radiated power components in a standard reference discharge.

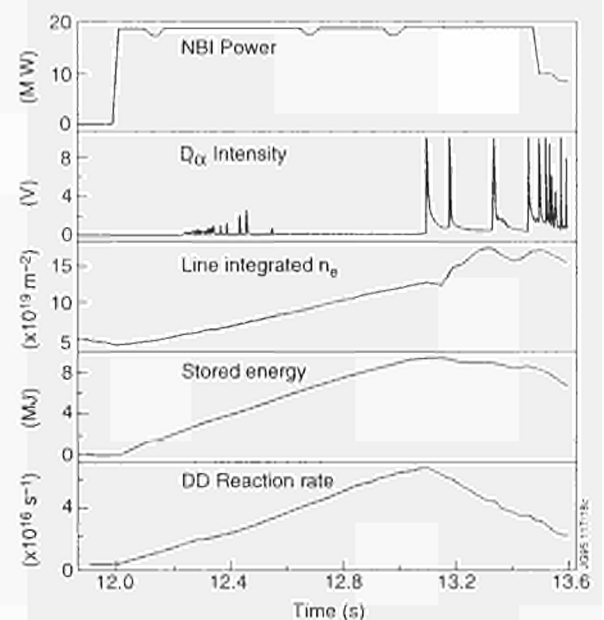


Fig.104: Main plasma parameters of a high performance hot-ion H-mode.

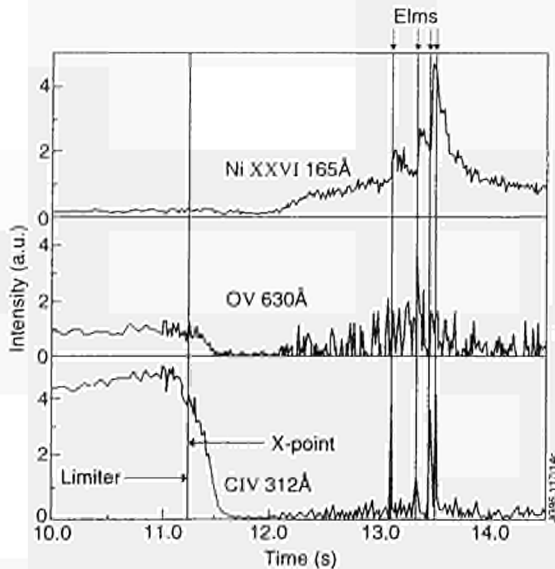


Fig.105: Time histories of three representative VUV lines for the high performance pulse in previous figure.

magnetic configuration. This behaviour is typical of the low  $Z$  elements. Figure 104 shows the main plasma parameters of a high performance H-mode discharge, heated by 19MW of neutral beam injection. The time histories of NiXXVI, OV and CIV are shown in Fig.105.

Again a marked decrease in the CIV and OV signals is found with the change of configuration. This behaviour is less pronounced for the more central NiXXVI ion and its intensity rises during the ELM-free period. Sharper increases in the NiXXVI intensity are seen with the occurrence of the giant ELMs. The ELMs correspond to spikes in the CIV trace.

### Bolometry (KB1,KB3 and KB4)

The old, modified bolometer system KB1 [3] has been used throughout the experimental campaign. The in-vessel installations of all 21 four-channel detectors of the new systems KB3D and KB4 [3,4] were completed in January 1994. The external work in particular on the termination of the anti-microphonicity cables between torus and basement continued. Electronics for 16 channels were installed and commissioned in April.

The new electronics system delivers a sinusoidal AC signal of 20kHz and 3.5Vrms as excitation to each bolometer bridge. The returning signal is rectified with a synchronous detection technique similar to a lock-in amplifier, after the subtraction of a constant amplitude sine-wave which accounts for the mismatch in the bridge resistors and effects of the cable capacitance. All channels are synchronised to avoid beating effects at the

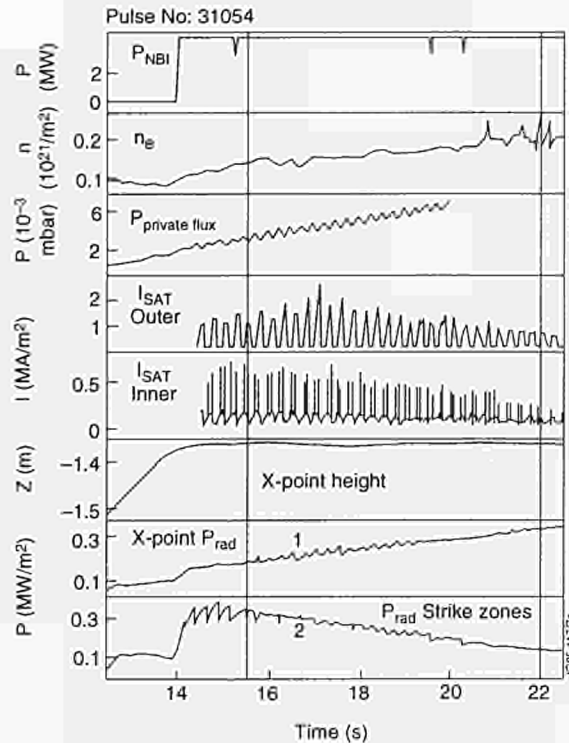


Fig.106: Overview of Pulse No: 31054: the plasma and the radiation detaches from the strike zones

detectors. The pre-amplifiers are located in the Basement to keep the cables as short as possible (i.e. 20m or 30m depending on port used). The connection to the main amplifiers in the Diagnostic Hall is via optical fibres. The analogue output of the main amplifiers is low pass filtered to either 200Hz or 1kHz bandwidth. It is digitised and stored in a PC based system from where all data are collected within seconds after each pulse.

With the 200Hz filter, the equivalent input noise of the electronics was less than 1mV(rms) in the absence of plasma. This is ten times better than the noise during plasma discharges. These figures have to be compared with steady state signal levels of 15mV measured in highly radiative regimes - equivalent to  $2\text{MWm}^{-2}$  of line-of-sight integrated radiated power. Since May, data have been taken regularly, and since August, calibrated traces of line integrated radiation power have been produced.

The 16 operational channels were chosen to cover the divertor region. The system was particularly useful for the investigation of radiative and detached divertor operation [5]. The radiation distribution was reconstructed from the measurements of all available lines-of-sight from the old and the new bolometer by using a method developed at IPP Garching, Germany [6].

Pulse No:31054 is a good example (Fig.106) of how the radiation evolves from an attached state to a detached

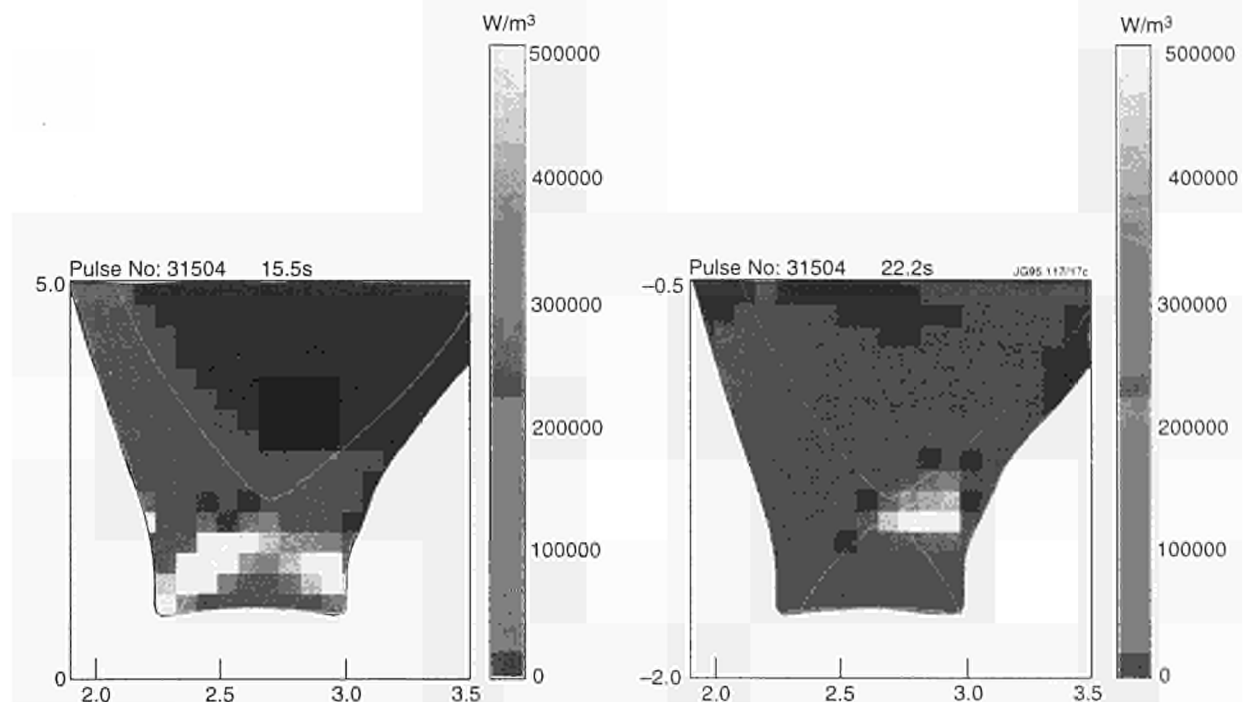


Fig.107: Radiation distribution in (a) the attached state and (b) the detached state

state as the density ramps up. This discharge has 4MW of neutral beam heating and stays in L-mode. The ion saturation currents at both strike zones are falling with increasing density and pressure in the private flux region. The radiation at the strike zone is falling whereas the X-point radiation is rising. Figure 107(a) shows the attached state of the discharge with radiation near the strike zones and figure 107(b) shows the detached state of the discharge with no radiation near the strike zones but a large radiation intensity just below the X-point.

In a short shutdown in Autumn, a fine mesh of nickel metal was installed in front of a few detectors, which improved the screening efficiency against interference from LHCD waves at 3GHz. At the end of 1994, the use of a bolometer signal measuring the X-point radiation was demonstrated in a feedback-loop controlling the radiation level by changing the impurity puff rate.

An ABEL-inversion code has been developed, which calculates on the basis of the EFIT equilibrium flux-surfaces, the local emissivity of the plasma, using the lower horizontal bolometer camera, which covers the X-point free upper half of the plasma cross-section. A reconstruction along the lines-of-sight of the remaining two KB1-cameras is possible and allows identification and analysis of asymmetric contributions to the total radiation. In discharges where nitrogen was seeded to increase the radiative power in the divertor and the

plasma edge, the width of the nitrogen radiation shell at the plasma boundary was about  $0.15^\circ$ .

### Divertor XUV/VUV Spectroscopy

A new VUV/XUV diagnostic (KT7D) has now been installed to observe line radiation of the main plasma impurities emitted from the divertor region. The instrument consists of three spectrometers, a double SPRED, which combines two VUV spectrometers in one instrument and a SOXMOS for the soft X-ray emission. All systems started to produce spectra on a regular basis at the end of 1994, although the SOXMOS only produces a weak signal. The reason for this is still under investigation.

The two toroidal gratings in the double SPRED spectrometer Fig.108 have groove densities of  $450\text{mm}^{-1}$  and  $2105\text{mm}^{-1}$ , which gives a spectral coverage of  $180\text{--}1490\text{ \AA}$  and  $140\text{--}440\text{ \AA}$ , respectively. The lines-of-sight of the two spectrometers are inclined by  $0.6^\circ$  and focus on the divertor target plates. The spatial resolution is about 10cm and it is foreseen to reduce this to 1cm by a modification of the entrance slit of the diagnostic. The VUV photons are detected by micro-channel plates followed by phosphor screens coupled to a 2048 pixel linear photo-diode array by a fibre-optic image conduit. The assembly is protected from neutrons and  $\gamma$ -rays by a minimum of 15cm thick stainless steel between plasma and detectors and 5cm, elsewhere. In addition, neutron moderator material, in

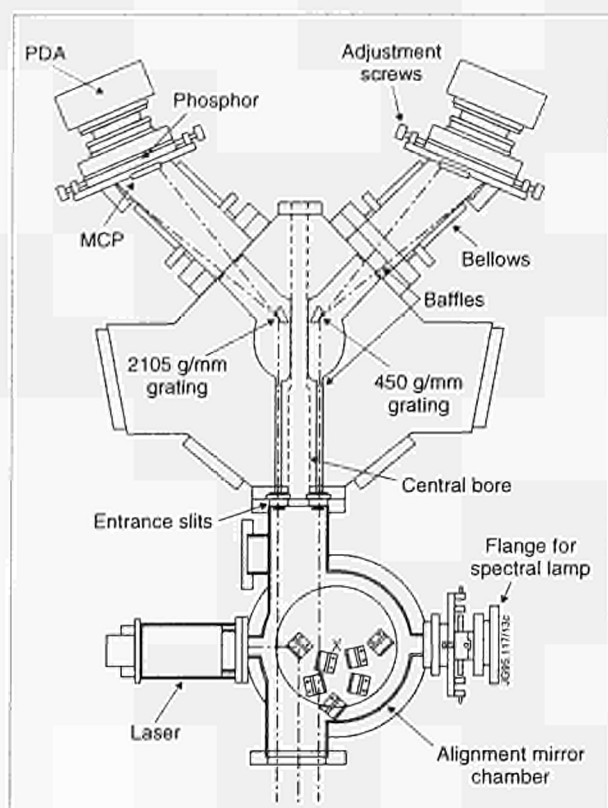


Fig.108: Double SPRED spectrometer and mirror changer for the alignment of the spectrometer assembly

particular hydrogen, has been avoided to minimise the production of secondary  $\gamma$ -radiation from neutrons in the range 0.8 -10MeV, which would readily penetrate the stainless steel. A line-of-sight in the visible wavelength range is planned to provide an absolute calibration by means of branching ratios. A wavelength calibration was performed using a hollow cathode source.

The double SPRED spectrometer has been commissioned during 1994 and is now routinely used in the study of the divertor plasmas. The diagnostic provides valuable data that will aid the modelling of the impurity transport in the divertor region. Spectra recorded at 16.3s in Pulse No:32779 are shown in Fig. 109. The two spectra from the double SPRED instrument, Figs.109(a) and (b), respectively, are compared with that recorded with the single detector SPRED instrument (KT2), whose near horizontal line-of-sight is close to the vessel midplane, (Fig.109(c)). The longer wavelengths observed with the double SPRED instrument match well the emission from the lower ionisation stages present in the divertor, its plasma having a lower  $T_e$  than the bulk plasma. The divertor spectra are, indeed, dominated by lower temperature emission and this contrasts with the bulk plasma VUV spectrum seen with KT2 which contains spectral lines from a wide range of ionisation stages characteristic of all regions of the plasma.

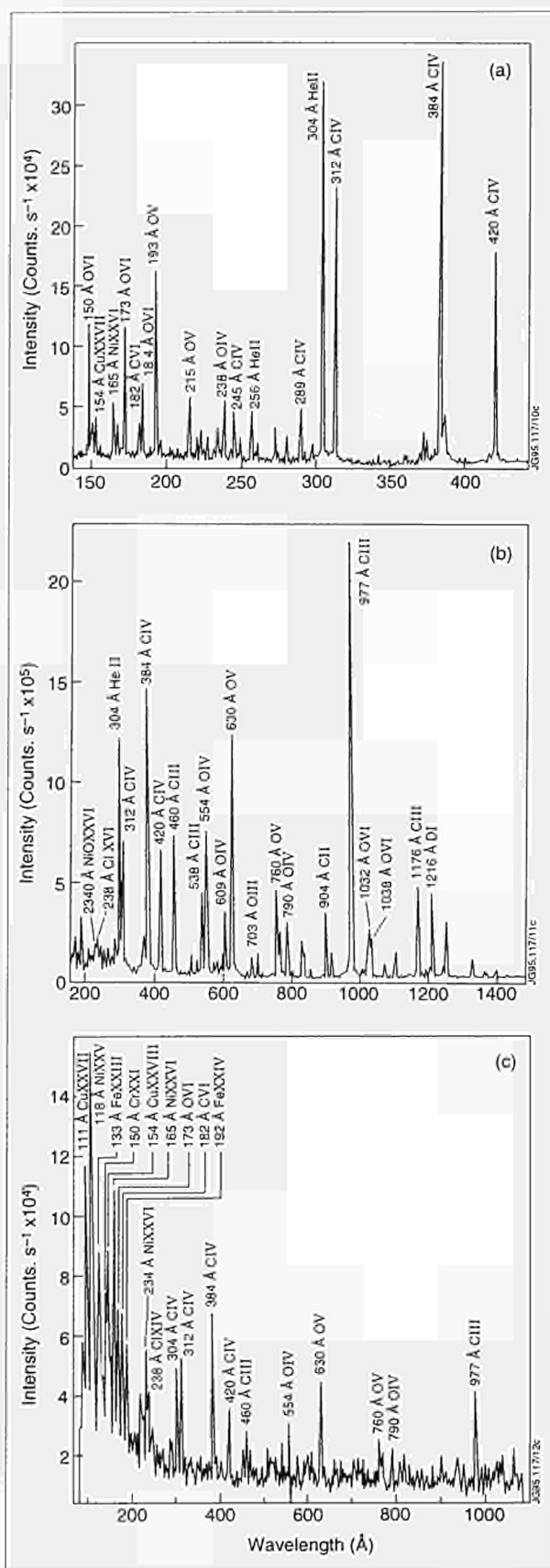


Fig.109: VUV spectra of the divertor plasma for Pulse No:32779 recorded at 16.3 s with (a) the 2105mm<sup>-1</sup> and (b) the 450mm<sup>-1</sup> grating of the double SPRED spectrometer. (c) shows the corresponding spectrum from the 450mm<sup>-1</sup> single SPRED viewing the bulk plasma horizontally

## Visible and Charge Exchange Spectroscopy

Most of the Visible and Charge Exchange Spectroscopy diagnostics were successfully implemented and commissioned. These included the visible spectroscopy instruments for impurity influx measurements at plasma walls and limiter region, continuum radiation measurements, bulk plasma charge exchange spectroscopy, high resolution plasma edge charge exchange spectroscopy, direct imaging of the divertor target to instruments in the roof laboratory, a lithium beam plasma edge spectroscopy, divertor periscopes and finally with resolution X-ray spectroscopy. The implementation of the toroidal divertor viewing system has been postponed to 1995, the He line-ratio periscope and the two spectrometers of the direct optical link will become operational in 1995. The total number of lines-of-sight, fibre connections, and of 'raw-data' produced for every plasma pulse, has increased by an order of magnitude.

The 'standard' visible spectroscopy systems, which did already exist in earlier operations, had to be adapted to the new divertor geometry, and more importantly, modified to account for the new magnetic axis positions. As a result of the new divertor and off-axis geometry almost the entire analysis procedures had to be rewritten and upgraded. For example, the calculation of line averaged  $Z_{\text{eff}}$  based on the measurement of continuum radiation, the deduction of ion temperatures for the new off-axis geometry of the high-resolution X-ray spectrometer, the beam attenuation code for the charge exchange analysis were substantially affected by the off-axis geometry of electron density and temperature diagnostics, asymmetric magnetic surfaces, flexible neutral beam positions etc.

The progress in tokamak operation was also reflected in the continuously changing spectral environment which has proven to be a major challenge to spectroscopists. There has been a notable increase in the multiplicity of spectra, in particular those emitted close to the divertor strike zone. A significantly enhanced neutral density at the plasma edge and divertor region has led to a boost of additional high quantum shell lines, molecular spectra and more complex charge exchange spectra. High resolution instruments have deduced from Zeeman line-splitting measurements (local magnetic fields) that a significant fraction of  $D_{\alpha}$  light created at the divertor is actually reaching instruments located at the top of the torus and at the torus mid plane via multiple reflections. The multi-

chord system of the lithium beam diagnostic has provided for the first time highly resolved edge measurements of passive low-Z line emission spectra. Active charge exchange measurements at the plasma edge have confirmed earlier measurements that the poloidal rotation velocities are less than a few  $\text{kms}^{-1}$  and that ion temperature gradients in hot-ion modes can reach values up to  $50\text{keVm}^{-1}$ . Low-Z transport experiments based on edge gas-puffing of helium, neon and nitrogen, were successfully monitored by the main charge exchange spectroscopy system and are currently evaluated.

## References

- [1] Taroni, A., et al., *Contrib. Plasma Phys.* **32** (1992) 438.
- [2] Stangeby, P C., Elder, J D., *Nucl. Mater.* **196-198** (1992) 258.
- [1] JET Progress Report, 1993 EUR 15722-EN-C (EUR-JET-PR11) page 83
- [2] JET Progress Report, 1992 EUR 15081-EN-C (EUR-JET-PR10) pages 80,81
- [3] R Reichle, N A C Gottardi, R M Giannella, H J Jäckel, A C Maas, "Divertor Radiation in JET", 36th APS Annual Meeting of the Division of Plasma Physics, November 1994, Minneapolis, Minnesota, USA, 7R01
- [4] J C Fuchs et al., 21st EPS on Controlled Fusion and Plasma Physics, Montpellier, France, June 27-July 1, 1994, Poster C107

## Summary of Machine Operations

During 1994, operations were essentially made up of two distinct periods.

### (a) First Period (Weeks W4 to W17)

The Divertor Shutdown ended in January 1994 with the start of the vacuum vessel pumpdown. This initiated the machine integrated commissioning phase. These overall commissioning activities were undertaken by the "Restart" Task Force (Task Force R). Its main objectives were the progressive and complete integration of the systems required for :

- producing the first plasma;
- establishing a 2MA divertor plasma with up to 10MW of additional heating.

Personnel access to the machine was maintained during Week W4 for final preparations and preliminary

inspections. This was followed by one seven hour long detailed machine inspection on 2 February 1994. The following day the first power pulse of 2.5-kA in each divertor coil was successfully achieved. This was obtained so early by virtue of extensive power supplies commissioning on dummy loads which had been carried out from October 1993.

Machine commissioning was conducted in double-shift (06.30 - 22.30 hours), six days a week. Progress was reviewed daily during Commissioning Progress meetings with the programme updated accordingly. Night shifts and Sundays were made available for the completion of ex-vessel installation work mainly for diagnostics and associated cabling.

Immediate priority was given to vacuum leak-testing of the vessel and all its attachments to eradicate leaks. This thorough and lengthy work, including repair work after vessel cooling and venting, represented 20% of the commissioning time. Time spent on the baking and cooling of the vessel and its attachments represented 10% of commissioning time. Assessments of the new static and dynamic loads resulting from the installation and operation of the divertor were also conducted. This was documented by several surveys of the vacuum vessel supports during the initial bakeout cycling and resulted in a new load distribution between the Octant joint spring supports, the main horizontal port spring supports and legs and the vessel restraints.

Integrated magnet and power supplies commissioning, first in CODAS-mode with pre-programmed references and then in PPCC-feedback mode represented the most important activity, taking one third of the time available.

Vessel conditioning work essentially consisted of two nitrogen gas purges of the main vessel, compatible with the induced thermal load on the divertor coils, and the commissioning and operation of the new glow discharge cleaning and the beryllium evaporators. The vacuum conditions for the first beryllium evaporation were met in early March 1994.

During this integrated commissioning phase, an assessment of heat transfer to the divertor coils structure and the Freon 113 cooling capacity was undertaken to ascertain the safe operating conditions during bakeout and/or plasma operations.

The first plasma pulse was followed by a period of initial operation for plasma commissioning with the Plasma Position and Current Control system (PPCC)

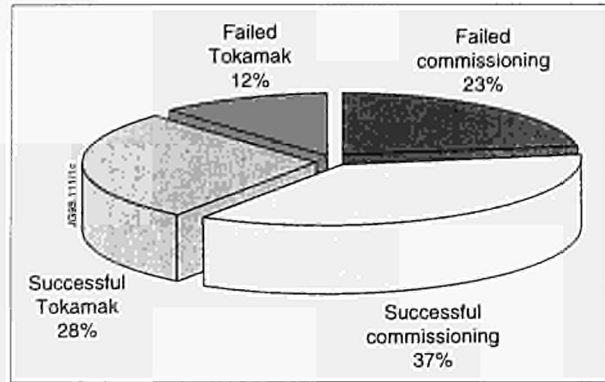


Fig.110: Analysis of Task Force R Pulse (Weeks W4-W17)

using the magnetic signals from the magnetic diagnostic (KC1). Development and commissioning of the new improved diagnostic magnetic (KC1D) was carried out in parallel and progressively integrated. The Task Force R work continued until the end of April 1994 to obtain reliable 3MA plasma discharges with additional heating.

Commissioning of the cryogenics plant was conducted in parallel with other activities. This led to the first filling of the divertor cryopump with liquid nitrogen during Week W21.

Figure 110 shows the breakdown of pulses achieved during the period corresponding to the Task Force R activities. A ratio of 65% successful pulses was obtained with only 35% failed pulses. As expected, the commissioning pulses represented 60% of the total, leaving 40% plasma pulses.

**(b) Second Period (Weeks W18 to W51)**

Operation time within the experimental programme was shared between the three main Task Forces; Divertor Assessment (D); High Performance (H); and Tokamak Concept Improvements (T). Some time was also devoted to plasma commissioning (C) and ICRF commissioning (within Task Force RF).

The experimental programme was carried out in double-shift operation days, six days a week. The number of shifts were distributed as follows:

Task Force	No: of Shifts	% of Total
Task Force D	104	32.30%
Task Force H	84	26.10%
Task Force T	76	23.60%
Task Force C	48	14.90%
Task Force RF	10	3.10%

The analysis of pulses during this main operational period are shown in Fig. 111. The overall ratio of successful pulses either for commissioning or plasma increased

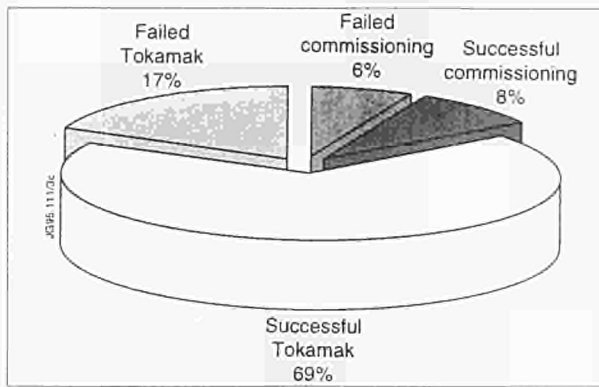


Fig.111: Analysis of Pulses in Operational Period (Weeks W18 - W51)

to 77% compared with 65% during the period devoted to Task Force Restart.

Meanwhile the portion of plasmas with currents <1MA corresponded to the limited number of non-sustained breakdowns encountered during plasma commissioning or after any deconditioning of the vessel and the divertor surfaces.

### Interruptions to Operation

The time available for operation was interrupted by four periods of shutdown or in-vessel interventions;

- The first interruption occurred during Weeks W12 and W13. Some large nickel influxes, sparks and sometimes a long afterglow were visible on the CCD

camera in most of the divertor or limiter plasmas. Detailed in-vessel inspection and completion of some diagnostic systems were possible over this non-operational period of seven days;

- The second shutdown matched the 400kV electricity outage and consequently spread over four operational days. This time was spent on machine subsystems maintenance and installation work for the plasma heating systems, the diagnostics and the fitting of electrical insulating breaks on the main vacuum pumping lines for safety purposes;
- The third shutdown, during Weeks W38 and W39, was spread over nine operational days. It was then possible, with an in-vessel intervention, to carry out repair work on the upper saddle coils, following some severe distortions which had occurred on the cross-over busbar sections. During the same period, several other activities were successfully completed such as the fitting of earth straps on the poloidal limiters, the cleaning of the beryllium evaporator heads and the installation of the E-mode reflectometer antennae and waveguides (KG8).
- The fourth interruption occurred during Weeks W44 and W45, when nine days were used for replacement inside the vessel of the three beryllium evaporator heads located at Octants Nos: 1, 5 and 7. These units

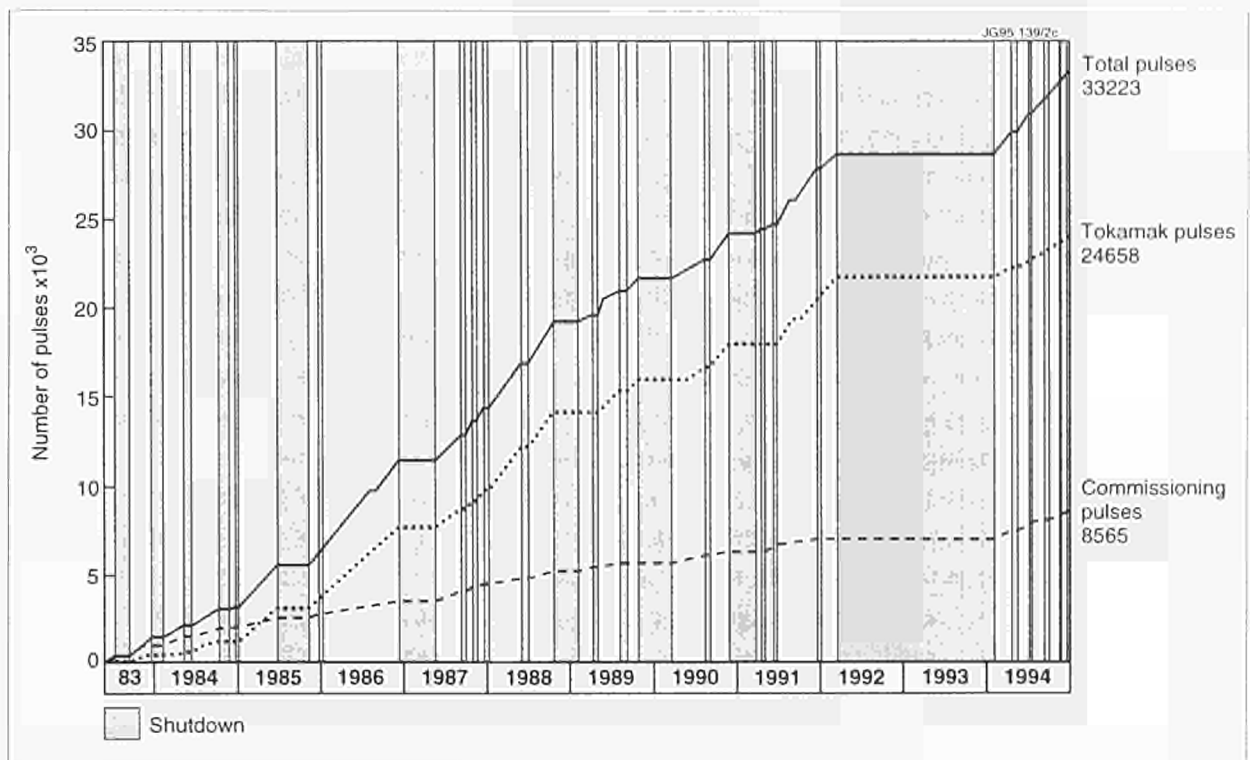


Fig.112: Cumulative totals of JET Pulses: 1983-1994

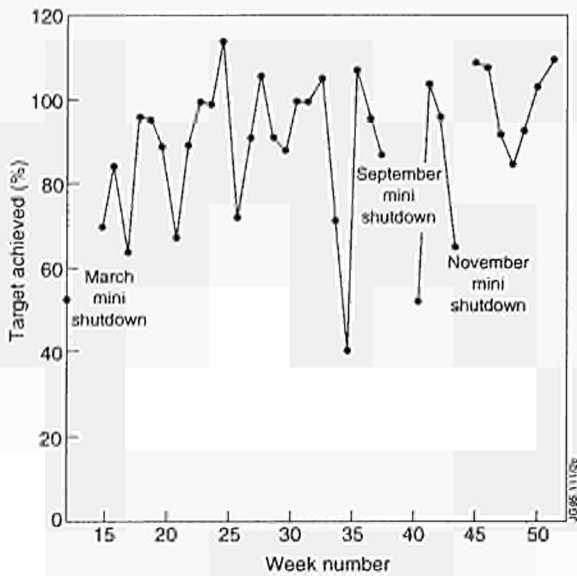


Fig.113: Performance trend for 1994

were fitted with new extension peices whilst the evaporator at Octant No: 3 was removed.

### Overall Summary

The total number of pulses carried out in 1994 was 4869 with an overall distribution over 1983-1994 as shown in Fig.112. An optimum target of 150 pulses a week (i.e. 25 pulses for a two-shift operational day) was set to evaluate overall weekly performance. The trend curve shown in Fig.113 plots the corresponding ratio of pulses achieved against this optimum. An analysis of the distribution of the plasma currents shows that currents of 2MA and 3MA have been routinely used during 1994. These represented 82% of the total plasma pulses (Figure 114). A total of 43 pulses above 4MA and up to 5MA were also obtained.

## Summary of Technical Achievements

During the major shutdown, installation of the axisymmetric pumped divertor had required a complete rebuild of the in-vessel structure, and, in addition new power supplies, new diagnostics and modification of several subsystems had been undertaken. With the completion of the shutdown in January 1994, operational flexibility of JET as an experimental device had been further extended. As a consequence, JET must be considered as a new machine. This required a thorough review of the engineering capability of the machine and of the global protection system for safe operation.

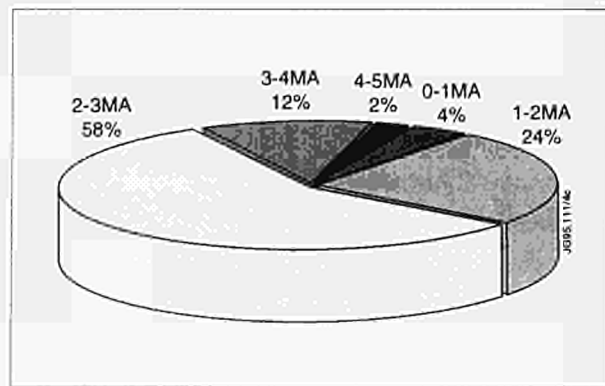


Fig.114: Plasma Current Distribution for 1994.

### The New JET

The main facilities available to tackle the key issues of the experimental programme, were the following:

- The inertially cooled *pumped divertor*, with strike-point sweeping capability for long plasma pulses and high energy deposition on the target plates;
- A flexible set of *AC/DC converters*, supplied directly from the 400kV Grid, to permit a wide flexibility of plasma scenarios and performance;
- A *machine protection system*, that can calculate mechanical stresses on major components, thus allowing an expanded parameter operating space;
- *Machine and plasma control system* (Plasma Position and Current Control (PPCC)) with a high degree of intelligence to produce and control the required plasma shapes and to actively control vertical instabilities;
- *Glow Discharge Cleaning* (GDC) with four graphite electrodes supplied at 5MHz;
- *Beryllium evaporation* using four beryllium evaporators, heated by an internal graphite resistance;
- Up to 58MW of *injected power* into the plasma, namely:
  - Neutral Beam Injection (NBI), 16 PINI's, 80kV-60A or 160kV-30A and up to 24MW of delivered power,
  - Radio Frequency (RF), eight Ion Cyclotron Radio Frequency (ICRF) antennae assembled in pairs supplied from 16 tetrodes (23-57MHz), and up to 24MW of delivered power,
  - Lower Hybrid Current Drive (LHCD), 24 generators, (3.7GHz), and up to 10MW of delivered power;
- *Fuel injection* by:
  - Gas filling, puffing and density feedback;
  - Pellet Injection, multi-pellet/pulse up to 0.6kms<sup>-1</sup> and single pellet up to 4kms<sup>-1</sup>;

- *Diagnostics*, specially designed and/or modified for divertor plasma measurement of all relevant plasma parameters in the divertor region with time and space resolution;
- *Advanced Gas Handling System (AGHS)*, for D-T fuel injection, recovery and re-processing;
- *Remote Handling* facilities, including *IVIS* (In-Vessel Inspection System), to inspect status of in-vessel components, when required by the development of the experimental campaign.
- *New Control and Data Acquisition System (CODAS)*, with Sun computers, using UNIX as the operating system and ETHERNET for communication.

### Readiness for JET Operations

In addition to these facilities, flexibility in safe operation in a wide variety of plasma scenarios relies on *Operating Instructions* and on a *Plasma Protection System* to minimize the adverse effects of disruptions on the vacuum vessel, on the in-vessel components, and on experimental time. A proper plasma recovery following a disruption, may take several pulses and/or several hours of glow discharge cleaning and/or beryllium evaporation.

The awareness of having to deal with a completely new machine required a well prepared approach to the re-start of JET.

The technical re-commissioning of the tokamak and of its major subsystem was prepared during the last six months of the shutdown by an 'ad-hoc' Group, which undertook the following tasks:

- *Planning* local commissioning with CODAS, and the integrated commissioning (the subsystem commissioning on dummy loads and eventually with the JET loads from the Central Control Room);
- *Machine active inspection*, preparing well defined plans and procedures of inspection following completion of the shutdown, in order to assure that power commissioning could proceed safely;
- *Machine protection and safety*, by verifying that all subsystems had adequate main and back-up protection, with particular attention to newly installed equipment;
- *Operating Instructions*, setting the allowed machine operating parameters, following a careful analysis of the implication of the operating scenarios for the safety of the tokamak and its major subsystems.

### Commissioning and First Operation

A special Task Force was set up to take care of the commissioning without plasma and later with plasma. The key goal of the *Task Force for Re-start* was to progressively bring all subsystems into operation and to produce a 2-3MA plasma, heated by up to 10MW of additional power with PPCC control. The commissioning with plasma was performed in steps (i.e. gas breakdown, fast rise plasma, limiter plasma with several seconds of flat-top, divertor plasma with strike-point sweeping and finally 2 and 3MA divertor plasma heated up to 10MW with RF and NB injection).

The main problem encountered was with vertical stabilization from parasitic signal inputs to PPCC led to FRFA delivering the maximum voltage (10kV) at the highest repetition frequency (~2kHz). This was corrected by modifying the internal control algorithm of the FRFA.

An extensive computer analysis supported by experimental work allowed assessment of the power scaling and the main heat transfer mechanism to the divertor coils. This led to the choice of 250°C, as the intrinsically safe maximum operating temperature of the vessel. However, wall conditioning procedure would require the vessel to be baked at 320°C. This required analysis in great detail of fault conditions (namely, loss of water cooling to the divertor structure, freon cooling to the divertor coils, vessel vacuum, site water and loss of 11kV electric power). Actions to be undertaken for each fault and maximum time required for intervention have been defined as a combination of automatic interventions and administrative procedures. These procedures have been shown to work well.

The well planned and well conducted re-commissioning allowed the physics programme to be started successfully at the end of April 1994.

### Overall Technical Achievements

The shutdown was successfully completed with pumpdown of the torus on 23 January 1994. The first plasma in the Pumped Divertor Characterisation Phase was produced on 14 February and by 15 March successful 2 MA diverted plasmas had been established. During 1994 the plasma current was increased to 5MA, the total heating power to 26MW, the stored energy to 11.3MJ and the neutron rate to  $4 \times 10^{16}$  neutrons/s.

1994 has seen significant progress in optimising peak fusion performance and extending operation to the reac-

tor relevant steady-state ELMy H-mode, which has now been obtained under a variety of conditions (plasma currents up to 4MA, power levels up to 26MW, in the high  $\beta_p$  regime, in discharges with negative central magnetic shear, and at high  $\beta_N$ ). The high  $\beta_p$  regime has also been extended to steady-state and to reactor relevant domains.

The high power handling capability of the Mark I divertor target has been demonstrated and the severe impurity influxes (carbon "blooms"), which previously terminated high performance plasmas, have been eliminated. The cryopump reduces recycling, eliminates the effects of wall saturation (observed in previous long pulse operation), allows effective particle control, and generally allows higher performance.

The two NB injectors have routinely injected up to 19MW and almost 140MJ of NBI power has been injected during a 20s ELMy H-mode. Up to 13MW of ICRF power has also been coupled, but this is limited by a combination of unsatisfactory control electronics, unequal coupling of the straps of the antennae array and low power transfer to the plasma under some phase conditions. New control electronics systems are currently being installed and will be tested with plasmas in February 1995. Further antenna modifications are scheduled for the beryllium tile exchange shutdown and the Mark II divertor shutdown planned to start in March and May 1995, respectively. Combined NB and ICRF heating powers up to 26MW have been injected and close to 3MA has been driven non-inductively with up to 6MW of LH power.

The saddle coils have been used for initial experiments on TAEs and the disruption feedback stabilisation system is in the final stages of commissioning. Only the lower saddle coils are now available for experiments, since the upper saddle coils were disabled in September 1994 after being damaged.

The prototype high speed pellet launcher has been brought into operation and used to deliver its first deuterium pellets into plasma in commissioning pulses.

During 1994/95, four manned in-vessel interventions were carried out in full air-suits (since beryllium evaporation has been used). In late March 1994, following first experiences with the restart of operations, an inspection showed that no significant in-vessel damage had occurred. In September/October 1994, damage to the upper saddle coils was stabilised and a further diagnostic system was installed. In early November 1994, the beryllium evaporator heads were removed, strengthened and rein-

stalled. At the end of January 1995, damaged RF excitation coils on the glow discharge electrodes and a broken reciprocating probe head were removed.

### JET Reliability Assessment

As one of the pre-conditions for consideration of an extension of JET beyond 1996, it was required to show that the main components of the JET machine and its major subsystems would be technically capable of fulfilling their roles without major failures. A Reliability Assessment Group, including both JET staff and experts from the Associations, was set up by the JET Scientific Council in March 1994.

This activity provided the opportunity of a complete review of JET design and construction and of the congruence of loading conditions for JET major components and subsystems. These were subdivided in three categories:

- (i) Items requiring a high degree of reliability, since their failure would lead to long and/or non-tolerable delays for repairs (toroidal, poloidal and divertor coils, vacuum vessel, mechanical structure and consequently machine protection);
- (ii) Items requiring a good degree of reliability, since their failure would have adverse effects on the experimental programme (central solenoid, flywheel generators, in vessel components, machine diagnostics);
- (iii) Items requiring a reduced degree of reliability, since their failure would require modification of the experimental programme (diagnostics, heating system, AC/DC rectifier units).

Therefore, the assessment dealt mainly with the first two categories of components.

A number of most demanding operating scenarios, including plasma disruptions, halo currents, and machine fault conditions were defined in some detail, to serve as inputs for the assessment work. Each subsystem considered has been evaluated on design, construction, analysis of tests performed through the years, modification and upgrading and operational experience. Wide use was made of computer modelling, and suggestions for improving reliability were made. The engineering analysis work performed through the years has been reviewed and served as background for further analysis under the new operating conditions.

The ASME codes were assumed as reference engineering standards to define allowable loads and stresses, analysis criteria and material properties. Results of me-

chanical tests on components and/or materials used to define, where necessary, the failure and yield strength.

Due to the pulsed operation, a key issue was the assessment of the fatigue life already used and the extrapolation to the life expectancy of the major components. The outcome of the study showed that only a small proportion of the fatigue life has been used so far for the main machine components (coils, mechanical structure, vessel and flywheel generators). This is mainly due to the large safety factors used in the JET original design, to the accurate electromagnetic analysis and to the extensive monitoring and interpretation of machine data performed throughout the years.

However, the study showed that while the design and construction of the main in-vessel structure is sound, some components would work close to the material yield strength limit in the extreme scenarios of JET operation. This is due mainly to the lack of space for installation, to the restricted choice of materials, that must be plasma compatible and, most of all, the severity and the uncertainty of the loads (plasma disruptions and halo currents).

The JET forward experimental programme foresees a D-T experimental phase (DTE1) toward the end of 1996, with a total production of  $\sim 2 \times 10^{20}$  neutrons. At this time, Mark IIA divertor (to be installed in the second half of 1995) should be replaced with Mark IIGB. These divertor structures are designed to allow remote handling replacement of the target plates, so that the loss of several months for in-vessel activation decay could be avoided. The feasibility of this activity was evaluated in detail by the Group, by reviewing the design of the two divertors and the extensive work already performed by the Remote Handling Group and plans for the replacement work.

The conclusions of the assessment, endorsed by the JET Scientific Council and, following a report of its Chairman, by the JET Council, can be summarized as follows:

- Only a small fraction of the fatigue life of JET main components is likely to have been used so far;
- Assessment of in-vessel components should continue as an on going activity, following the development of operating scenarios;
- With the plasma control techniques and the administrative control on operating scenarios by means of the Operating Instructions, the probability of major failures, of particular concern during DTE1, should be further reduced;

- It is entirely technically feasible to exchange remotely Mark IIA with Mark IIGB tile carriers, immediately following DTE1.

### Future Projects

The JET forward programme is focussed on divertor studies, progressively using configurations as close as possible to ITER requirements, since it is widely recognized that the power and particle exhaust may be the main remaining obstacle to overcome for the development of a tokamak fusion reactor.

Although the Mark I divertor has already proven to work satisfactorily, a Mark IIA divertor, which provides a more closed configuration and would be remote handling compatible, is well under construction and it will be installed during the 1995 shutdown. The gas-box divertor Mark IIGB, which would consist of a large volume divertor closed at the entrance with a narrow baffle, is under design and will be installed by full remote handling techniques. The spare vacuum vessel Octant has been prepared to serve as testbed for remote handling tests of the divertor replacement procedures.

Within the vessel, tile carriers will be handled and positioned by the Mascot IV manipulator mounted on the articulated boom transporter, using Octant No.5 port. Navigation and pre-positioning will be carried out automatically using *teach and repeat methods*. The required positioning of the boom, manipulator and cameras would be established using graphical modelling and verified in the mock-up. These positions would then be recorded in a 'teach' file and 'repeated' when modulating the actual job. Bolting of the tile carriers would be performed by the manipulator, handling a ratchet wrench motorized for fast run in. A shorter version of the articulated boom would be used for transfer of the tile carriers between the Torus Hall and the vessel through Octant No.1 port. For the removal of Mark IIA tile carrier, there would be a similar reverse sequence of events. This exercise would represent the first ever operation of the kind in a fusion device and would be of great interest to ITER.

Finally, preparation for DTE1 has been actively pursued and a special Group has been set up to identify technical and administrative work which needs to be completed before DTE1 can take place towards the end of 1996. In particular, the work which needs to be included in the 1995 shutdown has been identified.

# Scientific Achievements during 1994

## Introduction

For 1994, the system of operation of the scientific programme was the same as that employed since 1989. The programme operated for a series of campaign periods, the standard being of eight weeks duration (composed of six weeks tokamak operation and two weeks of maintenance/commissioning). Two Programme Leaders were appointed with responsibility for formulating near programme proposals (one campaign ahead) and outline plans (two campaign periods ahead). This was carried out in collaboration with the Head of Operations Division (A Tanga). These proposals were within the broad outline of the JET Development Plan and subject to guidelines provided by the Experiments Committee. These proposals were presented to the Experiments Committee for discussion and approval before implementation.

### Programme Leaders for 1994 were:

D Stork and M L Watkins.

Three Task Forces implemented the programme, as follows:

#### H) High Performance

(involving progression to full performance in the pumped divertor configuration with currents up to 6MA, with high energy content and including progression to the highest fusion product, long pulse operation and steady-state conditions, etc.)

(Task Force Leader: P J Lomas)

#### D) Divertor Assessment

(involving assessment of divertor performance on the vertical and horizontal target plates of the Mark I pumped divertor).

(Task Force Leader: D J Campbell)

#### T) Tokamak Concept Improvement

(involving studies of those physics areas in which JET can make important contributions to ITER and DEMO, including development of advanced tokamak Scenarios based on stable, long pulse discharges with a high bootstrap component).

(Task Force Leader: C Gormezano)

Task Force Leaders were appointed with responsibility for (i) interacting with and advising Programme leaders on programme requirements within that task area; (ii) devising and setting out a detailed programme for allocated time within a campaign period; (iii) driving through that task programme (including acting as a Control Room representative); (iv) analysing data (in conjunction with Topic Leaders, if appropriate); (v) disseminating information in the task area through internal meetings and publications (in conjunction with Topic Leaders, if appropriate).

In addition, Topic Groups were formed, as follows:

<i>Topic Group</i>	<i>Topic Leader</i>
(a) Transport and Fluctuations;	R Giannella
(b) MHD and Beta Limits	P Smeulders
(c) Divertor Physics	G Vlases
(d) Next Step Related Issues	B Tubbing

Topic Group subjects are of longer term interest than the immediate tasks undertaken by the Task Force Groups. The Topic Groups are responsible for analysis of results within many areas across the Task Force spectrum, but they also have responsibility for advising Programme Leaders on programme requirements which are topical and relevant to the Groups areas of activity. In addition, the Groups disseminate information through a number of internal meetings and in external publications.

## Programme Execution and Analysis

The main objectives of the 1994 campaign period were: to assess divertor performance on the vertical and horizontal targets of the Mark I divertor; to demonstrate the high performance capability of the JET pumped divertor; and to study those physics areas in which JET could make important contributions to ITER and DEMO.

The main themes of the programme were:

- to assess the performance of the Mark I pumped divertor configuration using both the horizontal and vertical divertor targets;
- to study quasi-steady H-modes at the highest powers;
- to study divertor pumping and exhaust, especially helium exhaust;
- to generate and understand high performance VH-modes up to 4.5MA;
- to develop very high power combined heating at high density in H-mode discharges up to 4.5MA and to move towards high values of the triple fusion product;
- to develop high current (towards 6MA), low q plasmas, defining the operating space and including the H-mode;
- to develop "advanced tokamak scenarios" based on stable, long pulse discharges with a "high-bootstrap" component to the total plasma current;
- to develop profile control techniques using Lower Hybrid Current Drive (LHCD) and Fast Wave Current Drive (FWCD); and
- to develop 100% non-inductive current drive up to 4MA;

Following the completion of shutdown work in January 1994, JET had been almost completely rebuilt internally and was essentially a new machine. As a consequence, a special Restart Task Force (Leader: J Jacquinot) was set up, with the objective of undertaking necessary initial commissioning and machine conditioning and to produce a 2-3MA diverted plasma with significant additional heating for a few seconds. This was achieved by late-April 1994 and then the regular Task Forces took over operation of this machine in May for the remainder of 1994. In addition, during 1994, a Tritium Study Group (Leader: A Gibson) undertook studies to make recommendations for future D-T experiments in JET.

The scientific achievements for 1994 are described in the following sections, within the Task Force, Topic Group and Study Group headings.

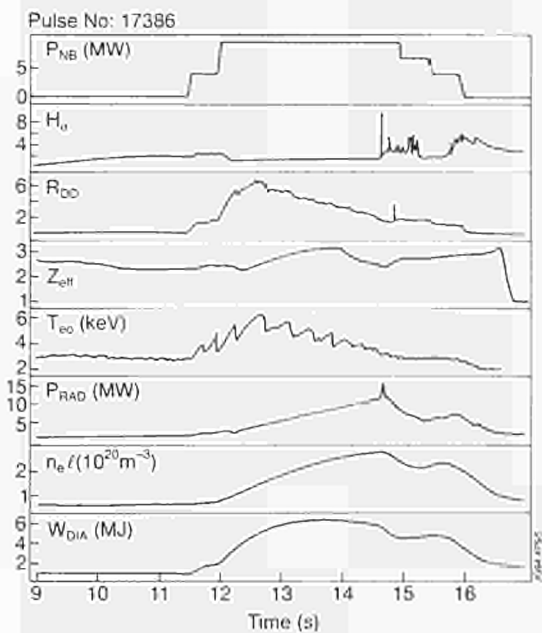


Fig.115: Typical H-mode behaviour in the old JET for 10MW of beams into a 3MA plasma. Note the long ELM-free period.

## High Performance

The major objective of this Task Force was to develop plasmas with high core plasma performance in the new configuration. This included the optimisation of parameters such as temperature, density stored energy and fusion yield, with a view to defining regimes of relevance to future D-T operation in JET and ITER. The pumped divertor was designed with a view to operation of diverted configurations with plasma currents up to 5MA (or even 6MA) with safety factors of, typically,  $q_{95} \sim 3$  (and down to 2.2), in line with mainstream ITER design. The improved current capability in diverted configurations opened up the domain of H-mode operation and raised the question of the scaling of confinement with plasma current at such low q. It was already appreciated [1] that the hot-ion H-mode regime, as demonstrated in the PTE pulses, offered potential for high  $Q_{DT}$  and, therefore, good prospects for studies of alpha-particle heating. It was thought possible to extend this regime to 4 or 4.5MA limited by plasma volume,  $q_{95}$  and degraded beam deposition arising from high axis position of the pumped divertor equilibria.

### H-mode Behaviour in Old and New JET

In the old JET, ELM-free H-modes of several seconds were the natural regime for any high power heated diverted configuration, as shown in Fig.115. Above a

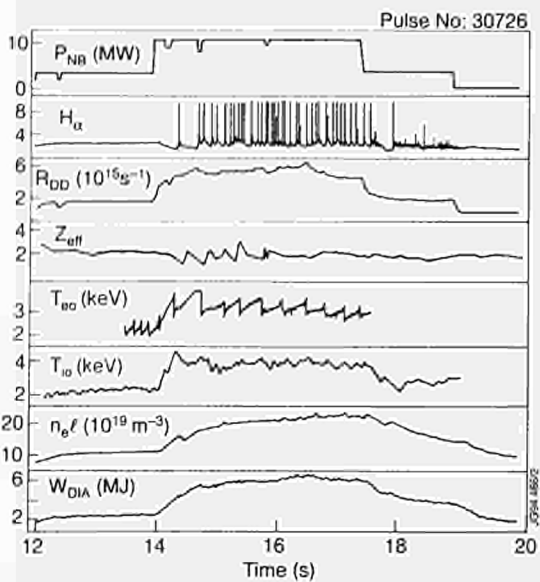


Fig.116: Typical H-mode behaviour for the standard FAT configuration in the new JET for 10MW of beams and plasma current of 3MA

clearly defined threshold power, the plasma would enter and remain in this regime until, typically, increasing radiated power reduced the exhaust power below threshold. In this case, optimisation of performance required low recycling, density control, optimum beam deposition but were limited in plasma current. The hot-ion H-mode regime in the old JET was transient limited by carbon blooms, earlier appearance of giant ELMs and, in some cases, limited by sawteeth and other internal MHD [2].

In the new JET, the natural H-mode regime is ELMy as shown in Fig. 116. In this case, the initial ELM-free period is relatively short and is followed by repetitive large ELMs. These large ELMs lead to steady-state conditions, which can be maintained for many energy replacement times. This is directly relevant to ITER, and, as such, has been exploited effectively.

This difference in behaviour has provided a challenge to the Task Force, which has had to rethink the strategy for performance optimisation. Four distinct lines of attack have emerged:

- the performance optimisation of ELMy regimes;
- an underlying physics study of the reasons for the difference in behaviour;
- optimisation of the ELM-free period;
- optimisation of the performance in regimes with longer ELM-free period.

These studies will continue into 1995 but already a picture is emerging whereby the optimisation of core

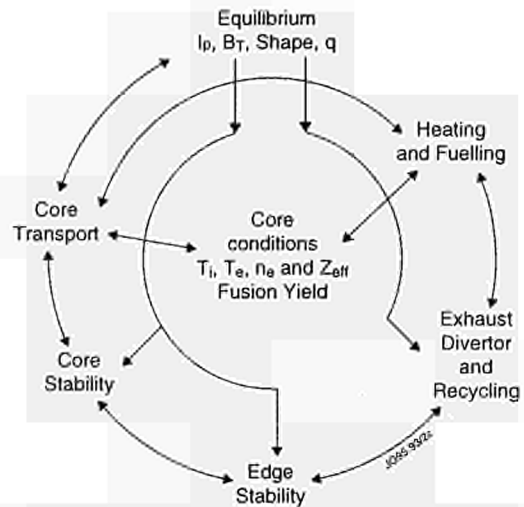


Fig.117: The complex web of inter-relations constraining the optimisation of core conditions

conditions is constrained by a complex web of interrelated physics, as illustrated in Fig.117. The Task Force has made progress in understanding some of the key links, such as that between configuration and ELM-free period, and between recycling and ELM-free period, between recycling, refuelling and core density profiles.

### Recycling and Conditioning

Experiments in ASDEX-Upgrade on divertor closure have established a link between main chamber recycling, requiring a high degree of neutral trapping in the divertor

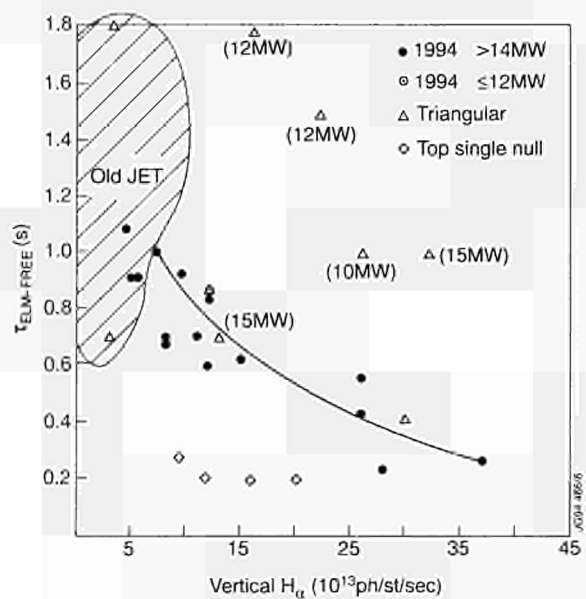


Fig.118: Correlation of ELM-free period with vertical  $H_\alpha$  radiation for various configurations. ELM-free period tends to be longer at low  $H_\alpha$  conditions

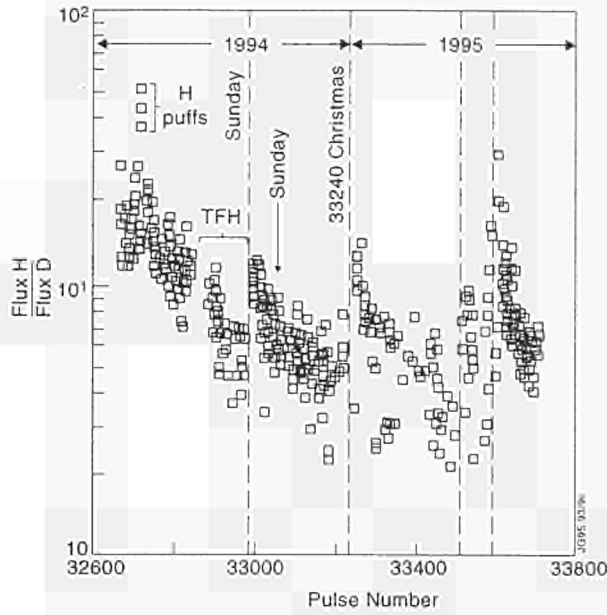


Fig.119: The ratio of fluxes H/D at 8keV measured by neutral particle analysis, at 8s after plasma initiation

chamber, to make ELM-free H-modes. This contrasts with the old JET with long ELM-free H-modes in an open divertor configuration. Many experiments were undertaken on the new JET to reduce the main chamber recycling, and as can be seen in Fig.118, a reduction in main chamber recycling, did significantly improve the ELM-free period from a few 100ms to about 1s, when the  $H_{\alpha}$  radiation was as low as previously. However, further examination has shown that the difference in  $H_{\alpha}$  radiation between the old JET and initial operation in the new JET can be explained by differences in the geometric views of the different plasma configurations. Nevertheless, it is clear from the figure that reduction in recycling for a given configuration does affect the ELM-free period. With the vessel baked at 250°C during operation, routine GDC in helium and regular beryllium evaporations did reduce the recycling, but the use of the torus cryopump had the strongest effect. In later experiments, it was

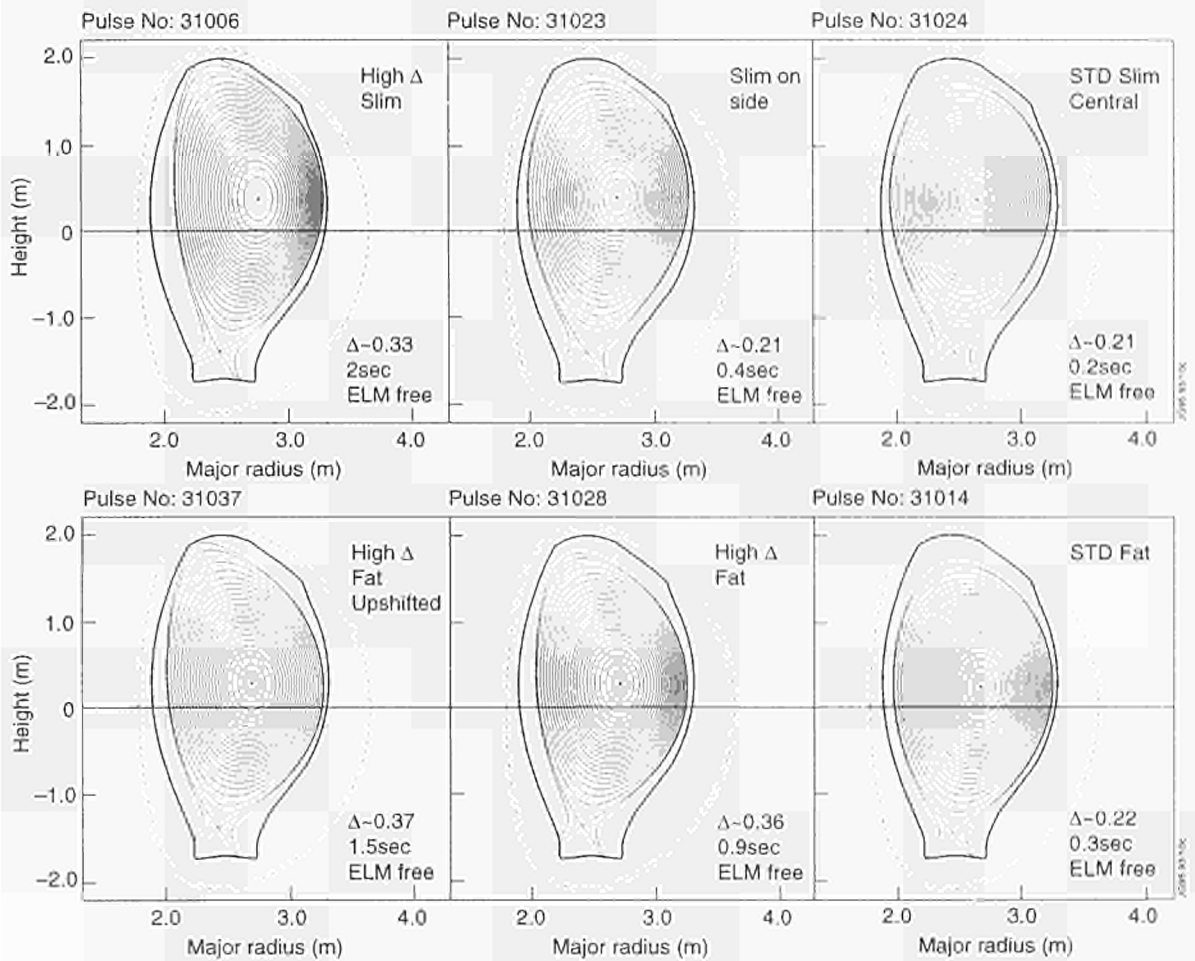


Fig.120: Variants of the standard FAT and SLIM configuration with high shaping and triangularity. The ELM-free period obtained with 10MW of beams at 2.5MA/2.8T is shown for each case

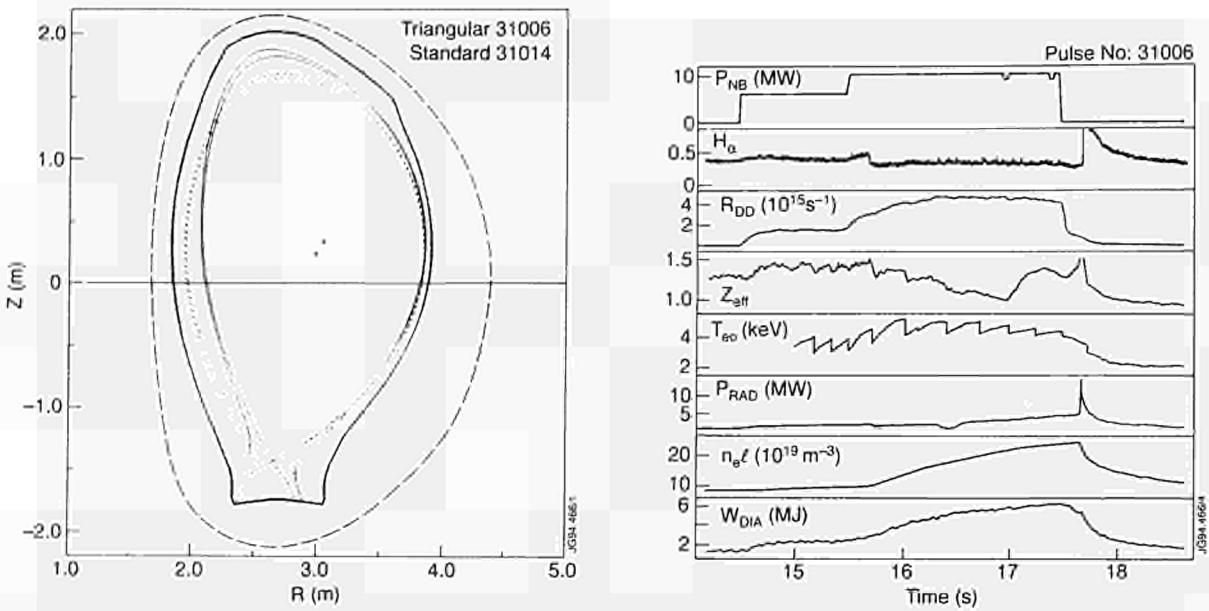


Fig. 121: (a) The SLIM-triangular configuration (solid) compared with the low triangularity FAT configuration (dashed); (b) time traces for the H-mode with moderate triangularity

shown that the pressure rise at the ELM was sufficient to allow strong pumping of deuterium in ELMy plasmas suggesting that the cryopump could deplete the deuterium reservoir in the torus and thus reduce the recycling source. However, in gas fuelled ELMy H-modes, the pumping is comparable to the fuelling. In beam fuelled ELMy H-modes, the pumping can exceed the beam fuelling by factors 2-4, but the net pumping is still comparable to the sum of gas fuelling during the limiter phase and beam fuelling in the X-point phase. Further experiments are outstanding to determine whether there remains any depletion of the deuterium inventory in the target tiles.

The old JET was routinely operated with the vessel at 300°C, but in the new JET the baking temperature was initially limited whilst the heat transfer to the divertor coils was being assessed. Since then, the vessel temperature has been progressively raised to 320°C. The higher vessel temperature has not significantly reduced the recycling levels, but has speeded up the recovery of torus conditions after an intervention.

In the old JET, the target tiles were at vessel temperature, whereas in the new JET the target tiles are indirectly cooled by the water cooled beams, on which they are located. It is possible, therefore, that a significant hydrogenic inventory remains in these tiles following exposure to air. Figure 119 shows that the hydrogen/deuterium ratio (as measured by the neutral particle analyser (NPA)) declines relatively slowly after an inter-

vention and has not yet reached the low (~2-5%) levels typical of previous operation. Modest baking of these tiles is only possible by removing the water and allowing the tile temperatures to float. This was carried out over the Christmas period, and the increase in H/D in the plasmas following this operation suggests that there is significant hydrogen in the target tiles, which was able to diffuse to the surface and dilute the plasmas.

Investigations of He GDC used routinely in the past on JET and other tokamaks to deplete hydrogenic inventories have shown that there is a considerable problem of helium implantation and release in subsequent tokamak discharges. Reference hot-ion H-mode pulses taken before and after helium GDC have revealed that though the  $H_\alpha$  radiation is reduced, the fusion yield is strongly reduced and triton burn-up analysis reveals that the deuterium concentration is halved consistent with helium contamination. This recovers on a timescale of about 5-10 pulses. Thus, the interpulse helium GDC used on DIII-D, for example, appears to be of questionable value.

### The Role of Plasma Shape

On the assumption that the ELM-free period is determined by the time it takes to reach the edge ideal ballooning and kink stability limit, plasma shape parameters are likely to be important in determining the nature of the H-mode. Figure 120 shows a range of equilibria, which were tested at constant plasma current field and beam power.

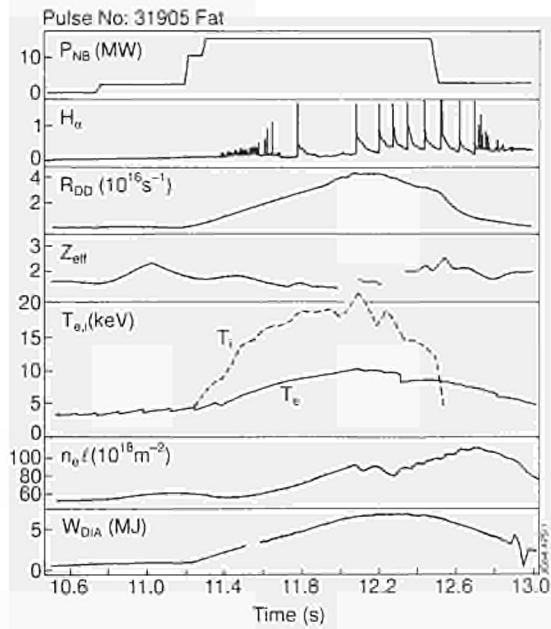


Fig.122: An example of the hot-ion regime in the standard FAT plasma configuration

This scan revealed a dramatic effect on ELM-free period and the most strongly shaped triangular configuration revealed a 2s ELM-free period, as shown in Fig. 121. Analysis of this scan and data over a range of currents confirm a strong correlation of plasma average pressure and edge pressure gradient with the predicted ideal ballooning edge gradient limit. Despite the spatial and temporal resolution limitations of the measurements, it is clear that increasing plasma current and edge shear are favour-

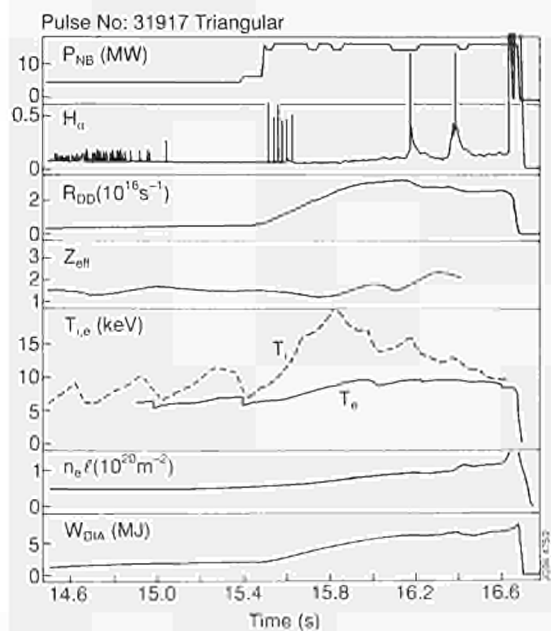


Fig.123: An example of the hot-ion regime in the so called FAT-triangular configuration.

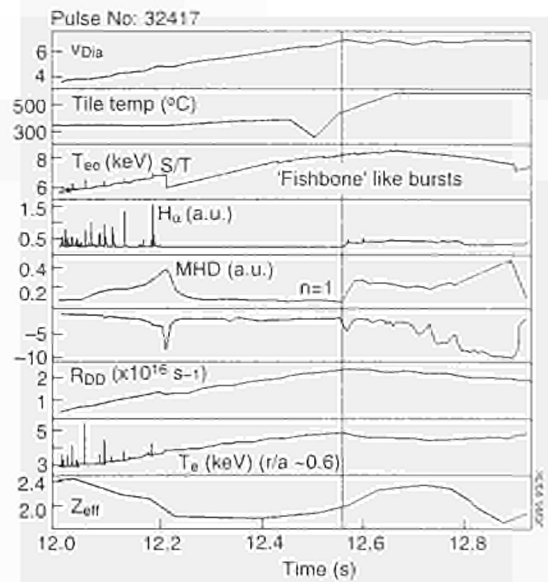


Fig.124: Example of the performance limiting "slow rollover" associated with internal MHD. In this case, the plasma configuration is similar to the high flux expansion case in Fig.125

able for long ELM-free periods. However, in this scan, the divertor plasma geometry was not held constant and it is not possible to separate out clearly the possible role of changed recycling on edge gradients. Experiments undertaken early in 1995 were able to scan separately plasma shape and divertor geometry and confirm that both divertor geometry and edge magnetic shear play a role, but that the latter dominates.

### The Hot-ion H-mode Regime

Initial experiments on the hot-ion H-mode regime were performed in the standard FAT plasma configuration, where it was necessary to pay careful attention to recycling optimisation, beam fuelling scenario, etc, in order to obtain reasonable performance. Figure 122 shows a typical example. Despite the high ion temperature, the fusion yield was only half the previous best performance, limited in this case by a giant ELM.

To avoid the limitation due to ELMs, the triangular configuration was developed towards the hot-ion regime, as shown in Fig.123. In this case, the low power fuelling phase is somewhat longer than the previous case dictated by the evolution from limiter phase and the transition into H-mode occurs at low power. The ELM-free phase is clearly longer than the last example, but despite this, the fusion performance is poorer as, in this case, confinement degrades part way through the ELM-free period associated with MHD activity in the plasma interior.

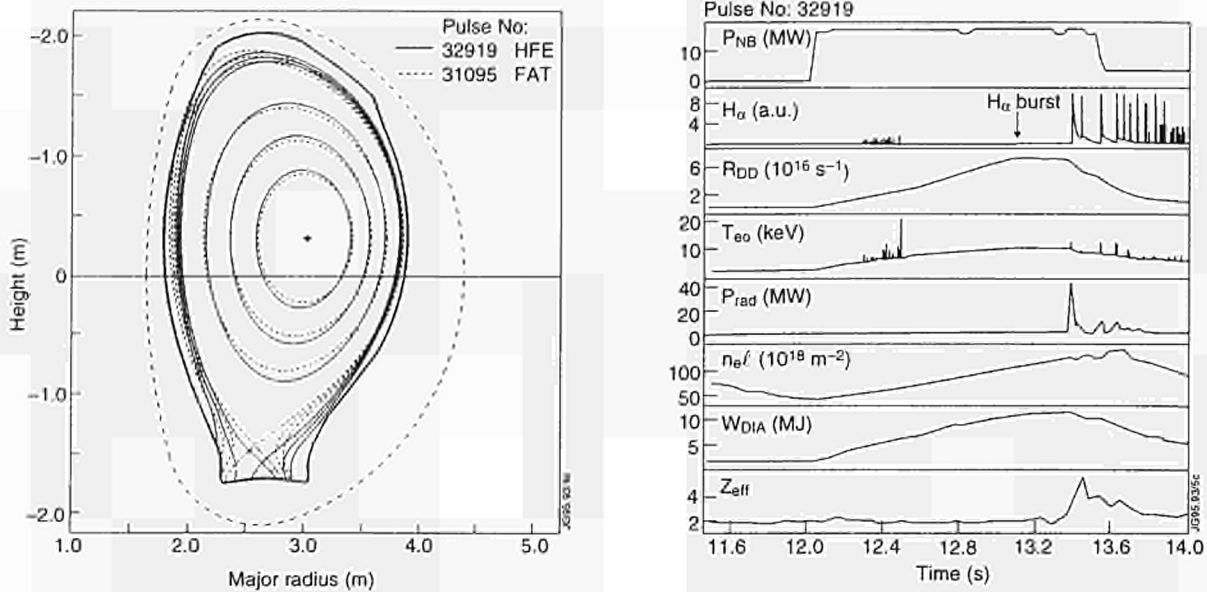


Fig.125:(a) Plasma equilibrium for the high flux expansion configuration (HFE) for highest fusion yield (Pulse No: 32919) compared with standard FAT configuration. Note the 1cm and 2cm scrape-off surfaces are also shown in each case; (b) Various time traces for the highest fusion yield pulse of 1994

This behaviour (the so-called slow termination) is illustrated in Fig.124. Here, early in the H-mode, the recycling level is low, but 300ms after the start of the ELM-free period, the rate of rise of stored energy decreases and at the same time the target temperature increases indicating higher energy loss from the core. The recycling radiation increases, the magnetic activity changes, in character, and the edge temperature clamps. However, the core transport within the 80% flux surface does not change.

In Fig.123, it can be seen that the ELMs, are somewhat different in character, with a slowly rising precursor and the final ELM leads to a disruption. During these ELM's the plasma position jumps up and inwards because of the rapid changes in poloidal beta,  $\beta_p$ , and plasma inductance,  $\ell_p$ . In the final ELM, the plasma contacted the inboard parts of the top saddle coils causing further damage and impurity influx. It is not surprising, therefore, that a disruption followed. After the September outage, further work on this configuration and position control was not able to solve the problems following the ELM's, and work on this configuration was held in abeyance.

A new configuration was then developed after the September outage with high edge magnetic shear to increase the stability margin and high divertor plasma flux expansion (similar to the PTE series plasmas). This configuration showed long ELM-free periods and low  $H_{\alpha}$  radiation levels during the H-mode. This was achieved even under the poor torus conditions following recovery

from the outage, when the standard FAT configuration showed high recycling and ELMy behaviour. Over a period of weeks as the torus conditions improved, this configuration was developed to fusion performance comparable to that achieved in the PTE series, as shown in Fig.125. In this case at 3MA, the triple fusion product,  $n_D \tau T_i$ ;  $\sim 8 \times 10^{20} m^{-3} s keV$  was achieved. As in previous hot-ion discharges, the transient high performance phase was limited by sawteeth, giant ELMs, slow rollover or a combination of these, such as a sawtooth together with a giant ELM. The plasma current was increased to  $\sim 4MA$ , but this revealed limitations in the neutral beam stray field compensation system, which led to power trips. These higher current cases will be exploited in 1995.

### High Plasma Current Operation

Already by September [3], the plasma current for routine operation in the FAT configuration had reached 4MA and promising performance in the ELMy H-mode had been established for pulse lengths of a few seconds.

By the end of 1994, these scenarios had been extended to 5MA, where ELMy H modes were demonstrated, as shown in Fig.126. The confinement demonstrated in these preliminary experiments is about 1.8 times L-mode as demonstrated in Fig.127, in line with expectation, showing little (if any) degradation at these low values of  $q_{05} \sim 3$ . These experiments will be continued in 1995 at still higher power levels. High flux expansion variants

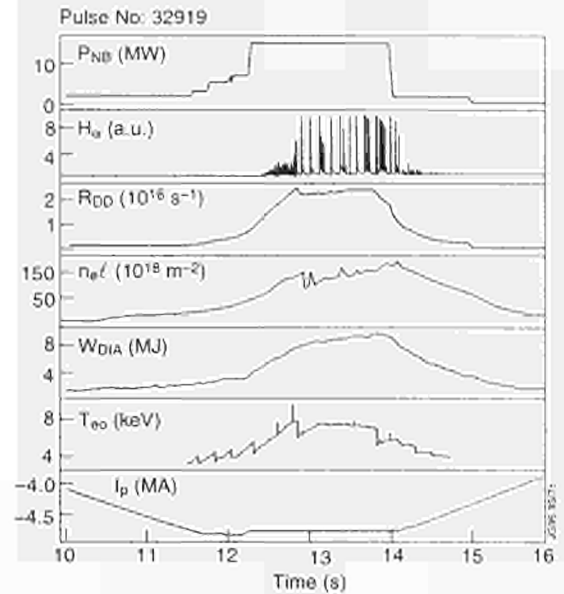
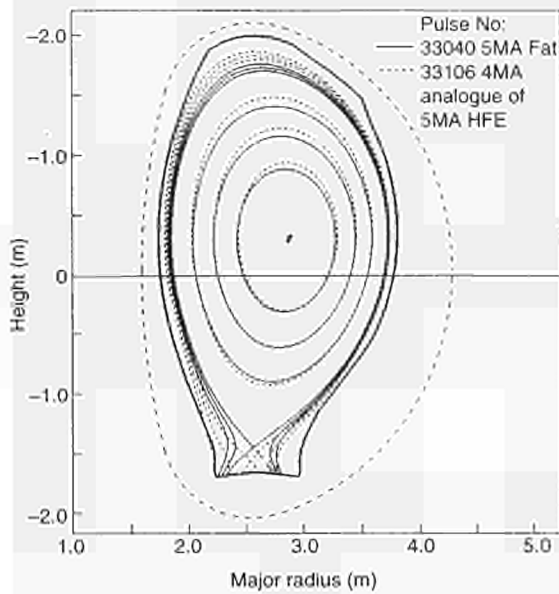


Fig.126: (a) FAT configuration employed for 5MA ELMy H-mode compared with high flux expansion analogue of 5MA showing ELM-free H-mode at 4MA/2.8T; (b) Time traces for 5MA ELMy H-mode in the FAT configuration

have been tested up to 4MA/2.8T in an analogue of 5MA scenario and these will be developed towards 5MA with the aim of exploiting ELM-free H-modes at the highest plasma current.

### Conclusions and Summary

The Task Force responded effectively to the challenge of exploitation of performance in the new JET. The surprise of finding the H-mode character somewhat different from that expected has led to increased understanding of the complex inter-relationships which determine H-mode character and, hence, influence performance. It is clear,

that both divertor plasma behaviour and edge magnetic shear strongly influence the H-mode behaviour.

There is evidence that both divertor closure and neutral retention influence the edge gradients and that high magnetic shear can, by raising the stability limits, allow open divertor geometries to show ELM-free H-modes. Whilst understanding is at yet incomplete, it has allowed, in a very short space of time to bring the fusion performance of the new up towards the previous best, looking forward

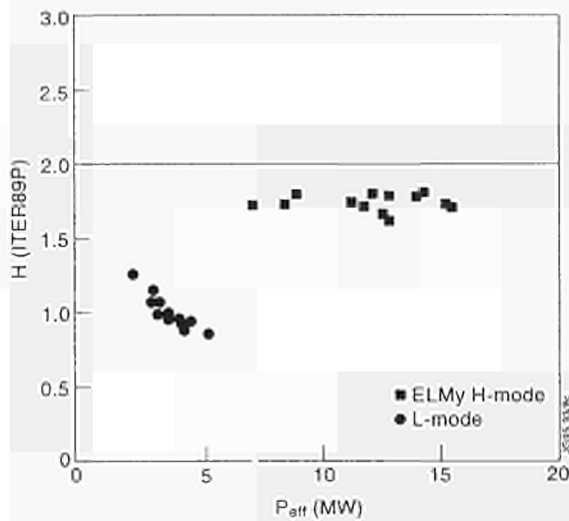


Fig.127: Confinement of 5MA plasmas in the FAT configuration showing both L-mode and ELMy H-mode

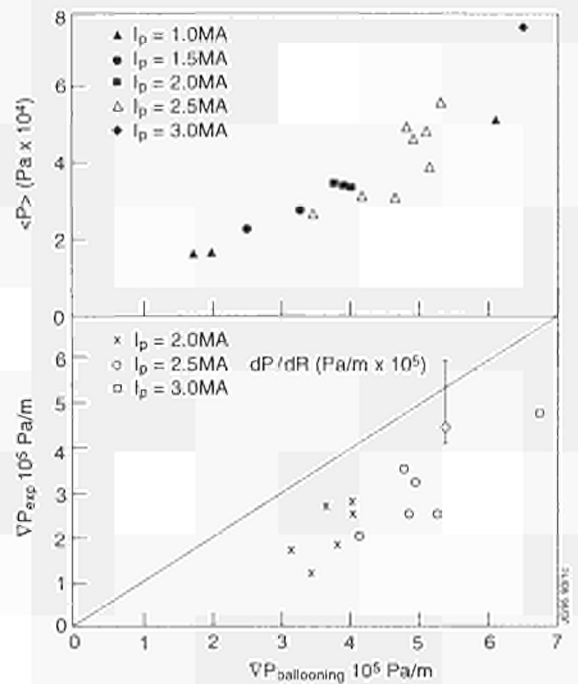


Fig.128: The relationship between average pressure and pressure gradient at the 95% flux surface with the ideal ballooning limit computed for equilibria at this surface

to further improvements in 1995. The conclusions indicate that the Mark II geometry offers improved prospects for recycling and neutral control and identify clear routes for the exploitation of fusion performance.

### References

- [1] A Gibson et al, JET Report, JET-IR(93)04;
- [2] D Stork et al, JET Report, JET-P(94)09;
- [3] The JET Team (presented by P J Lomas), 15th International Conference on Plasma Physics and Controlled Nuclear Fusion Research, (Seville, Spain, 1994) (Paper No: IAEA-CN-60/A-2-I-4).

## Divertor Assessment and Divertor Physics

The technical features of the inertially cooled Mark I divertor system were detailed in the JET Progress Reports for 1992 and 1993. The system can be described as a ribbed structure consisting of radially oriented water cooled rails on which the 2D CFC target tiles are mounted. (The CFC tiles will be replaced by Be tiles in March 1995). There are radial slots,  $\sim 1$ cm in toroidal extent, between the tile-carrier rail assemblies, through which neutrals can circulate, facilitating pumping. The use of four in-vessel coils not only enables sweeping of the strike points over the targets to reduce heat loads, but also makes it possible to produce a large variety of magnetic equilibria with independently varied X-point height and divertor connection length. This versatility has been greatly exploited during the 1994 campaign. The divertor is equipped with a toroidally continuous cryopump with an effective measured pumping speed near the liquid nitrogen shields of  $\sim 215,000 \text{ l/s}$ . The pump has proven to be effective in controlling the density during pulses. When covered with argon frost, it also pumps helium effectively.

During the installation of the divertor, considerable attention was paid to achieving the best alignment possible. The power handling of the new divertor has proven to be good, both on the horizontal and on the vertical targets (for which accurate alignment is more difficult). As a result, the carbon blooms which plagued high power/high energy discharges in previous campaigns have been effectively eliminated.

The Mark I divertor has had to fulfil two broad requirements. First, it has had to provide satisfactory power and particle exhaust, and impurity control, for the high per-

formance programme. Secondly, it has been used to successfully investigate many of the divertor physics issues crucial to the ITER divertor. During 1994, the Divertor Assessment Task Force and the Divertor Physics Topic Group worked closely together to plan, execute, and interpret experiments designed specifically to address ITER-related physics issues. In this effort, considerable emphasis was placed on the use of computational and analytical SOL/Divertor models, both in the planning and the interpretation phases. The campaign has been intensive and large quantities of data have been amassed; full interpretation will require considerable time after the end of the Mark I CFC campaign in March 1995. The experience gained with Mark I will be of direct use in laying the groundwork for the Mark IIA and Mark IIGB divertors, in which the effects of geometry, in progressively more closed systems, will be studied.

A broad range of divertor physics problems has been investigated in the Mark I divertor [1,2]. The main emphasis has been on medium to high density main plasma operation to access the high recycling and detached plasma regimes in the divertor. Both "pure" deuterium plasmas (i.e. those with only intrinsic impurities) and plasmas seeded with neon and nitrogen have been studied, to understand the approach to detachment, the mechanisms of power dispersal, the effect on impurity retention, and particle exhaust. A principal concern has been the compatibility of detached plasmas with high quality H-modes, as theory indicates that the window in parameter space for achieving this ITER requirement may become smaller in larger devices. A second main area of study has been that of the effect of divertor geometry, with particular emphasis on differences which arise between operating with the strike zones on the horizontal and vertical surfaces. Additional areas which were investigated include helium exhaust, the asymmetries associated with the direction of the ion  $\nabla B$  drift, the scaling of SOL widths, the effect of scrape-off layer flows induced by pumping and puffing, and the influence of divertor geometry on main chamber recycling, which affects main plasma performance.

The Divertor Task Force has also investigated steady-state H-modes, with considerable success. Whilst the drive to produce peak performance in ELM-free, hot ion moderate density H-modes is indisputably an important activity at JET, and will provide the quickest route to studying the important issues connected with the physics

of plasmas with significant alpha-particle content, it is likely that ITER will operate with higher density, ELMy H-modes with roughly equilibrated temperatures. During 1994, JET was able to achieve steady-state H-modes lasting 20s (restricted only by technical constraints), or about forty energy confinement times. This achievement is a major step forward in demonstrating ITER-relevant H-mode plasma operation. Progress has also been made on the L-H transition and the density limit in H-modes.

In summary, the 1994 Mark I CFC campaign has provided a wealth of data, and set the stage for further work to be carried out in Mark I and Mark II divertors. Each of the eight divertor R&D issues listed by ITER as "urgent" has been addressed, and significant progress made. In addition, most of the issues labelled as "high priority" or "longer term" have been examined on, at least, a preliminary basis. This data, together with that obtained by other divertor tokamaks throughout the world, is being analyzed in a coordinated manner to provide a credible basis for the ITER divertor design.

### Power Handling Capability of the Mark I Divertor

The study of divertor performance under steady-state conditions at high power has been a central goal of the programme. Particular care has, therefore, been taken in the design and installation of the power handling surfaces of the Mark I divertor target to optimise power handling, in particular by avoiding exposure of tile edges. The strike points can be swept over the target plates at 4Hz with an amplitude of  $\sim 10$ cm to increase the effective wetted area of the target. The Mark I divertor has shown excellent power handling capability during the current campaign, with no carbon blooms limiting the performance as in the past. The performance of the target has been investigated over a wide range of plasma conditions, at powers of up to 26MW and in steady-state H-modes lasting up to 20s. In no case, including hot-ion H-modes where performance was previously limited by impurity influxes, has a carbon bloom been observed. Indeed, the combined effects of sweeping and giant ELMs, which are now a feature of H-modes, are such that the surface temperature of the target has not exceeded  $1200^{\circ}\text{C}$ , even in cases where over 100MJ of energy has been delivered to the horizontal target. The vertical target plates have also proved robust in this respect, having sustained 80MJ of injected energy, of which 50MJ was deposited on the target.

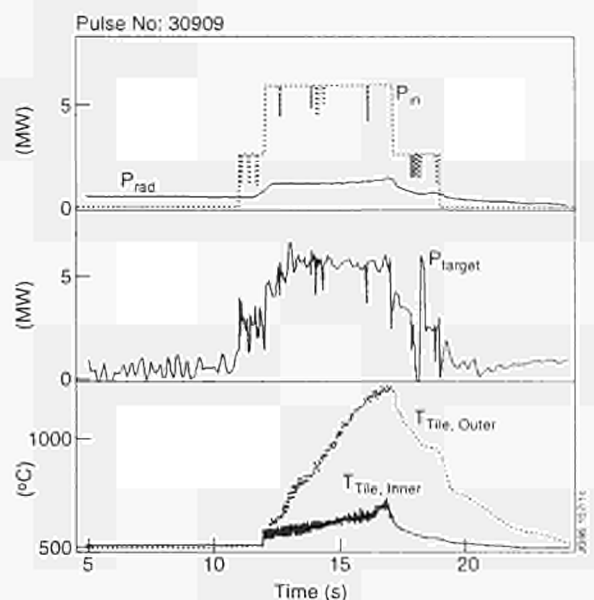


Fig.129: Total injected power, power radiated, power conducted to divertor plates, and time evolution of measured temperatures on the (a) outer and (b) inner target plates

### The Diagnostic

The surface temperature of the divertor tiles is measured by infrared thermography. A linear array of InGaAs diodes, sensitive in the 1.6 $\mu\text{m}$  region, views most of the horizontal target plates. The spatial resolution along this axis is 3mm. In the toroidal direction, a cylindrical lens is used to average the signal over approximately the width of four pairs of tiles; the temperature measured is representative of the areas of maximum temperature in each averaged region. The minimum detectable temperature varies with the setting of the camera and is between  $350$  and  $560^{\circ}\text{C}$  (the initial temperature of the tiles is measured by thermocouples embedded in the tiles). The time resolution is 2ms, which permits (marginally) the study of fast events such as ELMs.

### Static X-point Configuration

A quantitative analysis of the power deposition on the Mark I divertor tiles has been carried out for a real plasma case with the TILO code. TILO computes the power density on the tile surfaces, taking into account the shadowing patterns, and allows further thermomechanical analysis of the tile(s) considered. This permits the conducted power to the divertor to be deduced by comparing the calculated time evolution of the peak target temperatures on the inner and outer strike points with those measured with the infrared thermography.

A simulation has been performed for a simple case (Pulse No: 30909), with  $I_p=3.2\text{MA}$ ,  $B_t=3.2\text{T}$  with 6MW

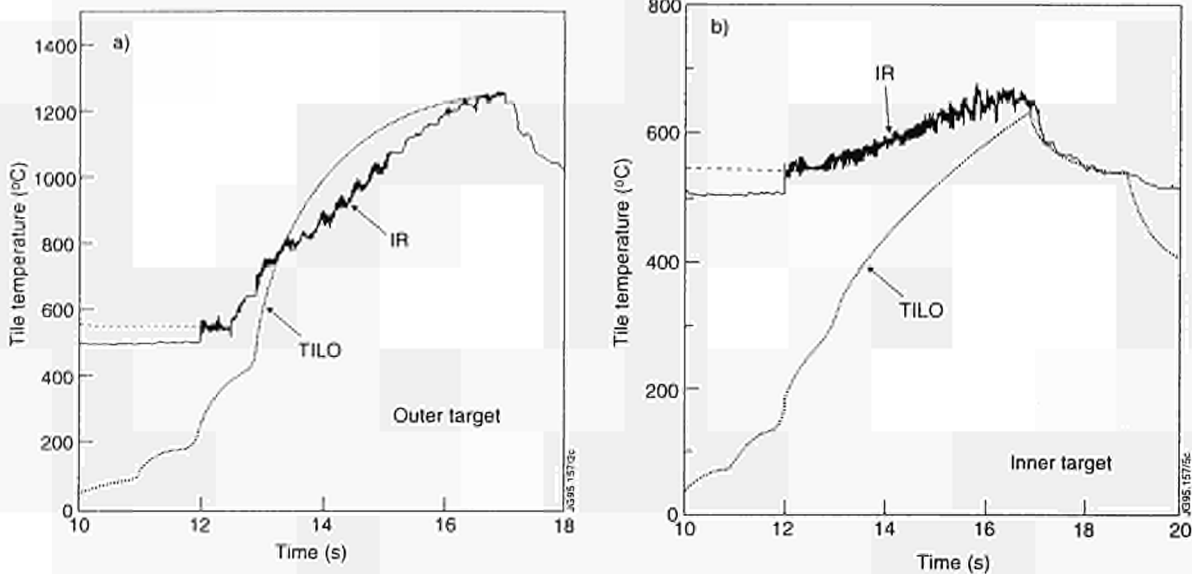


Fig.130: Evolution of calculated and experimental temperatures at the hottest points for inner and outer strike regions

NBI heating and no sweeping of the strike regions. This displayed only L-mode confinement and, hence, had no ELMs. The power density decay length in the edge plasma for this case was 1cm. The initial temperature of the tiles was measured by thermocouples embedded in the tiles, and was  $\sim 40^\circ\text{C}$ . Figure 129 shows the total injected power, the power radiated, the power conducted to the divertor plates, and the time evolution of the measured temperatures in the inner and outer strike regions. The experimental measurements have a background of  $\sim 560^\circ\text{C}$ , while the peak surface temperatures achieved in the inner and outer strike regions are 650 and  $1200^\circ\text{C}$ , respectively. Figure 130 shows the evolution of the calculated and experimental temperatures at the hottest points for inner and outer strike regions. The calculated power values, when the matching of the peak temperature is achieved, are:

$$P_{in} = 0.85(1/2P_{cond}) = 0.425P_{cond}$$

$$P_{out} = 1.40(1/2P_{cond}) = 0.7P_{cond}$$

where  $P_{cond}$  is the measured power conducted to the two divertor plates. This corresponds to  $\sim 3.85\text{MW}$  conducted to the outer strike zone, and  $2.3\text{MW}$  to the inner strike zone for 5s. The power is not equally shared between the inner and outer divertor plates. The different time evolution of the measured and the calculated temperatures reflects the fact that the power ratio between inner and outer strike regions is not constant with time, as assumed in the simulation. Nevertheless, the calculated conducted power is 112% of the measured conducted power. This is

a satisfactory power balance, considering the experimental error of 10-20% and scattering in the material properties of the tiles.

The ratio  $P_{out}/P_{in}$  differs only by 10% from the value of  $T_{out}/T_{in}$ , which means that the tiles behave as a semi-infinite solid to a reasonable approximation, and that the peak temperature values can reasonably be compared to make power imbalance assessments. The thermal analysis of the tiles shows that a uniform temperature is achieved only 7s after the power has been switched off. This is due to the excellent thermal conductivity of the CFC in the vertical and the radial directions.

The TILO code has been used to calculate the thermal conductance,  $K$ , between tiles and the support beam. It is observed that, after an initial fast variation, the longer term cooling of the tiles is represented by a simple decay expression, typical of a diffusion process. A good matching of the experimentally measured cooling time constant is achieved for  $\kappa \sim 40\text{W/m}^2\text{K}$ . This value is higher than foreseen in the design phase of the divertor, and, in fact, the power handling capability of the tiles is also higher than predicted. Figure 131 shows the predicted maximum power per divertor leg for different exposure times. The result of the TILO simulation, corresponding to 5s exposure, shows that the tiles are handling  $\sim 20\%$  more power than predicted.

S65B grade beryllium tiles will replace the currently installed CFC tiles for comparison purposes. Taking into account that the mechanism for attaching the tile to its

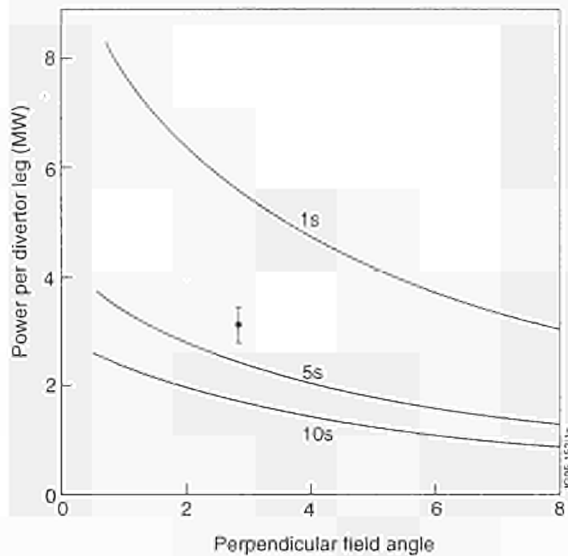


Fig.131: Predicted maximum power per divertor leg required to raise the target surface temperature by 1000°C in a given time (carbon target, unswept)

carrier will be the same as in the CFC case, it is expected that the beryllium system should have a similar value for the thermal conductance.

### Effects of Sweeping

Sweeping further improves the power handling capability of the tiles. An exact assessment is difficult to perform, since, during the sweep, the expansion of the magnetic flux lines at the divertor (and consequently also the power density) varies with separatrix radius.

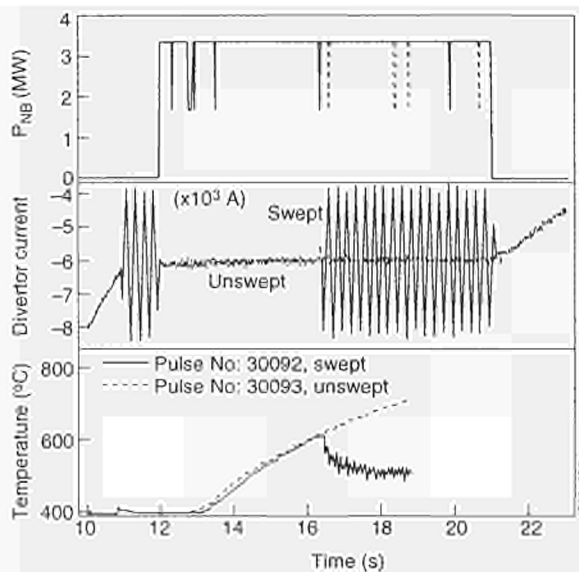


Fig.132: Time evolution of tile temperature during swept and unswept cases.

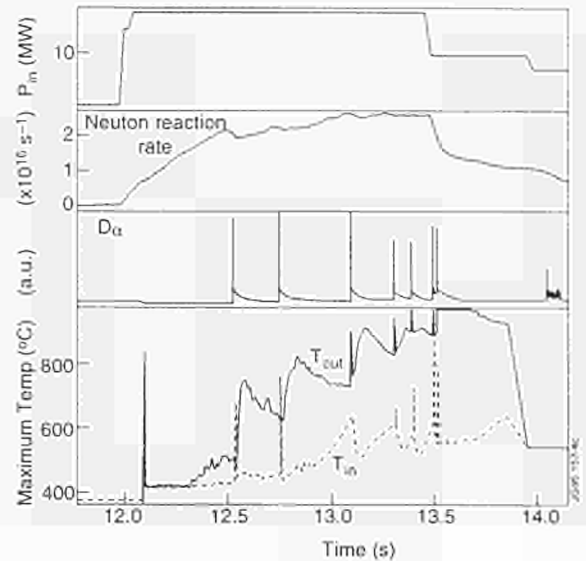


Fig.133: Time evolution of the surface temperature in the two strike regions for a discharge in the hot-ion mode (Pulse No: 34460)

Estimates have been made for long heating pulses at low power (Pulse Nos: 30092 and 30093, 3MW for 10s, swept and unswept). In these pulses,  $\lambda_p=8\text{cm}$  at the divertor and the peak-to-peak sweep amplitude was 18cm. Figure 132 shows the power injected in these two pulses, the current in the divertor coil D2 as an indicator of the sweep, and the time evolution of the maximum temperature of the tiles for the two cases. In the swept case, the peak temperature decreases when the sweep begins and stabilises at  $\sim 500^\circ\text{C}$ , in contrast to the unswept shot where the peak temperature continues to increase steadily. With sweeping, the effective power seen by the target is  $\sim 66\%$  of the power in the unswept case. This is slightly worse than the preliminary calculations predicted, but these assumed a perfect triangular sweep waveform, whereas the measurements show that more power is deposited at the extremes of the sweep.

### Effects of ELMs

From the power handling point of view, ELMs have two effects. Firstly, they deposit power on surfaces other than the strike zones, and secondly, since they create a spike in the radiated power, the power conducted to the strike zones decreases immediately after the ELM event. In this sense ELMs are extremely effective in alleviating the heat load on the strike zones, but the penalty is the uncontrolled deposition of power in zones which may have a poor power handling capability, particularly for giant ELMs. The initial power deposition occurs in

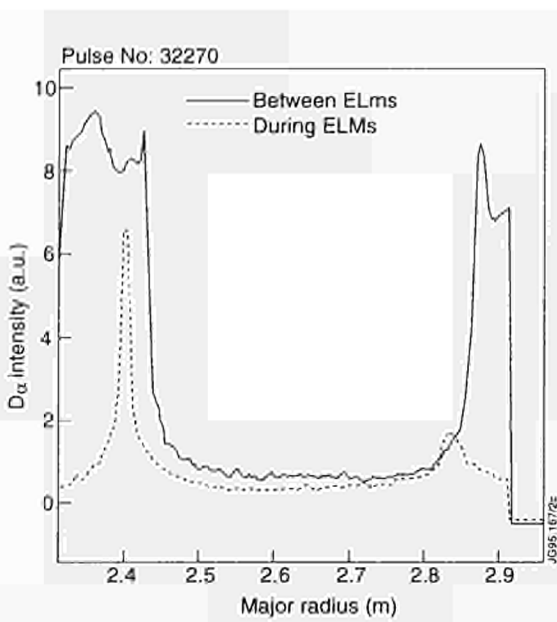


Fig.134:  $D_{\alpha}$  profile on the divertor plates between and during an ELM, Pulse No: 32270 (2.5MA, 2.7T,  $P_{NB}=14\text{MW}$ ,  $n=2.4 \times 10^{19}\text{m}^{-3}$ )

submillisecond times, and hence the infrared thermography time resolution (2ms) gives only an approximate sampling of the event. In Fig.133, the time evolution of the target temperature in the two strike regions is shown for a discharge in the hot-ion H-mode regime (Pulse No: 34460  $I_p=5\text{MA}$ ,  $B_t=3.4\text{T}$ ,  $P_{in}=20\text{MW}$ ). Between giant ELMs, the power imbalance changes between inner and outer strike zones.

High frequency small ELMs are produced in discharges with high gas fuelling. Small ELMs also tend to deposit power in the inner strike region, and, at the high repetition rates obtained, the net effect is a broadening of power deposition profiles on the target. During these very ELMy H-modes, the peak power density reaching the separatrix position was much lower than during the preceding non-ELMy L-mode phase at the same input power. By making use of sweeping to minimise the rises in both surface and bulk tile temperatures, a 20s H-mode has been obtained, at medium injected power (7MW, 140MJ), where the maximum tile temperature stayed below 550°C.

### Elm Characteristics and Interaction with Target Plates

The interaction of ELMs with the divertor plasma and the target plates has been studied in ELMy, high density H-modes. Typical discharge parameters were:  $B_t=2.4\text{--}3.4\text{T}$ ,  $I_p=2\text{--}3\text{MA}$ ,  $n_{\text{max}}=5\text{--}10.5 \times 10^{19}\text{m}^{-3}$ ,  $P_{NB}=10\text{--}18\text{MW}$ .

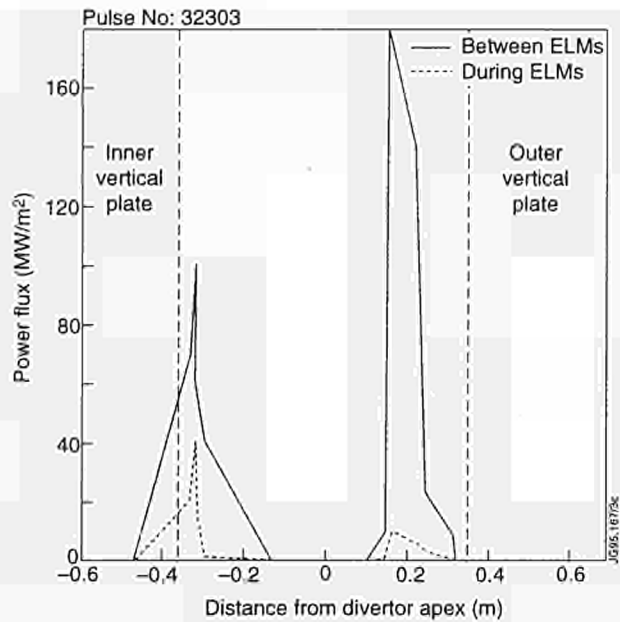


Fig.135: Power flux profile on the divertor plates between and during an ELM, Pulse No: 32303 (2.5MA, 3.4T,  $P_{NB}=15\text{MW}$ ,  $n=2.5 \times 10^{19}\text{m}^{-3}$ )

During an ELM, all the principal plasma parameters such as particle flux, power flux, electron temperature, electron and neutral density increased near the divertor target. The increase and its relative contribution to the inner and outer divertor leg depended on the individual ELM, but a factor of more than 10 was often observed for the particle and power fluxes. Moreover, the form of the spatial profiles of the main plasma parameters usually varied substantially (Fig.134). Complete loss of the exponential form, broadening of the profiles by a factor  $>2$  and the occurrence of multi-peak structures were common features. A tentative explanation for the observed profile changes may be a dramatic increase of the particle and energy transport in the SOL together with the occurrence of short lived magnetic islands.

In a typical ELM, the target probes show an increase of the ion saturation current, the electron temperature and the power flux at their maxima. Figure 135 shows an example of the power flux profile before and during an ELM. Integrating the increase of the power flux over the full divertor target and the duration of the ELM gives the additional amount of energy,  $\Delta E$ , hitting the target during this time. In this case  $\Delta E = 0.14\text{MJ}$ , which is  $\sim 6\%$  of the plasma energy content. The integration for the particle flux gives  $\Delta N = 6.5 \times 10^{20}$ , compared with the total particle content of the plasma of  $1.3 \times 10^{21}$ . Clearly, most of the additional particles are the result of increased recycling

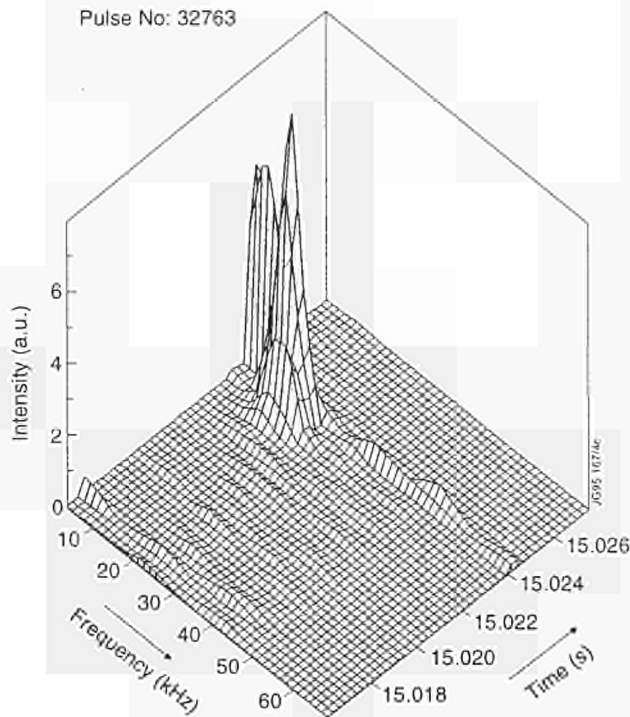


Fig.136: Frequency spectrum of the floating voltage perturbation in the outer SOL, Pulse No: 32763.

and/or particle release due to heating and sputtering. This means the intensity of the  $D_{\alpha}$  radiation from the target, usually taken as a measure for the ELM magnitude, is strongly influenced by the surface properties, which cannot be assumed to be constant.

The changes in the divertor plasma parameters during an ELM show characteristic time behaviour. The  $T_e$  perturbation is the shortest ( $\delta t \sim 0.2$ ms), followed by  $I_{sat}$  ( $\delta t \sim 0.6$ ms) and  $I_{D_{\alpha}}$  ( $\delta t \sim 1.0$ ms). Additionally, the  $T_e$  signal precedes the  $I_{sat}$  signal and the  $I_{D_{\alpha}}$  signal by  $\delta t > 0.2$ ms. The assumption of a conduction governed transport of electron energy and a convection governed transport of particles to the target plates, together with recycling and particle release due to heating and sputtering, qualitatively explains the behaviour.

The relationship between the arrival time of  $T_e$  perturbation and that of the particle flux perturbation, as well as that between the arrival of the perturbations on both sides of the divertor target, has been studied with a pair of high time resolution Langmuir probes ( $\delta t = 8$ ms). Clearly, all recorded ELMs show that the floating voltage perturbation, which is mainly governed by  $T_e$  perturbations, starts before the  $I_{sat}$  perturbation. On the other hand, there is no systematic time difference, within  $\pm 20$ ms, between the occurrence of the perturbations on both sides of the target

plates. The latter result means there is no experimental evidence of a localised expulsion of energy and particles near the outer midplane during an ELM. On the contrary, preliminary measurements show the perturbation arriving on both sides of the target approximately 500ms before it is seen on the reciprocating Langmuir probe near the top of the vessel. This points towards the X-point region being the "birthplace" of an ELM.

No systematic time delay has been found between signals from the closed flux surface region and from the divertor target at the start of an ELM. During ELMs broadband fluctuations have been observed on the reflectometer, magnetic probe and on the fast Langmuir probe signals. Only a fraction of the ELMs investigated show a precursor. Figure 136 shows the evolution of the frequency spectrum in time before and during an ELM. Here the main contributions to the signal are in the frequency range  $\Delta f = 0-20$ kHz and the precursor is concentrated around 15kHz. Typically, there is some continuous activity in the frequency range  $\Delta f = 20-45$ kHz before the ELM which disappears after the ELM.

## Effects of Fuelling and Pumping

Active particle control, including efficient helium exhaust, is required for steady-state operation in a reactor. The study of the effects of fuelling and active pumping on plasma properties has been one of the main topics of the Mark I campaign. In particular, an upgraded gas introduction system, characterised by toroidally and poloidally distributed gas sources in the vacuum vessel, and an entirely new internal cryopump capable of providing active pumping during plasma pulses have been extensively used.

## The Fuelling System

The plasma is fuelled by cold gas and neutral beam injection. The cold gas (room temperature) can be introduced into the machine from 10 modules, individually controllable. Each module feeds an internal manifold that provides a distributed source for the plasma. Two gas modules are located in the outer midplane and provide a point source in the main SOL, far from the plasma. Four other modules are located at the top of the machine, and provide fuelling in the main SOL, with poloidally distributed gas inlets. The last four modules are in the divertor region, and they fuel gas into the private flux region. The four manifolds are arranged to produce a uniform toroidal

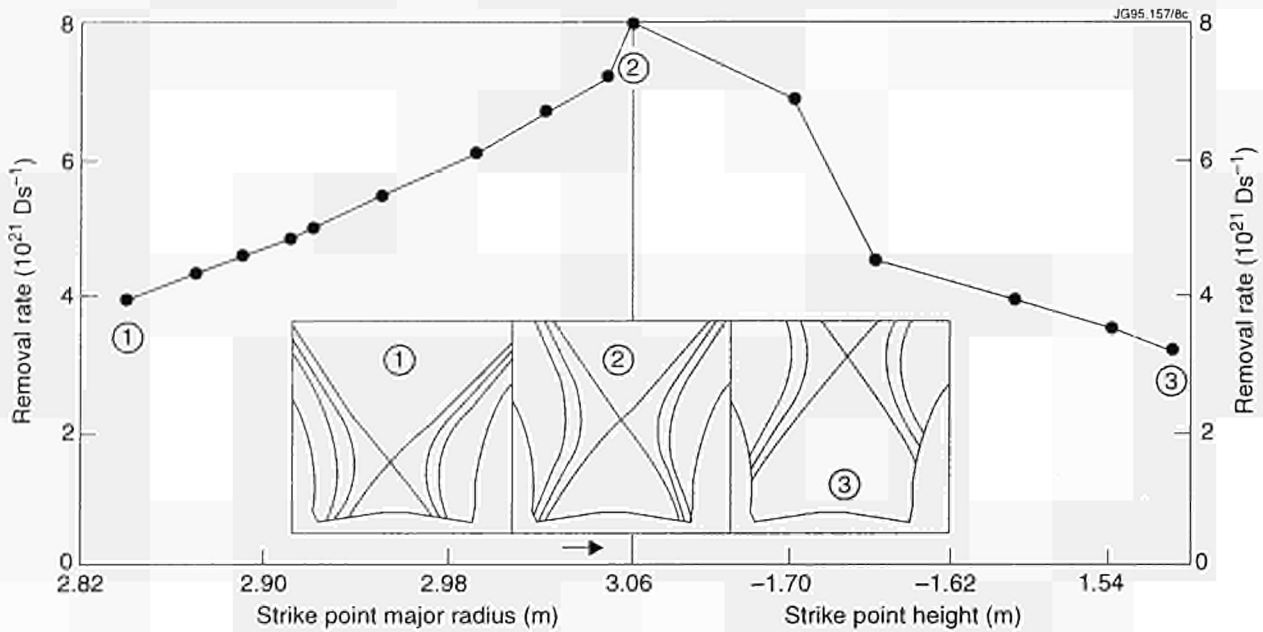


Fig.137: Pulse No: 31725 (2MA/2.8T): particle removal rate in atoms per second as a function of separatrix position on the horizontal plates (a) and on the vertical plates (b). The full sweep of the separatrix position is carried out in  $\sim 10$ s

distribution of the inlet gas. This system is used both to fuel the plasma and to inject gaseous impurities for specific experiments. The maximum capability for fuelling is  $\sim 5 \times 10^{22} D_0 s^{-1}$  for 10s steady state.

**The Pumping System**

Active particle removal during plasma discharges is provided by a toroidally continuous cryopump, located below the divertor plates. The cryopump is operated at 4.8K (supercritical He), and therefore all gases but H and He are efficiently pumped by cryosorption. In addition, the pump is equipped with internal nozzles to spray and condense Ar on the He panels, to pump He and H by cryotrapping. The cryopump has been exploited to control the plasma density and, by applying the argon frost layer, to simulate particle exhaust.

The overall effective pumping speed of the cryopump on the main vacuum vessel is about  $160 m^3 s^{-1}$ , while the speed of the pump, measured near the LN shields, is higher, and  $\sim 215 m^3 s^{-1}$ . The maximum amount of deuterium that can be condensed onto the pump has been limited to 1000barℓ for safety considerations rather than by the pump capacity. This amount of gas is sufficient for at least 2 weeks of normal plasma operation.

**Pumping during Plasma Discharges**  
**Particle Removal and Density Control**

Effective particle removal is achieved for all separatrix positions on both the horizontal and vertical plates of the

target. Optimum pumping is obtained with the outer divertor strike point located in the outer corner of the target (the closest point to the cryopump), but the particle removal rate falls by only a factor 2, as the strike point is swept along either the horizontal or vertical plate (Fig.137).

The particle removal rate is directly proportional to the neutral pressure built up in front of the cryopump. For a given separatrix position, this pressure depends on the plasma confinement regime and on recycling. As shown in Fig.138, the pressure in the divertor during the X-point phase increases with the plasma density during the ohmic

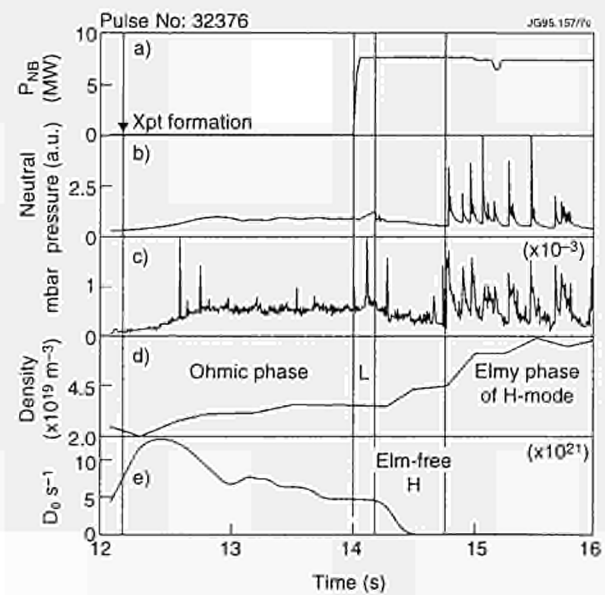


Fig.138: (a) Neutral beam power, (b) divertor  $D_0$  intensity, (c) neutral pressure in front of cryopump, (d) plasma density and (e) deuterium fuelling rate for Pulse No: 32376 (2.5MA/2.4T)

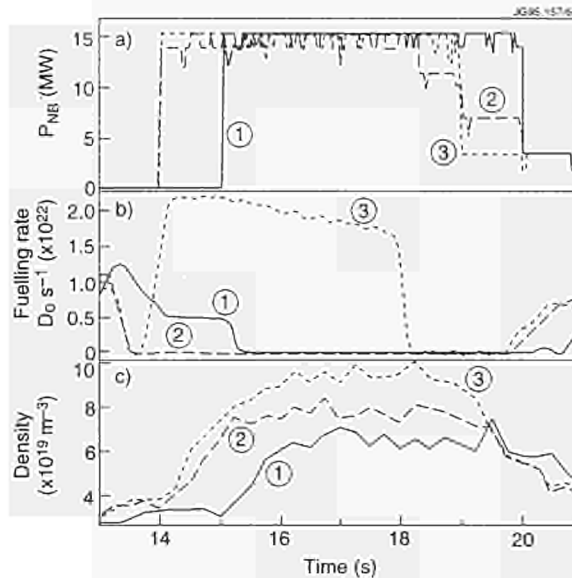


Fig.139: (a) Neutral beam power, (b) deuterium fuelling rate and (c) plasma central density for Pulse Nos: 32373 (1), 32745 (2) and 32747 (3), all at 3MA/2.8T. The neutral beam power is similar for the three discharges, whereas the separatrix position and gas fuelling during the H-mode were varied as follows:

Pulse No: 32373: strike point in the corners (max pumping position) - negligible gas fuelling;

Pulse No: 32745: strike point in middle position on the horizontal divertor plate - no gas;

Pulse No: 32747: strike point in middle position on the horizontal divertor plate - high gas flow.

The steady state density of these otherwise similar pulses vary by a factor 2

phase of the discharge. During the Elm-free phase both the  $D_\alpha$  and the pressure in front of the pump decrease, due to the improved particle confinement. Typical pressures in these cases vary from  $5 \times 10^{-4}$  to  $\sim 10^{-3}$  mbar.

In the ELM phase, pressure bursts in the divertor are measured in coincidence with the typical  $D_\alpha$  spikes. During ELMs, peak pressures at the pump can be as high as  $10^{-2}$  mbar, corresponding to peak particle removal rates  $\sim 10^{23}$  atom/s. The comparison between the plasma density drop and the particle removal associated with an ELM indicates that a large fraction of the particles removed by the pump originate from plasma induced desorption from material surfaces.

The particle balance of a discharge (difference between particle fuelling and particles removed by the cryopump) therefore depends on the discharge characteristics (density, separatrix position) as well as on the confinement regime and wall particle loading. For high density, high fuelling discharges in particular, the total particle exhaust equals or exceeds the gas input, indicating that some depletion of the deuterium wall inventory is achieved.

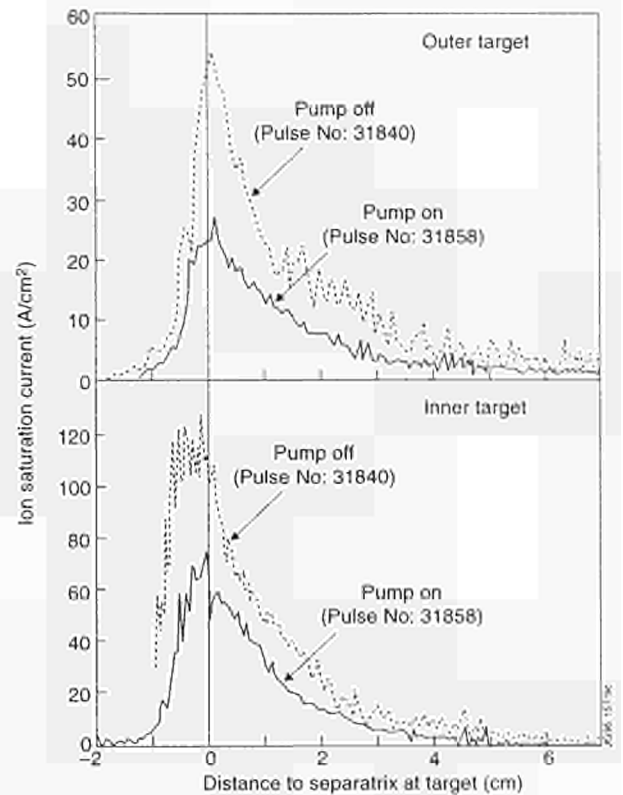


Fig.140: Changes of the ion flux profile at the target for two similar discharges: with the pump off (Pulse No: 31840) and the pump on (Pulse No: 31858). The two pulses were at 2.5MA/ 2.4T, 8-10 MW neutral beam heated H-modes. No gas feed during the H-mode phase.

In H-mode, density control in steady state is achieved during ELMy discharges, both for neutral beam only and gas fuelled discharges, Fig. 139. In contrast to unpumped cases, where the plasma density in steady state is determined by the beam fuelling, the combination of fuelling and active pumping allows the steady state density of H mode discharges to be varied by a factor of two. While it is intuitive that the pump should help to decrease the density in steady state, the interesting but less obvious feature is that active pumping also permits higher steady state density during H-modes than obtained without the cryopump. This is possibly related to the changes in the density profiles at the edge induced by the pumping.

### Effects on Plasma Parameters

H-mode discharges with the cryopump are characterised by a reduction of the  $D_\alpha$  level, both in the main chamber and in the divertor, by a decrease of the ion flux to the target  $J_{sat}$  (measured by Langmuir probes) and, in general, by a corresponding increase in the central ion temperature and neutron rate, when compared to similar discharges

carried out without active pumping. This effect can be correlated with the changes in the density profiles for pumped plasmas. For pumped discharges, the edge density (inside the separatrix) is generally reduced, and more peaked density profiles are measured. This is consistent with reduced recycling from the wall, and an improved neutral beam penetration. The decrease in edge density in H-mode with the pump on is generally observed for all types of discharges.

In the case of steady state ELMy H-modes at medium-high density, the peaking of the profile is particularly pronounced, both between and just after ELMs. This is in agreement with the observed increase of neutral pressure at the divertor and, therefore, of the particle removal rate.

The cryopump also significantly affects the plasma parameters in the divertor. The integrated ion flux to the target decreases approximately by a factor 2 compared to a similar discharge with no pumping (Fig. 140). The electron temperature and density at the target vary in a similar manner. The cryopump also affects the  $J_{\text{sat}}$ ,  $n_e$  and  $T_e$  profiles between ELMs, which become steeper. There is some evidence that active pumping affects the balance of fluxes between inner and outer strike zones. During ELMs, the ion flux to the outer strike zone (nearer to the pump) decreases more than the flux to the inner, and the ratio between  $J_{\text{sat}}(\text{in})$  and  $J_{\text{sat}}(\text{out})$  changes from 1.2 to 1.7. These imbalances in the divertor fluxes have no detrimental effect on the core plasma.

### *Neutral Pressure in the Divertor*

When the pump is on, the neutral pressure in the divertor is typically a factor 2 lower than for a similar unpumped discharge. Moreover, experiments were carried out where the separatrix was slowly swept across both horizontal and vertical divertor plates. From these experiments, it was possible to assess the influence of the separatrix position on the particle removal efficiency and to compare the pressure to the ion flux to the target. First calculations carried out for the pump-off case show that the integral of neutral flux and of the ion flux to the target are comparable. Broadening of the neutral pressure profile compared to the ion flux profile is consistent with neutral recirculation via the slots between divertor tiles playing an important role in the neutral distribution. This is also consistent with the small variation of the pressure in front of the pump with the plasma separatrix position,

and explains the weak dependence of pumping rate on strike point position.

### **Convection in the SOL**

SOL fluid models predict variation of the particle flows towards the divertor according to the location of the external particle source. The predicted changes can affect the natural convection in a measurable way only when the plasma density is high and the cryopump is on. Preliminary experiments were carried out in similar discharges, where the fuelling location was changed from the top of the torus to the divertor region, and the pattern of radiation changed. In particular, the bulk plasma radiation was higher in the case of top fuelling, whereas the divertor radiation was higher with fuelling in the divertor. Measurements carried out with a reciprocating Langmuir probe system located near the top of the machine show a strong flow towards the high field side, with a Mach number of about 0.2-0.3, the lower values of Mach number tending to be associated with fuelling from the top. This flow is only weakly associated with the fuelling location and the cryopump being on. Interestingly, the SOL flows change sign at high plasma density, and are observed to change sign in conditions near detachment. The link between flow reversal and changes in the recycling during detachment is still under study.

### **Helium and Neon Confinement and Exhaust Studies**

The confinement and transport behaviour of fully stripped helium and neon has been investigated. The experiment involved using argon-frost on the divertor cryopump to achieve active pumping of helium. Charge exchange spectroscopy measurements were used to monitor the evolution of ion density profiles of fully stripped helium following the injection of short (100ms) helium gas-puffs at the plasma edge. The characteristic profile response in the H-mode case is described by an instantaneous density increase and subsequent fast decay in the first 200ms in the outermost region of the confined plasma region ( $r/a > 0.7$ ). In the plasma core, there is a comparatively slow increase in the helium concentration, which reaches a steady state after 300-500ms. Steady-state helium profiles were very similar to the radial profile shape of electrons, both in H- and L-mode plasmas. The total helium content added by the gas puff was  $2-3 \times 10^{20}$  (<5% of the total plasma particle content). Typical  $\alpha$ -particle

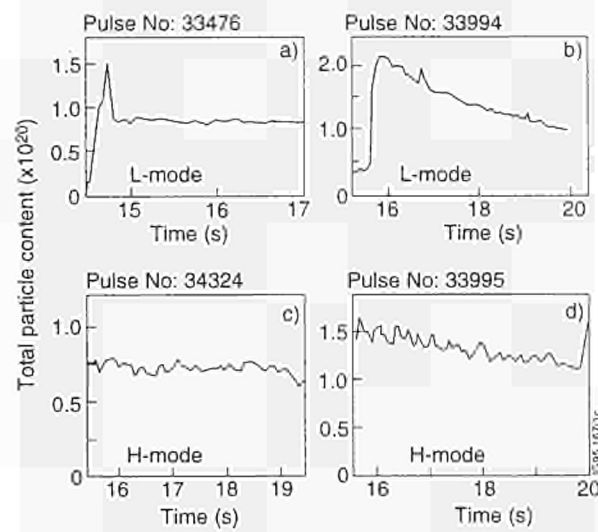


Fig.141: Time evolution of total helium content following a 100ms He gas puff: (a) L-mode, no argon frost; (b) L-mode, argon frost; (c) ELMy H-mode, no argon frost; (d) ELMy H-mode, argon frost. These curves allow the global helium confinement time,  $\tau_{\alpha}^*$ , to be deduced, as quoted in the text.

confinement times,  $\tau_{\alpha}^*$ , were 8-15s (H-mode) in the case of active argon-frost pumping, compared to 20-30s in the case of no argon-frost (Fig.141). Corresponding values for L-mode confinement were about half the values of the H-mode case. The observed alpha-particle confinement times exceeded energy confinement times,  $\tau_E$ , (~0.3-0.5s), by more than a factor of 20 (H-mode, argon-frost) and 10 (L-mode, argon-frost).

A slight time dependent variation of particle confinement time  $\tau_{\alpha}^*(t)$  following the initial pump phase indicated saturation effects in argon frost pumping. Sweeping of the X-point and the location of the strike zone with respect to the pump-duct led to significant changes in the observed particle decay time. The substantial decay times, characteristic for helium pumping, and comparable to the flat-top pulse length, make accurate alpha-particle confinement studies difficult. The role of wall pumping has been studied by comparing the alpha particle decay time in plasma conditions following intensive over-night helium glow discharges with an appreciable level of background helium densities ( $n > 10^{18} \text{m}^{-3}$ ) with those where helium puffs were introduced in plasmas with low helium recycling level. Comparable decay times in both cases suggest that wall pumping did not have a notable effect on helium exhaust.

Distinctively lower particle confinement times were observed for neon gas-puff experiments, carried out dur-

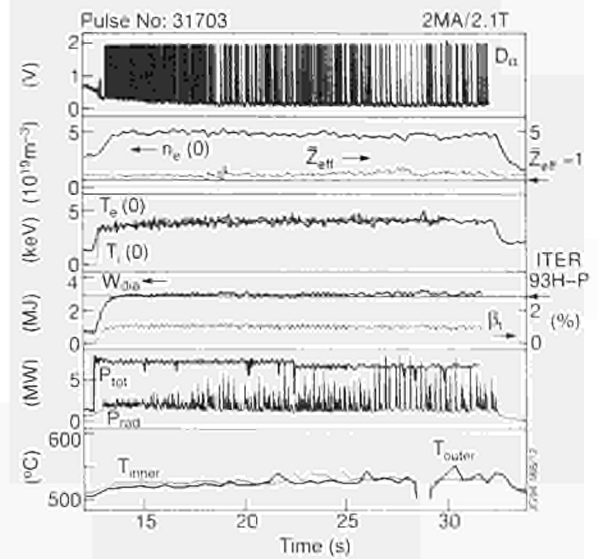


Fig.142: Time development of a long pulse steady-state ELMy H-mode at 2MA/2.1T.

ing radiative divertor cooling studies. As in the case of helium, the H-mode confinement time was about 2-3 times the L-mode case. Neon particle confinement times were about 5-10 times the energy confinement time.

Transients in the helium density profiles measured during the 0.5s interval following the gas-puff allow the deduction of diffusive and convective terms, which describe the perturbation and the subsequent relaxation of the density profiles. However, inconsistencies in the evaluation of the helium spectrum, in particular uncertainties in deduced ion temperatures, imply systematic errors in core helium density gradients. Therefore, experimentally derived values of diffusion coefficients  $D$  and convection velocities  $v$  describing helium transport can only be approximate. Characteristic core values ( $0.1 < r/a < 0.5$ ) for H-mode transport are  $D^a(0.3 \pm 0.2) \text{m}^2 \text{s}^{-1}$  and  $v^a(0.5 \pm 0.2) \text{ms}^{-1}$ .

The atomic physics involved in the analysis of NeX spectra is far less complex and transport data established in neon gas-puff experiments are generally more reliable than data derived from comparable helium experiments. Deduced values for diffusion coefficients  $D$  are for L- and H-mode phase below  $1 \text{m}^2 \text{s}^{-1}$ . The fact that observed neon density profiles (similar to the intrinsic impurity carbon) are consistently hollow is also reflected by outwards directed convection velocities over the major part of the profiles. In contrast to helium profiles, there is a poor correlation to the shape of electron density profiles.

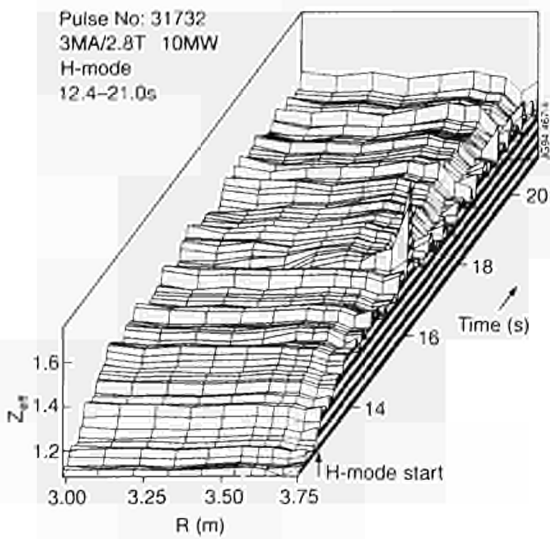


Fig.143:  $Z_{\text{eff}}$  profiles as a function of time for a 3MA/2.8T 9s ELMy H-mode with 10MW input power

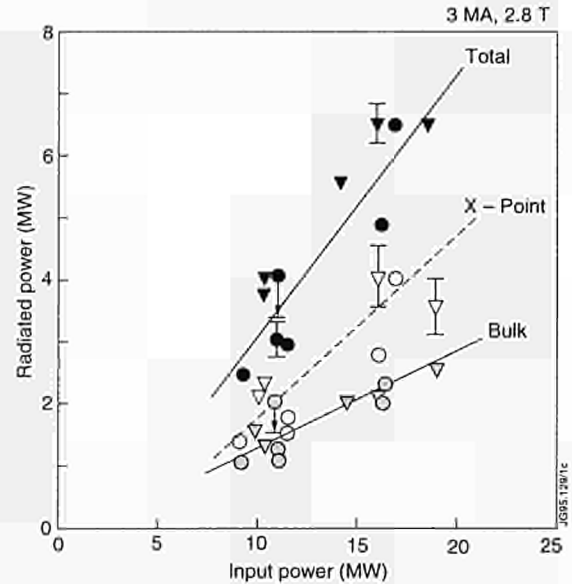


Fig.144: Radiated power and its distribution between the bulk plasma and X-point region, as a function of input power in a series of steady-state ELMy H-modes at 3MA/2.8T

### Steady-state H-modes

The excellent power handling capabilities of the divertor target, together with the in-vessel cryopump and the facility for sweeping the strike zone position, have been exploited to produce long pulse steady-state H-modes. The H-modes thus produced are characterised by frequent regular giant ELM behaviour, a regime which is now the most commonly observed in JET.

An example of the temporal evolution of a discharge of this type is shown in Fig.142. This shows the longest duration H-mode achieved, with a pulse length of 20s, limited only by machine engineering constraints. The H-mode phase in this 2MA/2.1T discharge lasts for  $\sim 50$  energy confinement times ( $50\tau_E$ ) and around 85% of the relevant resistive diffusion time ( $\tau_R$ ). The regime has been extended up to plasma currents of 3MA for at least 20 energy confinement times. The plasma density,  $Z_{\text{eff}}$ , stored energy, recycling conditions, plasma temperature,  $\beta$  and radiated power all remained constant for 20s. The radiated power (at 20-40% of input power) and  $Z_{\text{eff}}$  ( $\sim 1.6$ ) were typically low in the ELMy phase of these plasmas. An important result is that the divertor target temperature remained far below the design limit during the pulse.

The steady-state H-modes exhibited good confinement, and achieved the confinement level predicted by the ITER93H-P ELM-free scaling. Relative to ITER89-P L-mode scaling, an enhancement factor  $1.6 \leq H \leq 2.0$  is readily obtained at safety factor values,  $q_{95} \sim 3$ . Thus, the indicator  $H/q_{95}$  lies between 0.53 and 0.65, a regime which

has already been identified as being of interest for ignition scenarios in Next Step devices such as ITER-EDA.

The intrinsic impurity concentration in the steady-state H-modes remains low and constant through the evolution of the discharge. The ELMs are beneficial in keeping target impurities from entering the bulk plasma.  $Z_{\text{eff}}$  and carbon impurity profiles for a typical 3.0MA/2.8T steady-state H-mode lasting 9s are shown in Fig.143. Helium puffing experiments have also been performed in these discharges and the helium density profiles also become flat with no sign of accumulation.

The radiated power in these discharges is split approximately in the ratio 2:1 between the X-point region and the bulk plasma. Figure 144 shows the variation of radiated power with input power. It is possible to control the density during the steady-state H-modes using the pumped divertor cryopump, especially for discharges fuelled solely by NB injection and the accompanying recycling flux. This contrasts with previous operation in 1991 when wall pumping saturated after around 10s and no true steady-state could be achieved. A study has been made of the region in input power and density space over which the giant ELM steady-state regime can be obtained. The plasma density was varied in this study by extra fuelling with gas and by moving the outer strike zone of the plasma radially with respect to the entrance of the pumped divertor cryopump. The results are shown in Fig.145 where a density range of a factor 2 ( $0.5-1 \times 10^{20} \text{m}^{-3}$ ) can be obtained at powers of up to 18MW.

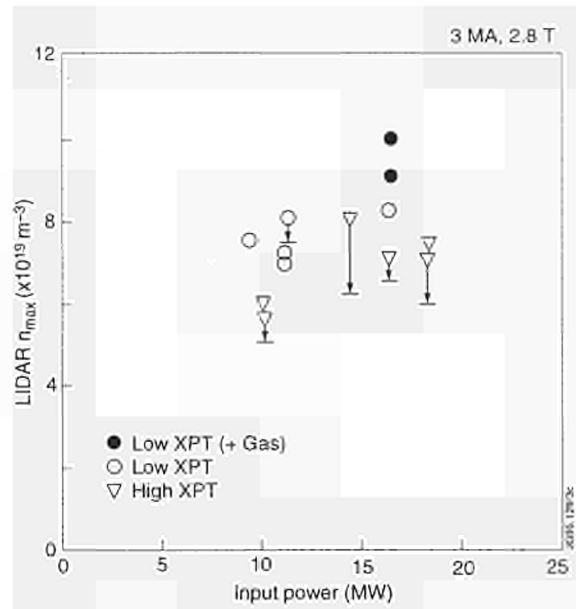


Fig.145: Existence diagram for the long pulse steady-state ELMy H-mode in the  $(n_e, P_{input})$  space for 3MA/2.8T plasmas.

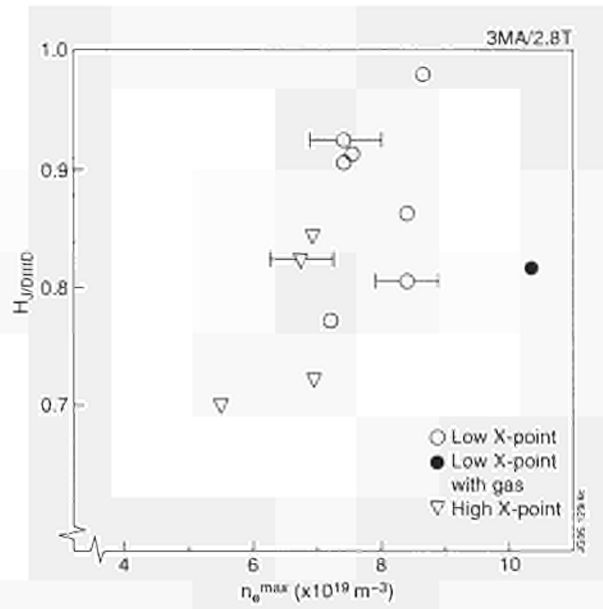


Fig.147: Confinement enhancement  $H_{JET/DIHD}$  (relative to the JET/DIHD scaling for ELM free H-modes), as a function of density for the 3MA/2.8T long pulse steady-state ELMy H-mode dataset.

At the higher density strong  $D_2$  puffing establishes a ‘grassy-ELM’ behaviour with  $\sim 50\%$  radiated fraction. This regime has a confinement enhancement (relative to ITER-89P L-mode)  $\sim 1.2-1.3$  and shares characteristics with the ‘radiative divertor’ regime. Figure 146 shows a discharge established with the gas puffing. It is clear that, as the power is stepped up (17s) and the conducted power to the target rises, the giant ELM regime returns.

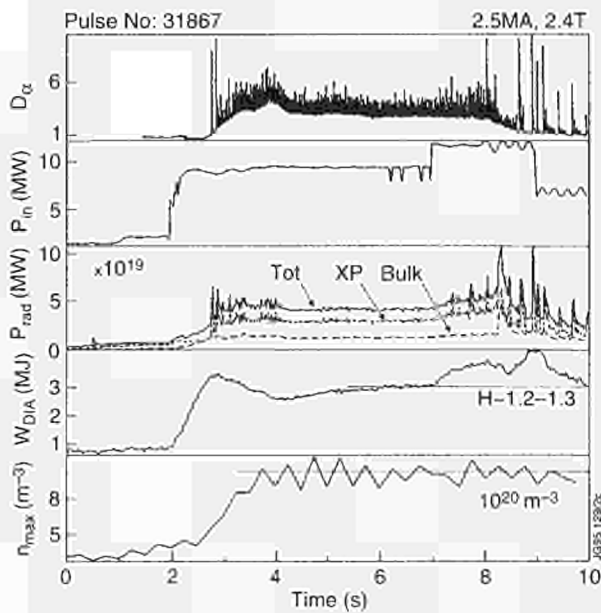


Fig.146: Typical discharge with small or ‘grassy’ ELMs, which occurs at high densities ( $> 10^{20} m^{-3}$ ) when strong gas puffing is applied to a steady-state ELMy H-mode.

The confinement across the range of the giant ELM H-modes does not show a monotonic dependence on density however. A dataset of 3MA/2.8T giant ELM H-modes with input powers up to 18MW is shown in Fig.147, where the confinement enhancement (H) is plotted relative to the JET/DIHD ELM-free H-mode scaling (which has no density dependence). The ELM behaviour in these discharges shows complex dependencies. In general, at fixed power, ELM-frequency tends to decrease with density but then increase at the high density end of the regime, close to the densities at which the grassy ELMs set in. It may be that this ELM behaviour accounts for the peaking in the dataset seen in Fig.147, but a more extensive analysis (based on further shots to be gathered in 1995) is needed to correlate this dependence. The dependence of ELM frequency on input power is more straightforward. At lower powers ( $\leq 10$  MW), the relatively infrequent ELMs are followed by short L-mode periods. At higher powers, the ELM frequency increases. This is a commonly observed feature in JET and other tokamaks.

Examination of two nominally identical shots in the Fig.147 database (‘A’ and ‘B’) shows that, for  $\sim 11$  MW of input NBI power, discharge ‘A’ achieves  $\sim 15\%$  more stored energy and about twice the neutron yield of discharge ‘B’. Examination of the profiles shows that the  $T_e$  profile is 30-40% higher in discharge ‘A’, than discharge ‘B’ ( $5 \pm 0.5$  keV compared to  $3.6 \pm 0.4$  keV), but also that  $T_e$

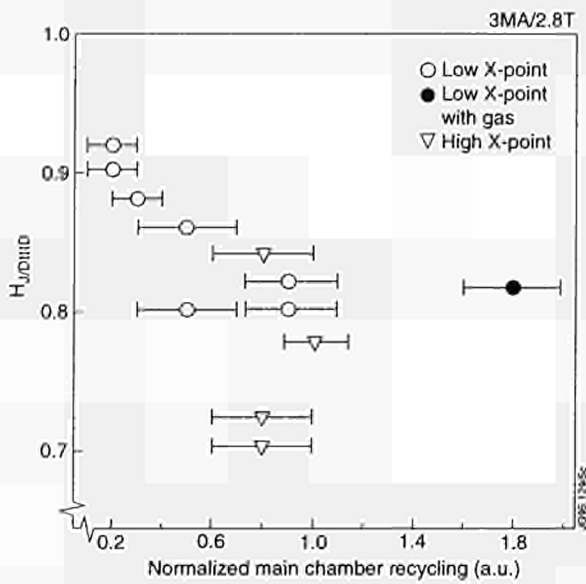


Fig.148: Confinement enhancement factor ( $H_{10DMD}$ ) versus normalised main chamber recycling, defined as ( $D_a$  photon flux in horizontal chord/Line integrated plasma density) for a series of 3MA/2.8T long pulse steady-state ELMy H-modes

and  $n_e$  are  $\sim 10\%$  and  $\sim 15\%$  higher respectively. One difference between the two discharges is that 'A' (Pulse No: 31731) has about half the recycling in the main chamber of that seen in 'B' (Pulse No: 32743). Across the dataset, the confinement enhancement seems to degrade slightly when the recycling (normalised to the plasma density) increases. This is shown for the 3MA/2.8T dataset in Fig.148. Even here, an exception can be seen where the recycling light is dominated by added gas (shot 'C' in Fig.148). A more thorough analysis on this effect is in progress.

Edge plasma and scrape-off-layer (SOL) measurements have been made in these plasmas and are still being analysed. Some clear indications have already emerged from this data showing the SOL fall-off lengths ( $\lambda$ ) to be significantly increased during ELMs. This applies especially to  $\lambda_{Te}$  which is increased approximately three-fold at the target during ELMs (up to  $\sim 6$ cm). Figure 149 shows how the SOL thickness for ion saturation current at the target ( $\lambda_{sat}$ ) is increased during ELMs in one of the discharges in the Fig. 147 dataset. Plasmas used for divertor physics studies are well situated for edge measurements with the new charge-exchange diagnostic, which is capable of measuring edge toroidal rotation, poloidal rotation, ion temperature and concentration for a chosen impurity. No poloidal rotation is seen in these ELMy H-modes (to within  $|v_{\perp}| < 5 \text{ km s}^{-1}$ ).

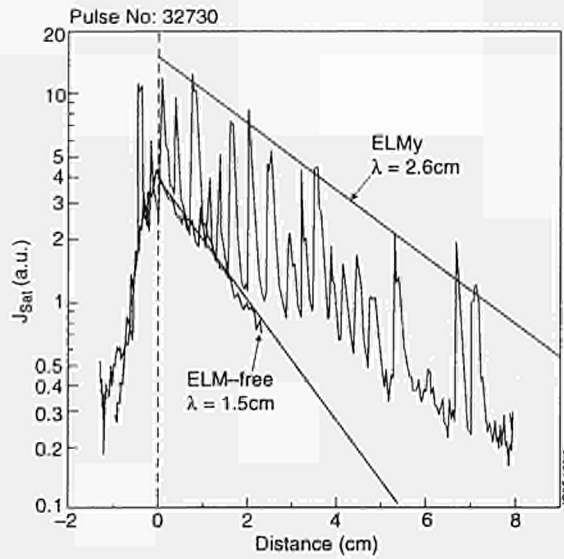


Fig.149: Comparison of the profile of ion saturation current ( $J_{sat}$ ) at the outer target for ELM-free and ELMy periods in a 3MA/2.8T long pulse steady-state ELMy H-mode

### Studies of Detached Divertor Plasmas with Intrinsic Radiation

While poloidal divertors have been employed successfully in many tokamaks to reduce impurity contamination of the plasma core, an operating scenario which scales to reactor plasmas has not yet been demonstrated. The exhaust of particles, momentum, and power from a burning plasma is such that, with reasonable estimates for SOL widths, the divertor target plates would not survive unless a significant fraction of the exhaust is redirected across magnetic field lines by volume loss processes. In addition, it has been shown [3] that radiation alone cannot be used to solve the power loading problem in a so-called high recycling divertor where there is no loss of momentum along the SOL field lines. A pressure drop of a factor of ten is consistent with a radiative fraction sufficient to satisfy constraints on ITER target loads ( $\sim 5 \text{ MW m}^{-2}$ ). Supersonic flow conditions at the target have also been considered, but are insufficient, by themselves, to provide the required effect.

When the core plasma density is increased by gas puffing, or some other fuelling method, the plasma density in the divertor typically increases, the dependence being as high as the third power in the simple two-point SOL model. This staggering rate of increase is self-limiting, however, because at the same time the temperature in the divertor and the SOL is rapidly decreasing and

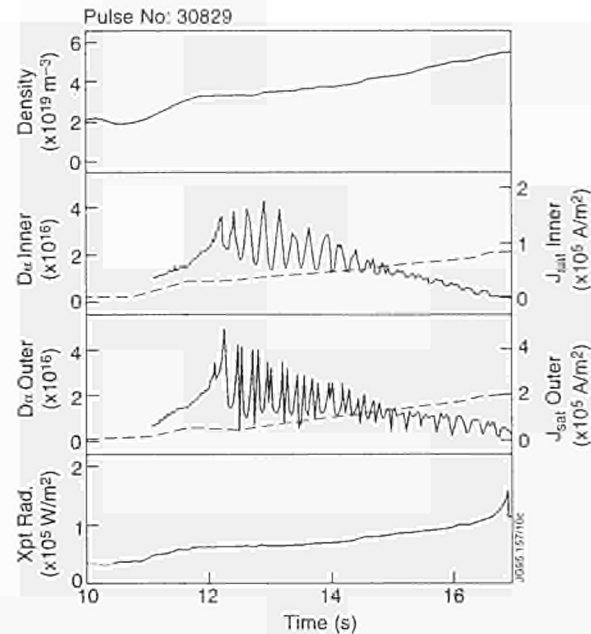


Fig.150: Time traces of an ohmic density ramp experiment: (a) line-averaged plasma density, (b)  $D_{\alpha}$  radiation from inner divertor leg (dashed curve) and ion saturation current flowing to a Langmuir probe in inner divertor target plate (solid curve), (c)  $D_{\alpha}$  radiation from outer divertor leg (dashed curve) and ion saturation current flowing to a Langmuir probe in outer divertor target plate (solid curve), and (d) radiated power integrated along a sight-line which passes through the X point. The currents oscillate because the plasma is being swept across the target at a frequency of 4Hz from 12s to the end of the shot

atomic physics loss terms, such as charge exchange and radiation, begin to dominate. At this stage, the density at the divertor plates decreases as the core density, is increased even further. This regime, where not only the density but also the flows of particles, momentum, and energy are decreasing functions of increasing core density is the so-called detached plasma regime and is the favoured candidate for future burning plasma tokamaks.

The onset of atomic volume losses is gradual as the SOL/divertor temperature drops and presents a problem of defining exactly when a plasma is detached. As an operational definition, the point is that at which the ion saturation current (and thus flow of particles to the divertor target plates) peaks and begins to decrease, or 'roll-over' with increasing core density. To distinguish between a detached divertor plasma, where volume losses are confined mainly to the SOL, and a more conventional detached core plasma, where the entire SOL is starved by losses inside the separatrix, the caveat is added that the  $D_{\alpha}$  radiation measured in the divertor must continue to increase. An example of detachment in a pulse where the core density was gradually increased is shown in Fig.150.

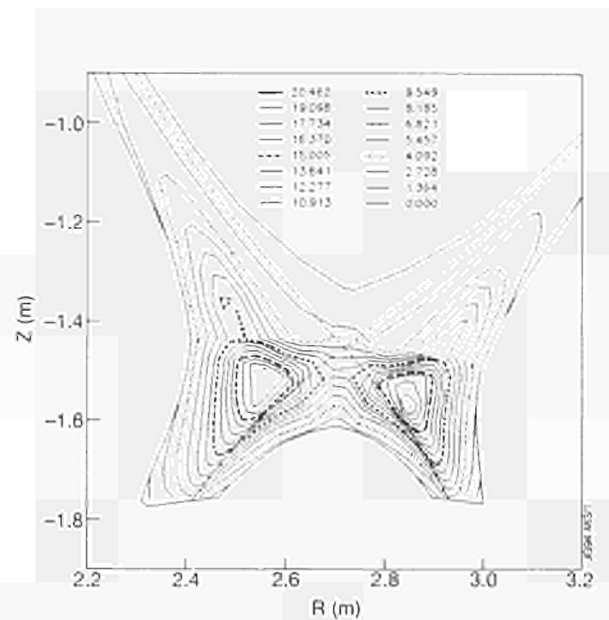


Fig.151: Profiles of radiated power, inverted from line-integrated bolometer measurements, for several time slices near the density limit. The peak radiation, which is initially near the X point but outside the main plasma, moves inside the separatrix and the pulse terminates with a MARFE and a disruption

As the atomic losses involved depend primarily on temperature, detachment cannot begin until the divertor plasma temperature falls to  $\sim 5\text{eV}$ . Thus, the density necessary to make the divertor detach is an increasing function of the power flow into the SOL. In fact, at the highest powers, detachment has not yet been attained, despite extremely high fuelling rates. The addition of recycling impurities can, in principle, reduce the density required for a given power.

One of the key questions in the understanding of detached plasmas is what species is the main contributor to the radiation and from which regions the radiation is predominantly coming. In particular, the fraction of radiation which is inside the separatrix is a key parameter. The new in-vessel bolometer system has provided, for the first time in JET, the capability of addressing this question. As the plasma detaches, the peak radiation is seen to move from near the strike points up the divertor towards the X-point. Finally, as the density reaches its limit, the radiation shifts quickly from the SOL near the X-point into the core plasma above the X-point.

### Numerical Modelling

It has been possible to reproduce the general features of divertor detachment using the 2-D fluid code EDGE2D

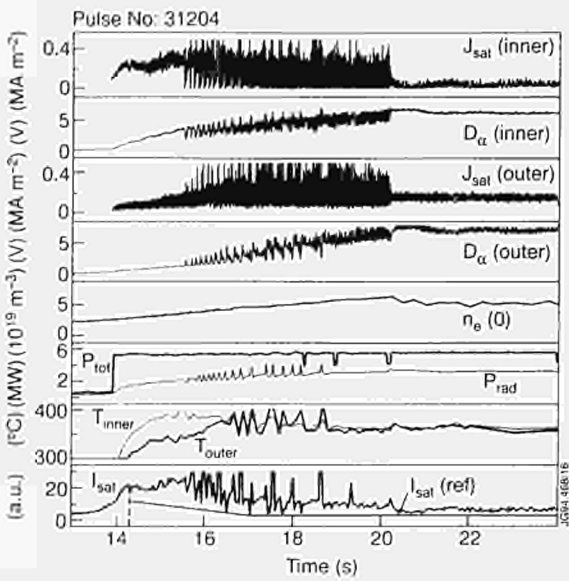


Fig.152: Time traces showing the evolution of an L-mode plasma into steady state detachment. In this pulse the gas fuelling rate was controlled using the ion saturation current shown in the lower box

[4], at least for Ohmic and L-mode discharges where the unknown physics of the H-mode transport barrier and of ELMs greatly complicates the analysis. As the core density is increased in the code, the flows of particles, momentum, and energy to the divertor plates are seen to decrease. At core densities comparable to those measured in experiment the divertor is seen to detach with the maximum density (see Fig. 151) and radiated power moving up the divertor legs toward the X-point. Such detachment is found to depend critically on radiation from impurities in order to lower the SOL temperature to the point where momentum losses become important. In the example shown in Fig.151 the total radiated power as calculated using the simulated carbon and deuterium densities is in good agreement with the measured value.

### Analytic Modelling

The main channel for momentum loss in a detached plasma is the transfer of momentum from ions to neutrals by elastic or charge exchange collisions (friction). In steady-state, the friction force exerted onto the neutrals must be balanced by either transverse losses of neutral momentum ( $i$ - $n$  induced transport or prompt losses, dynamic gas target) or by a neutral pressure gradient (Static Gas Target, SGT). The first two mechanisms dominate in a regime where is the neutral-ion mean free path  $\lambda_{e,i}$

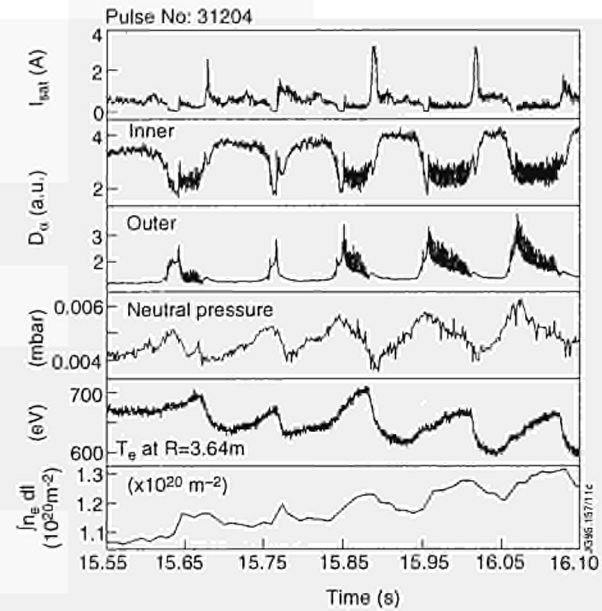


Fig.153: Experimental evidence for a divertor instability in a high density L-mode discharge: (a) the ion saturation current measured by a Langmuir probe in the inner divertor target plate, (b)  $D_\alpha$  radiation from the inner divertor leg, (c)  $D_\alpha$  radiation from the outer divertor leg, (d) the neutral pressure in the divertor, (e) the electron temperature near the edge of the core plasma, and (f) the core line-integrated electron density

exceeds the SOL width,  $D$  (weakly collisional regime). If  $\lambda_{n,i} \ll D$  (high collisionality regime) momentum losses are small and the plasma pressure gradient has to be balanced by a neutral pressure gradient.

The potential of SGTs to provide a drop of the plasma pressure along  $B$  has been investigated, both analytically and numerically, using the SOL-One I-D scrape-off layer transport code [5], which is coupled to a fluid neutral gas model. The main conclusion is that a significant pressure drop may only occur if the condition

$$\sin^2 \psi (L^*/\lambda_{n,i}) \gg 1$$

(where  $\psi$  is the field line pitch and  $L^*$  is the extension of the cushion along  $B$ ) is fulfilled, which is practically impossible to achieve in typical poloidal divertor configurations, where  $\sin \psi \ll 1$ . SGTs thus do not provide pressure drops in excess of the usual factor of two in typical tokamak configurations.

### Stability

In addition to the question of the conditions for establishing a detached divertor plasma, the stability of such plasmas must be assessed. Disruptions are a major concern in large, burning plasmas and detached plasmas mean necessarily operating near the density limit. It has

been possible to generate quasi-steady detached plasmas in JET using both pre-programmed control of the density and using a feedback system on the particle flow to the divertor plate (Fig.152).

During high density discharges with additional heating, instabilities are often observed when approaching detachment. As shown in Fig.153 for a 2MA, 2.8T discharge with 4MW of beam heating, the instabilities begin with a dramatic drop in the ion flow to the plates, rising neutral pressure in the divertor region and asymmetric  $D_\alpha$  emission from the inner and outer strike zones. After a period of ~50ms, in which the ion flow remains low (with additional fast fluctuations most clearly seen on the  $D_\alpha$  emission) and the central density rises, the ion flow to the divertor increases sharply with initially similar characteristics to an ELM. The period of decreased ion flow to the plates is also correlated with the radiation maxima moving from the strike zones to the X-point region and increasing edge electron temperature. It would appear that these instabilities begin with the formation of a transport barrier near the edge region of the main plasma that initially starves the SOL of power and particles. The subsequent escape of neutral particles previously confined by the divertor plasma is postulated to destroy the transport barrier by increasing the ionisation source inside the separatrix, leading to the large ion flux seen at the divertor plate. For example, the input power is well below the H-mode threshold for 2.8T, but similar behaviour can also be observed in discharges with higher additional heating power. In general, the instabilities are most evident when the strike points are located on the horizontal plates. This suggests that the neutral recycling pattern plays an important role in these instabilities and highlights the connection between divertor and core plasma behaviour.

### Radiative Divertor Experiments The ITER Relevant Regime

Estimates for the ITER H-mode power threshold are uncertain, but using the most commonly accepted scaling a core heating power of 320MW is required at the operating point of ITER. If this is confirmed then it would be difficult, if not impossible, for ITER to enter the H-mode at its intended operating density, since the alpha-particle heating power at the operating point is ~300MW. For this reason, it is planned that ITER enter the H-mode at low density, since the scaling says that the H-mode threshold power is proportional to density. It is then argued that

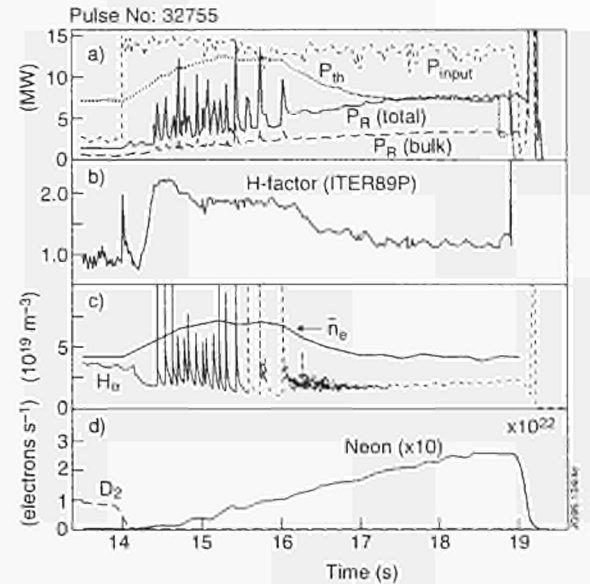


Fig.154: Traces for a discharge with 15MW of heating power with ramped feed of neon gas until 55s. The radiation level is typical of neon free discharges. Top panel shows:  $P_{input}$  - total input power,  $P_{th}$  - H-mode threshold power from the ITER database scaling,  $P_R(total)$  - radiated power for whole plasma,  $P_R(bulk)$  radiated power from inside the separatrix. Second panel shows: H-factor - ratio of energy confinement time to ITER89-P L-mode scaling. Third panel: Vertical  $H_\alpha$  - line averaged density. Bottom panel shows neon, Ne, and deuterium,  $D_2$ , injection rates in electrons per second.

hysteresis, the lower power threshold for the H-to-L "back-transition", will keep the plasma in H-mode at about half the power required to initiate an L-to-H transition at the same operating point. This still means that, in ITER, at least 160MW would be expected to flow into the plasma boundary and, without substantial dissipation of the power, the heat load and erosion rate at the divertor targets would be unacceptable.

In a typical ELMy H-mode without gas fuelling in JET, the intrinsic total radiated power is very low. Total radiated powers around 20% are typical as shown in Fig.154. Although it has neon injected, it is typical of neon free ELMy H-modes until about 5s. In this case, the energy confinement enhancement factor (H-factor) over the ITER89P L-mode scaling is 1.8. In the figure the total input power, total radiated and bulk radiated power are plotted with the H-mode threshold power calculated from the ITER database scaling. The intrinsic radiated power is a small fraction of the H-mode threshold power which generally agrees well with the ITER scaling. The spikes on the total radiated power are due to giant ELMs. In smaller machines such as ASDEX-U and DIII-D total radiated powers of ~50% are typical whilst the H-mode

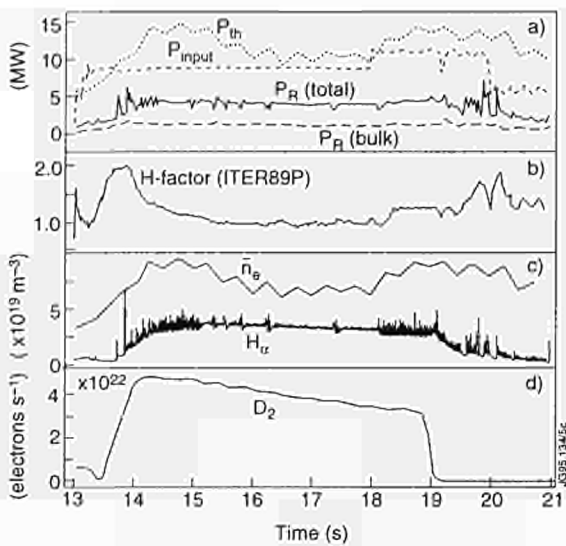


Fig.155: Traces for a discharge with 8.11 MW of heating power and a large deuterium gas feed which returns the discharge to L-mode ( $H=1$ ). The radiated fraction does not exceed 50%. Top panel shows:  $P_{input}$  - total input power,  $P_{th}$  - H-mode threshold power from the ITER scaling,  $P_R(total)$  - radiated power for whole plasma,  $P_R(bulk)$  radiated power from inside the separatrix. Second panel shows: H-factor - ratio of energy confinement time to ITER89-P L-mode scaling. Third panel: Vertical  $H_\alpha$  - line averaged density. Bottom panel shows neon, Ne, and deuterium,  $D_2$ , injection rates in electrons per second.

thresholds are at least 5 times lower than those in JET. This makes it difficult to do radiative divertor experiments close to the H-mode power threshold. In ITER, one would also expect a very low intrinsic radiated power, which means that a large increment in radiated power is required.

### Deuterium Injection into H-modes

Simulation of high density JET divertor plasmas with the EDGE2D/NIMBUS code have shown that it is difficult to lose significant power by radiation and charge exchange without using extremely high densities. Radiation losses do rise in JET with very strong deuterium puffing into H-modes and up to 50% radiated power fraction has been achieved, but the deuterium puffing forces the discharge back into L-mode. An example is shown in Fig.155, where the high main plasma density causes  $P_{LH}$  to exceed  $P_{input}$ . Higher radiated fractions can be achieved with higher gas input or lower input power but ITER requires a H factor of  $\sim 2$ . Qualitatively, therefore, the experiment agrees with code predictions that the power and particle flux to the targets are not readily reduced with deuterium alone, under conditions of density and power input compatible with H-mode operation.

### Neon injection

Since there is experimental and theoretical evidence that it is difficult to obtain sufficient radiated power with deuterium alone, the idea of seeding the plasma with non-intrinsic impurities has arisen. Code work with EDGE2D/NIMBUS has shown that it should be possible to radiate a significant fraction of the power and detach the divertor plasma at a moderate edge density, if impurities are introduced. Initial work has focused on neon impurity since this was reported to produce plasmas with radiated fractions as high as 90% in ASDEX-U with good energy confinement (CDH regime). The giant ELMs seen at low densities are regarded as unacceptable for ITER since they carry a significant fraction of the stored energy and would rapidly erode the divertor target. An attractive feature of the ASDEX-U results, therefore, was the production of small, high frequency ELMs. Similar results have been obtained in JET (Fig 154), but with the important difference that the H-factor declines to near unity (L-mode) at a radiative fraction of around 60%.

At this level of radiation, divertor probes show that the divertor plasma is still in an attached state. It is possible that the CDH regime has not been observed in JET neon experiments because they were carried out in an ITER relevant regime where the input power was close to the H-mode threshold power. Since 50% of the incremental radiation from the neon occurs inside the main plasma, this reduces the power flowing across the edge transport barrier to below that required to maintain H-mode energy confinement. In smaller machines, most of the work was carried out at  $>3$  times the H-mode threshold power, which means that high radiated fractions inside the edge transport barrier can be tolerated. JET also has a lower level of intrinsic radiation and so proportionately more non-intrinsic impurity radiation is required to obtain the high radiated power fractions needed for detachment.

### Nitrogen Injection

For ITER to maintain H-mode and a high fractional radiated power, it is necessary to confine most of the radiation to the divertor. In the high recycling regime, divertor electron temperatures were expected to lie in the range 2-20eV. Figure 156 shows the average power loss per neon neutral entering the plasma taken from the JET ADAS database, as well as the same curves for nitrogen. Unlike nitrogen, neon produces very little radiation in the temperature range of interest and for this reason nitrogen

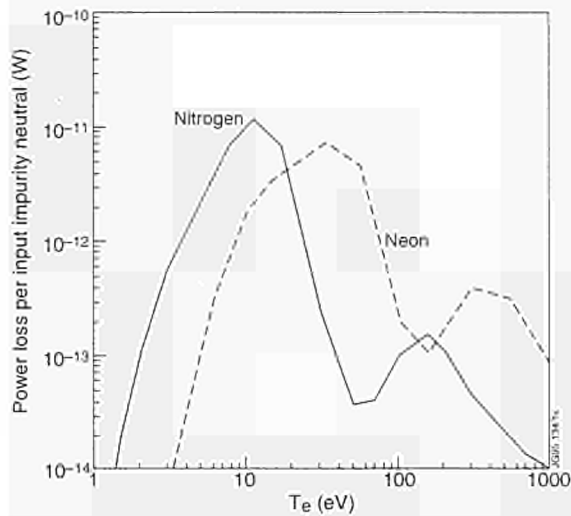


Fig.156: Average power loss per incident neon or nitrogen neutral for uniform plasmas at a range of electron temperatures. Data is taken from the ADAS database and corresponds to the case of coronal equilibrium. Non-coronal effects only influence the curves to the right of the maxima

seeded discharges are being carefully studied. Figure 157 shows an example of a discharge with nitrogen injected into the divertor plasma and deuterium injected into the main chamber. It has been predicted that with this fuelling configuration the flow of deuterium ions towards the divertor should improve the retention of impurities within the divertor. Various combinations of flow rate and fuelling position have been investigated. A secondary feedback loop was used to control the nitrogen flow rate and hence hold the total radiated power fraction at  $\sim 80\%$ . Higher radiated fractions have been achieved but were prone to instability.

As anticipated for nitrogen, the split between bulk and divertor radiation is much more favourable than for neon, with the incremental divertor radiation about 2 to 3 times higher than the incremental bulk radiated power. This means that better confinement is achieved for a given fractional radiated power. For the discharge shown in Fig.157, the H-factor was reduced to 1.4, which, although not acceptable for ITER, shows that enhanced confinement is possible at high radiating fraction whilst operating close to the threshold power. This plasma was also detached in the sense that the peak ion flux measured with Langmuir probes at the divertor targets was at least five times lower than in the equivalent reference discharge. Work is underway to determine the core dilution associated with impurity seeding and to obtain a more detailed understanding of the energy transport.

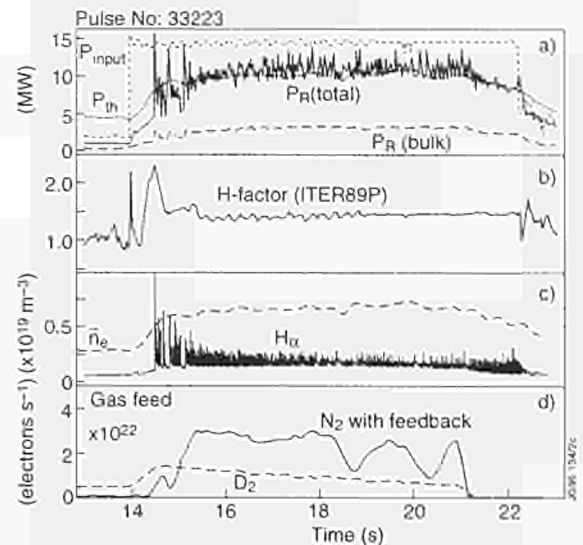


Fig.157: Traces for a discharge with 15MW of heating power with a pre-programmed deuterium feed and nitrogen feed in radiation feedback mode. The radiation level reaches 80% whilst the H-factor is around 1.5. Top panel shows:  $P_{input}$  - total input power,  $P_{th}$  - H-mode threshold power from the ITER scaling,  $P_R(total)$  - radiated power for whole plasma,  $P_R(bulk)$  radiated power from inside the separatrix. Second panel shows: H-factor - ratio of energy confinement time to ITER89-P L-mode scaling. Third panel: Vertical  $H_{\alpha}$  - line averaged density. Bottom panel shows nitrogen,  $N_2$ , and deuterium,  $D_2$ , injection rates in electrons per second

Up to 26MW of combined ICRF and neutral beam heating have been coupled into discharges with high fractional radiated powers. Figure 158 shows an example in which there was no sweeping of the divertor strike points and, despite a combined power of 24MW for 3s, the target temperature did not rise above the noise level of the IR camera. This suggests that the power loss was significantly more than the 75% indicated by the bolometer system. A further interesting feature of ICRF heating is that the energy confinement appears to improve when the RF is switched on. This leads us to speculate that some of the reduction in H-factor in the radiative divertor experiments may be due to changes in the heating profile.

### Comparison Between Horizontal and Vertical Plate Operation

The Mark I pumped divertor has made divertor operation possible with the strike zones positioned either on the horizontal or vertical section of the divertor target, allowing the study of the influence of the divertor geometry on the scrape-off layer (SOL) and main plasma behaviour. Modelling predictions for JET [6,7] have shown noticeable differences between the characteristics of the SOL and divertor plasma for the two configurations associated

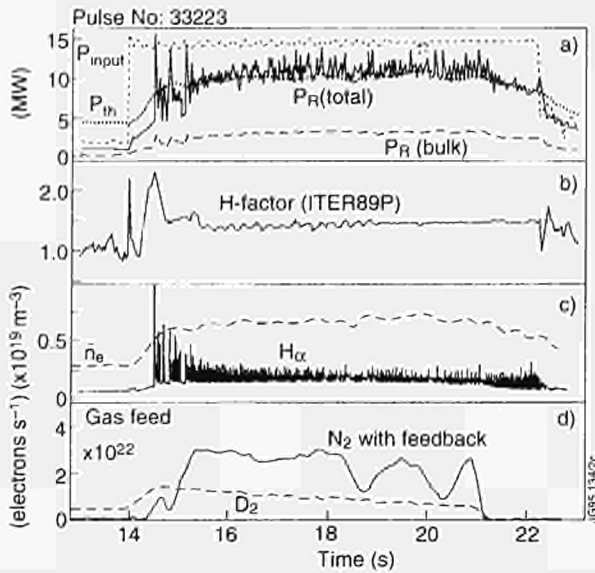


Fig.158: Traces for a discharge with 16MW of neutral beam power and 8MW of ICRF heating, giving a total input of 24MW including the ohmic contribution. More than 75% of the input power is dissipated with nitrogen and deuterium injection and no target heating is observed, even though the discharge was unswept. Top panel:  $P_{input}$  - total input power,  $P_{th}$  - H-mode threshold power from the ITER scaling,  $P_R(total)$  - radiated power for whole plasma,  $P_R(bulk)$  radiated power from inside the separatrix. Second panel: Vertical  $H_\alpha$  - line averaged density. Third panel: nitrogen,  $N_2$  and deuterium,  $D_2$  injection rates in electrons per second. Bottom panel: peak target temperature at inner and outer strike zones, which are below the noise level until the gas is switched off

with the different recycling patterns. In the horizontal plate configuration, the recycling neutrals are directed towards the outer part of the SOL, while the vertical plate configuration is expected to concentrate them towards the

separatrix. This effect is predicted to lead to lower neutral leakage from the divertor, more peaked density profiles in the divertor and the main SOL, and inverted electron temperature profiles at the divertor, with lower separatrix electron temperature for the vertical targets. This is expected to favour larger pressure drops from the midplane to the target in the vicinity of the separatrix (i.e. easier access to detachment), for the same main plasma density and input power.

To test these predictions, a series of experiments has been carried out comparing plasmas with various divertor configurations, confinement regimes (Ohmic, L-mode, H-mode), toroidal field directions (ion  $\nabla B$  drift towards/away from the divertor) and a wide range of densities. Two representative equilibria used in this investigation are shown in Fig.159. The parameters of the plasma in the main SOL and divertor target are determined by Langmuir probe measurements, spectroscopic measurements of the recycling species and neutral pressure gauges installed under the divertor plate. The spectroscopic measurements for the recycling species at the vertical plate are sparse and difficult to interpret because of geometric restrictions for the diagnostics. Most of the experiments were carried out with divertor sweeping which allows high spatial resolution divertor parameter profiles to be measured with Langmuir probes.

Although many of the predicted effects of the geometry are reproduced by the experiment, the overall behaviour of the discharges is similar for both divertor

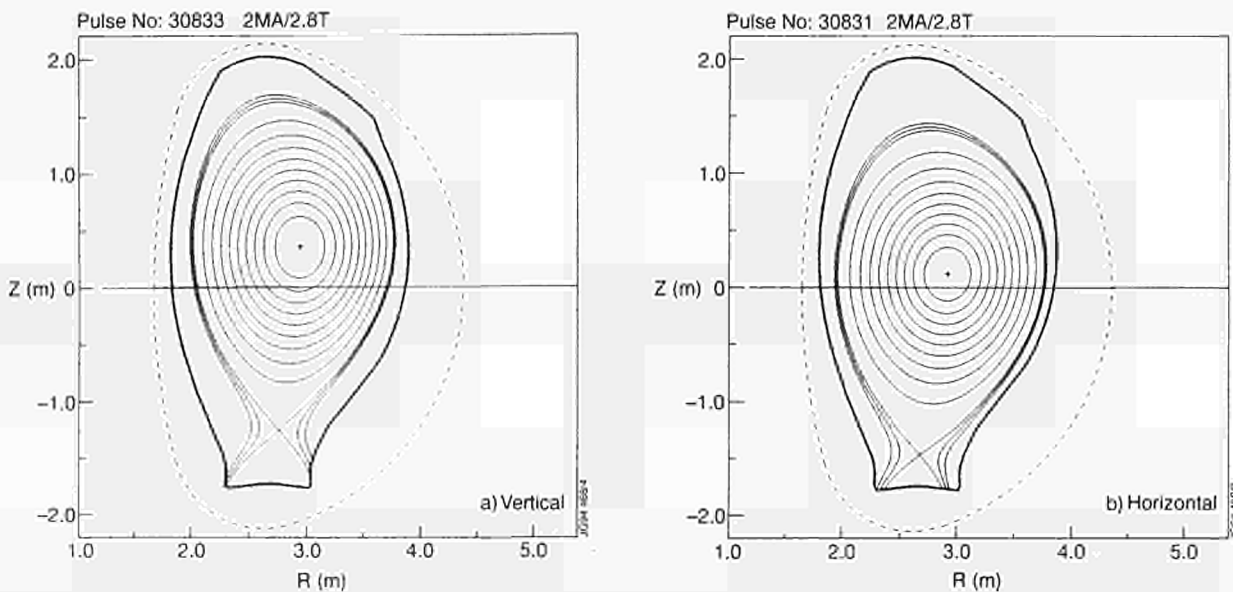


Fig.159: MHD equilibria for two representative discharges on the horizontal (a) and vertical (b) sections of the divertor target

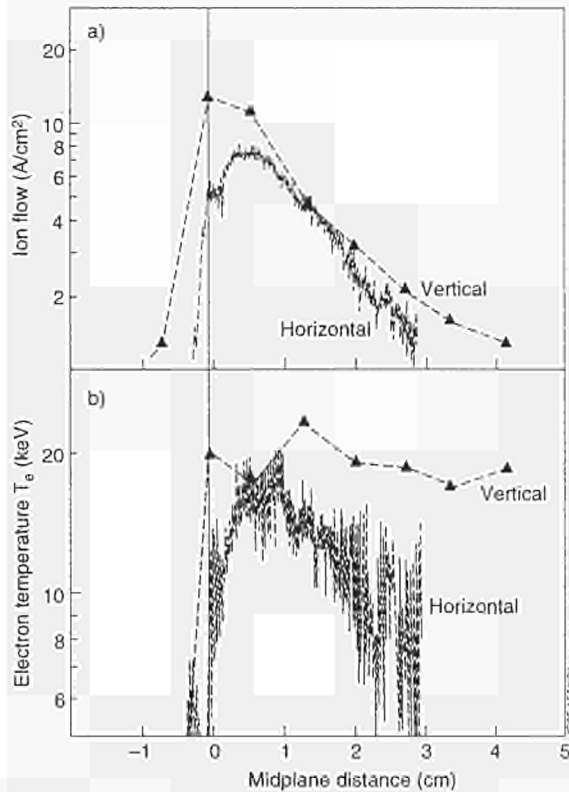


Fig.160: Divertor plasma flow and electron temperature profiles, mapped to the outer midplane, for two similar ohmic discharges ( $I=2MA$ ) on the horizontal and vertical section of the divertor

geometries, with the start of detachment occurring at similar main plasma densities. The discussion firstly considers the observed effects in the SOL and main plasma and how they compare with modelling predictions. Discrepancies and their relation to differences between model and experiment are then discussed.

### Plasma Flow and Temperature Profiles at the Divertor Plate

The trends predicted by the model with respect to the shape of the ion flow and temperature profiles at the divertor are reproduced in the experiment. When the strike zone is on the vertical plate, the plasma flow profiles tend to be more peaked and the electron temperature profiles are flatter than those for a similar discharge on the horizontal plate. An example of this is shown in Fig.160 for two ohmic density discharges in the horizontal and vertical configurations.

In the experiment, the plasma profiles at the divertor plate are very sensitive to the exact location of the strike zone on the vertical plate, which is not the case for discharges on the horizontal plate. Hence, while on the

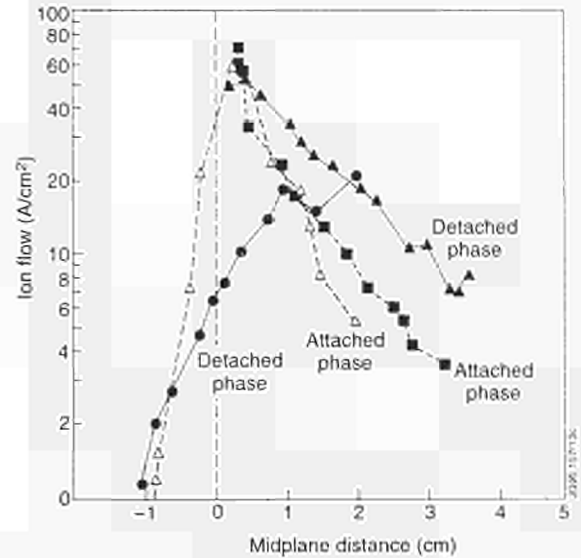


Fig.161: Divertor plasma flow profiles, mapped to the outer midplane, for two probes on the vertical plate during the attached and the detached phase of an additionally heated ( $P_{NBI}=3.5MW$ ) discharge

horizontal plate sweeping of the strike zones just displaces the profiles across the target (i.e. similar profiles are measured with probes located in various places), on the vertical plate the profile shape may change noticeably as the strike zone is moved across the target. This effect, which is not found in the modelling, not only affects the shape of the profiles but also the approach to detachment, which is more easily achievable when the strike zone is at the lower part of the vertical plate. This is shown in Fig.161 for an additionally heated discharge.

### Plasma Density Profiles in the SOL

Predictive modelling had shown that a vertical plate divertor should lead to a narrower density profile in the SOL, as it concentrates the recycling particles near the separatrix, depleting the outer part of the SOL. This prediction has been confirmed in the experiments, although the change in density e-folding length from horizontal to vertical divertor depends strongly on the main plasma density and input power, the largest difference being found in experiments at 4MW of power.

### Main Plasma Parameters

Despite the changes in the divertor and SOL, the bulk plasma has very similar parameters for equivalent discharges in both configurations. Radiation patterns are similar in both configurations apart from the differences associated with the location of the divertor strike zones.

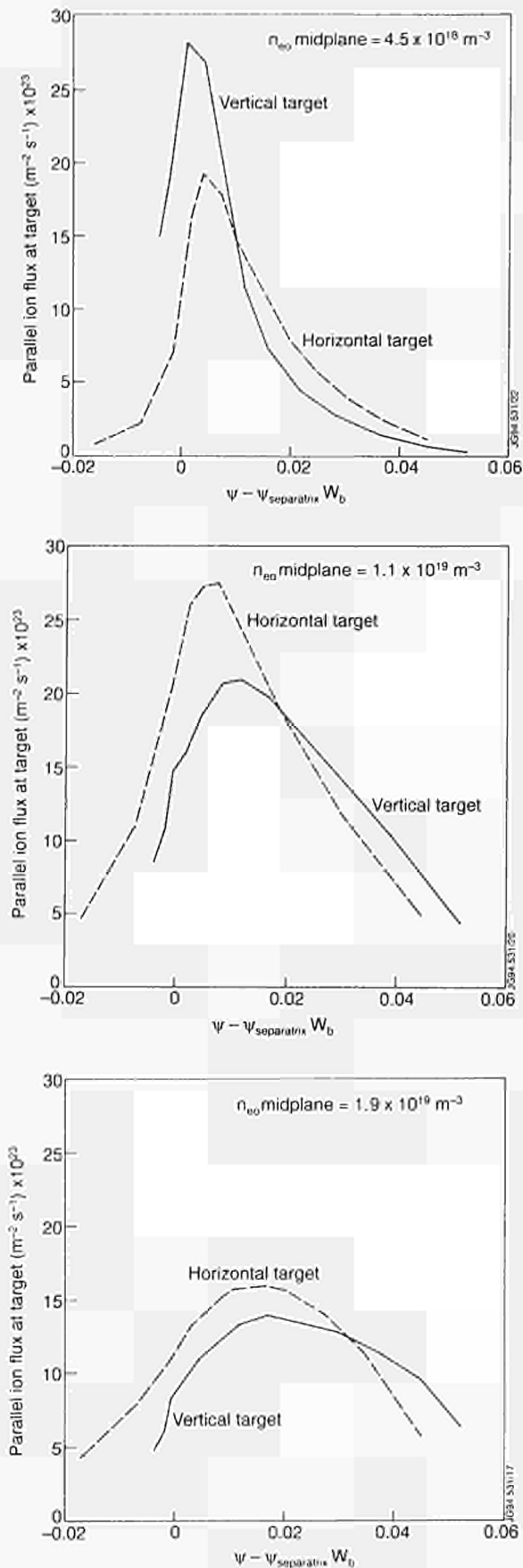


Fig.162: Modelled divertor plasma flow and temperature profiles for typical ohmic discharges on the horizontal and vertical sections of the divertor at three midplane plasma densities

For discharges with additional heating, the level of radiation is about 20% higher for discharges on the vertical plate, which is consistent with the observed somewhat higher level of impurities (oxygen in particular) in the main plasma. There are two possible explanations for this observation based on the effect of the divertor geometry on recycling: increasing recycling near the separatrix at the divertor, associated with vertical plates, may lead to plasma flow reversal near the separatrix, which degrades the retention of impurities in the divertor; in addition, the observed narrower main SOL density profiles favour the penetration of wall produced impurities to the bulk plasma.

No clear correlation has been found between the level of recycling, as determined by the  $H_{\alpha}$  intensity in the main chamber, and the strike zones being on the horizontal or the vertical section of the plate. While for ohmic discharges the level of recycling in the main chamber, which should be related to the neutral leakage from the divertor, is 1.6-2.0 times higher for vertical plate discharges, for additionally heated discharges cases with both higher and lower recycling have been observed. Hence, detailed modelling of the discharges, which takes into account the structure of the divertor target, is needed to assess the neutral leakage from both divertor geometries.

### Modelling

Predictive modelling for ohmic and L-mode additionally heated discharges has been carried out to investigate the effect of the divertor geometry. The calculated divertor target ion flux and temperature profiles for an ohmic density scan are shown in Fig.162 [7]. The ion flux and temperature profiles have values consistent with those shown in Fig.160, which correspond to typical ohmic conditions, although no attempt to model these discharges in detail was intended. The modelled density e-folding length in the main SOL is approximately 25% smaller for the vertical plate configuration.

One of the main discrepancies between modelling and experiment is that, in the modelling, detachment is obtained at lower separatrix densities, for a given  $P_{SOL}$ , than in the experiment. This is also shown in Fig.162, where the ion flow starts to drop at lower separatrix density for the vertical plate configuration, while in the experiment this effect is not so clear. This discrepancy is associated with the fact that most of the experiments were done with divertor sweeping or with the strike points located in the upper part of the vertical plate. As has already been noted,

experimental results seem to be very sensitive to the position of the strike zones on the vertical plate, so that only when the strike zones are located at the lower part of the vertical plate is the predicted vertical plate behaviour is observed. This sensitivity to the exact strike point location on the vertical plate does not appear clearly in the modelling and it is probably associated with the real 3-D structure of the divertor plate, which has toroidal gaps which influence the escape of neutrals from the divertor and which are not included in the model. Further experiments in which the strike zones will be positioned accurately on the upper and lower part of the vertical plate will be performed in 1995 to study in detail the effect of the divertor geometry, in particular, in the approach to detachment and the window of stable detached plasma operation.

### Influence of Ion $\nabla B$ Drift Direction on Divertor Asymmetries

Over the past few years, a considerable amount of information on the power sharing between the strike zones has been accumulated [9,10,11]. Excessive power load to the outer side was observed in the "normal" toroidal field direction (ion  $\nabla B$  drift directed towards the target), which led to overheating of the target and the occurrence of a high impurity influx which terminated the high performance phase of the discharge [11]. The "reversal" of the toroidal field (so that the ion  $\nabla B$  drift is directed away from the target) alleviated this problem by loading the two strike zones more symmetrically. Such a trend in the power distribution onto the divertor target, however, can only be noted as a statistically averaged observation, with the power asymmetries being strongly affected by the plasma core density, confinement regime, type and repetition of ELMs, etc. Extrapolation of the experimental data to reactor-relevant plasmas like ITER, therefore, requires knowledge of the underlying physical mechanisms responsible for the influence of the  $\nabla B$  drift direction.

To clarify the effect of the field reversal, a dedicated series of discharges with opposite  $\nabla B$  drift directions and variable plasma current and toroidal field has been performed. The discharges were  $\sim 4$  MW neutral beam heated L-modes with moderate to high density. Both the toroidal field and plasma current directions were reversed. Pairs of shots with similar absolute values, but opposite directions of  $B_T$  and  $I_p$  have been identified for comparison.

Profiles of the ion saturation current, density and temperature derived from Langmuir probe measurements for both a normal and reversed field pulse were compared. On reversing the field direction, it was observed that the profiles on the inner strike zone become narrower. The temperature profiles in the outer strike zone showed little difference in going from the normal to reversed field configuration. The temperature profile for the normal field case on the inner strike zone might be in error due to a problem in determining electron temperatures when densities  $\sim 10^{20} \text{m}^{-3}$  were encountered. The density was observed to decrease on the inner side and increase on the outer strike zone when going to the reversed field configuration.

There is currently a disagreement on the magnitude of the deposited power, calculated from the probe data, to the inner strike zone in the normal field configuration when compared to that deduced from the IR data. The Langmuir probe data give consistently higher powers than the IR camera and this is attributed to the overestimation of the electron temperature at high divertor densities. Generally the electron temperature is overestimated by a factor of two. Work is currently underway to model the Langmuir probe interpretation for high density plasmas so that the correct temperature may be calculated.

Verification of the power balance calculations can be made by comparing  $(P_{\text{input}} - P_{\text{rad}})$  with  $P_{\text{target}}$  calculated for the steady state conditions. This showed that good power balance was achieved. In three out of four pairs of the discharges with similar magnetic configurations but opposite toroidal fields, power was more uniformly shared between the two strike zones in the reversed toroidal field case. In pairs with  $q_{95} = 5.1$  and 4.2, however, more symmetric power sharing was found in normal field discharges. Radiation from around the inner strike zone, as well as the  $H_\alpha$  signals, were highest in normal field discharges with  $q_{95} = 5.1$  and 4.2, suggesting high density and low temperature plasma at the inner side. Highest ion saturation currents to the inner strike zone in these discharges have been confirmed by the Langmuir probe measurements. Estimates show that a significant fraction of power deposited on the inner side in these discharges could be attributed to the surface recombination of the ion flux to the target.

To explain the observed effect of the B reversal on the divertor asymmetries, various particle drift motions, which change direction with the direction of the  $\nabla B$  drift, have

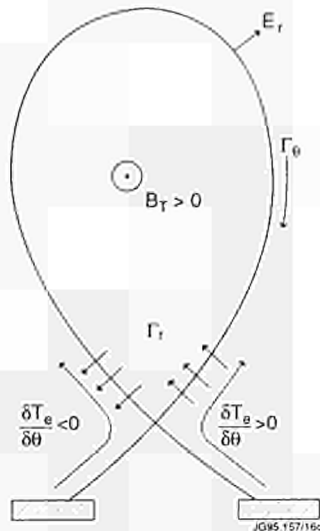


Fig.163: Direction of radial and poloidal  $E \times B$  drifts

been considered. Since the helicity of the magnetic configuration has not been changed in these experiments, the external input of the momentum associated with NBI (co-injection for the normal field and counter-injection for the reversed field) could not affect the divertor in-out asymmetries. Thus, the observed changes may be due to intrinsic plasma drifts. Density and temperature shifts associated with the B reversal appear to be broadly consistent with a recent model of radial  $E \times B$  drift based on shear viscous drag of the return flow along the SOL [13]. The radial drift, which should dominate in high recycling cases, is expected to cause opposite asymmetries to the ones caused by the poloidal drift (Fig. 163). The radial  $E \times B$  drift results from the temperature drop between the SOL and the target [14]. It would be useful to include poloidal and radial  $E \times B$  drifts in the edge modelling.

Significant difference between the two field directions has been observed approaching density limits. For Ohmic discharges, the threshold density for “roll-over” of ion saturation current at the inner side, which indicates the beginning of the detachment, was lower for the reversed field discharges. The “roll-over” at the outer strike zone, followed by the plasma detachment from the target, also started at lower densities in the reversed field plasmas. The density limit disruption follows almost immediately after detachment in the reversed field plasmas. In normal field discharges the operational density range was much wider, with substantially higher densities achieved (all the reversed field discharges, had  $B_T=2.7T$ ,  $I_p=2.7MA$ , while the normal field discharges had  $B_T=2.7T$ ,  $I_p=2.0MA$

and  $B_T=3.3T$ ,  $I_p=2.9MA$  in Pulse No: 31612). The distribution of plasma density and temperature between the strike zones was found to be more symmetric in the reversed field discharges, and the reason for the much narrower density range before the disruption in the reversed field case is unclear. It was found that earlier disruptions in reversed B plasmas were unlikely to be associated with “power starvation” of the scrape-off layer compared to the normal field discharges, since the behaviour of the calculated power to the target,  $(P_{input}-P_{rad})$ , was found to be similar for both field directions.

### SOL-width Scaling Studies

Knowledge of the scrape-off layer (SOL) width in tokamaks is important in Next-Step considerations for a variety of reasons: The power SOL width ( $\lambda_{q_{||}}$ ) directly determines the specific heat load on the divertor plates for attached plasmas, and thus the severity of the design problem. The density SOL width ( $\lambda_n$ ) affects the shielding of the main plasma from wall produced impurities as well as dictating whether major recycling contributions can originate from plasma facing components within the main chamber in addition to the target plates. Scalings of  $\lambda$  with toroidal field and plasma current are of interest inasmuch as the projected  $B_T$  and  $I_p$  values for ITER lie considerably above the level of present day experiments.

The reciprocating Langmuir probe (RCP) has produced a large SOL data set for varied conditions (Pulse Nos: 31462-31503, OH, L-mode, gas puff fuelling,  $I_p=2MA$ ,  $B_T=1.5, 2.2, 2.4, 3.3T$ ,  $P_{NI}=3-8MW$ ,  $\langle n_e \rangle = 2.2-5.6 \times 10^{19} m^{-3}$ ) for the reversed field configuration ( $\nabla B$  drift away from X-point, allowing L-mode operation at 8MW) with the strike zones near the corner of the divertor on the horizontal plates, or on the vertical plates. The measurements reported were carried out within dedicated scans and were performed up to or beyond the separatrix, with the resulting profiles capable of being well characterized by a single exponential fall-off length  $\lambda$ . The derived  $\lambda$  scalings for electron pressure,  $p_e$ , ion saturation current,  $J_s$ , electron temperature,  $T_e$ , electron density,  $n_e$  and convective power to the probe parallel to the field lines,  $q_{||}$ , are given in Tables XVIII and XIX.

Tables XVIII and XIX cover the more extensive horizontal target plate density and power scan at  $B_T=2.2, 2.4T$  and are divided into the power ranges  $P_{NI}=0-4MW$  (Table XVIII) and  $P_{NI}=4-8MW$  (Table XIX), as it was not possible to adequately parametrically characterize the

Table XVIII

SOL exponential falloff lengths mapped to the outer midplane for the case of: horizontal target plates,  $B_T=2.2, 2.4T$ ,  $\langle n_e \rangle = 2.2-5.6 \times 10^{19} m^{-3}$ ,  $P_{NI} = 0-4MW$ ,  $P_{tot} = 1.3-5.4MW$ .  $\langle n_e \rangle$  is the central chord line density and  $P_{tot}$  the total power input. Range gives the variation over the data set. R is the regression coefficient for the fit to the data given, for example, by:  $\lambda_{ne} = 1.15 n_e^{0.53} P_{tot}^{0.23}$ .

$\lambda[cm]$ for:	coefficient	$\langle n_e \rangle [10^{19} m^{-3}]$	$P_{tot} [MW]$	R	Range[cm]
$p_e$	0.36	$0.99 \pm 0.04$	0	0.994	0.8 - 2.0
$J_s$	0.76	$0.64 \pm 0.09$	$0.13 \pm 0.04$	0.985	1.2 - 2.9
$T_e$	1.03	$0.49 \pm 0.17$	$0.25 \pm 0.07$	0.962	1.6 - 4.0
$n_e$	1.15	$0.53 \pm 0.06$	$0.23 \pm 0.03$	0.998	1.9 - 4.0
$q_{  }$	0.30	$0.98 \pm 0.05$	0	0.989	0.7 - 1.6

profiles using the global parameters  $\langle n_e \rangle$  and  $P_{tot}$  for the combined range  $P_{NI} = 0-8MW$ . For each steady-state power level the density was scanned via a slow ramp at the rate  $\sim 0.5-1 \times 10^{19} m^{-3} s^{-1}$ . The density range was largely within the “rollover-detachment regime”, i.e. the peak  $J_s$  at the target plates depended only weakly on  $\langle n_e \rangle$ , with the highest density point effecting partial detachment at the inner divertor leg. The level of radiation in the main plasma, as determined by the bolometer array, was generally low, yielding  $P_{SOL}/P_{tot} \sim 0.83-0.92$ .

The parametric descriptions of Table XVIII fit the data well, with the greatest degree of uncertainty to be found in  $\lambda_{Te}$ .  $\lambda_{ne}$  and  $\lambda_{Te}$  are about the same, both in magnitude ( $\sim 1.6-5.6$  cm) and scaling:  $\lambda \sim \langle n_e \rangle^{0.4-0.5} P_{tot}^{0.23-0.86}$ , the exponential ranges arising from the different levels of  $P_{NI}$ .  $\lambda_{q||}$  varies between 0.7 and 2cm and does not manifest a statistically significant relationship to  $P_{tot}$ .

The  $P_{NI} = 4-8MW$  dataset of Table XIX is characterized by a much stronger power dependence. To some extent the exact scaling for  $P_{NI} \leq 4MW$  is questionable, since there is little overlap between the density ranges for OH and NI-heated discharges (see Fig.164), e.g. there exists some collinearity between  $\langle n_e \rangle$  and  $P_{tot}$ . In fact, generally

the 0-4MW dataset can be described almost as well by a linear  $\langle n_e \rangle$  relationship without any  $P_{tot}$  contribution (Fig.164). Nevertheless, the figure exhibits an undeniably clear power dependence for  $P_{NI} = 4-8MW$ .

With respect to the influence of toroidal field, data exists for  $\lambda(1.5, 3.3T)$  over a small density range ( $\langle n_e \rangle \sim 3-4 \times 10^{19} m^{-3}$ ). Furthermore, since the experimental  $P_{tot}$ -trends for  $\lambda(1.5T)$  and  $\lambda(3.3T)$  do not emerge as consistent, and since  $B_T$  is collinear with  $P_{tot}$  for OH discharges ( $P_{OH} \sim B_T^{-0.5}$ ), there exists no conclusive  $P_{tot}$ -scaling over the  $B_T$  range investigated. Thus, the formal results that  $\lambda_{ne}$  does not depend on  $B_T$  and  $\lambda_{ne} \sim B_T^{0.6}$  are of restricted application and are not presented in the table form.

SOL e-folding lengths associated with vertical target plate operation do not demonstrate a uniform  $\langle n_e \rangle$ ,  $P_{tot}$ -behavior which may be quantified in terms of regressions. For OH,  $\lambda_{ne}(vert)$  versus  $\langle n_e \rangle$  follows a characteristic similar to  $\lambda_{ne}(hor)$ , but is displaced to higher densities. At  $P_{NI} = 4MW$   $\lambda_{ne}(vert)$  does not change with  $\langle n_e \rangle$ , whereas  $\lambda_{ne}(hor)$  continually increases with density such that  $\lambda_{ne}(hor) > \lambda_{ne}(vert)$ . The  $\lambda_{ne}(hor)$  “detached” point, indicating partial detachment at the inner strike point, lies more than a factor of two above the vertical values.

Table XIX

SOL exponential falloff lengths for the case of: horizontal target plates,  $B_T=2.2, 2.4T$ ,  $\langle n_e \rangle = 3.6-5.6 \times 10^{19} m^{-3}$ ,  $P_{NI} = 4-8MW$ ,  $P_{tot} = 5.1-8.5MW$ .

$\lambda[cm]$ for:	coefficient	$\langle n_e \rangle [10^{19} m^{-3}]$	$P_{tot} [MW]$	R	Range[cm]
$p_e$	0.10	$0.76 \pm 0.10$	$0.99 \pm 0.05$	0.995	1.25 - 6
$J_s$	0.19	$0.59 \pm 0.15$	$0.97 \pm 0.07$	0.984	1.9 - 3.6
$T_e$	0.60	$0.41 \pm 0.22$	$0.65 \pm 0.14$	0.902	3.0 - 4.5
$n_e$	0.46	$0.44 \pm 0.16$	$0.86 \pm 0.08$	0.971	3.2 - 5.6
$q_{  }$	0.095	$0.75 \pm 0.16$	$0.90 \pm 0.08$	0.986	1.0 - 2.0

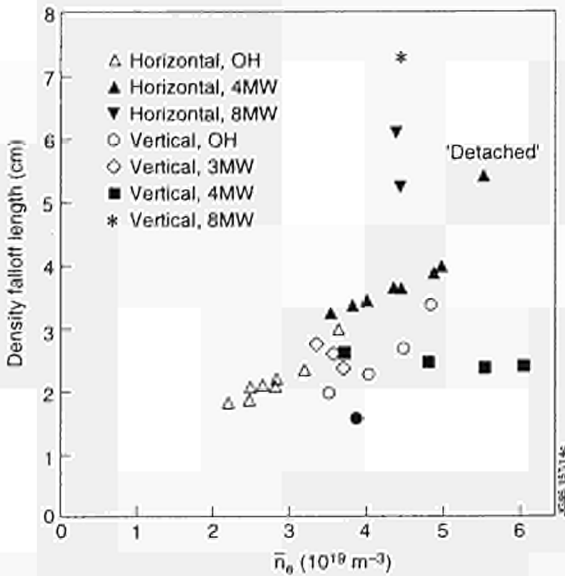


Fig.164: Measured main SOL density  $e$ -folding length for discharges on the horizontal and vertical plate versus main plasma density for ohmic and additionally heated discharges.

However, at  $P_{NI}=8\text{MW}$  both cases are typified by very large SOL widths whose differences cannot be regarded as being important.

At the target plate, well resolved profiles for the low flux expansion cases are most conveniently measured by periodically sweeping the strike point across one of the fixed Langmuir triple probes. For the high divertor densities associated with the rollover regime,  $T_e$  from the triple probe is subject to error, making it difficult to establish detailed profiles.  $J_{\text{sol}}$  does not suffer this limitation, and good exponential fits to the profiles outside the private flux region can be defined as long as detachment is not imminent. In Fig.165, a comparison is made between  $\lambda_{J_s}$  determined at the outer target plate strike point and in the SOL versus  $\langle n_e \rangle$  with  $P_{NI}$  as a parameter. The trends deviate substantially from those found in the SOL at 2.2-2.4T, i.e.  $\lambda_{J_s}(\text{tar})$  decreases both with  $\langle n_e \rangle$  and  $P_{NI}$  for  $P_{NI} \leq 4\text{MW}$ . However, at  $P_{NI}=8\text{MW}$  both target and SOL fall-off lengths evince the same proportional increase. On a relative basis, at the lower densities  $\lambda_{J_s}(\text{SOL}) \sim \lambda_{J_s}(\text{tar})$ , but thereafter they diverge, with the ratio  $\lambda_{J_s}(\text{SOL})/\lambda_{J_s}(\text{tar})$  changing as  $\sim \langle n_e \rangle^{1.5}$ , including the 8MW points, to reach a value of  $\sim 3.5$  at the highest  $\langle n_e \rangle$ . Quite clearly, as  $\langle n_e \rangle$  progresses into the rollover regime along the way to detachment, the target plate profiles no longer mirror the SOL profiles.

The above statements apply to OH and L-mode plasmas. No systematic RCP investigations of the H-mode have

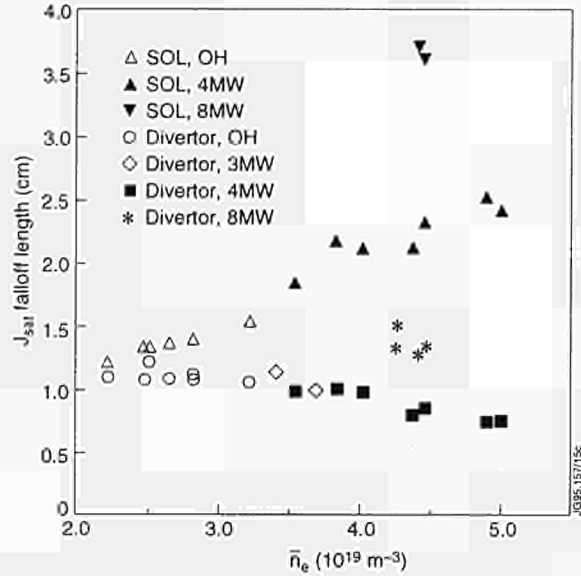


Fig.165: Comparison of the  $J_{\text{sol}}$  falloff lengths,  $\lambda_{J_s}$ , at the outer target plate and in the SOL versus  $n_e$ .  $\lambda_{J_s}$  is mapped to the outer midplane.  $B_T=2.2\text{-}2.4\text{T}$  and neutral injection power levels are indicated. The ratio  $\lambda_{J_s}(\text{SOL})/\lambda_{J_s}(\text{tar})$  is found to vary as  $\sim n_e^{1.5}$ .

been carried out as yet. Extensive target plate data during the ELM-free H-mode as well as with ELMs exists; however no overview has been reached. Typically  $\lambda_{J_s}$ , when mapped from the outer target plate to the outer midplane, lies in the range  $\sim 2\text{-}6\text{mm}$  during the quiescent phase and jumps to  $\geq 4\text{cm}$  at an ELM. Upon entering the ELM-free phase, the profiles display a sharp feature near the separatrix followed by a broader tail. As time progresses within the ELM-free phase, the profiles widen and the tail becomes less prominent.

In summary, for the OH and L-mode cases presented with the  $\nabla B$  drift away from the X-point, the behaviour of fall-off lengths in the SOL may be satisfactorily described by regressions based on the global parameters  $P_{\text{tot}}$  and  $\langle n_e \rangle$ , but only when  $P_{NI}$  is broken down into the ranges 0-4MW and 4-8MW.  $\lambda_{nc}$  and  $\lambda_{Tc}$  increase with  $P_{\text{tot}}$  and  $\langle n_e \rangle$  in a similar manner, having the range  $\sim 1.6\text{-}5.6\text{cm}$  (Tables XVIII and XIX). A cogent scaling with  $B_T$  cannot yet be advanced. Ideally, all scalings should be carried out in terms of "local" parameters instead of  $P_{\text{tot}}$  and  $\langle n_e \rangle$ , which then might allow a single scaling over the  $P_{\text{tot}}$  range. Unfortunately, lack of precise knowledge of the upstream separatrix position introduces too large an uncertainty at present to make such an approach credible.

$\lambda_{nc}$  versus  $\langle n_e \rangle$  exhibits a different functionality between vertical and horizontal target plates:  $\lambda_{nc}(\text{vert}) \leq \lambda_{nc}(\text{hor})$ , depending on the power level and density. At detachment  $\lambda_{nc}$  increases beyond that

expected from the global scaling. Comparing  $\lambda_{js}$  in the outer divertor leg to that at the outer midplane, it is found that they are about equal at pre-rollover densities and then diverge with increasing  $\langle n_e \rangle$ , whereby  $\lambda_{js}(\text{tar})$  becomes smaller and  $\lambda_{js}(\text{SOL})$  becomes larger in a very systematic way (Fig. 164).  $\lambda_{js}(\text{tar})$  in the quiescent H-phase - mapped to the midplane - can be more than ten times smaller than  $\lambda_{js}(\text{SOL})$  in the L-phase (0.2-0.6cm versus 1.2-3.6cm).

### Recycling and its Effect on Performance

In the early stages of the 1994 hot ion H-mode campaign, the ELM-free plasma performance in terms of D-D reaction rate  $R_{DD}$  lay considerably below that attained in 1991. Comparison of the absolutely calibrated  $D_\alpha$  signals (DAV), viewed along a vertical chord not intersecting the divertor, showed this recycling signal to be considerably higher than that encountered in 1991. On the positive side, there was clear indication that  $R_{DD}$  increased with decreasing DAV. As operational experience accumulated with the Mark I divertor, in the sense of learning to minimize recycling, implementing active divertor pumping, and optimizing shape parameters such as edge shear, triangularity and flux expansion,  $R_{DD}$  could be driven beyond the previous record value established in 1991. At this stage, recycling no longer appeared to restrict performance. Rather, internal MHD phenomena first limited the maximum value of  $R_{DD}$ , after which followed a giant ELM, ending the high performance ELM-free phase.

Against this background evidence was sought as to whether the largely inconel wall (versus graphite in 1991), or the target plates, or the mechanical bypasses from the divertor to the main chamber, were responsible for the larger DAV signal of 1994. The efficacy of the divertor configuration in regulating the neutral flux from the outer void of the main chamber to the SOL and into the core plasma was also investigated for various experimental flux expansion scenarios, as evidence existed that higher flux expansion was associated with lower DAV and higher  $R_{DD}$ . The approach used was to run the EDGE2D/NIMBUS code in a "predictive" fashion. That is, no attempt was made to model any one plasma condition exactly. Reasonable, generic values for transport coefficients ( $\epsilon_i = \epsilon_e = 0.3\text{m}^2\text{s}^{-1}$ ,  $D_{\text{perp}} = 0.03\text{m}^2\text{s}^{-1}$ , with no pinch term), input power ( $P_i = P_e = 3\text{MW}$ ) and edge density ( $n_{e,c} = 1 \times 10^{19}\text{m}^{-3}$ ), recycling only at the target, with and without divertor pumping were used for each of several divertor configurations.

The values produced by the code for recycling signals (horizontal, DAV, and at the target plate, DAT, in addition to DAV) compared well to experiment on an absolute basis, allowing for some adjustment of  $n_{e,c}$ . The relative ratios of the signals to each other matched the experiment ratios very closely. Hence, even in this first approach there appeared to be little room for significant additional neutral sources, e.g. from the wall or via bypasses, to enter the picture. That is, for the several classes of magnetic configurations used in the hot ion H-mode studies, the measured  $D_\alpha$  signals could be attributed to neutrals emanating from the target plates and escaping from the divertor. Another major result is that DAV of 1991 is found to be much smaller than for the 1994 configurations, for the same separatrix conditions, whereas the predicted total neutral flux to the main SOL is about the same. Thus, the differences in DAV between 1991 and 1994 are in large part due to the differences in viewing geometry between 1991 and 1994 and are not indicative of a generally higher level of recycling in 1994. The calculations also indicate an approximate factor of two reduction in neutral flux to the SOL when pumping is introduced. This is qualitatively in keeping with an enhancement in  $R_{DD}$  achieved when pumping is present. With respect to flux expansion, the main benefit is predicted to arise from fewer ionizations within the plasma core, i.e. poorer fuelling efficiency for recycling neutrals, for a given set of separatrix conditions. In the experiment, this should lead to a slower buildup of the density component of the edge pressure gradient, thereby pushing back the onset time of the giant ELM and prolonging the ELM-free period to permit a further increase in  $R_{DD}$ . However, detailed code work which considers experimental conditions more precisely is required on this subject before really definitive statements can be made.

### References

- [1] The JET Team (presented by D J Campbell), Proc. 15th IAEA Conf. Plasma Phys. & Control. Fusion Res., Seville, Spain, 1994, (IAEA-CN-60/A-4-I-4).
- [2] The JET Team (presented by L Horton), Proc. 15th IAEA Conf. Plasma Phys. & Control. Fusion Res., Seville, Spain, 1994, (IAEA-CN-60/A-4-I-5).
- [3] Borrass, K, Janeschitz, G, Nucl. Fusion **34** (1994) 1203.
- [4] Simonini, R, *et al.*, Controlled Fusion and Plasma Physics **18B** (1994) 694.

- [5] Borrass, K, Huysmans, G, SOL-One, A 1-D Scrape-off Layer Transport Code, in preparation.
- [6] The JET Team (presented by G C Vlases), Proc. 14th IAEA Conf. Plasma Phys. & Control. Fusion Res., Würzburg, FRG, 1992, 1 287.
- [7] Taroni, A, Corrigan, G, Simonini, R, et al., Proc. 11th Int. Conf. Plasma Surf. Interac. Control. Fus. Dev., Mito, Japan, 1994.
- [8] Lowry, C G, O'Brien, D, Campbell, D J, et al., 36th Ann. Meet. APS Div. Plasma Phys., Minneapolis, USA, 1994.
- [9] Reichle, R et al 1991 Proc. 18th Eur. Conf. on Contr. Fusion and Plasma Phys. (Berlin, 1991) vol 15C, part 3, p 105.
- [10] Janeschitz, G et al 1993 Proc. 20th Eur. Conf. on Contr. Fusion and Plasma Phys. (Lisboa, 1993) vol 17C, part 2, p 559.
- [11] Chankin, A V, Clement, S, Erements, S K et al., Plasma Phys. Control. Fusion 36 (1994) 1853.
- [12] Reichle, R, Summers, D D R and Stamp, M F, Journal of Nuclear Materials 176&177 1990 375-380
- [13] Stangeby, P C, Chankin, A V, submitted to Nuclear Fusion.
- [14] Hinton, F L, Staebler, G M, Nucl. Fusion 29 (1989) 405.

## Tokamak Concept Improvement

The main aim of the Task Force was to study those physics areas in which JET can make an important contribution to ITER and DEMO. A large series of experiments were planned along these lines. Some requiring a substantial amount of technical development were not ready to be carried out in 1994 and will be undertaken in 1995.

- The following experiments were started during 1994:
- High beta experiments
- Confinement of small volume plasmas with a high aspect ratio
- Shear reversal experiments
- Lower Hybrid Current Drive experiments:
- Current Drive efficiency
- Profile Control experiments
- Modelling and application to ITER
- Ion Cyclotron Resonance Heating experiments:
- Heating
- H-modes

- Direct electron heating.
- Toroidal Alfvén Eigenmodes excitation.

### High $\beta_p$ Experiments

A steady-state tokamak reactor is likely to need a substantial fraction of the plasma current to be provided by the neoclassical bootstrap effect. To achieve this requires that the poloidal beta ( $\beta_p$ ) be significantly greater than unity, which in turn requires good energy confinement without the use of very high plasma currents. Such a plasma would also need to exceed the Troyon  $\beta$  limit [1] if very high toroidal fields were to be avoided. Experiments have been performed with the demanding aim of simultaneously achieving these three conditions: high  $\beta_p$ , high confinement and high  $\beta_N (= B_T a \beta_p / I_p$  in mT/MA), in steady-state. The investigation of the stability and confinement characteristics of plasmas in this domain, the so-called 'Advanced Tokamak Scenario', is necessary to assess the prospects for steady-state reactor concepts.

In previous experiments, a bootstrap current fraction ( $I_{\text{Bootstrap}} / I_{\text{Plasma}}$ ) of 0.7 was obtained in plasmas with  $\beta_p \approx 2$  and high confinement compared with the usual L-mode and H-mode scalings [2]. However, these discharges were obtained at  $q_{95} > 10$  which would be uneconomic and technically difficult to achieve in a reactor. In such plasmas, high values of  $\beta_p$  can be achieved without reaching the Troyon  $\beta$  limit. Nevertheless, these discharges were not stable and collapsed with a large ELM after  $\approx 2$ s. The cause of the collapse has not yet been unambiguously identified. Theory predicts that high bootstrap fraction discharges will be prone to a large number of MHD instabilities on the current diffusion timescale, the more dangerous being the infernal modes due to the hollow current profile and external kink modes due to the large current density in the plasma periphery [3].

The new pumped divertor configuration has several features which are noticeably different to the old configuration. The plasma volume is smaller and consequently, for a similar plasma current and toroidal field strength,  $q(a)$  is lower. On the other hand, the power handling capability of the divertor is improved. Long ELM-free periods and very high confinement have not yet been obtained in the high  $\beta_p$  experiments with the new configuration. While the cause of this is still under investigation, the benefits of ELMy H-mode plasmas have been exploited to meet the aim of achieving quasi-steady-state plasmas at least with respect to density control.

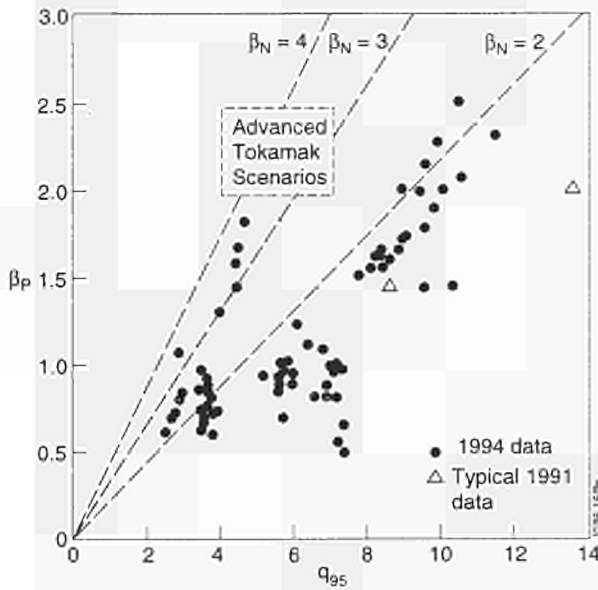


Fig. 166: Achieved values of  $\beta_p$  plotted against  $q_{95}$ .

High  $\beta_p$  plasmas have been investigated in a much wider range of plasma parameters (see Table XX) during 1994 than in previous JET campaigns. Figure 166 shows the achieved values of  $\beta_p$  plotted against  $q_{95}$ , and typical data from previous experiments are also shown for comparison. The 1994 data are significantly closer to the 'Advanced Tokamak Scenario' domain. Approximate lines of constant  $\beta_N$  have been added to the 1994 configuration as a guide. Whereas previous JET data were obtained at modest values of  $\beta_N$ , values up to 3.7 have now been achieved.

The time evolution of a typical high  $\beta_p$  plasma with a plasma current of 1MA and toroidal field of 2.8T is shown in Fig.167. The combined heating power of the NBI and ICRF heating systems was 20MW, which resulted in a  $\beta_p$  value of 2.0. However, in previous experiments, this value was achieved with <10MW of heating power in an ELM-free VH-mode plasma. The plasma in Fig. 167 has reached quasi-steady conditions with respect to stored energy, radiated power and density, whereas the previous VH-mode conditions were achieved only transiently.

Table XX  
Range of Plasma Parameters to Investigate High  $\beta_p$

Parameter	1991-92 Campaign	1994 Campaign
$I_p$ (MA)	1.0 - 1.5	1.0 - 2.0
$B_T$ (T)	2.8 - 3.1	1.0 - 2.8
$q_{95}$	8 - 14	2.5 - 12
$P_{add}$ (MW)	up to 10	up to 26

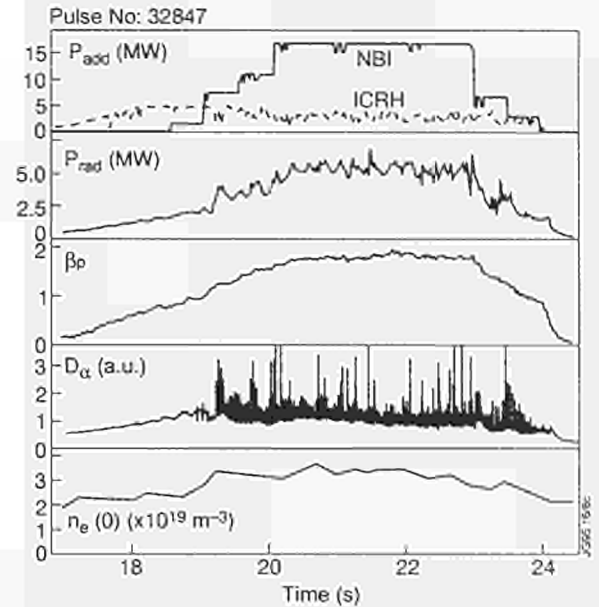


Fig. 167: Time history of heating and plasma parameters for a typical high  $\beta_p$  pulse

The bootstrap current fraction calculated for these pulses is about 0.6, somewhat lower than previously. This is largely due to the higher non-thermal fraction of the plasma stored energy (not included in the bootstrap current calculation) which results from the increased additional heating power. In some cases around 30% of the plasma stored energy is estimated as non-thermal. The calculated beam driven current can account for about 20% of the plasma current.

Figure 168 shows the confinement enhancement factor compared with the ITER89L-P L-mode scaling as a function of  $\beta_p$ . A domain is indicated in the bottom right-hand corner of the diagram which cannot be accessed at

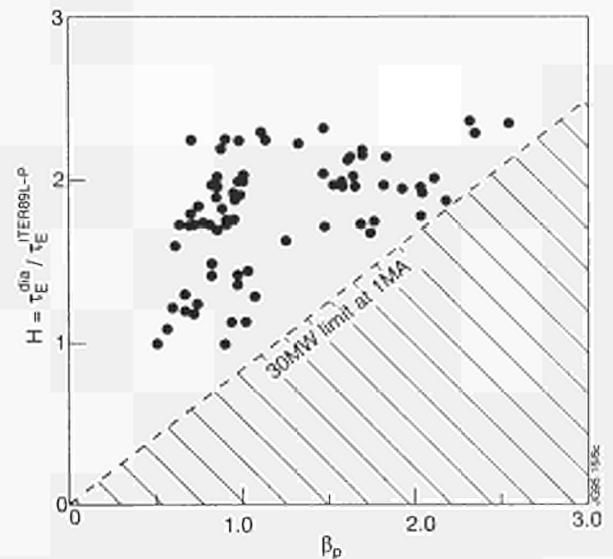


Fig.168: Confinement enhancement factor with respect to ITER89L-P scaling plotted against  $\beta_p$

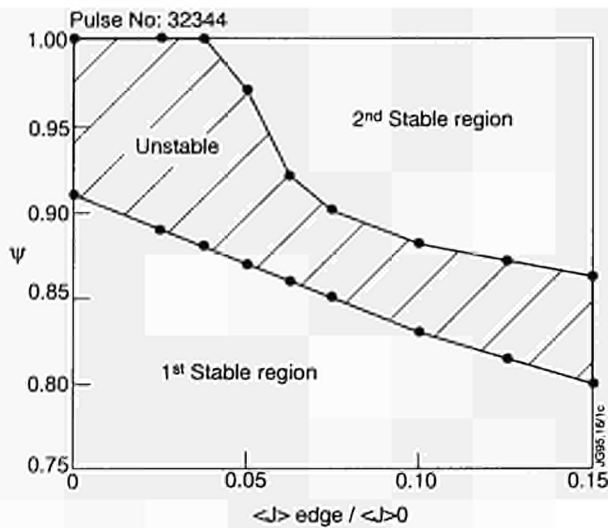


Fig.169: Unstable region for ideal ballooning modes as a function of poloidal flux index and the ratio of edge to central current density

the plasma currents used in these experiments without further increasing the additional heating power. This power limit defines the lower edge of the dataset. The highest values of confinement enhancement do not seem to depend significantly on  $\beta_p$ .

Transient phases of elevated confinement have been observed which resulted in the highest values of  $\beta_p$  ( $\approx 2.5$ ). An improvement in confinement was observed which was thought to be triggered by small variations in the total plasma current leading to large variations in the peripheral current density which may stabilise instabilities near the edge. Figure 169 shows the region of instability for high  $n$  ballooning modes calculated for this plasma. Calculations of the peripheral current density using the TRANSP code [4] suggest that the combination of the bootstrap effect and perturbations in the plasma current gave rise to values required to access the unconditionally stable (or second stable) region near the edge. Current ramp experiments have been performed in an attempt to provide sustained access to the unconditionally stable region near the plasma edge. Although some effects on the plasma confinement have been seen including short ELM free periods, the results are so far inconclusive.

High power heating experiments at a plasma current of 1MA and with a toroidal field strength of 1.4T have provided the closest conditions to those required for a steady-state reactor. Figure 170 shows the time evolution of such a plasma with 18MW of heating power. During the heating pulse, stationary conditions were achieved

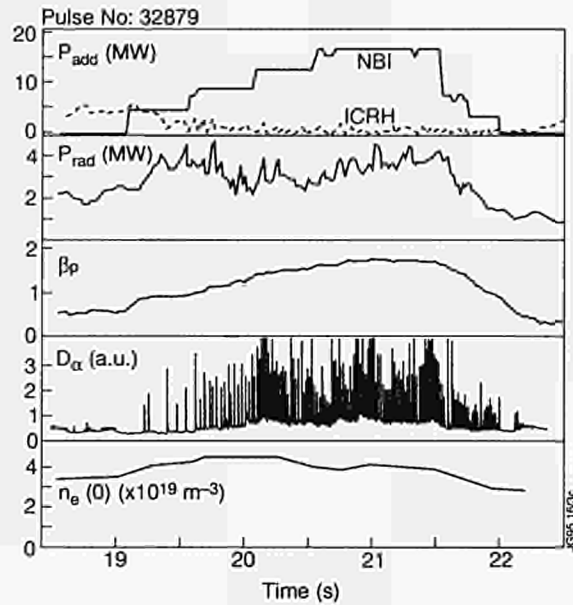


Fig.170: Time history of heating and plasma parameters for a high  $\beta_N$  plasma

with  $\beta_p \approx 1.8$ ,  $\beta_N \approx 3.7$  and  $q_{95} \approx 4.7$ . The confinement enhancement factor compared with ITER89L-P scaling was  $\approx 2.2$ . This quiescent phase was terminated by the end of the heating pulse.

Steady-state conditions approaching those required for a steady state reactor have been achieved in ELMy H-mode plasmas for pulse lengths in the range 1 - 7s. However, the effect on stability and confinement of poloidal field diffusion over a longer timescale has yet to be fully investigated.

### Confinement of Small Volume Plasmas with a High Aspect Ratio

The high aspect ratio configuration has become a prerequisite in the advanced tokamak concepts based on high bootstrap current operation, as it may offer a beneficial route to an ignition device in which the fusion triple product is significantly improved with the aspect ratio as predicted from the ITER89-P L-mode scaling. Experimental verification of this proposal has been required for ELMy plasmas with enhanced confinement at high- $\beta_p$  [5].

In a high- $\beta_p$  regime ( $\beta_p \leq 1.5$ ) of JET, confinement characteristics of ELMy plasmas with a high aspect ratio of  $\sim 3.7$  and a "small" volume of  $\sim 55\text{m}^3$  were investigated compared with those with an aspect ratio of  $\sim 3.1$  and a "large" volume of  $\sim 80\text{m}^3$  at the same major radius (Fig.171) where NBI heating up to 17MW and combined ICRF heating up to 6MW were applied. The results show no significant difference between the two configurations

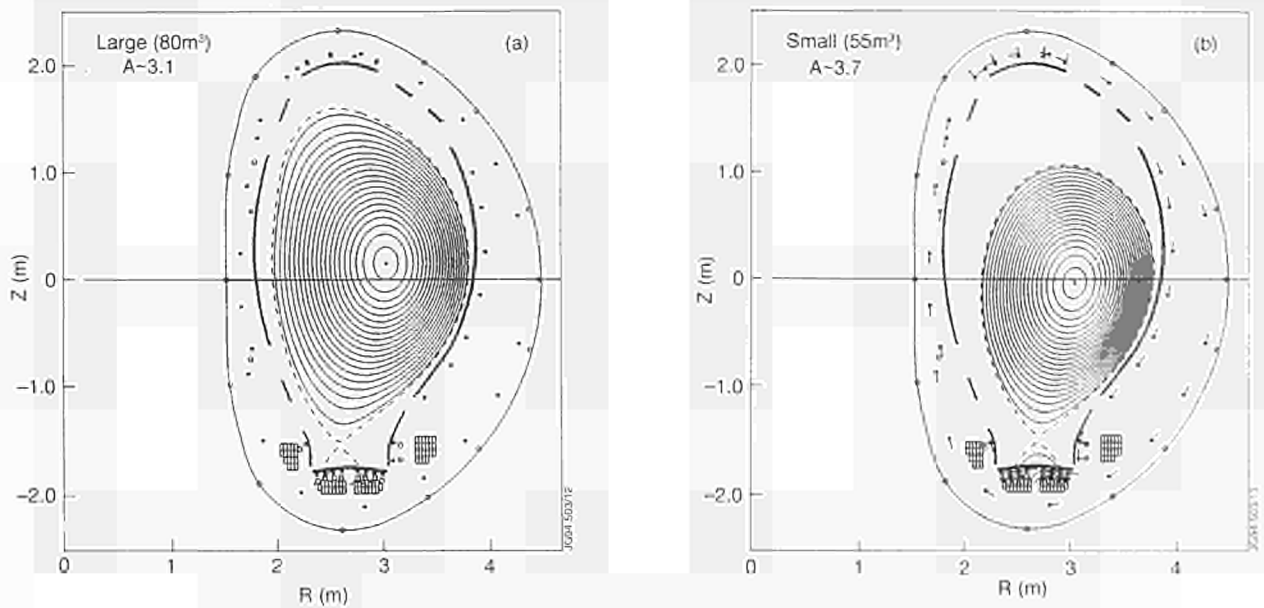


Fig.171: Typical configurations for (a) large and (b) small plasma size comparison

in energy confinement in spite of vastly reducing the plasma volume. The confinement enhancement factor (H-factor) against the L-mode scaling of  $\sim 1.8$  was achieved for both ELMy plasmas at 2.8T as shown in Fig.172, where the  $W_{dia}$  value is plotted against the total heating power at 1.5MA.

From these experiments, confinement follows ITER 89-P type of scaling law, although the major radius has not been varied. This is thought to be the dominant size parameter for determining energy confinement rather than the minor radius for ELMy plasmas at high- $\beta_p$ . This supports advanced tokamak concepts based on high aspect ratio.

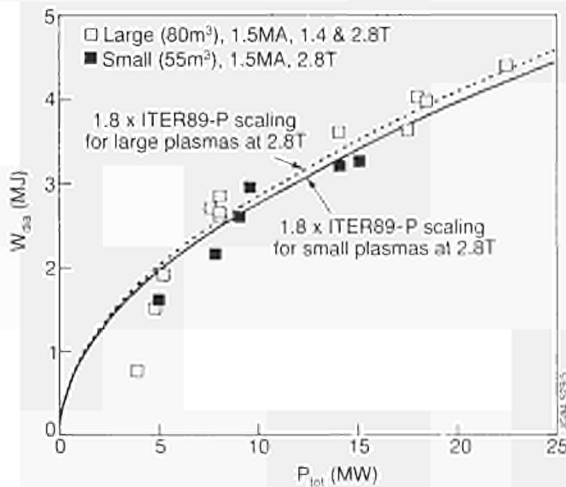


Fig.172:  $W_{dia}$  versus  $P_{tot}$  for the “large” and “small” plasma comparison

### Shear Reversal

Improved tokamak performance scenarios with high bootstrap current in high- $\beta_p$  operation will necessarily have hollow current profiles. These non-monotonic q-profiles with negative shear in the central high pressure region might provide superior confinement in the second stability region. Effort has been made to explore the possibilities for JET to work in this regime. Scenario studies have been carried out using a complex code system which includes LH and FW current drive codes, the 1.5D radial transport code JETTO and the MHD stability code CASTOR. Fast Waves (FW), Lower Hybrid (LH) Waves and Neutral Beam Injection (NBI) are used for heating and current drive, alternatively or in combination.

A stable route to non-monotonic q-profiles has been found from numerical models with a specific ramp-up scenario which combines LH-current drive (LHCD) and a fast Ohmic current ramp-up [6]. A hollow current profile with deep shear reversal over the whole central region is thereby formed in an early low- $\beta$  phase. Additional heating with FW and/or NBI is started at the end of the current ramp-up. The preconditioned hollow current profile is then frozen in and maintained into stationary conditions. MHD-unstable transitions during a discharge from positive to negative shear in regions of high pressure can be avoided by this scenario. Gradual variations between hollow and peaked current profiles for stability

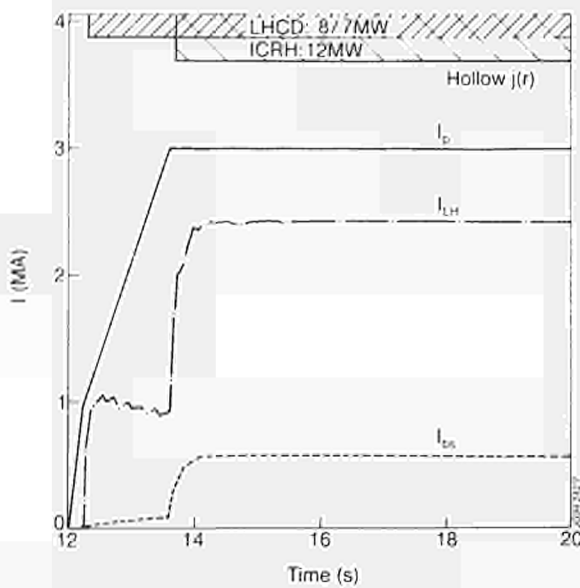


Fig.173: Waveforms of bootstrap, LH and total plasma current in a full non-inductive current drive scenario with non-monotonic q-profiles

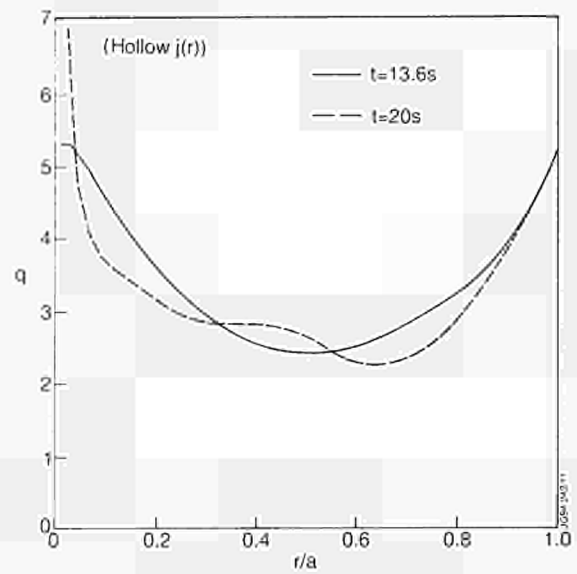


Fig.174: q-profiles at the end of the current ramp-up phase and late into the flat-top phase

and confinement studies can be obtained by power adjustments among FWCD and NBI for central current drive and LHCD for off-axis current drive. The temporal evolution of the currents and powers in a case with full noninductive current drive is plotted in Fig.173. A hollow q-profile with a minimum q value of about 2.5 and a wide region with negative shear in the centre is formed early during the current ramp-up and maintained into the flat top phase, (Fig.174), with two very similar q-profiles for two time slices at the beginning and the end of the current plateau phase.

With non-monotonic q-profiles, ballooning modes are stable in the region of negative shear without limit on the pressure gradient. The external kink mode is stable in these scenarios. In general, the growth rates are small and a narrow path to a second stability regime for infernal modes at higher  $\beta_p$  values ( $\beta_p > 1.7$ ) appears[7].

Current profile control experiments were performed on JET with the aim to establish deep shear reversal over a wide region in the plasma centre along the line found in the modelling calculations. Combined LHCD and ICRF heating were applied during a fast initial Ohmic current ramp to flat-top values of 2 and 3MA. Additional high power NBI heating was started still during the current ramp and continued over the whole flat-top period. The temporal evolution of plasma current, heating and current drive powers, central and boundary q-values,  $\ell_i$  and

central electron temperature in a 3MA discharge are shown in Fig.175. A hollow q-profile close to the theoretically required one with high  $q(0) \gg 1$  and  $q_{min} \approx 2.3$  is formed at the end of the current ramp with negative shear in the central region over more than half of the plasma radius. This profile reverts to a conventional monotonic shape soon after switch-off of the LHCD after begin of the current flat-top. The internal inductance is low, with  $\ell_i \approx 0.6$  during the shear reversal phase, and rises slowly afterwards. The central q-value  $q(0)$  stays above unity over the whole heating phase. The evolution of the q(r)-

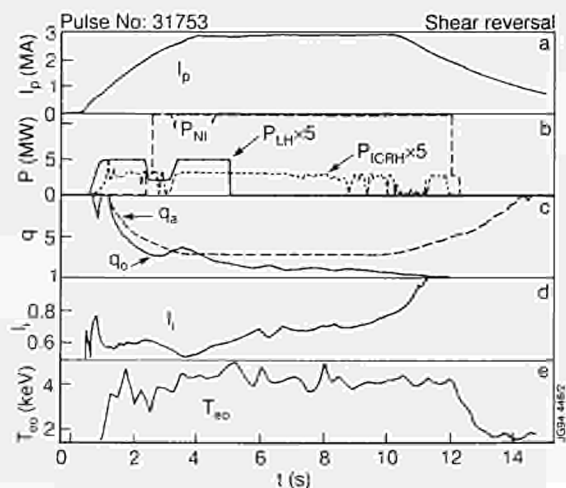


Fig.175: Time traces of a shear reversal discharge

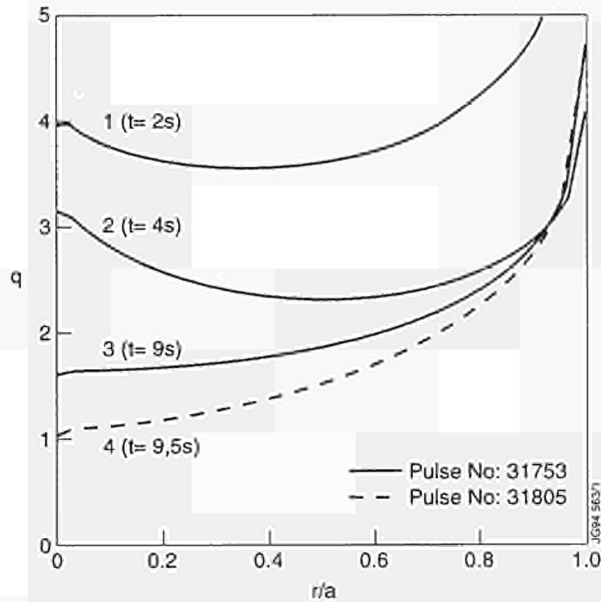


Fig.176: Evolution of the  $q(r)$  profile in the shear reversal discharge and comparison with the monotonic profile of a reference discharge

profile is shown in Fig.176 and compared with the monotonic profile of a reference discharge where the current is ramped up more slowly to keep the  $q$ -profile monotonic and attain higher  $\ell_i$  values. In these first experiments on the deep shear reversal scenario, no clear improvement in confinement has been found. However, longer preservation of the shear reversal configuration and more peaked heating power deposition profiles into the negative shear region might be required for a clear test of the potential of shear reversal scenarios.

## Lower Hybrid Current Drive (LHCD) Experiments

### Current Drive Efficiency

Current drive experiments have been performed with the full LHCD system on JET in the range of plasma currents  $I_p = 0.7 - 3\text{MA}$ . A maximum LH power of 6.5MW and a maximum energy of 36MJ have been coupled to the plasma so far. A representative 2MA discharge at a line averaged density  $\langle n_e \rangle = 1.8 \times 10^{19}\text{m}^{-3}$  is shown in Fig.177. The LH-current drive with 4MW coupled power replaces the ohmic flux consumption. The measured surface loop voltage  $U_{i,\text{surf}}$  drops to zero. The corrected resistive loop voltage  $U_{i,\text{corr}}$ , taking into account changes of plasma current and internal inductance, stays slightly positive. The electron temperature rises from 3 to 5keV and the total energy content doubles. A decrease of the internal inductance  $\ell_i$  indicates a broadening of the current profile.

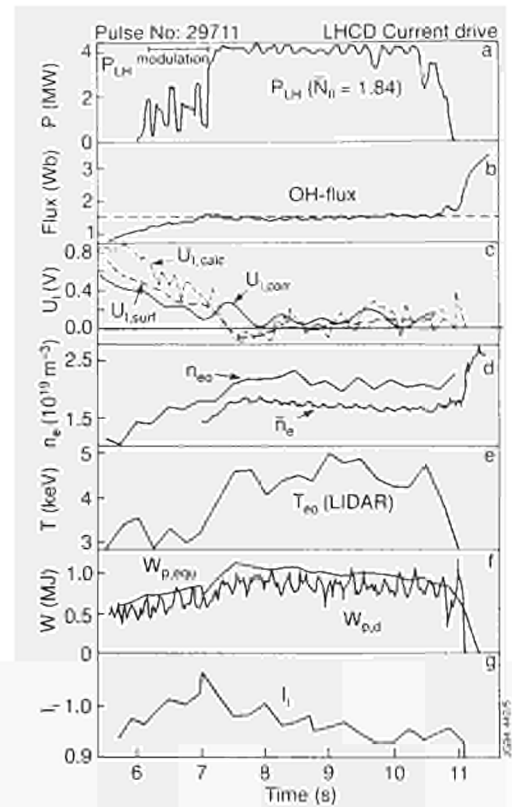


Fig.177: LHCD discharge at  $I_p = 2\text{MA}$ ,  $B_t = 2.8\text{T}$ . (a) LH power, (b) OH flux consumption, (c) measured, corrected and in TRANSP calculated loop voltage, (d) central and line averaged electron density, (e) central electron temperature, (f) energy content from diamagnetic and equilibrium field measurements and (g) internal inductance

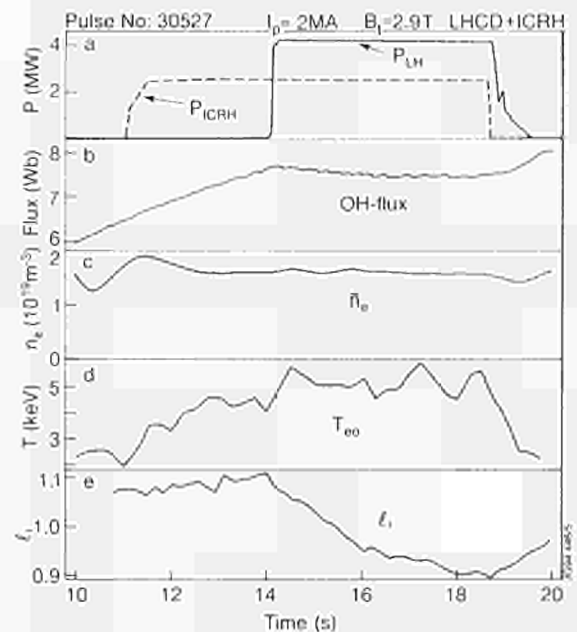


Fig.178: Combined operation of ICRF heating and LHCD

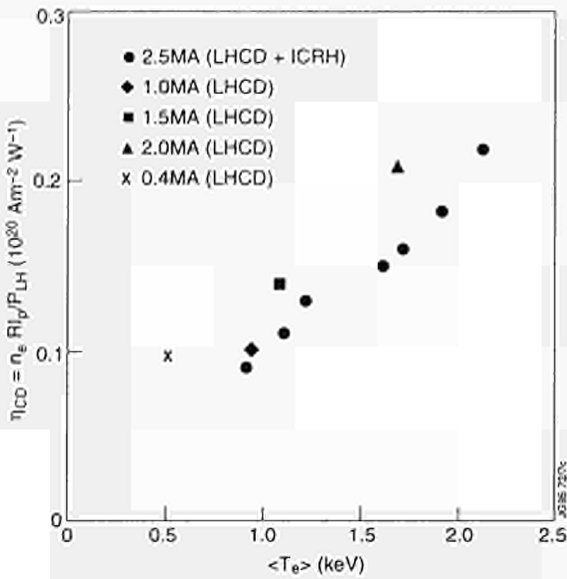


Fig.179: Scaling of the LH-current drive efficiency with volume averaged electron temperature

Full current drive conditions have been achieved at plasma current up to 2.5MA.

Preheating with ICRF power provides higher target electron temperatures and a wider temperature range is accessible. An example of LHCD into an ICRF-heated plasma is shown in Fig.178. The central electron temperature rises further from 4 to 5.5keV during LHCD. The Ohmic flux is constant, while the internal inductance is decaying, indicating a pronounced off-axis LHCD.

The current drive efficiency  $\eta_{CD}$  increases with electron temperature, for LHCD alone and in combined heating/current drive scenarios. The scaling of  $\eta_{CD}$  with the volume averaged temperature is shown in Fig.179 for full current drive discharges with LH alone and for partial and full current drive in combined operation with LHCD and ICRH over a wide range in powers. The variation due to  $Z_{off}$  is negligible in these discharges, while the central electron temperature varied between 2 and 7keV. The maximum current drive efficiency obtained is  $0.26 \times 10^{20} \text{Am}^{-2} \text{W}^{-1}$ .

**Current Profile Control Experiments**

The main goal of LH current drive application on JET is the active control of the plasma current profile in order to improve MHD stability and energy confinement and to explore scenarios for tokamak performance improvement in combination with heating and current drive by Fast Waves and NBI. In a first stage, the extent of

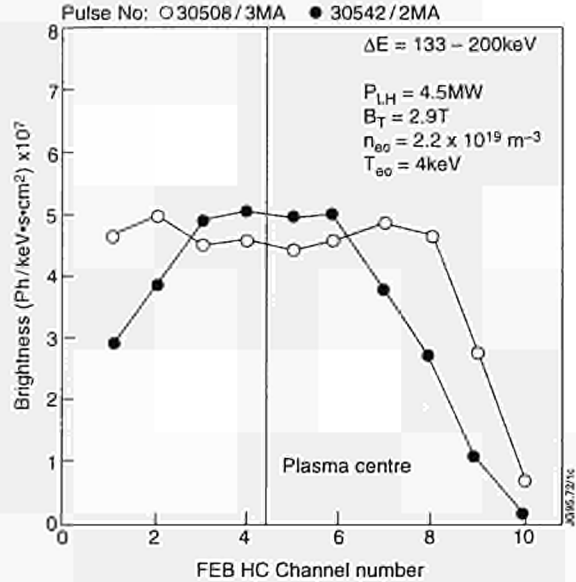


Fig.180: Fast Electron Bremsstrahlung (FEB) profiles during LHCD in two discharges with different plasma currents, 2 and 3MA

deposition profile variations and the resulting modifications of the current profile were assessed.

The current profile is broadened in most cases with LHCD, as seen from a reduction of the internal inductance  $\lambda_i$  and a transient negative overshoot of the loop voltage after start of the LH. Hard X-ray measurements of the fast electron bremsstrahlung (FEB) give consistently broad or hollow emission profiles in these cases, suggesting off-axis LH power deposition profiles. The FEB profiles are peaked at low electron density and temperature and broaden with increasing density and temperature. Variations of the launched LH wave spectrum by phase adjustments brought only small changes in the deposition profiles in cases where LH codes would predict multiple pass absorption.

A strong dependence of the LH deposition profile on plasma current and current profile was found. The FEB profiles broaden and the drop in  $\ell_i$  grew with the plasma current. Two discharges with 2 and 3MA at constant field  $B_T = 2.9\text{T}$  are compared in Fig.180. The time to reach steady-state became increasingly longer with off-axis shift of the LH deposition profile due to long inductive time scales for the current profile redistribution. Efficient local control of the current profile commands therefore intervention directly in the aimed at radial region.

Sawtooth stabilisation was achieved with nearly full LH current drive. The waveforms of a 3MA discharge at a density  $n_e(0) = 2 \times 10^{19} \text{m}^{-3}$  are shown in Fig.181. The LH

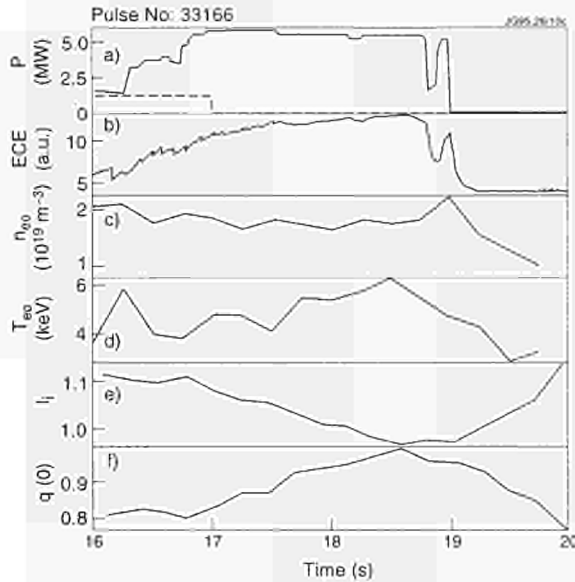


Fig.181: Temporal evolution of LH power, central ECE emission,  $n_e(0)$ ,  $T_e(0)$ , internal inductance and  $q(0)$  during sawtooth stabilisation with LHCD

power was ramped up within 1s to 5.5MW. The last sawtooth is seen on the ECE signal 1.5s after start of the LH.  $m=1$  oscillations continued for about 0.5s and then disappeared, but only transiently. The internal inductance dropped throughout the whole LH pulse and  $q(0)$  rises. The central electron temperature rose, with an increase from 3.8 to 5.4keV inside  $r/a = 0.3$ . FEB measurements showed distinct differences for the deposition profiles for different densities as given in Fig.182. In the lower density case, LH power reaches the centre, while in the higher density case the profile is peaked outside half

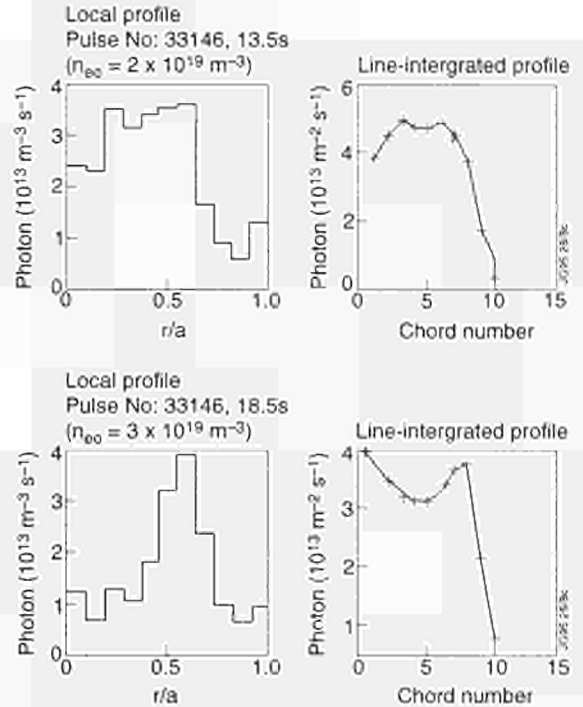


Fig.182: FEB profiles during LHCD at two different densities in 3MA discharges

radius. Transport code calculations for both cases give very different time-scales for the current profile readjustment in both cases. The off-axis deposition at higher density and high initial electron temperature (3keV) would require about 7s before sawtooth stabilisation through a rise of  $q$  above unity in the centre can be expected. These long delays can be avoided if the current profile is already preformed close to the requested shape before high power

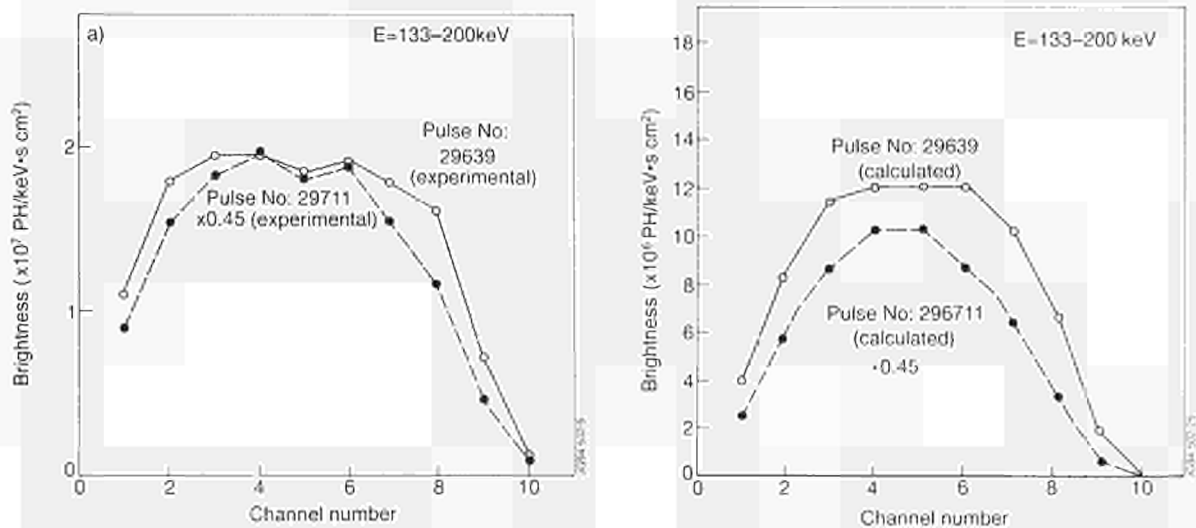


Fig.183: (a) Measured FEB profiles for Pulse No:29639 (solid line) and Pulse No:29711 (dashed line); (b) Calculated FEB profiles for Pulse Nos:29639 (solid line) and 29711 (dashed line)

heating and then frozen in. This scenario has been developed for deep shear reversal experiments [4].

### **Modelling and Application to ITER**

LHCD experiments have been modelled using a numerical code [8]. Results of modelling are in good agreement with experimentally observed LHCD efficiency [9]. Simulated fast electron bremsstrahlung (FEB) emission is compared with measured FEB profiles for a number of shots (Fig.183). The deposition profile varies with plasma density, temperature, and current. Simulations were carried out for a wide range of plasma parameters;  $n_{co}(0) = (0.9-4.0) \times 10^{19} \text{m}^{-3}$ ,  $T_{co} = 1.5-6 \text{keV}$ ,  $I_p = 0.5-3 \text{MA}$ ,  $B_T = 2.4-2.8 \text{T}$  up to the maximum available LH power of 6MW and different power spectra with  $N_{//max} = 1.4, 1.85, \text{ and } 2.3$ .

#### **Simulation of 2MA Current Drive Experiments**

Nearly full current drive of  $I_p = 2 \text{MA}$  was achieved in a discharge with  $n_e(0) \cong 2.3 \times 10^{19} \text{m}^{-3}$  by launching about 4MW of LH power for 3.5s. An LH-driven current  $I_{LH} = 1.86 \text{MA}$  and a current drive efficiency  $\eta = 0.22 \times 10^{20} (\text{Am}^2/\text{W})$  were calculated in the LHCD code. These values are close to the experimental values derived from the change in loop voltage and plasma resistance.

#### **Broadening of LH Current Profile with Density**

Current and power deposition profiles broaden when the density increases. Variations in the electron temperature have less impact. The discrepancy in the amplitude of the experimental and calculated FEB profiles can be attributed to deviations in the description of the fast electrons with the energy  $E > 250 \text{keV}$  by the Fokker Planck code (1D parallel momentum, 1D radius). In the framework of the model, the broadening of the profile is explained in a higher density plasma, waves propagate closer to the periphery, where the RF energy density increases. Ray trajectories experience a larger number of reflections. When reflection occurs in the top sector of the plasma boundary waves are strongly slowed down. This is the major mechanism for the 'spectral gap' filling. Higher power is absorbed and greater current is driven further off-axis than in lower density plasma (under the condition that the electron temperatures are not too different).

The results of modelling by the LHCD stand-alone code and the JETTO transport code are in qualitative agreement with the experimental data. The calculated LH-driven current profiles are systematically somewhat

narrower than the profiles deduced from the FEB data. Calculations show that in most cases multiple pass absorption of the LH waves takes place. Reflection of the waves as well as the process of the wave scattering requires additional investigation. When the plasma temperature increases, the number of reflections decreases. Extrapolation to the high temperature plasma shows that LH waves should be absorbed during the first pass. Under these conditions, the predictions of the LHCD code are reasonably reliable.

The models developed and validated on JET experimental results have been used to study the application of LHCD to ITER and reactor plasmas [10]. LH power and current deposition profiles are determined in these studies with ray tracing and beam tracing codes. The temporal evolution of the plasma profiles is calculated with the 1.5-D transport code JETTO. Full current drive and real time profile control on ITER can be achieved by a combination of LHCD and FW current drive with a high fraction of bootstrap current in the H-mode at high  $\beta_p$ . The off-axis current drive capability of LHCD is essential to establish and maintain stable shear reversal configurations. A scenario with 74% bootstrap current, 20% LH-driven current and a small fraction of FWCD-driven current for central q control has been developed. Steady-state operation at a plasma current of 13.5MA is then provided by a combination of FW and LH systems, with 50MW each.

### **Ion Cyclotron Resonance Heating**

The ion cyclotron resonance frequency heating (ICRF) system is used primarily for high power central heating of the plasma. The current straps of the four new A2 antennae are arranged in groups of four-straps each (total 16 straps) to provide increased directivity for fast wave current drive applications. Due to the change of grouping of antennae from two to four, and also to cope with the current drive applications, low power control electronics had to be changed. After the shutdown for the installation of the pumped divertor (including the installation of the new A2 antennae), the restart of operation began. The early operation revealed that the control electronics were not performing to specification. Also, the coupling resistance of the inner two straps out of four was significantly lower than expected due to a mismatch in the impedance of the so-called cross-over strip-line required to feed the inner straps and located within the antenna. Remedial action has been identified and will be carried out in the

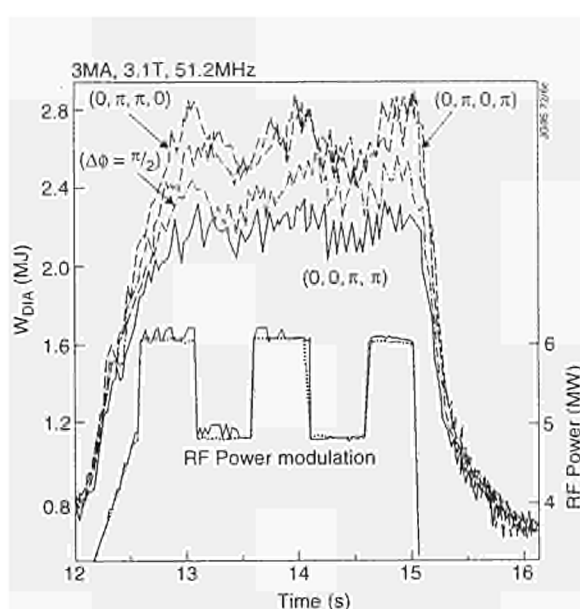


Fig.184: Stored energy in an ICRF modulated power experiment with different phasings of the A2-antenna four-straps

Mark II pumped divertor shutdown. The low power electronics have been modified.

Despite the above limitations, significant achievements in the operation of ICRF plant have taken place. Automatic real-time matching of four straps in an antenna with arbitrary phasing has been achieved. In operation with single-null divertor plasmas, ICRF power has reached a level of 10-12 MW and in combination with neutral beam heating, a total power of 26.5MW has been coupled [11].

As opposed to operation of the two-strap A1 antenna, the heating efficiency of the four-strap A2 antenna array appears to depend on the phase difference ( $\Delta\phi$ ) between straps. However, ICRF heating in the  $(0\pi0\pi)$  phasing and NBI have similar heating efficiencies. In Fig.184, the raw data of the resulting diamagnetic stored energy in several strap phasings is presented. The power coupled by one antenna-unit was modulated at 1Hz and its phasing was changed as shown. The remaining power was coupled in the  $(0\pi0\pi)$  phasing. Qualitatively, the  $(0\pi0\pi)$  and  $(0\pi\pi0)$  phasings have similar modulation on the stored energy and the  $(00\pi\pi)$  phasing is worse off. The  $(0000)$  phasing, which was not used in this combination, is the least efficient of all and also produces hot spots on the poloidal limiters located adjacent to the antenna. The excited  $k_{\parallel}$  spectrum (see Fig185) of the four-strap array was much narrower than  $A_{\parallel}$ , and in the  $(0000)$  phasing led to weak damping and cross-talk between antennae, making their operation much more difficult. However, the poorer

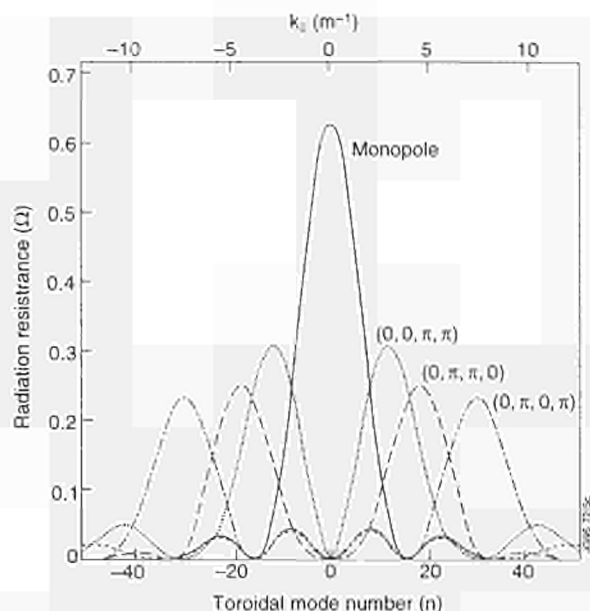


Fig.185: Theoretically calculated radiated power spectrum in the plasma for several phasings of the A2-antenna

heating efficiency in some phasings in the long toroidal array is attributable to the loss of power in the near-field RF sheath rectification effects. Hot spots were observed on the limiter during the power pulse for phasing other than dipole. It is believed that such effects could be reduced by installing bumper limiters in the middle of the four-strap array to reduce the net rectified sheath voltage.

The ICRF plant coped well in coupling power when the X-point of the diverted plasma was swept to spread the heat load. However, to maintain coupled power constant in an ELMy H-mode plasma was more difficult. During an ELM, the plasma loading changed typically from  $3\Omega$  to  $8\Omega$  in  $100\mu\text{s}$  and then relaxes back to  $3\Omega$  in  $1\text{ms}$ . The occurrence of an ELM in itself was not harmful, and in fact, it decreased the voltage on the antenna and the resonating transmission line. However, the large excursion of the loading caused a big mismatch in the normally matched generator output transmission line and the generator tripped. These problems can be solved by providing a signal that can distinguish between an arc and an ELM or by other engineering circuit design to cope with large and rapid excursions in the loading.

### H-modes with RF Alone

H-modes with ICRF alone have been achieved in the new pumped divertor configuration in different conditions of plasma current, toroidal field and phase of the injected wave. In all cases, the RF operating frequency was 42MHz.

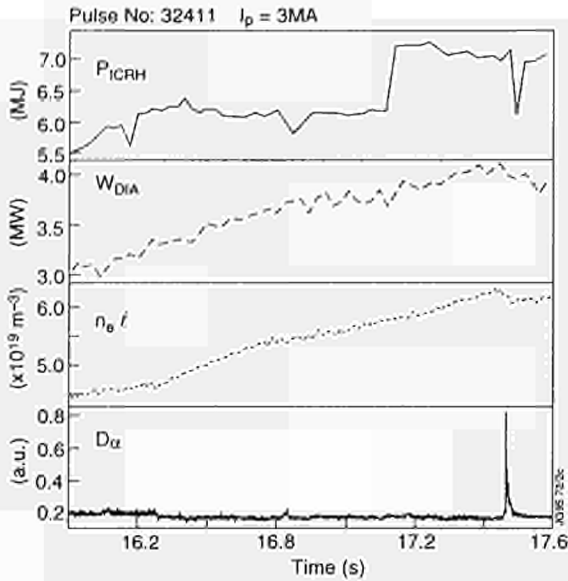


Fig.186: Time evolution of plasma parameters for an RF only H-mode at 3MA/2.8T

H-modes were first observed at 3MA/2.8T,  $f=42\text{MHz}$ , at both  $180^\circ$  (dipole) and  $90^\circ$  phasing of the antenna straps in the H-minority heating scheme. Although the signature of the H-mode was clear (Fig.186), the energy confinement time was found to be  $\sim 1.5 \times \tau_{\text{ITER-89}}$ . These discharges were characterised by a relatively high level (10% to 15%) of hydrogen, which increased steadily during the ICRF pulse; this is confirmed by data from the high and low energy Neutral Particle Analyser diagnostic, which showed the fast hydrogen tail decreasing with time. The fraction of ICRF power coupled to the bulk electron population was estimated from the rate of rise of the electron temperature after a sawtooth crash, and compared to simulations carried out with both the PION and PHANTOM codes. The agreement between experimental and numerical data is good under the assumption that up to 80% of the coupled RF power is absorbed by the minority ions. The degradation in high performance observed in these H-modes can be correlated to the decreased energy content of the fast ion tail, because of the increase in both the hydrogen content and bulk density and to the fact that half of the RF power was injected with a  $90^\circ$  phasing whose efficiency is lower than the dipole configuration.

At lower current  $\sim 1\text{MA}(2.8\text{T})$ , H-modes were produced in similar conditions, but at lower hydrogen concentration, and with use of the plasma radial position feedback on the RF coupling resistance. At power level  $\geq 7\text{MW}$ , the characteristic slow decrease in  $D_\alpha$  signal and increase in stored energy are observed; however, the RF

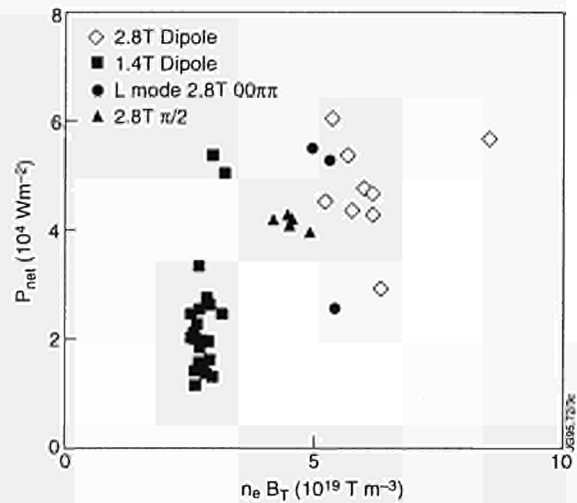


Fig.187: H-mode power threshold for RF only and combined RF + NBI discharges

coupling resistance continuously decreased during the ELM-free phase, thereby pulling the plasma closer and closer to the outer poloidal limiter, until contact with the limiter was observed and the H-mode phase terminated. After the H-mode, the level of radiated power remained high and no other L-H transition occurred. Attempts at operating with constant radial position, without RF coupling resistance feedback, were not conclusive. The L-H transition was, indeed, initiated, but the decreasing coupling resistance caused the RF system to trip and almost all the heating power was lost. H-modes were also produced at low power in the  $2\omega_{\text{CH}}$  heating scheme at 1MA/1.4T. These discharges, performed at a power level very near the power threshold, showed clearly the role of the net power flowing through the separatrix in the L-H transition.

The H-modes with the lowest power threshold have been obtained so far with positive ion  $\nabla B$  drift and either combined NBI+RF heating or RF heating alone at 1MA/1.4T (Fig.187). In the latter case, dipole ( $0\pi/0\pi$ ) phasing of the fast wave has given the best results, while for  $90^\circ$  phasing the threshold seems to be higher, although still comparable to that in dipole phasing. Attempts to produce H-modes with  $00\pi\pi$  phasing showed that, for this RF phasing, the power threshold is substantially higher than that in either dipole or  $90^\circ$  phasing.

### Direct Electron Damping Experiments

There are several reactor relevant scenarios for Fast Wave Heating and Current Drive that can be studied in JET plasmas. A scheme similar to the one proposed for ITER, i.e. injected wave frequency below all ion cyclotron

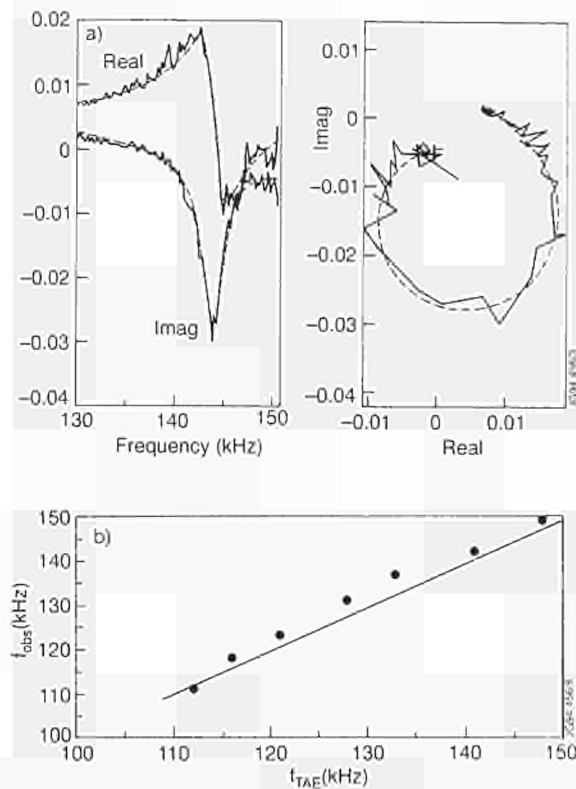


Fig.188: Example of a TAE resonance in the ohmic phase of Pulse No:31638

frequencies in the plasma [12], is considered: in the new divertor configuration by using fast waves at 33MHz in a 3.1T deuterium plasma only the fundamental  $\omega(\text{He}^3)$  resonance is present in the plasma. The single pass damping is predicted to be  $\sim 10\%$ , to be compared with about 50% for the ITER case. However, since there are no competing cyclotron absorption mechanisms, most of the injected power is expected to be absorbed by the electrons.

Experiments with predicted high single-pass damping, comparable to what is expected in ITER, are also planned at low toroidal field,  $B_T \sim 1.4\text{T}$ , high frequency,  $\sim 48\text{MHz}$ ; in similar conditions, non-negligible direct electron damping has already been demonstrated [13]. Scenarios characterised by a high fraction of mode conversion in the central plasma region, of the launched fast wave to an ion Bernstein wave [14] are being considered and numerical simulations of the predicted damping and current drive efficiency for JET plasmas are being carried out.

A fourth scheme was also studied. In deuterium plasmas at  $B_T = 1.8\text{-}2.1\text{T}$  and wave frequency 42 to 48MHz, the main resonance in the plasma centre is  $3w_{\text{CD}}$  while  $w_{\text{CD}}$  is either at the very edge or out of the plasma. In a similar scenario, significant direct electron damping and some current drive have been obtained in Tore Supra [15].

Preliminary experiments have been carried out at 2.1T, 42MHz in dipole phasing. The predicted single-pass damping for this case, given the low initial temperature, was  $\sim 5\%$ ; rising to 5% - 10% at the end of the ICRF pulse. Gamma ray radiation has been monitored to assess possible absorption by ions at  $3w_{\text{CD}}$  and consequent tail formation. No significant gamma ray emission has been measured, thereby excluding the presence of a high energy deuterium tail and eliminating a possible competing mechanism for the direct electron damping. Absorption at  $w_{\text{CD}}$ , located at  $\sim 0.7\text{m}$  off-axis on the high field side is estimated to be  $\sim 10\%$ , with no hydrogen tail formation expected [16]. The fast decrease of the central electron temperature at the ICRF switch-off suggests that direct electron damping of the fast wave is a non-negligible heating mechanism for this scenario.

Further studies of FW direct electron heating and current drive scenarios are planned for the remainder of the experimental campaign. Priority will be given to the high frequency scenarios, where higher ICRF power is likely to be available.

### Toroidal Alfvén Eigenmodes Excitation

The new active diagnostic for Alfvén eigenmodes, combining excitation by external antennae with coherent detection of various probing signals at the plasma edge and in the core, became operational during 1994. This method provides a direct measurement of the damping rates of the Alfvén eigenmodes in various plasma conditions, and, therefore, should permit an identification of the different damping mechanisms, which will determine the instability threshold of the Alfvén eigenmodes in reactor relevant plasma conditions.

The saddle coils are used as external antennae to excite the Alfvén eigenmodes. The exciter and detection systems cover the frequency range from 20 to 500kHz, including BAE, TAE and EAE. The exciter system comprises a function generator, a 3kW power amplifier, an impedance matching network, a power splitter and an isolation unit. The power distribution unit can drive 1, 2 or 4 saddle coils, allowing different combinations of antenna phasing which can preferentially excite specific low toroidal mode numbers ( $n$ ) and poloidal symmetry. The diagnostic method is based on repetitive sweeps of the driving frequency across the Alfvén continuum gap range. The driven component in the plasma response is extracted from background noise in various diagnostic

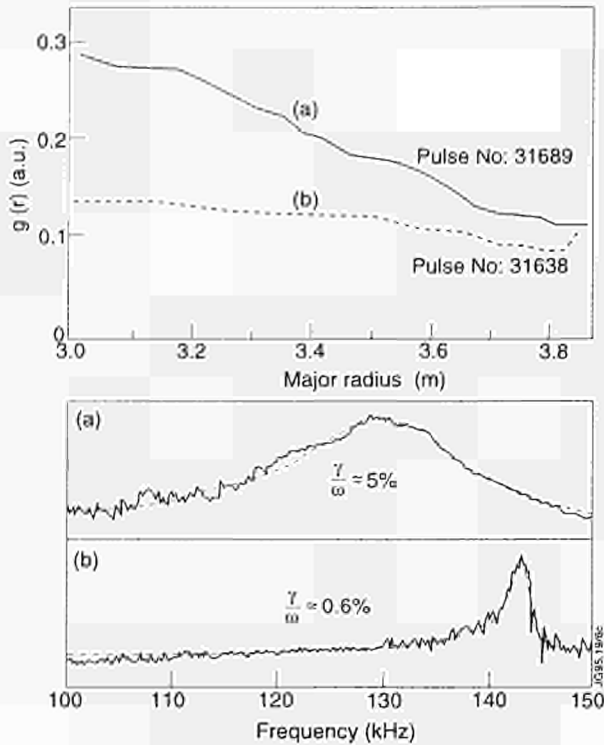


Fig.189: The relationship between the profile of  $\gamma(r)=1/(q(r)r(r)l/2)$  and the damping of TAE modes

signals using a set of synchronous detectors which provide the in-phase and quadrature components of the signals. Several probing channels are considered; the voltages induced on the unexcited saddle coils and the poloidal pick-up coils measure the perturbation of the radial and poloidal magnetic fields at several locations, allowing a mode analysis in the poloidal and toroidal conjugate plane. Fig. 188 shows an example, in which the toroidal magnetic field was varied from 2.2 to 3.0T, other parameters being held constant. The measured frequency agrees well with  $f_0(\text{TAE})$  evaluated assuming  $q=1.5$ , and using the line-averaged plasma density ( $n_l$ ) for calculating  $V_A$ .

The driven resonances toroidicity induced Alfvén eigenmodes. Damping of the TAE modes can be caused by several mechanisms. Firstly, continuum damping occurs when the eigenmode frequency intersects a shear Alfvén wave continuum within the plasma. As the gaps are centred at the local value of  $f_0(\text{TAE})$ , continuum damping is linked to the radial dependence of the quantity  $g(r)=1/(q(r)r(r)l/2)$ , where  $r$  is the minor radius of the magnetic surfaces on the tokamak mid-plane. Greatly differing damping rates were measured in similar discharges with different  $g(r)$ . Two examples are shown in Fig 189, where  $g(r)$  is shown together with the two measured eigenmodes and their damping rates. When there was a strong radial

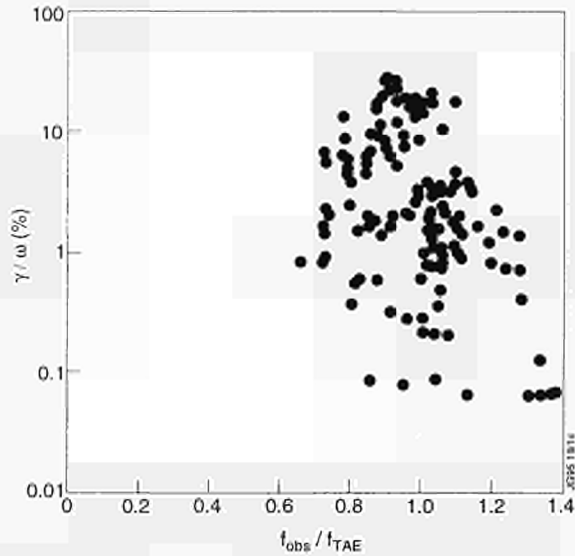


Fig.190: The measured damping rate plotted against the eigenmode frequency normalised to  $f_0(\text{TAE})$  ( $q=1.5$ ), for a series of ohmic discharges.  $1\text{MA} < I_p < 3\text{MA}$ ,  $1 \times 10^{19}\text{m}^{-3} < n_l < 5 \times 10^{19}\text{m}^{-3}$ ,  $1\text{T} < B_t < 3\text{T}$ ; all points correspond to excitation with one saddle coil, peaked at  $|n_l|=1$

dependence of  $g(r)$  (Fig.188(a)), the gaps were not aligned through the continuum structure and strong continuum damping occurred. The  $g(r)$  profile in Fig.188(b) was flatter and led to a more “open” gap structure and therefore to a much less effective continuum damping. The absorption mechanism in this case be sought in the kinetic interactions, such as ion and electron Landau damping. Ion Landau damping is negligibly small for the ohmic discharges considered, whereas for these relatively cold and dense plasmas,  $\omega\tau\eta_{ij} \sim V_A$  and thus electron Landau effects can contribute significantly to the damping. Kinetic damping can also be produced by trapped electron collisional absorption, occurring during the transition from trapped to passing orbits, caused by collisional pitch-angle scattering, or by radiative damping, a finite Larmor orbit effect of the bulk ions leading to a damping rate which is exponentially dependent on the magnetic shear and the poloidal mode number. An overview of the wide variation of the measured damping rates is shown in Fig.190 for ohmic plasmas and with an excitation spectrum dominated by  $l=1$ .

The measured values of  $\gamma/\omega$  span several orders of magnitude, suggesting that different absorption mechanisms must be dominant in different plasmas according to the configuration of each specific shot. A preliminary comparison with theory indicates that even in the case of flat  $\gamma(r)$  profiles, the measured  $\gamma/\omega$  is at least a factor of two larger than that calculated by local models consider-

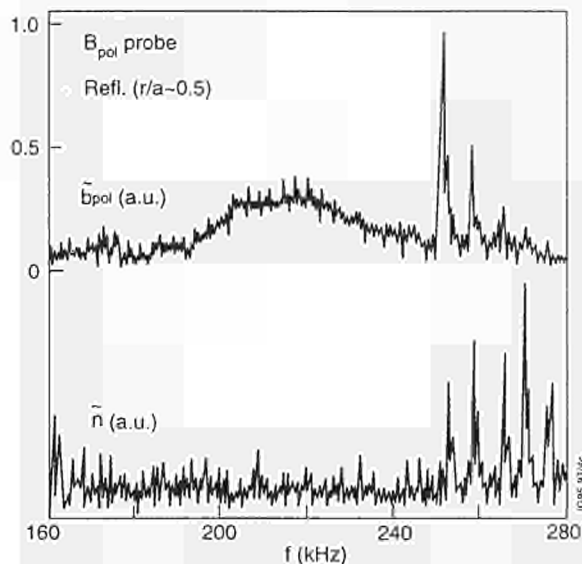


Fig.191: Example of multi-peak structure at  $f > f_{UH}$  (TAE) with additional heating (6MW ICRF). Peaks appear in the magnetic probe at the edge (top) and in the reflectometer signals, inside the plasma (bottom);  $B_1 = 3.3T$ ,  $I_p = 3MA$ ,  $n_e = 3 \times 10^{19} m^{-3}$

ing electron Landau and collisional damping. Contributions from either continuum damping at the plasma edge or by radiative damping in the core must therefore be significant. Preliminary TAE studies have been undertaken in the presence of additional heating, to extend the parameter range for the spectrum and damping measurements and to assess the driving effects in the presence of resonant fast particles. A reduction in the total  $\gamma$  of driven stable TAE modes was observed when high energy NBI at low B-field produced resonant particles, consistently with the predicted appearance of a finite mode growth rate. NBI heating for B-fields higher than 1.5T, ICRF at intermediate power and LH heating allowed investigations in absence of resonant particles, aimed at determining the TAE spectrum characteristics and the relative importance of the various damping mechanisms in regimes closer to reactor relevant conditions. In particular, high frequency resolution measurements have shown a sudden change in the excited AE spectra as the plasma temperature and b were increased by additional heating. Simple single peak structures were replaced by several very weakly damped peaks at frequencies corresponding to the lower part of the continuum above the TAE gaps. These spectra, of which one example is shown in Fig.191, could represent the first experimental observation of kinetic TAE, which are postulated to affect the performance of future ignition experiments.

## References

- [1] F. Troyon, et al., Plasma Phys. Control. Fusion 26 (1984) 209.
- [2] C. D. Challis, et al., Nucl. Fusion 33 (1993) 1097.
- [3] P. N. Yushmanov, et al., Nucl. Fusion 30 (1990) 1999.
- [4] R. J. Goldston, et al., J. Comput. Phys. 43 (1981) 61.
- [5] C. Gormezano, Plasma Physics & Controlled Nuclear Fusion Research 1994 (Proc. 15th Int.Conf. Sevilla, 1994)
- [6] F.X. Söldner, et al., 21st Europ. Conf. on Contr. Fusion & Plasma Physics, Montpellier 1994, Vol.II, 1126.
- [7] H. A. Holties, et al., 21st Europ. Conf. on Contr. Fusion & Plasma Physics, Montpellier 1994, Vol.I,234.
- [8] Y.F. Baranov, et al., 20th Europ. Conf. on Contr. Fusion & Plasma Physics, Lisbon 1993, Vol.III, 881.
- [9] F.X. Söldner, JET Team, Plasma Physics & Controlled Nuclear Fusion Research 1994 (Proc. 15th Int.Conf. Sevilla, 1994) IAEA-CN-60/A-3/I/2
- [10] ITER Task Report IVA-LH (1994), to be published.
- [11] F. Rimini, Plasma Physics & Controlled Nuclear Fusion Research 1994 (Proc. 15th Int.Conf. Sevilla, 1994)
- [12] V. Bhatnagar, J. Jacquinet, NET Report 103 EUR-FU/XII/163/94 (1994)
- [13] D.F.H. Start, et al., Nucl. Fusion 30 (1990) 2170
- [14] R. Majeskij, et al., Plasma Physics & Controlled Nuclear Fusion Research 1994 (Proc. 15th Int.Conf. Sevilla, 1994) IAEA-CN-60/A-3-I-4
- [15] B. Saoutic, et al., Plasma Physics & Controlled Nuclear Fusion Research 1994 (Proc. 15th Int.Conf. Sevilla, 1994) IAEA-CN-60/A-3-I-6
- [16] L-G. Eriksson, et al., Nucl. Fusion 33 (1993) 1037

## Transport and Fluctuations

During the year, progress was made on the study of both the low (L-mode) and high (H-mode) confinement regimes. From the analysis of experiments of the new campaign, and of the previous ones, it was shown that radial transport coefficients across the plasma promptly react to modifications occurring at the edge of the discharge **before** any substantial variation in the local density and temperatures occurs. Analysis of various

H-mode scenarios has shown that the reason for the different performance achieved in the various discharges can be ascribed to the levels of impurity radiation, as well as to the density- and power deposition-profiles, rather than to differences in transport properties.

The dependence of the power threshold for the L- to H-mode transition on operating parameters was extensively studied by comparing the results from previous campaigns with those obtained in the new configuration. Also the old database was systematically extended in dedicated experiments and a clear dependence of the threshold value for the net power flowing through the separatrix on the plasma density was established.

A considerable effort is being devoted in the present phase to transport studies on helium and other light impurities. This activity started in 1994 with gas-puff experiments. Significant progress is also reported, in the following account: on the study of transport of intrinsic impurities in high performance discharges; and on the technique used in the analysis of laser ablation injection experiments.

**Physics of L and H-mode Confinement**

It has been shown [1], that all perpendicular transport coefficients (electron and ion thermal diffusivities  $\chi_e$  and  $\chi_i$ , plasma diffusion coefficient D and perpendicular viscosity  $\eta$ ) in JET fell over a very wide radial region ( $0.5 \leq r/a \leq 1$ ) in a very short time scale ( $\Delta t \leq 3\text{ms}$  for  $\chi_e$ ) at the L-H transition. A possible explanation is that plasma turbulence is correlated in radial direction by the plasma toroidicity [2]. Therefore, any modification of the anomalous transport coefficients (at L-H and H-L transitions and during ELMs) could propagate across the magnetic field with the group velocity of plasma turbulence (which is much faster than the velocity of heat pulse propagation). This idea has been tested by the numerical simulation of the evolution of plasma parameters during L-H transitions, ELMy and ELM-free H-mode scenarios. Results of this analysis support this idea and allow development of transport models, which can describe the evolution of plasma parameters in L-, ELM-free and ELMy H-modes.

The evolution of electron ( $T_e$ ) and ion temperatures ( $T_i$ ) was simulated with the following model for electron and ion thermal diffusivities:

$$\chi_e = \alpha_e \frac{c \nabla(nT_e)}{eBn} a q^2, \quad \chi_i = \chi_i^{neo} + \alpha_i \frac{c \nabla(nT_i)}{eBn} a q^2 \quad (1)$$

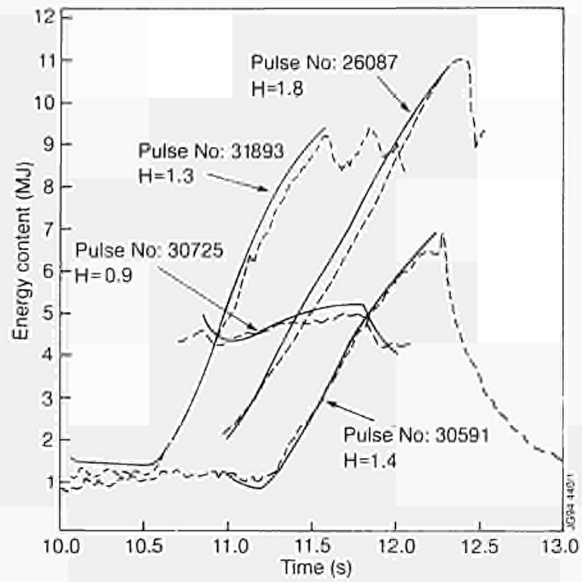


Fig.192: Time evolution of the total measured plasma energy content and that calculated with the model during the ELM-free H-mode phase for four JET discharges. The quantity H is the ratio of experimental energy confinement time to the JET-DIHD H-mode scaling for that time.

where  $\chi_i^{neo}$  is the ion neoclassical thermal conductivity and the second term on the right hand side of  $\chi_e$  and  $\chi_i$  is an empirical Bohm-like coefficient, proposed and used [3] to reproduce L-mode confinement in JET. Numerical analysis shows that the coefficients  $\alpha_e$  and  $\alpha_i$  should be chosen so that  $\alpha_i^L = 3\alpha_e^L = 9.9 \times 10^{-4}$  to fit JET L-mode discharges. Previous analysis [4] shows that the fast modification of electron temperature during the L-H transition only can be reproduced if it is assumed that both  $\chi_e$  and  $\chi_i$  are changed everywhere and not only near the separatrix. The best agreement with old and new JET shots was achieved if it was assumed that  $\alpha_e$  and  $\alpha_i$  were reduced from  $\alpha_i^L = 3\alpha_e^L = 9.9 \times 10^{-4}$  in L-mode to  $\alpha_i^H = 3\alpha_e^H = 0.54 \times 10^{-4}$  in H-mode plasma. New boundary conditions for  $T_e$  and  $T_i$  were used in the analysis, which corresponded to an assumption that the longitudinal heat flux in the SOL was proportional to the particle flow:  $\chi_{e,i} n \nabla T_{e,i} |_{r=a} = \beta_{e,i} D \nabla n |_{r=a}$  where  $D = \chi_e \chi_i / (\chi_e + \chi_i)$  and  $\beta_e \sim \beta_i \sim 0.3$  are numerical parameters. These boundary conditions allow the formation of the temperature pedestal to be reproduced, which emerges after the L-H transition. In the analysis, it was attempted to quantify the difference between local energy transport in hot-ion VH-mode and ELM-free H-mode.

To illustrate these points, the best hot-ion Pulse No:26087 ( $B_t=2.8\text{T}$ ,  $I_p=3.2\text{ MA}$  and  $P_{NBI}=14\text{MW}$ ) from the previous campaign and three ELM-free

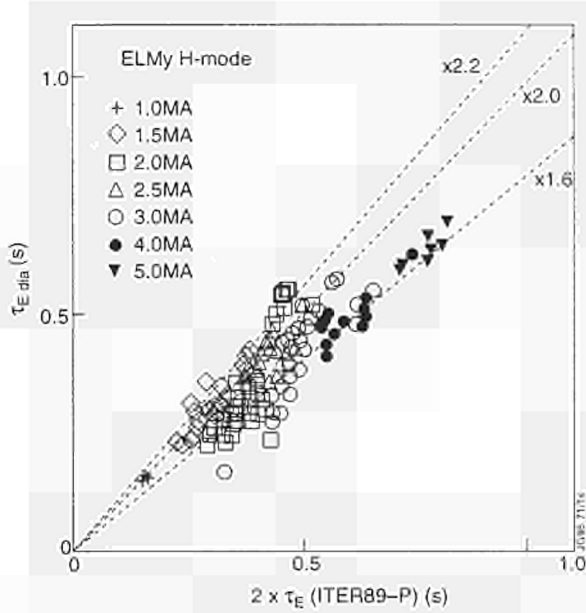


Fig.193: Measured diamagnetic energy confinement time ( $\tau_{E,dia}$ ) for 1994 JET ELMy H-mode dataset versus twice the prediction from ITER89-P scaling law ( $\tau_{E,ITER89P}$ ). Data selected are in quasi-steady-state ( $dW_{dia}/dt < 0.1P_{tot}$ )

H-modes from the current campaign: Pulse Nos:30591 ( $B_1=2.8T$ ,  $I_p=2.5$  MA and  $P_{NBI}=15$  MW), 30725 ( $B_1=2.3T$ ,  $I_p=3$  MA and  $P_{NBI}=7$  MW) and 31893 ( $B_1=2.8T$ ,  $I_p=4$  MA and  $P_{NBI}=18$  MW). The temporal evolution of the total measured plasma energy content and that calculated with the model during the ELM-free H-mode phase for all discharges are shown in Fig.192. These showed that, within experimental accuracy, all these pulses could be fitted with the same transport coefficients. The main differences between VH and ELM-free H-mode was not in transport properties but in the impurity radiation (the H-mode accumulated impurities much faster than the VH mode), power deposition profiles (centrally peaked for VH-mode and flat or even hollow for H-modes) and different levels of convective losses. This conclusion was recently confirmed by a TRANSP analysis.

Finally, the transport model was used for numerical simulation of the giant ELMs. The idea was to find the radial and temporal distribution of enhanced transport during giant ELMs and the magnitude of  $\alpha_p$  and  $\alpha_i$  increased. The analysis showed that giant ELMs in JET also have a global character and can be modelled as a temporary H-L transition triggered by an MHD event, during which at least electron thermal diffusivity is increased up to the level larger than those suitable for modelling of the L-mode phase.

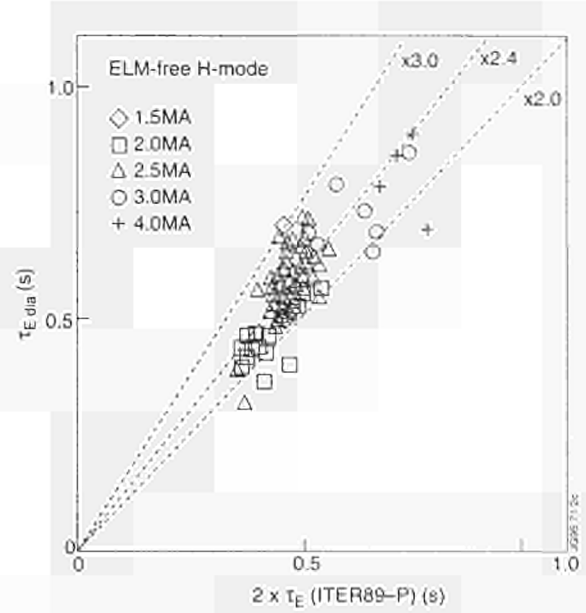


Fig.194: As for previous figure, but for 1994 ELM-free H-modes with  $\tau_{ELM-free} > 0.5$  s. Data selected have  $dW_{dia}/dt < 0.4P_{tot}$

### Confinement in ELM-free and ELMy H-mode Regimes

In previous operation, ELMs were rarely encountered in the H-mode and were only observed either just above the L-H transition threshold; with extremely strong gas puffing; at high  $\beta$  or with hydrogen plasmas. In the high recycling conditions, the ELMy H-mode is the standard. Long ELM-free periods ( $>1$  s) can only be obtained with special preparation. ELMs have the characteristics of 'giant' ELMs identified on other machines such as DIII-D and ASDEX-U. These include an ELM frequency which increases with input power and reduces with current.

An overview of the confinement enhancement in JET ELMy and ELM-free H-modes is shown in Fig.193 and Fig.194. The data are plotted against the predictions of the ITER89-P L-mode scaling law, as these are measurements for the total stored energy. The fast particle content of the diamagnetic energy ( $W_{dia}$ ) ranges from  $\sim 20\%$  for the high power discharges at 1.5 MA to  $< 5\%$  for the high power 4 and 5 MA plasmas. The dataset average is  $\sim 10\%$ .

In Figs. 193 and 194, the measured diamagnetic energy confinement time ( $\tau_{E,dia}$ ) is plotted against the prediction from the ITER89-P law ( $\tau_{E,ITER89P}$ ). It may be seen that the bulk of the data lies in the ranges

$$1.6 \times \tau_{E,ITER89P} < \tau_{E,dia} < 2.2 \times \tau_{E,ITER89P} \quad (\text{ELMy})$$

and

$$2.0 \times \tau_{E,ITER89P} < \tau_{E,dia} < 3.0 \times \tau_{E,ITER89P} \quad (\text{ELM free})$$

The ELMy dataset is dominated by steady-state and quasi-steady-state discharges ( $dW_{dia}/dt \sim 0$ ). The ELM-free dataset is not in steady-state, but a limit of  $dW_{dia}/dt < 0.4P_{in}$  has been applied. This confinement is generally maintained up to high values of loss power.

The small confinement advantage of the ELM-free over the ELMy H-mode is still under investigation, but may be due to a combination of poor deposition profiles and high recycling, which are encountered in this dataset. The exception to this is the good performance of the Hot-Ion H-modes with  $H_L \equiv \tau_{E,dia} / \tau_{E,ITER80P} > 2.4$ .

The limitations in the duration of the ELM-free periods have been especially severe at low current values. Consequently, the elevated confinement values relative to L-mode ( $H_L > 3$ ) achieved in the 1991/2 campaign have not yet been repeated. The ELMy discharges obtained have confinement approximately equal to the JET/DIII-D H-mode scaling law and, as a result, the 'efficiency' of achieving high  $\beta_p$  is now much lower. Nevertheless, values of  $\beta_p = 2.55$  have been recorded with combined NBI and ICRF power at IMA, and the discharges in the new configuration are not transient but present 'quasi-steady-state' conditions for 5-10 energy confinement times.

The confinement enhancement in the H-mode does not increase with  $\beta_p$  for the ELMy plasmas. In marked contrast to the results obtained in JT-60U, confinement appears to degrade as  $P^{0.5}$  in this dataset. There does appear to be some marginal gain in confinement enhancement with increasing  $\beta_p$  for discharges which have achieved longer ELM-free periods in JET. These latter discharges were performed in a double-null configuration.

**TRANSP Predictions and Analysis**

Investigations on transport have concentrated on high performance pulses where improved energy confinement and high neutron yields can be achieved (hot-ion H-modes). Local power balance analysis performed with the TRANSP code on these discharges shows that a significant improvement of the heat transport occurs in the bulk of the plasma immediately after the transition from L- to H-mode. At that time, the effective thermal conductivity,  $\chi_{eff}$ , falls by a factor  $\sim 3$  in the core of the discharge and then remains low ( $\chi_{eff} < 0.5 m^2/s$  for  $\rho < 0.5$ ) as the stored energy increases by a factor  $\sim 4$  [8].

JET pulses performed at the beginning of the new experimental campaign with higher  $Z_{eff}$ , broader density

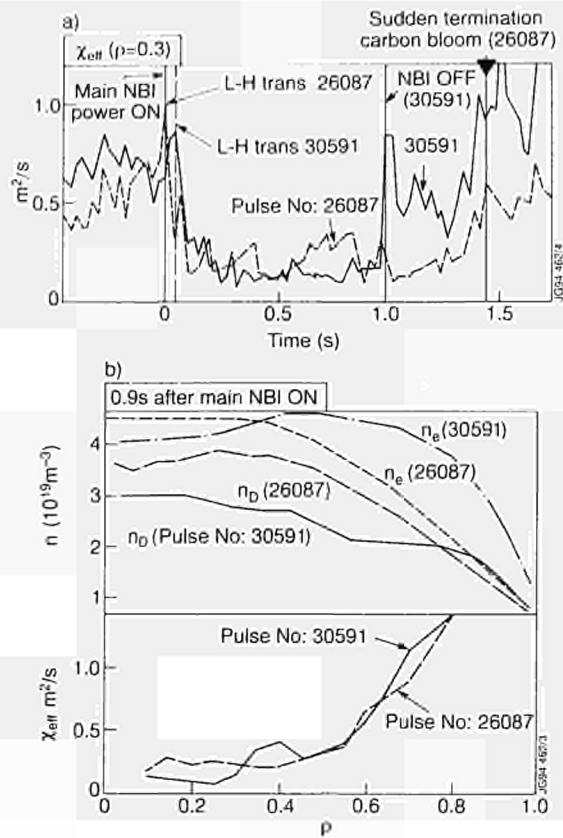


Fig.195: (a) Time evolution of  $\chi_{eff}(\rho=0.3)$  for two hot-ion discharges. Time is measured from application of the main neutral beam power; (b) Electron and deuteron density profiles during ELM-free phases for the above discharges; also shown are profiles of  $\chi_{eff}$  during the ELM-free phase

profiles and different edge fuelling rate appear, over the whole radial range where the local transport analysis is reliable ( $\rho \sim 0.2 - 0.75$ ), to have the same  $\chi_{eff}$  as higher performance pulses obtained during the previous campaign (Fig.195).

The TRANSP code has also been used in a predictive mode to assess the possible fusion performance of the future plasmas fuelled with a 50:50 mixture of D and T and the effect of alpha-particle heating on  $T_e$  and  $T_i$  [5]. These predictions are based on the best hot-ion H-mode D-D (Pulse No:26087) obtained during the 1991-92 campaign (single null, 2.8 T, 3.1 MA). These show that, if the very high confinement phase of tested discharges can be prolonged and providing the density and the impurity influxes can be controlled, a  $Q_{DT} \sim 1$  steady-state plasma can be achieved with significant alpha-particle heating. Furthermore, if MHD instabilities can be avoided at higher plasma currents ( $\sim 6.3$  MA), using a higher toroidal field ( $\sim 3.5$  T), to keep a reasonable  $\beta$  value, and if the

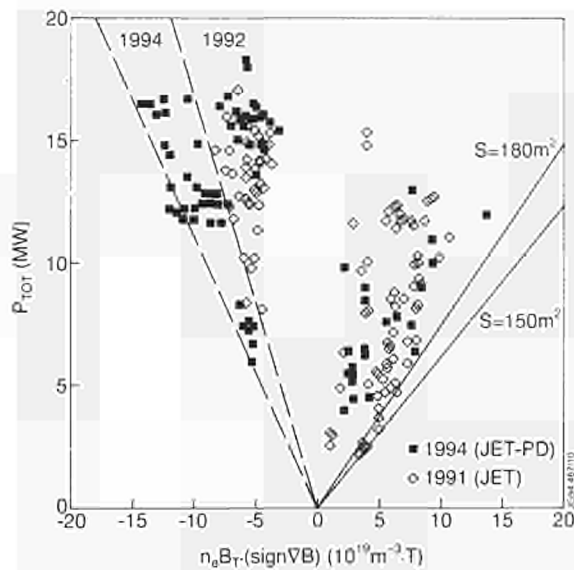


Fig.196: Existence diagram for 1994 JET-PD H-modes compared to 1991/92 data for carbon target, for positive and negative  $\nabla B$  against total input power in the discharge. Lines for the positive  $\nabla B$  data represent the scaling  $P_{th} = 0.004 n_e B_T S$  with  $S$  (plasma surface area) values shown

confinement scales as  $1/I_p$ , then a higher performance steady-state plasma, with  $Q_{DT} > 2.5$ , should be possible. The alpha-particle heating power of 4.9MW would lead to a 74% increase in  $T_e$ . Furthermore, if the energy confinement improved with the atomic mass number, even better fusion performance might be expected.

### The H-mode Power Threshold

During 1994, the analysis of the H-mode power threshold database from the 1991/92 campaign has been completed [6], and part of it has been incorporated into the international power threshold database. The important features of the 1991/92 database include the difference between discharges in double-null (DN) and single-null (SN) configurations, the latter with the ion  $\nabla B$  drift directed both towards (positive) and away (negative) from the target plates. The results of the analysis show that with both positive and negative ion  $\nabla B$  drift, the power threshold  $P_{th}$  scales linearly with the toroidal magnetic field  $B_T$ , while there is a weak positive dependence on plasma current, X-point position, and distance of the last closed flux surface from the limiter [6]. With positive ion  $\nabla B$  drift,  $P_{th}$  is in agreement with the  $n_e B_T$  scaling proposed by the H-mode Database Working Group [7], where  $n_e$  is the line averaged plasma density. With negative ion  $\nabla B$  drift, NBI heating and CFC target plates, the threshold as a function of  $n_e B_T$  is twice as high as that with positive ion  $\nabla B$  drift (Fig. 196).

However, a significantly lower threshold is found with RF heating alone and beryllium target tiles.

The data obtained in the present experimental campaign are characterised by both positive (co-injected NBI) and negative (counter-injected NBI) ion  $\nabla B$  drift on a type of CFC target plates different from that used in 1991/92, and by NBI, ICRH or combined heating. These substantially confirm the conclusions drawn from the 1991/92 database with both directions of the ion  $\nabla B$  drift.

Finally, in collaboration with the ITER Confinement Data Base and Modelling Expert Group and with the DIII-D Team, an experiment has been carried out for the first time to establish the power threshold over as wide a range as possible of densities and magnetic fields. The experiment has been carried out under carefully controlled conditions, with a constant edge safety factor  $q_{95} = 3$  and at 1MA/1T, 2MA/2T, 3MA/3T, and stepping up the NBI power in concert with the rise of density. For all three configurations, the threshold has been established, and for the first time it has been proven beyond doubt that a strong positive dependence, possibly linear, exists on the plasma density. Analysis of this new dataset is in progress.

### Analysis of Cold Pulses produced by Impurity Injection

Non-recycling metallic impurities have been injected to study the time evolution of the temperature profile due to increased edge radiation produced by these impurities as they enter the plasma periphery. Mo, Ni, and Al were ablated from a glass substrate by means of a ruby laser. The total impurities reaching the plasma scrape-off layer were estimated to a few  $\times 10^{18}$  particles/pulse. Although the laser pulse is very short ( $\sim 10$ ns), the influx of injected impurities at the plasma edge lasted a few milliseconds due to the spread in the time of flight of the ablated particles. Fig197 shows the visible light emission monitored on a line of sight coincident with the particle path.

Particular attention has been devoted to the temporal relation between temperature drop in the bulk plasma and that at the plasma periphery, since the cold pulse appears to propagate from the edge to the plasma centre on a time scale ( $\Delta t \leq 4$ ms) much faster than the typical diffusive times. Similar effects have been observed both in Ohmic and H-modes: these closely resemble the phenomena following the edge perturbations produced by giant ELMs.

Analysis with the JETTO transport code and with HPDIFFU (performed by the CNR Plasma Physics Insti-

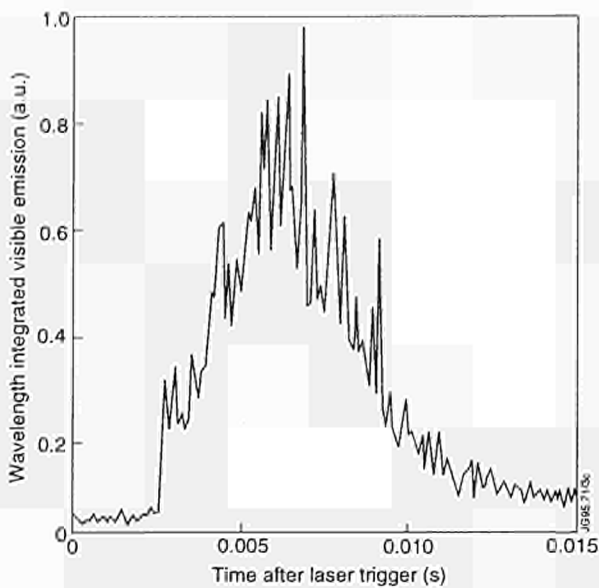


Fig.197: Visible light emission during laser blow-off injection of Ni. The emission is monitored along a line-of-sight coincident with the particles flight path

tute of Milan, Italy) indicates that, in order to explain the experimental evolution of the temperature profiles following the initial edge perturbation, a rapid increase of the thermal diffusivity  $\chi_e$  is required also at radial positions where no appreciable modifications of the local plasma parameters have yet taken place [8]

Figure 198 shows the time evolution of the electron temperature, measured with the new multi-channel electron cyclotron emission radiometer, at different radial positions. It can be seen that a prompt change of the  $T_e$  time derivative occurs over a very wide radial range. At intermediate radii (near field region:  $\rho \approx 0.6$  to  $\rho \approx 0.8$ ), the rapidity of the response to the edge perturbation is seen to decrease moving inwards, while further in (far field region:  $\rho < 0.6$ )  $dT_e/dt$  does not vary appreciably with the radius. This is also in agreement with the hypothesis of a fast  $\chi_e$  increase over a wide plasma range. In fact, the rapidity of the perturbations on  $T_e$  due to diffusive propagation is expected to decrease exponentially moving away from the source of such perturbation as observed in the near field. In the far field, where the diffusively propagating cold wave is progressively vanishing, the observed perturbation mainly consists of the response to the sudden modification on  $\chi_e$  and, therefore, its radial variation is much smaller. Radial analysis of the Fourier transformed temperature perturbation [9] also confirms the global behaviour of the radial propagation of such cold pulses [8].

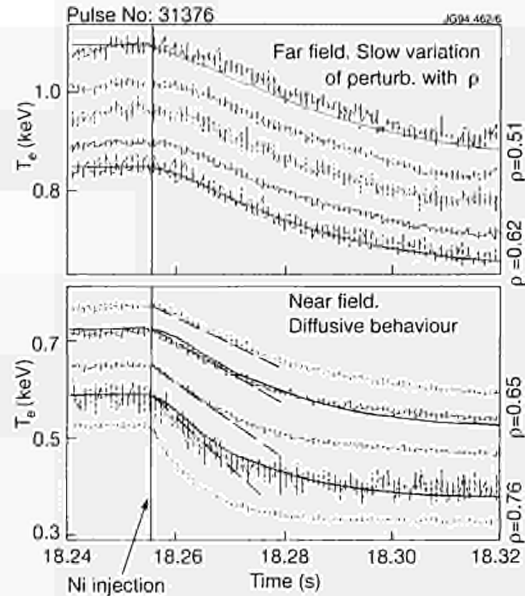


Fig.198: Time evolution of electron temperature at different radii following injection of Ni in an ohmic discharge. Solid lines are simulation of phenomena using the transport model

### Experimental Transport Data derived from Gas-puffing Experiments

Controlled transients in low-Z impurity density profiles caused by short gas-puffs introduced either in the divertor region or in the torus mid-plane allow the experimental deduction of diffusive and convective terms, which describe the perturbation and the subsequent relaxation of impurity density profiles. Several experiments were carried out in the 1994/95 experimental campaign including helium, neon and nitrogen edge gas-puffing. Neon and nitrogen were primarily added as an active agent for radiation cooling processes in the divertor. The main emphasis of low-Z transport experiments was directed, in particular, in view of its importance for future fusion ash control, towards investigation of the behaviour of helium. Two aspects of helium transport have been studied. The first, is the deposition of alpha-particles in the plasma core using neutral helium beam injection and the second type of experiments is edge gas-puffing, as described here.

Diffusion coefficients and convective velocities may be derived from particle flows and density gradients measured during the period of density perturbation following a brief plasma edge gas-puff. Neglecting source and sink terms, which is justified for core radii ( $\rho < 0.9$ ) and ion temperatures well above 1keV, values for diffusion  $D$  and convection velocity,  $v$ , may be derived from a plot of normalised particle flow versus normalised gradients ( $\Gamma_z/n_z = -D(\nabla n_z/n_z) + v$ ).

The key issue for particle transport experiments is the deduction of local particle densities from spectroscopic measurements. Therefore, the entire chain starting from the measurement of absolutely calibrated spectra (photons), the interpretation of spectral features, the accurate assessment of local donor densities (that is electrons, ions or neutrals), and finally the deduction of local impurity ion densities has been pursued. The most challenging part of this process is the verification of each stage by comprehensive consistency checks making use of complementary diagnostics.

Active charge exchange spectroscopy has proven to be the main tool providing access to local impurity density data. In the case of thermal and non-thermal alpha-particle diagnostics, substantial progress was achieved over the last decade in terms of atomic data, understanding of excitation processes, evaluation of spectra etc. In parallel with this activity, a significant number of supporting diagnostic techniques were also considerably refined providing for example reliable and highly resolved data on electron temperatures and densities, magnetic fields, etc..

In spite of this major effort, the present status of the analysis chain, leading eventually to the deduction of helium density data, is far from unambiguous or satisfactory in terms of data quality required for the deduction of local gradient and particle flows. Moreover, many of the standard consistency checks (e.g. comparison of temperatures), turn out to be irreconcilable with complementary diagnostics (X-ray spectroscopy  $\text{Ni}^{26+}$  temperatures, other low-Z impurity CX temperatures, or electron temperatures). Obviously, the deduction of density values of fully stripped helium can only be accepted as a viable quantity when its associated temperature value, which is derived from the same velocity distribution function, can be verified by independent diagnostics. The experience gained on all major fusion devices is that ion temperatures deduced from CX helium spectra are notoriously too low. The reasons for this discrepancy have been identified. One source of ambiguity in the spectral analysis is passive charge exchange emission at the plasma separatrix, and the second is the 'plume effect' introduced by singly ionised helium atoms moving from cooler plasma regions into the observation path. The addition of these features lead to errors which affect deduced temperature values and density gradients. In particular, this is the case for the core region ( $r < 0.5$ ) where, for example, simulation calcu-

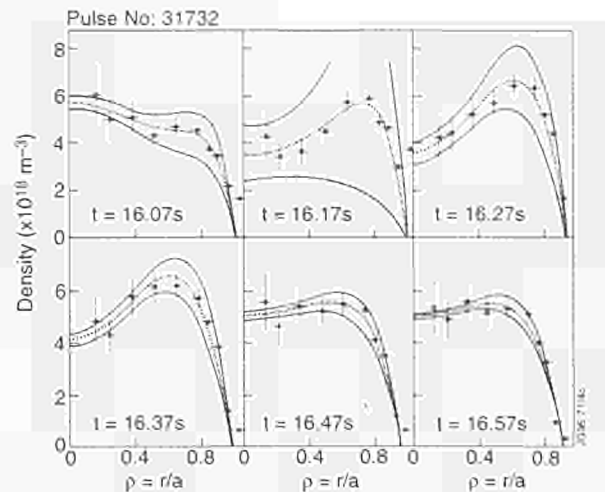


Fig.199: Radial helium density profiles following a 100ms gas puff at 16.1s into a cryo-pumped ELMy H-mode phase

lations predict up to 25% of the observed CX intensity being due to a helium 'plume'.

Systematic uncertainties in deduced helium densities are also introduced by errors in the electron density, magnetic field configuration, geometry and uncertainties in the actual impurity composition. The factors affect the calculation of the local neutral beam density and hence the radial gradient of the deduced helium density profile. Again the core region, and, therefore, core transport data, are most affected by the exponential error propagation along the beam path into the plasma core.

The main instrumental errors affecting directly transport data are errors in the relative calibration of each radial channel (the CX diagnostic uses up to 11 channels for the reconstruction of a radial density profile). To overcome the instrumental graininess of the profile, smooth functions (polynomial, spline, analytical) are fitted to experimental data. Similar smoothing procedures are also applied for the deduction of time derivatives.

The characteristic behaviour following a short (100ms) He puff into the plasma in a H-mode may be described by an instantaneous increase and subsequent fast decay at the outermost channels, and a slow increase at the plasma centre reaching steady-state after 300-500ms. The radial profile change from a flat to parabolic profile before the puff, to a distinctively hollow profile immediately after the puff and finally to steady-state profiles, which are similar to the electron density profile (Fig.199). The error bars on the experimental data include both statistical and systematic errors. The error propagation for gradients and particle flows as deduced from the spline fits are shown in

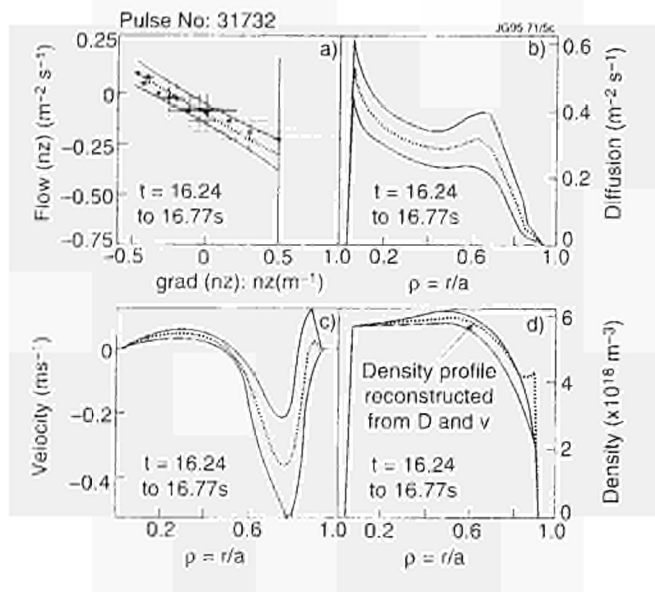


Fig. 200: (a) Deduction of transport data from  $G(n_z)/n_z$  versus  $\nabla(n_z)/n_z$ , (b) and (c)  $D$  and  $v$  profiles, (d) steady state reconstruction of density profiles from  $D/v$  integration

Fig.200 together with values for  $D$  and  $v$  as derived from the slope and interception of flow versus gradient.

### ITER JET DIII-D Scaling Experiments

The plasma cross-section envisaged for ITER shows strong resemblance's to the geometries that can be produced in JET and DIII-D. Therefore, it is possible to carryout experiments on both JET and DIII-D in which dimensionless parameters describing the plasma have the same values as intended for ITER. There may be 15-20 dimensionless parameters, but only a handful are found to have an impact on confinement. These variables are:

1. Normalised Larmor radius,  $\rho^*$ ;
2. Normalised collisionality,  $n^*$ ;
3. Plasma beta,  $\beta$ ;
4. Shape parameters like elongation, triangularity;
5. Safety factor,  $q_w$ , and aspect ratio.

The only difference between ITER, JET and DIII-D lies in  $\rho^*$ . Therefore, confinement scaling with  $\rho^*$  is crucially important to predictions of ITER's performance. Such predictions must include (i) L-mode confinement, (ii) the threshold power and density values needed to obtain an H-mode, and (iii) H-mode confinement scaling.

H-mode  $\rho^*$  scaling experiments have been carried out in JET. Preliminary investigations indicate that the power scaling on JET is closer to Bohm scaling ( $P \sim \rho^{*-5/2}$ ) than gyro-Bohm scaling ( $P \sim \rho^{*-3/2}$ ). Since the ITER/JET  $\rho^*$  ratio is 0.25, the power prediction for a ITER H-mode

could be uncertain by a up to a factor 4, unless the joint JET-DIII-D experiments can pin down the scaling more accurately.

### Impurity Transport in High Performance Discharges

Long sawtooth-free periods of Hot-Ion (HI) and Pellet Enhanced Performance (PEP) discharges have been analysed [10]. Depending upon the time duration of these quiescent phases, the degree of peaking of density and temperature profiles and the level of collisionality, as well as the shape of the  $q$ -profile, the light impurities' behaviour assumes different characteristics. In PEP discharges, these accumulate towards the plasma centre, leading to various levels of depletion of the main plasma ions. On the contrary, in hot-ion plasmas, hollow impurity profiles are measured, without any significant dilution effects on the fuel reactants. In general, medium and high-Z impurities play only a minor role.

The total radiation loss in the centre (up to  $\sim 50 \text{ kW/m}^3$ ) is in all cases much smaller than the local heating power. Also, the large excursion observed sometimes in the effective ion charge on axis (e.g. from  $Z_{\text{eff}} \sim 1$  to  $Z_{\text{eff}} > 4$  in some PEP discharges) does not lead to an important decrease of electric conductivity, because of a compensating effect due to the concomitant electron temperature rise. So the impurity behaviour appears not to be the cause of the MHD events [11,12] that normally terminate PEP or hot-ion discharges, with the possible exception of cases close to marginal stability.

**For PEP H-mode discharges**, the time evolution of broad band soft X-ray and neutron emissivity profiles provide the clearest evidence of strong **central impurity accumulation** (which develops over a timescale of  $\sim 1$ s); when the neutron emission profiles decline and broaden, the soft X-ray radiation from the central region increases. VUV- and crystal-spectroscopy indicate that the plasma main contaminants in the central region are light impurities (C and Be). Very high central carbon concentration and strong central dilution of the main plasma ions ( $n_b(0) \leq 0.3n_c(0)$ ) are obtained for some PEP pulses (Fig. 201). Simulations show that the impurity transport in the plasma core ( $\rho \leq 0.4$ ) is dominated by inward convection ( $v \sim 1-2 \text{ ms}^{-1}$ ) with a reduced diffusivity ( $D \sim 0.1 \text{ m}^2 \text{ s}^{-1}$ ).

**Hot-ion discharges** have a low impurity content in the high performance phase. Heavy impurities are present only as traces and among low-Z impurities, carbon is

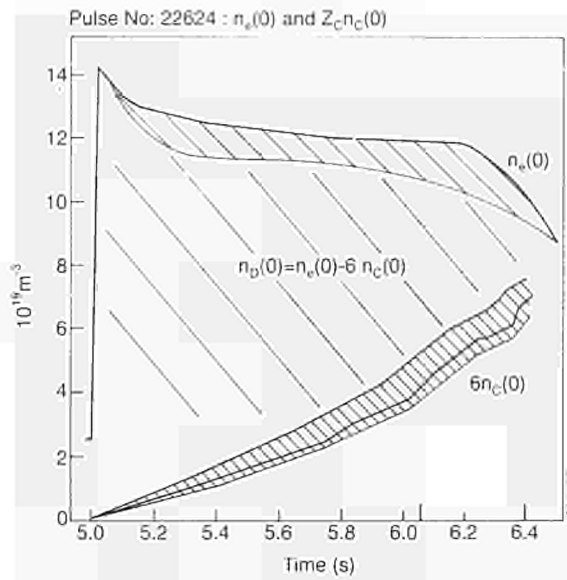


Fig. 201: Time evolution of central electron density,  $n_e(t)$ , of the central density of electrons accounted for by carbon ions (estimated from SXR emissivity). The difference represents an estimate of the central deuterium density,  $n_D(t)$

dominant. These pulses **do not show carbon central accumulation**, but the profiles observed by charge exchange spectroscopy are rather hollow. The carbon concentration in the plasma core ( $\rho \leq 0.4$ ) is about  $n_C/n_e \sim 1\%$ , with no major effects on the fuel dilution. The soft X-ray emissivity from the centre is an order of magnitude lower than in the PEPs (a few  $\text{kW/m}^3$  for HIs against a few tens of  $\text{kW/m}^3$  for PEPs); it can be accounted for mainly by bremsstrahlung radiation from the main plasma ions. The C transport in the central region is characterised in this case by a reduced diffusion ( $D \sim 0.1 \text{ m}^2 \text{ s}^{-1}$ ), but convection is smaller than in PEPs ( $v \sim 0.1 \text{ ms}^{-1}$ ) and directed outwards.

Due to the different plasma parameters in the two cases, during the PEP shots, C is well in the plateau collisionality regime, while it is in the banana regime during the HI pulses. In both cases, the predicted neoclassical diffusivity is low, of the same order as the observed values, but the neoclassical convection is expected to be very different in the two cases. In PEPs, where C is usually in the **plateau** regime, the neoclassical convection is  $v_c^{\text{neoc}} \propto [(\nabla n_D/n_D) + 1.3(\nabla T_e/T_e)]$ . In this case, the strong inward-directed term, proportional to  $(\nabla T_e/T_e)$  can allow the accumulation towards the centre to continue even after  $\nabla n_D$  changes sign, due to the depletion of deuterium ions. On the other hand, in hot-ion pulses, C is usually in the **banana** regime and  $v_c^{\text{neoc}} \propto [(\nabla n_D/n_D) - 0.3(\nabla T_e/T_e)]$ . In this case, the  $(\nabla T_e/T_e)$  term exhibits a slight screening

effect, inhibiting the accumulation for peaked T-profiles when  $\nabla n_D$  is small.

### Local Measurement of Transport Parameters for Laser Injected Trace Impurities

The local measure of transport parameters governing the radial propagation of particles in a tokamak discharge essentially amounts to measuring the density of those particles with adequate spatial and temporal resolution. For injected metallic trace impurities this depends on the possibility to deduce their density  $n_i(r,t)$  from the perturbation  $D_e$  induced by those impurities on the soft X-ray emissivity. However, the radiation coefficient  $Q_r$ , defined as the ratio of  $D_e$  to the product of  $n_i$  with the electron density  $n_e$  ( $Q_r = D_e / (n_i n_e)$ ), depends on the distribution of the injected impurity among the different charge states and is therefore a function of time, depending on the details of the transport of that impurity across the plasma. Due this, earlier attempts to deduce  $n_i$  from  $D_e$  by adopting for  $Q_r$  values appropriate for the coronal equilibrium [13] led to inconsistent determinations of the impurity diffusion coefficient  $D$  and convective velocity  $V$ : the experimental data  $D_e$  could not be reproduced using the obtained profiles of those parameters in transport simulations [14].

Based on this observation, a new procedure has been developed [15], where, using an initial guess,  $D^0(r)$  and  $V^0(r)$ , on the transport parameters profiles, first estimate,  $Q_r$ , of  $Q_r^{-1}(T_e, t)$  is worked out by running a simulation of the entire phenomenon,  $Q_r^{-1}(T_e, t)$  is then fed into the equation to obtain a first estimate of the density,  $n_i^{-1}(r, t)$ , and in turn of the transport parameters  $D^1(r)$  and  $V^1(r)$ . A new simulation is then run, using  $D^1$  and  $V^1$ , that leads to  $Q_r^2$ ,  $Q_r^{-2}$ ,  $D^2$  and  $V^2$ . In a few iterations convergence is reached.

This procedure intrinsically assures consistency of transport parameters with experimental emissivities. The error analysis, performed on a statistical basis, attributes to the different time slices and space points different weights according to the calculated uncertainties on the impurity fluxes  $\Gamma_i$  and on  $\nabla n_i$ . It shows that the most useful phase typically extends from 20 - 40ms to 100 - 200ms after the injection depending on the particular space point.

Analysis of impurity transport performed in this way essentially confirms results previously obtained with predictive analysis [16]. It also confirms the validity of the basic assumption that a diffusive/convective model is an adequate description of the impurity propagation in the

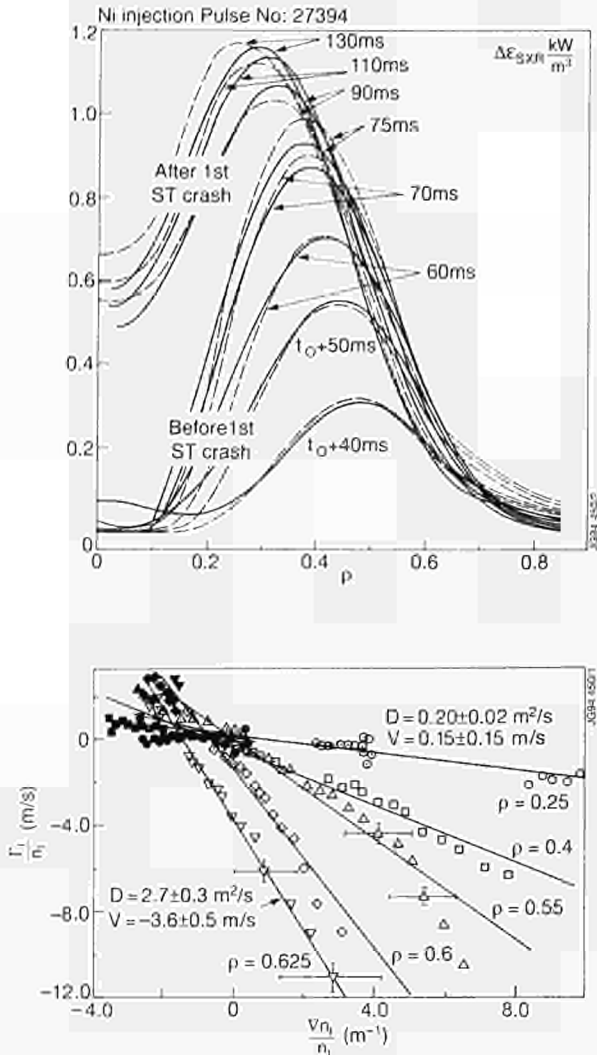


Fig.202: Measured (solid lines) and simulated (dashed lines) radial profiles of the perturbation to the soft X-ray emissivity  $D_{e,SXR}$  induced by the injection of Ni. Data refer to consecutive quiescent phases between sawtooth crashes (a). Local measurements of the transport parameters are obtained from linear regressions of the normalized Ni fluxes  $\Gamma_e n_e$  versus the normalized Ni density gradients  $V n_e / n_e$ . Data points are from the first three quiescent phases between sawtooth crashes (respectively, empty, dotted and filled shapes); different shapes refer to different radial positions

tokamak discharge; it shows that at the different radial positions the local transport is dominated by diffusion and that the local transport parameters remain the same during several successive quiescent phases between sawtooth crashes (Fig.202), until the injected impurities are lost from the discharge [16].

## References

- [1] Cordey, J.G., Muir, D.G., Neudachin, S.V., Parail, V.V., et al., Plasma Physics and Contr. Fusion, **36**, A267, (1994)
- [2] Connor, J.W., Hastie, R.J., and Taylor, J.B. Proc. Roy. Soc. London Ser. A **365**, 1 (1979)
- [3] Erba, M., Springmann, E., Taroni, A. and Tibone, F. accepted for publication in Plasma Physics and Contr. Fusion
- [4] Parail, V.V., Cordey, J.G., Springmann, E. and Taroni, A. accepted for publication in Nuclear Fusion
- [5] B. Balet, J.G. Cordey, A. Gibson, P. Lomas, P.M. Stubberfield and P. Thomas in Controlled Fusion and Plasma Physics (Proc. 21st Eur. Conf. Montpellier, 1994) Vol 18B, Part I, p. 58, European Physical Society, Geneva (1994).
- [6] D.F.H. Start et al., Proc. 21st EPS conference on Controlled Fusion and Plasma Physics, Montpellier (1994), vol. 18B, part I, p.314.
- [7] F. Rytter and the H-mode Database Working Group, Proc. 19th EPS Conference on Controlled Fusion and Plasma Physics, Lisbon (1992), vol.17C, part I, p.15.
- [8] The JET Team, in Plasma Physics and Controlled Nuclear Fusion 1994 (Proc. 15th Int. Conf. Seville, Spain, 1994) Paper CN-60/A-2-III-1, IAEA, Vienna (1995) to be published.
- [9] P. Mantica et al. Nucl. Fus. **32** (1992) 2203.
- [10] L. Lauro-Taroni et al, Impurity Transport of High Performance Discharges in JET, XXI EPS Conf. on Contr. Fusion and Plasma Physics, Montpellier (France), 1994, Vol.18b, Part I, p.102.
- [11] P. Smeulders et al, Survey of Pellet Enhanced Performance in JET Discharges, accepted for Nucl. Fus., 1994
- [12] J.C. Cordey et al, the Enhanced Confinement Regime in JET, JET-P(94)10.
- [13] The JET Team, in Plasma Physics and Controlled Nuclear Fusion 1990 (Proc. 13th Int. Conf. Washington, DC, 1990) Vol. 1, IAEA, Vienna (1991) 27
- [14] R. Giannella, L. Lauro-Taroni, M. Mattioli et al., Nucl. Fus. **34** (1994) 1185
- [15] R. Giannella and L. Lauro-Taroni, in Controlled Fusion and Plasma Physics (Proc. 21st Eur. Conf. Montpellier, 1994) Vol 18B, Part III, p. 1260, European Physical Society, Geneva (1994).
- [16] The JET Team, in Plasma Physics and Controlled Nuclear Fusion 1994 (Proc. 15th Int. Conf. Seville, Spain, 1994) Paper CN-60/A-2-III-1, IAEA, Vienna (1995) to be published.

## MHD and Beta Limits

During 1994, studies of magnetohydrodynamic (MHD) phenomena were undertaken in three principal areas:

- termination of high-performance phase by giant-ELMs;
- diminution of confinement by slow roll-over events;
- possible limitation of future plasmas by TAE modes.

Also, the study of tearing modes by actively controlled internal coil combinations has just started and is making rapid progress.

The high performance Hot-Ion H-Mode discharges in JET are limited by three classes of phenomena: giant ELMs at the plasma edge; MHD instabilities at intermediate radii; and central sawtooth events. These may appear separately from discharge to discharge or in the same discharge, sometimes occurring simultaneously. Figure 203 shows an example of the three phenomena occurring sequentially in one discharge. The appearance of the giant ELMs depends critically on the geometry of the discharge and the divertor configuration. Sawtooth events become more important at lower  $q$  at the edge.

### Termination of the High-Performance Phase by Giant ELMs

Depending on the precise magnetic divertor configuration, high performance discharges are terminated by giant edge localised modes (ELMs) at varying stages of their high energy development phase and well below the usual beta limits encountered at the low field low current discharges (typically  $B < 1.5\text{T}$  and  $I_p < 2\text{MA}$ ). In these low field and low current discharges, beta values of  $[\beta_N = \beta_T(T) a(m) / I(\text{MA})]$  well in excess of 2.8 (the Troyon limit) have been obtained. At higher fields and currents,  $\beta_N$  values of about 2.2 are rarely exceeded.

Experiments showed that divertor discharges which had high recycling properties also had frequent ELM occurrences. Frequent ELMs may not necessarily be a disadvantage, if sufficient power is available to maintain the plasma temperature at a sufficiently high level (ELMs may possibly lead to helium ash removal in a reactor). At present power levels (20MW), ion temperatures of 20keV cannot be achieved in ELMy discharges. Therefore, it is necessary to achieve ELM-free discharges in JET.

Studies are in progress to determine the cause of these limiting ELM events. Experimentally, plasma and target shape play an important role in improving the ELM-free period and maximum plasma energy achieved. In par-

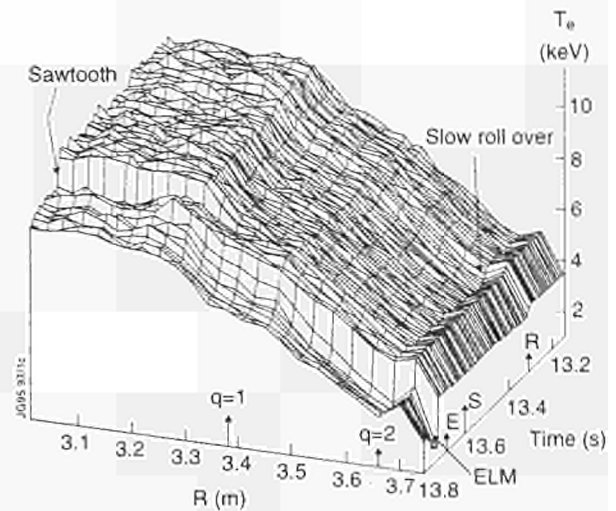


Fig.203: Evolution of electron temperature radial profile as a function of time from  $t=13.1 - 13.8\text{s}$  for Pulse No:33648. A slow roll-over can be seen at  $t=13.25\text{s}$  as a moderate decrease of the electron temperature, which starts near the  $q=2$  and/or  $q=3$  surfaces (at  $R=3.67$  and  $3.76\text{m}$ ). It propagates slowly inwards to the centre in  $0.1\text{s}$ . The roll-over in the neutron rate starts at  $t=13.25\text{s}$ . At  $t=13.6\text{s}$ , a sawtooth occurs with an inversion radius ( $q=1$ ) at  $R=3.39\text{m}$ . Finally, at  $t=13.7\text{s}$ , a giant ELM leads to rapid cooling of the plasma except for the centre

ticular, a detailed scan shows that increasing the plasma triangularity improves performance. This relationship to plasma shape is qualitatively consistent with ballooning modes limiting the maximum edge pressure gradients. Indeed, comparisons between edge ballooning limits and experimental edge pressure gradients at the time of the giant ELM show good agreement (see Fig.204).

High flux expansion of the scrape off layer (SOL) leads to low recycling at the target plates and, hence, to a low density build-up at the edge reducing therefore appreciably the build-up of edge pressure gradients.

In some of the highest performance discharges, the first studies indicate that, in the operation space of edge pressure gradient and edge current density, there is access to the second stable operating domain. Stability at the edge is set by low- $n$  kinks (driven by edge current gradients) and ballooning modes driven by pressure gradients. For highly shaped plasmas, the ballooning modes are stable, in agreement with previous pure ballooning stability analysis [1], for certain values of the edge current while the low- $n$  kinks are still in the stable regime at these currents.

### Limitation of High Performance Hot-Ion H-modes by Internal MHD Modes

In this section, the stability of the plasma is considered in relation to the effects of MHD modes at intermediate radii.

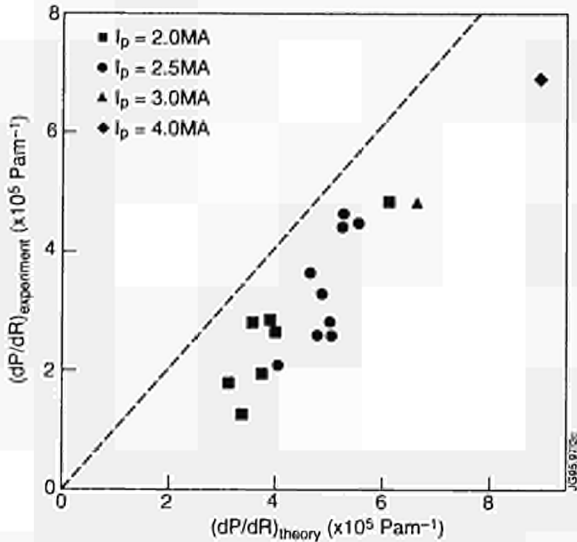


Fig.204: Experimentally determined pressure gradient at time of the giant ELM versus calculated marginal ballooning stable one for various plasma geometries and currents

These cause a change in the plasma performance, a slow roll-over usually occurs in the neutron emission and plasma energy. The MHD modes in this roll-over can persist for several hundred milliseconds. In some cases, a very rapid (<1ms) flattening of electron temperature profile is observed near the  $q=2$  surface. This flattening is accompanied by electron temperature and magnetic perturbations around the location of the  $q=2$  or  $q=3$  surfaces.

The enhanced heat and particle losses related to these MHD events lead to only a moderate heating of the divertor target plates in the new JET configuration. From shot to shot, the stored energy and neutron emission rises less vigorously, saturates or decreases slowly. In the previous divertor configuration, MHD events often led to large carbon blooms followed by a degradation of plasma parameters masking the MHD effects.

The slow roll-over starts close to a rational surface and then diffuses in- and outwards, as observed on the electron temperature profile measured by electron cyclotron emission. At the same time, the neutron yield saturates or drops. The typical features of the slow roll-over are low  $(m,n)$  MHD modes, in certain cases  $m=2$  and  $n=1$ , near the  $q=2$  surface with a frequency close to that caused by the plasma rotation, observed at about  $10^4$  Hz in the laboratory frame. In other cases,  $m=3$ ,  $n=1$  modes have been seen at the  $q=3$  surface. The roll-over always causes an increase in the observed edge recycling light (see Fig.205).

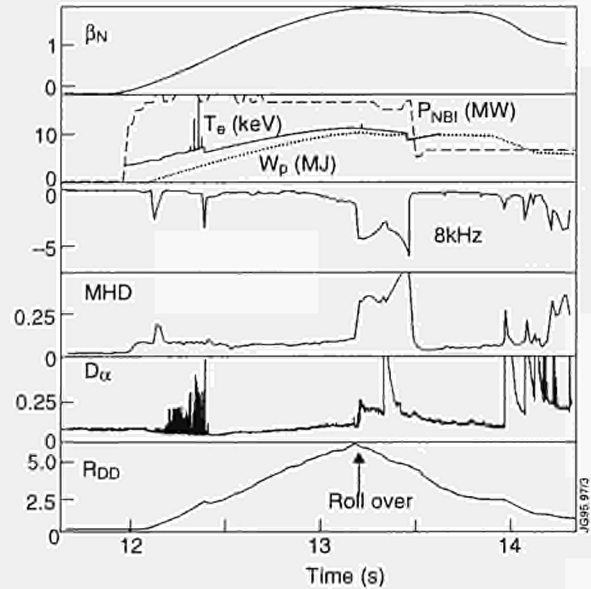


Fig. 205: Overview of a slow roll-over for Pulse No:33683 starting at  $t=13.2$ s: (a) the normalised beta,  $\beta_N$ ; (b) the neutral beam power,  $P_{NBI}$ , the central electron temperature,  $T_e$  from ECE, the total plasma energy,  $W_p$ ; (c) the 8kHz MHD activity from the comb filter; (d) the rectified signal from a pick-up coil in the torus midplane; (e) the  $D_\alpha$  neutral deuterium signal; (f) the D-D reaction rate

Calculations to study the stability of the core plasma as a function of the evolution of the  $q$  profile are in progress. The  $q$  profile has a tendency to evolve so that  $q(0)$  increases above unity (perhaps similarly to Pellet Enhanced Plasmas). It seems that control of the  $q$  profile is required for the core to remain MHD stable up to the Troyon limit, since many high performance discharges are presently limited to about three quarters of this limit.

### Alfvén Eigenmode Studies

Unstable Alfvén Eigenmodes (AE) could improve limitations on the operation of a tokamak reactor. To investigate systematically the physics of the Alfvén Eigenmodes (AE), and in particular, their stability properties, a new active diagnostic system has been installed on JET. This active system is based on direct mode excitation by saddle coils installed inside the vacuum vessel and synchronous detection of the plasma response in the frequency range from 30-500kHz. The magnetic perturbations induced in the plasma are  $(\delta B/B \ll 10^{-5})$ . Therefore, neither fast particle losses nor non-linear wave effects are generated. Selection of the toroidal mode number in the range  $1 < n < 4$  is achieved by imposing an appropriate phasing to the saddle coils used as antennae.

The excited mode structure is measured from a set of magnetic probes situated poloidally and toroidally around

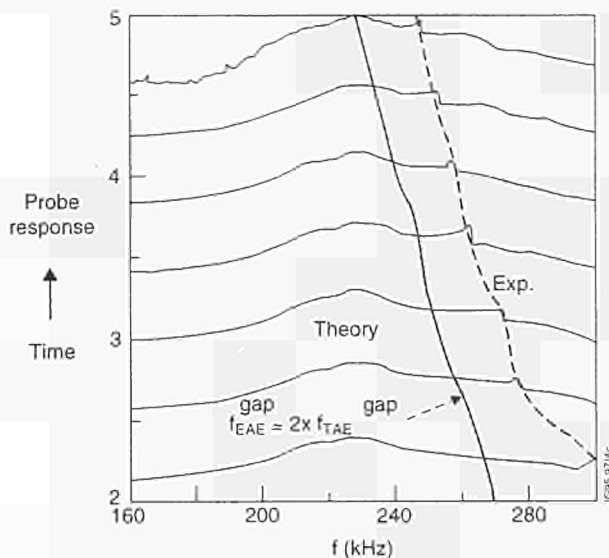


Fig.206: Example of observed ellipticity induced AE (Pulse No:33256). A poloidal magnetic coil signal is represented as a function of frequency for a number of successive scans ( $df/dt=140\text{kHz/s}$ ). Each scan takes 1s, the total time covered is 7s. The calculated frequency taking into account the variation of the plasma parameters corresponding to the centre of the ellipticity induced gap is also indicated  $f_{EAE}(gap) = 2 \times f_{TAE}(gap)$

the torus and from the radially resolved signals of the heterodyne ECE and reflectometer systems. MHD global modes have been excited and identified as Alfvén Eigenmodes (AE) by the dependence of their frequency upon density and toroidal field. In the range  $70\text{kHz} < f < 200\text{kHz}$ , toroidicity induced AE have been driven and analysed. Their damping has been measured directly, for the first time, for a variety of plasma conditions [1].

At higher frequencies ( $150\text{kHz} < f < 300\text{kHz}$ ), Alfvén Eigenmodes with frequencies lying in the ellipticity induced gap have been clearly identified. An example of the resonances observed over several frequency scans within the same discharge is shown in Fig.206. This constitutes the first unambiguous experimental observation of ellipticity induced Alfvén Eigenmodes. Their damping and mode structure appear to be similar, for the same plasma condition, to those of the TAE modes.

Preliminary AE studies have also been undertaken in the presence of additional heating, to extend the parameter range for the spectrum and damping measurements to regimes closer to reactor relevant conditions and to assess the driving effects in the presence of resonant fast particles. A reduction in the total growth rate  $g$  of driven stable TAE modes was observed, when high energy NB heating at low B-field produced resonant particles, consistently with the predicted appearance of a finite mode growth rate. NB heating for B-fields higher than 1.5T, ICRF heating at

intermediate power and LH heating allowed investigations in the absence of resonant particles. In particular, high frequency resolution measurements have shown a sudden change in excited AE spectra as the plasma temperature and  $\beta$  were increased. Simple single peak structures were replaced by several weakly damped ( $\gamma/\omega < 10^{-3}$ ) peaks at frequencies corresponding to the lower part of the continuum above the TAE gap,  $f_{TAE} = (v_A/4\pi q R_0)$ .

The presence of a finite density perturbations, measured by the reflectometer, highlight the non-ideal character ( $E_{\parallel} \neq 0$ ) of these modes. These observations are believed to be the first experimental proof of the existence of kinetic TAE. Their weak damping along with the simultaneous presence of a large number of modes, creating a large number of resonances over the particle phase space, make these modes particularly efficient in affecting the fast particle transport and, therefore, could be dangerous for the performance of future ignition experiments.

## References

- [1] A.Fasoli et al., Proc. of XV Int. Conf. on Plasma Phys. and Contr. Fusion, IAEA, Seville, Spain (1994).

## Physics Issues Relating to Next Step Devices

In this section, two areas of work are covered:

- a selection of experiments on JET, with a specific relevance to ITER;
- work in the physics areas carried out for ITER under Article 7 contracts with NET.

### Specific ITER Relevant Experiments.

ITER has selected as its main operating regime that of the Elmy H-mode. At present, this is the mode with the highest compatibility with the various requirements demanded of an ITER regime. This mode has a reasonable confinement enhancement factor,  $H \approx 2$ , it can be produced in steady-state, and it appears to have acceptable helium ash removal characteristics. On the other hand, the compatibility with the selected mode of divertor operation for ITER still needs to be demonstrated.

One of the main outstanding issues of plasma transport, that bears upon the choice of main machine parameters for ITER, is the uncertainty of the scaling of anomalous transport with the Larmor radius  $\rho$ . For the other

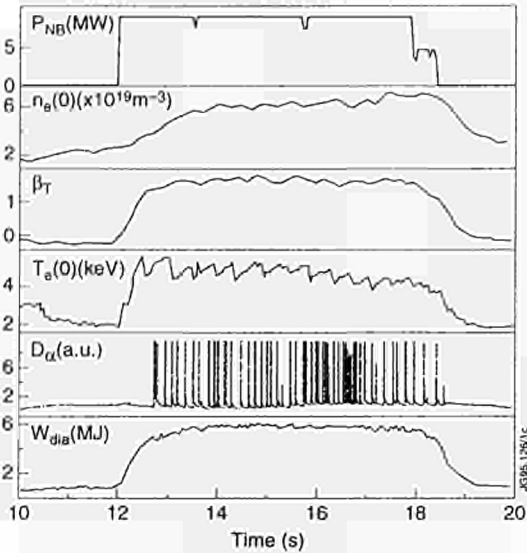


Fig.207: Traces of a representative JET pulse

dimensionless variables in the scaling relations, those of resistive MHD, the range foreseen by ITER can be covered by present day tokamaks. For the dimensionless parameter,  $r/a$ , where  $a$  is the typical minor radius, this is not the case.  $r/a$  for ITER is typically a factor 5 smaller than in JET, and much smaller than in machines smaller than JET. Hence, scaling anomalous transport from the present machines to ITER implies making a strong extrapolation in  $r/a$ .

To demonstrate the ITER relevance of this mode, both JET and DIII-D have produced discharges, which approximate as well as possible the intended ITER discharge in the critical dimensionless variables, except  $r/a$ . Figure 207 shows traces of a representative JET pulse.

In 1991, JET carried out an experiment in which only one of the two sets of toroidal field coils was energised. This increases the toroidal field (TF) ripple at the plasma edge from about 1% to about 10%. The effects of high toroidal field ripple on plasma behaviour in general, and on fast particle losses, in particular, were studied. Results from these experiments were sufficiently encouraging to prepare for a second ripple experiment. In this case, the two sets of coils will be operated at different currents. This modification will make possible the exploration of the intermediate ripple regimes, with ripples in the range 0.5% to 3%, in the pumped divertor configuration. Whereas the first ripple experiment showed that at the fixed high ripple level of 10% the plasma was strongly degraded, the second ripple experiment will allow quantification and investigation of threshold ripple values for the ripple

effects. These experiments have a strong relevance to Next Step devices, in general, as there will always be engineering pressure to minimise the number of TF coils. The constraints imposed by the physics on this minimisation need to be established.

Technical preparation for this experiment is now well advanced. A new busbar from the machine to the power supplies area and the TF mid-point busbar, have been installed. A new configuration for the TF power supplies has been prepared to allow sufficient voltage on each of the two coil sets. A study was made of the trajectories of lost particles and local heatloads on in-vessel components due to the ripple. As a result, maximum input powers and energies for the additional heating systems have been formulated.

## General Work for ITER

Specific tasks for ITER were undertaken under Article 7 Agreements with NET. In this section, a selection of the results from this work are described.

A configuration of the PROTEUS Grad-Shafranov code was set up to study the control and stability of ITER plasmas in the early current rise. The analysis was based on the ITER configurations described in the TAC-3 and TAC-4 Reports. Configurations down to a plasma current of 250kA were successfully calculated. Eddy currents did not change substantially the equilibrium or stability properties. The low current ITER configurations show the occurrence of an X-point on the plasma midplane. This has two implications: first, the low current plasmas may be radially unstable. Second, it will be impossible to find the plasma boundary by the usual simple method of first order flux extrapolation from the inner-wall. The ITER plasma starts to show vertically unstable behaviour only above a current of about 4MA, with growth rates of  $\sim 1.5s^{-1}$ .

A conceptual design for a Lower Hybrid (LH) Heating and Current Drive launcher for ITER was made in cooperation with NET and CEA, Cadarache, France. Current drive by LH has the feature, as opposed to other current drive systems, to retain a good current drive efficiency in plasma regions of low temperature, or in low  $\beta$  plasmas. These aspects are important for the 'Advanced Tokamak' scenarios, in which a hollow current profile, needed for shear reversal, needs to be established in the current ramp-up and maintained throughout the route to the burn phase. The conceptual launcher operates at 5GHz and couples typically 20MW through one main horizontal port. It uses

a combination active/passive waveguide grill with hyperguide and mode converters feeds to give a structure which combines a robust grill with simple supply networks and good neutron attenuation at the first wall.

A multivariable controller for the ITER poloidal plasma configuration is under design. Since the restart of operation in 1994 JET has been using a multivariable controller for the plasma shape based on a full decoupling matrix. The present controller allows the machine operator to control a mix of currents and plasma-wall distances (gaps) to best suit his pulse design and the different situations of the experimental campaign. The JET decoupling controller, while being based on a full multivariable approach, retains the possibility of an easy understanding of the decoupling matrix coefficients, an advantage which is not always present in optimal control techniques. This design choice enabled us to gain confidence in the model parameters before attempting to use a more sophisticated algorithm. With this background the study for the ITER control has been undertaken with the view that it is possible to design, implement and test different methods. The aim is to understand if a more refined controller is advantageous in the sense that it allows to cover a wider range of plasma configurations, is more robust to plasma disturbances and allows the designer to diagnose a system fault when some unexpected behaviour is found.

## Data Analysis and Modelling

The work on data analysis and modelling can be divided into three areas: Analytic Theory, Numerical Simulation and Data Processing and Analysis. However, there is a very strong interaction among these areas. The ultimate goal is to improve the modelling of the many physical processes taking place in both the core and edge regions of a tokamak. There is a strong interaction with experimental programme through Task Forces and Topic Groups.

### Analytic Theory

The Analytic Theory Group has supported the experimental programme by detailed interpretation of JET discharges and by predictive studies for specific experiments. The equilibrium identification was adapted to the new divertor configuration and its numerical performance has been significantly improved. Theoretical stud-

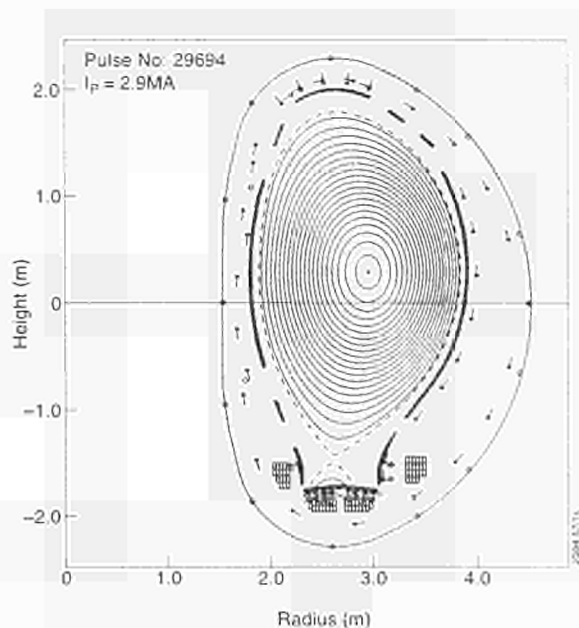


Fig. 208: Flux surfaces of a 3MA flat-top plasma with the pumped divertor configuration (Pulse No: 29694).

ies were performed of Global Alfvén wave excitation and the resulting energetic particle losses, and for the stability of advanced tokamak scenarios.

### Equilibrium Reconstruction of Discharges

Magnetic equilibrium reconstruction is basic to the tokamak operation and to plasma diagnostics. At JET, two codes for routine analysis are applied. One is the full equilibrium reconstruction code EFITJ[1], based on a Green's functions method. The other is the real-time boundary code XLOC[2], using local Taylor expansions. The codes EFITJ and XLOC have been modified to cater for the pumped divertor phase of JET.

The equilibrium codes played a pivotal role during start-up of operations of the machine after the shutdown [3,4]. Figure 208 shows one of the first good 3MA X-point equilibria of the JET restart campaign. EFITJ and XLOC now run routinely in intershot mode in the main processing chain of the IBM mainframe, providing equilibrium data for all divertor and limiter plasmas in the new JET configuration. The code EFITJ uses about five minutes CPU times for 100 time-slices. XLOC takes 25 seconds for 1000 time-slices, which includes boundary tracing and Lao-Hirshman fitting. EFITJ was also used for the commissioning of the new magnetic diagnostics KC1D, as it was capable of equilibrium reconstruction using the old magnetic diagnostics KC1.

The real-time display of the plasma boundary from XLOC has proved extremely useful in plasma develop-

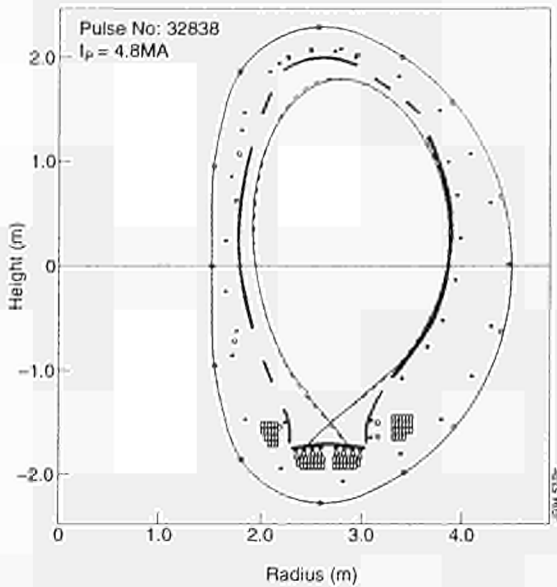


Fig.209: Real-time display of the plasma boundary of a SMA discharge in operation. The agreement with a full calculation by EFITJ, indicated by the dotted line, is good

ment during operations. A typical example is displayed in Fig.209. Software has been developed to calculate,  $\beta$ ,  $q_w$ ,  $V_{loop}$ ,  $W_{dia}$  in real-time, and this data will be used for display and plasma profile control.

A fast full equilibrium solver is under development to run, on specialised hardware, on a time scale applicable to plasma control. EFITJ was selected since it is tailored to JET, as the Green's function method is fast, and as the algorithm is based on a combination of parallelizable algorithms, like matrix operations.

The measurements of Faraday rotation and motional Stark effect, providing information about the current profile, have now been incorporated into EFITJ for the present configuration. This information is essential for an accurate description of the current and safety factor profile, which is necessary for stability calculations.

### Edge Plasma Physics

The tokamak edge plasma includes a core plasma part and a scrape-off-layer (SOL) part with completely different topology. The core plasma has closed magnetic surfaces, whereas the region outside the separatrix exhibits an open field line structure and the plasma interacts with the target plates in the divertor. These two regions around the separatrix, both typically ten ion Larmor radii wide, constitute the edge plasma. Due to MHD activity these two areas can interact. Therefore, this edge plasma plays a crucial role even for entire plasma behaviour, as investigation of the L-H transition has revealed. The near separatrix

region in tokamaks provides a new length scale parameter  $\chi_o = [-d(\ln p_o)/dx]^{-1}$ , the pressure gradient length, which is several ion gyro radii. The edge gradients in the profiles can drive resistive MHD and drift type instabilities, which depend on the conditions at the target plates. In the SOL, the instabilities have a flute, interchange character [5].

In the initial stage of the discharge evolution, the edge plasma is sufficiently cold and has low conductivity, which drives strong dissipative instabilities, such as the resistive interchange and drift mode, at the plasma boundary causing strong turbulent transport. The edge turbulence can be transmitted to the plasma centre by a pumping mechanism [6] or by a radially extending mode structure [7]. This plasma state corresponds to L-mode confinement. With increasing edge temperature, the dissipative instabilities become weaker, the transport coefficients are decreased and the gradients at the separatrix are increased. Thereby, the pressure profile (along with temperature and density) becomes increasingly more step-like. When this edge gradient is sufficiently steep, the Finite-Larmor-Radius (FLR) stabilisation [8,9] and the shear flow stabilisation [10,11] take place and the turbulence is strongly suppressed.

The H-mode is set up when the stabilisation of drift waves and of interchange modes becomes effective. This is equivalent to the condition  $\rho^* = \rho/\chi_o$  being of order unity, i.e. between 0.1 and 1. The L-H transition depends strongly on the longitudinal loss mechanism in the SOL. The resulting scaling of the L-H power threshold is very close to the dimensionally correct experimental scalings,  $P > 0.025 n_o^{0.75} B_o S$  and  $P > 0.4 n_o B_o R^{2.5}$ , where P denotes the total power which diffuses into the SOL and S the tokamak surface. With increasing edge temperature and with decreasing density the linear power threshold scaling with the toroidal field can change into a stronger dependence on  $B_o$  [11]. Moreover, the development of a step-like pressure profile in the H-mode will lead to unstable MHD surface modes [12], which may explain the essential properties of the ELM phenomenon. Firstly, the surface mode has a relatively weak radial dependence varying as  $\rho^{mq}$  for the internal plasma and as  $\rho^{-mq}$  for the external part. This explains the macroscopic character of the ELM. Secondly, this mode structure gives an estimate for the ELM repetition time (or ELM frequency)

$$(1/\tau) = (nq)[H \langle P \rangle] / (W P_{edge}) = (nq) \langle P \rangle / (P_{edge} \tau_E)$$

Here H is the heating power, W is the total energy content  $W \approx 2pa^2 \langle P \rangle$  per length, P the pressure and  $\tau_E$  is the

energy confinement time. This scaling yields a linear dependence on heating power and an inverse dependence on the plasma current. Thirdly, the surface-mode model explains the occurrence of two different timescales during a giant ELM [13]. The initial rise is caused by a fast MHD event with a characteristic time  $\tau_1 \approx (\rho_i R)^{1/2} / C_s \propto R^{1/2} T^{1/4} B_0^{-1/2}$  removing a plasma layer of width  $a/nq$ . The second phase is determined by the diffusive refilling of the expelled layer on a time of  $\tau_2 \approx \tau_e / (nq)^2$ .

For the theoretical investigation, macroscopic 'Reduced MHD' type equations for the SOL geometry were derived [14]. These equations include toroidal drifts in a natural way. Next, a stability analysis for general, non-axisymmetric perturbations was performed for Single-Null and double-null divertor configurations. It is found that for the same plasma parameters the single-null divertor is more stable, the anomalous transport processes are weaker and the SOL width is smaller [5, 15]. Applying the results of the stability analysis together with dimensional arguments and the mixing length approach allows a derivation of the power threshold scaling for the L-H transition [11].

### Stability of Low- $n$ External Kink Modes

Low- $n$  external kink modes constitute surface modes and are, thus, a possible cause for the giant ELM's which often terminate high performance discharges. Fast ECE temperature measurements show that the giant ELM affects a large volume of the plasma on a very short timescale ( $<1$ ms). Ballooning modes on the other hand are localised modes which would pose only a local limit on the pressure gradient, external kink modes are however more global modes. In addition, low- $n$  mode activity has been observed during large ELM's.

The stability of low- $n$  ( $n=1-4$ ) external kink modes has been studied (numerically using the CASTOR code) as a function of the edge pressure gradient and the edge current density for different shapes of the plasma boundary. The external kink mode is driven unstable by a finite edge current. The dependence on the edge pressure gradient is more complicated. Small pressure gradients at the edge have a stabilising effect on the external kink mode. However for pressure gradients of the order of the first ballooning stability limit, the external kink is destabilised especially for the  $n=3$  and  $n=4$  modes.

For plasmas with a low triangularity, access to the second ballooning stability region requires a large edge

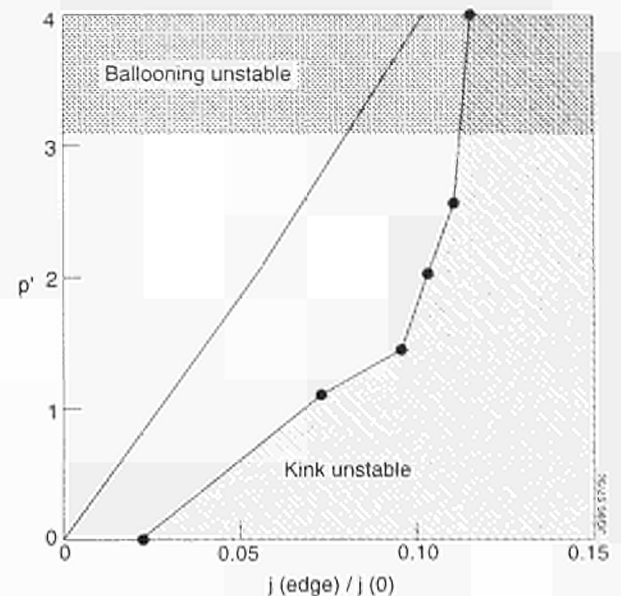


Fig.210: Ballooning and kink stability limits (Pulse No: 30591,  $t=12.2$ s)

current. These edge currents, however, can drive the external kink mode unstable and no stable route exists into second stability. For high triangularity a lower edge current is required and a stable window into second stability does exist. Figure 210 shows the ballooning and kink stability diagram for Pulse No:30591 in the plane of edge pressure gradient and edge current. It is clear that for this discharge with low triangularity there is no access to second stability.

### 1-D Scrape-Off Layer Code

A code has been developed to solve the scrape-off layer fluid equations along the field lines in the 1-D approximation. It solves the time evolution of the ion continuity and parallel momentum equations and the ion and electron energy equations. Two neutral models, for low and high collisionality are included. In the high collisionality limit, the neutrals are treated as a fluid and are described by a continuity equation and by the parallel and toroidal momentum equations. The equations are discretized using Petrov-Galerkin finite elements. A fully implicit scheme is used for the time evolution allowing for large timesteps. The code was designed with a view to allow easy implementation of different equations and physics models.

The model has been successfully applied to the investigation of a potential pressure drop in the high collisionality regime (high collisionality gas target). It is found that only poloidal friction tends to increase the pressure drop above a factor of two, while toroidal fric-

tion has even an adverse effect. So that poloidal friction may become efficient, the condition:  $\sin^2\psi \cdot (L^*/\lambda_{n-1}) \gg 1$  (where  $\psi$  is the field line pitch and  $L^*$  is the extension of the cushion along B) must be fulfilled. However, this is not achievable practically in typical poloidal divertor configurations, where  $\sin\psi \ll 1$ . The study of JET detached divertor plasmas is an ongoing activity.

## MHD Spectrum and Stability

### Toroidal Alfvén Eigenmodes (TAE) in JET

The confinement of fusion-born alpha-particles in D-T plasma is crucial for sustaining ignition in a tokamak reactor. For typical tokamak reactor plasmas (ITER), the alpha-particles are mainly super Alfvénic, i.e.  $v_\alpha > v_\Lambda$ , and yield the dominant source of plasma heating with extremely high energy contents,  $P_\alpha \sim 70\text{-}540$  MW, and highly-peaked alpha-particle, pressure profiles [16]. Weakly damped Global Alfvén Eigenmodes can be driven unstable by resonant interaction with high energy particles, satisfying  $v_{\text{res}} = v_\Lambda$  and  $v_{\text{res}} = v_\Lambda/3$ . This resonant interaction leads to the exchange of momentum and energy between the particles and the wave, which can cause anomalous losses of fast particles [17, 18] or a radial redistribution of fast particles and of plasma heating profile. These events will lead to a degradation of plasma confinement. In addition anomalous losses of alpha-particles can cause significant damage to the first wall.

A theoretical analysis of the TAE-phenomena and, in particular, of the experimental results from the new Alfvén Eigenmode Active Diagnostic, has been performed, and described in more detail in the section on Tokamak Concept Improvement.

The detailed analysis of the Alfvén spectrum, the gap structure and the global mode frequency, has been performed numerically using the MHD spectral code CASTOR. In collaboration with FOM Nieuwegein, the Netherlands, the plasma response due to an antenna drive was studied. The effect of continuum damping is resolved by introducing finite resistivity in the limit of asymptotically small resistivity. Other damping mechanisms, such as Landau damping and trapped electron collisional damping as well as the drive due to passing and trapped energetic ions is evaluated separately by a local analysis. A global treatment is currently implemented. A new aspect in the Global Alfvén wave physics appeared in 1994 with the discussion of the kinetic TAE spectrum in hot tokamak plasmas [19]. It is emphasised that the

number of occurring Global Alfvén modes has a crucial influence on the resulting energetic ion transport. With increasing plasma temperature not only the damping of the TAE's can vary, but in addition many new, weakly damped discrete Kinetic Toroidicity - Induced Alfvén Eigenmodes (KTAE) appear. This transition in the Alfvén spectrum from a single mode (TAE) to a multi-mode structure (KTAE's plus TAE) is determined by the dimensionless non-ideal parameter

$$\lambda \sim (\rho_{\text{ms}}/r\epsilon^{3/2})[(3/4) + (T_e/T_i)]^{1/2}$$

and the transition occurs if  $\epsilon\lambda \geq |\gamma_d/\omega|$  with  $\gamma_d$  being the damping rate. A number of experiments have been performed with the objective to identify such a KTAE spectrum. The high-resolution Alfvén Diagnostic was used with LH plasma heating, where no energetic ions were produced. It was found that even in the case of not very hot ions, but for a large temperature difference in electrons and ions,  $T_e/T_i \sim 3$ , the usual Alfvén eigenmode spectrum did not consist of a single TAE-mode but numerous weakly-damped ( $\gamma_d/\omega < 10^{-3}$ ) eigenmodes appear. This multi-peak structure of Alfvén eigenmodes was also found to be typical for ICRH - and NBI - heated plasmas. A theoretical stability analysis of the kinetic TAE-modes has been developed in [20, 21]. The MHD spectral code CASTOR has been modified toward a 'complex resistivity' for the study of KTAE-spectra in discharges [20, 22].

The energetic particle redistribution in the presence of high-amplitude Alfvén eigenmodes has also been studied. A new guiding centre code, HAGIS, which follows the particle motion in general tokamak equilibria in the presence of an arbitrary electromagnetic MHD perturbation, has been developed [18, 22]. This code is based on a Hamiltonian formalism to enhance the numerical accuracy. In this particular application the perturbation was a TAE normal mode computed by CASTOR. In preparation for the planned tritium discharges, DTE1, two main mechanisms for possible  $\alpha$ -particle losses have been identified as shown in Fig.211 (a) and (b).

There exists a resonant drift of an  $\alpha$ -particles into a loss cone, which can lead to the conversion of a barely passing  $\alpha$ -particles into a banana orbit, which intersects the wall. Then, stochastic radial diffusion of the  $\alpha$ -particle can occur. TAE-induced prompt  $\alpha$ -particle losses scale linearly with the amplitude of the applied TAE perturbation amounting to 1.5% for  $\delta B/B \sim 3 \times 10^{-3}$ .

The stochasticity threshold of the  $\alpha$ -particle motion in the presence of  $n=3$  TAE's have been found to be very

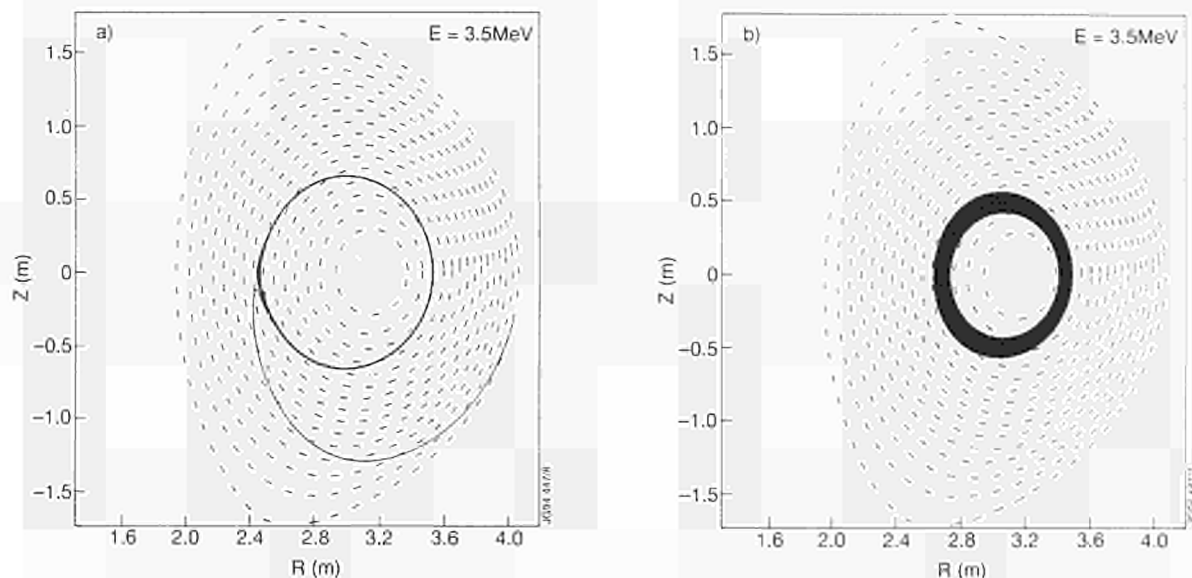


Fig.211: Alpha-particle loss mechanisms: (a) conversion of barely passing particles into lost banana orbits; (b) stochastic diffusion due to single  $n=3$  TAE mode

high,  $\delta B/B \sim 10^{-3}$ , for typical low-shear JET equilibria. Furthermore, just an additional 1% of the  $\alpha$ -particles are lost due to these  $n=3$  TAE's with an amplitude of  $\delta B/B = 3 \times 10^{-3}$ . These losses cannot lead to the degradation of the global confinement in JET, but can cause significant damage to the first wall or to the divertor due to a poloidally highly localised power deposition. The possible anomalous radial redistribution of the fast particle heating profile due to TAE's has to be studied in a self-consistent approximation; this problem is in progress in collaboration with the Institute for Fusion Studies, University of Texas, USA. The energetic particle behaviour in the presence of Alfvén waves with a multi-mode spectrum as well as the conditions for the stabilisation of these KTAE's are currently being investigated.

#### MHD Stability of Advanced Tokamak Scenarios

The limiting MHD instability in the advanced tokamak scenarios with an inverted  $q$ -profile is the infernal mode. This mode is driven by a large pressure gradient in the region of small shear. In collaboration with FOM Nieuwegein, the Netherlands, the resistive spectral code CASTOR was applied to a family of equilibria being of relevance to the experimental campaign. In particular, the stability of the ideal and resistive infernal mode has been studied for different shapes of the pressure and the  $q$ -profile in order to identify a stable operating regime for advanced tokamak scenarios [23]. The infernal mode can become unstable for relatively low values of poloidal beta

( $\beta_p \sim 0.5$ ). For equilibria with a sharp minimum in the  $q$ -profile, the infernal mode is well localised at the minimum and the growth rate is small. High beta ( $\beta_p > 2$ ,  $\beta_N \sim 4$ ) equilibria have been identified which are stable to infernal modes and ballooning modes. These equilibria are characterised by a  $q$ -profile with a shallow minimum near the plasma boundary ( $r/a \sim 0.8$ ). The pressure profile is peaked inside the minimum in  $q$ , outside this minimum, the pressure gradient is marginally stable to ballooning modes (see Fig.212).

#### Ion Cyclotron Resonance Frequency Heating

During Ion Cyclotron Resonance Frequency (ICRF) heating in a tokamak, ions receive a "kick" in velocity each time they pass a cyclotron resonance. Normally the "kick" in the velocity component perpendicular to the magnetic field is much greater than in the parallel component. However, the "kick" in the parallel velocity is important since it also leads to a change in the radial position of the turning point of a trapped ion. As a consequence, wave-particle interaction in a toroidal geometry leads to wave induced transport in both velocity and real space, making it necessary to solve a three dimensional Fokker-Planck equation to obtain the distribution function of the resonating ions [24]. Another complicating factor in the modelling of ICRH is the width of the orbits of ICRH accelerated ions. In JET, these acquire very wide orbits since they are often accelerated up to energies in the MeV range. In order to address these

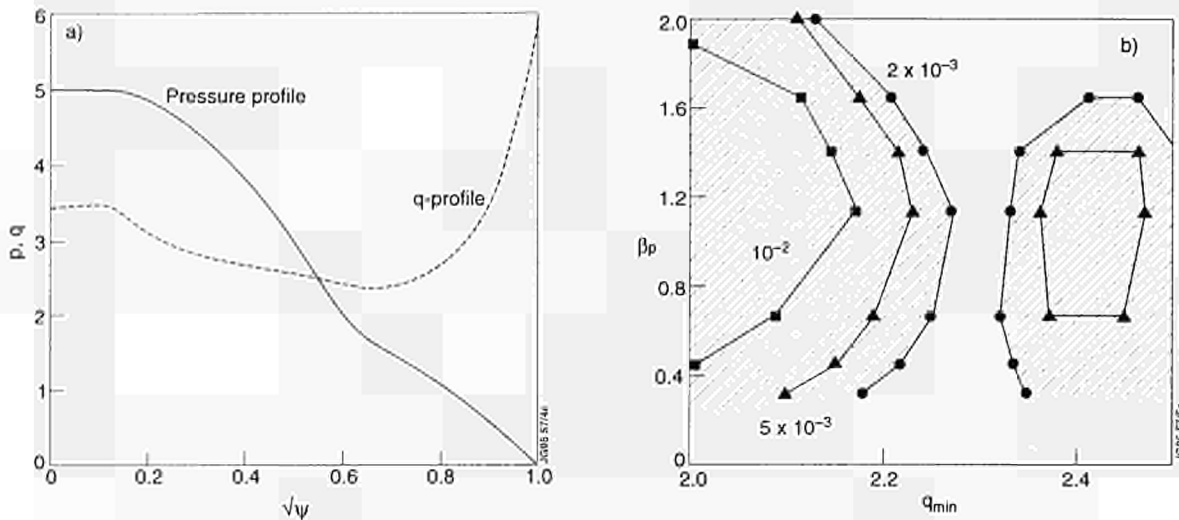


Fig.212: (a) Example of a non-monotonic  $q$ -profile obtained from the modelling of JET scenarios; (b) The growth rate of the ideal  $n=1$  and  $n=2$  infernal modes in the  $\beta_p - q_{min}$  plane

problems a code called FIDO [25] solving an orbit averaged Fokker-Planck equation with a Monte Carlo method [24] was developed.

The transport in real space due to ICRF heating has been found to be particularly important when the antennas launch toroidally directed waves. Such directed waves can be used for current drive, including current profile modification. To explore RF-driven currents, the new antenna system in JET has been designed to have the capability of launching toroidally directed waves with high directivity. One scenario which has been used for current profile modification is minority ion current drive [26], where minority ions are heated by directed waves. The influence of the wave induced radial transport on the resonating ions in this scenario has been studied with the FIDO code [27]. In particular, the wave induced radial drift of the turning points of trapped ions which appear, in addition to a diffusive component, when the resonating ions interact with directed waves was found to be important. Depending on the direction of the waves this drift is either inward or outward.

An example of the effect of this drift is shown in Fig.213, where the evolution of a typical ion orbit, as calculated with the FIDO code, is shown for a case where the wave induced drift is inwards. Initially the ion is passing, but due to the predominant increase in its perpendicular velocity during the heating it becomes trapped; the turning points of the trapped orbit then starts to drift inwards. Thus, in such a case many resonating ions drift inwards until they become marginally trapped, some of the marginally trapped ions will pitch angle scatter and

become passing particles. Many more passing ions are therefore created than would be the case without drift. When the drift is directed outwards there can instead be a depletion of resonating ions in the centre. The combination of large orbit width and the wave induced radial transport introduces a new current drive mechanism. This current drive mechanism is dominating in certain cases, especially when the ratio between ICRF power density and the density of resonating minority ions is high [27].

### Topological Transitions of Fast Ion Orbits

Fast ions in the MeV range, like fusion products and ICRF accelerated ions, frequently occur in JET plasmas. The

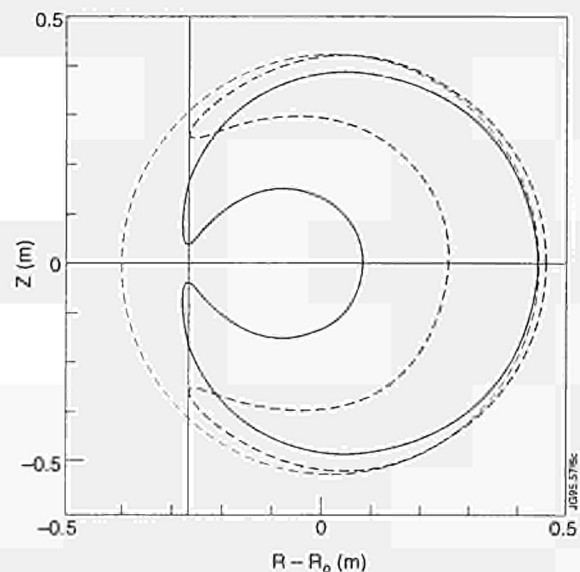


Fig.213: Evolution of the orbit of a resonating hydrogen ion interacting with a toroidally directed wave for JET-like parameters: dotted line - start of heating; dashed line; after 0.2s of heating; full line - after 1.3s of heating

standard treatment of such ions often break down since it assumes that the radial excursion of an orbit guiding centre across a magnetic surface is small compared with the distance of this surface to the magnetic axis [28]. The evolution of fast ion orbits as the ions slow down on thermal electrons, taking the finite width and non-standard character of the orbits into account, has been studied. The relevant Fokker-Planck equation is a first order partial differential equation, which can be solved with the method of characteristics. Branching of the characteristic curves to this equation occur, corresponding to topological orbit transitions. Transition probability functions, which determine the orbit evolution across the transition region, have been derived [29]. In addition, a significant inward drift experienced by ions with non-standard orbits as they slow down have been pointed out [29].

### ***Nonlinear Plasma Dynamics Magnetic Reconnection in Low Collisionality Plasmas and Fast Sawtooth Crashes.***

The observation of fast sawtooth crashes has motivated investigation of magnetic reconnection in low collisionality regimes. Following some work [30], the role of electron inertia on the reconnection rate has been analysed, initially working with a purely collisionless, zero-pressure reduced magnetohydrodynamics model [31] and later for the more general case, when finite Larmor radius effects and dissipation are taken into account [32-34].

The main result of the investigation, which is carried out by solving the relevant nonlinear model equations with analytic and numerical methods, is that reconnection rates at least an order of magnitude faster than the resistive rate predicted by the Sweet-Parker-Kadomtsev argument are expected for typical JET sawteeth. The predicted crash time turns out to be in the range of 30 to 100 $\mu$ s, as observed experimentally.

### ***Secondary Instabilities in Magnetohydrodynamics and Intermittent Magnetic Activity.***

The sequence of equilibria with magnetic islands has been investigated in collaboration with the University of Lecce, Italy, as a function of the stability parameter  $D'$  for a slab reduced magnetohydrodynamics (RMHD) model. Numerical tools previously utilized for ordinary fluids have been employed. These methods allow finding all the stable as well as unstable equilibria of the full set of RMHD equations. In this way, the sequence of bifurca-

tions from the initial axisymmetric state can be tracked systematically. As expected, the initial symmetric state becomes unstable when  $D'=0$ . The systems undergoes a symmetry-breaking bifurcation and develops an equilibrium with a small magnetic island, whose size grows as a function of  $D'$ .

At a critical value of  $D'$ , the system undergoes a second bifurcation (a saddle-node bifurcation or catastrophe): the equilibrium with a small island ceases to exist and the systems "jumps" to a new equilibrium with an island of macroscopic size. These preliminary results [35] are very intriguing. If confirmed in more realistic geometry, they could provide an explanation of MHD activity of intermittent nature (i.e., requiring a trigger) such as ELMs, and possibly certain types of disruptions [36].

### **Numerical Simulation**

The activity of the Simulation Group was directed along two main lines:

- Development and validation of models of energy transport inside the separatrix (JETTO code);
- Predictive and interpretive study of plasma in the boundary region (EDGE2D/U-NIMBUS codes).

A summary of results is given in the following sections. Other results are presented in the sections of the report dedicated to Transport and Fluctuations, and Divertor Physics Topics.

### ***Modelling of Energy Transport Ohmic and L-mode Regimes***

Ion energy transport has been studied with a transport model of the Bohm-type that was originally developed under the assumption of equal electron and ion thermal conductivity,  $\chi_e = \chi_i$  [37]. The study has shown that for a series of discharges where it is possible to separate the contribution of electron and ion energy loss channels, the ion conductivity is always larger than the electron one and a reasonable assumption is  $\chi_i = a \chi_e$  with  $a \approx 2-3$ . [38].

An analysis of ohmic discharges has also been performed showing that in the range 1-7 MA covered by JET data, the same Bohm model can be used for Ohmic and L-mode discharges. As an example of the model performance, Fig.214 shows a comparison of experimental and modelled values of the electron energy content for a series of discharges. A simple method of statistical analysis of computed temperature profiles versus the experimental ones has been used in this study. The results are

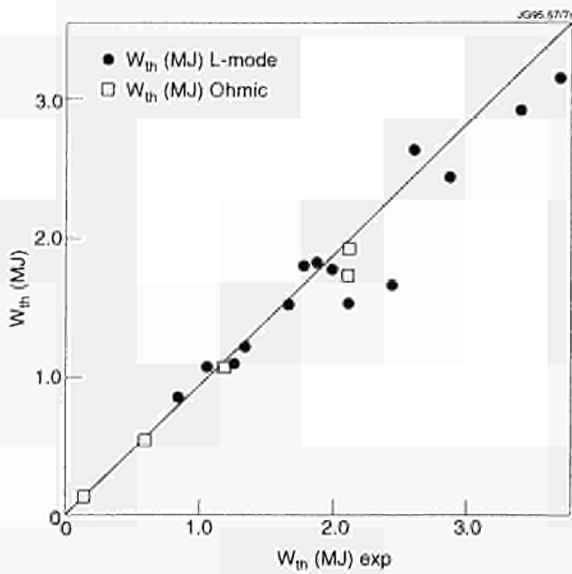


Fig.214: Comparison of thermal electron energy computed with the Bohm-like model and the experimental one

promising and it is planned to extend its use to the analysis of data available in the ITER profile data base.

**H-mode Regime and “Non-Local” Aspects of Energy Transport**

Predictive transport simulations [39] have clearly shown that JET H-mode discharges, when free of ELMs and other MHD activity, can be modelled by simply reducing (by a factor  $\approx 10$ ) the coefficients in front of the  $\chi_e$  and  $\chi_i$  expressions used for L-mode discharges. Whether or not a small residual gyro-Bohm like transport has to be taken into account in this regime remains to be properly assessed. The analysis carried out so far does not yet allow any definite conclusion on this point.

The simulations indicate that limitations of the H-mode performance are related to processes other than pure local and diffusive energy transport, such as ELMs, internal MHD activity, recycling and impurity radiation. An important result is that in various situations a transition from a low local energy transport regime (pure VH-mode) to high local transport regime (L-mode) takes place over a wide region of the plasma cross section on a time scale much shorter than expected from local and diffusive energy transport. Thus, some aspects of energy transport appear as non local when studied on the standard L-mode transport time scale.

So far the “non local” features of transport have been found in the L-H transition, ELMs (Fig.215) and cold pulse propagation due to injection of impurities. In all

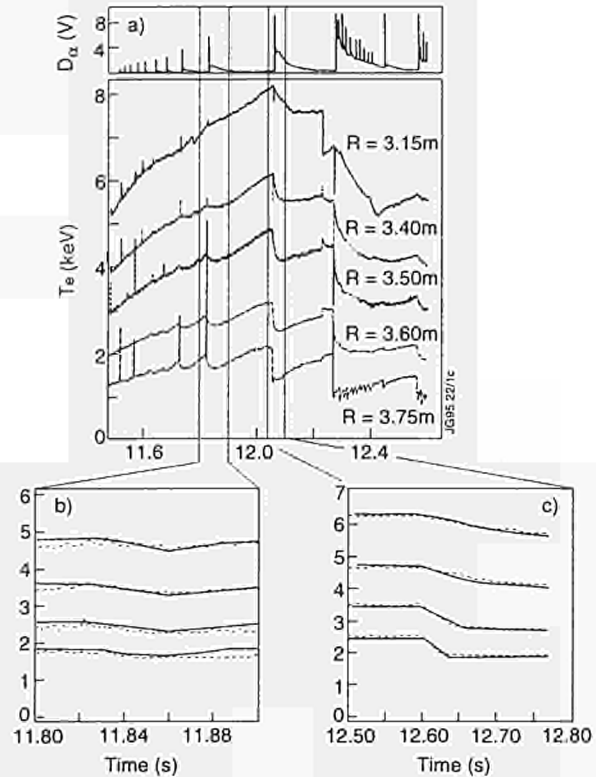


Fig.215: (a) shows the evolution of temperature measured by the ECE heterodyne system at various plasma positions having an H-mode with large ELMs. Two of these ELM's were simulated numerically (b) and (c)

these cases, they seem to originate in the plasma boundary region. Whether they can also be connected to internal perturbations is presently being investigated.

**Modelling of Edge Plasmas Code Development**

The set of boundary conditions determining a solution in the 2D boundary region dealt with by the EDGE2D/U code has been revised in such a way to simulate as closely as possible the external constraints and experimental “knobs” determining the plasma state for both steady state and time dependent situations [40].

Several schemes of particle circulation concerning recycling, pumping and puffing of hydrogenic and impurity particles can now be treated in a realistic way. The model of particle transport across field lines used in the code has been modified by including a pinch term similar to that required to simulate transport in the inner region. This term is required to obtain a decay length of density in the SOL compatible with experimental observations in the entire SOL density range observed in JET [41].

A post-processor allowing a user-friendly analysis of code results has been developed. The post-processor is

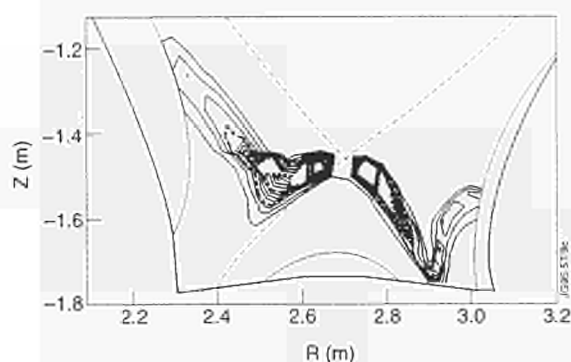


Fig.216: Impurity radiation density evaluated by EDGE2D/U for a detached plasma, showing peaks in proximity of the separatrix X-point

also linked to JET PPFs and can be used for direct comparison of computed and experimental results. Figure 216 is an example of a 2D figure produced by the post processors.

### Study of Power Exhaust Problem in JET and ITER

The problem of plasma detachment as a means to reduce the power load onto divertor targets has been studied numerically for the Mark I [42] and a possible gas box divertor configurations [43]. In particular the dependence of detachment on mid-plane separatrix density, power entering the SOL and impurity radiation has been examined. The results show that plasma detachment in JET is likely to require a non-negligible level of impurity radiation (> 50% of the input power) in discharges with significant auxiliary heating, thus linking the problem of power exhaust to that of controlling impurities.

Preliminary comparisons of predicted and experimental results show that this prediction is correct [41]. In addition features such as the drop in the ion saturation current and the drift of the radiative zone away from the targets towards the X-point are also well simulated (Fig.216). Predictive computations for ITER also show that strong impurity radiation will also be required in this device [44].

Clearly, the ideal situation would be for a radiative divertor, with most of the radiating impurities entrenched in the divertor region. The possibility of achieving such a situation by means of puffed neon has been extensively studied for the case of a JET gas box divertor [7]. It is found that generally most of the impurities tend to reside outside the divertor, thus leading to a potentially dangerous situation where impurities enter the main plasma and can dilute it in the central region. The study also shows that a sufficiently strong plasma flow towards the targets,

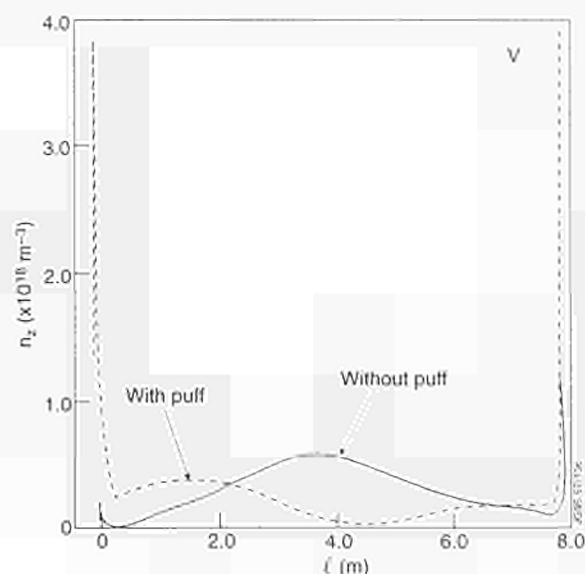


Fig.217: Poloidal distribution of average impurity density in the plasma boundary region with and without flux induced by pumping in the divertor and puffing deuterium at the top (JET gas box divertor configuration)

induced e.g. by pumping in the divertor region and puffing at the top of the device, might improve the situation (Fig.217). Even in this case, however, a non negligible fraction of impurities (~50%) would reside outside the divertor (albeit not far from the divertor entrance in our simulations).

The improvement in the impurity entrenchment due to an induced flow might be larger in a deep divertor such as the one considered for ITER [44]. However, a better understanding is required to derive any firm conclusion on the feasibility of a radiative divertor, and the effect of phenomena, such as ELMs, which might deeply influence the situation, should also be taken into account.

### Data Processing and Analysis

During 1994 the main activity in data processing and analysis has been in modifying and re-establishing the processing chains in the new JET configuration. Extensive changes have had to be made to the TRANSP code also to accommodate the new JET geometry. JET has continued to play a full part in the ITER database activities and analytic work has been completed on both divertors and the convection of turbulence.

### Upgrading of Intershot Analysis

The data analysis programs in use up to 1992 had to be modified in order to process data in the new JET configuration. The first programs in CHAIN 1 of the intershot

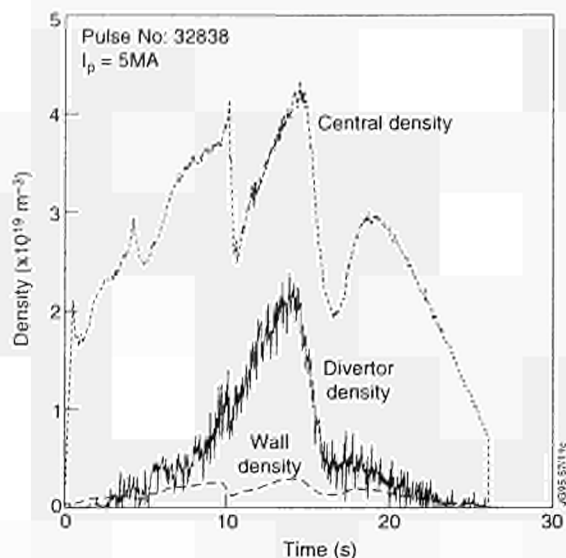


Fig.218: Density evolution with time and how it compares with the axial and edge densities.

analysis is JPFPPF processing data from the diagnostic KCID. The new pick-up coil configuration and the use of four divertor coils has had a substantial impact on magnetic data processing. The vacuum-field boundary XLOC has replaced the wire code LACWIR while the EFIT full equilibrium code has replaced IDENTC. Both of the new codes allow for up-down asymmetries in the representation of the boundary and internal surfaces. A new and fast tracking method is applied to data from diagnostic sightlines intersecting the asymmetric plasma surfaces (ECE, LIDAR, interferometer, visible Bremsstrahlung). The addition of lateral channels on the interferometer allows for an estimate of the density in the divertor region.

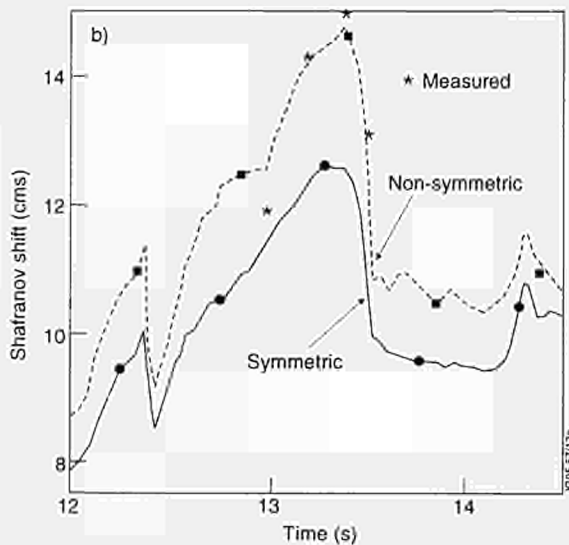
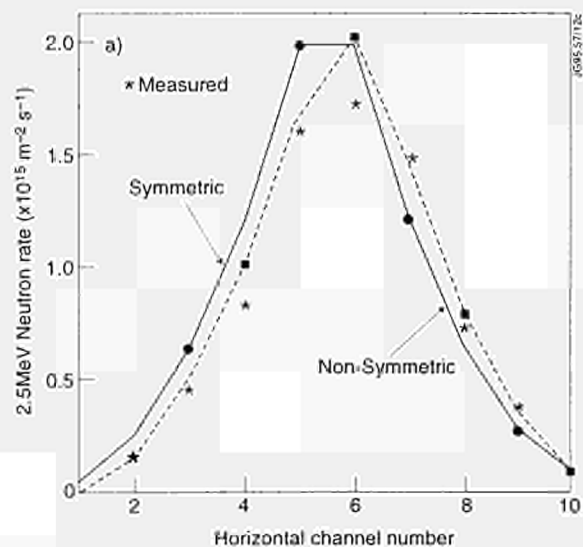


Fig. 219: (a) Comparison between predicted and experimental values for the horizontal collimated neutron channels at 13.2s: (b) compares the calculated Shafranov shift with values estimated by the IDENTC2 code

Figure 218 shows the density evolution with time and how it compares with the axial and edge densities.

The program calculating power deposition and total power from the NBI, ICRF and LH systems have also been upgraded because of plasma configuration changes as well as changes to the beam lines and ICRF antennae. The selection of data for the CPF has been upgraded following the increased time resolution of the LIDAR system.

During 1994, these changes have been gradually introduced to the data processing analysis. Sequences of reprocessing data have thus frequently occurred to ensure that the best data possible is available to the JET project.

### TRANSP Code Development

The code was successfully modified during the year by the joint JET/PPPL code development team to be able to model up-down asymmetric plasmas. Modifications included altering the fixed boundary version of the VMEC equilibrium code to support both symmetric and asymmetric plasmas and generalising the flux surface geometry to include both sine and cosine terms in the Fourier representation of R and Z. To simulate neutral beam heating the TRANSP Monte Carlo fast ion code has been upgraded to support computation of deposition, orbiting and slowing down of fast ions in an asymmetric plasma.

Simulations of Pulse No:26087 show that the new version provides significantly better estimates of relevant diagnostic quantities. Figure 219(a) shows a comparison between predicted values and measurements for the horizontal collimated neutron channels at 13.2s. Figure 219(b) compares the calculated Shafranov shift with values

estimated by the IDENTC2 code. Plasmas in the divertor configuration are now being studied with this version.

### Multi-machine Database Collaboration

The multi-machine data base assembly and analysis activities have been ongoing for the last five years, these were initially under the framework of the ITER conceptual design activity and now under the ITER engineering design activity. During 1994, the framework for the database activity has been modified and extended. The work is now steered by one of the ITER Physics Expert Groups and as well as assembling global data (L, H and H-mode power threshold), the work has been extended to include the assembly of a profile database and I-D model testing.

### ITER L-mode Database

The L-mode database has been expanded by adding more information about the experimental configuration, conditioning, heating and radiative power, and fast ion energy content. The database has also been extended by new data from various devices. These changes have made the L-mode database more complete and compatible with the ITER H-mode database. The updated L-mode database consists of data from eleven different tokamaks i.e. ASDEX, DIII, DIII-D, FTU, JET, JFT-2M, JT-60, PBX-M, PDX, TORE SUPRA and TEXTOR.

The scaling analysis of total and thermal confinement time have not yet been completed. However, preliminary results from the scaling analysis have been presented at recent International Conferences [45,46].

### ITER H-mode Database

The second version of the H-mode database has been released [47]. No further changes to the database have been made this year. The scaling of thermal H-mode confinement using two-term power law models has been studied [48]. In this study, an offset linear scaling has been assumed for the thermal energy content  $W_{th}$ , i.e.  $W_{th} = W_o + \tau_{inc} P$  with  $W_o$ ,  $\tau_{inc}$  and  $P$  being the offset incremental confinement time and loss power, respectively. Using the standard dataset of the H-mode database, the following ELM-free and ELMy power laws for  $W_o$  and  $\tau_{inc}$  have been obtained from non-linear least squares regression:

ELM-free:

$$W_o = 0.0117 I^{1.0} B^{0.5} n^{0.75} M^{-0.25} R^{3.2} \kappa^{0.05} (a/R)^0$$

$$\tau_{inc} = 0.0493 I^{1.0} B^{-0.3} n^{-1.0} M^{2.0} R^{-1.0} \kappa^{2.3} (a/R)^0$$

ELMy:

$$W_o = 0.0055 I^{0.67} B^{0.2} n^{0.8} M^{-0.1} R^{4.0} \kappa^{-1.5} (a/R)^{0.3}$$

$$\tau_{inc} = 0.085 I^{1.05} B^{-0.1} n^{-0.45} M^{1.5} R^{-1.1} \kappa^{-0.35} (a/R)^{0.3}$$

The units are [ $W_o$ (MJ),  $\tau_{inc}$ (s), I(MA), B(T), n, M, R(m), k].

In the above scalings the aspect ratio dependences have been assumed as the database consists of data from six different tokamaks (ASDEX, DIII-D, JET, JFT-2M, PBX-M and PDX) and this is not sufficient to determine two constants and six geometrical exponents. The database is also poorly conditioned in other respects (e.g. the mass exponent is not accurately determined [48]). Further improvements of the condition of the database for fitting this type of confinement scalings is expected from a decoupling, as far as is experimentally possible, of the plasma current, input power and machine size.

### ITER H-mode Threshold Database

The H-mode threshold database has been extended and improved by the addition of new data. The database now consists of data from ALCATOR C-MOD, ASDEX, ASDEX Upgrade, COMPASS-D, DIII-D, JET, JFT-2M and PBX-M. In previous work, the threshold was essentially studied for easy transition, well-known conditions for which the threshold is low: single null configuration with the ion  $\nabla B$ -drift toward the X-point, deuterium target plasma, as well as some criteria specific to each device such as distance from the wall and avoidance of low  $q_{95}$  region [49]. It was suggested that the threshold power increases linearly with the product  $nB$  for each device and that the plasma surface area,  $S$ , could be used to unify the multi-machine database. The same analyses have been redone and extended with the new data [45,46,50]. The form  $P \sim nBS$  is not dimensionally correct [51]. Assuming that the dependence of  $P$  on two of the parameters in this form is correct, the scaling can be made dimensionless (i.e depends only on dimensionless parameters  $\beta$ ,  $n^*$  and  $r^*$ ). Three forms are possible:

$$P \sim n^{0.75} BS \quad (1)$$

$$P \sim nB R^{2.5} \quad (2)$$

$$P \sim nB^{0.6} S \quad (3)$$

Figure 220(a) and (b) shows tests of Eqs (1) and (2). The straight lines are approximate lower bounds to the threshold power, and are given by the expressions  $P = 0.035 n^{0.75} BS$  (Fig.220(a)) and  $0.4 nBR^{2.5}$  (Fig. 220(b)) in units of  $10^{20} m^{-3}$ , T,  $m^2$ , m. Assuming  $n = 5 \times 10^{19} m^{-3}$  for ITER the first scaling yields a threshold power of  $\approx 100$  MW, while the second gives  $\approx 200$  MW.

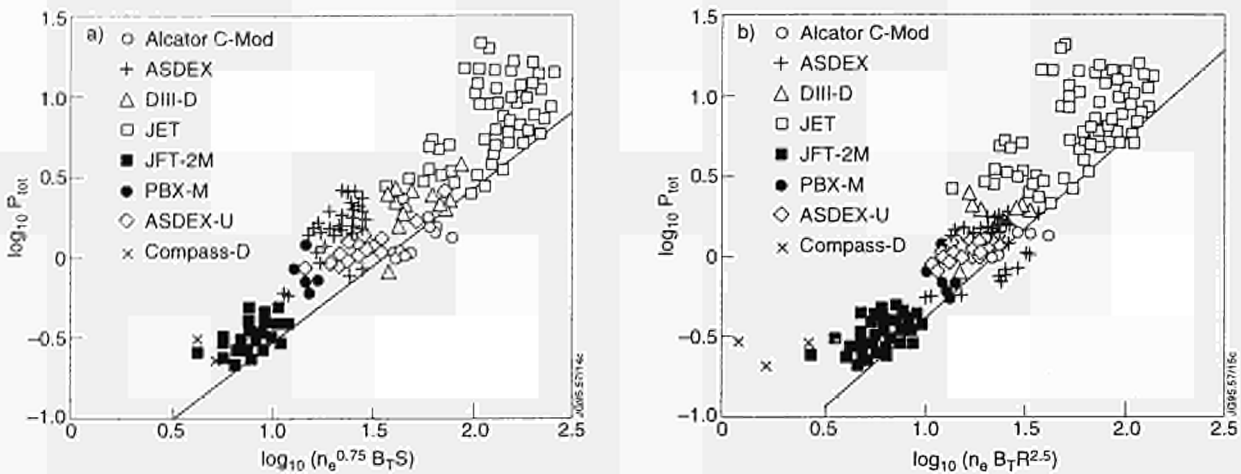


Fig.220: Tests of the variations (a)  $P \sim n^{0.75}BS$ , and (b)  $P \sim nBR^{2.5}$

**ITER Profile Database**

The profile database definition has been finalised and JET has so far released data from one pulse to the database. The first round of analysis of the profile data has commenced and will be completed in early-1995.

**Divertor Heat Pulses**

A proposed solution to the problem of high heat flux to the divertor target plates is to remove the heat by atomic processes in the scrape-off layer plasma. However, the resulting shield is susceptible to heat pulses. A computer code has been used to explore the response of a radiation cooled scrape-off layer to heat pulses emanating from the bulk plasma. Figure 221 shows the result for a particular case in the form of a sequence of temperature profiles along the scrape-off layer. It is seen that the temperature is raised and the shielding is removed.

**Turbulent Drift Motion**

Heat and cold pulses, L to H transitions, termination of high performance, are all physics processes which apparently propagate across the plasma on timescales 2 to 3 orders of magnitude shorter than the confinement time itself. To explain such rapid speeds of propagation a theory is being developed with its origin in turbulent kinetic drift motions.

A set of fluid equations have been derived for the evolution of plasma density and parallel perpendicular energy. These equations clearly show which kinetic drifts become associated with transport driven by gradients and transport driven by a toroidal equilibrium configuration.

A preliminary but simplified turbulence model applied to these equations shows that plasma fluctuations can lead to characteristic propagation speeds which scale as the drift motion, i.e. drift speeds proportional to energy (or temperature). A second study of these equations is underway. In this study, a standard small amplitude approximation is made. The resulting linearised set of three coupled equations contain so many parameters that solutions to a cubic equation giving growth rates must be computed.

**Diagnostic Software**

The Diagnostic Software section is responsible for the design and maintenance of diagnostic control, data acqui-

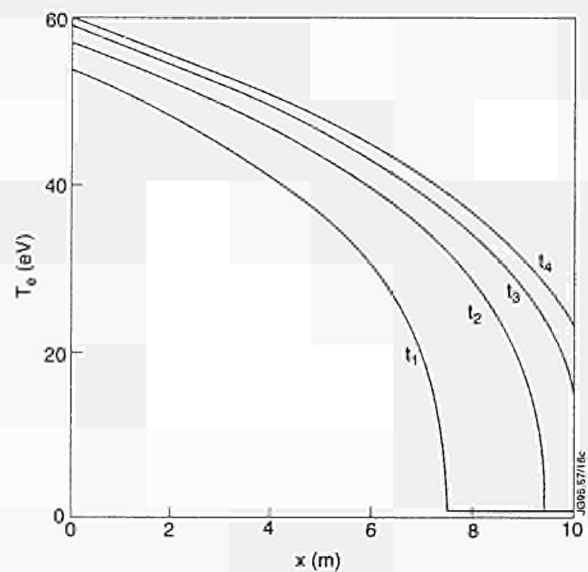


Fig.221: Time sequence of electron temperature profiles along the scrape-off layer during propagation of heat pulse to target plate

sition, calibration and display software for a considerable number of diagnostics. It also provides support to diagnosticians with the commissioning of diagnostics and trouble-shooting during operations.

In 1994 considerable effort was expended in further development of the Central Acquisition and Trigger System (CATS), the Diagnostic Data Acquisition Network (DIAGNET) and the Real Time Plasma Boundary Display (XLOC-RT). Both CATS and DIAGNET serve a multitude of diagnostic systems. Major contributions were made to the development of software for the Space and Time Resolved Velocity Distribution of Alpha Particles diagnostic (KE4), to the Plasma Boundary probes control and commissioning and the development of a data collection system for the fast CCD camera diagnostic (KL1.3). A new development is a data acquisition control system which serves all neutron diagnostics at JET (NEUTS).

The section maintains some general purpose software products such as a JPF data retrieval and display package, a General Data Acquisition and Control package and various subroutine libraries. It also supplies data analysis support on the IBM system mainly for the KS1, KS2 and KS6 spectroscopy diagnostics.

### **Central Acquisition and Trigger System**

The new Central Acquisition and Trigger System (CATS) [52] has been installed and is collecting data for several fast diagnostics. These diagnostics are used to study high frequency plasma phenomena such as the sawtooth crash and other MHD effects, and includes the Soft X-Ray (KJ3/4), fast Magnetic (KC1D-Fast), ECE (KK3), H-(KS3) and Reflectometry (KG3/8).

At the heart of the system is a Parallel Digital Signal Processor (a form of microprocessor optimised for numerical calculations). Twenty five of these processors each read data at a rate of 10Mbytes/s, the data handled by this system being approximately 12 Gigabytes per shot. For obvious reasons, only a small subset of this data can be collected. To reduce the amount of data collected, decisions are made in real-time, throughout the shot as to when the data is of value and should be saved. This "trigger system" can be pre-programmed with many algorithms running in parallel to evaluate the data.

During initial operation, the system was operated in a recording mode, where large blocks of data were collected. This provided the largest continuous datasets

recorded at JET, totalling up to 120 Mbytes. With the experience gained from this data, the trigger system is being programmed with algorithms that will collect a representative subset of these events. In addition, it is also used to spot unusual or unknown events. The methods used are neural networks able to spot sawteeth and conventional spectrum analysis to detect MHD modes.

This system is designed to be relevant to next step devices, such as ITER, which will have much longer pulse times, and therefore will require more sophisticated methods of data acquisition.

### **The Diagnostic Data Acquisition Network**

The Diagnostic Data Acquisition Network provides automatic data acquisition for PC-based diagnostics. In a single pulse, the network handles ~40MB of data. Some of these diagnostics use CCD cameras for spectroscopy or for imaging, some use transputer-based fast ADCs for transient recording, others use PC-based ADCs.

The network comprises four AST network file-servers, a VME crate with connections to CODAS control and data-acquisition systems, and the diagnostic PC's. The servers run Windows NT and our DIAGNET software which translates CODAS signals to a file-based protocol.

At the start of a JET pulse, the DIAGNET servers write pulse initialisation files in diagnostic-specific directories. The diagnostics wait, periodically looking for these files. When the files arise, the diagnostics execute their own instrument control procedures, finally writing JET pulse data files back to the diagnostic directories. The DIAGNET servers look for the JET pulse data files and send the data back to the CODAS systems.

The PC-based Data Acquisition Network provides the required high capacity, high speed and high reliability. Based on industry standard components, the network is easy and cheap to maintain. Furthermore, the system can evolve to use new technology and do new science, without displacing the existing components.

### **The Real Time Plasma Boundary Display**

The Real Time Plasma Boundary Display system (XLOC-RT), uses magnetic flux data from the diagnostic KC1D to determine the boundary of the plasma, in real time. The system uses a network of thirteen transputers to compute the flux, a second network to buffer the data during the JET pulse and compute the flux contour and a Windows PC to display the flux contour overlaid on a picture of the

vessel. The transputers are arranged to compute the flux in five regions of the vessel and fit the result at the boundaries, in parallel.

The system is installed in the Control Room and is used to give real-time and slow-motion replay of recent JET pulses during normal (and abnormal) operations. Currently, the XLOC-RT system is being developed to include calculation of the pressure ratio,  $\beta$ , and the plasma inductance  $\ell_i$ , in real time. These and the X-point coordinates will be calculated on a dedicated DEC alpha RISC processor (which provides very high performance at very reasonable cost), and then sent to a Real-Time Signal Server for subsequent distribution to display and control systems.

### **Space and Time Velocity Distribution of Alpha-particles**

This is a microwave scattering experiment (KE4) designed to measure the alpha-particle velocity distribution within the JET plasma. This system is currently being installed and undergoing commissioning tests.

A high power gyrotron microwave source injects modulated radiation vertically into the torus, where it is scattered by the electrons surrounding the alpha-particles. This scattered radiation is collected and analysed by a specially designed Real-Time Signal Averager (RTSA), which is a 36 channel spectrometer, that sums multiple repetitive samples to generate an average, which has a higher signal to noise ratio.

This is a complex diagnostic system, requiring a dedicated workstation to control and monitor the high voltage power supplies to the gyrotron; PLC systems control and monitor lower-power supplies and cooling systems; VME systems controlling stepper and servo motor drives for mirrors and polarisers. The multiple systems communicate with each other across Ethernet, and to the central CODAS systems.

### **The Fast CCD Camera**

A data collection system the fast CCD camera diagnostic (KL1.3), has been designed, built and tested. The system is centred around two ADC racks placed near the two CCD cameras and a PC system located in the Diagnostic Hall. Each ADC rack contains two ADC data acquisition cards and a fibre optic link module card plus T800 transputer. Each ADC card is equipped with four 1 MHz ADC channels and a T800 transputer. The PC contains

two T800 transputer module cards and is connected via fibre optic cables to the two ADC racks.

Each camera contains a row of 256 pixels which will be focused on the divertor. The conversion speed of the ADC's is determined by a clock signal generated by the cameras. An image of the pixel row can be obtained every 64 ms. The periods of data acquisition are determined by trigger signals or by a signal from the camera. The programs on the transputer network control the data acquisition, the image construction and the transport of the images to the PC disk where they are available for the CODAS system. The diagnostic is ready for final testing before being brought into operation.

### **Neutron Diagnostics Data Acquisition Control System**

A new data acquisition control system, called NEUTS, was designed to control the data acquisition for all neutron diagnostics at JET. The system acts as an interface between the UNIX sub-systems and the GAP tree. It manages to hide the complexity of the GAP tree from the user, thus allowing hardware to be controlled in an easy-to-use manner. The system caters for fast and slow windows of interest. In addition, the software allows diagnosticians to optionally impose specialised data taking sequences, for example, pre-plasma and post-plasma data collection, which allows background measurements to be made. The system is aware of the inter-relationship between timing and data taking modules, and the hardware limitations such as the maximum sampling frequency offered by the hardware. It prevents hardware from being over clocked, thus preventing the loss of valuable data. It also allows many diagnostics to be synchronised to the same time vector.

Although the system was developed for the neutron diagnostics, it is currently being extended and generalised to support any diagnostic system.

### **References:**

- [1] D. O'Brien et al., Nuclear Fusion **32**, 1351 (1992)
- [2] D. O'Brien et al., Nuclear Fusion **33**, 467 (1993)
- [3] J.J. Ellis et al., IAEA TCM on Magnetic Diagnostics, Kharkov, Ukraine (1994)
- [4] W. Zwingmann et al., IAEA TCM on Magnetic Diagnostics, Kharkov, Ukraine (1994)
- [5] O. Pogutse and W. Kerner "The SOL width and MHD Interchange Instability in Tokamaks", JET-P(94) 44.

- [6] B.B. Kadomtsev, *Plasma Phys. and Contr. Fusion* 34 1931, 1992.
- [7] F. Romanelli and F. Zonca, *Phys. Fluids*, B2, 754, 1993.
- [8] J.G. Cordey, W. Kerner and O. Pogutse, *Workshop on Transport in Fusion Plasmas*, Aspenas, Goteborg, Sweden 1994.
- [9] J. Drake et al, 15th IAEA Conf. on Plasma Phys. and Contr. Fusion Res., Seville, Spain, 1994, IAEA-N-60/D-P-I-A.
- [10] A.B. Hassam, *Phys. Fluids*, B4, 485, 1992.
- [11] J.G. Cordey, W. Kerner and O. Pogutse, *JET Preprint JET-(94)* 66.
- [12] J.G. Cordey, W. Kerner and O. Pogutse, to be published.
- [13] V.V. Parail et al, 15th IAEA Conf. on Plasma Phys. Contr. Fusion Res., Seville, Spain, 1994, IAEA-CN-60/A-2-II-3.
- [14] W. Kerner, O. Pogutse and R. Van der Linden, to be published.
- [15] W. Kerner, O. Pogutse, 21st EPS Conf. on Contr. Fusion and Plasma Phys., Montpellier, 1994, Vol. II, p.882.
- [16] S. Putvinski, et al., 15th IAEA Conference, Seville, Spain, 1994, IAEA-E-P-4.
- [17] D.J. Sigmar, C.T. Hsu, R. White, C.Z. Cheng, *Phys. Fluids* B4, 1506 (1992).
- [18] W. Kerner, et al., IAEA Conference, Seville, Spain, 1994, IAEA-CN-60/D-P-11-4.
- [19] R.R. Mett, S.M. Mahajan, *Phys. Fluids* B4, 2885 (1992).
- [20] J.W. Connor, et al. *Proceed. of 21st EPS*, Montpellier, France, 1994, p.616.
- [21] B.N. Breizmann and S. Sharapov, *Preprint IFSR-671*, 1994 (submitted to *Phys. of Plasmas*).
- [22] S. Sharapov, et al, 36th APS Conf., Minneapolis, 1994. *Bull. Amer. Phys. Soc.*, **39**, 1566 (1994).
- [23] H.A. Holties and J.P. Goedbloed, *Rijnhuizen Report* 94-221.
- [24] L.-G. Eriksson and P. Helander, *Phys. Plasmas* 1 (1994) 308.
- [25] J. Carlsson, L.G. Eriksson and T. Hellsten in *Theory of Fusion Plasmas (Proceedings of the Joint Varenna-Lausanne Workshop, 1994)* Editrice Compositori Bologna (1994) 403.
- [26] D. Start et al., *International Conf. on Plasma Physics (Proc. 19th EPS Conf. Innsbruck, 1992, vol. 16C, Part II, EPS Geneva 1992, 897.*
- [27] T. Hellsten, J. Carlsson and L.-G. Eriksson in *Theory of Fusion Plasmas (Proceedings of the Joint Varenna-Lausanne Workshop, 1994)* Editrice Compositori Bologna (1994) 403.
- [28] F. Porcelli, L.-G. Eriksson and H.L. Berk, in *Proc. 21st EPS Conference on Contr. Fusion and Plasma Physics (Montpellier, 1994)*, Vol. II. p.648.
- [29] F. Porcelli, L.-G. Eriksson and I. Furno, *JET Report JET-P(94)* 72.
- [30] J. Wesson, *Nucl. Fusion* 30, 2545 (1990).
- [31] M. Ottaviani and F. Porcelli, *Phys. Rev. Lett.* 71, 3802 (1993).
- [32] M. Ottaviani and F. Porcelli, *Proc. of the 21st EPS Conf. on Contr. Fusion and Plasma Phys., Montpellier (1994)*, Vol. 18B, part II, p. 532.
- [33] M. Ottaviani and F. Porcelli, in "Theory of Fusion Plasmas", *Proc. of the Joint Varenna-Lausanne Workshop, Varenna (1994)*, E. Sindoni Ed., p. 33.
- [34] M. Ottaviani and F. Porcelli, 15th IAEA Conference on Plasma Physics and Controlled Fusion Research, Seville, Spain, 1994.
- [35] C. Tebaldi, M. Ottaviani and F. Porcelli, to be published
- [36] J. Wesson, A. Sykes and M. F. Turner, IAEA, London (1994), paper IAEA-CN-44/E-I-3, Vol II, p. 23.
- [37] A. Taroni, M. Erba, F. Tibone, E. Springmann, *Plasma Phys. Control. Fusion* **36** (1994) 1629.
- [38] M. Erba, V. Parail, E. Springmann, A. Taroni, Extension of a Bohm Model for L-mode Electron Heat Transport to Ion Heat Transport and to the Ohmic Regime, *JET Report in Press*.
- [39] V.V. Parail, et al., Paper IAEA-CN-60/A-2-II-3, 15th IAEA Conference on Plasma Physics and Controlled Fusion Research, Seville, Spain, 1994.
- [40] A. Taroni, et al., *Proceedings of the Workshop on Theory of Fusion Plasmas, Varenna, 22-26 August, Editrice Compositori, Bologna, Italy.*
- [41] JET Team (presented by L. Horton), Paper IAEA-CN-60/A4-I-5, 15th IAEA Conference on Plasma Physics and Controlled Fusion Research, Seville, Spain 1994.
- [42] A. Taroni, et al., 11th International Conference on Plasma Surface Interaction in Controlled Fusion Devices, Mito, Japan, May, 1994. (To appear in *Journal of Nuclear Materials*).
- [43] R. Simonini, et al., 21st EPS Conference on Controlled Fusion and Plasma Physics, Montpellier, France, 1994.

- [44] S. Weber, et al., Proceedings of the Workshop on Theory of Fusion Plasmas, Varenna, August 1994, Editrice compositori, Bologna, Italy.
- [45] ITER Confinement Database and Modelling Group (by S. Kaye), 15th Int. Conf. on Plasma Physics and Controlled Nuclear Fusion Research, Seville, 1994, IAEA-CN-60/E-P-3.
- [46] ITER Confinement Database and Modelling Group (by S. Kaye), APS, Minnesota, 1994.
- [47] ITER H-mode Database Working Group, Nuclear Fusion **34** (1994) 131-167.
- [48] H-mode Database Working Group (by O. Kardaun), EPS, Montpellier, 1994.
- [49] H-mode Database Working Group (by F. Ryter), Controlled Fusion and Plasma Physics, Proc. 20th European Conference, Lisbon I (1993) 15.
- [50] H-mode Database Working Group (by F. Ryter), EPS, Montpellier, 1994.
- [51] K. Lackner, Comments on Plasma Physics and Controlled Fusion **13** (1990) 163-171.
- [52] K. Blackler, A. W. Edwards, IEEE Transactions on Nuclear Science, January 1994.

## Summary of Scientific Progress and Perspective

The general objectives of the experimental programme with the Mark I divertor were to assess the performance of the pumped divertor configuration, using the horizontal target tiles and, within their limitations, the vertical side tiles. The relatively open geometry of the Mark I divertor accepts a wide range of plasma equilibria, and divertor physics studies, high performance operation and advanced tokamak concept studies are possible for this configuration within the designed maximum plasma current capability of 6 MA.

The execution of the experimental programme was shared by three Task Forces: Task Force D to assess divertor performance on the vertical and horizontal target plates; Task Force H to demonstrate the high performance capability of the JET pumped divertor; and Task Force T to study those other physics areas in which JET can make important contributions to ITER and DEMO.

### Power Handling and Particle Control

The careful design and superior thermal properties of the carbon fibre composite (CFC) divertor target tiles have

resulted in significantly improved power handling. The ability to "sweep" the plasma footprint over the inertially-cooled tiles has proved to be very effective in limiting the temperature of the tiles. For example, with 25MW combined NB and ICRF heating, 72MJ of energy is conducted to the tiles and their surface temperature increases to  $<650^{\circ}\text{C}$ . In other discharges, almost 140MJ of NB energy has been injected during ELMy H-mode plasmas, raising the surface temperature of the tiles to  $<550^{\circ}\text{C}$ . In the "Old" JET X-point configuration of 1991/92, an input energy of about 15MJ could raise the tile temperature above  $1500^{\circ}\text{C}$  and provoke a severe impurity influx (carbon "bloom") which quenched the discharge.

The vertical side tiles, intended primarily as protection for the divertor coils, have also been used as the targets for ohmic and ELM-free H-modes with NB heating. In line with model predictions, the density scrape-off layer is narrower and the temperature profile is inverted with operation on the vertical target. This result gives confidence that the basic modelling assumptions are correct and with further validation and refinement will provide the tools to help design a reliable ITER divertor.

The torus cryopump has proven to be effective for plasma purity and density control, removing neutral deuterium for a wide range of strike point positions on both the horizontal and vertical target tiles. The variation in the removal rate is useful in facilitating density control in steady-state ELMy H-mode plasmas. The particle removal rate is several times the maximum NB fuelling rate (1MW of "80kV" NB corresponds to a particle source rate  $\approx 10^{20}$  atoms/s) and this helps deplete gas reservoirs in plasma facing surfaces and reduce recycling. The efficiency of the cryopump in reducing recycling has been exploited in high performance hot-ion H-modes to the point where the NB particle source dominates fuelling from recycling. Hence, peaked density profiles, favoured for improved NB penetration, are maintained and lead to improved fusion performance.

### H-mode Threshold and Confinement

The transition to the high confinement H-mode has been achieved with similar powers to those required during previous experimental campaigns. In the present campaign a more thorough study has been carried out and, when combined with the results (yet to be obtained) from other tokamaks operated with the same geometry (for example, ASDEX-Upgrade and COMPASS in Europe),

a more accurate size scaling of the threshold power will be determined and used in predictions for ITER. RF only H-modes have also been produced using either minority or second harmonic heating. The threshold power is similar to that required for NB produced H-modes.

Following the transition from the L-mode to H-mode, the evolution of the electron temperature across the whole plasma has been measured using a new 48 channel ECE heterodyne radiometer. These results confirm the earlier result of a very rapid temperature response over the entire plasma volume. This can be simulated with a global model in which the dominant L-mode transport term is reduced across the whole plasma by a factor  $\approx 15$  at the L-H transition.

After a period free of ELM instabilities, the plasma in the new JET configuration develops regular ELMing behaviour. As a result, two approaches to high performance can be pursued: long pulse, ELMy H-modes which maintain steady plasma conditions for many energy confinement times (this is considered the most credible mode of operation for ITER); and ELM-free, hot-ion H-modes in which the highest performance is achieved transiently.

In ELMy H-modes, confinement is typically a factor  $H \approx 1.8$  higher than low confinement (L-mode) scalings such as ITER89P, but at high  $\beta_p$  this can rise to  $H \approx 2.5$ . In ELM-free discharges, the enhancement factor is typically 2.2. This is not significantly different from the past, although the absolute level of confinement is, as expected, about 15% lower, since the plasma volume with the Mark I divertor is smaller. Energy confinement during the ELM-free phase of H-mode discharges with widely different enhancement factors can be modelled, however, using the same transport model (referred to above) and with the same numerical coefficients.

Preliminary similarity experiments have been undertaken for ITER in which all dimensionless parameters ( $\beta$ ,  $n^*$ ,  $\kappa$ ,  $q_w$  etc.) are kept constant, except for the dimensionless Larmor radius,  $\rho^* = r/L$ . Further experiments will be undertaken in early-1995.

### **Long pulse Steady-state ELMy H-modes**

The high heat load capability of the Mark I divertor target and the degree of density control afforded by the cryopump allows ELMy H-mode plasmas which are essentially steady state. For example, at 2MA with 7MW NB power, the plasma density,  $Z_{\text{eff}}$ , stored energy, recycling signal, plasma temperatures,  $\beta$ , and radiated power all remain

constant for 20s. The radiated power ( $\approx 20\text{-}30\%$  of the input power) and  $Z_{\text{eff}}$  ( $\approx 1.6$ ) are typically low throughout the ELMy H-mode phase. The temperature of the divertor target tiles, which are not actively cooled, increases slowly, but remains well below the design limit.

During the H-mode phase of this discharge, plasma fuelling was by NBI alone and the divertor cryopump controlled the density, with no saturation of the pumping occurring. This contrasts with previous operation in 1991 when wall pumping saturated after about 10s and no true steady-state could be achieved. The present pulse length is about fifty times the energy confinement time which, itself, is enhanced by a factor  $H \approx 1.8$  above L-mode. The demonstration of these steady-state H-modes with edge safety factors,  $q_{95}$ , as low as 2.9 and  $H/q_{95} \approx 2/3$  (identified by the ITER Physics Group as a relevant ignition scenario) is a significant step along the road to the successful operation of ITER.

### **Gas Target/Radiative Divertor Plasmas**

Complete detachment and the concomitant reduction of heat flux to the divertor target plates was first reported during 1991/92. With the Mark I divertor, this regime has been extended to cover a broad range of plasma conditions and magnetic configurations at high density in ohmic and L-mode plasmas. For example, in an ohmic detached discharge, the particle flux density to the target first increases with density (the high recycling regime), and then decreases dramatically with the onset of detachment. The emission from recycled deuterium increases as the number of excitations per ionisation increases rapidly at very low temperature. The carbon influx from the target begins to decrease during the high recycling phase as the divertor plasma temperature falls below that required for significant sputtering, and then decreases further as the temperature and particle flux decrease during the detached phase.

Detachment has been achieved in an L-mode discharge at a power level of 5MW by controlling the gas input by feedback from the ion saturation current of one of the Langmuir probes close to the inner target. There is a gradual fall in the ion saturation current, while the density is increasing. The pressure at the probe falls while the total radiated power is of the order of 50%. Plasma radiation is localised near the target plates during the attached phase of such discharges, and near the X-point during the (partially) detached phase. EDGE2D can model many of the

features of the edge/SOL for both attached and detached divertor plasmas. Studies are in progress to control, and properly model, the location of the radiating region.

Attempts to achieve complete detachment in H-mode plasmas, by puffing deuterium into steady state H-modes, precipitate an increase in the ELM frequency and eventually the plasmas return to L-mode before complete detachment can occur. So far, similar attempts by puffing a mixture of neon and deuterium also precipitate a return to L-mode when the net input power falls below the H-mode threshold. There is, however, evidence for both the screening and the compression of neon in the divertor as the deuterium flow is increased. This is in line with theoretical predictions.

### **High performance operation**

The high heat load capability of the Mark I divertor target means that carbon "blooms", which previously terminated high performance, have been eliminated. This has shown, as previously suspected, that MHD modes, which precede fast collapses (ELMs) and slow "roll-overs" of stored energy and neutron yield, can be a limit to high performance.

The ELM-free period and the fusion yield are strongly affected by vessel conditioning, gas recycling from in-vessel components and the magnetic configuration. Recycling in the new configuration was, at first, higher than in 1991/92 and special attention has been paid to identifying and reducing the source of higher recycling. In particular, divertor targets and vacuum vessel have been baked to high temperatures (200°C and 320°C, respectively) and subsequent operation has been with a vessel temperature of 250°C and water-cooled divertor targets.

Helium glow discharge cleaning has proven to be particularly effective, beryllium evaporation has been used routinely and the cryopump has been used to deplete neutral gas reservoirs. Specific magnetic configurations ("high magnetic flux expansion" in the divertor) have been developed to reduce the leakage of neutrals into the main plasma from the divertor and these studies have also helped to establish the role of the magnetic configuration in improving edge stability and reducing the occurrence of giant (DIII-D Type I) ELMs. Studies at constant input power ( $\approx 10$  MW NBI), current ( $I \approx 2.5$  MA) and toroidal magnetic field ( $B \approx 2.5$  T) show that the ELM-free period increases with flux expansion (at high edge shear) and with edge shear and triangularity (at high flux expansion).

In practice, increasing the ELM-free period cannot always be exploited for increasing the stored energy and neutron yield due to the onset of a slow "roll-over" phenomenon (perhaps a soft limitation of the plasma pressure profiles in the region of the  $q=3$  surface) which is accompanied by a variety of MHD activity whose origins are still under analysis. It is this phenomenon (already noted in some of the best hot-ion H-modes of 1991/92) that appears to limit plasma pressure to a normalised  $\beta_N \approx 2$ . In hot-ion H-modes at higher plasma current (3.5-4 MA), the phenomenon is much weaker, or entirely absent. The limitation then appears to be giant ELMs or sawteeth.

### **High plasma current, stored energy and fusion yield**

Experiments, so far in 1994, have been with plasma currents up to 5 MA and ELMy H-modes have been achieved at 5 MA with up to 15 MW of NBI. Such operation requires tight margins on plasma shape control, forces and stresses, the temporal evolution of the discharge and the magnetic flux consumption. Disruption forces have been less severe than expected because instability growth rates are slower than expected ( $300\text{s}^{-1}$  rather than  $700\text{-}800\text{s}^{-1}$ , previously).

The best steady-state results (achieved in ELMy H-modes at 4 MA/3.4 T with more than 18 MW of additional heating) show a stored energy of  $\approx 8$  MJ and a fusion triple product ( $n_D T_i \tau_E$ ) of  $2.6 \times 10^{20} \text{m}^{-3} \text{keVs}$  being maintained for more than four energy confinement times. The best transient results (achieved at the end of the ELM-free phase of hot-ion H-modes) are comparable to the best of the past even though plasmas are now  $\approx 15\%$  smaller in volume. The highest stored energy is 11.3 MJ and the fusion triple product ( $n_D T_i \tau_E$  greater than  $8 \times 10^{20} \text{m}^{-3} \text{keVs}$ ) and neutron rate ( $4 \times 10^{16} \text{s}^{-1}$ ) are within 10% of the best obtained with deuterium in 1991/92.

### **Advanced Tokamak Studies**

The domain of the steady-state tokamak reactor plasma is bounded by:  $\beta_p \geq 2$  (to provide a high bootstrap current fraction);  $H \geq 2$  (to provide high  $\beta_p$  without excessive power requirements); and  $\beta_N \geq 3$  and  $4 \leq q_{95} \leq 6$  (to avoid the need for an excessively high toroidal magnetic field). This high  $\beta_p$  regime was first studied on JET in 1991/92 where, at very high  $q_{95} (\geq 10)$ ,  $\beta_p \approx 2$  was achieved in 1-1.5 MA plasmas with "VH-mode" levels of confine-

ment ( $H \approx 3.5$ ). Although this level of confinement has not yet been realised during 1994, the high  $\beta_p$  regime has been extended to the reactor relevant domain with lower safety factors,  $q_{95}$ , higher normalised plasma pressure,  $\beta_N$ , and, by virtue of the frequent ELMs, to quasi steady-state.

With 18MW of input power and a toroidal magnetic field of 1.7T,  $\beta_p \approx 1.9$  and  $\beta_N \approx 3.2$  were maintained simultaneously for the full 3s of the heating pulse at  $q_{95} \approx 5.5$  with  $H \approx 2.2$ . The bootstrap current fraction was  $\approx 60\%$ . With 13MW of input power,  $\beta_N \approx 3$  (with  $\beta_p = 1.6$  and  $H \approx 2$ ) has been maintained for the duration of the heating pulse (7s) in a 1MA/1.4T plasma. With 21MW of input power,  $\beta_p \approx 2.8$  has been obtained transiently at 1MA/2.8T.

Up to 7.3MW, and up to 46MJ, of LH power has been coupled to plasmas using position feedback control. With high LH power at low density, sawteeth disappear,  $q(0)$  rises eventually above unity and the central electron temperature increases to well above 8keV.

A plasma current of 3MA has been driven non-inductively in a plasma with a central density of  $1.5 \times 10^{19} \text{m}^{-3}$  with 6.5MW of LH power being coupled for 6s. The loop voltage was zero at nearly constant internal inductance.

During current ramp experiments the H factor can rise above 3 but the phenomenon responsible for the improved confinement is not yet under control, since the current ramp is proving difficult to control at the low plasma currents (1.0-1.2MA) used. There is a strong increase in edge electron temperature during the current ramp.

Configurations with negative central magnetic shear have also been produced by heating with LH and ICRH and NBI early in the current rise. Stable discharges at very low  $\ell_i$  have been produced, but these initial experiments have not yet led to enhanced confinement.

In view of their possible potential for provoking  $\alpha$ -particle losses in ITER, the first experiments have been carried out in which Alfvén Eigenmodes have been externally excited using the Saddle Coils driven by a high frequency amplifier with a 3kW capability. In ohmic plasmas, the Alfvén nature of the observed resonances has been verified by scanning the toroidal magnetic field and comparing the measured resonance frequency with that calculated. The measured damping of the modes ( $\gamma/\omega$  in the range 0.1 to 0.01) are being compared with predictions.

# Developments and Future Plans

In 1978, the original objectives of JET were set out in the JET Design Proposal, EUR-JET-R5, as follows:

*'The essential objective of JET is to obtain and study a plasma in conditions and dimensions approaching those needed in a thermonuclear reactor. These studies will be aimed at defining the parameters, the size and the working conditions of a Tokamak reactor. The realisation of this objective involves four main areas of work:*

- i) the scaling of plasma behaviour as parameters approach the reactor range;*
- ii) the plasma-wall interaction in these conditions;*
- iii) the study of plasma heating; and*
- iv) the study of  $\alpha$ -particle production, confinement and consequent plasma heating.*

*The problems of plasma-wall interaction and of heating the plasma must, in any case, be solved in order to approach the conditions of interest.*

*An important part of the experimental programme will be to use JET to extend to a reactor-like plasma, results obtained and innovations made in smaller apparatus as a part of the general tokamak programme. These would include: various additional heating methods, first wall materials, the control of the plasma profiles and plasma formation.'*

At the start of 1994, JET was nearing the end of the longest and most extensive modifications since initial assembly of the device. During the long shutdown, the interior of the vacuum vessel was essentially replaced. Following completion of this work, JET was in a position to begin its planned programme of operations to demonstrate effective methods of power exhaust and impurity control in conditions close to those envisaged for ITER.

Since the beginning of its experimental campaign, extensive studies had been made in the first and third

areas of work of JET's objectives: reactor relevant temperatures (up to 30 keV), densities (up to  $4 \times 10^{20} \text{m}^{-3}$ ) and energy confinement times (up to 1.7s) had been achieved in separate discharges. The second area of work had been well covered in the limiter configuration for which JET was originally designed. However, the highest performance JET discharges had been obtained with a 'magnetic limiter', (or X-point configuration). The duration of the high performance phase of these discharges exceeded 1.5s; this was achieved by careful design of the targets and specific operation techniques, but is limited, ultimately, by an unacceptably high influx of impurities, characterized by a rapid increase in electron density, effective ionic discharge and radiated power (referred to as the 'bloom').

The fourth area of work had been started by earlier studies of energetic particles produced as fusion products or by ion cyclotron resonance heating (ICRH). It was addressed further during 1991 by the first tokamak plasma experiments in deuterium-tritium mixtures. The high performance achieved in deuterium discharges, together with the experience gained in making substantial modifications to JET in a beryllium environment and with significant vessel activation, gave confidence that an experiment with about 10% tritium in the plasma could be performed and would provide data that could be used to plan an effective campaign of deuterium-tritium experiments in 1996.

During 1991, the JET Council had approved the policy of a step-wise approach to the introduction of tritium in advance of the full D-T phase of JET operations. As a first such step, after having obtained all necessary regulatory approvals, JET successfully carried out a preliminary tritium experiment (PTE-1) in November 1991 (as already described). A release of fusion energy in the megawatt range in a controlled fusion device had been achieved for the first time in the world.

In the 1991/92 campaign, JET achieved plasma parameters approaching breakeven values for about a second, resulting in large bursts of neutrons. However, in spite of the plasma pulse continuing for many seconds after reaching peak plasma values, the neutron count fell away rapidly as impurities entered the plasma and lowered its performance. This limitation on the time for which the near-breakeven conditions could be maintained was due to the poisoning of the plasma by impurities (the 'bloom'). This further emphasised the need to provide a scheme of impurity control suitable for a Next Step device.

In late 1991, the Council of Ministers approved a modification to the JET Statutes, which prolonged its statutory lifetime by four years until 31st December 1996. The extension will allow JET to implement the new Pumped Divertor Phase of operation, the objective of which is to establish the effective control of plasma impurities in operating conditions close to those of the Next Step. This programme of studies will be pursued before the final phase of full D-T operations in JET.

During 1993, a large proportion of JET's effort was devoted to shutdown work for the pumped divertor phase of operations. The first stage of the shutdown in 1992 had involved removal of components and replacement of faulty toroidal magnetic field coils. The second stage in 1992/93 involved assembly of the four divertor coils and casings inside the vacuum vessel. The third stage of the shutdown began in mid-1993, with the final positioning of the coils. The shutdown was successfully completed with pumpdown of the torus in January 1994. The first plasma in the Pumped Divertor Characterisation Phase was produced in mid-February and by mid-March successful 2MA diverted plasmas had been established. During 1994, the plasma current was increased to 5MA, the total heating power to 26MW, the stored energy to 11.3MJ and the neutron rate to  $4 \times 10^{16}$  neutrons/s.

1994 saw significant progress in optimising peak fusion performance and extending operation to the reactor relevant steady-state ELMy H-mode, which has now been obtained under a variety of conditions (plasma currents up to 4MA, power levels up to 26MW, in the high  $\beta_p$  regime, in discharges with negative central magnetic shear, and at high  $\beta_N$ ). The high  $\beta_p$  regime has also been extended to steady-state and to the reactor relevant domain.

The high power handling capability of the Mark I divertor target was demonstrated and the severe impurity

influxes (carbon "blooms"), which previously terminated high performance plasmas, have been eliminated. The cryopump reduces recycling, eliminates the effects of wall saturation (observed in previous long pulse operation), allows effective particle control, and generally allows higher performance.

Overall, these achievements show that the main objectives of JET are being actively addressed and substantial progress is being made. The overall aim for JET can be summarised as a strategy "to optimise the fusion product ( $n_i T_i \tau_E$ ). For the energy confinement time,  $\tau_E$ , this involves maintaining, with full additional heating, the values that have already been reached. For the density and ion temperature, it means increasing their central values  $n_i(0)$  and  $T_i(0)$  to such an extent that D-T operation would produce alpha-particles in sufficient quantities to be able to analyse their effects on the plasma.

The enhancements to JET aim to build up a high density and high temperature plasma in the centre of the discharge (with minimum impurity levels) where alpha-particles could be observed, while maintaining an acceptably high global energy confinement time  $\tau_E$ . The mechanisms involved are to decouple the temperature profile from the current density profile through the use of lower hybrid current drive and neutral beam injection to ensure that, at higher central temperatures, the current density in the centre does not reach the critical value that causes sawtooth oscillations.

This involves the following:

- a) Increasing the Central Deuterium Density  $n_D(0)$  by:
  - injecting deuterium pellets and high energy deuterium beams to fuel the plasma centre and dilute impurities;
  - injecting pellets to control the influx of edge material;
  - stabilising the  $m=2, n=1$  magnetic oscillations present at the onset of a disruption with magnetic perturbations produced from a set of internal saddle coils which will be feedback controlled;
- b) Increasing the Central Ion Temperature,  $T_i(0)$  by:
  - trying to lengthen the sawtooth period;
  - controlling the current profile (by lower hybrid current drive in the outer region, and by counter neutral beam injection near the centre) to flatten the profile;
  - on-axis heating using the full NB and ICRF additional heating power (24MW, ICRH, and 20MW, NB)
- c) Increasing the Energy Confinement time  $\tau_E$  by:
  - increasing to 6MA the plasma current in full power, H-mode operation in the X-point configuration;
- d) Reducing the impurity content, by:

- using beryllium as a first-wall material to decrease the impurity content;
- controlling new edge material by using the pumped divertor configuration.

In parallel, preparations for the D-T phase of operations have continued. In particular, JET has completed installation of all the main components of the active gas handling system and pre-tritium commissioning has continued. During 1994, the inactive commissioning phase of subsystems continued in accordance with the JET programme for D-T operations in 1996. Some subsystems were almost ready for active commissioning with tritium trace amounts, which is planned for mid-1995.

JET is now continuing its programme of operations to demonstrate effective methods of power exhaust and impurity control in operational conditions close to those envisaged for ITER before the final phase of full D-T operations. ITER relevant studies will provide stimulation to JET and JET's results will make an important contribution to the development of the ITER design.

The following sections describe various developments underway on JET to implement these systems.

## Pellet Injection

The pellet injection effort deals with two systems:

- the pellet centrifuge for shallow deposition of pellet mass beyond the recycling layer at high equivalent flow rate as an intermediate particle source tool in connection with divertor pumping.
- the high-speed pellet launcher, on the basis of a two-stage gun technology which has been under development for some years.

### The Pellet Centrifuge

A more detailed description of the design and the functions of the various components of the pellet centrifuge have been detailed in the 1991 and 1992 JET Progress Reports and the basics will only briefly be presented in this Report.

The centrifuge has been conceived to deliver long strings (~1 minute duration) of 2 and 3mm pellets at repetition frequencies of up to 40s<sup>-1</sup> with velocities between 50 and 600ms<sup>-1</sup>. Its purpose is for shallow fuelling with minimum recycling beyond the separatrix for investigations in connection with the divertor programme. It accelerates pellets mechanically from the hub to the tip of a rotor arm (R = 0.35 m) from which they leave at about

1.4 times the rotor tip speed. Each size of deuterium ice pellet will be launched from one of up to four possible individual extruder units into the central part of the centrifuge rotor hub, into which protrudes, hanging from the stationary crown on top of the rotor housing, the stationary stop cylinder. The latter features a hole that can be azimuthally adjusted to ensure the proper starting conditions for the pellet on the rotor arm.

The design of centrifuge rotor and stop cylinder follows very closely that of the centrifuge developed for ASDEX Upgrade by IPP Garching, Germany, who also advise JET under contract. The extruder is of a new design by JET to provide a much larger number of pellets per tokamak pulse, and is novel, in the sense that, its final version will attempt to make use of "dynamic cooling". A large LHe cryopump of more than 10<sup>5</sup>ℓs<sup>-1</sup> pumping speed is to cope with the gas losses stemming from pellet acceleration and guidance and is to keep the pressure below 10<sup>-3</sup>mbar. To operate on the machine for a 1-2 days, the capacity of the cryopump was designed for 2500barℓ of deuterium. As a consequence, this demanded stringent safety measures against hydrogen deflagration after regeneration, with implications for the design and pressure classing of the main vacuum vessel and the cryopump.

This year, assembly of the cryopump and its initial commissioning was completed. The LHe tank with its cryopanel cylinder had been pre-assembled into the toroidal LN<sub>2</sub> tank with the LN<sub>2</sub> baffle structure shielding the LHe parts from room temperature radiation. The part of the cryovalve system, damaged in a lifting incident, was repaired in the first two months of 1994. The four internal coaxial go-and-return cryogenic feeds, through which each of the four possible extruders are to be supplied from the 300ℓ LHe reservoir of the cryopump, were fitted to the LHe system and closed with temporary short-circuits. The main vessel lid was then brought onto the cryopump assembly and the respective cryostructure supports, as well as the cryovalves and cryocouplings for the supply of cryogenics, were integrated into the lid by welding them into their respective lid nozzles and to internal distribution manifolds. The main vessel was then closed and lifted onto its support which was erected in the Assembly Hall for off-line commissioning. Cryogenic and control services were connected and, during early Summer preliminary cryogenic tests, (without pumping of deuterium) were conducted. The cryopump performed

as expected from the design.  $\text{LN}_2$  consumption was about 10ℓ/h and that of LHe was 8-10ℓ/h.

The main vacuum vessel, had been classed as a pressure vessel with an operational pressure range of -1 to 22bar gauge to cope with the aspects of a hydrogen deflagration and an operational temperature range of -198 to 80°C to cope with the problem of an internal spill of cryogenics in connection with the deflagration case. The latter specification was mainly to guarantee under all circumstances that a possible tritium fraction of the deuterium would be confined. The flange bolts are highly stressed due to the CEFILAC metal seal requirements and it turned out that those delivered with the vessel had a problem with their ductility at low temperatures. A bolt material compatible with specifications was finally found, and new suitable bolts are now on order. To permit limited use of the vessel for commissioning with deuterium, a safety scheme was worked out that would guarantee absolute safe working practice against deflagration but might not provide final containment in case of an additional spillage. In this assessment, the heat transfer from the cryopump to the bottom of the vessel and, to the centrifuge rotor was calculated for the case of a prolonged non-evacuated status of the system after cryopump regeneration. Although only model estimates are available, the highest value that can be imagined is ~3kW.

Since the turbopump rotor of the centrifuge would also suffer from this cooling event, the rotor area has been covered with electrically heated, temperature controlled copper cladding, and, in addition, the vessel bottom flange with the critical bolt area has been temperature controlled by external heater fans and jackets. Certain bolt temperatures will also be monitored: the centrifuge rotor speed will be limited to half its maximum operational speed (i.e. 1/3 of its design value or about 1/10 of its maximum rotational energy) and the deuterium capacity will be limited to 1250 barℓ.

The vacuum/pressure pipe and target vessel to contain the pellet track to the torus were also drawn into the bolt problem. A contract was placed to procure the pipework for the commissioning loop to measure the pellet strings equivalent particle flow rate with the actual deuterium gas being returned to the outside of the main vessel cryopump. This contract ran into problems with the unexpected difficulties of contractors handling the metal seal requirements. The initial plans to extend this contract to include the bellow section of the flight tube with the use

of already procured stainless steel bellows had therefore to be abandoned. As an emergency measure, this section is now being constructed in-house, with only part manufacture and final testing sub-contracted. The pellet track has mainly been built. The section inside the torus was assembled at the end of the shut-down; the sections inside the flight tube have been virtually completed apart from movable part to connect the in-vessel and external track through the vacuum valve to the torus. The latter vacuum valve with the capability to also withstand the 22bar gauge from the potential hydrogen deflagration was also fitted before the end of the shutdown. It needs re-commissioning when the track is installed, then to be mutually interlocked with the connecting track section above.

The stop cylinder unit on top of the centrifuge rotor was brought through its final adjustment and the centrifuge unit again re-commissioned to 300Hz. The microwave cavities for the pellet mass and integrity control and monitoring have been produced and tuned. However, the microwave diagnostics as well as the other diagnostics (in-flight flash photography, track entrance position detector and stroboscopic photography of the extruders and rotor hub area) suffered a severe set-back when the physicist for these diagnostic facilities fell seriously ill by the middle of the year and could not carry out the work.

The most challenging components of the system is the pellet generating unit, or extruder. The equivalent flow rate of 1000mbarℓs<sup>-1</sup> for about 1 minute amounts to about 100cm<sup>3</sup> of deuterium ice. The technical solution adopted to create the cubicle pellets was by extrusion of an ice rod with the cross-section of the pellet cube and then these were chopped off at suitable lengths. At maximum rate 3mm pellets need to be extruded at 10cms<sup>-1</sup> and chopped off at about 40s<sup>-1</sup>. To limit the forces, deuterium ice can only be extruded at the higher temperatures of around 14°K whereas pellets should be accelerated at about 7°K. Therefore, it was attempted to cool the deuterium ice "dynamically" during extrusion at 14°K while it was sliding along the wall of a sufficiently long channel (~200mm). This should permit the thermal conductivity of the deuterium to cool the ice while it is moving towards the chopper at the speed of about 10cms<sup>-1</sup>. Since there are uncertainties involved, operation is intended to start with the less ambitious scheme of cooling down evenly the 200mm long ice column to 7°K and then feeding the colder part into the chopper, limiting the total number of delivered pellets per tokamak pulse to 40-50, initially.

Two extruder units, occupying two of the four possible positions in the stop cylinder acceptance sector, are being prepared for nominal 2 and 3mm pellets, with the latter one planned for first commissioning. Each unit has a hydraulic actuator ( $\sim 10^4$ N force), internal to the main vessel vacuum, working into a deuterium ice piston/cylinder arrangement featuring the nozzle portion where the dynamic cooling takes place and being fabricated in friction welded copper (Cu) and stainless steel (SS) sections to separate the various temperature stages required in this scheme. Starting from coldest point, the nozzle, towards the cylinder LHe - first in the two-phase, then in the gaseous state - flows through channels between the inner Cu-SS parts and an outer SS jacket forming a double wall with the former. Finally it flows through the various heat exchangers and shields.

The double-bellow units for the in-vessel hydraulic piston actuator, crucial in the assembly sequence were finally delivered. However, several difficulties contributed to further delays. The chopper lever, with a combined mass of  $\sim 100$ g, uses a CoSm magnet section in a powdered iron core and develops 60N force leading to a stroke of 4 mm over  $2 \times 10^{-3}$ s at 40Hz repetition frequency. The magnet is bi-stable so that only pulses with a minimum of ohmic losses are needed in the coils for the cutter action. The CoSm magnet needs to be jacketed in a stainless steel case to prevent chemical reactions with hydrogen, and the windings of the iron core are thermally connected to a helium return flow heat exchanger to keep its operational temperature  $\sim 40^\circ$ K. After investigating various schemes for the manufacture of a strong lever, to withstand the high dynamic forces and to encapsulate the magnet, an elegant method of laser welding of laser-cut stainless steel sheet metal elements was found.

In the main, the first extruder for 3mm pellets has now been assembled, with some minor work still to be performed. It has undergone warm pre-testing of its piston action inclusive of its force and travel instrumentation. The extruder will be installed in the waiting main vessel unit in early 1995 and be commissioned and made operational from initial cool-down to ice extrusion and pellet formation phases with the aim of early application of pellet injection into the torus.

### The High-speed Launcher

This launcher is to accelerate sabots supported 6mm deuterium pellets to speeds up to 4 kms $^{-1}$  by using two-

stage light gas gun driver technology (1.5m long, 6mm ID barrel in combination with a 3m long, 60mm ID pump tube and a  $\sim 0.6$  kg titanium piston, foreland and driver gas being hydrogen), for deep to central plasma fuelling purposes. Sabots are small plastic (mostly polypropylene) pistons, set behind the deuterium pellets to protect them from the hot driving gas. These sabots are needed for pellet velocities exceeding 3kms $^{-1}$  and are being accelerated with the pellet. These are made from two halves of equal mass, which split after leaving the barrel due to aerodynamic forces and can be eliminated from the pellet path by a shear cone. Pellets are formed by cryo-condensation into bushings ( $\sim 20$ mm long barrel sections) and are pre-loaded with bursting discs and sabots. The cryo-condensation is performed outside the gun breech in a cryostat with the capability of forming 10 pellets in one thermal cycle and then storing them in their bushings. These can be moved one per tokamak pulse into the breech immediately before the shot. The transport is performed by a "chain" imbedded in a stainless steel cold box operating at less than 20°K.

A series of shots on the testbed had achieved a 50% success rate for delivering a 6mm diameter, 5mm long deuterium pellet at speeds exceeding 3.1kms $^{-1}$  into the target in a geometry compatible with the conditions at the torus site. A decision was then taken to implement the launcher behind the Pellet Injector Box (PIB) on the torus. Installation was carried out in the last possible period of the divertor shut-down and re-commissioning took much effort during the start-up of operations. Although no major obstacles were encountered in the change-over, it was not before the second half of the year that systematic shooting could commence.

There were several decisive differences to the operation of the launcher at the testbed besides the remote control feature which was already exercised there. An important part of the pellet diagnostics could not be activated. The only available pellet diagnostic was the microwave interferometer, providing size and speed of the pellet and with progressing time this suffered detuning. Another difference was the state of the LHe supplied from a dewar via a valve box which required new tuning of the cryogenic operational parameters for the pellet formation. Also, in preparation for a tokamak pulse in synchronous operation, the waiting times, with a pellet ready for loading and the gun armed, were frequently much longer than encountered on the testbed and the loss

of pellets into the launcher cold box after an aborted or early disrupted tokamak pulse led to undesirable condensation of deuterium elsewhere in the cold box with subsequent cryogenic instabilities. Several modifications on the pellet formation cells, mostly to the ram inserts, were made until finally the condensation process could be controlled in a satisfactory way. The transport chain movement and the loading of the breech thereafter functioned without flaw. The two-stage gun performed with few problems and no further modifications were required. Some limited experiments have been performed with pellet injection using polypropylene (impurity injection experiment) and deuterium .

## Advanced Divertor Development

The Mark I divertor currently installed in JET has been successful from several points of view. In particular, its power exhaust capability in the sweeping mode has been very good, and the cryopump works effectively. The fact that Mark I is relatively wide has made it possible to investigate a large variety of magnetic equilibria with strike points on both the horizontal and vertical sections of the target tiles.

However, the openness of the divertor also has drawbacks. As described in the 1992 JET Progress Report, such an open divertor is not as effective at retaining neutrals in the divertor region as a more closed design, particularly at high powers and low to moderate main chamber densities. Under these conditions, the divertor plasma itself is not opaque enough to re-ionize the recycling neutrals. Thus, it was decided to design and construct a series of more closed divertors, beginning with Mark IIA, to be installed in 1995, and followed by Mark IIGB (Gas-Box) in 1997. The purpose of these closed divertors is to permit a high neutral density in the divertor volume while maintaining a low neutral density in the main chamber. The first condition is required to exhaust power to a large fraction of the total divertor wall area by the volumetric processes of radiation and charge exchange; i.e. to operate in the highly radiating, partially or fully detached regime. The second requirement, that of low neutral density in the main chamber, is necessary for highest main plasma performance, as has been demonstrated at JET as well as in other tokamaks.

### The Mark IIA Divertor

The design and construction features of Mark IIA divertor were described in considerable detail in the 1992 and 1993 JET Progress Reports, and will only be briefly summarized here. Mark IIA is a moderately closed semi-V divertor which flares out at the upper region of the side plates in order to accommodate a wide variety of equilibria. These include several low X-point equilibria of varying degrees of flux expansion, which have strike zones on the "outward facing" dome targets, as well as higher X-point equilibria which contact the "inward facing" vertical targets. The target tiles are 40cm long in the poloidal direction, providing a high toroidal wetted length, relative to Mark I. This feature, along with the inclination of the targets, gives a wetted area sufficiently large that the need for sweeping is eliminated. Monte Carlo simulations indicate that the pumping performance should be somewhat better than that of Mark I. Mark IIA is intended to satisfy the dual and sometimes conflicting needs of performing well in both the high performance campaigns (low to moderate density, magnetic axis) not too far above the midplane) and ITER-related high density radiating divertor studies.

The design of Mark IIA was finalized in 1992 and procurement and fabrication went ahead throughout 1993/94. It is scheduled to be installed starting in May 1995.

### The Mark II GB (Gas-Box) Divertor

The term "Gas-box" is used to denote a divertor characterized by a close fitting baffle near the X-point, below which there is a relatively large volume in which the recycling neutrals (both hydrogenic and any seeded recycling impurity which may be used) can circulate freely in order to re-enter the divertor plasma along its entire surface. This promotes the volume loss of energy and momentum required to prevent excessive energy deposition on the target "strike zones". The JET Gas-Box divertor uses the same coils, pump, and support structure as the Mark IIA divertor, but has new target tiles and tile carriers to change the geometry from moderate V to Gas-Box configuration. The system has been designed so that the changeover can be carried out via remote handling, following the D-T campaign scheduled for late 1996.

To provide a specific test of the Gas-Box concept, the range of equilibria must be restricted to allow for a baffle which is long enough, and close fitting enough, to prevent the back-flow of neutrals into the main chamber. In

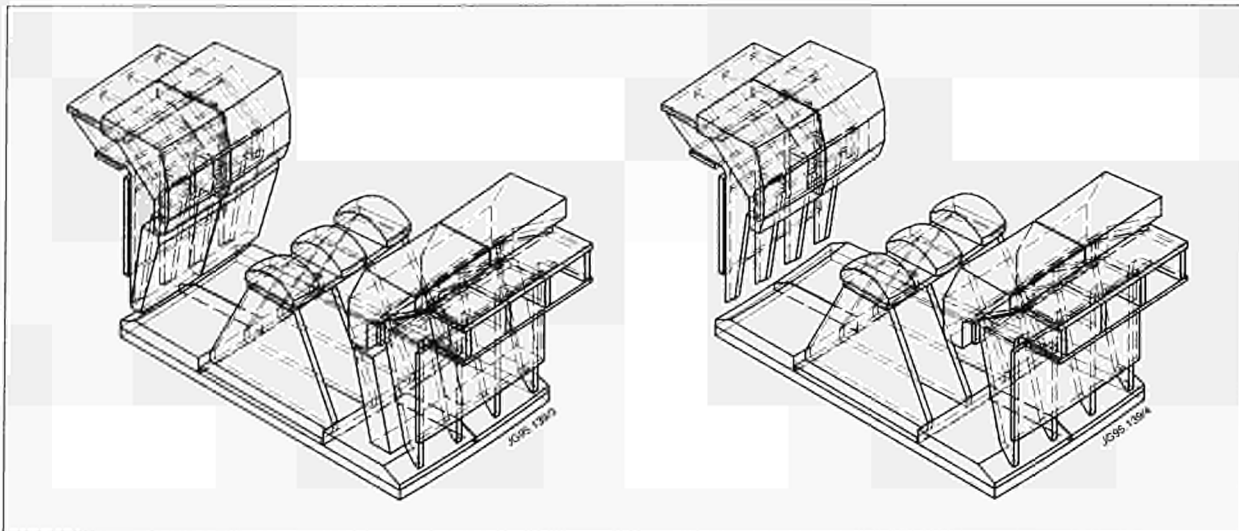


Fig.222: Mark II Gas-Box divertor (a) with lower side-wall tiles, and (b) without lower side-wall tiles

practice, this means that only high X-point equilibria can be investigated.

Two versions of the gas-box are being designed and are shown in Figs.222(a) and (b). These use a common baffle, base target, and septum assembly. The "vertical target" version shown in Fig.222(a) has a nearly vertical tile placed just below the baffle on both the inside and outside legs, and operates with the strike points on these vertical tiles. In this case, the recycling of neutrals takes place through the private flux region only. Such vertical target divertors have certain advantages, and current ITER thinking favours such a design. Among the advantages are a higher wetted surface for handling power during non-detached phases of the discharge, such as start-up or in ELMs. In the second Gas-Box configuration, the vertical target tiles are removed and the strike points are placed on the bottom plates. The wetted surface is now smaller, but the pumping is somewhat stronger. In this case, recycling neutrals can circulate around both sides of the divertor plasma, rather than just from the private flux region. This version is closer to the original ITER EDA design. The precise location of the baffles, the targets, and the septum are still being iterated by calculations using the multi-fluid EDGE2D code.

In contrast to the design of Mark IIA, the tile carriers for Mark IIGB will probably be fabricated from CFC plates. The anticipated radiative loads on the carriers, including the septum, are sufficiently high that bare inconel could not be used, and would need to be clad. Thus, the adoption of CFC as the structural member should lead to a simpler engineering solution, and tests are in progress to validate this approach. The material of

both the target plates and the baffles is CFC. In principle, beryllium could be used for a later version, if justified by continuing interest from ITER and favourable results from the Mark I beryllium tile test in Spring 1995.

At present, it is planned to test both versions of the Gas-Box divertor. However, the scheduling is very tight, and it may be necessary to omit one of them. The vertical target version is the one currently favoured by JET (as well as by ITER), but the design is sufficiently flexible to permit either version to be operated first.

## Tritium Handling

The purpose of the JET Active Gas Handling System (AGHS) is to pump the JET torus, to collect gases from various systems (the torus, neutral beam injection, pellet injection and various diagnostics), to purify and isotopically separate these gas mixtures (consisting of the six hydrogen molecules, helium and impurities such as hydrocarbons, oxygen, nitrogen, etc) and to re-inject pure tritium and deuterium gas into the torus.

The AGHS is situated in a separate building (Building J25) and can be separated into sub-systems as shown in the block diagram (Fig.223). During the year, the inactive commissioning phase of the sub-systems continued in accordance with the JET programme for D-T operations in 1996. Some sub-systems are almost ready for active commissioning with tritium trace amounts which is planned for mid-1995.

With the commissioning of the individual sub-systems being substantially complete, the emphasis has been on operation of the system in an integrated way under conditions relevant to the actual tritium processing cycle. For

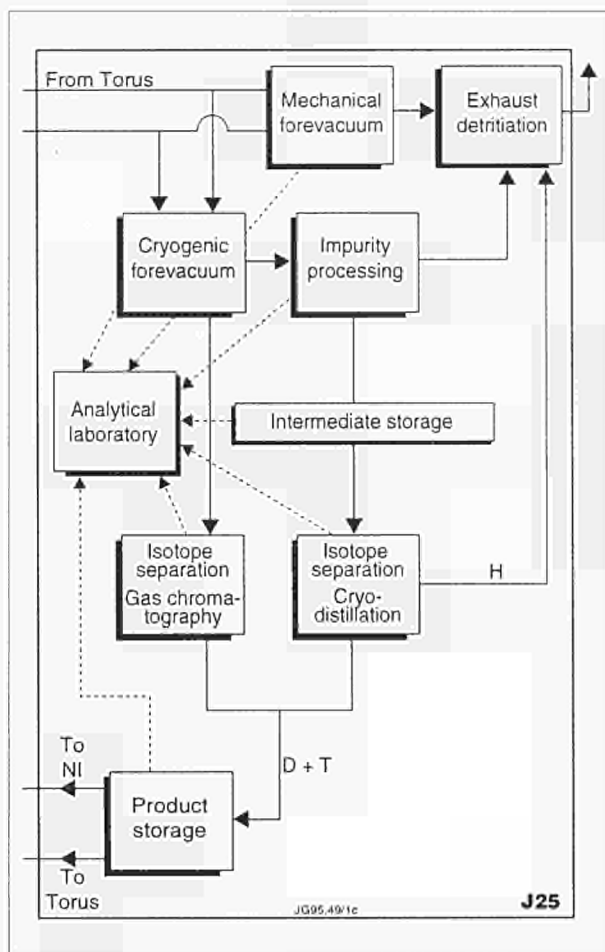


Fig.223: Block Diagram of Active Gas Handling System (AGHS)

example the gas chromatography isotope separation system has been operated in conjunction with the intermediate and product storage using uranium beds in these sub-systems for hydrogen isotope pumping.

Some of the achievements during the year are set out in more detail below.

### Cryoforevacuum

The cryoforevacuum system (see Fig.224) consists of five double containment modules, each containing a number of individual cryogenic pumping components. Modules 1 and 2 are designed for removal of air and trace quantities of water, Module 3 is designed to pump hydrogen isotopes, and Modules 4 and 5 will pump mixtures of hydrogen isotopes, helium and impurities allowing separation by distillation of these groups of gases during warm-up.

Module 4 contains two identical pump pairs. The maximum capacity of each pump is 300 standard litres of hydrogen gas. The pumping rate is about  $180\text{ l/s}^{-1}$  at 0.1 mbar pressure measured upstream of the pump entrance flange (CF100). Module 3 contains two identical pumps of larger

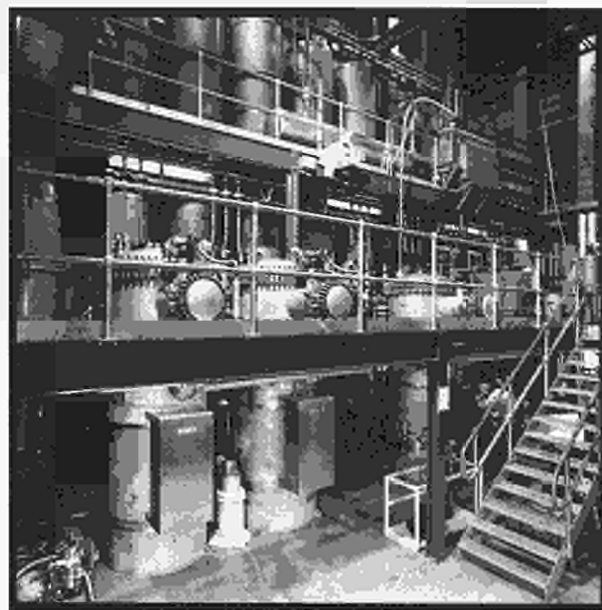


Fig.224: Cryoforevacuum Module

size. The maximum gas capacity pumped by each pump was 3,200 standard litres of hydrogen gas. The pumping rate was about  $450\text{ l/s}^{-1}$  at 0.4 mbar pressure measured upstream of the entrance flange (CF100) to the pump. These pumping speeds and capacities meet the specification for handling of machine exhaust gases.

### Cryodistillation System

The Cryodistillation system (see Fig.225) was connected via doubly-contained lines into the AGHS interconnecting duct to the intermediate storage and product storage systems. A number of tests runs in this configuration have now been carried out.

The 800 l volume of the Cryodistillation system was filled at room temperature with 2 bar pure protium ( $\text{H}_2$ ) of purity 99.995%. After the system was cooled down to 18°K and run in recycle mode, a sample was taken from the bottom of Column 3 (if the Cryodistillation system is filled with protium, deuterium, tritium, the bottom of Column 3 should supply pure tritium gas) and analysed with the gas chromatography system. The analysis showed a gas mixture of 47.1%  $\text{H}_2$ , 5.7% HD and 47.2%  $\text{D}_2$ . Considering that the total deuterium gas amount was less than 0.08 l and the volume collected during sampling was about 0.2 l, the Cryodistillation system is very well capable of enriching deuterium in protium and will even perform better in the case of tritium in protium. This situation will arise during D-D operation after DTE1 when it will be necessary to collect tritium which will continue to be evolved from the machine.

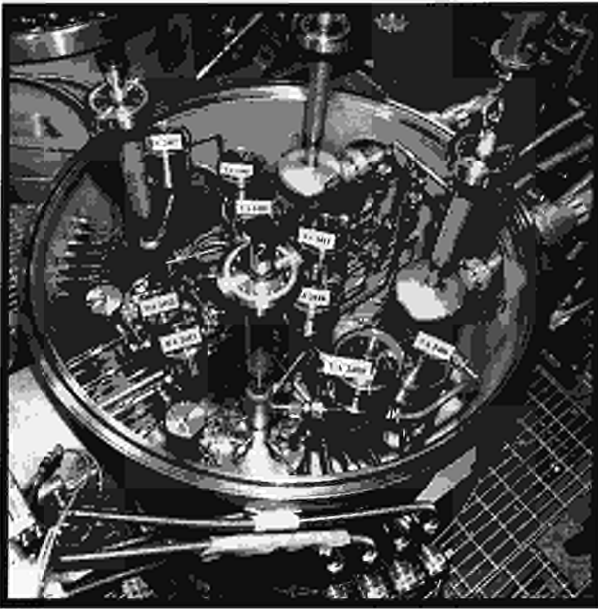


Fig.225: External view of cryodistillation system

The columns were filled with various gas mixtures, (eg 66.8% H<sub>2</sub>, 26.5% HD and 6.7% D<sub>2</sub> via Feed 1 and/or Feed 2). At the top of Column 1, "pure" protium was measured and at the bottom of Column 3 "pure" deuterium was measured. "Pure" means that, with the AGHS diagnostic, no HD and/or D<sub>2</sub> (H<sub>2</sub> and/or HD) signals were observed in the H<sub>2</sub> (D<sub>2</sub>) product streams (detection limit was 100ppm). The separation was relatively independent of the Cryodistillation controller parameters.

The overall conclusion for the Cryodistillation system is that satisfactory product quality can be obtained. (The deuterium quality was much better than that of the deuterium gas supplied, which contains HD of about 0.2%).

### Gas Chromatography

The Gas Chromatographic isotope separation system has also been operated in an integrated way. Hydrogen isotope separation was performed with various protium/deuterium gas mixtures in the palladium-filled columns using the displacement technique. The main result is that any gas mixtures from 0.02 to 98% can be separated into "pure" product streams. ("Pure" means about 0.3% HD and 99.7% D<sub>2</sub>). The transition between the product streams is very sharp and the amount of interfractions small. Correct valve switching is essential especially if the amount of product gas is small.

### Analytical Laboratory

The analytical laboratory glovebox has been commissioned and connected via sampling lines to the other

AGHS sub-systems. The analytical gas chromatograph, which had been previously tested with tritium in a "stand-alone" mode, was installed in the glovebox.

### Exhaust Detritiation

The Exhaust Detritiation (ED) system was designed to provide depression in the torus in the event of a large vacuum leak and to collect any tritium evolved. It was also designed to provide depression and clean-up facilities in the AGHS and during remote maintenance activities on the machine. Experience during the Preliminary Tritium Experiment in 1991 showed that tritium evolution from components, in particular in the Neutral Beam system, could continue at a significant level for several months after cessation of operations. The original ED dryers operate on a 12 hour regeneration cycle. To improve the reliability of the ED system, when it is required to be operated for extended periods, for example during the remote tile exchange, an additional high pressure air dryer is being incorporated. This is a continuously regenerating system which can be used when relatively low levels of tritium (<37GBq/m<sup>3</sup>) are present and torus systems are ventilated with air. With an output dewpoint of lower than -50°C, this permits the period between regenerations of normal ED dryers to be increased by a factor ~100, thus significantly increasing the reliability.

### Oxygen-in-Hydrogen Detector

For safety reasons, it is necessary to detect the presence of oxygen (due to potential air leakage into the torus or neutral injector beams (NIBs)) in hydrogen isotope mixtures returned after plasma discharges, prior to processing in the Active Gas Handling System. An instrument, installed in Building J25, performs this task by catalytic combustion of a sample in a vessel at 77K by means of a hot (600°C) platinum filament. Pressure change after combustion ( $2\text{H}_2 + \text{O}_2 \rightarrow \text{H}_2\text{O}$ ) directly measures the oxygen concentration (1% O<sub>2</sub> → 3% pressure drop since H<sub>2</sub>O at 77K has a negligible vapour pressure). This instrument, processes only individual samples and is therefore not suitable for continuous monitoring. Therefore, JET has developed and tested a differential calorimetric instrument, measuring the heat of recombination of a reactive gas mixture on a wet-proof catalyst. This instrument can detect O<sub>2</sub> in H<sub>2</sub> at low pressures (signal >1mV for O<sub>2</sub> concentration of 0.2% at 10mb pressure). These monitors will be installed in the NIB and torus crown.

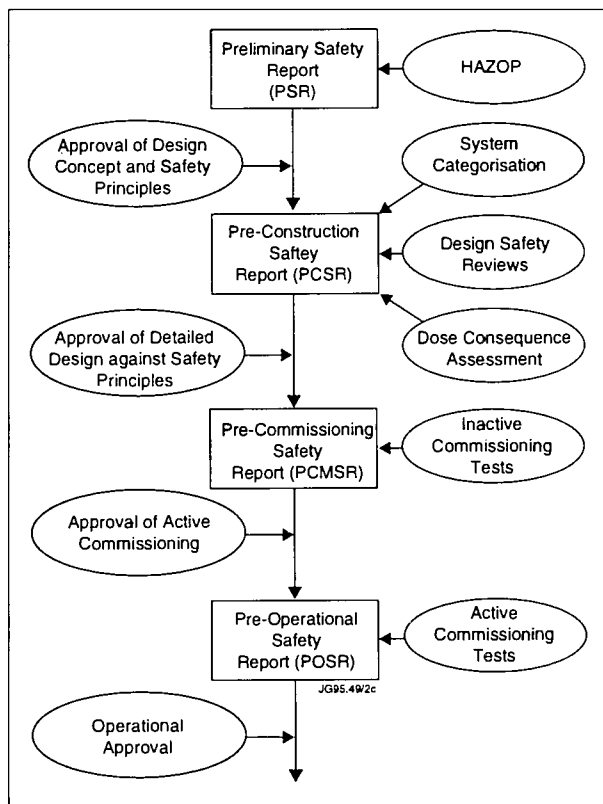


Fig.226: JET safety submissions

## Accounting

In all radioactive laboratories, accounting of radioactive isotopes must be carried out at regular intervals. In the case of radioactive gases which are volatile, accounting is very important to know where the gases are stored. In the case of tritium, accountancy is even more difficult and important due to the potential of tritium to permeate through metal and to dissolve in many materials.

The most common method for accountancy in the case of radioactive gases is to determine the pressure (P) and temperature (T) of the radioactive gas within well known volumes (V). For this purpose, the values of over 300 volumes were determined with an accuracy of about 0.5%. Three different techniques were used:

- A few large volumes were filled with water after manufacture. From the weight change, the measured temperature and known density of the water, the volume of the tanks was calculated;
- Volumes were calculated by simple expansion of gas from known volumes into unknown volumes using the ideal gas equation and a high precision pressure gauge;
- Large volumes were determined by observing the weight loss of a dewar filled with liquid nitrogen due to the evaporation of the nitrogen and by measuring the pressure increase in the volume.

In the case of tritium, in addition to PVT measurements, the amount of tritium in the gas mixture must be determined. In the AGHS, this can be undertaken in the following way:

- Ionisation chambers were added to large volumes, which will detect any radioactive gas. In the AGHS, the main radioactive gas expected is tritium. Thus, the ionisation chamber signal will be tritium specific, but it is known that ionisation chamber response varies with gas pressure and gas species in the gas mixture due to different multiplication processes;
- Mass spectrometry: quadrupole and omegatron mass spectrometers were installed for the characterisation of the various gas mixtures in the analytical laboratory, which were connected via sampling lines to the other sub-systems;
- Gas chromatography: an analytical gas chromatographic system was developed for the specific needs of the AGHS. The advantage of gas chromatography is that the composition of the gas mixture during analysis will not be changed in contrast to mass spectrometry. The main disadvantage is that a full analysis takes about half an hour;
- Calorimetry: the tritium content can be calculated from the temperature rise of containers filled with tritium. The decay heat generated by one gram of tritium is 0.324W. At JET, this method will be used to determine the inventory of tritium-filled U-beds which are used for the tritium delivery before the tritium is transferred to the AGHS.

Further development of an "inertial guidance" thermostat resulted in a calorimeter with a base line stability of  $\pm 10\mu\text{W}$ . It will be used to measure as-received tritium batches in transport uranium beds. The achievable absolute accuracy is only limited by the instruments used for calibration and measurement to  $\sim \pm 300\text{ppm}$ . However, the inherent base line stability will permit measuring, for example, the half life of tritium to within  $\pm 1\%$  in a 24 hour period (tritium decay rate is  $\sim 100\text{ppm/day}$ ).

## Safety Related Commissioning Procedures

The completion of these procedures is a pre-requisite for obtaining approval for the start of commissioning with tritium. These cover specific conditions such as leak rates, ability to transfer gas to special tanks for processing, and verification of the correct operation of all valves

from the control system. A block diagram of the safety submissions required are set out in Fig.226.

All process lines of the sub-systems of the AGHS are surrounded by independent secondary containments. Most are filled with nitrogen, but some are evacuated. The purpose of the secondary containment is to contain tritium released or permeated from the primary containment.

All these nitrogen-filled valve boxes were leak tested to the specification of less than one volume percent in-leakage in 24 hours with a starting pressure inside the box of about 30mbar below atmosphere. The over/underprotection system to protect the flat wall boxes against evacuation or overpressurising and the purge mechanism to remove activities were checked and commissioned for all twelve valve boxes. This required a tremendous effort in sealing feedthroughs and penetrations.

The AGHS is controlled by a distributed control system and can be operated in automatic mode or in "single mode" where the operator can control valves, and pumps. This control system is capable of detecting faulty and slightly incorrect process conditions and can correct those conditions via software interlocks. Although these software interlocks increase the safety of the plant, almost no credit is given to the control system in the probabilistic safety analysis of the AGHS due to the difficulty of demonstrating software reliability. To achieve the requested safety standards, a protection system based on hardwired interlocks must be installed in the AGHS.

The main purpose of a hardwired interlock system is to bring all systems, sub-systems or part of a sub-system before the occurrence of dangerous conditions into a safe state. This is achieved by turning off heaters, pumps, etc, and closing or opening valves, etc, by means of simple, well proven electrical or pneumatic equipment (excluding sophisticated equipment such as computers, etc). There are 220 hardwired interlocks installed in the AGHS. A test procedure was written for every hardwired interlock and the correct operation of the hardwired interlock was demonstrated and witnessed by a representative of the UKAEA's Safety and Reliability Directorate (SRD).

### **Safety Approval and other preparations for Tritium Commissioning of AGHS**

The formal safety documents which comprise the safety case for the AGHS have been endorsed by the Fusion Safety Committee and the UKAEA's SRD. In particular, the Pre-Commissioning Safety Report (PCMSR) was endorsed

during 1994 and a number of procedural aspects requiring resolution were identified. Once these are cleared, approval for tritium commissioning of the AGHS is expected from UKAEA, which should enable it to proceed in mid-1995.

With the endorsement of the PCMSR, any changes to the AGHS became subject to a formal modification procedure. This procedure, which categorises modifications by their safety significance, has been in operation in 1994 and about 40 modifications arising from commissioning have been dealt with.

A number of features of the AGHS Building have been completed as a result of the requirements of tritium operation. These include sealing of penetrations, formation of a sub-change area for the Analytical Laboratory to allow freer access to the remainder of the building plant area and more effective deployment of personnel, and provision of inactive and active area Health Physics laboratories. Procedures have been prepared to transfer 40TBq of tritium recovered after the PTE in 1991 into the AGHS to enable the first stage of trace tritium commissioning to start.

### **Safety Approval for Torus D-T Operation**

The UKAEA's Safety Directorate Group (SRD) endorsed the Preliminary Safety Report (PSR) for the torus which provides part of the required documentation to use tritium. Work then began on the next phase of documentation, the Pre-Construction Safety Report (PCSR). This report will provide a comprehensive description of the torus and its auxiliary systems, as well as safety analyses of postulated accidents and probabilistic risk assessments.

An analysis was undertaken to assess the torus and its auxiliary systems for their intrinsic radiological hazard. This work was completed and conclusions accepted by the UKAEA and the Fusion Safety Committee. More detailed analyses in the PCSR will be provided for those systems categorised as potentially hazardous. Much of the supporting work for the PCSR analyses was completed in 1994 and a few remaining jobs initiated. This work is expected to be completed in early 1995.

## **Technical Preparations for D-T Experiments**

A DTE1 Technical Preparations Group was set up (under the Chairmanship of Dr A Gibson) to identify the technical work which needed to be completed before DTE1 could take place in 1996. In particular, it was important

to identify all the work which needed to be included in the 1995 shutdown, bearing in mind that this would be the last major shutdown before DTE1. The group also took note of additional work which would be required for DTE2 in 1999, but the main emphasis was on DTE1. For this purpose, DTE1 was taken to be a programme producing  $\sim 2 \times 10^{20}$  D-T neutrons in a three-month period at the end of 1996, with provision for a remote handling divertor configuration change immediately after the experiment.

The boundary conditions set for the Group were that:

- (a) all major work in operation areas was to be completed during the 1995 shutdown;
- (b) the planned short shutdown in 1996, prior to DTE1 was to allow systems not required for DTE1 to be removed or valved off. No new components could be introduced into the vacuum envelope at this time.

### Planning Summary

The main items of work identified are listed, as follows:

#### AGHS Plant

The commissioning milestones for the Active Gas Handling System (AGHS) plant are summarised in Table XXI.

#### Prepare Case for UKAEA Agreement to Operate

A large effort would be required to ensure that all elements in the reference configuration were properly documented and demonstrably safe for tritium operation.

#### Emergency : Planning and Training

- Emergency Planning : during 1995
- Training : AGHS Operations : 1994/95
- EiC, NB, RF, Cryo,
- Shift Technicians : 2nd half of 1995
- Emergency Control Centre : end 1995

#### Vacuum System

- Bake plant upgrade to Helium : 1995
- Tritium Admission System
- (Torus & NIBs) : 1995
- Vacuum interspace manifolding : 1995
- Torus exhaust & ventilation to
- Exhaust Detritiation System : 1995/96

#### Neutral Injection

- PINI Upgrades : 1995
- Water drainage : 1995

Table XXI : AGHS Commissioning

Jan 1994	Successful high quality D/H Separation demonstrated with both Gas Chromatography (GC) and Cryodistillation(CD)
April 1995	Use AGHS to maintain JET vacuum during operation periods including cryopump regeneration
June 1995	Start three-month commissioning programme to separate the $T_2$ recovered from PTE (1000 Ci) Main Aims: (a) Purify $D_2$ to release levels using CD (b) Purify $T_2$ to re-use level using GC (c) Leak test system with trace $T_2$
Sept 1995	Process $D_2$ through AGHS to clean up to a level where it could be used to supply $D_2$ to JET. Carry out safety tests
Nov 1995	Start full tritium commissioning of AGHS off-line at the level of few $gmT_2$
Early 1996	Use AGHS to pump down JET including on-line trials of exhaust detritiation system
Mid 1996	Complete commissioning AGHS off-line at the level of a few gm of $T_2$ Main aims : (a) confirm U-bed performance with $T_2$ (b) test impurity processing (c) test GC with realistic $T_2$ batch size
Mid 1996	Use AGHS to supply $D_2$ to JET and pump plasma exhaust
Late 1996	Supply $T_2$ and exhaust pumping for DTEI

#### RF Systems

- Modest upgrading for tritium : 1995

#### Remote Handling Development

- Provide for Remote Tile Exchange : 1995/96
- Practice Remote Tile Exchange : in shutdown plan
- Identify systems for removal : in progress
- Preparation of Remote Handling
- Access for ex-vessel tasks : 1996

#### Machine Services

- Freon system: Review and secure : 1995
- Water System: enhancements : 1995

**Access and Fire Systems**

Extend Access Control	:1995/96
Complete N <sub>2</sub> TH Fire Suppression	:1995
Associated Oxygen Monitoring	:1995/96

**Technical Services**

Shielding and Penetration Sealing	:1995
Depression Plant Commission and Operate	:1995/96
JIT Ventilation Systems (remote tile exchange, control dresser unit, ISO containers)	:1995/96
Backing Pump exhaust to J25	:1995/96

**Diagnostics**

Categorise for operation, isolation or removal	:1995
Upgrade to tritium standard	:1995/96
Review window security	:1995
Removal, Refurbishment and Replacements of after DTE1	:1997

**Summary of Work to be Completed**

The technical preparations to be completed before DTE1 could take place are summarised in the following sections. Most of these actions should be completed during the 1995 MarkII shutdown.

**Reference Configuration**

A referenced configuration has been defined to enable the Safety Report to be produced. A change control system is being defined so that developments from the reference configuration could be properly recorded and approved for tritium operation in due time.

The IVIS cameras will be removed during DTE1 to prevent neutron damage. It is considered that the cameras can be replaced manually during DTE1 to allow an IVIS inspection, if necessary. Such an operation would require operations to be interrupted for a few days to allow for: decay of short-lived activation; Torus Hall ventilation; radiation surveying and barriering off. The plasma viewing systems suffer from the same difficulty that neutrons would degrade and eventually render exposed cameras inoperable. These systems are so important that the cameras could be periodically replaced. Ways are being examined of sheltering the cameras from the neutron flux, for instance, by using optical relays and neutron shields.

**Vacuum Interspaces**

All interspaces are identified and a general policy has been agreed.

**Remote Maintenance**

A comprehensive survey and assessment has been completed of ex-vessel components and a number of actions identified. The expected activation radiation levels are such that most required operations can be hands-on, subject to the usual dose control procedures. Eventually, it is expected that a small number of required ex-vessel remote handling developments would be identified.

**Waste Management and Activated Material Handling**

The waste management implications of DTE1 have been assessed. In view of the fact that the tile modules due to be removed following DTE1 will be stored for possible re-use and thus will not be declared waste, existing JET procedures are adequate for dealing with all of the operational waste anticipated following the experiment.

It will be necessary to modify some existing JET facilities to handle activated and tritiated components for storage. These modifications are mainly in non-operational areas and, therefore, need not be carried out during the 1995 shutdown. However, it will be necessary to install a ventilation system in the Torus Hall during the 1995 shutdown, to enable tritiated components to be stored in the torus hall whilst their associated dose rates decay. The design of these modifications is underway.

Currently, no significant machining work has been identified to be carried out on activated components. If such work does arise, it will have to be carefully assessed and the necessary facilities located.

**Tritium Introduction**

Provision is being made to introduce tritium to a single gas introduction point on the main horizontal point of Octant No:6 and to any quadrant on either or both NIB boxes.

The deuterium torus gas admission system will be the one currently in operation and will continue to use a bottled gas supply. For tritium, the main introduction route is considered to be by neutral injection, where both the T<sub>2</sub> and the D<sub>2</sub> will be supplied from the AGHS. The restriction to one torus tritium gas admission point needs to be examined to confirm that this will be sufficient for

high density ICRF heating scenarios. Provision of additional feed lines would be difficult and costly but could be done if a clear requirement was identified.

### **Gas Collection and Analysis System**

Considerations are in progress to decide whether requirements can be met within the AGHS or whether the West Wing D<sub>2</sub> system (GCS) be upgraded and qualified to tritium standards. An outline proposal for carrying out on-line analysis of the gas stream from the torus during tritium operation, in the AGHS has been prepared. The main shortcoming is that samples cannot be collected for off-line analysis. If this is accepted, the AGHS system would be implemented and the GCS isolated during DTE1 and restored for D<sub>2</sub> operation in subsequent experiments, when the tritium exhaust level had fallen to a low level.

### **Torus Ventilation during Remote Tile Exchange**

A concept has been agreed to permit control of tritium outgassing from the torus through the AGHS detritiation system and to provide, from a separate system, sufficient ventilation in the Remote Handling enclosures. The ventilation system will ensure that operation of the two booms does not divert torus exhaust air away from the detritiation system.

### **Cryosystems**

Each cryopump will be regenerated after any day on which it has been exposed to a significant quantity of tritium (in the 100 Ci range). The operation of the AGHS depends on the supply of cryogen from the cryoplant. Reliable operation of the cryoplant is thus essential to the continuance of tritium operation, although failure would not lead to any tritium hazard.

### **Health Physics Aspects**

The Health Physics systems and procedures already in place at JET are, in general, adequate for DTE1. It should be noted:

- (a) The Depression Stack monitors must be operational;
- (b) The N<sub>2</sub> fire suppression system must be operational;
- (c) Vacuum systems connected to the torus must exhaust to the AGHS;
- (d) Items for removal from the Torus Hall after DTE1 will be subject to radiation and contamination control procedures;

- (e) Upgrade of Health Physics Laboratory tritium assay capability must be completed;
- (f) The existing tritium site monitoring programme must be reviewed and extended if necessary.

### **Staff Training**

The overall training requirement has been assessed based on the experience from the PTE. A general tritium and radiation familiarisation course will be needed for all staff who need to enter operational areas. Specialised training will be required for all staff operating systems with tritium contact. In particular, they must be trained to recognise potentially hazardous operations and to call for expert staff when necessary.

### **Approvals Required for D-T Operation**

Approvals required from UK authorities have been compiled. In addition, the Director would need to seek the specific approval of the JET Council before commencing DTE1, although the Council has already endorsed DTE1 as a programme item.

The final requirement is that JET shall satisfy the UKAEA that its arrangements conform to UKAEA standards, before D-T operations commence. As with the Preliminary Tritium Experiments (PTE), the UKAEA Director of Safety would be asked to agree that he is satisfied. Responsibility for safe operation would rest with JET.

In collaboration with the UKAEA Safety and Reliability Directorate (SRD), the UKAEA responsible body, the studies and documentation necessary in order to prepare for D-T operation and to allow the UKAEA to be satisfied with the procedures are well advanced and will be completed in time for DTE1 to take place in 1996.

### **Emergency Preparations**

A number of actions are in progress to ensure that systems and procedures will be in place before DTE1 to ensure that any incident can be controlled and will not present a hazard either to the public or to workers on site.

### **Site Emergency Organisation and Exercises**

The preparation of necessary procedures is in progress. The main units involved are: CSU (including Health Physics); Fusion Technology Division and Machine Operations Group. The procedures used for the PTE will suffice for the 'trace tritium' commissioning of the AGHS but the full procedures must be in place before DTE1.



### ***Torus Hall Fire Suppression***

The radiation levels in the Torus Hall immediately after a high performance D-T pulse will be sufficiently high to make manual fire fighting difficult. Consequently, the nitrogen enhancement (oxygen depletion) fire suppression system should be operational before DTE1.

Access to the Torus Hall during DTE1 will be limited by two factors:

#### **(a) The Oxygen Level**

The oxygen level would have to be restored from the suppression level of 13% to a working level ~21%. This will be obtained after ~2.5 hour with the ventilation system in flushing mode. Earlier entry would require breathing assistance and would be restricted by radiation.

#### **(b) The Radiation Level**

It is estimated that the radiation level would permit limited access at the Torus Hall wall floor level two hours after D-T operation (i.e. compatible with the ventilation requirement above). More extensive controlled access to ex-vessel areas would be possible after 24-hour subject to radiation monitoring and exclusion barriers.

### ***Cooling Water Systems***

Minor cooling water spillages are a common feature of interventions on JET systems, it is probably not feasible to eliminate these spillages. On occasions large spillages have occurred due to disconnections, etc. This type of spillage should not occur during DTE1.

It has been decided to introduce sampling points into PINI and poloidal field (PF) water circuits to allow batch monitoring of the tritium in water levels. The PINI loop water, which is expected to be the main source of tritium, will be kept separate from the PF loop unless monitoring shows acceptably low tritium levels. The necessary work will be carried out during the MkII shutdown.

### **Conclusions**

The technical work required to prepare for DTE1 has now been identified and in-vessel work to be accomplished in 1995 has been included in the in-vessel planning (the major item is Remote Handling installation of tiles and carriers in two Octants). The ex-vessel work has been included in the ex-vessel planning. A large amount of ex-vessel work can be accomplished within the planned shutdown duration.

The Group has shown that there are no technical or approval obstacles which cannot be overcome in time for

DTE1 to take place at the end of 1996 and our experience with the PTE means that there is confidence that the programme will be executed in a safe and professional manner. However, it is clear that an improvement in the reliability of JET operation is required before DTE1 can take place efficiently. The 1994 campaign has already revealed some weaknesses in a number of in-vessel components and these will be corrected in the 1995 shutdown.

The lessons learned from the MarkI Divertor operation have been incorporated into MarkII designs and as a consequence it is expected that the in-vessel components after the 1995 shutdown should be much more robust. The planned 1996 deuterium experimental campaign before DTE1 should expose the new in-vessel components to loads at least equal to those to be imposed in DTE1. This should enable any suspect elements to be strengthened or removed so that DTE1 can be carried out with a proven in-vessel structure.

The 1994 campaign, as with previous JET campaigns, has required frequent interventions into the Torus Hall. This will not be practicable during DTE1 because of the overheads imposed by the need: to allow short-lived activation to decay; to ventilate the Torus Hall; to undertake radiation survey and barrier-off access routes. Even entry to the Basement areas would be more time consuming, with an oxygen deficient atmosphere in the Torus Hall. Particular consideration is being given to the following systems:

- (a) Diagnostic systems as a whole, where many interventions have been necessary in 1994. In part, this was due to the fact that many systems were not fully completed during 1994 and the need for intervention should markedly decrease now that these are completed;
- (b) Diagnostic windows, where there have been a number of failures. Again, weaknesses have been identified and corrected, and the situation should improve;
- (c) Configuration turns-change where it now seems possible that manual changes may be possible in a timescale of a few days. Clearly alternation of turns configurations as seen in 1994 would not be possible, but one or two changes should be possible during DTE1.

To address the question of improving reliability to the level required for effective D-T operation a number of actions are required, they are listed below.

- (a) All interventions which are caused by a failure of the vacuum boundary or which require the vessel to be vented are being logged and categorised;
- (b) The number of interventions into the Torus Hall each week should be reported on the weekly statistics and a database should be kept of the reasons for the intervention.
- (c) Towards the end of the 1994/1995 operating period an attempt should be made to operate for two weeks without any Torus Hall access over a 14 day period.

When the present operating campaign comes to an end, the process of specifying the content of the DTE1 programme in more detail should be started. This will, be difficult in 1995 when there is no experience of MarkII operation. Nevertheless, the preparation of specific experiment proposals should begin. The proposals should address the main areas already identified:

- (a) refine the objectives of each experiment;
- (b) estimate the experiment time required;
- (c) estimate the required neutron production;
- (d) define the D-D comparison discharges and
- (e) specify the plasma performance to be demonstrated in D-D before the experiment can proceed.

## Future Plans

The JET Programme was divided into phases governed by the availability of new equipment and fitting within the accepted life time of the Project. Phase I (Ohmic Heating Studies) was completed in September 1984, and Phase II (Additional Heating Studies) in October 1988. Phase III (Full Power Optimization Studies) ended in February 1992. The scientific aims of Phase III were to obtain maximum performance in limiter configuration (currents up to 7MA) and to optimize X-Point Operation (currents up to 6MA) including a comparison of H-modes in X-point configuration using beryllium (lower X-point) with carbon (upper X-point) dump plates.

JET future plans are dominated by the insertion of a new phase of the Project (Phase IV: Pumped Divertor Configuration and Next-Step Oriented Studies). This phase is subdivided into a Divertor Characterization Plasma and an ITER Support Phase. This new phase extended the lifetime of the Project up to the end of 1996. The present campaign on divertor characterization (scheduled to end in May 1995) has still to address: high power combined heating; further exploration of the detached divertor regime and its compatibility with ELMy H-mode

operation; helium pumping and transport using argon frost on the cryopump; current profile control; toroidal magnetic field ripple studies; use of the saddle coils with the disruption feedback controller and for generating error fields; and the extension of X-point operation towards 6MA. In March 1995, the present CFC divertor target tiles will be exchanged for a set of beryllium target tiles and a comparison will then be made between the CFC and beryllium tiles for a few specific plasma configurations.

The next major milestone is then to demonstrate compatibility between the high confinement reactor-relevant ELMy H-mode regime and detached divertor operation. This might require the more closed Mark II divertor structure, which will be installed in 1995 and tested in 1996 with particular emphasis on the effect of geometry on gas target/radiative divertor plasmas, which forms the physics basis for the divertor concept favoured by the ITER Joint Central Team.

### **Extension of the Programme to end of 1999**

An extension of the JET Programme to the end of 1999 is currently being proposed. It would include divertor studies aimed at providing experimental data in support of the ITER divertor while satisfying the requirements of JET high performance D-T operations.

The basis for D-T operation of ITER needs to be broadened by establishing the confinement properties of D-T divertor plasmas. In addition, the power threshold for H-modes in D-T plasmas must be defined. Two periods of D-T operation are foreseen for the JET programme to the end of 1999, subject to the necessary approvals. JET will make important contributions to D-T physics for ITER (including H-mode threshold, ELM and confinement behaviour, and some radio frequency heating studies). The first period (DTE-1), scheduled for the second half of 1996, would check whether the more favourable confinement found during D-T operation in TFTR extends also to the ITER-relevant divertor and operating conditions in JET. In addition it would demonstrate long pulse fusion power production. JET alone can provide these with its divertor configuration. The second period (DTE-2), scheduled for 1999, would permit  $\alpha$  thorough study of D-T plasmas with enhanced levels of  $\alpha$  particle heating, capitalising on the performance improvements achieved in the preceding experimental campaigns with deuterium.



During 1996 the experimental programme will develop toward long pulse, high performance operation. The Mark IIA Divertor target structure can accommodate a wide range of plasma configurations and operating conditions, making possible high power, high current operation on both the horizontal and vertical target plates. The programme will therefore extend many of the issues now being addressed initially with the Mark I Divertor and give further emphasis to studies of the effect of geometry on gas target/detached plasmas which form the physics basis for the divertor concept favoured by the ITER Joint Central Team.

A period of D-T operation (DTE-1) is scheduled for the last four months of 1996. It will assess whether the more favourable confinement found during D-T operation in TFTR extends also to the ITER-relevant divertor and operating conditions in JET. These experiments will allow more accurate scalings for the size and heating requirements of ITER to be determined. In addition, it will demonstrate long pulse fusion power production (fusion amplification factor,  $Q \approx 1$  with more than 10 MW of fusion power). As a result, DTE-1 could last up to four months and produce up to  $2 \times 10^{20}$  neutrons. DTE-1 will also address the important technology issues of reactor relevant tritium processing and remote handling. In particular, DTE-1 will demonstrate the ability of the JET Active Gas Handling System to process tritium while supporting a reacting tokamak plasma.

In a six month shutdown in the first half of 1997, the Mark IIA Divertor target structure will be exchanged for a second target structure, an ITER-specific divertor of the "Gas-Box" class (Mark IIGB). The exchange will be accomplished by remote handling because radiation levels will be too high during 1997 for a manned in-vessel intervention. This remote handling operation will dem-

onstrate for the first time one of the central technologies required for ITER and for a fusion reactor.

In a divertor of the "Gas-Box" type, such as the Mark IIGB, energy and momentum are removed from the divertor plasma and spread more uniformly over the divertor sidewalls. Neutrals can recirculate freely through a large relatively open volume below a fairly narrow entrance baffle which is placed as high as possible near the X-point. The 1997/98 operations period will validate experimentally high power, high performance physics in a closed divertor configuration similar to that currently proposed for ITER.

### ***Final Phase of D-T Operation (mid-1998 to end-1999)***

A four month shutdown in 1998 will permit any necessary modifications to the divertor and final preparations for DTE-2. Manned interventions will again be possible in this shutdown. The subsequent experimental programme in late 1998 and early 1999 will then prepare for the final phase of D-T operation by optimising plasma performance and establishing reliable operation.

A period of high performance D-T operation (DTE-2) is scheduled to take place in 1999. This will capitalise on the performance improvements achieved in the preceding experimental campaigns with deuterium. DTE-2 experiments could last up to 8 months and could produce up to  $5 \times 10^{21}$  neutrons. Actual neutron production, within this defined limit, will be reassessed in light of the experience gained on JET (DTE-1 in 1996) and on TFTR (in 1994/95). Every effort will be made to reduce the activation produced while still satisfying JET's role in supporting ITER and the World Fusion Programme. This period of D-T operation will also provide a full-scale test of the technology of processing tritium in conjunction with an operating tokamak.



## Appendix I

**JET Task Agreements 1994**

<i>Title</i>	<i>Association</i>	<i>JET Responsible Officer</i>
<b>RF HEATING DIVISION</b>		
Wave induced current drive experiments on JET	EUR-CEA, Cadarache, France	C. Gormezano
RF transport code development	EUR-IPP Garching, Germany	C. Gormezano
Fast ion and electron kinetic effects on JET	EUR-UKAEA Culham, UK	C. Gormezano
Confinement studies in profile control experiments	EUR-ENEA Frascati, Italy	F.X. Soldner
<b>EXPERIMENTAL DIVISION I</b>		
Edge plasmas and plasma surface interactions	EUR-UKAEA Culham, UK	P.E. Stott
Plasma wall interactions	EUR-IPP Garching, FRG	P.E. Stott
Neutron production related physics and associated diagnostics	EUR-NFR Sweden	P.E. Stott
Plasma surface interactions	EUR-NFR Sweden	P.E. Stott
Neutron production related physics	EUR-UKAEA Harwell, UK	P.E. Stott
Collective scattering measurements on ions in JET plasmas	EUR-ENEA, Frascati, Italy	P.E. Stott

<i>Title</i>	<i>Association</i>	<i>JET Responsible Officer</i>
Microwave reflectometry	EUR-CFN/IST Lisbon, Portugal	P.E. Stott
Feedback stabilization of disruptions	EUR-ENEA CNR-Milan, Italy	P.E. Stott
Neutron production related physics and associated diagnostics	EUR-ENEA Frascati, Italy	P.E. Stott
Physics of turbulent and convective transport, MHD and related diagnostics	EUR-FOM The Netherlands	P.E. Stott
Work on collector probes	EUR-NFR Sweden	P.E. Stott

## EXPERIMENTAL DIVISION II

Measurement and interpretation of divertor and plasma edge impurity ion temperatures	EUR-KFA Julich, Germany	R. Konig
Dynamics of ions and of neutral particles in tokamak plasmas	EUR-ENEA Frascati, Italy	R. Gianella
Spectroscopic measurements: interpretation and impurity analysis	EUR-CEA Cadarache, France	P.R. Thomas
Charge exchange recombination spectroscopy	EUR-FOM Amolf, The Netherlands	M. von Hellerman
Impurity analysis and plasma diagnostics using spectroscopic measurements	EUR-NFR Sweden	P.R. Thomas
Impurities and other topics	EUR-UKAEA Culham, UK	P.R. Thomas

## DATA ANALYSIS & MODELLING

Plasma stability	EUR/UKAEA Culham, UK	J.G. Cordey
------------------	-------------------------	-------------

<i>Title</i>	<i>Association</i>	<i>JET Responsible Officer</i>
Modelling of anomalous transport and study of energetic particle collective effects	EUR-ENEA Frascati, Italy	A. Taroni
Physics of shaped cross-sections	EUR-UKAEA Culham, UK	W. Kerner
Analysis of local transport in JET and comparison with theoretical models	EUR-UKAEA Culham, UK	J.G. Cordey
Transient transport analysis in JET	EUR-ENEA CNR-Milan, Italy	A. Taroni
Comparison between JET profile data and the predictions of a transport model based on ITG and trapped electron modes	EUR-NFR Sweden	J.P. Christainsen
MHD spectroscopy and advanced tokamak scenarios	EUR-FOM The Netherlands	W. Kerner
<b>OPERATIONS</b>		
Alfven eigenmodes	EUR-CRPP Lausanne, Switzerland	J. Jacquinot
Feedback stabilization of disruptions	EUR-ENEA CNR-Milan, Italy	D.J. Campbell
The control of instabilities and disruptions	EUR-UKAEA Culham, UK	D.J. Campbell
Study of density evolution and recycling of JET plasmas during (pumped) divertor operation as a function of fuelling method and wall conditioning state	EUR-ENEA Frascati, Italy	G. Saibene

## Appendix II

# List of Articles, Reports and Conference Papers Published in 1994

1. ELM precursors in JET.  
Ali-Arshad S Campbell D Colton A Cripwell P  
deKock L Kramer G J Nave M F F Neill G F  
1992 Int. Conf. on Plasma Physics: Joint Conf. of 9th  
Kiev Int. Conf. on Plasma Theory; 9th Int. Conf. on  
Waves and Instabilities in  
Plasmas; 19th EPS Conf. on Controlled Fusion and  
Plasma Physics, Innsbruck, 29 June - 3 July 1992. 3  
vols. EPS. 1994. p.I-227.
2. Observation of TAE activity in JET.  
Ali-Arshad S Campbell D J  
Joint European Torus (JET). March 1994. 12p.  
Preprint JET-P(94)12 Submitted to Plasma Physics  
and Controlled Fusion.
3. MHD limiting phenomena in high performance JET  
plasmas.  
Alper B Edwards A Gill R Pasini D Smeulders P  
1992 Int. Conf. on Plasma Physics: Joint Conf. of 9th  
Kiev Int. Conf. on Plasma Theory; 9th Int. Conf. on  
Waves and Instabilities in Plasmas; 19th EPS Conf. on  
Controlled Fusion and Plasma Physics, Innsbruck, 29  
June - 3 July 1992. 3 vols. EPS. 1994. p.I-331.
4. Effects of sawteeth on neutron emissivity profiles in  
ohmic discharges.  
Anderson D Eriksson L G Lisak M Wising F  
Odblom A  
Joint European Torus (JET). March 1994. 12p.  
Preprint JET-P(94)17 Submitted for publication in  
Plasma Physics and Controlled Fusion
5. Modelling of sawtooth induced redistribution of  
ICRF heated minority ions  
Anderson D Eriksson L-G Lisak M Odblom A  
Joint European Torus (JET), December 1994 13p.  
Preprint JET-P(94)64
6. ITER H Mode Database Working Group.  
Authors include Thomsen K Campbell D J Cordey  
J G JET Team  
Nuclear Fusion, vol.34 no.1 January 1994 p.131.
7. Asymmetry modifications to the TRANSP Monte  
Carlo fast ion code.  
Balet B Stubberfield P McCune D C Goldston R J  
Gann R T and others  
Bulletin of the American Physical Society, vol.39  
no.7 November 1994 (Abstracts of the Thirty-Sixth  
Annual Meeting of the Division of Plasma Physics,  
7-11 November 1994, Minneapolis). p.1680.
8. Heat transport with strong on/off axis heating.  
Balet B Boucher D Cordey J G Muir D Neudatchin  
S V Schmidt G  
1992 Int. Conf. on Plasma Physics: Joint Conf. of 9th  
Kiev Int. Conf. on Plasma Theory; 9th Int. Conf. on  
Waves and Instabilities in Plasmas; 19th EPS Conf. on  
Controlled Fusion and Plasma Physics, Innsbruck, 29  
June - 3 July 1992. 3 vols. EPS. 1994. p.I-59.
9. Heat transport with strong on- and off-axis heating.  
Balet B Cordey J G  
Nuclear Fusion, vol.34 no.8 August 1994 p.1175.
10. Particle transport during the tritium experiments in  
JET.  
Balet B Cordey K G Jones T T C Konig R Marcus  
F Sadler G Stubberfield P M von Hellebrand M  
1992 Int. Conf. on Plasma Physics: Joint Conf. of 9th  
Kiev Int. Conf. on Plasma Theory; 9th Int. Conf. on

- Waves and Instabilities in Plasmas; 19th EPS Conf. on Controlled Fusion and Plasma Physics, Innsbruck, 29 June - 3 July 1992. 3 vols. EPS. 1994. p.I-263.
11. Up-down asymmetry modifications to the flux surface geometry in TRANSP.  
Balet B Stubberfield P Wieland R M McCune D C Terpstra T B  
Bulletin of the American Physical Society, vol.39 no.7 November 1994 (Abstracts of the Thirty-Sixth Annual Meeting of the Division of Plasma Physics, 7-11 November 1994, Minneapolis). p.1680.
  12. Power deposition and driven current profiles in lower hybrid current drive experiments on JET.  
Baranov Y F Ekedahl A Froissard P Gormezano C Lennholm M Rimini F Soldner F X  
Bulletin of the American Physical Society, vol.39 no.7 November 1994 (Abstracts of the Thirty-Sixth Annual Meeting of the Division of Plasma Physics, 7-11 November 1994, Minneapolis). p.1628.
  13. Components of  $P_{\text{rad}}$  and  $Z_{\text{eff}}$  derived from X-ray spectroscopy of the main impurities in JET.  
Barnsley R Brzozowski J Coffey I H Lawson K D Melnick I M Patel A Patel T K Peacock N J  
1992 Int. Conf. on Plasma Physics: Joint Conf. of 9th Kiev Int. Conf. on Plasma Theory; 9th Int. Conf. on Waves and Instabilities in Plasmas; 19th EPS Conf. on Controlled Fusion and Plasma Physics, Innsbruck, 29 June - 3 July 1992. 3 vols. EPS. 1994. p.I-291.
  14. Observations of suprathreshold electrons in the edge region on JET H-mode plasmas.  
Bartlett D V Porte L Costley A E Jones S E Smith R Zolfaghari A  
1992 Int. Conf. on Plasma Physics: Joint Conf. of 9th Kiev Int. Conf. on Plasma Theory; 9th Int. Conf. on Waves and Instabilities in Plasmas; 19th EPS Conf. on Controlled Fusion and Plasma Physics, Innsbruck, 29 June - 3 July 1992. 3 vols. EPS. 1994. p.I-163.
  15. Millimetric FSS Waveguide Beamsplitter  
Bartlett D, Cahill R, Porte L, Rookes A  
Preprint JET-P(94)60
  16. Transient thermal analysis of cryocondensation pump for JET.  
Baxi C B Obert W  
Advances in Cryogenic Engineering, vol.39 pt.A August 1993 pp.1577-1582.
  17. Tritium technology and safety at JET.  
Bell A C and the JET Team  
Joint European Torus (JET), August 1994 14p. Preprint JET-P(94)33 Preprint of a paper to be presented to ANS Topical Meeting on Fusion (New Orleans 21 June 1994).
  18. Measurements of fusion neutron energy spectra at JET by means of time-of-flight techniques  
Belle PV, Elevant T Jarvis ON Sadler G  
Preprint JET-P(94)53
  19. Impact of JET experimental results and engineering development on the definition of the ITER design concept.  
Bertolini E and the JET Team  
Joint European Torus (JET) November 1994 17p. Preprint JET-P(94)36 Invited talk at the Third International Symposium on Fusion Nuclear Technology, 27 June-1 July 1994, Los Angeles, USA
  20. JET with a pumped divertor: design, construction, commissioning and first operation  
Bertolini E and the JET Team  
Preprint JET-P(94)56
  21. JET with a pumped divertor: design, construction, commissioning and first operation  
Bertolini E and the JET Team  
(Invited Paper) 18th Symposium on Fusion Technology (SOFT-18) (Karlsruhe, Germany, 1994)
  22. Fast wave heating and current drive in ITER.  
Bhatnagar V Jacquinet J editors  
Next European Torus. 1994 51p. Report NET 103
  23. Initial FWCD results using the JET A2 antenna arrays and experience with phased operation.  
Bhatnagar V Bures M Dobbing J A Fechner B Start D F H Wade T J Goulding R H Bell G L Hoffman D J Ryan P M

- Bulletin of the American Physical Society, vol.39 no.7 November 1994 (Abstracts of the Thirty-Sixth Annual Meeting of the Division of Plasma Physics, 7-11 November 1994, Minneapolis). p.1566.
24. Fast-wave heating and current-drive scenarios for JET and ITER.  
Bhatnagar V P Jacquinot J JET Team  
Joint European Torus (JET). April 1994. 28p. Preprint JET-P(94)23 Invited papers at 5th Toki Conf. on Plasma Physics and Controlled Fusion (ITC-5), Toki, Japan, 16-19 November 1993.
  25. An ICRF antenna for the next step tokamak operating in a wide frequency band.  
Bhatnagar V P Jacquinot J  
Nuclear Fusion, vol.34 no.6 June 1994 pp.886-896.
  26. Local magnetic shear control in a tokamak via fast-wave minority-ion current drive: Theory and experiments in JET.  
Bhatnagar V P Start D F H Jacquinot J Chaland F Cherubini A Porcelli F  
Joint European Torus (JET). April 1994. 48p. Preprint JET-P(94)22
  27. A scheme for demonstrating fast-wave electron current-drive in present-day large tokamaks.  
Bhatnagar V P Jacquinot J Lashmore-Davies C  
Joint European Torus (JET), November 1994 28p. Report JET-R(94)12
  28. Local magnetic shear control in a tokamak via fast wave minority ion current drive: theory and experiments in JET  
Bhatnagar V P and others  
Nuclear Fusion, vol. 34 no. 12 December 1994 p.1579
  29. A quantitative study of scattering from electromagnetic fluctuations in plasmas.  
Bindslev H  
Joint European Torus (JET). September 1994. 11p. Preprint JET-P(94)30 Submitted to Journal of Atmospheric and Terrestrial Physics (ESGAP Workshop, Aussois, France, 20-24 March 1994).
  30. Low temperature models of non-linear wave mixing in plasmas  
Bindslev H  
Preprint JET-P(94)71
  31. The new millimetre wavelength optical constants of some potential window materials at elevated temperatures.  
Birch J R and others  
Joint European Torus (JET), October 1994 14p. Preprint JET-P(94)46 Submitted for publication in Journal of Infrared Physics.
  32. The JET fast central acquisition and trigger system.  
Blackler K Edwards A W  
IEEE Transactions on Nuclear Science, vol.41 no.1 February 1994 (Selected papers from the IEEE 8th Conf. on Real-time Computer Applications in Nuclear, Particle, and Plasma Physics (RT'93), Vancouver, 8-11 June 1993) p.111.
  33. Pseudo-spectrum of the resistive MHD operator: resolving the resistive alfvén paradox.  
Borba D Riedel K S Kerner W Huysmans G T A Ottaviani M Schmid P  
Joint European Torus (JET). January 1994. 26p. Preprint JET-P(94)04 Submitted for publication in Phys of Plasmas (Phys of Fluids B).
  34. Estimation of the maximum divertor radiative fraction in the presence of a neutral cushion.  
Borrass K Janeschitz G  
Nuclear Fusion, vol.34 no.9 September 1994 p.1203. Preprint JET-P(93)107
  35. Modelling of the density limit in JET beryllated limiter discharges.  
Borrass K Campbell D Clement S Vlases G  
1992 Int. Conf. on Plasma Physics: Joint Conf. of 9th Kiev Int. Conf. on Plasma Theory; 9th Int. Conf. on Waves and Instabilities in Plasmas; 19th EPS Conf. on Controlled Fusion and Plasma Physics, Innsbruck, 29 June - 3 July 1992. 3 vols. EPS. 1994. p.II-735.
  36. Li-beam measurements of edge electron density and impurity profiles on JET.

- Breger P Summers D Pietrzyk A Viacoz B Vince J  
Bulletin of the American Physical Society, vol.39  
no.7 November 1994 (Abstracts of the Thirty-Sixth  
Annual Meeting of the Division of Plasma Physics,  
7-11 November 1994, Minneapolis). p.1566.
37. Window transmission monitoring and cleaning  
schemes used with the LIDAR Thomson scattering  
diagnostic on the JET tokamak.  
Brown B W Goers C W Nielsen P Schunke B  
Joint European Torus (JET). April 1994. 7p. Preprint  
JET-P(94)21 Submitted to Review of Scientific In-  
struments
38. Determination of the suprathreshold electron distribu-  
tion function during lower hybrid current drive in  
JET.  
Brusati M Bartlett D V Ekedahl A Froissard P  
Airoldi A Ramponi G da Silva R P Peysson Y  
Nuclear Fusion, vol.34 no.1 January 1994 pp.23-  
42.
39. Long pulse operation in JET.  
Brusati M Bures M Clements S Ehrenberg J Horton  
L Jones T T C Lawson K Lomas P Morgan P  
Nielsen P Sartori R Schmidt G Stamp M  
Summers D  
1992 Int. Conf. on Plasma Physics: Joint Conf. of 9th  
Kiev Int. Conf. on Plasma Theory; 9th Int. Conf. on  
Waves and Instabilities in Plasmas; 19th EPS Conf.  
on Controlled Fusion and Plasma Physics, Inns-  
bruck, 29 June - 3 July 1992. 3 vols. EPS. 1994. p.I-  
307.
40. The sawtooth collapse in rotating JET plasmas.  
Buchse R Campbell D J Edwards A W Gill R D  
1992 Int. Conf. on Plasma Physics: Joint Conf. of 9th  
Kiev Int. Conf. on Plasma Theory; 9th Int. Conf. on  
Waves and Instabilities in Plasmas; 19th EPS Conf.  
on Controlled Fusion and Plasma Physics, Inns-  
bruck, 29 June - 3 July 1992. 3 vols. EPS. 1994. p.I-  
375.
41. Enhanced performance of neutral beam heated  
hot-ion H-modes on JET by central ICRF heating.  
Bures M Balet B Campbell D Cottrell G A Elevant  
T Erksso L-G Jacquinet J Jarvis O N Jones T  
Konig R Lomas P Marcus F Righi E Sadler G Start  
D F H Tanga A van Belle F von Hellermann M  
1992 Int. Conf. on Plasma Physics: Joint Conf. of 9th  
Kiev Int. Conf. on Plasma Theory; 9th Int. Conf. on  
Waves and Instabilities in Plasmas; 19th EPS Conf. on  
Controlled Fusion and Plasma Physics, Innsbruck, 29  
June - 3 July 1992. 3 vols. EPS. 1994. p.II-881.
42. Millimetric FSS waveguide beamsplitter  
Cahill R and others  
Joint European Torus (JET), December 1994 4p.  
Preprint JET-P(94)60 preprint of a paper submitted  
for publication in Electronic Letters
43. The JET programmes I and II  
Campbell DJ  
Preprint JET-P(94)62
44. H-modes under steady-state conditions in JET  
Campbell D J  
Preprint JET-P(94)01
45. Comparison of vertical and horizontal target plate  
operation with the JET mark I divertor.  
Campbell D J Clement S Horton L Lingertat H  
Lowry C Monk R Saibene G Taroni A Vlases G and  
the JET Team  
Bulletin of the American Physical Society, vol.39  
no.7 November 1994 (Abstracts of the Thirty-Sixth  
Annual Meeting of the Division of Plasma Physics,  
7-11 November 1994, Minneapolis). p.1565.
46. H-modes under steady-state conditions in JET.  
Campbell D J Ali Arshad S Gondhalekar A  
Thomas P R  
Plasma Physics and Controlled Fusion, vol.36 no.7A  
July 1994 (Papers from 4th H-Mode Workshop  
(IAEA Technical Committee Meeting on H-Mode  
Physics) Naka, Ibaraki, Japan, 15-17 November  
1993) p.A255. Preprint JET-P(94)01
47. The JET Programme I & II  
Campbell D J  
Joint European Torus (JET), November 1994 36p.  
Paper submitted for publication in the Proceedings  
of 36eme Cours de Perfectionnement de AVCP,  
(March 1994)

48. Review of neutral beam heating on JET for physics experiments and the production of high fusion performance plasmas.  
Challis C D and the JET Team  
Joint European Torus (JET). November 1993. 31p. Preprint JET-P(93)90 Submitted for publication in Fusion Engineering and Design (proceedings of the 5th Toki Conference).
49. The effect of the diamagnetic drift on the boundary conditions in tokamak scrape-off layers and the distribution of plasma fluxes near the target.  
Chankin A V Stangeby P C  
Joint European Torus (JET). April 1994. 18p. Preprint JET-P(94)18 Submitted for publication in Plasma Physics and Controlled Fusion
50. The effect of radial electric field on fast ion losses in divertor tokamaks.  
Chankin A V Summers D D R McCracken G M  
1992 Int. Conf. on Plasma Physics: Joint Conf. of 9th Kiev Int. Conf. on Plasma Theory; 9th Int. Conf. on Waves and Instabilities in Plasmas; 19th EPS Conf. on Controlled Fusion and Plasma Physics, Innsbruck, 29 June - 3 July 1992. 3 vols. EPS. 1994. p.II-779.
51. The generation of edge toroidal momentum due to ion orbit losses and its effect on the scrape-off layer.  
Chankin A V Kerner W Pogutse O P  
Joint European Torus (JET). January 1994. 14p. Preprint JET-P(94)03 Submitted for publication in Nuclear Fusion.
52. Infrared measurements of the divertor power at JET.  
Chankin A V Summers D D R Jackel H J LeSourd M Matthews G F Reichle R  
Plasma Physics and Controlled Fusion, vol.36 no.3 March 1994 p.403.
53. Current scaling of plasma confinement.  
Christiansen J P Challis C Cordey J G Gormezano C Gowers C Kramer G J O'Rourke J Taroni A Tibone F Tubbing B Stubberfield P M  
1992 Int. Conf. on Plasma Physics: Joint Conf. of 9th Kiev Int. Conf. on Plasma Theory; 9th Int. Conf. on Waves and Instabilities in Plasmas; 19th EPS Conf. on Controlled Fusion and Plasma Physics, Innsbruck, 29 June - 3 July 1992. 3 vols. EPS. 1994. p.II-723.
54. The rapid determination of plasma equilibrium parameters at JET from external magnetic measurements  
Christiansen J P Garribba M Milani F O'Brien D Puppin S Sartori F Van der Goot E Zwingmann W
55. The testing of transport models against data.  
Christiansen J P Cordey J G Taroni A  
Nuclear Fusion, vol.34 no.3 1994 pp.375-386.
56. Development of a visco-mach probe for simultaneous measurement of viscosity and flow velocity in tokamak edge plasma.  
Chung K-S  
Joint European Torus (JET). March 1994. 20p. Preprint JET-P(94)11
57. Report on ITER task: fatigue studies of S65b beryllium  
Ciric D Deksnis E B Martin D  
Report JET-R(94)04
58. In situ determination of the JET neutral heating beam divergence by beam emission spectroscopy  
Ciric D Konig R W T Wolf R C  
Preprint JET-P(94)68
59. The JET fast power supplies  
Claesen R  
Preprint JET-P(94)67
60. Edge measurements in the divertor region in high density discharges at JET.  
Clement S Erents S K Gottardi N Harbour P J Jaekel H Janeschitz G de Kock L Loarte A Lowry C Saibene G Summers D Tagle J A Vlases G  
1992 Int. Conf. on Plasma Physics: Joint Conf. of 9th Kiev Int. Conf. on Plasma Theory; 9th Int. Conf. on Waves and Instabilities in Plasmas; 19th EPS Conf. on Controlled Fusion and Plasma Physics, Innsbruck, 29 June - 3 July 1992. 3 vols. EPS. 1994. p.II-723.
61. The effect of  $B_r$  reversal on the asymmetries between the strike zones in single null divertor discharges: experiment and theories.

- Clement S Harbour P J Janeschitz G Lingertat J Loarte A Matthews G F Reichle R Summers D D R Joint European Torus (JET), October 1994 11p. Preprint JET-P(94)39 Submitted for publication in Plasma Physics and Controlled Fusion.
62. Redeposition effects on the target plates of the JET tokamak.  
Coad J P Farmery B  
Vacuum, vol.45 no.4 April 1994 p.435.
63. An appraisal of deuterium retention in JET and the implications for tritium retention in TFTR  
Coad J P  
Report JET-R(94)11
64. Ne IX and Ne X spectra in the JET tokamak.  
Coffey I H Barnsley R Keenan F P Peacock N J  
Journal of Physics B: Atomic, Molecular and Optical Physics, vol.27 no.5 14 March 1994 p.1011.  
Preprint JET-P(93)78
65. The enhanced confinement regime in JET.  
Cordey J G Reichle R Stork D JET Team  
Joint European Torus (JET). February 1994. 10p.  
Preprint JET-P(94)10 Submitted to Plasma Physics and Controlled Fusion.
66. The evolution of the transport through the L-H transition in JET.  
Cordey J G Muir D G Parail V V Vayakis G Ali-Arshad S Bartlett D V Campbell D J Colton A L Costley A E Gill R D Loarte A Porte L Sips A C C Springmann E M Stubberfield P M Taroni A Thomsen K von Hellermann M G  
Joint European Torus (JET). April 1994. 29p. Preprint JET-P(94)19 Submitted to Nuclear Fusion
67. The time behaviour of the thermal conductivity during L-H and H-L transitions in JET.  
Cordey J G Muir D G Neudatchin S V Parail V Ali-Arshad S Bartlett D V Campbell D J Costley A E Colton A L Edwards A W Porte L Sips A C C Springmann E M Stubberfield P M Vayakis G von Hellermann M G Taroni A  
Plasma Physics and Controlled Fusion, vol.36 no.7A 1994 (Papers from 4th H-Mode Workshop (IAEA Technical Meeting on H-Mode Physics) Naka, Japan, November 1993) p.A267. Preprint JET-P(94)14
68. Dimensionless form for the L-H power threshold  
Cordey J G Kerner W Pogutse O  
Joint European Torus (JET), December 1994 16p  
Preprint JET-P(94)66
69. A numerical simulation of the L-H transition in JET with local and global models  
Cordey J G Muir D G Neudatchin S V Parail V V Springmann E Taroni A  
Nuclear Fusion, vol.35 no.1 January 1995 p.101
70. Distortion and temperature anisotropy of the ion distribution functions in NBT tokamak plasmas  
Core W G F  
Preprint JET-P(94)57
71. The effect of sawteeth on fast ion confinement in JET during ICRH.  
Core W G  
Joint European Torus (JET). January 1994. 15p.  
Preprint JET-P(94)02 Submitted for publication in Nuclear Fusion (letters).
72. Distortion and temperature anisotropy of the ion distribution functions in NBH tokamak plasmas  
Core W G F  
Joint European Torus (JET), December 1994 18p  
Preprint JET-P(94)57
73. Measurement of the toroidal motion of fine-scale density structures in JET plasmas.  
Costley A E Cripwell P Fukuda T  
1992 Int. Conf. on Plasma Physics; Joint Conf. of 9th Kiev Int. Conf. on Plasma Theory; 9th Int. Conf. on Waves and Instabilities in Plasmas; 19th EPS Conf. on Controlled Fusion and Plasma Physics, Innsbruck, 29 June - 3 July 1992. 3 vols. EPS. 1994. p.I-199.
74. Ion cyclotron absorption by fusion alpha-particles  
Cottrell G A Eriksson L G  
Report JET-R(94)10
75. Identification of ion cyclotron emission from fusion  $\alpha$ -particles during JET deuterium-tritium experiments.

- Cottrell G A Bhatnagar V P da Costa O Dendy R O Edwards A Jacquinet J Nave M F F Schmid M Sibley A Smeulders P Start D F H  
1992 Int. Conf. on Plasma Physics: Joint Conf. of 9th Kiev Int. Conf. on Plasma Theory; 9th Int. Conf. on Waves and Instabilities in Plasmas; 19th EPS Conf. on Controlled Fusion and Plasma Physics, Innsbruck, 29 June - 3 July 1992. 3 vols. EPS. 1994. p.1-327.
76. The behaviour of divertor and scrape-off layer parameters in the JET pumped divertor.  
Davies S Altan B Erements S K Loarte A Matthews G F McCormick K Monk R D Taroni A Weber S Bulletin of the American Physical Society, vol.39 no.7 November 1994 (Abstracts of the Thirty-Sixth Annual Meeting of the Division of Plasma Physics, 7-11 November 1994, Minneapolis). p.1565.
77. Beryllium high heat-flux tests at JET.  
Deksnis E B Altmann H Falter H Ibbott C Pick M Viola A  
Workshop on Beryllium for Fusion Applications, Karlsruhe, Germany, 4-5 October 1993. Proceedings. pp.277-283.
78. The VH-mode at JET.  
Deliyanakis N O'Brien D P Balet B Greenfield C M Porte L Sips A C C Stubberfield P M Wilson H Plasma Physics and Controlled Fusion, vol.36 no.7 July 1994 pp.1159-1170.
79. Laser blow-off injected impurity particle confinement times in JET and tore supra  
Demichelis C Denne-Hinnov B Dukok de Wit T Giannella R Mattioli M Myrnas R
80. Superthermal ion cyclotron harmonic emission from fusion and space plasmas: a single physical mechanism.  
Dendy R O Lashmore-Davies C N McClements K G Kam K F Cottrell G A  
Physica Scripta, vol.T52 1994 (Proceedings of the International Workshop on Acceleration & Radiation Generation in Space & Laboratory Plasmas, Kardamyli, Greece, 29 August - 4 September 1993.) p.135-138.
81. JET divertor coils, manufacture, assembly and testing.  
Dolgetta N Bertolini E D'Urzo C Last J R Laurenti A Presle P Sannazzaro G Tait J Tesini A  
IEEE Transactions on Magnetics, vol.30 no.4 pt.II July 1994 (13th Int Conf on Magnet Technology (MT-13), Victoria, Canada, 20-24 September 1993) pp.2150-2153.
82. A comparison of JET sawtooth behaviour in plasmas with co- and counter-neutral beam injection.  
Edwards A W Bickley A Buchse R Challis C D Konig R Marcus F B O'Rourke J Stork D  
1992 Int. Conf. on Plasma Physics: Joint Conf. of 9th Kiev Int. Conf. on Plasma Theory; 9th Int. Conf. on Waves and Instabilities in Plasmas; 19th EPS Conf. on Controlled Fusion and Plasma Physics, Innsbruck, 29 June - 3 July 1992. 3 vols. EPS. 1994. p.1-379.
83. Measurements of fusion neutron energy spectra at JET by means of time-of-flight techniques  
Elevant T van Belle P Jarvis O N Sadler G  
Joint European Torus (JET), November 1994 14p Preprint JET-P(94)53
84. New parametrizations of d-d fusion cross sections.  
Erba M  
Journal of Physics D: Applied Physics, vol.27 no.9 14 September 1994 pp.1874-1877.
85. Simulation of L-mode tokamak discharges and ITER performance with energy transport coefficients of Bohm and gyro-Bohm type.  
Erba M Springmann E Taroni A Tibone F  
Joint European Torus (JET). January 1994. 11p. Preprint JET-P(94)06 Paper presented to Varenna Workshop on Transport, Varenna, September 1993.
86. A model for calculating ICRH power deposition and velocity distribution.  
Eriksson L-G Hellsten T  
Joint European Torus (JET). June 1994. 28p. Preprint JET-P(94)25 Submitted to Plasma Physics and Controlled Fusion
87. Field error instabilities in JET.

- Fishpool G M Haynes P S  
Nuclear Fusion, vol.34 no.1 January 1994 pp.109-120.
88. Level of error field in the pumped divertor phase of JET.  
Fishpool G M Campbell D J  
Bulletin of the American Physical Society, vol.39 no.7 November 1994 (Abstracts of the Thirty-Sixth Annual Meeting of the Division of Plasma Physics, 7-11 November 1994, Minneapolis). p.1565.
89. Calculations of ion/atom collision cross-sections for beam-driven diagnostics.  
Fritsch W  
Joint European Torus (JET), August 1994 36p. Report JET-R(94)05
90. Report on vertical stability studies during the plasma start-up of ITER  
Garribba M Milani F  
Report JET-R(94)
91. Poloidal asymmetry of impurity in co- and counter-injection experiment at JET.  
Giannella R Christenen M De Angelis R Gottardi N Lauro-Taroni L Mattioli M Pasini D  
1992 Int. Conf. on Plasma Physics: Joint Conf. of 9th Kiev Int. Conf. on Plasma Theory; 9th Int. Conf. on Waves and Instabilities in Plasmas; 19th EPS Conf. on Controlled Fusion and Plasma Physics, Innsbruck, 29 June - 3 July 1992. 3 vols. EPS. 1994. p.I-279.
92. Role of current profile in impurity transport in JET L mode discharges.  
Giannella R Lauro-Taroni L Mattioli M Alper B Denne-Hinnov B Magyar G O'Rourke J Pasini D  
Nuclear Fusion, vol.34 no.9 September 1994 p.1185. Preprint JET-P(93)81
93. Spectroscopic diagnostics and measurements at JET.  
Giannella R  
Plasma Physics Reports, vol.20 no.1 1994, (Papers presented to the 6th Symposium on High-Temperature Plasma Diagnostics, St. Petersburg, May 26 - June 1, 1993) p.56.
94. Effects of neutrons on the JET soft x-ray detectors.  
Gill R D Alper B Edwards A  
1992 Int. Conf. on Plasma Physics: Joint Conf. of 9th Kiev Int. Conf. on Plasma Theory; 9th Int. Conf. on Waves and Instabilities in Plasmas; 19th EPS Conf. on Controlled Fusion and Plasma Physics, Innsbruck, 29 June - 3 July 1992. 3 vols. EPS. 1994. p.II-1051.
95. Generation and loss mechanisms of runaway electrons following disruptions in JET.  
Gill R D Edwards A W  
1992 Int. Conf. on Plasma Physics: Joint Conf. of 9th Kiev Int. Conf. on Plasma Theory; 9th Int. Conf. on Waves and Instabilities in Plasmas; 19th EPS Conf. on Controlled Fusion and Plasma Physics, Innsbruck, 29 June - 3 July 1992. 3 vols. EPS. 1994. p.I-355.
96. MHD spectroscopy: free boundary modes (ELMs) & external excitation of TAE modes.  
Goedbloed J P Holties H A Poedts S Huysmans G T A Kerner W  
Joint European Torus (JET). October 1993. 19p. Preprint JET-P(93)94 Submitted for publication in Plasma Physics and Controlled Fusion.
97. Investigations of impurity control in JET using fuelling, and interpretation of experiments using the LIM impurity code.  
Gondhalekar A Stangeby P C Elder J D  
Nuclear Fusion, vol.34 no.2 February 1994 pp.247-260.
98. Perturbative measurement of suprathreshold electron diffusion in JET.  
Gondhalekar A Bartlett D Lomas P Martin-Solis R O'Brien M  
1992 Int. Conf. on Plasma Physics: Joint Conf. of 9th Kiev Int. Conf. on Plasma Theory; 9th Int. Conf. on Waves and Instabilities in Plasmas; 19th EPS Conf. on Controlled Fusion and Plasma Physics, Innsbruck, 29 June - 3 July 1992. 3 vols. EPS. 1994. p.I-147.
99. Lower-hybrid current drive experiments, synergism with the fast wave near ion cyclotron resonance and future plans on JET. (Invited).

- Gormezano C  
Radio Frequency Power in Plasmas. 10th Topical Conf., Boston, April 1993. New York, American Institute of Physics. 1994. pp.87-98.
100. Power compensators for phased operation of antenna arrays on JET and DIII-D.  
Goulding R H Hoffman D J Ryan P M Bosia G Bures M Start D Wade T Petty C C Pinsker R I  
Radio Frequency Power in Plasmas. 10th Topical Conf., Boston, April 1993. New York, American Institute of Physics. 1994. pp.351-354.
101. Comparison of single and triple probe operation with the JET divertor probe array.  
Guo H Y Monk R D Matthews G F Loarte A  
Bulletin of the American Physical Society, vol.39 no.7 November 1994 (Abstracts of the Thirty-Sixth Annual Meeting of the Division of Plasma Physics, 7-11 November 1994, Minneapolis). p.1566.
102. The boundary of a fusion plasma: some problems in rarefield gas/plasma dynamics  
Harbour P J  
Preprint JET-P(94)45
103. Departures from sonic flow at the sheath on a divertor target or limiter.  
Harbour P J Loarte A  
Contributions to Plasma Physics, vol.34 no.2-3 1994 (4th Int. Workshop on Plasma Edge Theory in Fusion Devices, Varenna, 4-6 October 1993) p.312. Preprint JET-P(94)05
104. The scrape-off layer in a finite aspect-ratio torus: The influence of limiter position.  
Harbour P J Loarte A  
Joint European Torus (JET). October 1993. 31p. Preprint JET-P(93)96 Submitted for publication in Nuclear Fusion.
105. Change in electron cyclotron emission during a sawtooth collapse.  
Hastie R J  
Joint European Torus (JET). May 1994. 10p. Report JET-R(94)03
106. The behaviour of fast ions in tokamak experiments.  
Heidbrink W W Sadler G J  
Nuclear Fusion, vol.34 no.4 April 1994 pp.535-616. Preprint JET-P(93)63
107. High resolution tritium calorimetry based on inertial temperature control.  
Hemmerich J L Serio L Milverton P  
Joint European Torus (JET). December 1993. 16p. Preprint JET-P(93)38 Submitted for publication in Review of Scientific Instruments.
108. High pressure atmosphere detritiation for JET and future devices.  
Hemmerich J L Milverton P  
Joint European Torus (JET). August 1994. 14p. Preprint JET-P(94)31 Submitted to Fusion Technology
109. Thermal design of a metal hydride storage bed, permitting tritium accountancy to 0.1% resolution and repeatability.  
Hemmerich J L  
Joint European Torus (JET). May 1994. 11p. Preprint JET-P(94)24 Paper submitted to Fusion Technology
110. High-beta(sub p) MHD activity in JET.  
Hender T C Alper B Ali-Arshad S DeBlank H J Challis D C Gimblett C Han J Jacquinet J Kramer G J Kerner W Nave M F O'Brien D P O'Rourke J Smeulders P Stamp M Summers D Tibone F Tubbing B Zolfaghari A Zwingmann P W  
1992 Int. Conf. on Plasma Physics: Joint Conf. of 9th Kiev Int. Conf. on Plasma Theory; 9th Int. Conf. on Waves and Instabilities in Plasmas; 19th EPS Conf. on Controlled Fusion and Plasma Physics, Innsbruck, 29 June - 3 July 1992. 3 vols. EPS. 1994. p.I-335.
111. Studies of line emission from collisions of multiply charged ions on He and Li targets for tokamak diagnostics.  
Hoekstra R  
Joint European Torus (JET). March 1994. 16p. Preprint JET-P(94)16 Preprint of paper submitted to Procs. 9th APS Topical Mtg. on Atomic Processes in Plasmas, San Antonio, USA, 20-24 September 1993.

112. Antireflection treatments for JET millimetre wave diagnostic windows.  
Hughes T P Richards S D Bartlett D V  
International Journal of Infrared and Millimeter Waves, vol.15 no.1 January 1994 p.61.
113. Diffusion of fast electrons after a monster sawtooth crash.  
Hugon M Bartlett D Brusati M Froissard P Gormezano C Morgan P Porte L Rimini F Stamp M  
1992 Int. Conf. on Plasma Physics: Joint Conf. of 9th Kiev Int. Conf. on Plasma Theory; 9th Int. Conf. on Waves and Instabilities in Plasmas; 19th EPS Conf. on Controlled Fusion and Plasma Physics, Innsbruck, 29 June - 3 July 1992. 3 vols. EPS. 1994. p.I-119.
114. Similarity in divertor studies  
Hutchinson I H Vlases G C  
Joint European Torus (JET) August 1994. 19p.  
Preprint JET-P(94)32  
Submitted for publication in Nuclear Fusion
115. Modelling the excitation of global alfvén modes by an external antenna in JET  
Huysmans G  
Preprint JET-P(94)49
116. MHD stability model of edge localized modes in JET discharges.  
Huysmans G T A de Blank H J Kerner W Goedbloed J P Nave M F F  
1992 Int. Conf. on Plasma Physics: Joint Conf. of 9th Kiev Int. Conf. on Plasma Theory; 9th Int. Conf. on Waves and Instabilities in Plasmas; 19th EPS Conf. on Controlled Fusion and Plasma Physics, Innsbruck, 29 June - 3 July 1992. 3 vols. EPS. 1994. p.I-247.
117. A hierarchy of empirical models of plasma profiles and transport  
Imre K Riedel K S Schunke B  
Preprint JET-P(94)59
118. New trends in tokamak concepts and initial results  
Jacquinot J and The JET Team  
Preprint JET-P(94)65
119. The JET Joint Undertaking: scientific advances and future challenges.  
Jacquinot J  
Fusion Technology, vol.25 no.2T, March 1994, Part 2, (Proceedings of the First Carolus Magnus Summer School on Plasma Physics, Vaals, The Netherlands September 6-17, 1993) p.377.
120. Launching fast waves in large devices.  
Jacquinot J Bhatnagar V P Kaye A Brown T  
Joint European Torus (JET). December 1993. 15p.  
Preprint JET-P(93)105 Presented to IAEA TCM on RF Launchers, Naka, Japan, 10-12 November 1993,
121. Radial carbon flux profiles in the upper divertor in JET at high target load.  
Jaekel H J Clement S Lesourd M Lingertat J Maggi C F Matthews G F Summers D D R Summers H P  
1992 Int. Conf. on Plasma Physics: Joint Conf. of 9th Kiev Int. Conf. on Plasma Theory; 9th Int. Conf. on Waves and Instabilities in Plasmas; 19th EPS Conf. on Controlled Fusion and Plasma Physics, Innsbruck, 29 June - 3 July 1992. 3 vols. EPS. 1994. p.II-823.
122. High power operation with a radiative divertor in JET.  
Janeschitz G Clement S Gottardi N Lesourd M Lingertat J Lowry C Radford G Saibene G Stamp M Summers D Taroni A Thomas P R Vlases G
123. 1992 Int. Conf. on Plasma Physics: Joint Conf. of 9th Kiev Int. Conf. on Plasma Theory; 9th Int. Conf. on Waves and Instabilities in Plasmas; 19th EPS Conf. on Controlled Fusion and Plasma Physics, Innsbruck, 29 June - 3 July 1992. 3 vols. EPS. 1994. p.II-727.
124. Neutron measurement techniques for tokamak plasmas.  
Jarvis O N  
Plasma Physics and Controlled Fusion, vol.36 no.2 February 1994 p.209.
125. Comparison of high beta regimes between JET and JT-60U on confinement and fusion reactivity.  
JET and JT-60 teams

- Bulletin of the American Physical Society, vol.39 no.7 November 1994 (Abstracts of the Thirty-Sixth Annual Meeting of the Division of Plasma Physics, 7-11 November 1994. p.1564.
126. First results with the modified JET.  
JET Team Tanga A presenter  
Joint European Torus (JET). August 1994. 15p.  
Preprint JET-P(94)35 Submitted for publication in the Proceedings of the 21st EPS Meeting on Controlled Fusion and Plasma Physics, Montpellier, 1994
127. Overview of high performance H-modes in JET.  
JET Team Stork D presenter  
Plasma Physics and Controlled Fusion, vol.36 no.7A July 1994 (Papers from 4th H-mode Workshop (IAEA Technical Committee Meeting on H-mode Physics) Naka, Ibaraki, Japan, 15-17 November 1993) p.A23.
- JET divertor research in support of ITER.  
JET Team Watkins M presenter  
Plasma Physics and Controlled Fusion, Vol. 36 supplement (12)B, December 1994 (invited papers from the 21st European Conference on Controlled Fusion and Plasma Physics, Montpellier, 27 June-1 July 1994) p.B241
128. Update of statistical analysis of JET disruptions.  
Johnson M F  
Joint European Torus (JET). Report JET-R(94)02
129. High current, high power H-modes in JET.  
Jones T T C Balet B Brusati M Bures M Hugon M Lawson K D Lomas P J Morgan P D Morsi H Nielsen P Sadler G Sartori R Start D F H Summers D D R Tanga A Taroni A Thomsen K Ward D J  
1992 Int. Conf. on Plasma Physics: Joint Conf. of 9th Kiev Int. Conf. on Plasma Theory; 9th Int. Conf. on Waves and Instabilities in Plasmas; 19th EPS Conf. on Controlled Fusion and Plasma Physics, Innsbruck, 29 June - 3 July 1992. 3 vols. EPS. 1994. p.I-3.
130. Present and future JET ICRF antennae.  
Kaye A Brown T Bhatnagar V Crawley P Jacquinot J Lobel R Plancoulaine J Rebut P-H Wade T Walker C  
Fusion Engineering and Design, vol.24 nos.1&2 February 1994 pp.1-22.
131. Present state of nuclear fusion research and prospects for the future.  
Keen B E Watkins M L  
Proc. Instn. Mech. Engrs., vol.207 no.4 pt.A 1993 pp.269-278. Preprint JET-P(93)67
132. JET physics in support of ITER: results and future work  
Keilhacker M and the JET Team  
Preprint JET-P(94)69
133. The JET programme to 1996 and beyond.  
Keilhacker M  
Joint European Torus (JET). March 1994. 8p. Preprint JET-P(94)13 Submitted to Contributions to High Temperature Plasma Physics.
134. Stability of global Alfvén waves (TAE, EAE) in JET tritium discharges.  
Kerner W Borba D Huysmans G T A Porcelli F Poedts S Goedbloed J P Betti R  
Plasma Physics and Controlled Fusion, vol.36 no.5 May 1994 pp.911-924. Preprint JET-P(93)100
135. Measurements of MeV energy ICRF driven minority ions in JET.  
Khudoleev A V Afanasyev V I Corti S Gondhalekar A Maas A C Petrov M P  
1992 Int. Conf. on Plasma Physics: Joint Conf. of 9th Kiev Int. Conf. on Plasma Theory; 9th Int. Conf. on Waves and Instabilities in Plasmas; 19th EPS Conf. on Controlled Fusion and Plasma Physics, Innsbruck, 29 June - 3 July 1992. 3 vols. EPS. 1994. p.I-151.
136. Alpha particle physics in thermonuclear reactors (Report on the Third IAEA Technical Committee Meeting, Trieste, Italy, 10-14 May 1993).  
Kolesnichenko Y I Sadler G J  
Nuclear Fusion, vol.33 no.12 December 1993 p.1905. Preprint JET-P(93)85
137. High performance plasmas with the JET pumped divertor in JET.

- Konig R JET team  
Bulletin of the American Physical Society, vol.39 no.7 November 1994 (Abstracts of the Thirty-Sixth Annual Meeting of the Division of Plasma Physics, 7-11 November 1994, Minneapolis). p.1565.
138. JET TF coil faults - detection, diagnosis and prevention.  
Last J R Bertolini E Bonicelli T Dolgetta N Presle P Zullo G  
IEEE Transactions on Magnetics, vol.30 no.4 pt.II July 1994 (13th Int Conf on Magnet Technology (MT-13), Victoria, Canada, 20-24 September 1993) pp.2154-2157.
139. Particle and impurity transport in JET versus neo-classical theory.  
Lauro-Taroni L Giannella R  
1992 Int. Conf. on Plasma Physics: Joint Conf. of 9th Kiev Int. Conf. on Plasma Theory; 9th Int. Conf. on Waves and Instabilities in Plasmas; 19th EPS Conf. on Controlled Fusion and Plasma Physics, Innsbruck, 29 June - 3 July 1992. 3 vols. EPS. 1994. p.I-287.
140. Plasma characteristics during soft disruptions.  
Lazzaro E Simonetto A Tanga A  
1992 Int. Conf. on Plasma Physics: Joint Conf. of 9th Kiev Int. Conf. on Plasma Theory; 9th Int. Conf. on Waves and Instabilities in Plasmas; 19th EPS Conf. on Controlled Fusion and Plasma Physics, Innsbruck, 29 June - 3 July 1992. 3 vols. EPS. 1994. p.I-443.
141. Activation of first wall tiles in JET.  
Loughlin M J  
Joint European Torus (JET). January 1994. 22p. Report JET-R(94)01
142. Effects of sawtooth crashes on beam ions and fusion product tritons in JET.  
Marcus F B Adams J M Bond D S Hone M A Howarth P J A Jarvis O N Loughlin M J Sadler G J Van Belle P  
Nuclear Fusion, vol.34 no.5 May 1994 p.687.
143. Neutron profile measurements during the tritium experiments in JET.  
Marcus F B Adams J M Bond D S Conroy S Howarth P J A Jarvis O N Loughlin M J Sadler G Smeulders P van Belle P Watkins N  
1992 Int. Conf. on Plasma Physics: Joint Conf. of 9th Kiev Int. Conf. on Plasma Theory; 9th Int. Conf. on Waves and Instabilities in Plasmas; 19th EPS Conf. on Controlled Fusion and Plasma Physics, Innsbruck, 29 June - 3 July 1992. 3 vols. EPS. 1994. p.I-251.
144. Modification of the carbon and beryllium walls in JET by erosion, redeposition and deuterium trapping after the 1991 discharge period.  
Martinelli A P Behrisch R Peacock A T  
Journal of Nuclear Materials, vol.212-215 1994 part B (Proceedings of the Sixth International Conference on Fusion Reactor Materials (ICFRM-6), Stresa, Italy, 27 September - 1 October 1993). p.1245.
145. Tokamak plasma diagnosis by electrical probes.  
Matthews G F  
Plasma Physics and Controlled Fusion, vol.36 no.10 October 1994 pp.1595-1628. Preprint JET-P(94)15
146. Plasma detachment from divertor targets and limiters  
Matthews G F  
Preprint JET-P(94)63
147. Transitions in boron-like Ni XXIV, Ge XXVIII, Kr XXXII and Mo XXXVIII, and fluorine-like Zr XXXII and MO XXXIV, observed in the JET tokamak.  
Myrnas R Jupen C Miecznik G Martinson I Denne-Hinnov B  
Physica Scripta, vol.49 no.4, April 1994 p.429.
148. Energetic particle driven instabilities at JET.  
Nave M F F Borba D Cripwell P von Hellermann M Kerner W Porcelli F Sadler G Smeulders P  
1992 Int. Conf. on Plasma Physics: Joint Conf. of 9th Kiev Int. Conf. on Plasma Theory; 9th Int. Conf. on Waves and Instabilities in Plasmas; 19th EPS Conf. on Controlled Fusion and Plasma Physics, Innsbruck, 29 June - 3 July 1992. 3 vols. EPS. 1994. p.I-439.
149. MHD activity in JET hot ion H-mode discharges.  
Nave M F F Ali-Arshad S Alper B Balet B Borba D Challis C D de Blank H J von Hellermann M

- Hender T C Huysmans G T A Kerner W Kramer G Porcelli F O'Rourke J Porte L Sadler G Smeulders P Sips A C C Stubberfield P M Stork D Reichle R Wesson J Zwingmann W  
Joint European Torus (JET). December 1993. 37p.  
Preprint JET-P(93)79 Submitted for publication in Nuclear Fusion.
150. Experience of electromagnetic forces during JET divertor operation  
Noll P Andrew P Barabaschi P Garribba M Miele P Sannazzaro G Sborchia C Verrecchia M  
Preprint JET-P(94)55
151. The JET cryosystem, overview and experience.  
Obert W  
Advances in Cryogenic Engineering, vol.39 pt.A August 1993 pp.493-500.
152. The liquid nitrogen and supercritical helium cooling loop for the JET pumped divertor cryopump.  
Obert W Mayaux C Perinic G  
Advances in Cryogenic Engineering, vol.39 pt.A August 1993 pp.1569-1576.
153. Questions on collisionless magnetic reconnection.  
Ottaviani M Porcelli F  
Joint European Torus (JET), October 1994 8p.  
Preprint JET-P(94)50 Submitted for publication in the Proceedings of the 1994 ICPP, Brazil, 31 October-4 November 1994.
154. Turbulent transport of diluted impurities  
Ottaviani M  
Preprint JET-P(94)74
155. Evolution of the current profile in JET high bootstrap current plasmas.  
O'Rourke J Challis C D Jacquinot J O'Brien D Stamp M F Stork D Stubberfield P Tibone F Tubbing B J Zwingmann W  
1992 Int. Conf. on Plasma Physics: Joint Conf. of 9th Kiev Int. Conf. on Plasma Theory; 9th Int. Conf. on Waves and Instabilities in Plasmas; 19th EPS Conf. on Controlled Fusion and Plasma Physics, Innsbruck, 29 June - 3 July 1992. 3 vols. EPS. 1994. p.I-311.
156. Measurements of the electron source distribution and implications for particle transport.  
O'Rourke J Kramer G J Simonini R Sips A C C  
1992 Int. Conf. on Plasma Physics: Joint Conf. of 9th Kiev Int. Conf. on Plasma Theory; 9th Int. Conf. on Waves and Instabilities in Plasmas; 19th EPS Conf. on Controlled Fusion and Plasma Physics, Innsbruck, 29 June - 3 July 1992. 3 vols. EPS. 1994. p.I-259.
157. The JET in-vessel divertor cryopump design, manufacture, assembly, testing and operational safety.  
Papastergiou S Obert W Thompson E  
Joint European Torus (JET). September 1994. 13p.  
Preprint JET-P(94)37 Submitted to Fusion Engineering and Design
158. Materials selection, qualification and manufacturing of the in-vessel divertor cryopump for JET.  
Papastergiou S Obert W Thompson E  
Advances in Cryogenic Engineer Materials, vol.40 pt.A August 1993 pp.1429-1436.
159. Scaling of impurity transport in JET.  
Pasini D Giannella R Lauro-Taroni L Magyar G Mattioli M  
1992 Int. Conf. on Plasma Physics: Joint Conf. of 9th Kiev Int. Conf. on Plasma Theory; 9th Int. Conf. on Waves and Instabilities in Plasmas; 19th EPS Conf. on Controlled Fusion and Plasma Physics, Innsbruck, 29 June - 3 July 1992. 3 vols. EPS. 1994. p.I-283.
160. Neutral particle analysis in the MeV range in JET.  
Petrov M P Afanasyev V I Corti S Gondhalekar A Khudoleev A V Korotkov A A Maas A C  
1992 Int. Conf. on Plasma Physics: Joint Conf. of 9th Kiev Int. Conf. on Plasma Theory; 9th Int. Conf. on Waves and Instabilities in Plasmas; 19th EPS Conf. on Controlled Fusion and Plasma Physics, Innsbruck, 29 June - 3 July 1992. 3 vols. EPS. 1994. p.II-1031.
161. Review of tritium retention in first wall materials.  
Pick M A Andrew P L  
Joint European Torus (JET). October 1993. 16p.  
Preprint JET-P(93)93 Submitted to Procs. of 6th Int. Conf. on Fusion Reactor Materials, Stressa, Italy, 1 October 1993.

162. The resistive interchange convection in the edge of tokamak plasmas.  
Pogutse O Kerner W Gribkov V Bazdenkov S Osipenko M  
Joint European Torus (JET). January 1994 34p.  
Preprint JET-P(93)106 Submitted for publication in Plasma Physics and Controlled Fusion.
163. The SOL width and MHD interchange instability in tokamaks.  
Pogutse O Kerner W  
Joint European Torus (JET), October 1994 12p.  
Preprint JET-P(94)44 Submitted for publication in Physics of Plasmas.
164. Resistive internal kinks and ICRF phasing current drive.  
Porcelli F Bhatnagar V P Bosia P Cherubini A Jacquinet J Start D Taroni A  
1992 Int. Conf. on Plasma Physics: Joint Conf. of 9th Kiev Int. Conf. on Plasma Theory; 9th Int. Conf. on Waves and Instabilities in Plasmas; 19th EPS Conf. on Controlled Fusion and Plasma Physics, Innsbruck, 29 June - 3 July 1992. 3 vols. EPS. 1994. p.II-901.
165. On the modelling of fast particle ripple losses in tokamaks.  
Putvinskij S V Tubbing B J D Eriksson L-G Konovalov S V  
Nuclear Fusion, vol.34 no.4 1994 pp.495-506.
166. Interaction of lower hybrid waves with fast ions in JET.  
Ramos de Andrade M C Brusati M Baranov Y Eriksson L G Gormezano C Righi E Rimini F Sadler G  
Plasma Physics and Controlled Fusion, vol.36 no.7 July 1994 pp.1171-1188.
167. Characterization of LH induced current carrying fast electrons in JET.  
Ramponi G Airoidi A Bartlett D Brusati M Froissard P Gormezano C Rimini F da Silva R P Tanzi C  
1992 Int. Conf. on Plasma Physics: Joint Conf. of 9th Kiev Int. Conf. on Plasma Theory; 9th Int. Conf. on Waves and Instabilities in Plasmas; 19th EPS Conf. on Controlled Fusion and Plasma Physics, Innsbruck, 29 June - 3 July 1992. 3 vols. EPS. 1994. p.II-973.
168. Divertor radiation in JET.  
Reichle R Gottardi N A C Giannella R M  
Bulletin of the American Physical Society, vol.39 no.7 November 1994 (Abstracts of the Thirty-Sixth Annual Meeting of the Division of Plasma Physics, 7-11 November 1994, Minneapolis). p.1709.
169. Electron impact excitation of Cl.  
Reid R H  
Joint European Torus (JET). August 1994. 114p.  
Report JET-R(94)06
170. Large minority ion orbit effects in ICRF heating experiments on JET.  
Righi E  
Joint European Torus (JET). August 1994. 166p.  
Report JET-R(94)08 Ph.D. Thesis
171. Electrical characterization of the JET A(sub 2) antenna: Comparison of model with measurements.  
Ryan P M Goulding R H Bhatnagar V Kaye A Wade T  
Radio Frequency Power in Plasmas. 10th Topical Conf., Boston, April 1993. New York, American Institute of Physics. 1994. pp.355-358.
172. Effects of enhanced toroidal field ripple on JET plasmas.  
Sadler G Barabaschi P Bertolini E Conroy S Deksnis E Dietz J de Esch B Green B Huguet M Huart M Jacquinet J Jarvis O N Khudoleev A Loughlin M J Konig R Last J Maas A Petrov M Putvinskii S Sborchia C Stork D Tubbing B van Belle P  
1992 Int. Conf. on Plasma Physics: Joint Conf. of 9th Kiev Int. Conf. on Plasma Theory; 9th Int. Conf. on Waves and Instabilities in Plasmas; 19th EPS Conf. on Controlled Fusion and Plasma Physics, Innsbruck, 29 June - 3 July 1992. 3 vols. EPS. 1994. p.I-167.
173. Determination of the ion thermal diffusivity from neutron emission profiles in decay.

- Sasao M Adams J M Conroy S Jarvis O N Marcus F B Sadler G van Belle P  
Plasma Physics and Controlled Fusion, vol.36 no.1  
January 1994 p.1.
174. Determination of the ion thermal diffusivity from neutron emission profiles in decay.  
Sasao M Adams J M Conroy S Jarvis O N Marcus F B Sadler G van Belle P  
1992 Int. Conf. on Plasma Physics: Joint Conf. of 9th Kiev Int. Conf. on Plasma Theory; 9th Int. Conf. on Waves and Instabilities in Plasmas; 19th EPS Conf. on Controlled Fusion and Plasma Physics, Innsbruck, 29 June - 3 July 1992. 3 vols. EPS. 1994. p.1-67.
175. Fuelling of JET limiter, X-point plasma by deuterium pellet injection.  
Schmidt G L Bartlett D Baylor L Bures M Edwards A Gadeberg M Gottardi N Jones T Kupschus P Lomas P Morgan P Morsi H Nielsen P O'Rourke J Sadler G Start D F H Stubberfield P Tanga A Ward D  
1992 Int. Conf. on Plasma Physics: Joint Conf. of 9th Kiev Int. Conf. on Plasma Theory; 9th Int. Conf. on Waves and Instabilities in Plasmas; 19th EPS Conf. on Controlled Fusion and Plasma Physics, Innsbruck, 29 June - 3 July 1992. 3 vols. EPS. 1994. p.1-255.
176. Parametric dependencies of JET LIDAR profiles: Comparison of Ohmic L and H-modes.  
Schunke B Imre K Riedel K S  
Bulletin of the American Physical Society, vol.39 no.7 November 1994 (Abstracts of the Thirty-Sixth Annual Meeting of the Division of Plasma Physics, 7-11 November 1994, Minneapolis). p.1566.
177. Fast particle losses due to TAE-modes in JET.  
Sharapov S Appel L C Borba D Hender T C Huysmans G T A Kerner W Pinches S D  
Bulletin of the American Physical Society, vol.39 no.7 November 1994 (Abstracts of the Thirty-Sixth Annual Meeting of the Division of Plasma Physics, 7-11 November 1994, Minneapolis). p.1566.
178. Models and numerics in the multi-fluid 2-D edge plasma code EDGE2D/U.  
Simonini R Corrigan G Radford G Spence J Taroni A  
Contributions to Plasma Physics, vol.34 no.2-3 1994 (4th Int. Workshop on Plasma Edge Theory in Fusion Devices, Varenna, 4-6 October 1993) p.368.
179. ICRF heating of plasma in the new JET divertor configurations.  
Sips A C C Bures M Gormezano C Jacquinet J Righi E Rimini F Start D Tubbing B Goulding R  
Bulletin of the American Physical Society, vol.39 no.7 November 1994 (Abstracts of the Thirty-Sixth Annual Meeting of the Division of Plasma Physics, 7-11 November 1994, Minneapolis). p.1566.
180. Survey of pellet enhanced performance in JET discharges.  
Smeulders P Appel L C Balet B Hender T C Lauro-Taroni L Stork D Wolle B Ali-Arshad S Alper B de Blank H Bures M de Esch B Giannella R Konig R Kupschus P Lawson K Marcus F Mattioli M Morsi H O'Brien D O'Rourke J Sadler G Schmidt G Stubberfield P Zwingmann W  
Joint European Torus (JET). March 1994. 45p. Preprint JET-P(94)07 Submitted to Nuclear Fusion
181. Lower hybrid launchers on JET.  
Soldner F X Brusati M Ekedahl A Froissard P Gormezano C Jacquinet J Kaye A Lennholm M Plancoulaine J Rimini F Schild P  
Joint European Torus (JET). December 1993. 18p. Preprint JET-P(93)108 Submitted for publication in the Proceedings of the IAEA Meeting on Radio-Frequency Launchers for Plasma Heating and Current Drive, Naka, Japan.
182. Measurement of sputtering yields at the JET beryllium and carbon X-point tiles.  
Stamp M F Thomas P R  
1992 Int. Conf. on Plasma Physics: Joint Conf. of 9th Kiev Int. Conf. on Plasma Theory; 9th Int. Conf. on Waves and Instabilities in Plasmas; 19th EPS Conf. on Controlled Fusion and Plasma Physics, Innsbruck, 29 June - 3 July 1992. 3 vols. EPS. 1994. p.11-819.
183. The effects of flow reversal on impurity behaviour in tokamaks.

- Stangeby P C Elder J D Reiter D  
Maddison G Contributions to Plasma Physics, vol.34  
no.2-3 1994 (4th Int. Workshop on Plasma Edge  
Theory in Fusion Devices, Varenna, 4-6 October  
1993) p.306.
184. Observation of fast wave ion current drive effects on  
sawteeth in JET.  
Start D Bhatnagar V Bosia G Brusati M Bures M  
Campbell D Cottrell G Cox M de Esch H Edwards  
A Eriksson L-G Gormezano C Jacquilot J Lomas  
P Marcus F O'Brien M R Porcell F Rimini F Stork  
D Tanga A Tubbing B Warrick C D Wesson J  
1992 Int. Conf. on Plasma Physics: Joint Conf. of 9th  
Kiev Int. Conf. on Plasma Theory; 9th Int. Conf. on  
Waves and Instabilities in Plasmas; 19th EPS Conf. on  
Controlled Fusion and Plasma Physics, Innsbruck, 29  
June - 3 July 1992. 3 vols. EPS. 1994. p.II-897.
185. High beta studies in the H-mode and hot ion H-mode  
in JET.  
Stork D Alper B Ali-Arshad S De Blank H J de Esch  
H P L Edwards A Hender T C Konig R Kramer G  
Marcus F B Nave M F O'Brien D P O'Rourke J  
Smeulders P Stamp M Tibone F Tubbing B J D  
Zolfaghari A Zwingmann P W  
1992 Int. Conf. on Plasma Physics: Joint Conf. of 9th  
Kiev Int. Conf. on Plasma Theory; 9th Int. Conf. on  
Waves and Instabilities in Plasmas; 19th EPS Conf. on  
Controlled Fusion and Plasma Physics, Innsbruck, 29  
June - 3 July 1992. 3 vols. EPS. 1994. p.I-339.
186. The ion velocity (Bohm-Chodura) boundary condi-  
tion at the entrance to the magnetic pre-sheath in the  
presence of diamagnetic and ExB drifts in the  
scrape-off layer  
Strangeby P C Chankin A V  
Joint European Torus (JET), October 1994 20p.  
Preprint JET-P(94)51 Submitted for publication in  
Physics of Plasmas.
187. A note on the Bohm-Chodura plasma sheath  
criterion.  
Strangeby P C  
Joint European Torus (JET) November 1994 10p.  
Preprint JET-P(94)52 Submitted for publication in  
Physics of Plasmas.
188. Non-ambipolar neoclassical transport.  
Stringer T E Joint European Torus (JET). September  
1994. 6p.  
Preprint JET-P(94)38 Submitted to Nuclear Fusion
189. Energy confinement in high performance JET-  
D-T plasmas.  
Stubberfield P M Balet B Cordey J G O'Brien D P  
Thomsen K von Hellermann M  
1992 Int. Conf. on Plasma Physics: Joint Conf. of  
9th Kiev Int. Conf. on Plasma Theory; 9th Int.  
Conf. on Waves and Instabilities in Plasmas; 19th  
EPS Conf. on Controlled Fusion and Plasma Phys-  
ics, Innsbruck, 29 June - 3 July 1992. 3 vols. EPS.  
1994. p.I-63.
190. Global and local energy confinement properties of  
simple transport coefficients of the Bohm type.  
Taroni A and others  
Plasma Physics and Controlled Fusion, vol.36 no.10  
October 1994 pp.1629-1646.
191. Overview of high performance H-modes in JET.  
The JET Team presented by D Stork  
Joint European Torus (JET). February 1994. 24p.  
Preprint JET-P(94)09 Submitted for publication in  
Plasma Physics and Controlled Fusion (Proceedings  
of 4th IAEA TCM on H-mode Physics).
192. Improved tokamak concepts for JET and the future.  
Thomas P R and the JET Team  
Joint European Torus (JET), September 1994 p.12.  
Preprint JET-P(94)34 Submitted for publication in  
Plasma Physics and Controlled Fusion.
193. Steady state H-modes in JET.  
Thomas P R Campbell D J Gondhalekar A  
Lowry C J  
1992 Int. Conf. on Plasma Physics: Joint Conf. of 9th  
Kiev Int. Conf. on Plasma Theory; 9th Int. Conf. on  
Waves and Instabilities in Plasmas; 19th EPS Conf.  
on Controlled Fusion and Plasma Physics, Inns-  
bruck, 29 June - 3 July 1992. 3 vols. EPS. 1994. p.I-  
239.
194. Global and local confinement analysis of JET's VH-  
mode pulses.

- Thomsen K Balet B Campbell D J Challis C D Cordey J G Deliyannis N Ellis J J Greenfield C M Hawkes N Muir D G O'Brien D P Reichle R Stork D Stubberfield P Thomas P R JET Team Plasma Physics and Controlled Fusion, vol.36 no.7A July 1994 (Papers from 4th H-Mode Workshop (IAEA Technical Committee Meeting on H-Mode Physics) Naka, Ibaraki, Japan, 15-17 November 1993) p.243. Preprint JET-P(93)101
195. An assessment of theoretical models based on observations in the JET tokamak. II: Heat transport due to electron drift waves, electromagnetic and resistive fluid turbulence, and magnetic islands. Tibone F Connor J W Stringer T E Wilson H R Plasma Physics and Controlled Fusion, vol.36 no.3 March 1994 p.473.
196. Dependence of confinement on plasma ion species in JET. Tibone F Balet B Bures M Cordey J G Jones T T C Lomas P J Lawson K D Morsi H W Nielsen P Start D F Tanga A Taroni A Thomsen K Ward D J 1992 Int. Conf. on Plasma Physics: Joint Conf. of 9th Kiev Int. Conf. on Plasma Theory; 9th Int. Conf. on Waves and Instabilities in Plasmas; 19th EPS Conf. on Controlled Fusion and Plasma Physics, Innsbruck, 29 June - 3 July 1992. 3 vols. EPS. 1994. p.I-19.
197. The new phase of JET and prospects for future operation. Tubbing B J D and JET Team Bulletin of the American Physical Society, vol.39 no.7 November 1994 (Abstracts of the Thirty-Sixth Annual Meeting of the Division of Plasma Physics, 7-11 November 1994, Minneapolis). p.1516.
198. Geometry free of singularities for fusion duplex components. Viola R Deksnis E B Joint European Torus (JET), November 1994 18p. Preprint JET-P(94)54 Submitted for publication in Fusion Technology and Design.
199. Analytical approximation of cross-section effects on charge exchange spectra observed in hot fusion plasmas. von Hellermann M Breger P Frieling J Konig R Mandl W Maas A Summers H P Joint European Torus (JET). April 1994. 36p. Preprint JET-P(94)20 Submitted to Plasma Physics and Controlled Fusion
200. Investigation of alpha particle slowing-down features in helium neutral beam fuelling experiments at JET. von Hellermann M Core W G F Frieling J Horton L D Konig R Mandl W Summers H P Wolle B 1992 Int. Conf. on Plasma Physics: Joint Conf. of 9th Kiev Int. Conf. on Plasma Theory; 9th Int. Conf. on Waves and Instabilities in Plasmas; 19th EPS Conf. on Controlled Fusion and Plasma Physics, Innsbruck, 29 June - 3 July 1992. 3 vols. EPS. 1994. p.II-1035.
201. Quantitative spectroscopy for fusion plasmas. von Hellermann M G Joint European Torus (JET). February 1994. 17p. Preprint JET-P(94)08 Submitted for publication in 'Contributions to High Temperature Plasma Physics' Editors: KH Spatschek, J Uhlenbusch, Akademie Verlag, Berlin.
202. Progress in spectroscopic plasma diagnostics and atomic data Von Hellermann M and others Joint European torus (JET), November 1994 10p. Report JET-P(94)58 Preprint of a invited paper presented to ICPP 1994, Iguacu, Brazil, 1994
203. Development of the JET ICRH plant. Wade T J Jacquinot J Bosia G Sibley A Schmid M Fusion Engineering and Design, vol.24 nos.1&2 February 1994 pp.23-46.
204. Sawteeth and transport in tokamaks. Ward D J Plasma Physics and Controlled Fusion, vol.36, no.4, April 1994 p.673.
205. Transitions in tokamak edge confinement. Ward D J Nuclear Fusion, vol.34 no.8 August 1994 p.1169.
206. Energy exhaust through neutrals in a tokamak divertor.

- Watkins M L Rebut P-H  
1992 Int. Conf. on Plasma Physics: Joint Conf. of 9th Kiev Int. Conf. on Plasma Theory; 9th Int. Conf. on Waves and Instabilities in Plasmas; 19th EPS Conf. on Controlled Fusion and Plasma Physics, Innsbruck, 29 June - 3 July 1992. 3 vols. EPS. 1994. p.II-731.
207. JET divertor research in support of ITER  
Watkins M L  
Preprint JET-P(94)47
208. Numerical simulation of hydrogenic atomic losses in a divertor plasma.  
Weber S Simonini R Taroni A  
Contributions to Plasma Physics, vol.34 no.2-3 1994 (4th Int. Workshop on Plasma Edge Theory in Fusion Devices, Varenna, 4-6 October 1993) p.374.
209. Motional stark effect measurements of the local ICRH induced diamagnetism in JET plasmas.  
Wolf R C Eriksson L G von Hellermann M Konig R Mandl W Porcelli F  
Nuclear Fusion, vol.33 no.12 December 1993 p.1835. Preprint JET-P(93)24
210. The-dependent neutron rate interpretation for deuterium injection into deuterium plasmas.  
Wolle B Eriksson L-G Hubner K Morgan P D Sadler G Tsintsadze L N von Hellermann M G  
1992 Int. Conf. on Plasma Physics: Joint Conf. of 9th Kiev Int. Conf. on Plasma Theory; 9th Int. Conf. on Waves and Instabilities in Plasmas; 19th EPS Conf. on Controlled Fusion and Plasma Physics, Innsbruck, 29 June - 3 July 1992. 3 vols. EPS. 1994. p.II-1485.
211. Time-dependent neutron-rate interpretation for neutral-beam-heated tokamak plasmas.  
Wolle B Eriksson L-G Gerstel U Sadler G  
Plasma Physics and Controlled Fusion, vol.36 no.6 June 1994 pp.1051-1074.
212. First measurements of fast MHD fluctuations in JET by ECE correlation radiometry.
- Zolfaghari A Bartlett D V Costley A E Crippwell P Jones S E Kasner J Luckhardt S C Porte L Ramos J J Smith R J Woskov P P  
1992 Int. Conf. on Plasma Physics: Joint Conf. of 9th Kiev Int. Conf. on Plasma Theory; 9th Int. Conf. on Waves and Instabilities in Plasmas; 19th EPS Conf. on Controlled Fusion and Plasma Physics, Innsbruck, 29 June - 3 July 1992. 3 vols. EPS. 1994. p.I-407.
213. JET papers presented to 21st EPS Conf. on Controlled Fusion and Plasma Physics, Montpellier, France, 27 June - 1 July 1994.  
Joint European Torus (JET). July 1994. 240p. Preprint JET-P(94)29
214. JET papers presented to 18th Symp. on Fusion Technology (SOFT-18), Karlsruhe, Germany, 22-26 August 1994.  
Joint European Torus (JET). September 1994. 180p. Preprint JET-P(94)40
215. JET papers presented at the 15th IAEA conference on plasma physics and controlled nuclear fusion research.  
Joint European Torus (JET) October 1994. 148p. Preprint JET-P(94)48 To be published in the Proceedings of 15th IAEA Conference, Seville, Spain, 26 September-1 October 1994
216. Papers presented to 11th Int. Conf. on Plasma Surface Interactions in Controlled Fusion Devices (11th PSI), Mito-shi, Japan, 23-27 May 1994.  
Joint European Torus (JET). July 1994. 169p. Preprint JET-P(94)28
217. JET Annual Report 1993.  
JET Joint Undertaking 1994. Edited and compiled by B.E.Keen and G.W.O'Hara. 129p. EUR 15723-EN-C (EUR-JET-AR16).
218. JET Progress Report 1993.  
JET Joint Undertaking 1994. Edited and compiled by B.E.Keen. 188p. EUR 15722-EN-C (EUR-JET-PR11).









